NANOSTRUCTURES: PHYSICS AND TECHNOLOGY

16th International Symposium

Vladivostok, Russia, July 14–18, 2008

Co-Chairs
Zh. Alferov
L. Esaki

PROCEEDINGS

Vladivostok, 2008

Published by
Ioffe Physico-Technical Institute
26 Politekhnicheskaya, St Petersburg 194021, Russia
http://www.ioffe.ru/

Publishing license ΛP No 040971 of June 16, 1999.

ISBN 978-5-93634-024-4

The International Symposium "Nanostructures: Physics and Technology" is held annually since 1993. The first Symposium was initiated by Prof. Zh. Alferov and Prof. L. Esaki who are its permanent co-chairs. More detailed information on the Symposium is presented on the World Wide Web **http://ntc.dvo.ru/nano2008/**

The Proceedings include extended abstracts of invited talks and contributed papers to be presented at the Symposium. By tradition this book is published before the beginning of the meeting.

The volume was composed at the Information Services and Publishing Department of St Petersburg Physics and Technology Center for Research and Education from electronic files submitted by the authors. When necessary these files were converted into the Symposium style without any text revisions. Only minor technical corrections were made by the composers.

Design and layout: N. Vsesvetskii
Desk editors: E. Solovyova and E. Savostyanova

Information Services and Publishing Department
St Petersburg Physics and Technology Center for Research and Education of RAS
8, bld. 3 Khlopina, St Petersburg 195220, Russia
Phones: (812) 534-58-58
Fax: (812) 534-58-50
E-mail: nano@mail.ioffe.ru

Printed in Russian Federation

The Symposium is held under the auspices of
the Russian Academy of Sciences

Organizers

Institute of Automation and Control Processes of Far Eastern Branch of the RAS
Scientific Engineering Center for Microelectronics at the Ioffe Institute
St Petersburg Physics and Technology Center for Research and Education of RAS
Ioffe Physico-Technical Institute

in association with

Division of Physical Sciences of the Russian Academy of Sciences
Far Eastern Branch of the Russian Academy of Sciences
St Petersburg Scientific Center of the Russian Academy of Sciences
Ministry of Education and Science of the Russian Federation

Acknowledgments

The Organizers gratefully acknowledge the following
for their contribution to the success of the Symposium:

Russian Academy of Sciences
Russian Foundation for Basic Research
Ministry of Education and Sciences of Russian Federation
Administration of Primorsky Region of the Russian Federation
AIXTRON AG, Germany
State Unitary Scientific-industry enterprise "Inject", Russia
Carl Zeiss, Germany
NT MDT, Russia
SPECS GmbH, Germany

Location and Date

Symposium is held in Vladivostok, July 14–18, 2008.

Advisory Committee

G. Abstreiter (*Germany*)
Zh. Alferov (*Russia*)
Y. Arakawa (*Japan*)
A. Aseev (*Russia*)
G. Bastard (*France*)
D. Bimberg (*Germany*)
L. Eaves (*United Kingdom*)
L. Esaki (*Japan*)
S. Gaponov (*Russia*)
E. Gornik (*Austria*)
Yu. Gulyaev (*Russia*)
N. Holonyak Jr. (*USA*)
L. Keldysh (*Russia*)
G. Landwehr (*Germany*)
J. Merz (*USA*)
M. Shur (*USA*)
M. Skolnick (*United Kingdom*)
R. Suris (*Russia*)

Programme Committee

R. Suris, Chair (*St Petersburg, Russia*)
V. Evtikhiev, Secretary (*St Petersburg, Russia*)
A. Andronov (*Nizhny Novgorod, Russia*)
N. Bert (*St Petersburg, Russia*)
C. Chang-Hasnain (*Berkeley, USA*)
A. Chaplik (*Novosibirsk, Russia*)
V. Dneprovskii (*Moscow, Russia*)
V. Dubrovskii (*St Petersburg, Russia*)
A. Gippius (*Moscow, Russia*)
S. Gurevich (*St Petersburg, Russia*)
S. Ivanov (*St Petersburg, Russia*)
P. Kop'ev (*St Petersburg, Russia*)
Z. Krasil'nik (*Nizhny Novgorod, Russia*)
V. Kulakovskii (*Chernogolovka, Russia*)
M. Kupriyanov (*Moscow, Russia*)
X. Marie (*Toulouse, France*)
I. Merkulov (*St Petersburg, Russia*)
V. Panov (*Moscow, Russia*)
O. Pchelyakov (*Novosibirsk, Russia*)
E. Poltoratskii (*Moscow, Russia*)
H. Sakaki (*Tokyo, Japan*)
N. Sibel'din (*Moscow, Russia*)
M. Stutzmann (*Garching, Germany*)
V. Timofeev (*Chernogolovka, Russia*)
V. Volkov (*Moscow, Russia*)
L. Vorobjev (*St Petersburg, Russia*)

Organizing Committee

Yu. Kulchin, Co-Chair (*Institute of Automation and Control Processes FEB RAS*)
S. Dar'kin, Co-Chair (*Administration of Primorsky Region of the Russia*)
N. Galkin, Secretary (*Institute of Automation and Control Processes FEB RAS*)
A. Dyshljuk (*Institute of Automation and Control Processes FEB RAS*)
K. Ignatovich (*Institute of Automation and Control Processes FEB RAS*)
A. Konoshenko (*Financial-economic department of the Russian Academy of Sciences*)
V. Kurilov (*Far Eastern National University*)
M. Mizerov (*Center for Microelectronics*)
S. Nikiforova (*Institute of Automation and Control Processes FEB RAS*)
A. Saranin (*Institute of Automation and Control Processes FEB RAS*)
N. Sibeldin (*Lebedev Physical Institute of RAS*)
E. Solovyova (*St Petersburg Physics and Technology Center for Research and Education of RAS*)
S. Voznesensky (*Institute of Automation and Control Processes FEB RAS*)
V. Zayats (*Division of Physical Sciences of RAS*)
A. Zotov (*Institute of Automation and Control Processes FEB RAS*)

Award Committee

Zh. Alferov, Chair (*Russia*)
A. Aseev (*Russia*)
M. Heuken (*Germany*)
J. Johansson (em Sweden)
A. Kovsh (*Russia*)
Z. Krasil'nik (*Russia*)
Yu. Kulchin (*Russia*)
X. Ren (*China*)
R. Suris (*Russia*)
S. Tarucha (*Japan*)
A. Yoshikawa (*Japan*)

Contents

Nanostructures and Life Science

Metal Nanostructures

Tunneling Phenomena

Nanostructure Characterization

Nanostructure Characterization — Silicides

Nanostructure Devices

Nanostructure Technology — Epitaxy

Nanostructure Technology — Surface Controlled Nanostructure Formation

Quantum Wells and Quantum Dots

Spin Related Phenomena in Nanostructures

Transport in Nanostructures

Microcavity and Photonic Crystals

Nitride Nanostructures

Closing Plenary Session

Unprinted Papers

The papers listed below are included in the Symposium Programme, but not printed in the Proceedings, as the authors had not submitted electronic files in due time.

OPS.01pl *S. Tarucha*
Electron manipulation of electron and nuclear spins in quantum dots
SCNF.13p *S. Arzhannikova*
Nucleation and crystallization in a-Si:H films during femtosecond laser irradiation
QW/QD.11p *V. Mikhajlov*
Temperature and particle number oscillations of the electron canonical heat capacity
TN.06p *L. Magarill*
Photocurrent and photovoltage in curved 1D systems
CPS.02pl *Ian Appelbaum*
Silicon Spintronics
CPS.03pl *V. I. Konov*
Single wall carbon nanotubes — a new photonic material

AIXTRON Young Scientist Award

In 1999, the Symposium Programme Committee and the Board of AIXTRON AG (Germany) established a special award to honour a young scientist who will present at the Symposium the best paper in the field of solid state nanostructures. The award comprises a diploma and since 2004 a $1000 reward sponsored by AIXTRON.

The AIXTRON Young Scientist Award recipients are:

1999 **Alexey R. Kovsh**, Ioffe Institute, St Petersburg, Russia
2000 **Thomas Gruber**, Physikalisches Institut, Universität Würzburg, Würzburg, Germany
2001 **Ivan Shorubalko**, Department of Solid State Physics, Lund University, Lund, Sweden
2002 **Scott Kennedy**, Department of Electrical and Computer Engineering, University of Alberta, Edmonton, Canada
2003 **Sergey A. Tarasenko**, Ioffe Institute, St Petersburg, Russia
2004 **Ivan A. Dmitriev**, Ioffe Institute, St Petersburg, Russia
2005 **Matthias Kuntz**, Institut für Festkörperphysik, Technische Universität Berlin, Germany
2006 **Dmitry S. Sizov**, Ioffe Institute, St Petersburg, Russia
2007 **Sassine Sami**, GHMFL, CNRS, Grenoble, France

Dr. S. Sassine
became the recipient of AIXTRON Award for the presentation of the paper:

"Ratchet" effect in Galton-board-like 2DES with broken spatial inversion symmetry

Co-author: *U. Krupko, Z. D. Kvon, V. T. Renard, J.-C. Portal, R. Murali, K. P. Martin, G. Hill and A. D. Wieck.*

PROCEEDINGS

16th Int. Symp. "Nanostructures: Physics and Technology"
Vladivostok, Russia, July 14–18, 2008

Nanostructured matrix sorption materials — promising media for low-energy nanotechnology and ecology

V. I. Sergienko and V. A. Avramenko
Institute of Chemistry, Far East Branch, Russian Academy of Sciences, Vladivostok, Russia

Abstract. Prospects of development of nanosrtuctured sorption materials are discussed. A principal scheme of these materials synthesis from xerogels is presented. The efficiency of new materials for liquid radioactive waste is shown. The focus was made on the materials stability and substantial reduction of the formed solid waste to be sent for final disposal.

Among the functional materials widely used during development of prospective technologies of aqueous and organic-aqueous solutions decontamination from heavy metals and radionuclides, inorganic sorbents tend to continuously find more extensive application. It was demonstrated by numerous studies that monocrystalline sorbents appeared to be the most prospective in this regard from the practical point of view. Reduction of the monocrystal size results in substantial improvement of the sorbents performance parameters and, at the same time, is accompanied by temporary decrease of their properties stability over time and significant dependence on the method and degree of the initial material crushing. An ideal solution for such a problem can be transition to nanosize sorbents stabilized by a specific method.

Nanosize crystalline sorbents in which nanosize crystals are stabilized by some method have sorption properties differing from those of macrocrystalline selective sorbents. Obtaining stabilized nanosize particles of selective sorbents is a prospective direction that enables one to improve significantly their selectivity and produce principally new sorption materials. The report discusses some theoretical and experimental aspects of synthesis of nanosize sorption materials as well as the results of nanosize sorbents application in liquid radioactive waste (LRW) management practice.

Stabilization of nanosize particles of sorption materials can be performed whether by porous matrix of xerogel or by cross-linked organic polymer gel as well as by fixation of nanosize particles on carbon fibers of micron and sub-micron diameter by different methods.

One of the ways to obtain nanosize sorption structures can be synthesis of ion-exchange xerogels with using the sol-gel technology (sols of silicon, titanium, zirconium and aluminum hydroxides can be taken as precursors) and performing the process directly in the xerogel matrix pores [1]. The principle of producing ion-exchange xerogels from a sol coagulated by ions of polyvalent metals is shown in Fig. 1.

Formation of insoluble precipitate of a selective sorbent can proceed in two ways — inside the xerogel porous space or on the outer surface of the xerogel particles, as shown in Fig. 2

The xerogel pores have usually the size from 1 up to 20 nm. The critical diameter of the xerogel pore in which the formation of a nanoparticle is possible is determined from the condition of heterogeneous equilibrium of a binary low-soluble substance AB:

$$\Delta G = nRT \ln \frac{c_{\mathrm{A}}^* c_{\mathrm{B}}^*}{\Pi \mathrm{P}_{\mathrm{AB}}} - 4\pi\sigma_{mr} r^2, \qquad (1)$$

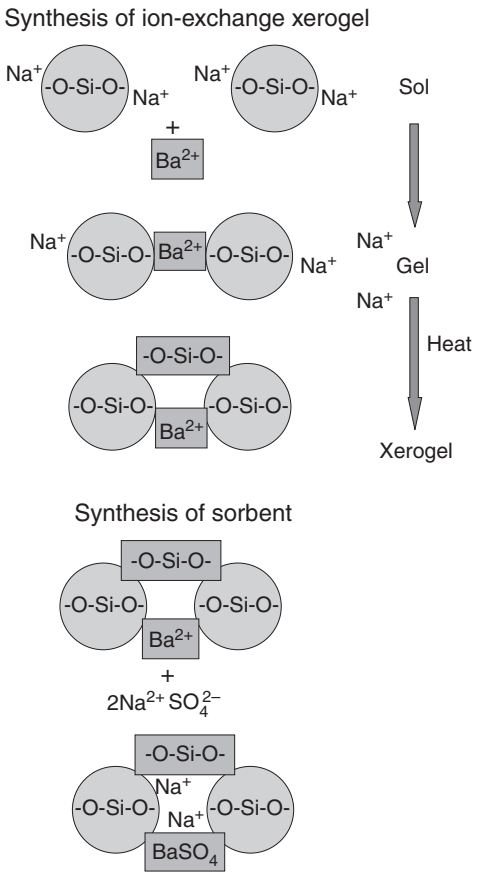

Fig. 1. Scheme of synthesis of ion-exchange of xerogels and sorbents on their basis: (upper part) synthesis of ion-exchange xerogel-sol-gel-(heat)-xerogel, (lower part) synthesis of sorbent.

while the minimum radius of a particle at given degree of saturation λ is determined as:

$$r_v = \frac{2\sigma_{mr} M}{\rho RT \ln \lambda_{\mathrm{AB}}}. \qquad (2)$$

It is evident that the process of precipitate formation in a porous particle has, aside from thermodynamic limitations, kinetic limitations related to the substances diffusion from solution through the boundary layer.

In the course of the study, theoretical aspects of synthesis of nanosize particles of crystalline sorbents in a porous medium were discussed. Thermodynamic conditions of the formation of an insoluble compound inside a porous particle and on its outer surface were determined. A theoretical model was developed for growth of nanosize particles in a porous medium.

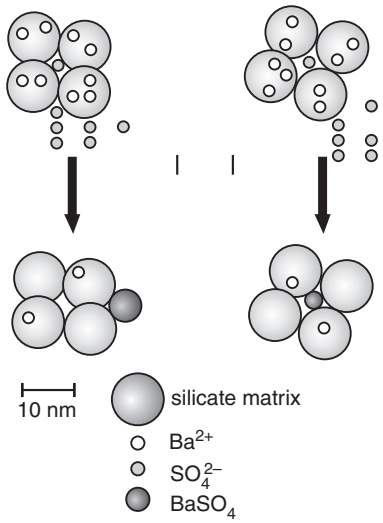

Fig. 2. Different directions of synthesis of sorbents on the basis of porous matrices: (top to bottom) — silicate matrix, barium sulfate, barium ions, sulfate ions (10 nm).

Extensive studies were devoted to growth of nanoparticles and xerogel matrix destruction over time as well as to changes in sorption and ion-exchange properties of a system related to the process. The methods of synthesis of composite matrices of xerogels blocking the destruction of matrix and growth of particles of crystalline sorbents and nanosorbents on their basis were developed.

The results of experimental studies of synthesis of nanosize sorbents on the basis of porous xerogels of silicon, titanium and zirconium are presented. The synthesized selective sorbents for radionuclides of cesium and strontium on the basis of nanosize ferrocyanides of transition metals and barium sulfate, respectively, are described. Another class of sythesized sorption materials comprises nanosize sorbents on the basis of insoluble dithiocarbamates stabilized by cross-linked gels of chitosan that are selective to extremely stable complexes of cobalt radionuclides with ethylenediaminetetraaacetic acid. The efficiency of nanosize sorbents on the basis of insoluble dithiocarbamates is shown in Figs. 3, 4.

Fig. 2 shows that the synthesis conditions completely determine the structure of the sorbents formed. For example, increase of the synthesis pH results in formation of macrocrystals of insoluble dithiocarbamates. At the same time, by using relatively low pH values, one is capable to obtain nanosize particles of dithiocarbamates. From the results of studies of the sorption capacity of composite sorbents, one can see that the size of crystals formed determines to a great extent the sorption properties (Fig. 4).

The tests were performed for the most prospective composite nanosorbents in view of their applicability for decontamination of liquid radioactive waste from long-lived radionculides. The methods of production of nanosize selective sorbents stabilized by active carbon fibers were discussed, and the results of studies of their structure and sorption properties are presented. The report also focuses on chemical and electrochemical methods of production and fixation of nanosize crystalline ferrocyanides of metals and manganese oxides selective to radionuclides of cesium and strontium, respectively.

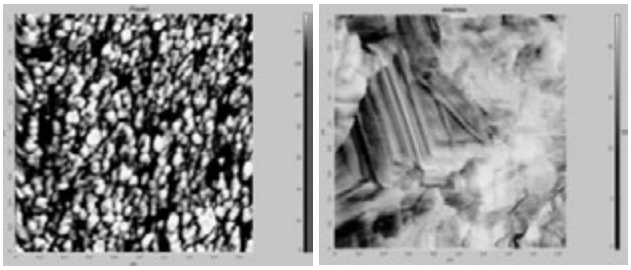

Fig. 3. AFM-images of the surface of sorbents on the basis of insoluble manganese dithiocarbamate stabilized by cross-linked chitosan gel: (left) nanosize crystals, sample 12, (right) microcrystals, sample 1.

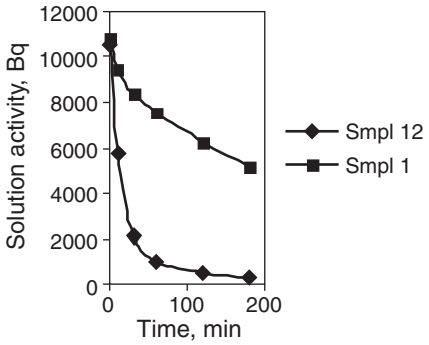

Fig. 4. Sorption of cobalt radionulcides by different samples of dithiocarbamate sorbents.

Application of the methods of scanning electron microscopy (SEM) and X-ray phase analysis have demonstrated the difference in composition, structure and morphology of manganese oxides precipitated on the surface of carbon fiber (CF) under chemical and electrochemical modification conditions. During chemical precipitation one can observe the presence of two phases on the fiber surface: both of them belong to the type of K-burnessite represented by two compounds ($K_{0.46}Mn_{1.54}Mn_{0.46}O_4(H_2O)_{1.4}$ and $K_{0.5}Mn_2O_{4.3}(H_2O)_{0.5}$) having the exchangeable potassium ion. Burnessite represents layered compounds of manganese oxides. Besides, the phase of α-Mn, which formation is possible due to reduction of manganese salts on the CF surface, is also present. During manganese oxides precipitation by means of electrochemical method one can observe on the CF surface the phase of manganese oxide with slight deficit of oxygen ($MnO_2/Mn_{1.937}$) and precipitation of synthetic ramsdellite MnO_2 belonging to the group of minerals with a tunnel-like structure.

A method was also developed to produce nanosize ferrocyanide sorbents stabilized by carbon fibers that is concerned with modification of the CF surface by means of doping with metal-containing organic compounds followed by their thermal destruction. The chemical form of metals on the carbon fiber surface depends insignificantly on the type of organic compound used for doping while a great role is played by the thermal destruction conditions. The stability of ferrocyanide fixation depends on the thermal destruction temperature and the type of organic compound. The suggested method of modification of CF surface enables one to obtain ferrocyanide sorbents with a stable fixation of ferrocyanides independently of the type of active CF. The sorption properties of the obtained ferrocyanide sorbents were studied, and prospects of their application in high-salinity liquid radioactive waste (LRW) de-

contamination from cesium radionuclides were demonstrated.

The examples were given for application of selective nanosize sorbents for decontamination of LRW at different nuclear power facilities. For example, during management of radioactive waste formed at operation and dismantlement of nuclear submarines, application of nanosize sorbents stabilized by silica gels (sorbents SNi and SRM) developed in the Institute of Chemistry FEBRAS enabled us to substantially reduce the volume of solid radioactive waste sent for final disposal.

References

[1] V. A. Avramenko *et al*, *IAEA TECDOC-1336* (2003).

16th Int. Symp. "Nanostructures: Physics and Technology"
Vladivostok, Russia, July 14–18, 2008

Far infrared and terahertz devices based on graphene heterostructures

V. Ryzhii[1,4], M. Ryzhii[1,4], N. Ryabova[1,4], V. Mitin[1,2] and T. Otsuji[3,4]

[1] Computational Nanoelectronics Laboratory, University of Aizu, Aizu-Wakamatsu 965-8580, Japan
[2] Department of Electrical Engineering, University at Buffalo, Buffalo, NY 14260-1920, USA
[3] Research Institute Electric Communication, Tohoku University, Sendai 980-8577, Japan
[4] Japan Science and Technology Agency, CREST, Tokyo 107-0075, Japan

Abstract. We overview some novel concepts of far infrared (FIR) and terahertz (THz) devices based on graphene heterostructures — graphene FIR/THz laser and phototransistor. The device operation priciples are considered. Using the developed models, we evaluate the characteristics of these devices.

Introduction

The demonstration of exceptional electronic properties of graphene, i.e., a monolayer of carbon atoms forming a dense honeycomb two-dimensional structure [1,2,3], has led to a surge of experimental and theoretical publications. This, in particular, is due to the potential of the graphene-based heterostructure in developing of novel electronic and optoelectronic devices. A linear dispersion relations the for electron and hole energy spectra with zero energy band gap provides nontrivial features of graphene and graphene-based heterostructures in far infrared (FIR) and terahertz (THz) spectral ranges. The utilization of the patterned graphene, the arrays of the so-called graphene nanoribbons (GNRs), opens up additional new opportunities for the band engineering by varying the width or shape of GNRs (by lithography, nanoscratching, and so on). In this paper, we consider two concepts which can result in creation of novel FIR/THz devices.

1. Population inversion and FIR/THz lasing in optically pumped graphene

We consider a graphene-based heterostructure (see Fig. 1a) illuminated by light with the photon energy $\hbar\Omega$, where $\hbar$ is the reduced Planck constant and Ω is the photon frequency [4]. The illumination results in the photogeneration in graphene of electrons and holes with kinetic energy $\varepsilon_0 = \hbar\Omega/2$. Due to a very short time of the optical phonon emission τ_0, the photogeneration of electrons and holes leads to the emission of a cascade of optical phonons, so that the photogenerated electrons and holes occupy the states with the energies close to $\varepsilon_N = \hbar(\Omega/2 - N\omega_0)$. Here $\hbar\omega_0$ is the optical phonon energy and N is the number of emitted optical phonons ($N \le N_m$, where N_m is determined by the integer part of $\Omega/2\omega_0$). When $\varepsilon_{N_m} = \hbar(\Omega/2 - N_m\omega_0) \simeq 0$, the photogenerated electrons and holes after the cascade emission of optical phonons are concentrated near the bottom of the graphene conduction band and the top of the graphene valence band, respectively. In this case, the energy distribution of electrons and holes corresponds to that shown schematically in Fig. 1b.

Taking into account that in graphene $\hbar\omega_0 \simeq 0.2$ eV, when it is illuminated by a semiconductor laser with the photon energy $\hbar\Omega = 0.8$ eV, one obtains $N_m = 2$.

The calculation of the interband and intraband (Drude) contributions (generalizing the results of Ref. [5] for nonequilibrium electron-hole system) leads to the following formula for the net dynamic ac conductivity [4]:

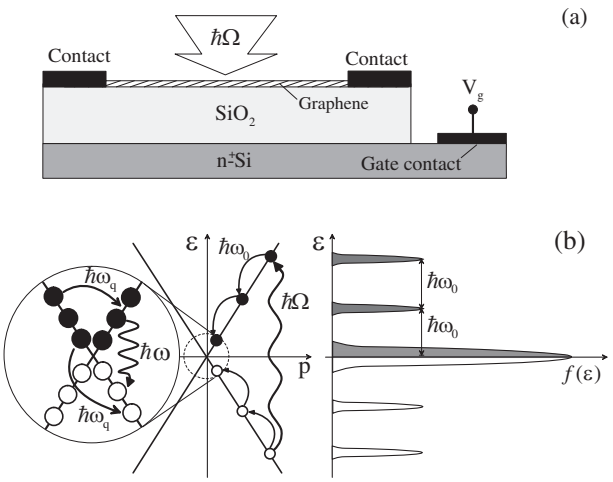

Fig. 1. Schematic view of graphene heterostructure under optical pumping (a) and its band diagram as well as distribution function (b) with different electron transitions showed by arrows (generation of electrons and holes by optical photon with energy $\hbar\Omega$), relaxation due to emission of optical and acoustic phonons with energies $\hbar\omega_0$ and $\hbar\omega_q$, , and radiative recombination accompanied by emission of photon with energy $\hbar\omega$.

$$\mathrm{Re}\,\sigma_\omega \simeq \frac{e^2\overline{g}}{8\hbar}\left[1 + \frac{3}{2}\left(\frac{\omega - \overline{\omega}}{\overline{\omega}}\right)^2 - \frac{I_\Omega}{\overline{I_\Omega}}\right]. \qquad (1)$$

Here, I_Ω is the intesity of optical pumping,

$$\overline{I_\Omega} = \frac{(4\ln 2/\pi)^{1/3}}{12\alpha}\left(\frac{k_B T}{\hbar v}\right)^2 \xi^{1/3}\frac{\hbar\Omega}{\tau_R} \qquad (2)$$

is the threshold intensity of optical radiation,

$$\overline{g} = \left(\frac{4\ln 2\,\xi}{\pi}\right)^{1/3}, \qquad \overline{\omega} = \left(\frac{32\ln 2}{\pi\,\xi^2}\right)^{1/3}\frac{1}{\tau},$$

e is the electron charge, τ is the momentum relaxation time, τ_R is the nonradiative recombination time, $v \simeq 10^8$ cm/s is the characteristic velocity of electrons and holes in graphene, e is the electron charge, $\alpha \simeq 1/137$, T is the temperature, k_B is the Boltzmann constant, and $\xi = (\hbar/k_B T\tau)$. As follows from

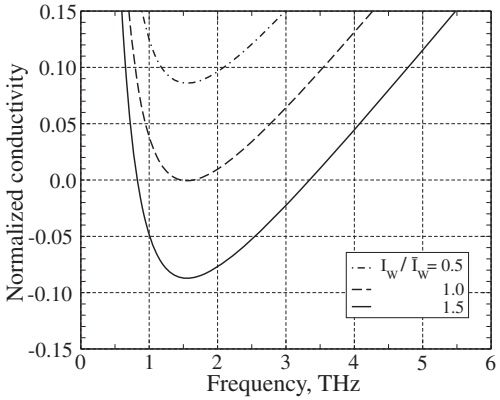

Fig. 2. Normalized dynamic ac conductivity versus frequency for different intensities of optical excitation.

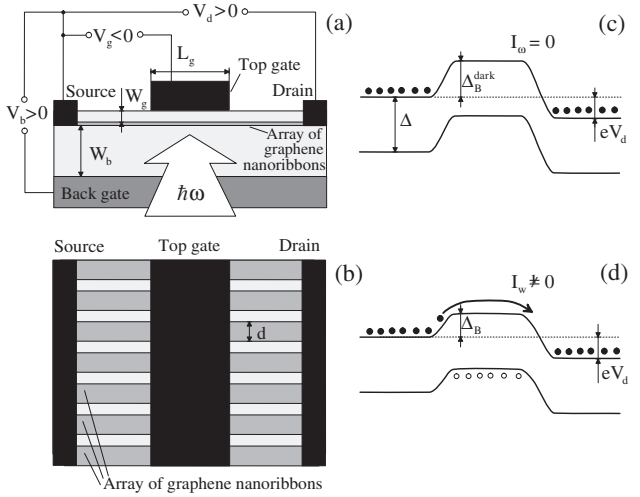

Fig. 3. GNR-phototransistor (GNR-PT) structure side (a) and top (b) schematic views as well as the device band diagrams under dark condition (c) and under irradiation (d). Circles correspond to electrons (•) and holes (○).

Eq. (1), $\mathrm{Re}\,\sigma_\omega = 0$ at

$$\omega = \omega_\mp = \overline{\omega}\left(1 \mp \sqrt{\frac{2}{3}}\sqrt{\frac{I_\Omega}{\overline{I_\Omega}} - 1}\right), \qquad (3)$$

so that $\mathrm{Re}\,\sigma_\omega < 0$ in the frequency range $\omega_- < \omega < \omega_+$.

At $T = 77$ K, $\tau = 1 \times 10^{-12}$ s, $\hbar\Omega \simeq 0.8$ eV ($\hbar\Omega = 4\hbar\omega_0$, where the optical pnonon energy in graphene is assumed to be $\hbar\omega_0 = 0.2$ eV,), and $\tau_\mathrm{R} = 10^{-7} - 10^{-9}$ s, we obtain $\overline{\omega} \simeq 1.5$ THz, $\overline{g} \simeq 0.4$ and $\overline{I_\Omega} \simeq 0.07 \times (1 - 100)$ W/cm^2. If $\tau = 3 \times 10^{-12}$ s and the same as above other parameters, $\overline{\omega} \simeq 1$ THz, $\overline{g} \simeq 0.3$ and $\overline{I_\Omega} \simeq (0.05 - 5)$ W/cm^2. Figure 2 shows the frequency dependence of the ac conductivity normalized by the characteristic conductivity $e^2/2\hbar$ at different intensities of optical radiation. As follows from Eq. (1) and can be seen from Fig. 2, the range of frequencies in which $\mathrm{Re}\,\sigma_\omega \leq 0$ widens when the intensity of incident optical radiation increases beyond its threshold value.

If the real part of dynamic ac conductivity is negative, the optically pumped graphene or GNR array can be used for generating of terahertz radiation. One option is associated with the utilization of the optically pumped graphene (GNR array) as an active region for a FIR/THz laser provided that the pertinent conditions for effective reflection of the generated photons are satisfied by proper design of the graphene heterostructure edges. Another option is associated with the self-excitation of THz plasma waves in graphene [5, 6]. This is because a two-dimensional electron-hole system, in particular in the graphene, can serve as a resonant plasma cavity [7]. The self-excitation of plasma waves due to the negative ac conductivity in the THz range followed by their conversion into electro-magnetic radiation can also be used in sources of THz radiation.

Varying the voltage, V_g, between the contacts to the graphene layer and the back gate (highly conducting substrate as shown in Fig. 1a), one can control the dark electron (hole) density, the dynamic ac conductivity $\mathrm{Re}\,\sigma_\omega \leq 0$, and, hence, the output FIR/THz radiation. Similar effect of negative dynamic conductivity in the FIR and THz ranges of frequencies can occur in the heterostructures with a patterned graphene layer (GNR array similar to that shown in Figs. 3a and 3b). Manipulating the density of state by a proper choice of the GNR width, one can optimize the spectral dependence of $\mathrm{Re}\,\sigma_\omega$ and the performance of the FIR/THz lasers based on the optically pumped graphene heterostructures.

2. Graphene nanoribbon phototransistor

The interband absorption in different graphene-based structures can be used in photodetectors for FIR/THz radiation. An example of the device structure of FIR/THz photodetector on the basis of a GNR array [8] is show in Figs. 3a and 3b. The structure of such a device is similar to the GNR field-effect transistor [9, 10, 11, 12] and can be called the GNR-phototransistor (GNR-PT). Its operation is associated with the control of the electron source-drain current by varying of the potential barrier (the phototransistor effect) by the charge of the holes photogenerated and accumulated in the the depleted region of the channel (beneath the central gate) as shown in Figs. 3c and 3d. The utilization of a GNR array with a bandgap Δ between the valence and conduction bands instead of a heterostructure with uniform graphene and $\Delta = 0$ is due the necessity to avoid the interband tunneling at the points in the channel near the edges of the top gate. Apart from this, the lateral quantization in GNRs and, hence, the appearance of the density of state maxima, promotes higher quantum efficiency and the photodetector performance.

The source-drain current along GNRs associated with the electrons propagating from the source to the drain and overcoming the barrier in the center section of the channel (beneath the top gate), can be presented in the following form:

$$J = e\Sigma_\mathrm{b} v_\mathrm{T} \exp\left(-\frac{\Delta_\mathrm{B}}{k_\mathrm{B}T}\right)\left[1 - \exp\left(-\frac{eV_\mathrm{d}}{k_\mathrm{B}T}\right)\right]. \qquad (4)$$

Here, $\Sigma_\mathrm{b} = (\varkappa V_\mathrm{b}/4\pi e W_\mathrm{b})$ is the electron density induced in the channel by the back gate voltage, $v_\mathrm{T} = v\sqrt{4k_\mathrm{B}T/\pi\Delta}$ is the electron thermal velocity [12], Δ_B is the height of the barrier in the central section of the channel (see Figs. 3c and 3d), and $\varkappa$ is the dielectric constant. Equation (4) is valid if $V_\mathrm{d} \ll V_\mathrm{b}$ (but ratio $eV_\mathrm{d}/k_\mathrm{B}T$ can be arbitrary). The quantity Δ_B are determined by the gate voltages V_b and V_g as well as by the electron and hole densities in the central section. The dependence of Δ_B

on the drain voltage V_d is weak under the conditions that V_d is not too large and the length of the top gate layer $L_g \gg W_b$, W_g. Here W_b and W_g are the thicknesses of the layers separating the GNR array from the back and top gates, respectively. Considering the balance between the photogeneration of holes and their escape from the depleted region of the channel, we obtain the following equation for the variation of the barrier height under irradiation:

$$\Delta_B - \Delta_B^{dark} \simeq -\frac{4\pi\, e^2 W}{\varkappa}\Sigma_g \simeq -\frac{4\pi\, e^2 L_g W}{\varkappa\, v_T}\frac{\exp(\Delta_B^{dark}/k_B T)}{[1+\exp(-eV_d k_B T)]}G_\omega, \quad (5)$$

where Σ_g is the density of photogenerated holes accumulated in the depleted region of the channel, $W = W_b W_g/(W_b + W_g)$, and G_ω is the rate of photogeneration of electrons and holes due to the interband absorption of incoming radiation. Calculating this rate taking into account the features the energy dependence of the density of states in the array of GNRs, one can arrive at the following equation for the GNR-PT responsivity:

$$R \simeq \left(\frac{W}{W_b}\right)\left(\frac{eV_b}{k_B T}\right)\left[\frac{1-\exp(-eV_d/k_B T)}{1+\exp(-eV_d/k_B T)}\right] \times \sum_{n=1}^{\infty}\frac{2\pi\, e\alpha\Delta\,\Theta(\hbar\omega - n\Delta)}{\hbar\omega\sqrt{\hbar^2\omega^2 - n^2\Delta^2}}. \quad (6)$$

Here, Δ is the energy gap between the valence and conductance bands associated with the lateral quantization in GNRs, $\hbar\omega$ is the energy of detected photons, and $n = 1, 2, 3, \ldots$. It is instructive that the GNR-PT responsivity is independent of Δ_B^{dark}. This is because the effective life-time of the photogenerated holes in the depleted section of the channel and, therefore, their density increase as $\exp(\Delta_B^{dark}/k_B T)$ (see Eq. (5)). Using Eq. (6) and setting $W \simeq W_b/2$ and $eV_d \gg k_B T$, the responsivity maximum (at $\hbar\omega \geq \Delta$) and its ratio to the responsivity minimum (at $\hbar\omega \leq 2\Delta$) can be estimated, respectively, as follows:

$$\max R \simeq \frac{e\beta}{2\sqrt{2\Gamma\Delta}}\left(\frac{eV_b}{k_B T}\right) \propto \Delta^{-1/2}T^{-1}, \quad (7)$$

$$\frac{\max R}{\min R} \simeq \sqrt{\frac{6\Delta}{\Gamma}}. \quad (8)$$

Assuming that $\Delta = 100$ meV, $\Gamma = 2$ meV, $V_b = 1 - 5$ V, and $T = 300$ K, we obtain max $R \sim 50 - 250$ A/W. Figure 4 shows the spectral dependences of the responsivity, R, of GNR-PTs with different energy gaps Δ (different width of GNRs) calculated using Eq. (6). It is assumed that $W/W_b = 0.5$, $V_b = 1$ V, $V_d = 0.05$ V, and $T = 300$ K.

The obtained values of the responsivity significantly exceed those for intersubband quantum-well, -wire, and -dot photodetectors for the IR and THz ranges. This is primarily due to higher quantum efficiency and higher photoelectric gain, which might be exhibited by GNR-PTs. The latter is associated with a long life-time of the photogenerated holes in the central section of the channel because these holes are confined in this section by relatively high barriers. The maximum responsivity of GNR-PTs can also exceed the responsivity of the customary photodetectors made of narrow gap semiconductors (for example, PbSnTe and CdHgTe), whose responsivity is about a few A/W, because the former can exhibit rather high quantum efficiency at the resonances $\hbar\omega = n\Delta$ arising due to the lateral quantization in GNRs.

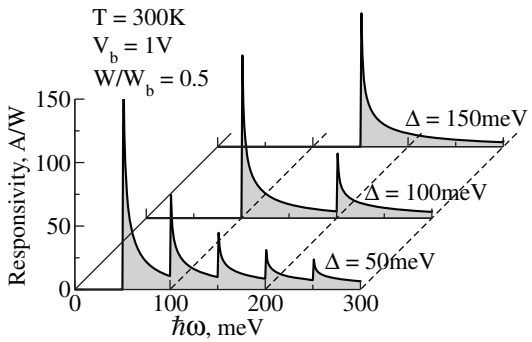

Fig. 4. Responsivity as a function of energy of incident photons for GNR-PTs with different band gaps.

Acknowledgements

This work was supported by the Japan Science and Technology Agency, CREST and by the Japan Society for Promotion of Science, Japan.

References

[1] C. Berger, Z. Song, T. Li, X. Li, A. Y. Ogbazhi, R. Feng, Z. Dai, A. N. Marchenkov, E. H. Conrad, P. N. First, and W. A. de Heer, *J. Phys. Chem.* **108**, 19912 (2004).

[2] K. S. Novoselov, A. K. Geim, S. V. Morozov, D. Jiang, M. I. Katsnelson, I. V. Grigorieva, S. V. Dubonos, and A. A. Firsov, *Nature* **438**, 197 (2005).

[3] A. K. Geim and K. S. Novoselov, *Nat. Mater.* **6**, 183 (2007).

[4] V. Ryzhii, M. Ryzhii and T. Otsuji, *J. Appl. Phys.* **101**, 083114 (2007).

[5] L. A. Falkovsky and A. A. Varlamov, *Europhys. J.* **56**, 281 (2007).

[6] V. Ryzhii, A. Satou, and T. Otsuji, *J. Appl. Phys.* **101**, 024509 (2007).

[7] M. Dyakonov amd M. Shur, *IEEE Trans. Electron. Devices* **43**, 1640 (1996).

[8] V. Ryzhii, V. Mitin, M. Ryzhii, N. Ryabova, and T. Otsuji, unpublished.

[9] B. Obradovich, R. Kotlyar, F. Heinz, P. Matagne, T. Rakshit, M. D. Giles, M. A. Stettler and D. E. Nikonov, *Appl. Phys. Lett.* **88**, 142102 (2006).

[10] B. Huard, J. A. Sulpizio, N. Stander, K. Todd, B. Yang, and D. Goldhaber-Gordon, *Phys. Rev. Lett.* **98**, 236803 (2007).

[11] G. Fiori and G. Iannaccone, *IEEE Electron Device Lett.* **28**, 760 (2007).

[12] V. Ryzhii, M. Ryzhii and T. Otsuji, unpublished.

16th Int. Symp. "Nanostructures: Physics and Technology"
Vladivostok, Russia, July 14–18, 2008

Millimeter wave dynamics of Josephson junctions with antiferromagnetic layer

Y. V. Kislinskii[1], I. V. Borisenko[1], K. Y. Constantinian[1], P. V. Komissinskiy[1,2], G. A. Ovsyannikov[1,2] and A. V. Shadrin[1]

[1] Institute of Radio Engineering and Electronics, RAS, Moscow, Russia
[2] Chalmers University of Technology, Gothenburg, Sweden

Abstract. Nb/Au/$(Ca_{1-x}Sr_x)CuO_2$/$YBa_2Cu_3O_{7-\delta}$ thin film structures, with antiferromagnetic $(Ca_{1-x}Sr_x)CuO_2$ layer were deposited by laser ablation and patterned by ion etching. Superconducting currents with density $j_C = 1$–100 A/cm^2 were measured at 4.2 K for the Josephson effect heterojunctions. Bottom electrode $YBa_2Cu_3O_{7-\delta}$ has d-wave symmetry of superconducting order parameter, that is likely cause appearance the second harmonic in current-phase relation. Our estimations for second harmonic were 10–40 percents of j_C.

Introduction

Unusuall properties of superconducting hybrid junctions with an interlayer comprising magnetic materials are of great interest for fundamental physical and electronic applications. Recently was predicted [1] an anomalously strong magnetic field dependence of superconducting current I_C in Josephson junction with an artificial multilayer antiferromagnetic (AF) barrier, offering an opportunity for manipulation by weak external magnetic field. The giant proximity effect: an anomalously large value of the superconducting current has been found in the cuprate structures with thick AF oxide inter-layers [2,3], but a question also exists whether the micro-shorts [4] may explain these observations. Recently heterojunctions Nb/Au/$Ca_{1-x}Sr_xCuO_2$/$YBa_2Cu_3O_7$ with antiferromagnetic interlayer ($Ca_{1-x}Sr_xCuO_2$) have been developed [5]. Our experimental results show that the superconducting current is increased in hetero junctions in comparison with Nb/Au/$YBa_2Cu_3O_7$ structures [6] without AF layer. It was found also that the critical current in structures with AF layer is very sensitive to external magnetic field as predicted in [1]. Josephson junctions driven far from equilibrium at microwave frequencies may demonstrate noticeable deviations of high frequency dynamical characteristics known for usual Josephson junctions. The deviation from sinusoidal superconducting current-phase relation (CPR) could be observed, e.g. in form: $I_S(\varphi) = I_{C1}\sin(\varphi) - I_{C2}\sin(2\varphi)$, where amplitudes I_{C1} and I_{C2} are the first and the second harmonics of superconducting current. Non-sin type of CPR yields in appearance of non-integer $I_{1/2}$ Shapiro steps and specific behavior of integer I_1, I_2 ones vs. applied microwave field. In this connection studies of high frequency dynamics in such structures become important for development of novel elements for quantum computer, the qubit, utilizing Josephson junctions with nonzero phase difference $0 < \varphi_0 < \pi/2$ in the background state [7,8]. For estimation of parameter $q = I_{C2}/I_{C1}$ in CPR a millimeter wave signal was applied to the heterojunctions and the Shapiro steps and detector responses were measured.

1. Experimental

Experimental structures were fabricated in square topology with sizes L, ranges from 10 to 50 μm. Epitaxial films of $YBa_2Cu_3O_7$ (YBaCuO) and $Ca_{1-x}Sr_xCuO_2$ (CaSrCuO) were grown by laser ablation on $NdGaO_3$ substrates. $Ca_{1-x}Sr_xCuO_2$ ($x = 0.15$ or 0.5) films were prepared with thickness $d = 20$–70 nm. The top electrode, log-periodic antenna, contact areas and wiring were made from Nb 200 nm, and 300 nm thick Au layers. The I–V curves were measured by four-probe method. The measurement system gives us possibility to record Shapiro steps down to 0.5 μA in height. Frequency range of microwaves was 40–120 GHz. Detector response dependences were measured by modulation — demodulation technique using lock-in amplifier with resolution of 2 nV/(Hz)$^{1/2}$.

2. Magnetic field dependencies of critical current

Dependencies of critical current versus the field $I_C(H)$ for junctions with $L = 10$–20 μm show deviation from usual ones for ordinary Josephson junctions with Fraunhofer pattern. The $I_C(H)$ dependences have oscillating periods about 20 times smaller, than the corresponding periods observed for Nb/Au/YBaCuO junctions with the same geometry, but without AF layer [9]. Qualitatively this can be explained by giant magnetic oscillations, which were predicted by theoretical model [1] where critical current depends on antiferromagnetic order parameter M_S, affected by an external magnetic field. By the model I_C oscillates with H increase:

$$I_C(H) \sim I_C(0)\,(2/\pi M_S\beta)^{-1/2}\,abs\cos(M_S\beta - \pi/4)\,.$$

Here $\beta = (t_0/T_C)(d/\xi_0)$, t_0 is amplitude of electron hopping parameter in the model, T_C — critical temperature of superconductor, ξ_0 — coherence length in superconductor. Formula was derived for thick antiferromagnetic: $d \gg \xi_0$. Decrease in periods of 2–3 times with increase of thickness d from 20 to 50 nm was observed experimentally. For example, the periods decrease from 50 to 20 μT, that was observed for junctions with fixed size $L = 20$ μm.

3. Current-phase relations of the junctions

If the CPR has I_{C2} term in addition to the first Shapiro step at voltage $V_1 = hf/2e$ the half integer one originating at $V_{1/2} = hf/4e$. The integer step amplitude I_1 depends on microwave power P according to [6]:

$$i_1(P) = 2\max_\Theta\,(J_1(x)\sin\Theta + q\,J_2(x)\sin 2\Theta)\,.$$

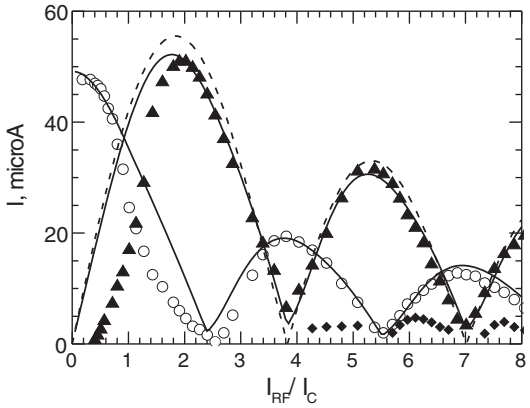

Fig. 1. Shapiro steps at $f = 56$ GHz, $\omega = 0.8$, I_C — circles, I_1 — triangles, and $I_{1/2}$ — rhombuses. Solid lines — fit by the model. Dashed line is J_1 approximation. The junction has $d = 50$ nm and $L = 10$ μm.

Here $i_1 = I_1(P)/I_C$ is normalized height of the first step, J_1 and J_2 are the first and second order Bessel function, $x = (I_{RF}/Ic)/\left(\omega(\omega^2\beta_C^2+1)^{1/2}\right)$ — normalized microwave amplitude, $\omega = 2eI_CR_N/hf$ — normalized frequency, R_N — normal resistance, β_C — McCumber parameter: $4\pi eI_CR_N^2C$, C — capacitance of the junction. Θ is the phase difference between external signal with frequency f and the self Josephson generation. The minima of $i_1(P)$ become non-zero, caused by the second harmonic in the CPR. Critical current is:

$$i_0(P) = \max_\Theta \left(J_0(x)\sin\Theta + q\,J_0(2x)\sin 2\Theta\right),$$

that gives nonzero minima, caused by the second harmonic. Model was derived in high frequency limit $\omega \gg 1$ [6]. Experimental data demonstrate good agreement with this model: see Fig. 1. For data shown on Fig. 1 we obtain the second harmonic term $q \approx -0.2$. Half integer steps should be observed according to the model. At high frequencies $\omega \gg (2/\beta)(\beta/q-1)^{1/2}$ formula for half integer steps is:

$$i_{1/2}(P) = 2\max_\Theta \left(q\,J_1(2x)\sin\Theta\right).$$

Detector response $\eta(V)$ dependences from heterojunctions were measured in high frequency limit at $f = 90$–120 GHz. The q-factor could be estimated from ratio of integer detector response amplitude η_1 at V_1 with differential resistance R_{D1} and $\eta_{1/2}$ half integer response at $V_{1/2}$, with $R_{D1/2}$: $\eta_{1/2}/\eta_1 = 4q^2(R_{D1}/R_{D1/2})$.

Experimental detector response curve is shown in Fig. 2. The half integer response at $V_{1/2} = 124$ μV and integer response at $V_1 = 250$ μV are shown. Applied microwave power P was of order 6 pW, which is insuring quadratic detection in small signal regime. The ratio of $\eta_{1/2}/\eta_1 = 0.5$ allows us to estimate $|q| \approx 0.5$, in approximation of small capacitance.

4. Summary

In conclusion, the S-AF-S Josephson junctions with antiferromagnetic interlayer with thickness 20–70 nm were fabricated. The I_CR_N products were of 150–300 μV at 4.2 K, which are corresponding to the critical frequency 70–150 GHz. High enough resistances were observed: $R_N = 20\Omega$ for $d = 50$ nm and $R_N = 0.15\Omega$ for $d = 20$ nm, for junctions 20 μm in size.

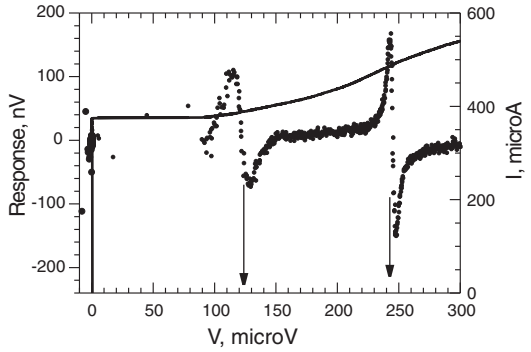

Fig. 2. Detector response (circles) on 119 GHz signal, $\omega = 1$, I–V characteristic — solid line. The junction had $L = 10$ μm, $d = 20$ nm. Bias voltages for integer and half integer responses were shown by arrows.

A portion of the second harmonic in superconducting current-phase relation was estimated as order 10–40 percent of critical current from experimental data of Shapiro steps and detector responses.

Acknowledgements

The work was supported by EU proj. NMP3-CT-2006-033191, projects ISTC-3743, RFBR 08-02-00487, Scientific School-5408.2008.2 and RAS Programs.

References

[1] L. P. Gorkov, V. Z. Kresin, *Physica C* **367**, 103 (2002).
[2] Y. Tarutani, T. Fukazawa, U. Kabasawa *et al*, *Appl. Phys. Lett.* **58**, 2707 (1991).
[3] I. Bozovic, G. Logvenov, M. A. J. Verhoeven *et al*, *Phys. Rev.Lett.* **93**, 157002 (2004).
[4] K.-U. Barholtz, M. Yu. Kupriyanov, U. Hubner *et al*, *Physica C* **334**, 175 (2000).
[5] G. A. Ovsyannikov, P. V. Komissinski, I. V. Borisenko *et al*, *JETP Lett.* **84**, 262 (2006).
[6] Y. V. Kislinski, P. V. Komissinski, K. Y. Constantinian *et al*, *JETP* **101**, 494 (2005).
[7] E. Goldobin, D. Koelle, R. Kleiner *et al*, *Phys. Rev. B* **76**, 224523 (2007).
[8] M. H. S. Amin, A. Yu. Smirnov, A. M. Zagoskin *et al*, *Phys. Rev. B* **71**, 064516 (2005).
[9] Y. V. Kislinskii, K. Y. Constantinian, G. A. Ovsyannikov *et al*, *JETP* **106**, 800 (2008).

16th Int. Symp. "Nanostructures: Physics and Technology"
Vladivostok, Russia, July 14–18, 2008

Amplification of terahertz radiation due to plasmonic instability in the field-effect transistor array

V. V. Popov[1], G. M. Tsymbalov[1] and M. S. Shur[2]

[1] Institute of Radio Engineering and Electronics (Saratov Branch), Russian Academy of Sciences, 410019 Saratov, Russia
[2] Department of Electrical, Computer, and System Engineering and Center for Integrated Electronics, C119015, Rensselaer Polytechnic Institute, Troy, 12180 New York, USA

Abstract. We study the amplification of terahertz radiation due to instability of the collective plasmon mode in an array of field-effect transistors. The terahertz amplification develops at small DC drain currents in the array having an entirely planar design, which makes this device very attractive for its potential applications as terahertz amplifiers and emitters.

Unstable plasma oscillations in field-effect transistors (FETs) with two-dimensional (2D) electron channels can be used for the generation of terahertz (THz) radiation [1]. Hydrodynamic instability of plasmons in 2D channel of FET with a single gate was predicted in a seminal paper [2]. This type of the instability develops at small electron drift velocities (which may be much less than the plasmon phase velocity) if asymmetrical boundary conditions for plasmons are realized at different ends of the gated portion of the 2D electron channel: short-circuit regime at the source and open-circuit regime at the drain ends of the gated part of the channel. Since then the observation of THz emission from unstable plasmons was reported in several papers [3–5].

In all previous works the problem of coupling the unstable plasmons to THz radiation was left aside, although it is very important in order to ensure the THz generation regime. It is known that the gated plasmons, in general, couple very poorly to THz radiation due to an acoustical nature and, hence, small net dipole moment of this plasmon mode [6] so that a special antenna elements are needed to couple the gated plasmons to THz radiation. This is consistent with very small output THz emission power (of nanowatt level or less) observed in experiments [3–5] without using special coupling elements.

In earlier paper [1], it was suggested that the coupling between plasmons in the FET channel and THz radiation might be more effective if FET units were arranged in an array. Later, in a recent paper [7], we showed that the enhancement of the coupling grows proportionally to the number squared of FET units in the array due to a formation of collective plasmon mode delocalized over the entire array of FET's. Coupling of the gated plasmons in the FET array to THz radiation drastically grows also because the charge distributions in the gate and side contacts of the FET unit have the same symmetry as excited by the ether gated plasmon mode or incoming/outgoing THz radiation [7]. Because of all this the FET array itself acts as an aerial matched antenna coupling the plasmons to THz radiation.

In this paper, we theoretically study the amplification of THz radiation in a one-dimensional planar FET's array with isolated 2D electron channels and conjugate side contacts of adjacent FET units (Fig. 1). External THz wave is incident upon the FET array at normal direction to its plane. Terahertz amplification takes place due to hydrodynamic instability of

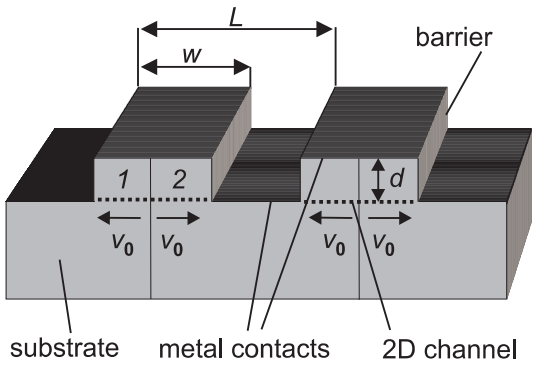

Fig. 1. Schematic of the FET array. Incoming THz radiation is incident normally from the top.

plasma waves developed in the FET channels. As was mentioned above, asymmetrical boundary conditions at the source and drain ends of the channel are mandatory for the hydrodynamic plasmon instability to develop in a single-gate FET. This is hard to realize using a planar technology but may need a special design involving lamped elements. Alternatively, large drain currents close to saturation regime may produce needed asymmetry of the channel [3]. In the FET array shown in Fig. 1 symmetrical boundary conditions at the source and drain ends of the channel in each FET unit take place because of planar geometry of the FET array. Necessary condition for the plasmon instability to develop is ensured by the excitation of a specific plasmon mode in the FET array. Incoming THz wave with the electric field polarized across the FET array (x-direction) induces anti-symmetrical vertical electric field under source and drain edges of gate contacts in each FET unit. Such electric field excites plasmon modes with the nodes of the vertical component of the oscillating electric field under the centers of the gate contacts. It means that one has the short-circuited condition for the vertical electric field under the center of the gate contact, while close-to-open-circuited conditions at the edges of the gate contact, in each FET unit. In order to ensure the plasmon instability in such a device one has to apply counter-directed DC drain currents in different half-parts 1 and 2 of the FET unit (see Fig. 1). In this sense each FET unit in the array is similar to two single-gated FET's with combined gates and merged source contacts, which are short-circuited in the center of the FET unit (hidden wire source contacts at the centers of the FET-unit channels are not shown in Fig. 1), and different

open drain contacts on both sides of the FET unit.

We solve the linear electromagnetic problem using a self-consistent approach similar to that described in [6–8]. However, in distinction from [6–8], here we have to use the Ohm's law, which accounts for not only a spatial periodicity of the FET array but also for a spatial dispersion of the conductivity of 2D electron system arising from (counter-directed) DC electron drift in different half-parts of every FET unit. The oscillating current density, $j^{(1,2)}(x)$, in each part of the channel can be related to the electric field in the channel as (harmonic time-dependence is omitted)

$$j^{(1,2)}(x) = \sum_{-\infty}^{\infty} \sigma^{(1,2)} E_{x,m} \exp(i q_m x), \qquad (1)$$

where $E_{x,m}$ are the amplitudes of the Fourier harmonics of the in-plane electric field in the channel and

$$\sigma_m^{(1,2)} = i \frac{\omega e^2 N_{2D}}{m(\omega \mp q_m v_0)(\omega \mp q_m v_0 + i\nu)} \qquad (2)$$

for every Fourier harmonic having plasmon wavevector $q_m = 2\pi m/L$. Here N_{2D} is the equilibrium electron density in the FET channel, e and m are the electron charge and effective mass, respectively, ν is the electron momentum scattering rate, v_0 is the DC electron drift velocity. Superscripts (1,2) and signs $\mp$ refer to the left 1 and right 2 half-parts of the channel in each FET unit (see Fig. 1), respectively (we assume that counter-directed DC electron drift velocities have the same value in each of the two half-parts of the FET unit). The gate and side metal contacts are described by the frequency independent conductivity of gold.

Figure 2 shows the evolution of THz absorption spectrum of the FET array at the fundamental plasmon resonance when the DC electron drift velocity/bias current in each part of the FET unit increases. At small DC bias current, the plasmon absorption resonance decreases in intensity becoming narrower due to decreasing the radiative lilnewidth of the plasmon resonance. At some threshold value of the DC drift velocity the absorption becomes negative, which corresponds to the amplification of the incoming THz wave. The width of the amplification line is by an order of magnitude narrower than the plasmon absorption linewidth because in the former case the dissipation linewidth and the radiation linewidth of the unstable plasmons (which is negative in the amplification regime) cancel each other. Amplification develops at small DC drift velocities $v_0/v_{ph} < 1$, where v_{ph} is the plasmon phase velocity, in accordance with [2]. However, the strongest amplification with the utmost amplification factor up to 400 takes place at much smaller DC drift velocities (which correspond the drain currents far below the saturation value) than those ensuring the largest plasmon instability increments predicted in [2]. The reason for this is that the condition for the plasmon instability and the condition for optimal coupling the unstable plasmons to THz radiation differ so that one can obtain less THz amplification even under stronger plasmon instability.

In conclusion, we have shown that the array of FET's can effectively amplify THz radiation via the plasmon instability mechanism at the small drain DC currents far below the saturation current regime. This makes FET arrays very attractive for its potential applications as THz emitters and amplifiers with entirely planar geometry.

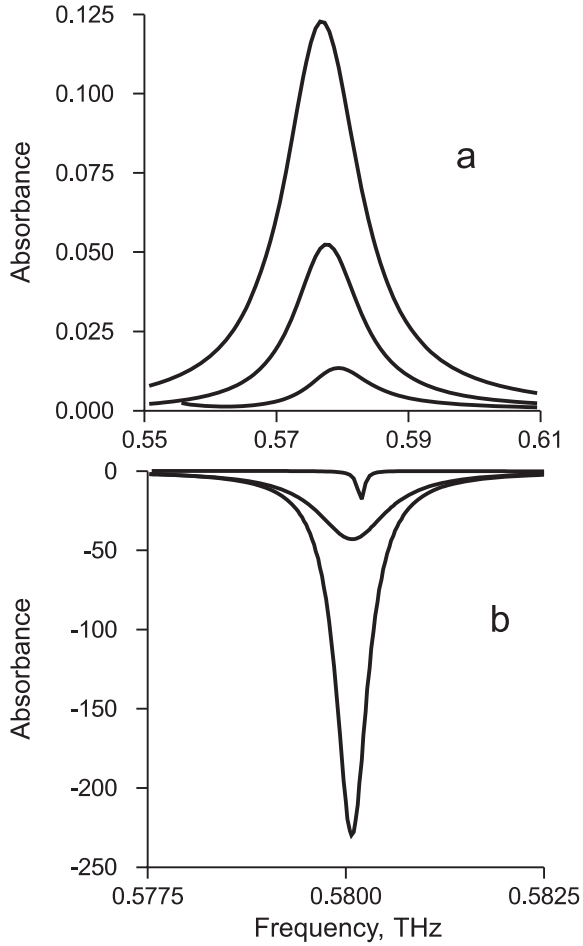

Fig. 2. Spectra of THz absorption (a) and amplification (b) in the FET array at the fundamental plasmon resonance. Electron DC drift velocities in the FET channel are (from the top to bottom): 1×10^4, 4×10^5, 5.5×10^5, 1×10^6, 1×10^7, 7.35×10^6 cm/s. Other FET parameters are $N_{2D} = 2.57 \times 10^{11}$ cm^{-2}, $\nu = 1.5 \times 10^{10}$ s^{-1}, $L = 4$ μm, $w = 2$ μm, $d = 0.4$ μm, $m = 0.067m_0$, where m_0 is the free electron mass.

Acknowledgements

This work has been supported by the Russian Foundation for Basic Research (Grant 06-02-16155) and the Russian Academy of Sciences program "Quantum Nanostructures". M.S.S. acknowledges a support from the Office of Naval Research (Project Monitor Dr. Colin Wood) and from the National Science Foundation under the auspices of the I/UCRC "Connection One".

References

[1] M. Dyakonov and M. Shur, *IEEE Trans. Electron Devices* **43**, 380 (1996).
[2] M. Dyakonov and M. Shur, *Phys. Rev. Lett.* **71**, 2465 (1993).
[3] W. Knap *et al*, *Appl. Phys. Lett.* **84**, 2331 (2004).
[4] T. Otsuji *et al*, *Appl. Phys. Lett.* **85**, 2119 (2004).
[5] N. Dyakonova *et al*, *Appl. Phys. Lett.* **29**, 435 (1979).
[6] V. V. Popov *et al*, *J. Appl. Phys.* **98**, 033510 (2005).
[7] V. V. Popov *et al*, *Appl. Phys. Lett.* **89**, 23504 (2006).
[8] V. V. Popov *et al*, *J. Appl. Phys.* **99**, 124303 (2006).

16th Int. Symp. "Nanostructures: Physics and Technology"
Vladivostok, Russia, July 14–18, 2008

Difference frequency generation in GaAs-based butt-joint diode laser with germanium substrate

V. Ya. Aleshkin and A. A. Dubinov
Institute for Physics of Microstructures RAS, 603950, Nizhny Novgorod, Russia

Abstract. The difference frequency generation arising by mixing of two near-infrared modes with a wavelength of about 1 μm in a GaAs based butt-joint diode laser with germanium substrate are studied theoretically. It is shown that the power of the difference mode in the 5–50 THz range generated by 1-W near-infrared modes in a 100-μm-wide laser at room temperature can be $\sim$40 μW.

Introduction

Semiconductor lasers operating in the middle and far-infrared (IR) regions attract considerable interest in view of their high potential for different applications. The quantum cascade medium-IR lasers capable of room-temperature operation have been successfully implemented [1], whereas with far-IR lasers based on cascade structures generation has been achieved only at cryogenic temperatures [2]. However, an extremely complicated band diagram of cascade structures and high requirements for control of parameters restrict their application. Moreover, these lasers cannot to radiate in 7–10 THz range fundamentally as a result of strong phonon absorbtion in this frequency range.

This limitation is surmounted for noninversion generation schemes. One such approach might be that where far- or middle-IR radiation is generated in a quadratically nonlinear semiconductor structure [3] by extracting the difference frequency $\omega = \omega_2 - \omega_1$ resulting from mixing two near-IR fields at frequencies ω_1 and ω_2.

For the difference frequency generation we propose to use the scheme of butt-joint diode laser (the two-chip laser with compound resonator, which consist snap-together two lasers on common heat sink). In the suggested scheme both CW lasers generate the fundamental modes of different near-IR frequencies. The radiation of one laser be put in another laser, in which cavity the difference frequency generation will take place. Our recent experiments have demonstrated a possibility to introduce about one half laser radiation inside the cavity of an other laser diode [4].

1. Laser waveguide design for the difference frequency generation

In order to attain effective difference frequency generation, the phase-matching condition should be satisfied, which means that the phase velocities of the polarization wave, produced by nonlinearity-induced interaction between near-IR modes, and the difference frequency propagating mode must be the same. Moreover, the low losses of difference frequency radiation by optical phonons and free carriers should be satisfied.

For realization these conditions in this work, we propose to use un- or low-doped germanium (Ge) substrate for the InGaAs/GaAs/InGaP heterolaser, in which cavity the difference frequency generation will take place. Since the lattice constant of Ge is close to that of GaAs, GaAs can basically be grown on a Ge substrate and capacity for work of lasers with Ge substrate was demonstrated [5]. The refractive index of Ge in the middle and far infrared range is higher than that of GaAs; therefore, the phase-matching condition for fundamental modes of the near-IR range is satisfied in this case. This is impossible for GaAs-substrate laser [6]. An advantage of this method is that the overlap factor for the difference near-IR mode is not small (the modes are not orthogonal). Moreover, Ge substrate plays a part of a oversize waveguide for difference frequency radiation. So absorbtion of the difference frequency is low, because phonon absorbtion in Ge is depressed strongly as compared with GaAs, and free carriers are not in undoped Ge. It is significant, that the loss decreasing of the difference frequency leads to more mild phase-matching condition in the oversize waveguide, because this condition was satisfied for large mode number.

2. The calculation of the difference frequency power

In the case when the laser waveguide is grown on the (001)-plane substrate and the near-IR modes have TE polarization and propagate along the [110] direction, the nonlinear polarization in GaAs is normal to the plane of layers and the TM mode is generated at the difference frequency [6]. The Z-axis is directed along the crystallographic direction [001] (see Fig. 1). The TM mode propagating along the X-axis has one magnetic field component directed along the Y-axis. The layer parameters of the laser, in which difference frequency is generated, is shown in Table 1.

The difference frequency power is calculated as approximation, that $\alpha L \gg 1$ (α — the absorption factor by difference frequency, L — laser length). In this case the difference frequency power don't depend on L. In the calculation waveguide

Table 1.

#	Layer composition	Type conductivity	Carrier concentration, cm^{-3}	Layer thickness, μm
1	Ge	-	-	130
2	GaAs	n	10^{18}	0.1
3	InGaP	n	10^{18}	0.8
4	GaAs	-	-	0.6
5	InGaP	p	2×10^{18}	0.8
6	GaAs	p	10^{19}	0.2
7	Au	-	-	0.2

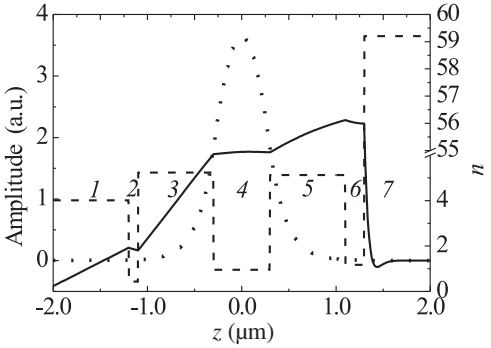

Fig. 1. Spatial profiles of the value of the magnetic field amplitude of the difference mode (solid curve). The amplitude of near-IR modes is shown by dotted line, and the real part of the refractive index n at the frequency 8.6 THz is shown by dashed line. The layers are numbered in accordance with the table data.

wide is 100 μm and near-IR modes powers are 1 W each.

The calculated difference frequency power for suggested butt-joint diode laser is shown in Fig. 2. The longest wavelength for a near-infrared mode λ_1 is fixed in our calculation. The wavelength of the difference mode is changed by variation of the wavelength of another near-IR mode. The spectral dependence of power features great number of resonance peaks. Each peak corresponds to oversize waveguide mode, for which the phase-matching condition is satisfied. The results of our calculations indicate that the difference mode can be generated with a power of $\sim$40 μW in the ranges 5–50 THz. It is significant, that the difference frequency mode propagates in Ge substrate for the most part, and near-IR modes interaction takes place in GaAs-based laser, which was grown by this Ge substrate.

Figure 2 shows that the radiation power in mid-IR range of the same order with a power, which can be generated by using transverse modes of a different order for pumping [6]. Although the overlap factor for the difference near-IR mode is small. This effect is related with then that the refractive index of Ge exceeds the refractive indexes of GaAs and InGaP substantially. So the magnetic field of the difference frequency mode penetrates to laser structure region faintly from Ge substrate, and the overlap factor for the difference frequency mode and the polarization wave is small.

We also note a feature of the radiation generation in range 7–10 THz. In this range the radiation absorbtion of GaAs and InGaP, the quadratically nonlinearity of GaAs rise sharply (Fig. 2), because they have common phonon nature [3]. Moreover, refractive indexes of GaAs and InGaP change strongly. So, there is a frequency region between transverse phonon frequencies of GaAs (8.02 THz) and InGaP (9.2 THz), where the phonon absorbtion of GaAs falls sharply, but the phonon absorbtion of InGaP does not rise sharply also, and the nonlinearity of GaAs is higher substantially than in mid-IR range, and the refractive index of InGaP is larger the refractive index of Ge also. In this case the magnetic field of the difference frequency mode penetrates to laser structure sufficiently freely from Ge substrate (Fig. 1). It lead to large extension of the radiation power in this frequency range.

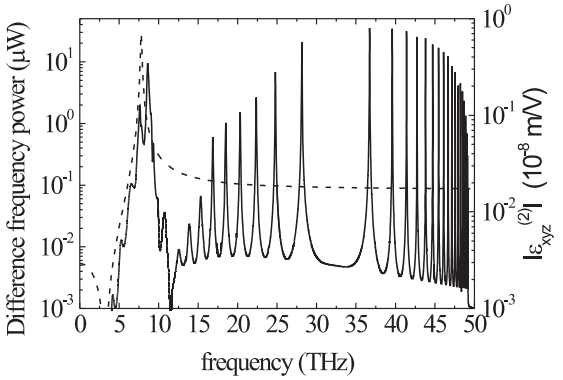

Fig. 2. The difference mode power versus the difference mode frequency in GaAs-based butt-joint diode laser with Ge substrate at room temperature (solid curve, $\lambda_1 = 1.13$ μm). Broken curve corresponds to the dependence of the $\varepsilon^{(2)}_{xyz}$ component (quadratically nonlinearity) in GaAs on the difference mode frequency.

3. Conclusions

The results of our calculations indicate that for near-IR modes power around 1 W in a 1-μm region, the difference mode can be generated with a power of $\sim$40 μW in the ranges 5–50 THz in GaAs-based butt-joint diode laser with germanium substrate and 100-μm-wide waveguide.

Acknowledgements

This work has been supported by grants from the RFBR (07-02-12177, 07-02-00486, 08-02-90054, 08-02-97034), the RAS "Coherent optical emission of semiconductor materials and structures" and "Electromagnetic waves of the terahertz range" Programs, the Russian President (MK-3344.2007.2), and the state contract of Ministry of Education and Science of the Russian Federation No. 02.518.11.7031.

References

[1] J. Faist *et al*, *IEEE J. of Quantum Electron.* **38**, 533 (2002).
[2] B. S. Williams *et al*, *Optics Express* **13**, 3331 (2005).
[3] C. Flytzanis, *Phys. Rev. B* **6**, 1264 (1972).
[4] A. A. Biryukov *et al*, *J. Mod. Opt.* **52**, 2323 (2005).
[5] M. D'Hondt *et al*, *J. Crystal Growth* **195**, 655 (1998).
[6] V. Ya. Aleshkin *et al*, *Semiconductors* **35**, 1203 (2001).

16th Int. Symp. "Nanostructures: Physics and Technology"
Vladivostok, Russia, July 14–18, 2008

Resonant-tunneling heterostructures: new approach in the development of low noise microwave semiconductor devices

N. V. Alkeev[1], S. V. Averin[1] and A. A. Dorofeev[2]

[1] Institute of Radioengineering and Electronics, Russian Academy of Sciences, Fryazino, Moscow region, Russia
[2] Federal State Unitary Enterprise Scintific and Product Enterprise "Pulsar", Moscow, Russia

Abstract. It is shown that properly designed resonant tunneling diodes (RTDs) and transistors containing such RTDs in the emitters are characterized by the reduced level of intrinsic noise. The application of these devices for the microwave technology will increase the sensitivity of the relevant equipment and will allow one to increase the speed and reliability of information transfer through microwave telecommunication channels.

Last decades essential progress has been achieved in the mesoscopic physics. Due to the development of semiconductor technology the fabrication of structures with nanometric characteristic sizes is now feasible. In such structures, the electron de Broglie wavelength exceeds the structure size, and the transport of electrons is mainly controlled by their wave prop-erties, which results in a large variety of new effects. Some of these effects have practical applications.

One mesoscopic structure is the resonant tunneling diode (RTD) suggested for the first time by Esaki and Tsu [1]; this is one of the first nanoelectronic devices. It consists of a narrow-gap semiconductor layer, i.e., quantum well (QW), sand-wiched between two semiconductor layers (barriers) with a wider band gap. In turn, these layers are placed between layers (spacers) of lightly doped narrow-gap semiconductor followed by heavily doped emitter and collector layers. One or several size-quantization levels arise in the QW. As a bias voltage is applied, the current through the RTD flows only when the emitter contains electrons which can resonantly (i.e., with con-servation of energy and transverse momentum) tunnel to the QW level and then to the collector. The RTD features a very fast response; e.g., it is known that its nonlinear properties are retained up to 10 THz [2]. The RTD has other unique proper-ties: in particular, it is one of few nanoelectronic devices oper-ating at room temperature, and its current-voltage (I–V) char-acteristic contains regions of negative differential conductance (NDC). Originally RTDs were supposed to be used in micro-wave oscillators and high-speed digital devices. The maximum oscillating frequency and the minimum switching time achieved in specially designed RTDs is 712 GHz and 1.5 ps, respectively. These results are in strong competition with other high-speed semiconductor devices.

There are two basic mechanisms of electron transport in the RTD. The coherent transport implies that electrons pass through RTD barriers in the same way as the light wave passes through the Fabry Perot cavity. The sequential one implies that an electron tunnels through the RTD in two steps: first, from the emitter through the first barrier to a QW level, and then from this level through the second barrier to the collector. It is assumed in this case that both tunneling events are independent, i.e., the information on the initial phase of the electron wave function is completely lost due to inelastic collisions while the electron stays in the QW. We have shown theoretically and confirmed experimentally that the coherent mechanism of electron transport through RTD barriers exhibits the essential suppression of the shot noise [3]. This phenomenon can be explained as follows. As a result of interaction between the electrons passing through the RTD barriers and the charge in the QW, the Poisson flow of electrons transforms into a sub-Poisson one (antibunching of electrons takes place). This leads to the suppression of shot noise. A similar mechanism of the shot noise suppression is observed in a non-saturated vacuum diode in which electrons passing to the an-ode interact with a cloud of negative charge between the cathode and the anode. It is interesting to note that if electrons tunnel through the RTD barriers by the sequential transport mechanism, the shot noise is reduced appreciably less. De-tailed simulations explaining this effect are given in [3]; nevertheless, the difference in the shot noise suppression of coherent and sequential transport can be explained in the following way. In the coherent mechanism of transport the total transparency of two RTD barriers for electrons is close to unity, and they tunnel through the barriers without any reflection. On the contrary, in the sequential mechanism of electron transport, they tunnel through the first and second RTD barriers independently. Thus, some part of electrons is reflected from the first barrier and this gives rise to additional noise. This noise is analogous to the noise that occurs in multielectrode vacuum tubes due to the current redistribution between the electrodes of the tube. In this study, we propose a new class of low noise semiconductor devices based on the shot noise suppression in RTDs. One can show that if a QW is narrow enough the resonant level in the QW lies above the Fermi levels in the emitter and collector and appreciable nonlinearity is formed in the vicinity of zero voltage in the RTD I-V curve. The authors of [4] have suggested using the RTD with such nonlinearity as an active element of a subharmonic mixer (SHM). These mixers are widely employed at the terahertz frequencies, where they have some advantages over conventional mixers. We carried out a simulation of an RTD-based SHM. The conversion losses, noise figure, and other parameters of this mixer were calcu-lated as a function of RTD characteristics. In [5], we have car-ried out an optimization of the thickness of the active layers of RTDs designed for the operation in SHMs at room tempera-tures. The optimization was carried out for two types

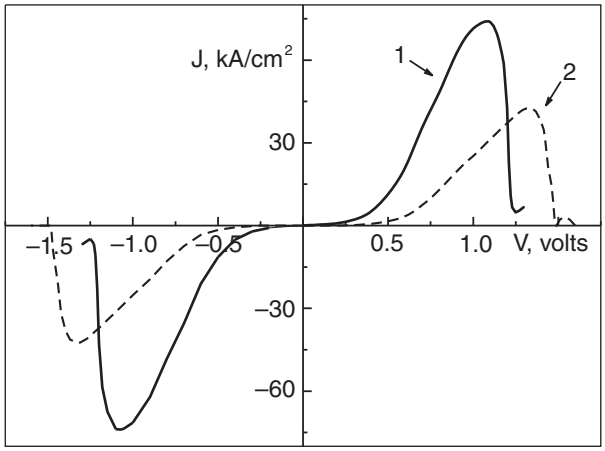

Fig. 1. The optimized I-V curve (1) for the InGaAs/InAlAs heterosystem and (2) for the InGaAs/AlAs heterosystem.

of het-erosystems: matched — $In_{0.53}Ga_{0.47}As/In_{0.52}Al_{0.48}As$ and pseu-domorphic — $In_{0.53}Ga_{0.47}As/AlAs$. Figure 1 shows the simulated I-V curves for these RTDs. In addition to the low noise figure, RTD-based SHMs have other advantages over conventional mixers. In particular, the local oscillator (LO) power could be essentially reduced as compared with the optimal LO power of widely used SHMs based on two antiparallelly connected Schottky diodes. This is especially important in the terahertz frequency range.

The effect of the shot noise suppression in RTD can also be used in other semiconductor devices, for example, in heterojunction bipolar transistors (HBTs). The intrinsic noise intensity of these transistors is several times higher than that of field effect transistors (FETs) and high electrons mobility transistors (HEMTs). This is due to the fact that the dominant noise in FETs and HEMTs is the thermal noise of their channel, which can be reduced by cooling the device. In contrast to FETs and HEMTs, the dominant noise in HBTs is the shot noise of the emitter-base junction, which is much greater than the thermal noise of these transistors under their operating conditions. We propose a method which allows one to reduce considerably the intrinsic noise of HBTs and HETs. We place RTDs in the emitters of these transistors. In this case, if electrons tunnel through RTD barriers coherently, the shot noise in the emitter base junction is reduced, and thus the noise of the whole transistor is also reduced. In [6,7] it was reported on the design of an HBT with the RTD in the emitter (RBT). The author's main goal was to use these transistors in various functional devices and, in particular, in multiple-valued logic circuits. It should be noted that we are not aware of any noise measurements on RBTs. However, one may expect that, if properly designed, RBTs will have much lower intrinsic noise than that of conventional HBTs. RBTs may find the applications in low noise amplifiers (LNAs) at the frequencies of up to 2 GHz. At these frequencies FETs and HEMTs usually used in LNAs possess very high input impedance, which does not allow one to design broadband and stable amplifiers on the basis of these devices. However, the use of RBTs in microwave oscillators to re-duce the phase noise intensity seems to be more promising. It is known that this noise is the main factor limiting the speed and the reliability of information transfer in telecommunication channels. The phase noise arises in oscillators during nonlinear transformation of noise, and its intensity is deter-mined by the whole noise spectrum of all active and passive elements of the circuit. Today, when designing a microwave oscillator with low level of phase noise, one prefers to use HBTs but not FETs and HEMTs. In spite of smaller noise at microwave frequencies of the latter transistors, their $1/f$ niose is essentially higher than that of HBTs. One may expect that the use RBTs in microwave oscillators will lead to the reduc-tion phase noise of these oscillators Note that RBTs can find application also in frequency multipliers with low phase noise level of the output signal. Moreover, one can use RTDs with nonlinearity at as a frequency tripler with a low level of phase noise. In spite of the fact that the cutoff frequencies of pHEMTs and HBTs have already reached 400 GHz, RTDs are potentially higher frequency devices, which gives them advantage over the above-mentioned transistors as low phase noise multipliers in the short-millimeter and submillimeter wavelengths. Thus, it is shown that properly designed RTDs and transistors containing such RTDs in the emitters are characterized by the reduced level of intrinsic noise. The application of these devices for the microwave technology will increase the sensitivity of the relevant equipment and will allow one to increase the speed and reliability of information transfer through microwave telecommunication channels.

Acknowledgements

This work was supported by the Russian Foundation for Basic Research, project Nos. 07-02-01121 and 07-07-00009.

References

[1] R. Tsu, L. Esaki, *Appl. Phys. Lett.* **22**, 562 (1973).
[2] W. R. Frensley, *Appl. Phys. Lett.* **51**, 448 (1987).
[3] V. Ya. Aleshkin *et al*, *Phys. Rev. B.* **70**, 115321 (2004).
[4] W. Y. Liu, D. P. Steenson, *IEEE Trans.* **MTT-48**, 757 (2000).
[5] N. V. Alkeev *et al*, *Proc. 16th Int. Conf. MIKON-2006*, Krakow, Poland (2006).
[6] T. Futatsugi *et al*, *Jpn. J. Appl. Phys.* **26**, L131 (1987).
[7] F. Capasso *et al*, *IEEE El. Dev. Letters.* **EDL-7**, 573 (1986).

16th Int. Symp. "Nanostructures: Physics and Technology"
Vladivostok, Russia, July 14–18, 2008

Intermode plasmon-plasmon scattering in a nanotransistor with partially gated two-dimensional electron channel

O. V. Polischuk[1], V. V. Popov[1], W. Knap[2,3] and A. El Fatimy[2,3]

[1] Institute of Radio Engineering and Electronics (Saratov Branch), Russian Academy of Sciences, 410019 Saratov, Russia
[2] Research Institute of Electrical Communication, Tohoku University, 2-1-1 Katahira, Aoba-Ku, Sendai
[3] GES UMR-5650, Universite Montpellier 2 and CNRS, 34095 Montpellier, France

Abstract. We calculate the terahertz absorption spectrum of the field-effect transistor with a short recessed gate and show that the main contribution to the linewidth of the gated plasmon resonance can be attributed to the intermode plasmon-plasmon scattering. The physics of the intermode plasmon-plasmon scattering is discussed compared to the other possible plasmon damping mechanisms.

High-frequency response of field-effect transistors (FET) with two-dimensional (2D) electron channels is strongly affected by plasma oscillations in the channel. This phenomenon in its various manifestations can be used for the detection, frequency multiplication and generation of terahertz (THz) radiation [1–3]. In a typical high-frequency FET [2] there are a short gated region of the channel as well as (much longer) ungated access regions on the source and drain sides of the channel (Fig. 1). Accordingly, two different types of plasma oscillations can exist in a FET device. They are plasma oscillations excited either in gated or ungated regions of the electron channel, which are termed as gated and ungated plasmons, respectively. The gated plasmons have a linear dependence of their frequency on the plasmon wavevector, whereas the frequency of the ungated plasmon mode is proportional to a square root from the plasmon wavevector. The gated plasmons were considered to be more attractive for electronic applications because their frequencies can be effectively tuned by varying the gate voltage.

Obviously, the gated and ungated plasmon modes can exist independently only in ideal structures. However, in a real FET structure having the gated as well as ungated portions of the channel the gated and ungated plasmons can interact with each other. The effect of the ungated portions of the channel on the resonant frequencies of the gated plasmons was studied in recent theoretical papers [4,5], where the ungated portions of the channel were considered as resistive regions. Interaction between the gated and ungated plasmons was originally discussed in [6], where was shown that the resonant gated plasmons can excite plasmons in the ungated regions via their scattering at the edges of the gate contact. Such intermode plasmon-plasmon scattering must contribute to the total linewidth of the gated plasmon resonance along with the other plasmon damping mechanisms. These other mechanisms can be related to electron momentum relaxation in the channel and/or to radiative damping of plasmons related to the electromagnetic emission from oscillating plasmon mode.

Due to acoustic nature of the gated plasmons (and, hence, vanishingly small net dipole moment of this plasmon mode) the gated plasmons weakly couple to THz radiation. That is why the gated plasmon resonances are not pronounced in the THz absorption spectra of the FET. They merge into much stronger background originated from the plasmon and free-electron absorption in long ungated access regions of the channel. However, the gated plasmon resonances can be observed in the THz photoresponse spectra of FET [7] because the photovoltaic response is due to the gated plasmon nonlinearity [1]. In [7] the plasmon photoresponse of InGaAs/InGaAs HEMT with nanometer (50 nm) gate and the ungated access regions of the channel of a micron length was measured at temperature 10 K (Fig. 2a). Electron mobility in the HEMT channel was greater than 36000 $cm^2/V\,s$ that corresponds to the electron relaxation time 0.8 ps. Amazingly, the measured in [7] linewidth of the plasmon resonance by an order of magnitude exceeded the dissipative contribution $1/2\pi\tau \approx 0.2$ THz.

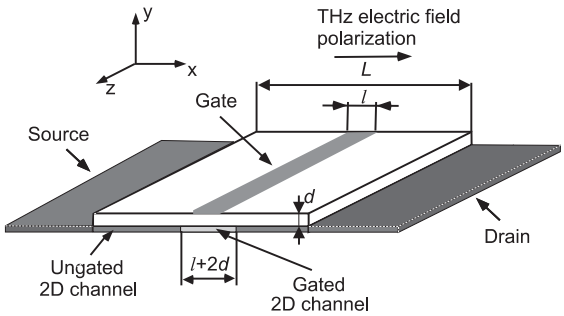

Fig. 1. Schematic of the transistor structure and coordinate system. The external THz radiation is incident normally from the top.

In this paper, we calculate the THz absorption spectra of a FET with a short recessed gate (Fig. 1) and characteristic parameters corresponding to those indicated in [7]. Earlier it has been shown that plasmons excited in the ungated regions of the channel via the intermode plasmon-plasmon scattering typically decay before they reach the side (source and drain) contacts [6]. Because of that in our present calculations we use a model structure of FET with infinitely long access regions of the channel [6]. In such model structure the ungated plasmons can not be excited by incoming THz wave and, hence, the gated plasmon resonances alone survive in the THz absorption spectrum. Free-electron Drude absorption also can be easily subtracted from the total calculated absorption in such a model structure. This makes the gated plasmon resonances very well pronounced and the effective width of the plasma resonances can be easily determined from the calculated THz absorption spectrum.

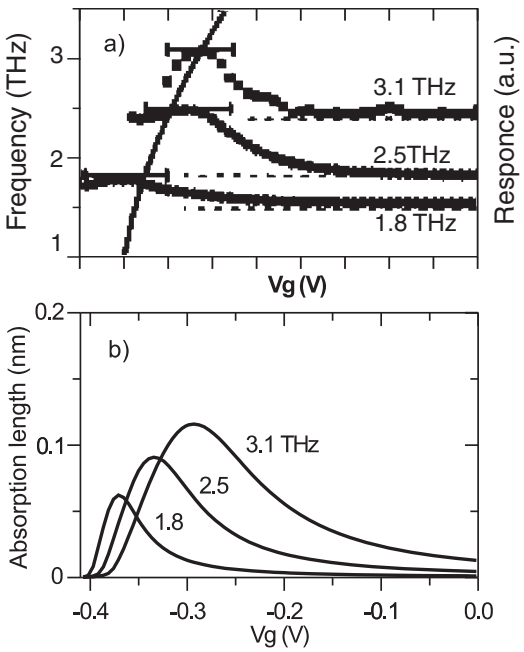

Fig. 2. (a) Measured plasmon photoresponse [7] and (b) calculated THz absorption lengths of the fundamental gated plasmon mode in InGaAs/InAlAs nanotransistor with a short recessed gate versus the gate voltage for three different frequencies of incident THz radiation. Electron channel depletion threshold voltage is $V_{\rm th} = 0.41$ V for the gate-to channel distance 20 nm.

The results of calculations are shown in Fig. 2b. The linewidths of the calculated gated plasmon resonances (Fig. 2b) practically coincide with the experimental linewidths of the FET photoresponse resonances of Ref. 7 (shown in Fig. 2a). As have been already mentioned the total line-width of the plasmon resonance exceeds by an order of magnitude the electron relaxation contribution $1/2\pi\tau$. The radiative contribution to the total linewidth of the plasmon resonance is also very small (due to acoustic nature of this plasmon mode). It complies with extremely short THz scattering length of the device (the calculated THz scattering length is four orders of magnitude shorter then corresponding absorption length shown in Fig. 2b). It means that almost the entire linewitdth the plasmon resonances comes from the intermode plasmon-plasmon scattering.

In general, a non-resonant plasmon-plasmon scattering takes place because plasmon wavevector does not conserve in this scattering process (frequency of the both gated and ungated interacting plasmon modes is dictated by the frequency of incoming THz wave). The gated plasmons have a quantized wavevectors due to confinement of this plasmon mode under the gate contact while, in our model structure with the infinite access regions, the wavevector of the non-resonant ungated plasmons is defined by the dispersion law of this plasmon mode. Because the ungated plasmons are non-radiative modes, the intermode plasmon-plasmon scattering provides additional non-radiative damping channel for the gated plasmons.

If the length of the ungated access regions is commensurate with the ungated plasmon wavelength, then the resonant ungated plasmons having quantized wavevectors can be excited in the access regions of the channel. In this case the resonant interaction between the gated and ungated plasmons (plasmon mode anticrossing) is, in principle, possible. However, this anticrossing is hard to resolve in a real FET device due to destructive effect of the electron scattering.

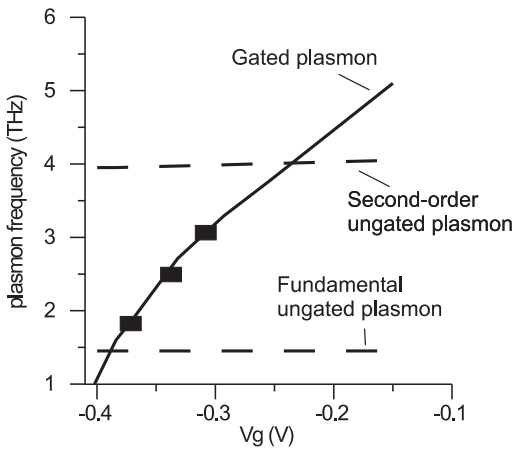

Fig. 3. Frequencies of the fundamental gated (solid curve) and ungated (dashed curves) plasmon resonances versus the gate voltage in the FET with characteristic parameters [7].

Figure 3 shows the calculated frequencies of the fundamental gated plasmon mode and two ungated plasmon modes as functions of the gate voltage in the FET structure with characteristic parameters corresponding to those indicated in [7]. Full squares indicating positions of the plasmon resonances shown in Fig. 2a fall away from the ungated plasmon resonance frequencies. Therefore in our case the main plasmon decay mechanism (determining the calculated linewidth) corresponds to the non-resonant intermode plasmon-plasmon scattering.

In conclusion, we have shown that the experimentally observed gated plasmon resonance linewidth in FET's with a short recessed gate can be explained by the nonresonant intermode plasmon-plasmon scattering. This mechanism appears to be much stronger then dissipative and radiative damping mechanisms.

Acknowledgements

This work has been supported by the Russian Foundation for Basic Research through Grant 06-02-16155 and by the Russian Academy of Sciences Program "Quantum Nanostructures". We acknowlendge also support from GDR-E "Semiconductor Sources and Detectors" and the Region of Languedoc-Roussillon "Terahertz Platform" projects.

References

[1] M. S. Shur and J.-Q. Lü, *IEEE Trans. Microwave Theory and Techniques* **48**, 750 (2000).
[2] W. Knap *et al*, *Appl. Phys. Lett.* **84**, 2331 (2004).
[3] A. Satou *et al*, *Semicond. Sci. Technol.* **18**, 460 (2004).
[4] A. Satou *et al*, *J. Appl. Phys.* **95**, 2084 (2004).
[5] V. Ryzhii *et al*, *J. Appl. Phys.* **99**, 084507 (2006).
[6] V. V. Popov *et al*, *J. Appl. Phys.* **98**, 033510 (2005).
[7] A. El Fatimy *et al*, *Appl. Phys. Lett.* **89**, 131926 (2006).

16th Int. Symp. "Nanostructures: Physics and Technology"
Vladivostok, Russia, July 14–18, 2008

Violet-green injection laser converter based on II–VI quantum dot nanostructures

S. V. Ivanov[1], E. V. Lutsenko[2], S. V. Sorokin[1], I. V. Sedova[1], S. V. Gronin[1], A. G. Voinilovich[2], N. P. Tarasuk[2], G. P. Yablonskii[2] and P. S. Kop'ev[1]

[1] Ioffe Physico-Technical Institute, St Petersburg, Russia
[2] Stepanov Institute of Physics of NAS Belarus, 68, Independence Ave., Minsk 220072, Belarus

Abstract. Violet-green integrated laser converter with a quantum efficiency of 1% at a wavelength of 515 nm has been fabricated on the basis of CdSe/ZnSe/ZnMgSSe quantum dot (QD) laser heterostructure optically pumped by a 416 nm emission of a commercial InGaN/GaN pulse laser diode, supplied to II–VI structure via a microlens system. Different designs of CdSe QD laser structures grown by molecular beam epitaxy have been employed, with the maximum efficiency being achieved in the structure comprising five CdSe QD active layers embedded in a ZnSSe/ZnSe superlattice waveguide.

Introduction

The lack of green semiconductor laser diodes (LD) stimulates numerous attempts to solve the problem using different materials and designs. Most natural for this spectral range (500–550 nm) II–VI wide gap nanos-tructures suffer from instability of nitrogen acceptor, that causes slow degradation of ZnSe LDs [1]. Recent progress in development of blue-violet III-Nitride based LDs has yielded the maximum operational wavelength of 485 nm at 300 K and faced the problem of degradation of the quantum efficiency at higher In content in the InGaN quantum wells [2]. Nevertheless, high quantum efficiency ($\sim$40%) and very low threshold power density (2.5 kW/cm^2 at 300 K) achieved in the optically pumped undoped ZnSe-based laser structures with CdSe quantum dot (QD) active region [3], demonstrating much better degradation stability than ZnSe LDs, enable one to consider these structures as promising candidates for active elements of high performance electron beam pumped lasers [4]. Another way to use the unique lasing properties of the ZnSe-based nanostructures in the green range, suggested by us earlier, is to integrate them as an active part of the violet-green laser converter pumped by emission of a III-Nitride laser [5].

In this paper we report for the first time on fabrication and studies of violet-green injection laser converter comprising a green CdSe QD laser structure chip pumped by a 416 nm pulse radiation of commercial III-Nitride LD. Room temperature lasing at 515 nm and output power of 8 mW per facet has been demonstrated at a violet-to-green conversion efficiency of 1%.

1. Experiment

A II–VI QD laser heterostructure has been grown by molecular beam epitaxy (MBE) on a GaAs epitaxial buffer layer [3]. The structure comprises bottom and top ZnMgSSe cladding layers with the thickness of 1.1 μm and 20 nm, respectively, and a 180-nm-thick $ZnS_{0.15}Se_{0.85}$/ZnSe short-period alternately-strained SL waveguide. Five CdSe/ZnSe QD active layers with the CdSe nominal thicknesses of $\sim$2.5 ML are separated by 5-nm-thick barriers consisting of a tensile-strained 3-nm-thick $ZnS_{0.15}Se_{0.85}$ layer for partial compensation of compressive stress induced by CdSe QD sheets and two 1-nm-thick ZnSe spacers at both sides of the ZnSSe layer. The whole multiple

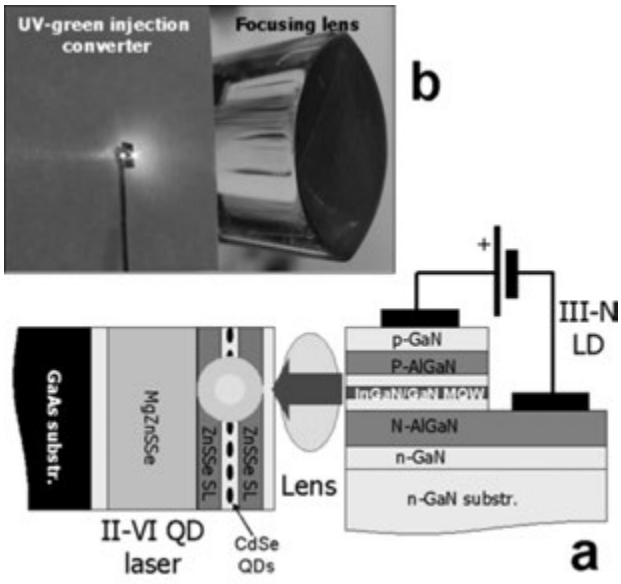

Fig. 1. Schematic design of the violet-green injection laser converter composed of the violet InGaN/GaN commercial LD and elaborated green II–VI QD laser heterostructure (a). General view of the converter under operational conditions (b).

QD active region is asymmetrically placed at 50 nm from the top cladding. Owing to additional inter-dot stress compensation the laser structure remains pseudomorphic as a whole and demonstrates bright photoluminescence at 515 nm at 300 K (not shown hear).

Schematic design of the fabricated laser con-verter is shown in Fig. 1a along with the picture demonstrating a general view of the injection converter under the operational conditions (Fig. 1b). Edge-emitting III-N multiple QW LD operated at a wavelength of 416 nm in pulse regime (pulse duration of 50 ns, repetition rate of 1 kHz) pumps the II–VI laser heterostructure in a transverse geometry via a lens focusing LD radiation in a stripe on the II–VI structure surface normally to the cleaved resonator facets. The resulting edge emission of the II–VI QD laser is registered by a CCD camera. Output light power was measured using Laser Probe Rm 3700 universal radiometer. No reflecting coatings on the facets were used, as well as no special optimization of microlens system was performed.

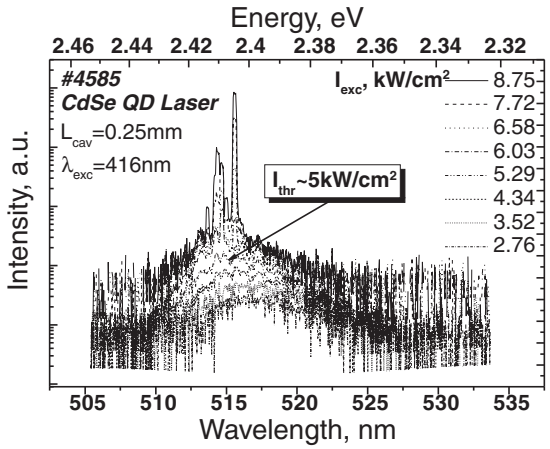

Fig. 2. Photoluminescence spectra of II–VI QD laser structure under the optical excitation with 416 nm line of InGaN/GaN LD at different excitation powers.

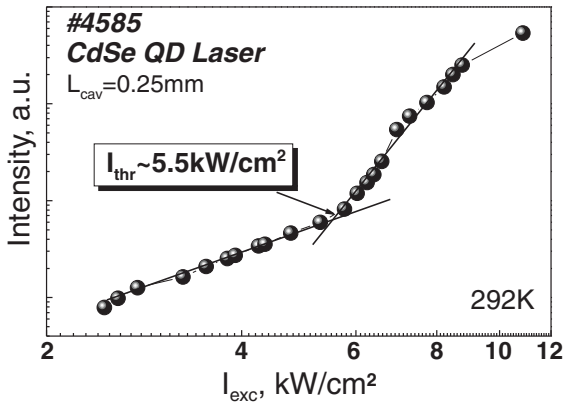

Fig. 3. Edge photoluminescence intensity of the II–VI QD laser structure versus III-N LD excitation power density.

2. Results and discussion

Figure 2 demonstrates edge photoluminescence spectra of the II–VI QD laser structure pumped by the III-N LD at different excitation power densities. Clearly distinguished stimulated emission lines appear at power densities above 5 kW/cm^2 in the vicinity of the PL maximum, increasing fast with power density rising.

The dependence of integral PL intensity of the II–VI structure on the excitation power density of III-N LD, presented in Fig. 3, exhibits typical threshold behavior with the threshold defined at about 5.5 kW/cm^2. Although this value is among the lowest reported, it exceeds twice the lowest threshold power density value achieved in a II–VI QD laser structure of the similar design, but having two electronically coupled QD sheets in the active region [3]. It was unexpected, because the as-grown five-QD-sheet laser structure demonstrated twice higher surface PL intensity as compared to the best structure. The reason for that might be a partial stress relaxation in the studied II–VI laser chip indicated by arising cracks on the surface and some decreasing the surface PL intensity after wafer thinning down to 100 μm. This evidences for not optimum strain engineering in the II–VI structure with multiple CdSe QD sheets.

Figure 4 illustrates variation of the light output power at 515 nm of the II–VI/III-N injection laser converter as a function

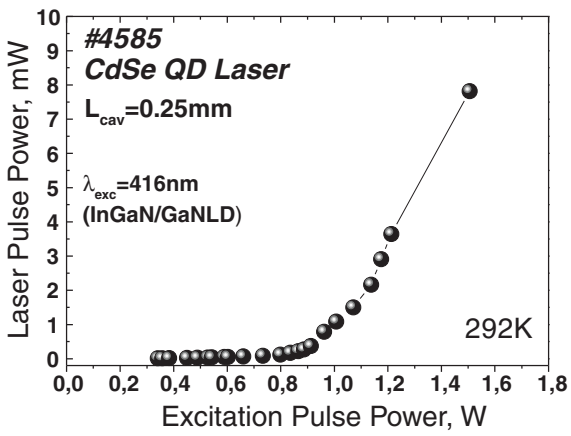

Fig. 4. Light output power at 515 nm of the II–VI/III-N injection converter versus excitation power supplied by III-N LD.

of pulse pumping power supplied by the InGaN/GaN LD. The maximum output power in green per one facet is 8 mW at the excitation of 1.5 W, that gives the value of violet-to-green conversion efficiency of $\sim$1%.

It is expected that decrease of the threshold power density of the II–VI laser heterostructure by optimizing its design and improvement of the laser converter design as a whole to avoid the losses of exciting radiation of a III-N LD will enable us to increase the conversion efficiency of the injection converter at least by order of magnitude.

Summarizing, we have demonstrated for the first time operation of integrated injection laser converter which yields 8 mW pulse laser power in green (515 nm), using violet excitation by a commercial InGaN/GaN LD. This result paves the way to development of compact semiconductor green injection lasers based on II–VI optically pumped nanostructures.

Acknowledgements

The work was partly supported by ISTC Project No. 3754, RF FASI Contract and Belarus State Program Photonics 2.01.

References

[1] S. V. Ivanov, *Phys. Stat. Sol. (a)* **192** (1), 157 (2002).
[2] T. Jang, O. H. Nam, K. H. Ha, S. N. Lee, J. K. Son, S. H. Chae, Y. H. Kim, and Y. Park, *Proc. SPIE* **6473**, 64730X (2007).
[3] S. V. Ivanov *et al*, *Phys. Stat. Sol. (c)* **3** (4), 1229 (2006).
[4] M. M. Zverev *et alTech. Phys. Lett.* **33** (12), 1032 (2007).
[5] S. V. Sorokin *et al*, *Electron. Lett.* **43** (3), 162 (2007).

16th Int. Symp. "Nanostructures: Physics and Technology"
Vladivostok, Russia, July 14–18, 2008

3 watt scanning blue VCSEL with electron-beam pumping based on MBE grown ZnCdSe/ZnMgSSe structure

S. V. Alyshev[1], A. O. Zabezhaylov[1], R. A. Mironov[1], V. I. Kozlovsky[2] and E. M. Dianov[1]

[1] Fiber Optics Research Center, 119333 Moscow, Russia
[2] P. N. Lebedev Physical Institute, 119991 Moscow, Russia

Abstract. ZnCdSe/ZnMgSSe MQW structures were grown by molecular beam epitaxy on GaAs substrates. Cathodoluminescence was used for structure characterization. Electron-beam pumped VCSEL based on the 6 μm thick 28 periods ZnCdSe/ZnMgSSe MQW structure was produce. Maximum output power was as high as 2.8 W with efficiency of 3.5% at electron beam energy of 45 keV. Threshold current was as low as 35 μA.

Introduction

The blue continuous wave laser can be useful as low-cost high saturation and high brightness light source for projection television [1]. In this context a vertical cavity surface emitting laser (VCSEL) based on multiple quantum well (MQW) structure is sufficiently adequate. To produce this laser a wide band gap compound structure should be used. ZnMgSSe with $E_g = 3.0$ eV is a suitable material for barrier layers while ZnSSe, ZnCdSe or ZnSe may be used as the QW material in the blue spectral range. Unfortunately, a big problem relating to p-type doping for ZnMgSSe with high Mg and S contents has been found [2]. To avoid this problem, undoped ZnSSe/ZnMgSSe or ZnCdSe/ZnMgSSe structures as gain layers for the VCSEL with optical or electron beam pumping can be used.

Lasing on the undoped ZnSSe/ZnMgSSe MQW structures grown by metal organic vapour phase epitaxy (MOVPE) was observed in work [3]. Using Cd of small content in the ZnSe QW was offered for improving the blue lasers [4]. However the blue laser based on the MQW structures grown by molecular beam epitaxy (MBE) was inferior to the laser on MOVPE grown structure until [5]. In this work we studied cathodoluminescence (CL) and laser properties of MBE grown ZnCdSe/ZnMgSSe structures and obtained essential improving of blue laser characteristics.

1. Experimental

ZnCdSe/ZnMgSSe structures were grown by MBE on GaAs substrates misoriented by 3° from (100) to (111)A. Growth runs were accomplished on a TSNA 18 MBE machine with help of solid Zn, ZnS, Mg, Se and Cd sources. The substrate temperature during growth was 280 °C.

First a few single QW structures were grown at different II/VI relations that was controlled by reflection high electron energy diffraction (RHEED) during growth. The structures consisted of the 100 nm thick ZnSe/ZnSSe buffer, the 200 nm thick ZnMgSSe layer, the 5 nm thick ZnSe QW and the 200 nm thick ZnMgSSe layer.

Then we grew the 3 ZnCdSe QW structure with different Cd content in each QW to study Cd influence on QW emission intensity. The 6 nm thick QWs were separated by the 100 nm thick ZnMgSSe barrier layers. The first and the last ZnMgSSe layers were 200 and 100 nm in thickness. The Cd content was about 5% in the first QW while 0% in the second and 2.5% in the third QW.

Finally, the 6 μm thick 28 periods ZnCdSe/ZnMgSSe MQW structure was grown as gain layers for VCSEL. The period was approximately equal to λ/N, where λ is the desired laser wavelength and N is the average refractive index along the period. The MQW region was grown on the 60 nm thick ZnSe buffer. The QW thickness was about 6 nm and the ZnMgSSe barrier had the band gap of 3 eV at room temperature (RT). The structure was completed by the ZnMgSSe layer with thickness equalled to the thickness of the ZnMgSSe barrier layer and was followed by the 6 nm thick ZnSe cap layer. The ZnMgSSe lattice period was close to that of GaAs substrate although not precisely matched.

The CL spectra were recorded at $T < 14$ K and 300 K, electron energy $E_e = 3$, 10, 30 keV, current $I_e = 1$ μA and electron beam diameter $d_e = 1$ mm. When preparing the laser etalon, first the dielectric mirror with the reflectance $R = 0.97$ was deposited on the structure, then the sample was glued by epoxy to a sapphire holder and the GaAs substrate was removed by selective etching. A second closed mirror containing dielectric layers and thin Al layer was deposited on the etched surface. The microcavity length was about 6 μm. Active element was excited by scanning electron beam with $E_e = 30$–50 keV, $I_e = 0$–2 mA and $d_e = 25$–50 μm increasing with the increase of pumping current and the decrease of electron energy. The scanning rate was 4×10^5 cm/s.

2. Results and discussion

It has been found that the factor of the II/VI beam equivalent pressure (BEP) ratio is very important in achieving of high intense luminescence. The best results were obtained at the slightly group VI-reach growth conditions with the dominance of (2×1) surface reconstruction pattern observed by RHEED.

Low temperature CL spectra of the 3 QW structure are presented in Fig. 1 at different electron energy $E_e = 3$, 10 and 30 keV. There are emission lines of ZnMgSSe layers (near 405 nm), ZnSSe buffer layer (427 nm) and three lines of different QWs (438 nm from the second QW, 442 nm from the third QW and 447 nm from the first QW). The characteristic penetration depth of electrons increases from 0.05 μm at $E_e = 3$ keV to 0.25 μm at 10 keV and to 2.3 μm at 30 keV. It is seen that the line intensity changes with increasing E_e. At 3 keV excitation, the upper ZnMgSSe layer is excited by the electron beam only.

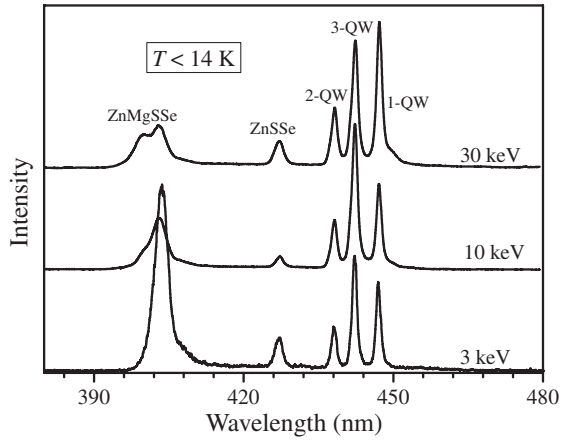

Fig. 1. CL spectra ZnCdSe/ZnMgSSe structure for different electron-beam energy at $T < 14$ K.

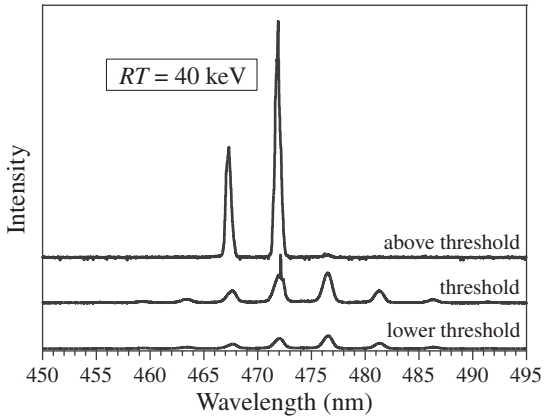

Fig. 2. Generation spectra VCSEL based on ZnCdSe/ZnMgSSe MQW structure at RT. $E_e = 40$ keV.

Other layers are excited by emission of the upper ZnMgSSe layer or as a result of carrier diffusion. Therefore the emission line of ZnMgSSe is the most intense at 3 keV. One can see that the intensity of the second QW emission line is less than the intensity of the emission lines from other QWs. It means that the addition of Cd in the ZnSe QW enhances the QW emission.

We suppose that one of the reasons of such an enhancement is improving carrier capture by the QWs. Indeed in [6] they measured an energy barrier for carrier capture in the ZnSe/ZnMgSSe MQW structures. Probably the Cd addition decreases this barrier.

The emission spectra of the laser etalon at different excitation levels were depicted in Fig. 2. Excitation level was changed by changing d_e at the same $I_e = 1.5$ mA and $E_e = 40$ keV. At the excitation being lower the threshold, the emission spectrum consists of several longitudinal modes of the etalon. At the threshold, lasing occurs in one of the etalon modes at 472 nm. At the smallest d_e the laser spectrum consists of two longitudinal modes at 467 and 472 nm.

Fig. 3 represents the dependences of the output power and the electron beam current on the electron energy. Maximum output power was 2.8 W with efficiency of 3.5% relative to electron beam power at $E_e = 45$ keV. Threshold current was in the range 35–40 μA.

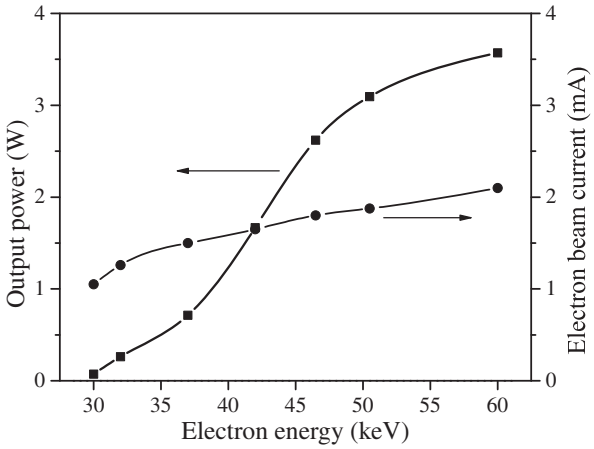

Fig. 3. Dependences of output power and electron beam current on electron energy.

Efficiency can be increased by using the output mirror with higher transmission and matching the period of structure to cavity mode. In this case we should obtain one-mode generation regime.

3. Conclusion

The 2–5% Cd addition in ZnSe QW enhances the cathodoluminescence intensity of the blue ZnSe/ZnMgSSe MQW structures grown by MBE. The 2.8 W power lasing in blue range (470 nm) at 45 keV electron energy was achieved under longitudinal pumping by scanning electron beam.

Acknowledgements

This work was supported in part by Russian Foundation of Basic Researches, Grants 07-02-01139, 08-02-00796 and Program "Scientific Schools of Russia", Grant 6055-2006-2.

References

[1] M. D. Tiberi, V. I. Kozlovsky, *Proc. of SPIE* **60**, 5740 (2005).
[2] D. C. Grillo *et al*, *Electron. Lett.* **30**, 2131 (1994).
[3] V. I. Kozlovsky *et al*, *Proc. of 15th Int. Symp. "Nanostructures: Physics and Technology" Novosibirsk, Russia, June 25–29*, 40–41, (2007).
[4] V. I. Kozlovsky *et al*, *Proc. of Symp. "Coherent optical emission of semiconductor compounds and structures", Zvenigorod, Russia, November 27–29*, (2007).
[5] I. P. Kazakov *et al*, *Quantum Electronics,* **37**, 857–862 (2007).
[6] V. I. Kozlovsky *et al*, *Vestnik Ryazanskoy Gosudarstvenoy Radiotehnicheskoy Academii,* **16**, 79–84 (2005).

16th Int. Symp. "Nanostructures: Physics and Technology"
Vladivostok, Russia, July 14–18, 2008

Effective electron beam pumped green semiconductor lasers based on heterostructure with multiple CdSe/ZnSe QD active layers

S. V. Sorokin[1], I. V. Sedova[1], S. V. Gronin[1], M. M. Zverev[2], N. A. Gamov[2], D. V. Peregoudov[2], V. B. Studionov[2] and S. V. Ivanov[1]

[1] Ioffe Physico-Technical Institute, St Petersburg, Russia
[2] Moscow Institute for Radio Engineering, Electronics and Automation, Vernadskogo 78, Moscow 119454, Russia

Abstract. The laser characteristics of electron beam pumped semiconductor ZnSe-based lasers consisted of a 0.6-m-thick superlattice waveguide involving 10 equidistantly placed CdSe/ZnSe quantum dot active layers has been studied in detail. The maximum values of an light output pulse power of 12 W and an efficiency of 8.5% per one facet at a wave-length of 542 nm have been obtained at room temperature. The ways to further improvements of the characteristics are discussed.

Introduction

The progress in physics and technology of semiconductor heterostructures determines a possibility of commercial fabrication of injection lasers in the near-IR, red and blue-violet ranges of the spectra. However, the commercial development of laser diodes emitting in green part of visible spectrum is currently impracticable due to the set of unresolved problems of fabrication of such lasers. Among these is the achievement of relatively high and stable p-type doping with the simultaneous maintenance of degradation stability of the laser structures based on wide-gap II–VI compounds. Nevertheless, green semiconductor lasers have a large number of potential applications such as optical communications, location and navigation systems, medicine applications etc.

Due to the no requirements of both contacts and p-n junction, the electron beam pumped (EBP) lasers looks very perspective for the development of semiconductor green lasers. Moreover, the maximum conversion efficiency of electron beam energy to light is as high as 30%. The non-equilibrium carriers are generated within the relatively high volume of the material, which, in turn, is governed by the penetration depth of the electron beam into the crystal as well as its cross-section. EBP laser provides the ability to vary the thickness of excited region and output light power within the wide range by adjusting the electron beam energy. The EBP laser also allows the wide-range modulation of light output power, the electronic control of the directivity diagram, and synchronization of light and pump pulses at a level of a part of nanoseconds. However, the applications of monocrystal-based EBP lasers are limited by both high threshold current density and energy of electron beam.

The possibility of using quantum-size ZnSe-based heterostructures for the EBP green lasers was demonstrated during the last few years. The compact laser device operating at $E_e = 10$ keV in pulsed mode with an average output power up to 30 mW has been realized at cryogenic temperatures [1]. The using of quantum-size heterostructures with short-period superlattice (SL) waveguide and single CdSe/ZnSe quantum dot (QD) active region has resulted in room-temperature lasing at $E_e < 5$ keV and extremely low threshold current density $j_{\text{th}} = 0.4$–0.5 A/cm^2 ($E_e = 8$–10 keV) [2]. The structure consisted of extended 0.4 μm-thick SL waveguide and three ZnSe/CdSe QD sheets has demonstrated laser generation with efficiency (per one facet) as high as ∼4% [3].

This paper present the latest results on fabrication and study of green EBP ZnSe-based laser heterostructure with 10 active CdSe/ZnSe QD sheets equidistantly placed within 0.6 μm-thick ZnSe/ZnSSe SL waveguide with the effectiveness of electron beam to light energy conversion up to 8.5% per facet.

1. Experiment

ZnMgSSe/ZnSSe/Zn(Cd)Se laser heterostructure has been grown by molecular beam epitaxy (MBE) pseudomorphically to GaAs(001) substrate via a GaAs buffer epilayer at growth temperature $T_s = 270$–280 °C. The structure consists on bottom and top $Zn_{0.9}Mg_{0.1}S_{0.15}Se_{0.85}$ cladding layers with the thickness of 1.65 μm and 20 nm, respectively, and the 2.4 nm-$ZnS_{0.15}Se_{0.85}$ / 0.9 nm-ZnSe SL waveguide with the whole thickness of ∼0.6 μm. The 10 CdSe/ZnSe QD sheets were placed equidistantly within the SL waveguide. The nominal thickness of CdSe layers is as high as 2.5 ML.

All measurements were carried out at room temperature in transverse excitation geometry. No reflecting coatings on the facets were used. The electron beam parameters were the followings: energy $E_e = 10$–30 keV, pulse duration time of ∼50 ns, repetition rate up to 10 Hz. The 0.25mm-size diaphragm has been used to limit the electron beam size in the direction normal to laser cavity axis. The lasing spectra were measured using CCD-rules-based recorder mounted at the output of MDR-2 monochromator. The calibrated coaxial photocell has been used to measure both the shape of light pulse and light output power.

2. Results and discussion

Figure 1 demonstrates the schematic energy diagram of the laser structure along with the spatial distribution of an electron beam losses within ZnSe at different electron beam energies (E_e). The lasing has been observed at the wavelength of 542 nm. The FWHM of the emission line is of ∼2–3 nm.

The dependencies of pulsed output power per facet on electron beam current (I_e) at different electron beam energies are

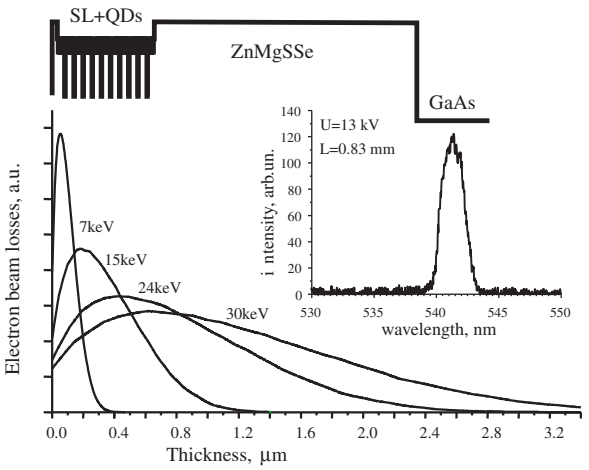

Fig. 1. Schematic energy diagram of the laser structure along with spatial distribution of an electron beam losses within ZnSe at different E_e (7, 15, 24, and 30 keV). The spectrum of laser generation at $E_e = 13$ keV is shown in the inset.

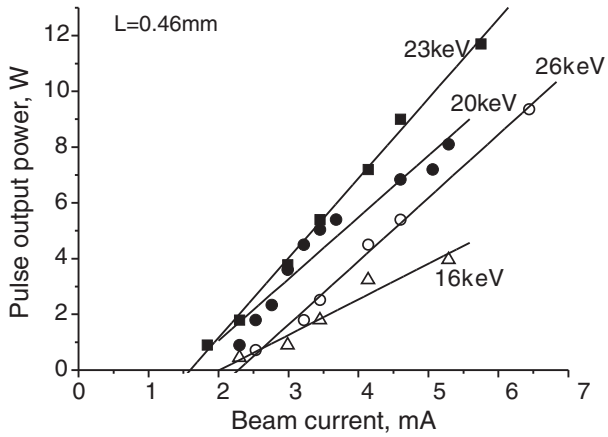

Fig. 2. The dependencies of pulse output power on electron beam current registered at different E_e.

presented in Fig. 2. The cavity length and the width of laser crystal are $L = 0.46$ mm and $d = 0.25$ mm, respectively. The maximum output power of 12 W has been obtained at $E_e = 23$ keV.

Figure 3 demonstrate the dependence of emission efficiency per a facet on electron beam current at an electron beam energy of 23 and 26 keV, respectively. The maximum registered efficiency (8.5%) has been obtained at electron beam energy of 23 keV and electron beam current $I_e = 5.7$ mA. To obtain the real value of efficiency we should multiple twice the recorded value taking account of two laser facets. The main reason of the increase of laser efficiency is likely the more effective utilizing of pumping energy due to the adjustment of structure geometric parameters and penetration depth of electron beam into the sample. The dependencies presented in Fig. 2 demonstrate no saturation of light output power with the increase of electron beam current, though the values of I_e were raised (at any E_e) to its maximum values, which are the characteristics of the electron gun used for pumping. Presumably the increase of I_e keeping constant their energy E_e should allow the further increase of light output power. The optimum number of active CdSe QD sheets to reach maximum light output power and

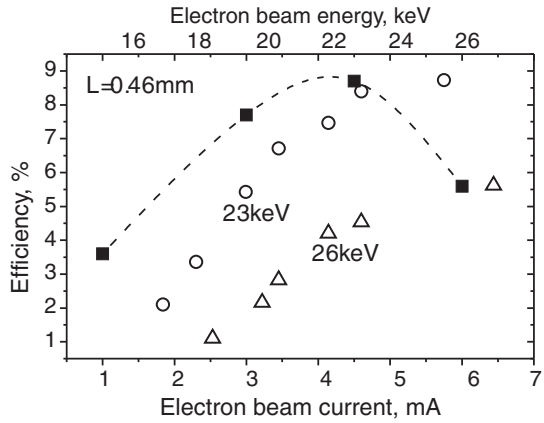

Fig. 3. The dependence of emission efficiency on electron beam current (bottom scale) at an electron beam energy of 23 (white circles) and 26 keV (white triangles), respectively. The filled squares reflects the dependence of maximum emission efficiency on electron beam energy (top scale).

efficiency is also under consideration. Anyway, the optimum number of QD sheets will depends both on working energy of an electron beam matched to the thickness of the waveguide and carrier diffusion length because of the latter should be less the distance between the neighbor QD sheets.

The dependence of maximum value of efficiency on electron beam energy is also shown in Fig. 3 (black squares). The maximum is corresponded to $E_e = 23$ keV. The decrease of the efficiency could be explained by a loss of a part of pumping energy within the GaAs substrate at higher E_e (see Fig. 1).

Summarizing, the emission parameters of EBP ZnSe-based lasers with the SL waveguide and 10 CdSe/ZnSe QD sheets in the active region have been studied in detail. The pulsed output power of 12 W per facet along with extremely high value of efficiency ~8.5% has been obtained at electron beam energy of 23 keV and electron beam current $I_e = 5.7$ mA.

Acknowledgements

The work was partly supported by RFBR grants, ISTC — Project No. 3754 and FASI Program.

References

[1] D. Herve, R. Accomo, E. Molva, L. Vanzetti, J. J. Paggel, L. Sorba, A. Francioci, *Appl. Phys. Lett.* **67 (15)**, 9, 2144 (1995).

[2] M. M. Zverev, N. A. Gamov, E. V. Zhdanova, D. V. Peregudov, V. B. Studenov, S. V. Ivanov, I. V. Sedova, S. V. Sorokin, S. V. Gronin and P. S. Kop'ev, *Tech. Phys. Lett.* **33(12)**, 1032 (2007).

[3] M. M. Zverev, S. V. Sorokin, I. V. Sedova, S. V. Ivanov, D. V. Peregudov, P. S. Kop'ev, *Phys. Stat. Sol. (c)* **2**, 923 (2005).

16th Int. Symp. "Nanostructures: Physics and Technology"
Vladivostok, Russia, July 14–18, 2008

Optical properties of MBE grown Cr^{2+}:ZnSe layers and Cr^{2+}:ZnSe/ZnMgSSe waveguide structures for mid-IR lasers

A. O. Zabezhaylov, S. V. Alishev, R. A. Mironov, S. A. Vasiliev, M. V. Grekov and E. M. Dianov
Fiber Optics Research Center, Russian Academy of Sciences, 119333 Moscow, Russia

Abstract. The results of photoluminescence study of Cr^{2+}:ZnSe epitaxial layers in the spectral range of 2–3 μm at room temperature are presented. The films were grown by MBE on GaAs substrates by using CrSe compound as a chromium dopant source. The optimal Cr concentration in the Cr^{2+}:ZnSe epitaxial layers for achieving bright mid-IR emission was found to be $10^{18} - 10^{19}$ cm^{-3}. According to our measurements the Cr^{2+} emission lifetime in these layers was about 5 μs. Optically active Cr^{2+}:ZnSe/ZnMgSSe waveguide structures with total thickness of about 5 μm were prepared and characterized.

Introduction

One of the best choices for affordable 2–5 μm mid-infrared sources is wide-bandgap II–VI compound semiconductors doped with divalent transition metal ions (TM^{2+}) [1]. Nanostructures based on TM^{2+}:II–VI are the promising laser media not only for optical but also for direct electrical pumping [2,3]. In spite of successful demonstration optically active Cr^{2+}:II–VI epitaxial layers [4,5] the waveguide-confinement structures have not been fabricated yet. There are some difficulties to grow ZnMgSSe cladding layers matched to GaAs substrate and having thickness high enough for efficient light guiding in mid-IR region. In this work we report the results of our study of photoluminescence (PL) properties of Cr- doped ZnSe epilayers and waveguiding parameters of ZnSe(ZnSSe)/ZnMgSSe structures grown by molecular beam epitaxy (MBE).

1. Experimental

A series of undoped and Cr- doped ZnSe epilayers and ZnSe/ZnMgSSe structures were grown in a MBE system with solid Zn, Se, Mg, ZnS sources on undoped 40 mm diameter semi-insulating GaAs (100) substrates. Chromium incorporation was performed from a crucible based effusion cell containing CrSe. The CrSe compound is sublimated better than metallic Cr, and therefore the application of CrSe allows one to reduce the undesirable substrate heating due to thermal radiation of molecular sources [6]. The 300–700 nm thick ZnSe buffer layers followed the 1000–2000 nm thick Cr:ZnSe layers were grown at the growth temperature of 300 °C. The growth rate was 0.5–0.8 μm/h. The doping concentration was controlled by varying the temperature of the CrSe source. The Zn/Se flux ratio was adjusted to ensure stoichiometric or slightly Se- rich growth conditions that were proved by the appropriate surface reconstructions.

Waveguide structures were grown at 280 °C under closely stoichiometric conditions. The waveguide structure is schematically shown in Fig. 1. The ZnMgSSe solid solution with energy gap $E_g \approx 2.9$ eV and lattice-matched to GaAs was used as a cladding layer. Active waveguide layers were made of both Cr:ZnSe and closely lattice matched Cr:ZnSSe. Thicknesses of the cladding and waveguide layers were 1–2 and 2–3

PL spectra at $^5E \rightarrow {}^5T_2$ mid-IR transition of Cr^{2+} ions have been measured using an optical monochromator and a PbS detector. A lock-in-amplifier connected to a computer has been used to measure the PL signal. Emission of CW Er/Yb-doped double-clad fiber laser ($\lambda = 1600$ nm) has been modulated with the help of mechanical chopper ($f = 450$ Hz) and used for PL excitation.

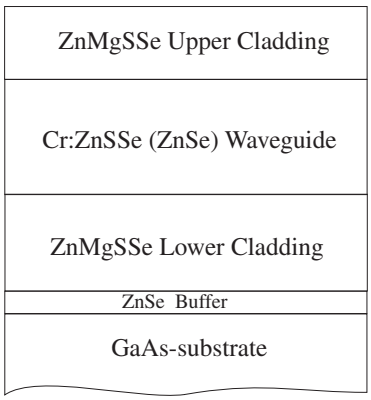

Fig. 1. Schematic drawing of the Cr:ZnSe(ZnSSe)/ZnMgSSe waveguide structure.

2. Results

Laser mass-spectroscopy and electron probe micro-analysis (EPMA) of Cr:ZnSe layers showed that the Cr concentration was $10^{18} - 10^{21}$ cm^{-3}. Incorporation of Cr in the active Cr^{2+} state in thin MBE grown epilayers was further verified by the comparison of the PL spectra of thin films with the spectra measured in bulk Cr^{2+}:ZnSe samples. All PL measurements of series Cr:ZnSe-based epilayers were studied with the same geometry and the laser power. Thus it was possible to compare the PL intensity normalized to the thickness of the different samples. Infrared PL spectra measured for some our films are depicted in Fig. 2 together with the spectrum obtained for the bulk crystal.

It is seen that the spectra of thin films and bulk crystal are quite similar, indicating that Cr has been successfully incorporated in MBE grown thin films in active Cr^{2+} state. The difference of the PL spectra for thin films and the bulk crystal is explained by the presence of interference in a Fabry–Perot cavity formed by the film interfaces [5]. The positions of the interference extremums occurred at different wavelengths due to different thickness of the epilayers.

The PL kinetics was measured at room temperature using Q-switched fiber laser ($\lambda = 1600$ nm) with 50 ns pulse dura-

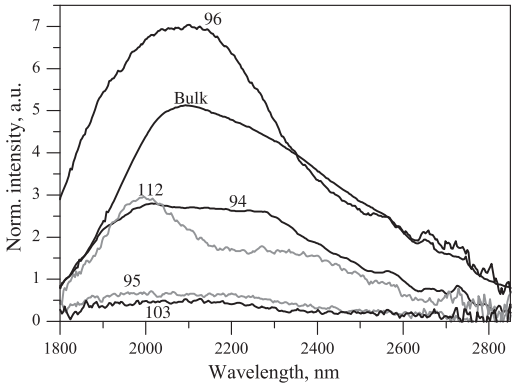

Fig. 2. Room temperature PL spectra of the ${}^5E \rightarrow {}^5T_2$ transition of Cr^{2+} ions in Cr:ZnSe epilayers and bulk crystal with different Cr concentration: 2×10^{18} cm^{-3} (112); 1×10^{19} cm^{-3} (96); 2×10^{19} cm^{-3} (94); 5×10^{19} cm^{-3} (95); 2×10^{20} cm^{-3} (103); and 5×10^{19} cm^{-3} (Bulk).

tion and 10–15 μJ pulse energy. A liquid-nitrogen cooled InSb detector with a time response of 0.5 μs was used to perform time-resolved measurements of the PL intensity in all wavelength range (2–3.2 μm).

Thickness normalized PL intensities (at $\lambda \sim 2000$ nm) and PL decay times for Cr^{2+}:ZnSe epilayers with different dopant concentration are shown in Fig. 3. PL decay times of epilayers were agreed with that reported for bulk crystals having similar dopand concentrations [7]. It should be noted that PL intensity and decay time are quenched for Cr concentration larger than 10^{19} cm^{-3} indicating that non-radiative recombination should be taken into consideration at such ion concentrations and this phenomenon limits the population of the excited Cr^{2+} levels. The optimal chromium concentration for mid-infrared Cr^{2+} emission was found to be $10^{18} - 10^{19}$cm^{-3}.

To study Cr-related PL in waveguide structures the stripes with dimensions 5×0.5 mm were cleaved out from the samples. The pump beam was precisely focused on the edge of the shorter cleaved structure side. To compare the PL spectra and the emission intensities of the waveguide structures and single epilayers the same methods of sample preparation were used for epilayers. The PL signal was collected by the lens from the opposite side of the sample. The Cr-related PL intensities in waveguide structures were measured to be more than one order of magnitude higher than for the epilayers with the same dopant concentration.

We found that the PL intensity measured in waveguides linearly depends on the input CW pump power. We failed to observe any line narrowing of the luminescence that could indicate stimulated processes in the waveguide structure in spite of the presence the Fabry–Perot cavity formed by the cleaved waveguide endfaces. The same result was observed for pulsed-light excitation. In our opinion the main reason of this failure is a high optical losses due to relatively large substrate refractive index. Application of thicker ($\sim 3\mu$m) ZnMgSSe lower cladding layers and/or ARROW structures would help to overcame this problem [8].

In conclusion, measurements of mid-IR photoluminescence spectra of MBE grown epitaxial layers Cr^{2+}:ZnSe and waveguide structures Cr^{2+}:ZnSe/ZnMgSSe in the spectral range 2–3 μm at room temperature were performed. The optimal Cr concentration in Cr^{2+}:ZnSe epitaxial layers for achieving bright mid-IR emission was defined to be from 10^{18} to 10^{19} cm^{-3}. Optically active Cr^{2+}:ZnSe/ZnMgSSe waveguide structures with total thickness of about 5 μm were produced. The Cr-related PL intensities in waveguide structures were measured to be more than one order of magnitude higher than for the epilayers with the same dopant concentration.

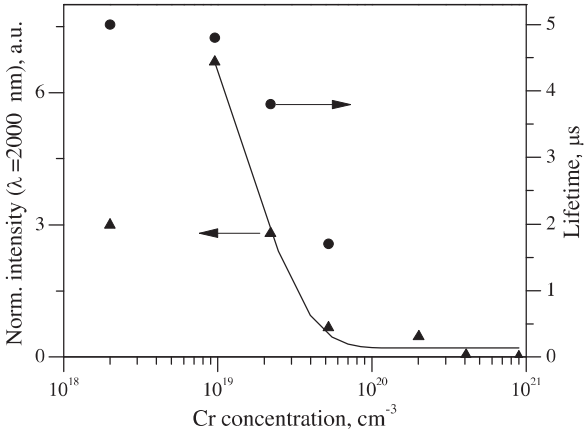

Fig. 3. Thickness normalized PL intensities (at $\lambda \sim 2000$ nm) and decay PL lifetime of Cr^{2+} ions for Cr:ZnSe epilayers with different Cr concentration.

Acknowledgements

The study was supported by the Russian Foundation for Basic Research, Grant 05-02-08176.

References

[1] L. D. DeLoach *et al*, *IEEE J. Quant. Electron* **32**, 885 (1996).
[2] A. Gallian *et al*, *Appl. Phys. Lett.* **86**, 091105 (2005).
[3] S. B. Mirov *et al*, *IEEE J. of Sel. Top. In QE* **13**, 810 (2007).
[4] M. Luo *et al*, *Appl. Phys. Lett.* **97**, 013518 (2005).
[5] I. P. Kazakov *et al*, *Int. J. of Nanoscience* **6**, 00448 (2007).
[6] Y. G. Sadofyev *et al*, *J. Vac. Sc. & Tech. B* **19**, 1483 (2001).
[7] V. E. Kisel *et al*, *Optics and Spectroscopy* **99**, 663 (2005).
[8] R. A. Mironov, A. O. Zabezhaylov *et al*, *to be published*.

16th Int. Symp. "Nanostructures: Physics and Technology"
Vladivostok, Russia, July 14–18, 2008

Single photon solid state emitters

V. A. Haisler
Institute of Semiconductor Physics, Novosibirsk, Russia

Abstract. In this contribution the recent progress in the development of the single photon emitters based on the semiconductor quantum dots is reviewed. The special attention is given to the development of the electrically driven single quantum dot single photon sources, which are very attractive for the practical implementation of the efficient light emitters for the quantum cryptography and quantum computing systems.

Introduction

The ideal single photon emitter (SPE) is determined as a device that, when one pulls the trigger, and only then, emits one and only one photon [1–3]. In such a way the another name of SPE is a photon gun. The ideal SPE generates nonclassical light states or photon Fock states. A mode which is excited in Fock states is occupied by exactly N photons and the variance $N = 0$, as distinct from photon Glauber states which are generated by classical light sources there the photon number distribution is determined by Poisson statistics. The efficient single photon emitters are in demand for the implementation of quantum cryptography and quantum computing systems as well as for the realization of the precise optical power standards and the precise spectroscopic systems [1–3]. Starting with the first observation of a sub-Poisson photon statistics (antibunchig phenomenon) using the single atoms [4,5], a large number of studies on single photon emission have been carried out for a wide variety of isolated quantum systems including single atomic ions, single dye molecules, single crystal defects and semi-conductor quantum dots (QDs) [2,6–8]. In semiconductor QDs, photon emission originates from the decay of exciton, biexciton or trion QDs states. Semiconductor QDs offer the advantages of narrow spectral linewidth, optical stability, wide tunability of wavelengths and the possibility of the electrical excitation in contrast to all other mentioned above isolated quantum systems where only the optical pumping is possible. An electrical excitation is required to allow for the fabrication of integrated compact devices and to avoid large-scale external pump sources. Moreover, semiconductor QDs can be easily embedded into an appropriate semiconductor microcavity in order to achieve a high external quantum efficiency of SPE. A single photon emission has been demonstrated for a wide variety of isolated semiconductor QDs such as GaN/AlN, InGaN/GaN, CdSe/ZnS, InP/GaInP, InAs/GaAs and InAs/InP QDs [2,9–12]. The obvious advantage of the wide bandgap QDs is a possibility of a single photon emission at relatively high temperatures. A single photon emission at 200 K has been demonstrated for GaN/AlN, CdSe/ZnS QDs systems. The indisputable advantages of InAs QDs systems is a possibility of a creation of the miniature and efficient completely solid state electrically driven SPE for a near infrared wavelength range including a telecom wavelength range 1.3–1.55 μm [2,5,13–18].

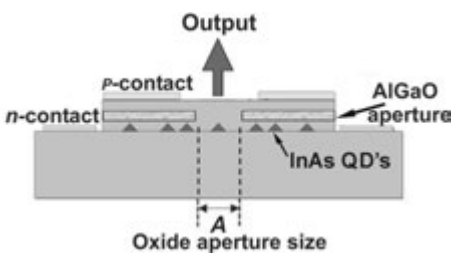

Fig. 1. Schematic cross section of the device structure.

1. Electrically driven InAs QDs SPE

A promising approach for single-photon generation based on electrical pumping uses a micronsize aluminumoxide aperture to restrict the current flow to a single quantum dot. Thus, electrical excitation of more than one dot was significantly suppressed, and non-classical statistics of the electroluminescence was measured. The structure of electrically driven InAs QDs SPE developed in [13-15] is shown in Fig. 1.

The *pin*-structure consists of an undoped GaAs layer with a low density layer of InAs QDs, a 60 nm thick aperture layer of high aluminium content AlGaAs, and p- and n-type GaAs electrical contact layers. To reduce the influence of current spreading, the distance between the AlGaAs aperture layer and the InAs QDs layer is minimized down to only 20 nm. The structures were grown by Riber-32P MBE system on semi-insulating (100) epi-ready GaAs substrates. The low density (10^8 cm^{-2}) InAs QDs layers were grown in the Stranski–Krastanow mode with deposition of 1.8 ML of InAs. The growth rate and the ratio of As to In were kept at 0.04 ML/s and 50, respectively. All layers were grown at $T = 580\,^{\circ}$C, except the QD layer which was grown at $T = 510\,^{\circ}$C. Cylindrical mesas were processed by inductively coupled plasma reactive ion etching, using chlorine based recipes. The submicron size oxide current apertures were created by selective oxidation of the high aluminium content aperture AlGaAs layers. Tapered oxide current apertures were used to enhance the stability of the oxide structure and to improve the injection characteristics of the electrically driven SPE. The oxidation was performed in a H_2O-N_2 environment at $T = 420\,^{\circ}$C. After the selective oxidation, SiN_x deposition was performed, followed by Au/Pt/Ti and Au/Au-Ge/Ni metallization to form p- and n-contacts, respectively. The electroluminescence spectrum of the device with 0.85 μm oxide aperture at continuous wave current injection (870 pA, 1.65 V) and a temperature of 10 K shows super monochromatic light emission (Fig. 2), what demonstrates a high efficiency of the electrical excitation. Line X in the electroluminescence spectrum corresponds to decay of exciton in a single InAs quantum dot.

No other emission is observed in a spectral range of 550 to

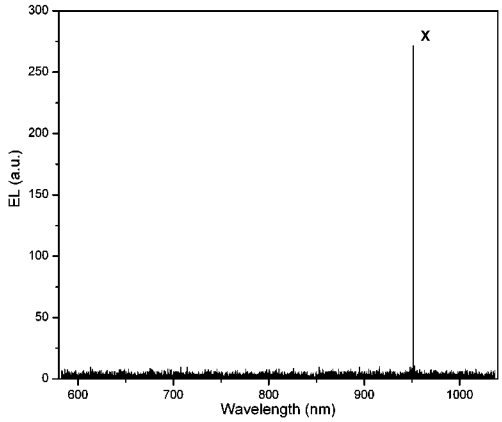

Fig. 2. Electroluminscence spectrum at a current of 870 pA and 1.65 V bias voltage.

1050 nm, even no wetting layer or GaAs, AlGaAs bulk emission is detected. At current higher 0.9 nA, a few additional biexciton and trion lines appear. Non-classical photon statistics was characterized by the second-order intensity correlation function via a Hanbury–Brown and Twiss setup (HBT) [2] consisting of a 50:50 beam splitter and two avalanche photo diodes (APDs). In contrast to all previous HBT setups related to quantum dot experiments, no spatial or spectral filtering of the exciton line was needed (except a 10 nm FWHM band pass filter centered at 953 nm in front of one APD to avoid cross-talk between the detectors). The measured autocorrelation function contains a clear dip at zero time delay, what proves that developed InAs quantum dot diode with a submicron oxide aperture represents indeed an ideal electrically pumped single-photon emitter [13–15].

2. DBR microcavity for electrically driven QD SPE

One of the most important parameter of SPE is an external quantum efficiency. External quantum efficiency of *pin* SPE described above is only $\sim 10^{-2}$ due to a total internal reflection. The emission of electrically driven QDs SPE can be enhanced and directed into distinctive modes by using semiconductor distributed Bragg reflectors (DBR) microcavity. In that case the structure of the electrically driven QDs SPE will be similar to a resonant cavity light emitting diode (RCLED) structure or a vertical-cavity surface-emitting laser (VCSEL) structure [2,19]. The structure of such RCLED-type electrically

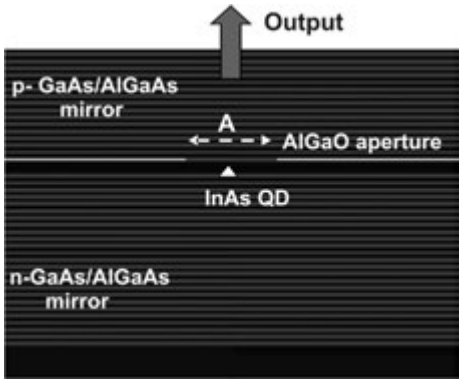

Fig. 3. Schematic cross section of RCLED-type electrically driven QDs SPE.

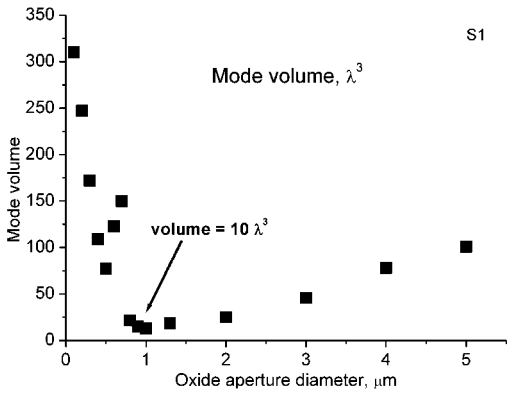

Fig. 4. Fundamental mode volume (in λ^3 units) vs oxide aperture diameter.

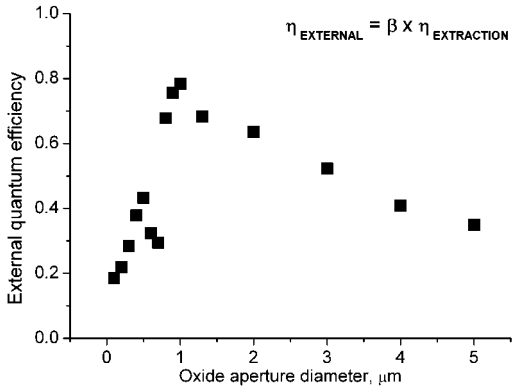

Fig. 5. External quantum efficiency vs oxide aperture diameter.

driven QDs SPE is shown in Fig. 3. The structure contains 1λ thick cavity with one low density InAs QDs layer, top output 10 pairs GaAs/AlGaAs DBR, bottom 25 pairs GaAs/AlGaAs DBR and high Al content aperture layers above QDs layer. The following parameters of fundamental mode of this microcavity have been calculated: 1) quality factor Q, 2) mode volume V, 3) Purcell factor F_{P}, 4) mode wavelength λ, 5) spontaneous emission coupling factor β [2] and 6) external quantum efficiency η_{ext}.

This microcavity was designed to $\sim$965 nm resonance wavelength (at room temperature). The quality factor of a fundamental mode in this microcavity and resonance dip width are $\sim 10^3$ and $\sim$1 nm, correspondingly. Mode volume is a non-monotonic function of an oxide aperture size (Fig. 4).

A minimum of mode volume $\sim 10\lambda^3$ is achieved at oxide aperture diameter ~ 1 μm, correspondingly, the maximum of Purcell factor F_{P} and maximum of spontaneous emission coupling factor are achieved at the same oxide aperture diameter, $F_{\mathrm{P}}^{\max} \sim 5$ and $\beta_{\max} \sim 0.83$. The final dependence of the external quantum efficiency vs oxide aperture diameter is presented in Fig. 5. This function contains a clear maximum at oxide aperture diameter ~ 1 μm and parameter of the external quantum efficiency achieves a level of 80 percents.

In conclusion, the presented experimental and simulation data demonstrate the possibility of a creation of new miniature completely solid state electrically driven QDs SPE without spectral filtering with the external quantum efficiency as high as 0.8.

Acknowledgements

This work has been supported in part by NATO Science for Peace grant ICS.NR.NRSFPP982735.

References

[1] D. Bouwmeester, A. Ekert and A. Zeilinger (ed.), *The Physics of Quantum Information: Quantum Cryp-tography, Quantum Teleportation, Quantum Computation* (Berlin Heidelberg New York: Springer-Verlag), p. 315, (2001).

[2] P. Michler (ed.) *Single Quantum Dots: Fundamentals, Applications and New Concepts* (Berlin Heidelberg New York: Springer-Verlag), p. 352, (2003).

[3] M. Grundmann, *The Physics of Semiconductors: An Introduction Including Devices and Nanophysics*, (Berlin Heidelberg New York: Springer-Verlag), p. 689, (2006).

[4] H. J. Kimble, M. Dagenais, L. Mandel, *Phys. Rev. Lett.* **39**, 691 (1977).

[5] K. Takemoto, M. Takatsu, S. Hirose *et al*, *J. Appl. Phys.* **101**, 081720 (2007).

[6] F. Diedrich and H. Walther, Phys. *Rev. Lett.* **58**, 203 (1987).

[7] B. Lounis and W. E. Moerner, *Nature* **407**, 491 (2000).

[8] C. Kurtsiefer, S. Mayer, P. Zarda, H. Weinfurter, *Phys. Rev. Lett.* **85**, 290 (2000).

[9] C. Santori, S. Gotzinger, Y. Yamamoto, S. Kako, K. Hoshino and Y. Arakawa, *Appl. Phys. Lett.* **87**, 051916 (2005), *Nature*, 22 October, 1 (2006).

[10] K. Sebald, P. Michler, T. Passow, D. Hommel, G. Bacher, A. Forchel, *Appl. Phys. Lett.* **81**, 2920 (2002).

[11] A. F. Jarjour, R. A. Taylor, R. A. Oliver, M. J. Kappers, C. J. Humphreys, A. Tahraoui, *Appl. Phys. Lett.* **91**, 052101 (2007).

[12] V. Zwiller, T. Aichele, W. Seifert, J. Persson and O. Benson, *Appl. Phys. Lett.* **82**, 1509 (2003).

[13] A. Lochmann, E. Stock, O. Schulz, F. Hopfer, D. Bimberg, V. A. Haisler, A. I. Toropov, A. K. Bakarov, A. K. Kalagin, *Electronics Letters* **42**, 774 (2006).

[14] A. Lochmann, E. Stock, O. Schulz, F. Hopfer, D. Bimberg, V. A. Haisler, A. I. Toropov, A. K. Bakarov, M. Scholz, S. Buttner, O. Benson, *phys. stat. sol.(c)* **4**, 547 (2007).

[15] M. Scholz, S. Buttner, O. Benson, A. I. Toropov, A. K. Bakarov, A. K. Kalagin, A. Lochmann, E. Stock, O. Schulz, F. Hopfer, V. A. Haisler, D. Bimberg, *Optics Express* **15**, 9107 (2007).

[16] D. J. P. Ellis, A. J. Bennett, A. J. Shields *et al*, *Appl. Phys. Lett.* **88**, 133509 (2006).

[17] D. J. P. Ellis, A. J. Bennett, A. J. Shields *et al*, *Appl. Phys. Lett.* **90**, 233514 (2007).

[18] M. B. Ward, T. Farrow, P. See *et al*, *Appl. Phys. Lett.* **90**, 063512 (2007).

[19] H. E. Li, K. Iga (ed.) *Vertical-Cavity Surface-Emitting Laser Devices*, (Berlin Heidelberg New York: Springer-Verlag), p. 365, (2003).

16th Int. Symp. "Nanostructures: Physics and Technology"
Vladivostok, Russia, July 14–18, 2008

High-power wavelength stabilized laser based on the tilted cavity concept

L. Ya. Karachinsky[1,2], I. I. Novikov[1], G. Fiol[2], M. Kuntz[2], Yu. M. Shernyakov[1], N. Yu. Gordeev[1], M. V. Maximov[1], M. B. Lifshits[1], T. Kettler[2], K. Posilovic[2], V. A. Shchukin[1,2], N. N. Ledentsov[1,2], S. S. Mikhrin[3] and D.Bimberg[2]

[1] Ioffe Physico-Technical Institute, St Petersburg, Russia
[2] Technische Universität Berlin, Institut für Festkorperphysik and Center of NanoPhotonics, EW 5-2, 10623 Berlin, Germany
[3] Innolume GmbH, Konrad-Adenauer-Allee 11, 44263 Dortmund, Germany

Abstract. We studied wavelength stabilized all-epitaxial 970-nm spectral range Tilted Cavity Lasers (TCLs). Optical cavity of a TCL favors propagation of only one tilted optical mode ensuring wavelength-selective operation. The possibility of full control of the thermal shift of the lasing wavelength $d\lambda/dT$ in TCL including positive, zero or negative shift, is proved theoretically. Broad-area (100 μm) devices have been fabricated showing a high temperature stability of the lasing wavelength (0.13 nm/K), a high power operation (>7 W in pulsed mode and >1.5 W in continuous wave (cw) mode), and a narrow vertical far-field beam divergence (FWHM ∼20°). Single transverse mode edge-emitting 4 μm wide ridge TCLs demonstrated high-power spatial and spectral single mode cw operation with a longitudinal side mode suppression ratio (SMSR) up to 41.3 dB.

Introduction

Wavelength-stabilized lasers are required for a wide range of applications, such as pumping of Er- and Yb-doped fibres at about 975 nm, solid state laser pumping at 808 nm, frequency conversion at 1060 nm and 920 nm and in telecom for wavelength division long haul transmission in multiplexing (WDM) etc. Currently used approaches for stable wavelength operation are either relatively expensive (e.g., external cavity optical disc lasers) and/or of relatively low power (single-mode distributed feedback (DFB) lasers, volume fiber grating-coupled lasers). To overcome these deficiencies and create a low cost all-epitaxial wavelength-stabilized device the Tilted Cavity Laser (TCL) concept has been recently proposed [1]. A TCL combines the advantages of an edge-emitting laser (high power operation) and a VCSEL (high temperature stability of the lasing wavelength) and is based on the resonance properties of multilayer structures revealed in optical reflectivity spectra at tilted incidence of light [2–4]. In this paper we report on the possibility of full control of the thermal shift of the lasing wavelength in TCL and also on experimental high-power high temperature stability operation of the TCLs (lasing wavelength shift 0.13 nm/K) and high-power spatial and spectral single mode continuous wave (cw) operation with a longitudinal side mode suppression ratio (SMSR) up to 41.3 dB.

1. Approach to control the thermal shift of the lasing wavelength

The possibility to control $d\lambda/dT$ is related to a strongly nonlinear dependence of the refractive index thermal coefficient dn/dT on alloy composition x, e.g. for $Ga_{1-x}Al_xAs$, when the energy band gap comes close to the photon energy. Thus, at 975 nm, dn/dT dramatically increases for pure GaAs as compared to GaAlAs. This allows replacing one or a few GaAlAs layers in a TCL by a GaAs/GaAlAs superlattice (SL), as shown in Fig. 1, by keeping the same average refractive index n_{av} at room temperature [2]. Then the thermal coefficient

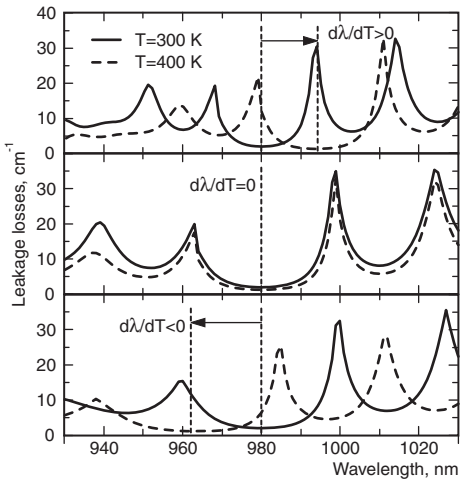

Fig. 1. Positive, zero, and negative thermal shift of the TCL lasing wavelength.

dn_{av}/dT can be strongly varied. For different realizations of a superlattice, the leakage loss minimum that governs the lasing wavelength may exhibit positive, zero or negative shift upon temperature (Fig. 1).

2. Experiment

The epitaxial structure was grown using molecular beam epitaxy (MBE) on a Si-doped GaAs (001) substrate (Fig. 2). The multilayer interference reflector (MIR) consists of 17 periods of a 448-nm $Ga_{0.8}Al_{0.2}As$ / 150-nm $Ga_{0.4}Al_{0.6}As$. The n-doped part of the cavity contains 105 periods of a 3-nm GaAs / 22-nm $Ga_{0.2}Al_{0.8}As$ superlattice (SL), the p-doped part consists of 1620-nm $Ga_{0.2}Al_{0.8}As$ layer, covered by the 300-nm GaAs contact layer. The active area includes two InGaAs QWs. The epitaxial wafer was processed into $W = 100$ and 4 μm wide ridge lasers with various cavity lengths and as cleaved facets. The lasers were characterized in wide temperature and pump current range in pulsed mode (300 ns, 1 kHz) and cw mode.

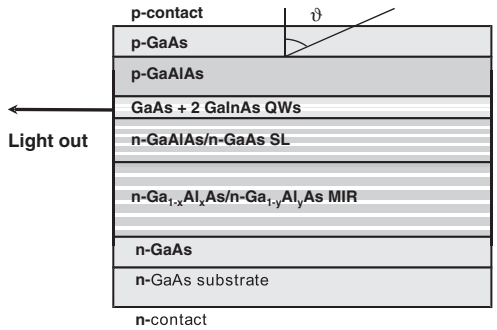

Fig. 2. Cross-sectional view of the TCL.

3. Results and discussion

Fig. 3 depicts lasing of a 2000 μm cavity length broad area TCL, which occurs in a tilted cavity mode in a broad temperature range revealing a weak temperature shift of 0.13 nm/K versus 0.4 nm/K for conventional 975 nm-range GaInAs/GaAs edge-emitters. TCL also shows a low threshold current density at room temperature (300 A/cm^2) and good temperature stability, where the characteristic temperature T_0 is 270 K below 50 °C and 75 K in the temperature range 50–150 °C. The 2000 μm cavity length broad-area TCL demonstrates a high power pulsed operation (>7 W). The cw operation is limited by catastrophic optical mirror damage (COMD) accelerated by Joule heat due to a high contact resistance of the laser (10^3 Ωcm^2). Thus, the maximum total optical output power >1.5 W is achieved in cw mode, which indicates a very good potential of the device with further optimization of the resistance. The full width at half maximum (FWHM) of the vertical far field pattern both below and above lasing threshold was found about 20°, in agreement with the modeled beam divergence of the tilted cavity optical mode.

Narrow 4 μm wide ridge TCL with a cavity length of $L = 870$ μm under cw excitation at 23 °C heat sink temperature showed a maximal total optical output power of 150 mW, limited by thermal rollover (Fig. 4). The far field pattern measured in the direction parallel to *p-n* junction clearly proved single mode emission of the laser. Inset in Fig. 4 shows the spectrum of the 4 μm wide ridge laser with a cavity length of $L = 870$ μm for a cw current of $I = 190$ mA at 23 °C. It can be seen that 41.3 dB SMSR was achieved at a total output power of 93 mW. Such a result is similar to the range of values achieved for DFB lasers in the same spectral range [5], while at the same time TCL laser fabrication benefits from a much simpler and robust processing. With increase of the pump current above $I = 190$ mA the SMSR decreases. It is still possible to achieve the high value of 26 dB even at a current of 290 mA, when the total output power is 142 mW.

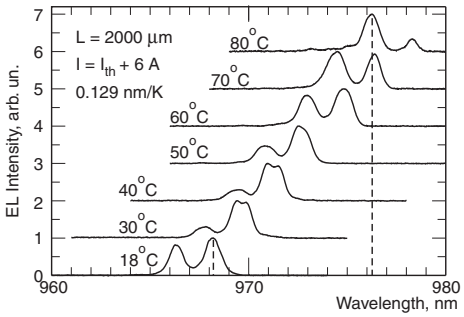

Fig. 3. EL spectra of the TCL ($L = 2000$ μm) at different temperatures under pulsed excitation far beyond the lasing threshold $I_{\text{th}} = 0.6$ A ($I = I_{\text{th}} + 6$ A).

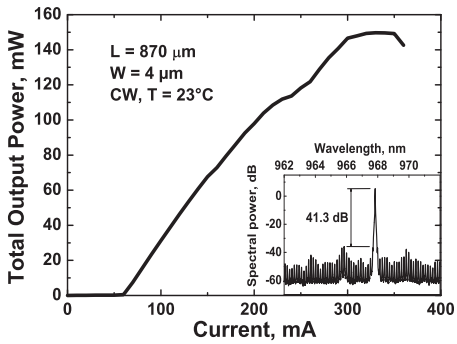

Fig. 4. CW Light-Current characteristic of a 4-μm wide ridge TCL ($L = 870$ μm) at 23 °C. The insert shows a spectrum of a laser at the output power 93 mW.

4. Conclusion

We have demonstrated that tilted cavity laser (TCL) provides the possibility of full control of the thermal shift of the lasing wavelength: positive, zero, or negative thermal shift can be realized. We have shown the operation of the 970 nm range TCL with a high temperature stability of the lasing wavelength (0.13 nm/K), low threshold current density (300 A/cm^2), a high power operation (>7 W in pulsed mode and >1.5 W in cw mode), and a narrow vertical far-field beam divergence (FWHM ∼20°). We have also shown single spatial and spectral mode cw operation of a narrow stripe TCL. A high side mode suppression ratio up to 41.3 dB has been achieved at 93 mW output power. Such a result is similar to the best values achieved for DFB lasers in the same spectral range, while no etching and overgrowth is used in our case. The results obtained indicate that TCLs are promising candidates for low cost high-power single mode 970 nm range edge emitters with a narrow beam divergence.

Acknowledgements

The work was supported by the German CoE NanOp, funded by BMBF, DFG (SFB 787), EU Project 'SANDiE' (NMP4-CT-2004-500101), SPbRC RAS, St Petersburg Government and RFBR. LYaK acknowledges the President grant (MK-4232. 2007.2) and the Alexander von Humboldt Foundation. IIN acknowledges the President grant (MK-5162.2008.2).

References

[1] N. N. Ledentsov, V. A. Shchukin, *Opt. Eng.* **41**, 3193 (2002).
[2] M. B. Lifshits *et al*, *Semicond. Sci. Techn.* **22**, 380 (2007).
[3] V. A. Shchukin *et al*, *Semicond. Sci. Techn.* **22**, 1061 (2007).
[4] L. Ya. Karachinsky *et al*, *Appl. Phys. Lett.* **91**, 241112 (2007).
[5] H. Wenzel *et al*, *IEEE Photon. Technol. Lett.* **18**, 737 (2006).

16th Int. Symp. "Nanostructures: Physics and Technology"
Vladivostok, Russia, July 14–18, 2008

Circular polarized electroluminiscence in diodes with InGaAs/GaAs quantum wells and Mn δ-layer

S. V. Zaitsev[1], M. V. Dorokhin[2], Yu. A. Danilov[2], P. B. Demina[2], V. D. Kulakovskii[1] and B. N. Zvonkov[2]

[1] Institute of Solid State Physics, Russian Academy of Sciences, 142432 Chernogolovka, Russia
[2] Physical-Technical Research Institute, N. I. Lobachevskii University, 603950 Nizhny Novgorod, Russia

Abstract. Strong enhancement of electroluminescence intensity and high degree of its circular polarization (up to 50% at low temperature $T = 1.5$ K and magnetic field $B = 9$ T) are demonstrated in Schottky diodes with near contact InGaAs/GaAs quantum wells and Mn δ-layer. High values of polarization are suggested due to effective exchange interaction of holes with magnetic moments of Mn atoms in the nearby δ-layer.

Introduction

A unique combination of magnetic properties in diluted magnetic semiconductor (DMS) makes them very interesting for different spintronics applications [1]. (Ga,Mn)As is extremely attractive after discovering of ferromagnetism in this DMS compound with a record value of the FM transition temperature T_c in epi-layers of 173 K [2]. Mn atom in (Ga,Mn)As acts not only as a local magnetic moment but also as an acceptor in the Ga cation position which results in appearance of the free holes [2]. The main difficulty to achieve high T_c is a technological problem to introduce Mn exactly to the cation sublattice and obtain high hole concentration. Despite microscopic FM mechanisms in (Ga,Mn)As are still discussed, at present it is convincingly shown that free holes and/or holes in acceptor zone play determining role in formation of FM state, interacting with magnetic atoms [2]. Introducing of a two-dimentional (2D) channel by means of δ-doping with Mn allowed to increase T_c up to 250 K due to combined effect of enlarged overlap of high concentration 2D-holes with the Mn δ-layer [3]. What is especially important for applications, the layers of (Ga,Mn)As can be used for injection of spin-polarized holes in light emitting diodes (LEDs) and obtain high degree of the electroluminescence (EL) circular polarization [4].

In this contribution we present results of investigations of LEDs with InGaAs/GaAs quantum well (QW) and nearby Mn δ-layer. The choice of Mn δ-layer was invoked by a possibility to increase T_c in such structures as compare to homogeneously doped (Ga,Mn)As layers [3]. We found that using of a low temperature growth technic for Mn δ-layer allows to achieve high values of the EL polarization and increase LED efficiency.

1. Experimental

A combined technique of metal-organic vapor phase epitaxy (MOVPE) at atmospheric pressure and laser ablation was applied for growing of the studied structures on the n^+-GaAs (001) substrate. Structure design is shown in inset in Fig. 1. First, n-doped GaAs buffer layer, 10 nm thick $In_xGa_{1-x}As$ QW ($x = 0.1$–0.2) and a thin undoped GaAs spacer with thickness $d_S = 2$–10 nm) were grown by use of MOVPE at temperature 550 °C. Then in the same reactor a δ-layer of Mn with nominal thickness of 0.4 monolayer and a cap layer of GaAs (20 nm) were formed by the laser ablation of metallic Mn and undoped GaAs, respectively, with a focused beam of pulsed YAG:Nd laser (pulse length 20 ns, rate 12.5 Hz, pulse power 0.1 J). Using of the laser ablation allows to decrease the growth temperature down to 400 °C and minimize Mn diffusion inside the active area of LED. Top contact of 30 nm thick Au film was thermally evaporated. The ohmic contact to the substrate were formed by alloying of the tin pad. The reference LED was grown with a Be δ-layer.

The electrical current-voltage (I–V) characteristics at room temperature show two regions with exponential dependencies of the direct I–V branch. The ideality factor n for the first region (0.1–0.6 V) is 2.3–2.6 and for the second one (0.6–1 V) $n = 1.6$–1.8. The barrier height of ∼0.65 eV, as defined by the initial region, is less than that for the ideal Shottky barrier Au/GaAs (∼0.9 eV), which points to the additional current channels in the structure [5].

Optical measurements in the Faraday geometry (perpendicularly to the sample surface and the easy magnetization axis of the FM film) in a magnetic cryostat with superfluid He (temperature $T \sim 1.5$ K) with magnetic fields up to $B = 10$ T. The EL emission was collected from the back side of the transparent substrate. The degree of circular polarization $P_C(B)$ was defined as $P_C(B) = (I^+ - I^-)/(I^+ + I^-)$, where I^+ and I^- are the intensities of the right- and left-hand polarized EL emission spectrum, corresponding to optical transition in the QW.

2. Electroluminescence in a magnetic field

The EL spectra of the LEDs with and without Mn δ-layer are shown in Fig. 1. One can see that in the structure with Mn the EL intensity is more than one order larger as compare to reference one. This is in agreement with our previous investigations [6] where we have shown that the LED efficiency increases significantly when acceptor C δ-layer is included into the cap layer, thus promoting hole injection in Schottky contact. The mechanisms of such enhancement are discussed in Ref. [6].

In Fig. 2 the magneto-EL spectra at low $T = 1.5$ K are depicted. They show two spectrally wide bands: the first one in the range 1.41–1.46 eV (depending on the structure) which corresponds to the QW emission and another band at 1.49 eV, close to the transition free electron — hole bound at C acceptor [7], which is expected for the organic precursors in MOVPE. Note much smaller intensity in the structure with $d_S = 2$ nm which correlates with very wide (>20 meV) QW line. Reasonable EL

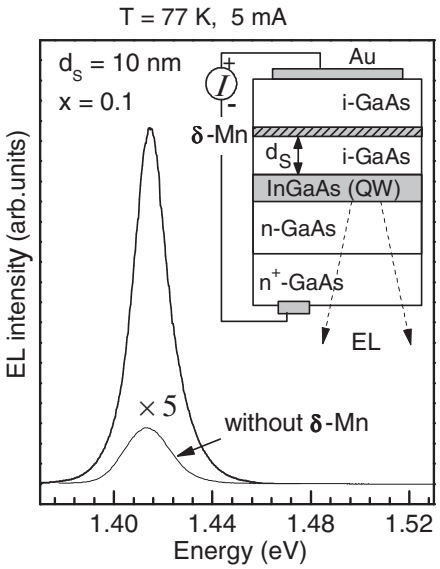

Fig. 1. The EL spectra of the LED with Mn d-layer ($d_S = 10$ nm) and of the LED without δ-layer at $T = 77$ K. In inset is shown the design of LED-structures.

signal of the QW emission in this LED appears at much higher current 20 ($\sim$30 mA at $B = 0$ T) as compare to 5 mA for the LED with $d_S = 5$ nm (Fig. 2). Mn impurity is known as a strong non-radiative center which quenches photoluminescence (PL) at very low contents (>0.13%) when introduced directly to the QW, which reflects the increasing density of crystalline defects with Mn doping [8]. Such behavior is explained by diffusion of Mn atoms and introducing inside the QW at $d_S = 2$ nm which gives rise to a strong disorder and non-radiative recombination. On the other hand, at $d_S \geq 3$ nm the linewidth of the QW transition shrinks to 8–10 meV, typical for all LEDs. This gives an estimation of the spatial width of the Mn δ-layer of $\sim$3 nm at used growth conditions.

In LEDs with Mn d-layer EL spectra are strongly circular polarized at $B > 0$ (Fig. 2). The dependencies of $P_C(B)$ are given in (Fig. 2(c)). While $P_C(B) < 10\%$ in the reference structure is small, linear with B and related to small Zeeman splitting (<0.5 meV) in the QW, $P_C(B)$ in LEDs with Mn are significantly nonlinear: they show a fast increase up to $B \sim 1$ T and slower rise at higher fields, with saturation at $B > 7$ T. Saturation value P_{sat} depends on d_S and shows a non-monotonic behavior: it increases with decreasing d_S, reaches maximum of $P_{sat} \sim 50\%$ for $d_S = 3$ nm and then drops for $d_S = 2$ nm (Fig. 2(c)).

We suggest that the injected holes are polarized after capturing into QW, interacting via strong $p - d$ exchange with Mn atoms [9] at the nearby δ-layer, similar to [10]. For confirmation of this interpretation we measured PL and found also high values of $P_C(B)$ which correlate with $P_C(B)$ of the EL. The increase of the P_{sat} for smaller d_S is explained by a larger overlap between heavy hole wave function in the QW and Mn ions in the δ-layer, which accelerates the hole spin relaxation to the ground state. Note that the confinement and the internal strain in the InGaAs/GaAs QWs both push light-hole levels to higher energies [11]. The decrease of P_{sat} for $d_S = 2$ nm is not clear at the moment and can be connected with a very fast non-radiative processes thus limiting the efficiency of the

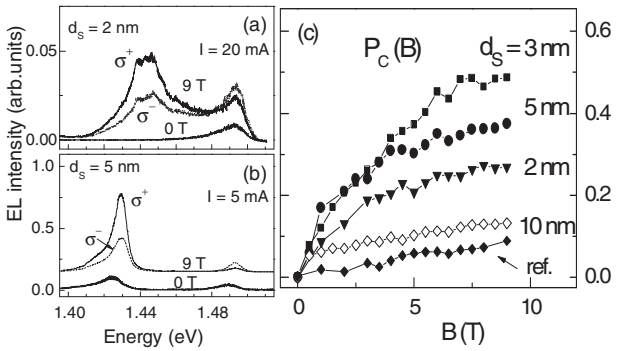

Fig. 2. Magneto-EL spectra of LEDs with $x = 0.1$ and (a) $d_S = 2$ nm (20 mA) and (b) $d_S = 5$ nm (5 mA) at $B = 0$ and 9 T ($T = 1.5$ K). In (b) spectra are shifted for clarity. (c) The dependencies of $P_C(B)$ for all LEDs (marked in figure).

hole spin-flip. It is consistent with a monotonous decrease of intensity in all LEDs with narrowing of the spacer d_S between QW and Mn δ-layer.

Thus, a possibility to increase the intensity and obtain strongly circular polarized EL at low temperature is experimentally demonstrated in Schottky diodes by δ-doping with Mn magnetic atoms. High values of polarization are supposed due to the exchange interaction of magnetic Mn atoms in the δ-layer and heavy holes in the QW giving rise to a spin polarization of holes.

Acknowledgements

This work has been supported by the Russian Foundation of Basic Research Grant 07-02-01153.

References

[1] I. Žutić *et al*, *Rev. Mod. Phys.* **76**, 323 (2004).
[2] T. Jungwirth *et al*, *Rev. Mod. Phys.* **78**, 809 (2006).
[3] A. M. Nazmul *et al*, *Phys. Rev. Lett.* **95**, 017201 (2005).
[4] Y. Ohno *et al*, *Nature* **402**, 790 (1999).
[5] E. H. Roderick and R. H. Williams, *Metal-Semiconductor Contacts* (Oxford, 1988).
[6] N. V. Baidus *et al*, *Semicond. Sci. Technol.* **19**, S469 (2004).
[7] M. A. Herman and H. Sitter, *Molecular Beam Epitaxy* (Springer, Berlin, 1996).
[8] M. Poggio *et al*, *Phys. Rev. B* **72**, 235313 (2005).
[9] J. K. Furdyna, *J. Appl. Phys.* **64**, R29 (1988).
[10] R. C. Myers *et al*, Phys. Rev. B **69**, 161305(R) (2004).
[11] G. Hendorfer and J. Schneider, *Semicond. Sci. Technol.* **6**, 595401 (1991).

16th Int. Symp. "Nanostructures: Physics and Technology"
Vladivostok, Russia, July 14–18, 2008

Quantum dot comb-laser as a light source for optical interconnect technologies

A. Kovsh[1], A. Gubenko[1], I. Krestnikov[1], D. Livshits[1], S. Mikhrin[1], J. Weimert[1], L. West[2], G. Wojcik[2], D. Yin[2], C. Bornholdt[3], N. Grote[3], M. V. Maximov[4] and A. Zhukov[4]

[1] Innolume GmbH, Konrad-Adenauer-Allee 11, 44263, Dortmund, Germany
[2] Innolume Inc., 3333 Bowers Ave, Suite 190, 95054 Santa Clara, CA, USA
[3] Fraunhofer-Institut für Nachrichtentechnik Heinrich-Hertz- Institut, Einsteinufer 37, 10587, Berlin, Germany
[4] St Petersburg Physics and Technology Centre for Research and Education of the RAS, Khlopina 8(3), 194021, St Petersburg, Russia

Abstract. We report on edge-emitting InAs/GaAs quantum dot laser promising as multiple wavelength light source for Dense Wavelength Division Multiplexing systems. Broad and flat gain spectrum of quantum dots as well as pronounced gain saturation effect facilitate simultaneous lasing via more than 200 longitudinal modes with uniform intensity distribution (comb spectrum). A bit error rate less than 10^{-13} is demonstrated for ten spectrally filtered and externally modulated at 10 Gb/s Fabry–Perot modes owing to a low (<0.3% in the 0.001–10 GHz range) relatively intensity noise of each individual mode. This result shows aptitude of using these individual Fabry–Perot modes as independent optical channels for Dense Wavelength Division Multiplexing.

Introduction

The use of optical signals having different wavelengths results in greatly increased information carrying capacity by emplying dense wavelength-division-multiplexing (DWDM). This technique requires an optical source which is capable of providing a sufficiently large number of signals having different wavelengths (channels). It is currently a common practice to build an optical source for a DWDM system by using a plurality of single-frequency distributed feedback lasers (DFB) operating at different wavelengths (Fig. 1). However, complexity of fabrication of DFB laser results in its high cost further multiplied by the number of lasers to be integrated. Furthermore, an operation wavelength should be independently determined for each laser. This makes it difficult to build an array of single-frequency lasers with pre-selected wavelength separation. In addition each laser requires its own system of wavelength stabilization. Thinking about possible integration of a multiwavelength laser source with silicon optoelectronic components for future computing, an array of DFB lasers has disadvantage of its large footprint. As the number of required optical channels increases and the wavelength separation between channels decreases, all the aforementioned problems of a conventional optical source are enhanced.

1. Dense wavelength-division-multiplexing system based on a single optical source

A very promising approach for developing a compact and cheap DWDM system is the use of single laser, capable of emitting a sufficient number of spectrally separated channels (Fig. 2). Such approach is especially advantages for future silicon photonic integrated circuits since all the system or at least its major part can be integrated together on one Si photonic chip. A required number of optical signals can be selected from the single source by bandpass filter and then spectrally separated by a demultiplexer, e.g. an arrayed waveguide (AWG). Electrical to optical signal transfer occurs in silicon photonic modulators.

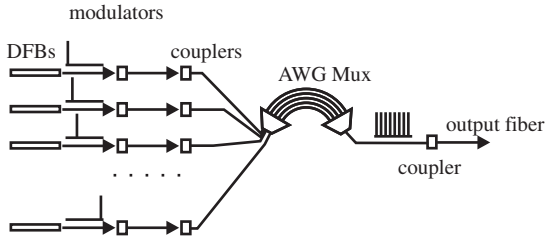

Fig. 1. Schematic of DWDM source based on a plurality of single-frequency DFB lasers.

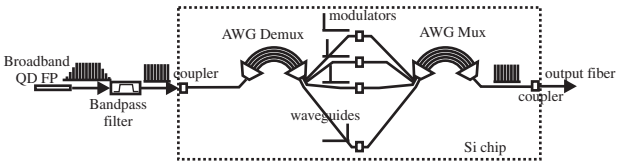

Fig. 2. Schematic of DWDM source based on one broadband QD laser. Individual Fabry–Perot modes serve as independent optical channels.

Modulated channels are then jointed together by an AWG multiplexer. These modulators and WDM elements can be coupled to each other by means of planar waveguides and integrated together on one Si photonic chip (shown in the frame in Fig. 2). The cost of most silicon photonic devices can be relatively low, like that of silicon electronics.

As efficient lasing in silicon-based devices still remains a challenge, future optical integrated circuits will likely include a III–V laser integrated into Si chip. An attractive candidate for such multi-wavelength emitter is a Fabry–Perot laser. This approach reduces requirements for the precision of lasing wavelengths because a channel separation is naturally predetermined by only one parameter which is a resonator length. In this case, all channels can be stabilized and tracked simultaneously. Typical dimensions of diode lasers are very well suitable for providing the desired channel spacing. For example, a 50 GHz intermodal spacing would require a cavity length of about 1 mm ($\Delta f = \frac{c/n}{2L}$).

A multi-wavelength emitter should satisfy several preconditions. First, lasing spectrum should be broad to provide a sufficient number of optical channels. Second output power of each channel should be high enough. Third, wavelengths should fall into a spectral interval appropriate for optical communication, e.g. around 1.3 or 1.55 μm. And, finally, intensity noise of each of longitudinal modes should be low enough in order to obtain a low bit error rate for each optical channel at high modulation speeds, acceptable for use in a multi-channel optical communication system. Below we will show that these requirements can be met by semiconductor quantum dot lasers.

2. Broadband emission in quantum dot laser

Quantum dots are especially favorable for broadband emission owing to the inhomogeneous broadening of quantum states caused by inevitable non-uniformities of dimensions, chemical composition, shape, strain, as well as other parameters of quantum dots affecting the energy levels in quantum dots. Spectral width of few tens of nanometers is typical for InAs self-organized quantum dots. Additional broadening of QD laser gain spectrum can be achieved by the use of vertically stacked QDs arrays with slightly shifted gain maxima. In this case the resulting gain curve is a superposition of gain curves of individual QD sheets. The total gain spectra width can be easily controlled by adjusting the spectral positions of gain maxima for individual QD layers. However, the sequence and number of the QD stacks should be optimized to obtain flat gain spectrum, high optical confinement factor and efficient carrier injection. If necessary, further gain spectrum broadening can be realized due to excited state contribution. At elevated pump levels excited states are populated with carriers and, therefore, contribute to gain spectrum at shorter wavelengths. If the ground and excited states overlap the resulting gain spectrum width can exceed 200 nm.

A multi-wavelength emitter for DWDM should provide simultaneous lasing via a large number of different wavelengths within gain spectrum. The spectral width of lasing spectrum in QW lasers is typically below 10 nm because of very fast carrier excitation/relaxation processes in a quantum well. As soon as empty electronic states become available after a photon emission, charge carriers quickly refill these states making them ready for another photon emission event. A very different situation takes place in an array of QDs. In contrast to a quantum well, QD electronic states of different energy belong to spatially separated dots. Therefore, in a QD laser, only a certain portion of the available QDs contributes to the lasing process, namely those quantum dots which have optical transition energy approximately equal to the lasing transition. Other QDs act as a reservoir providing charge carriers to the lasing dots. However, such an interaction can be strongly suppressed because a charge carrier should be first excited from the first quantum dot to a matrix or a wetting layer, then travel across the active region to a second dot, and finally be captured by the second dot. As a result, a refilling process may be significantly slowed down.

A possibility of achieving unusually broad room temperature lasing spectra, up to 15 nm, has been already mentioned in [1,2]. A 21-nm-wide spectrum with a power of 500 mW has been demonstrated in [3]. Recently, we have reported on QD laser with extremely broadband emission spectrum of 75 nm and high output power of 750 mW [4]. Fig. 3 shows an example of broadband and flat lasing spectrum of a QD laser having more than 220 modes.

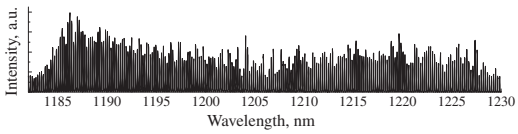

Fig. 3. Broadband emission spectra of a quantum-dot laser.

3. Low-noise quantum-dot laser

A prerequisite for application of multi-wavelength light source in DWDM systems is low relative intensity noise of each longitudinal mode (modal RIN). In single frequency lasers with large side mode suppression ratio (SMSR $>$ 40 dB) the values of RIN are rather low and these lasers are suitable for telecomm applications. In case of the multi mode (multi frequency) lasers the value of RIN rises significantly [5] and lasers cease complying with telecom applications requirements. The main reason of RIN rising is "beating effect" which is connected with random redistribution of mode intensity between longitudinal laser modes [6]. Thus, spectral division into single spectral line in case of QW lasers is possible but it does not allow realizing error-free data transmission that currently prevents the use of FP lasers in DWDM systems. The other situation is realized for semiconductor laser with nonlinear gain saturation or in other words where relaxation oscillations are strongly dumped. In Ref. [7] it was shown that the presence of nonlinear gain saturation lead to decreasing of RIN for fundamental mode of two-frequency laser. Computational modeling of characteristics of 21 longitudinal laser modes have proved that strong damping of relaxation oscillations suppresses fluctuation of the photon density in the cavity and considerably decrease the value of RIN [8]. As it was mentioned above the relaxation oscillations in QD lasers are strongly damped due to large values of gain compression factor. The typical value of gain compression factor for QD lasers is 5×10^{16} cm^3 [9,10] that is at least one order of magnitude larger than for QW lasers and opens a way for use of FP QD lasers in DWDM systems.

QD laser structure was grown by molecular-beam epitaxy. Active area contained of 10 planes of InAs/$In_{0.15}Ga_{0.85}As$ QDs. 3-μm-wide ridge waveguide FP lasers were fabricated, cavity length was about 1 mm. For eye-diagram and bit error rate (BER) evaluations, an individual longitudinal mode of the optically isolated laser was filtered out using a fibre Fabry–Perot

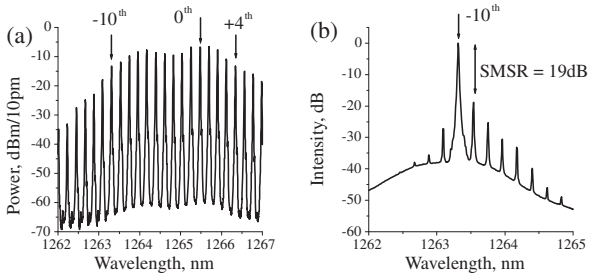

Fig. 4. Lasing spectra: overall spectrum around mode of the maximum intensity (a), spectrally filtered mode (b).

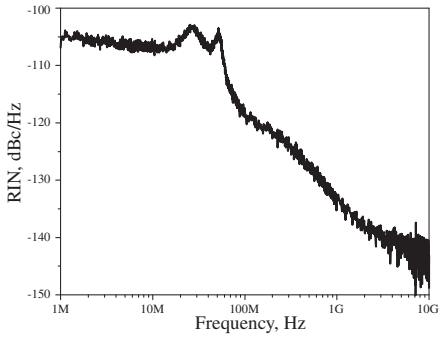

Fig. 5. Spectrum of relative intensity noise of filtered mode at 1265.2 nm.

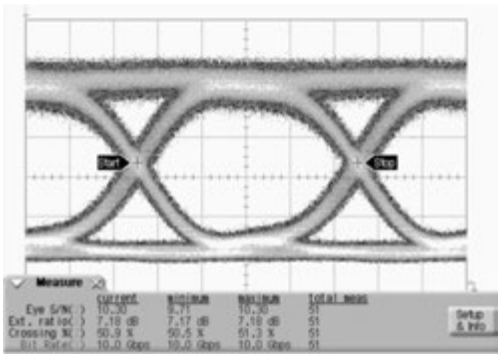

Fig. 6. Eye-diagram generated by a 10 Gb/s digital modulation for one of ten filtered longitudinal mode for which BER $< 10^{-13}$ was measured.

tunable filter. The spectrally filtered mode was amplified by passing through optical amplifiers (SOA) and externally modulated.

Fig. 4,a shows an overall emission spectrum of the QD laser taken at CW current of 85 mA, which is 5-times above the threshold. An output power is 50 mW per two facets. The spectrum comprises a series of longitudinal FP modes separated by 0.22 nm. The 0^{th}-order mode, i.e. the mode of the maximum intensity is centred at 1265.5 nm. The full width at half maximum is about 2 nm. An external FP etalon can be adjusted to transmit only one longitudinal mode while intensity of the other modes is significantly suppressed. Experiments were undertaken for longitudinal modes that fall into a wavelength interval from 1263.3 to 1266.4 nm. These modes are indicated in Fig. 4,a by an index ranging from -10^{th} to $+4^{\text{th}}$. Fig. 4,b shows a filtered intensity of -10^{th} longitudinal mode. In this case, as well as for other filtered modes, side mode suppression ratio better than 19 dB was achieved.

Relative intensity noise spectrum for the spectrally filtered FP mode (modal RIN) is shown in Fig. 5. In low frequencies, the RIN spectrum is nearly flat at a level of -105 dB/Hz. In higher frequencies, the modal RIN drops from -120 to -145 dB/Hz in the 0.1–10 GHz range. If a received power is sufficiently high, BER is governed by the total RIN, i.e. an integral over the relative intensity noise spectrum. Assuming a 100% modulation depth and a 1/2 decision level, minimum Bit Error Rate (BER) as a function of the total RIN can be estimated as $\text{BER} = (1/2)\text{erfc}[(2\sqrt{2\text{RIN}})^{-1}]$ (no photodetector noise), where erfc is the complementary error function. Our calculation has shown that the total RIN of less than 0.4% would be acceptable for error-free transmission (BER less than 10^{-15}). From the data of Fig. 5, the total RIN was calculated to be 0.21% over the full frequency range of analysis (0.001–10 GHz). These results show that the use of multi-mode QD laser for high-speed data transmission looks feasible.

An individual longitudinal mode after spectral filtering was modulated at 10 Gb/s by a $2^{31} - 1$ pseudorandom binary non-return-to-zero (NRZ) sequence by an external $LiNbO_3$ modulator. Fig. 6 shows eye pattern for the 0^{th} mode at -3dBm received power at the photodetector. For this case we obtained error-free operation with a bit error rate less than 10^{-13}.

Similar BER was achieved for the modes with the highest intensity (mode order ranges from -7^{th} to $+2^{\text{nd}}$), which wavelengths are close enough to the central wavelength of the overall lasing spectrum. BER increases for shorter-wavelength modes, as well as for longer-wavelength modes having lower modal power. It is worth emphasizing that the mode intensity was pre-amplified with an external SOA. Our result correlates well with an experimentally observed recovery of the signal-to-noise ratio for spectrally filtered light from an FP laser after passing through an external SOA [12]. We expect that modal RIN as well as BER do not degrade or even improve by using a monolithically integrated combination of a multi-mode QD laser and a SOA section.

Acknowledgements

This work was supported in part by Program of Presidium of RAS "Quantum nanostructure" and Presidents grants MD-3858.2007.2 (A.E.Z.).

References

[1] M. Grundmann, F. Heinrichsdorf, N. N. Ledentsov, C. Ribbat, D. Bimberg, A. E. Zhukov, A. R. Kovsh, M. V. Maximov, Yu. M. Shernyakov, V. M. Ustinov and Zh. I. Alferov, *Jpn. J. Appl. Phys.* **39**, 2341 (2000).

[2] D. A. Livshits, A. R. Kovsh, A. E. Zhukov, N. A. Maleev, S. S. Mikhrin, A. P. Vasil'ev, E. F. Nikitina, V. M. Ustinov, N. N. Ledentsov, G. Lin and J. Chi, *Tech. Phys. Lett.* **30**, 9 (2004).

[3] H. S. Djie, B. S. Ooi, X.-M. Fang, Y. Wu, J. M. Fastenau, W. K. Liu and M. Hopkinson, *Optics Letters* **32**, 44 (2007).

[4] A. Kovsh, I. Krestnikov, D. Livshits, S. Mikhrin, J. Weimert and A. Zhukov, *Optics Letters* **32**, 793 (2007).

[5] C. H. Henry, P. S. Henry and M. Lax, *J. Lightwave Technol.*, **LT-2**, 209 (1984).

[6] R. Schimpe,*Z. Phys. B — Condensed Matter* **52**, 289 (1983).

[7] G. P. Agrawal, *Phys. Rev. A* **37**, 2488 (1988).

[8] L. V. T. Nguyen, *Defense Science and Technology Organization (Australia) research report* **DSTO-RR-0244** (2002).

[9] H. Su and L. F. Lester, *J. Phys. D: Appl. Phys.* **38**, 2112 (2005).

[10] S. Ghosh, S. Pradhan and P. Bhattacharya, *Appl. Phys. Lett.*, **81**, 3055 (2002).

[11] A. Gubenko, I. Krestnikov, D. Livshtis, S. Mikhrin, A. Kovsh, L. West, C. Bornholdt, N. Grote and A. Zhukov, *Electron. Lett.* **43**, 1430 (2007).

[12] K. Sato and H. Toba, *IEEE J. Select. Topics Quantum Electron.* **7**, 328 (2001).

16th Int. Symp. "Nanostructures: Physics and Technology"
Vladivostok, Russia, July 14–18, 2008

Intracavity difference-frequency generation in butt-joint diode lasers

V. Ya. Aleshkin[1], A. A. Biryukov[2], V. I. Gavrilenko[1], A. A. Dubinov[1], Vl. V. Kocharovsky[3], K. V. Maremyanin[1], S. V. Morozov[1], S. M. Nekorkin[2] and B. N. Zvonkov[2]

[1] Institute for Physics of Microstructures RAS, 603950, Nizhny Novgorod, Russia
[2] Physico-Technical Research Institute, University of Nizhny Novgorod, 603950 Nizhny Novgorod, Russia
[3] Institute of Applied Physics RAS, 603950, Nizhny Novgorod,Russia

Abstract. The room-temperature difference-frequency generation in mid-infrared spectral range have been observed in a butt-joint GaAs/InGaAs/InGaP quantum-well laser diode which supports lasing at two closely spaced wavelengths in the near-infrared range around 1 μm. A special asymmetric waveguide design and a low-doped substrate that minimize mid infrared losses and phase mismatch for the difference-frequency generation process were used in butt-joint lasers.

Introduction

Compact mid-far-infrared semiconductor sources are now under active development stimulated by a variety of applications. Remarkable progress has been achieved with quantum cascade (QC) lasers that work at and above room temperature in the continuous-wave regime in the mid-infrared range [1] and at cryogenic temperatures in the far-infrared range [2]. However, the perspectives of their room temperature operation in the far-infrared range are uncertain. Besides, QC lasers are quite complex devices including thousands of thin epitaxial layers. The intracavity difference-frequency generation in semiconductor diode lasers provides an alternative way to room temperature injection-pumped source in the mid-far-IR range, which recently also has been realized in QC lasers [3]

It would be very attractive to implement DFG process in the cavity of a laser diode generating radiation in the near-IR range [4]. In this work, we report the observation of DFG in a butt-joint diode lasers generating two wavelengths in the near-IR range that serve as a pump for the intracavity DFG process.

1. Butt-joint diode lasers

The four factors are important for the DFG efficiency. The first factor is the power of the short-wavelength pump radiation. The most powerful diode lasers are based on GaAs structures and operate at wavelengths around 1 μm. Therefore, we use GaAs/InGaAs/InGaP lasers operating in this wavelength range. The second factor is a relatively high optical nonlinearity of the laser waveguide material. The second order optical susceptibility of GaAs is 1.3×10^{-8} cm/V, which is a very high value. The third factor is phase matching, which can be satisfied for DFG in GaAs in the mid-IR range when near-IR pump modes have different transverse orders [5]. In butt-joint lasers we used the fundamental mode at a longer pump wavelength and the first order mode at a shorter pump wavelength. The fourth factor is the low losses for the difference frequency radiation. To minimize these losses, we used a low-doped substrate and a specially designed waveguide in chip where the DFG process took place.

To achieve simultaneous generation of two wavelengths around 1 μm, we used the butt-joint two-chip laser design [6]

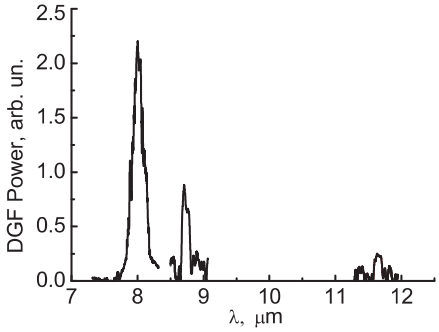

Fig. 1. Photo of butt-joint laser with heat sink. Enlarged photo laser is present on insert at right upper corner.

shown in Fig. 1. It provides independent control of power of the two modes by varying the corresponding currents in which diode. Such device promises a good degree of flexibility and spectral tunability. The weak point of the design is outcoupling losses of radiation. However, we have demonstrated that mounting the chips episide down on a common heat sink provides precise alignment of two waveguides and a reasonably high (around 20%) coupling of the TE_0 mode of one chip (LD1) into the TE_0 mode of another chip (LD2). The chips are approximately 1 mm length and separated by no more than a 1 μm wide gap.

Laser structures were grown by metal-organic chemical vapor deposition epitaxy on GaAs substrates. Active regions are formed by $In_xGa_{1-x}As$ quantum wells of 10 nm thickness with InAs fraction $x = 0.35, 0.32, 0.29$ for radiation at wavelength $\lambda_1 = 1.13, 1.107, 1.077$ μm and $x = 0.2$ for radiation at wavelength $\lambda_2 = 0.99$ μm, respectively. Waveguide cladding is formed by $In_{0.49}Ga_{0.51}P$ layers lattice matched to GaAs.

The waveguide of the LD1 laser that generates the fundamental mode at wavelength λ_1 is of a standard design. Its facet facing the second laser. The waveguide of the LD2 laser generating at λ_2 has a special asymmetric design with an extra InGaP layer to ensure laser operation at the first order transverse mode [7]. The layer sequence starts from the low-doped $\sim(1-2) \times 10^{17}$ cm^{-3} n-GaAs substrate of 150 μm thickness followed by a 780 nm $In_{0.49}Ga_{0.51}P$ layer n-doped to $\sim 10^{18}$ cm^{-3}, undoped 88 nm of GaAs, a 10 nm InGaAs quantum well, 102 nm GaAs layer, then a 100 nm p-$In_{0.49}Ga_{0.51}P$ layer, 400 nm p-GaAs, and a 780 nm p-$In_{0.49}Ga_{0.51}P$ layer, all

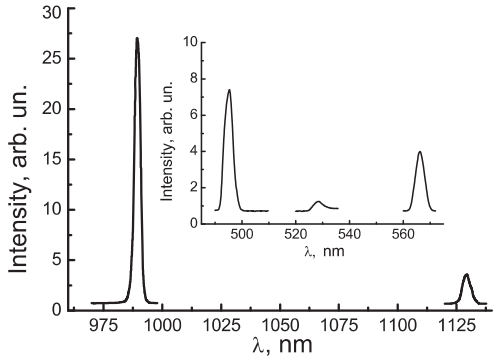

Fig. 2. Typical laser generation spectrum of a butt-joint laser. Inset: the spectrum of intracavity second-harmonic and sum-frequency generations.

three doped to 2×10^{18} cm^{-3}, followed by a 200 nm p$^+$-GaAs contact layer doped to 10^{19} cm^{-3}.

Efficient frequency mixing takes place in the LD2 laser between TE_0 and TE_1 modes of the near-IR fields at frequencies ω_1 and ω_2, respectively, generated in the composite LD1–LD2 cavity of the butt-joint laser. Due to the large relative spectral widths ($\sim$0.3%) of the two lasing lines, there are up to 20–30 longitudinal modes of the cavity which are involved in the nonlinear mixing process. They produce approximately the same number of difference-frequency longitudinal modes. Most of them are expected to be of the same TM_n transverse structure which is phase matched to two lasing modes, where $n \approx 40$. The index n of a phase-matched mid-IR mode is known approximately and may differ slightly from sample to sample. We choose the substrate thickness so that for a given longitudinal mid-IR mode, the frequency difference of neighboring transverse TM modes is approximately equal to the DFG line width. Therefore, a nearly perfect phase matching is unavoidable in our laser design. However, these high transverse order mid-IR modes are spread into the whole substrate, what reduces the overlap of three interacting modes.

2. Experimental results

Radiation in the near-IR, mid-IR, and visible range was detected from the output facet of the LD2 laser generating at the wavelength λ_2. All spectra were measured in the pulsed regime with pulse duration of 500 μs and repetition rate of 1 kHz. Figure 2 shows typical near-IR spectra. We have also detected the signals at the second harmonics and sum frequency at the nanowatt level. Their spectra are shown in the inset of Fig. 2. All spectra were measured by a diffraction grating monochromator.

Mid-IR radiation at the difference frequency was detected by a liquid nitrogen cooled CdHgTe detector with bandwidth 2–12.5 μm. Spectra were measured by the same grating monochromator. Mid-IR radiation was filtered by a pure Ge filter. The observed difference-frequency spectra for three different lasers are shown in Fig. 3. The estimated total power of the difference-frequency radiation is about 0.1 μW for line with peak around 8 μm and powers of two other lines are sufficiently lower. Thus we experimentally have demonstrated the possibility of difference frequency generation in mid-infrared region in butt-joint diode lasers at room temperature.

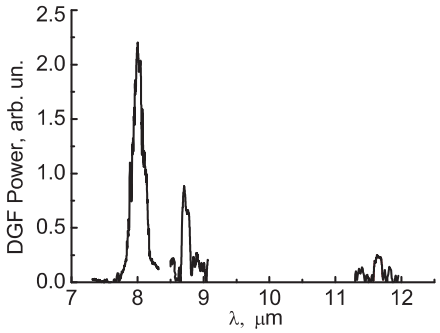

Fig. 3. Difference-frequency generation spectra for three butt-joint lasers.

Acknowledgements

This work has been supported by grants from the RFBR (07-02-00486, 07-02-12177ofi, 08-02-90054, 08-02-97034), Presidium of the Russian Academy of Sciences (the program "Terahertz electromagnetic radiation"), Department of Physics Science of the Russian Academy of Sciences (the program "Optical coherent emission of semiconductor materials and structures"), Ministry of Education and Science of the Russian Federation (BRHE, REC-NN-001 Grant No. Y1-P-01-06), the state contract of Ministry of Education and Science of the Russian Federation No. 02.518.11.7031, President of the Russian Federation (MK-3344.2007.2), and INTAS YS (05-109-4705).

References

[1] A. Evans, J. S. Yu, S. Slivken, and M. Razeghi, *Appl. Phys. Lett.* **85**, 2166 (2004).

[2] B. S. Williams, *Nat. Photonics* **1**, 517 (2007).

[3] M. A. Belkin, F. Capasso, A. Belyanin, D. L. Sivco, A. Y. Cho, D. C. Oakley, C. J. Vineis, and G. W. Turner, *Nat. Photonics* **1**, 288 (2007).

[4] V. Ya. Aleshkin, A. A. Afonenko, and N. B. Zvonkov, *Semiconductors* **35**, 1203 (2001).

[5] M. Jager, G. I. Stegeman, M. C. Flipse, M. Diemeer, and G. Mohlmann, *Appl. Phys. Lett.* **69**, 4139 (1996).

[6] A. A. Biryukov, S. M. Nekorkin, B. N. Zvonkov, V. Ya. Aleshkin, A. A. Dubinov, V. I. Gavrilenko, K. V. Maremyanin, S. V. Morozov, A. A. Belyanin, V. V. Kocharovsky, and Vl. V. Kocharovsky, *Laser Phys.* **17**, 684 (2007).

[7] A. A. Biryukov, B. N. Zvonkov, S. M. Nekorkin, V. Ya. Aleshkin, A. A. Dubinov, V. V. Kocharovsky, and Vl. V. Kocharovsky, *Semiconductors* **41**, 1364 (2007).

16th Int. Symp. "Nanostructures: Physics and Technology"
Vladivostok, Russia, July 14–18, 2008

Semiconductor nanostructure mirror for ultrashort-pulse laser

A. A. Kovalyov[1], N. V. Kuleshov[2], V. E. Kisel[2], S. V. Kurilchik[2], O. P. Pchelyakov[1], V. V. Preobrazhenskii[1], M. A. Putyato[1], N. N. Rubtsova[1] and T. S. Shamirzaev[1]

[1] Institute of Semiconductor Physics, Siberian Division of Russian Academy of Sciences, Academica Lavrentieva prospect, 13, Novosibirsk, 630090, Russia
[2] Institute for optical materials and technologies, Belarus National Technical University, Nezavisimosti ave., 65, bd. 17., 220013, Minsk, Belarus

Abstract. GaAs/$In_xGa_{1-x}As$/GaAs multiple quantum well grown by molecular beam epitaxy was investigated with femtosecond resolution by pump-probe technique. In the spectral area of excitonic transition fast absorbtion bleaching was observed. The recovery revealed two types of decay, the fast and the slow one. The fast recovery time of 0.38 ps corresponds to excitons localized in quantum wells; the slow one of 188 ps corresponds to free carriers recombination. Optical properties at room and liquid nitrogen temperatures and the kinetics of bleaching and recovery of the sample shown promising results for development of saturable absorbers based on such kind of semiconductor nanostructures. The all-in-one type mirror including saturable absorber based on that structure, wide-band total reflector and the Zhires–Tournois type interferometer as group delay dispersion compensator was designed and grown in a single cycle. This all-semiconductor mirror provided reliable and stable regime of Nd^{3+}: $KGd(WO_4)_2$ laser self-mode-locking.

Introduction

Compact ultra-short pulse lasers are of great importance for scientific, medico-biological and technological applications. In an optimal case, the pulse duration is determined by accessible spectral range of laser gain covered by equally-spaced generation modes. Phase-synchronous operation of all above mentioned modes can be triggered by optical losses modulation. The most efficient and cheap way to make laser to operate in a regime of modes self-synchronization is semiconductor mirror with saturable absorption (SESAM). This regime delivers a train of ultrashort pulses of radiation.

The saturable absorber (SA) should respond very rigid requirements in order to obtain pulses as short as possible for a given laser gain width, and SESAM designers are sometimes forced to make a set of different optical elements to satisfy all the requirements. The first requirement is fast bleaching and recovery of SA. Actually the fastest optical nonlinearity originates from the excitonic transitions [1,2]. Modern semiconductor nanotechnology permits to operate with excitons localized in nanostructures (wells, wires, dots), and it was already used in our previous works [3,4]. Saturable absorber in actual work is also based on nanostructures; its optical properties including the bleaching and recovery kinetics were tested (look below). The second requirement is low non-saturable losses and simultaneously the wide spectral range of high reflectivity of SESAM. This point was satisfied by multilayer structure (Bragg mirror) of sequential quarter-wavelength layers of semiconductors with different refraction indexes. Last but not least requirement is the compensation of group delay dispersion (GDD) arising from active and passive elements of the laser cavity. There are two principal approaching for the design of such optical element. One is related to application of Zhires–Tournois type interferometer, another uses a double-chirped mirror. In our design the first approach proved optimal.

This work demonstrates semiconductor SESAM grown in single technology cycle, responding all essential requirements, and integrating three functions in one chip. Optical testing of SESAM is essential part of technology.

1. Saturable absorber

Saturable absorber based on quantum wells of $In_xGa_{1-x}As$ separated by thick GaAs barriers was grown by low temperature molecular beam epitaxy [5,6,7] under continual control of the structure crystal quality by reflection high energy electrons diffraction (RHEED). The barriers thickness of 22.3 nm guaranteed the non-overlapping of wave functions of electrons and holes localized in the quantum wells. The wells thickness (8.7 nm) and alloy content ($x = 0.25$) were chosen in such a way that to place E1HH1 exciton transition near the laser gain spectrum.

The probe sample containing 10 periods of QW/barrier nanostructures grown at GaAs epi-ready substrate was used for investigation of optical properties. Transmission spectrum recorded at room temperature in polarized weak radiation and in the geometry corresponding to the Brewster angle incidence onto the sample plain showed clearly exciton absorption. Photoluminescence spectra of the structure detected both at room temperature and at the liquid nitrogen temperature shown high contrast exciton radiation.

The most important characteristics of saturable absorber is its bleaching and recovery kinetics. This research was made by pump-probe technique [8] by using a passively mode-locked Yb:KYW laser, producing pulses of 168 fs at central wavelength of 1036 nm. An average output power was of up to 1.5 W, and the pulse repetition frequency was 70 MHz. The pump and probe beams were formed from the same laser beam, focused into the sample to an overlap spot radius of 10 μm ($1/e^2$ level). To reduce the background arising from the scattered pump light a non-collinear scheme was chosen, and the pump and the probe beams had linear and mutually orthogonal polarizations. The pump intensity on the sample was chosen of 1.8 GW/cm^2 (0.3mJ/cm^2) using another calibrated neutral intensity filter. Additionally, the intensity of probe beam was varied by filter 1 to achieve a better signal/noise ratio. The signal from the photodiode as a function of delay time was am-

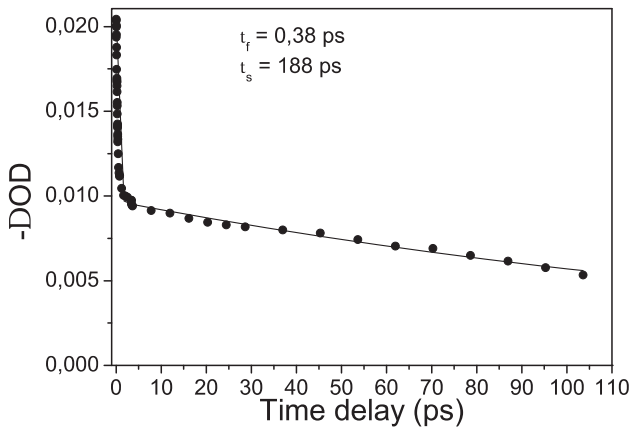

Fig. 1. Fast and slow recovery of saturable absorber based on 10 periods of GaAs/InGaAs/GaAs quantum wells.

plified by a lock-in-amplifier tuned at a frequency of 880 Hz. The bleaching value is defined as a differential optical density $\Delta D = -\log(T/T_0)$ where T and T_0 are transmissions of the sample with and without pump beam, respectively.

The pump-probe testing of multiple quantum wells shows clearly fast bleaching effect with time equal to laser pulse duration. The absorption recovery kinetics (bleaching relaxation curve) presented in Fig. 1 shows double-exponential decay. The curve fitting was made by the expression $\Delta D(t) = A_\mathrm{f} \exp(-t/\tau_\mathrm{f}) + A_\mathrm{s} \exp(-t/\tau_\mathrm{s})$, where A_s, A_f, τ_f and τ_s are the amplitudes and relaxation time constants of the fast and slow bleaching components. The fast and slow relaxation times were 0.38 ps and 188 ps, correspondingly. The optical damage threshold was estimated to be approximately 10 GW/cm^2. This kinetics has clear interpretation. The fast process corresponds to contribution of localized excitons, while the slow one should be referred to the recombination of free charge carriers. The results proved encouraging to use such a structure in SESAM construction.

2. SESAM construction

As it was mentioned earlier, the whole SESAM mirror should perform not only the optical losses switching. It should provide also high wide-band reflectivity. Besides, SESAM should accomplish the compensation of group delay dispersion of laser optics. That is why our mirror construction shown in Fig. 2 contains all three functional elements: the saturable absorber, the Bragg reflector, and group delay dispersion compensator.

3. Compact ultrashort-pulse laser with SESAM

Compact laser Nd^{3+}:$KGd(WO_4)_2$ pumped by semiconductor laser at $\lambda = 812$ nm operates near $\lambda = 1.06$ microns and has relatively high gain as compared to other compact lasers of this spectral region. Above described SESAM mirror for this laser including in one chip the saturable absorber, Gires–Tournois interferometer and total reflector was placed into the beam waist. This one-chip mirror produced self-starting mode-locking regime of the laser with pulses duration of about 1 ps. Mode synchronization regime was enough stable, and optical losses introduced by the mirror were relatively low (not over 1%).

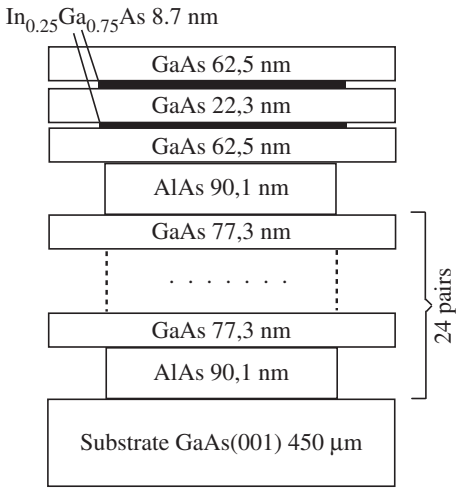

Fig. 2. One-chip SESAM contains SA of quantum wells inserted inside the GDD compensator grown on Bragg mirror over GaAs substrate.

4. Conclusions

In conclusion, we have realized SESAM mirror for near infrared compact laser, which operates simultaneously as saturable absorber, wide-band total reflector, and GDD compensator. Another important point of this mirror design is its preparation in the united cycle semiconductor nanotechnology.

Acknowledgements

Financial support of Russian Foundation for Basic Research grant 06-02-16527, Russian-Byelorussian RFBR grant 08-02-90010-Bel, and Integrated Project between Byelorussian National Academy of Sciences and Siberian Branch of Russian Academy of Sciences are acknowledged.

References

[1] P. W. Smith, Y. Silberberg, D. A. Miller, *JOSA* **B 2**, 1228–1236 (1985).

[2] W. H. Knox, *Phys. Rev. Lett.* **54** No. 12, 1306 (1985).

[3] E. Sorokin, S. Naumov, I. T. Sorokina, N. N. Rubtsova, V. V. Preobrazhenskii, A. A. Kovalyov, M. A. Putyato, O. P. Pchelyakov, *Proc. of 11-th International Symposium "Nanostructures: Physics and Technology" (St Petersburg, 23–28 June 2003)* Ioffe Institute 2003, pp. 18–21.

[4] O. P. Pchelyakov, V. V. Preobrazhenskii, M. A. Putyato, A. A. Kovalyov, N. N. Rubtsova, E. Sorokin, S. Naumov, I. T. Sorokina, *Proc. of 12-th International Symposium "Nanostructures: Physics and Technology" (St Petersburg, 21–25 June 2004)* Ioffe Institute 2004, pp. 297–298.

[5] A. B. Boitsov, N. A. Bert, Yu. G. Musikhin, V. V. Chaldyshev, M. A. Yagovkina, V. V. Preobrazhenskii, M. A. Putyato, B. R. Semyagin, *Fizika i Tekhnika Poluprovodnikov* **40** No. 7, 778 (2006).

[6] V. V. Preobrazhenskii, M. A. Putyato, B. R. Semyagin, *Fizika i Tekhnika Poluprovodnikov* **36** No. 8, 897 (2002).

[7] J. Herfort, V. V. Preobrazhenskii, N. Boukos, G. Apostolopoulos, and K. H. Ploog, *Physica E* **13**, 1190 (2002).

[8] E. U. Rafailov, S. J. White, A. A. Lagatsky, A. Miller, W. Sibbett, D. A. Livshits, A. E. Zhukov, V. M. Ustinov, *IEEE Photon. Technol. Lett.* **16**, 2439 (2004).

16th Int. Symp. "Nanostructures: Physics and Technology"
Vladivostok, Russia, July 14–18, 2008

The efficient generation of the TE_1 waveguide mode in the InGaAs/GaAs/InGaP heterolaser

V. Ya. Aleshkin[1], A. A. Biryukov[2], A. A. Dubinov[1], V. V. Kocharovsky[3,4], Vl. V. Kocharovsky[3], S. M. Nekorkin[2] and B. N. Zvonkov[2]

[1] Institute for Physics of Microstructures RAS, 603950, Nizhny Novgorod, Russia
[2] Research Physical-Technical Institute of the Nizhny Novgorod State University, 603950, Nizhny Novgorod, Russia
[3] Institute of Applied Physics RAS, 603950, Nizhny Novgorod, Russia
[4] Department of Physics, Texas A&M University, College Station, TX 77843-4242, USA

Abstract. The generation of the first excited transverse mode (TE_1) in a new InGaAs/GaAs/InGaP diode heterolaser with a thin InGaP layer at the waveguide center had been studied. This laser design decreases the competition of the first and fundamental modes and provides TE_1 mode lasing at a threshold current comparable to that of a conventional laser generation at the fundamental TE_0 mode.

Introduction

Recently, great interest has arisen in GaAs-based laser diodes, which generate excited modes in the laser waveguide. Among the possible applications of such lasers is the generation of a difference frequency in the mid-infrared wavelength region using butt-joint diode lasers [1,2]. In order to attain effective difference frequency generation, the phase-matching condition should be satisfied, which means that the phase velocities of the polarization wave, produced by nonlinearity-induced interaction between near-IR modes, and the difference frequency propagating mode must be the same. It was shown that the phase matching condition can be satisfied by using transverse modes of a different order for pumping [3,4]. In the suggested scheme one laser generates the TE_0 mode, and it radiation be put in another laser, which generated the TE_1 mode. This study is devoted to the development of an efficient laser diode based on the InGaAs/GaAs/InGaP heterostructure with a quantum well for lasing of the first excited mode of a waveguide with wavelength $\lambda \sim 1$ μm. The using of conventional laser waveguide design leads to low efficiency TE_1 mode lasing, high threshold currents, low power and concurrent TE_0 mode lasing. To increase the efficiency, an unusual design of the laser waveguide was proposed and implemented, which provides single TE_1 mode lasing at a threshold current comparable to that of the conventional laser generating the TE_0 mode.

1. Laser waveguide design for the first mode lasing

To accomplish this goal, a thin layer of a coating material (InGaP) with a smaller refractive index n was placed to the central laser waveguide layer (GaAs). This additional layer should be displaced from the waveguide center (Table 1 and Fig. 1) so that the central waveguide GaAs layer would be partitioned into wide and narrow sections. In such a waveguide, the fundamental and first modes are mostly localized in the wide and narrow sections of the waveguide GaAs layer, respectively. In this laser, it is reasonable to place a quantum well at the maximum of the first mode field in the narrow waveguide section.

Table 1.

Layer description	Layer composition	Carrier concentration, $\times 10^{17}$cm^{-3}	Layer thickness, μm
Substrate	n-GaAs	1	150
Confining	n-InGaP	10	0.78
Waveguide	i-GaAs	—	0.088
QW	i-InGaAs	—	0.01
Waveguide	i-GaAs	—	0.102
Intermediate	p-InGaP	20	0.1
Waveguide	p-GaAs	20	0.4
Confining	p-InGaP	20	0.78
Contact	p-GaAs	100	0.2

2. Experimental results

The InGaAs/GaAs/InGaP laser heterostructure was grown by metal-organic vapor-phase epitaxy at atmospheric pressure. As quantum well, InGaAs layer 10 nm thick was used. To minimize losses by difference frequency, we used a low-doped substrate ($\sim 10^{17}$ cm^{-3}), which must be a mid-IR waveguide.

Laser diode with active region 100 μm wide was fabricated by chemical etching of the contact layer outside the active

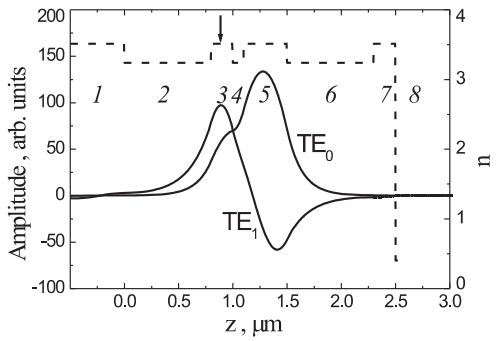

Fig. 1. Dependence of the real part of the refractive index n (broken line), electric fields in TE_1 (solid curve) and TE_0 (dotted curve) modes on the z coordinate (across the p-n junction) for laser. The arrow indicates the optimal position of the quantum well for TE_1 mode lasing. Structure layers are (*1*, *3*, *5*, *7*) GaAs, (*2*, *4*, *6*) InGaP, and (*8*) Au.

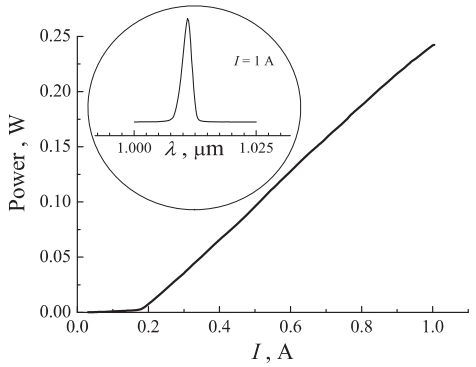

Fig. 2. Power-current characteristic of the laser diode under study. The insets show the spectral characteristic.

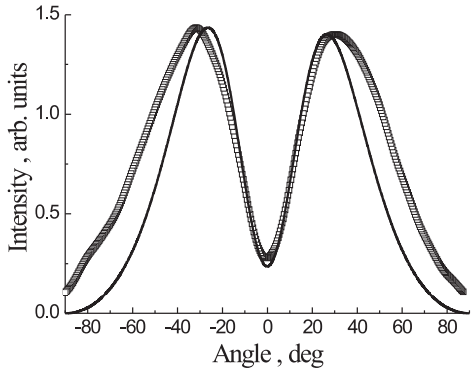

Fig. 3. Calculated (solid curve) and measured (squares) directional patterns of radiation in the plane perpendicular to the *p-n* junction of the laser.

stripe, followed by proton implantation of the exposed InGaP surface. After cleaving, chip was soldered (structure downward) onto copper heat sinks to provide the cw lasing mode. As mirrors, (110)-face cleavages were used. The cavity length was 1 mm.

Figure 2 shows the power-current and spectral characteristics of the fabricated laser. The lasing threshold was 150 mA and comparable to lasing threshold of the conventional laser generating the TE_0 mode. The differential quantum efficiency from a single laser facet was 28%. Spectral characteristic was measured using an MDR-23 grating monochromator during dc pumping of the laser. Figure 2 (insets) shows the spectral dependence of the intensity of laser emission.

To study the mode composition of laser radiation, we measured directional pattern, i.e., the angular dependence of the intensity of laser diode radiation in the plane perpendicular to the *p-n* junction. These patterns are shown in Fig. 3. As seen from the figure, the intensity of stimulated radiation of laser has two maximums at angles $\pm 30°$, whose positions and relative amplitudes are in agreement with those calculated for the TE_1 mode.

3. Conclusions

The TE_1 mode lasing was obtained and studied in the new design diode laser with a thin lower-refractive index layer at the waveguide center. This laser design reduces the competition of the first and fundamental modes and provides single TE_1 mode lasing at a threshold current comparable to that of the conventional laser generating the fundamental TE_0 mode. The difference frequency generation in mid-IR range was obtained in this laser using butt-joint diode laser scheme [2].

Acknowledgements

This work has been supported by grants from the RFBR (07-02-12177, 07-02-00486, 08-02-90054, 08-02-97034), the RAS "Coherent optical emission of semiconductor materials and structures" and "Electromagnetic waves of the terahertz range" Programs, the Russian President (MK-3344.2007.2), the Russian Ministry of Education (BRHE, REC-NN-001, #Y1-P-01-06), and the state contract of Ministry of Education and Science of the Russian Federation No. 02.518.11.7031.

References

[1] A. A. Biryukov *et al*, *J. Mod. Opt.* **52**, 2323 (2005).
[2] B. N. Zvonkov *et al*, *Appl. Phys. Lett.* **92**, 021122 (2008).
[3] M. Jager *et al*, *Appl. Phys. Lett.* **69**, 4139 (1996).
[4] V. Ya. Aleshkin *et al*, *Semiconductors* **35**, 1203 (2001).

16th Int. Symp. "Nanostructures: Physics and Technology"
Vladivostok, Russia, July 14–18, 2008

Effect of carrier generation rate pulsations on quantum wells population in optically-pumped dual-wavelength semiconductor disk laser

Yu. A. Morozov[1], M. Yu. Morozov[1], T. Leinonen[2] and M. Pessa[2]

[1] Institute of RadioEngineering and Electronics (Saratov Branch), Russian Academy of Sciences, 410019, Saratov, Russia
[2] Optoelectronics Research Center, Tampere University of Technology, P.O. Box 692, 33101 Tampere, Finland

Abstract. The influence of pump wave reflections on the carrier generation rate and a uniformity of the carrier population in the quantum wells of the dual-wavelength semiconductor disk laser is numerically analyzed. We have applied the approach which enables us to study the carrier distribution over the barrier and the quantum well layers of quite general structure and for an arbitrary function of the local carrier generation rate. We have shown that the optimal location of the blocking layers can provide the quantum wells carrier population with very high uniformity. The pump reflections are demonstrated to be of great importance with regard to the carrier distribution in such the device.

Introduction

Semiconductor disk lasers (SDLs), also known as vertical external-cavity surface-emitting lasers (VECSELs), are the subject of growing interest in a variety of applications. SDLs emit nearly diffraction-limited gaussian beams, have potentiality for power scaling to multi-watt level and demonstrate availability of radiation in different ranges because of semiconductor band-gap engineering [1]. Besides, SDLs allow for location of non-linear crystals in their external cavity thus providing a possibility for a nonlinear frequency conversion [2]. An intracavity nonlinear frequency conversion is known to be far more effective as compared with an extracavity one [3]. However, until recently, an intracavity nonlinear optical wave interaction was mainly restricted to second harmonic generation because of a lack of SDLs emitting more than one parent wavelength. Just after first realization [4] and the improvement [5] of the dual-wavelength SDLs, the possibility occurs to achieve an intracavity emission at combinative frequencies, including sum- [6] and, what is even more important, difference-frequency generation corresponding to mid- and far-infrared ranges [7]. Even though quantum-cascade lasers operate in the above regions, there are still considerable drawbacks since those lasers require cryogenic freezing and pulsed operation when wavelength of radiation exceeds 10 microns [8].

1. Mathematical model and simulations

In this report, we perform the theoretical analysis and numerical simulation of optical pumping of a dual-wavelength SDL's active region. The mathematical model of an active region is stated for a quite general structure including any number of quantum wells (QWs) located in N sections (Fig. 1). Wide-band blocking layers separating the adjacent sections are supposed to be transparent for pump and laser emission but impenetrable for carrier transport. The section numbered by i consists of m_i identical quantum wells. The quantum wells are not required to be the identical ones in the different sections. Our model enables carrier generation rate and pump power decay to differ from those dictated by the Beer–Lambert law. Such the distinctions are caused by pump wave reflections which arise readily in the device due to imperfect pump wave absorption and multilayered laser structure.

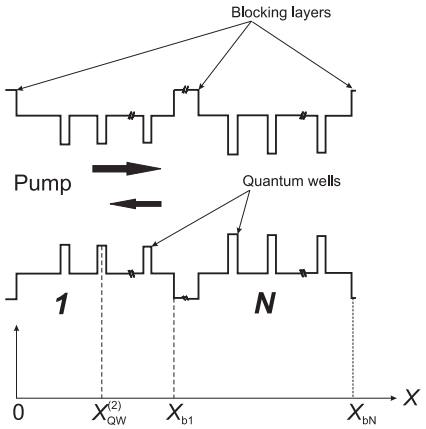

Fig. 1. Band diagram for the SDL's active region.

The general model is applied to the analysis of the dual-wavelength SDL [5]. The laser structure includes two active regions ($AR_{S,L}$) designed to emit at the wavelength $\lambda_S \approx 966$ nm and $\lambda_L \approx 1047$ nm. Both the active regions are composed of four sections. Each section of AR_S contains two 7 nm quantum wells made of $In_{0.14}Ga_{0.86}As$. The barrier layers GaAs efficiently absorb the incident pump power at the wavelength 808 nm. The "long-wavelength" active region AR_L consists of 7 quantum wells $In_{0.25}Ga_{0.75}As$ which are located by pairs in three sections and one additional QW is in fourth section. To enhance the achievable gain coefficient, all the quantum wells are placed nearly at the antinodes of their own standing waves. As it was already mentioned, the sections are separated by the wide-band blocking layers $GaAs_{0.7}P_{0.3}$ working as the strain compensating layers at the same time. The short-wavelength active region is grown close to the surface of the device and the long-wavelength one is deeper in the structure. The active regions are separated by the long-wave-pass filter which is transparent for the pumping and strongly reflective for the short-wavelength radiation. Moreover, the stop-band of said filter is chosen to have λ_L at one of the reflection minima of the filter.

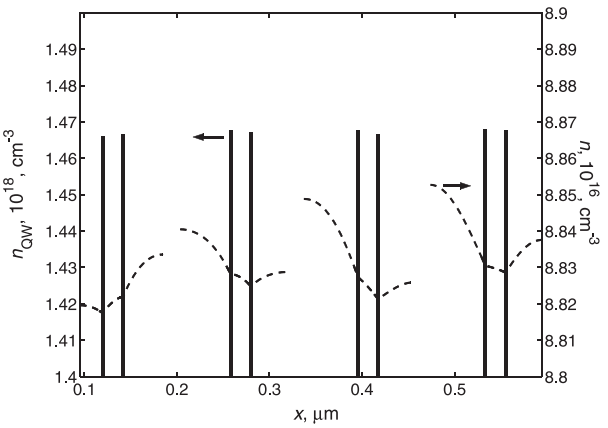

Fig. 2. Carrier density in the QWs (solid line) and the barrier layers (dotted line) of AR_S.

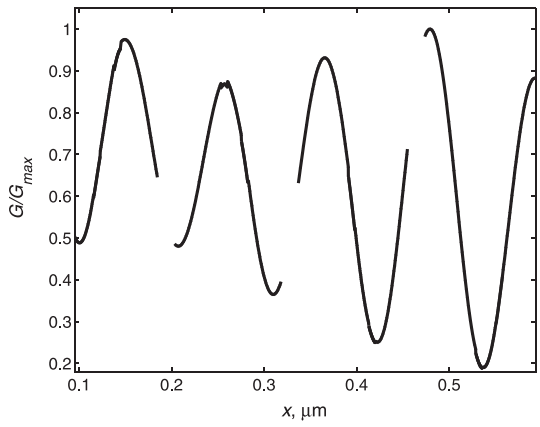

Fig. 3. Carrier generation rate in the barrier layers of AR_S.

By optimizing the position of the blocking layers in the active regions one could equalize carrier population in the quantum wells. Fig. 2 shows the carrier distribution in the QWs and the barrier layers of AR_S provided that the blocking layers location is optimal. To obtain these findings, the diffusion equation for the carriers generated by the pumping in the barrier layers was solved self-consistently with the balance equations determining carrier exchange between the QW's confined states and the continuous states above the QWs [9]. We used the following typical parameters of the structure in these calculations: the ambipolar diffusion coefficient $D_a = 10$ cm^2/s; the carrier lifetime τ and loss coefficient α of the pump radiation in the barrier layers correspond to 5 ns and 13200 cm^{-1}, respectively; the capture time $\tau_c = 0.3$ ps and the escape time $\tau_{esc} = 5$ ps for the short-wavelength QWs. The laser structure was supposed to be pumped at the wavelength $\lambda_p = 808$ nm with the incident power $P_{in} = 0.2$ W and the spot diameter $d = 100$ μm. One could easily see from Fig. 2 that the carrier concentration profile in the barrier region breaks at the blocking layers positions. It is because of carrier transport impenetrability of these layers. Therefore, the pumping of all the sections appears to be independent and the possibility arises for quantum wells population to be perfectly uniform. The calculations performed for the data of Fig. 2 result in the QW's non-uniformity $\chi = \sigma/a$ being less than 0.1 percent. Here σ and a are the standard deviation and the mean value of the QW's carrier concentration. The carrier distribution shown in Fig. 2 corresponds to the normalized carrier generation rate which is displayed in Fig. 3.

The carrier generation rate G was determined as follows:

$$G(x) = -\frac{dS}{dx}\frac{\lambda_p}{hc},$$

where $S(x)$ is the pump power density, h is the Planck's constant and c is the light velocity. In linear regime of absorption, the pump power density being determined according to $S = 0.5\mathrm{Re}[\mathbf{E}\mathbf{H}^*]$ must be found as the solution of the Helmholtz equation for the pump wave. Here $\mathbf{E}$, $\mathbf{H}$ are the complex amplitudes of the electric and magnetic fields of the pumping. Fig. 3 demonstrates clearly the carrier generation rate to be greatly different from the ordinary exponential dependence

$$G(x) = \frac{4P_{in}}{\pi d^2}\frac{\alpha\lambda_p}{hc}e^{-\alpha x}.$$

The last formula is valid provided that there is the incident pump wave only (i.e., the Beer–Lambert law holds). The pump wave reflections manifest themselves as the carrier generation rate pulsations superimposed on the exponential decay. Note, that the magnitude of these pulsations is quite comparable with an average value of G.

In conclusion, we have analyzed the carrier density profile in the optically-pumped dual-wavelength SDL. The quite general model of the laser structure has been applied to the study. The analysis shows that the carrier distribution in the barrier layers and the uniformity of the QW carrier population is greatly determined by the pump wave reflections in the laser structure. With the blocking layers properly located, nearly perfect uniformity of the carrier concentration in the QWs could be obtained. The pump wave reflections have to be taken into account when the dual-wavelength SDLs, like those studied in [4,5] or an ordinary optically-pumped VECSELs, are designed.

Acknowledgements

This work has been supported in part by the Academy of Finland under projects 115810 and 109080.

References

[1] A. Tropper *et al*, *J. Phys. D.* **37**, R75 (2004).
[2] G. Kim *et al*, *Appl. Phys. Lett.*, **89** 181106 (2006).
[3] V. G. Dmitriev, L. V. Tarasov, *Applied nonlinear optics*, Moscow: Physmatlit, 2004.
[4] T. Leinonen *et al*, *IEEE Phot. Techn. Lett.* **17**, 2508 (2005).
[5] T. Leinonen *et al*, *Optics Express* **15**, 13451 (2007).
[6] A. Harkonen *et al*, *IEEE Phot. Techn. Lett.* **19**, 1550 (2007).
[7] Yu. Morozov *et al*, *Proc. 15th International Symp. Nanostructures: Physics and Technology. (Novosibirsk, Russia, 2007)*, Ioffe Institute, 48 (2007).
[8] M. Beck *et al*, *Science* **295**, 301 (2002).
[9] Yu. A. Morozov *et al*, *IEEE JQE* **42**, 1055 (2006).

16th Int. Symp. "Nanostructures: Physics and Technology"
Vladivostok, Russia, July 14–18, 2008

Optimization of waveguide properties for mid-IR Cr^{2+}: ZnSe laser

R. A. Mironov, A. O. Zabezhaylov, S. V. Alyshev and E. M. Dianov
Fiber Optics Research Center, 119333 Moscow, Russia

Abstract. We present the numerical calculations of the waveguiding properties and optimization of Cr^{2+}:ZnSe/ZnMgSSe/GaAs based planar structures for lasing in 2–3 μm wavelength range. Propagation loss value is predicted to be less than 1 dB/cm for 3.2 μm lower cladding layer thickness. Two types of ARROW (antiresonant reflecting optical waveguide) based on MgS and GaAs compounds are proposed to reduce losses. A propagation loss of less than 0.1 dB/cm for TE_0 mode is predicted for the structure with three MgS buried layers.

Introduction

Transition metal doped wide-band-gap semiconductors were proposed as effective tunable mid-infrared laser sources [1]. Active interest to this lasers is inspired by their possible application in medicine, trace gas monitoring, spectroscopy, optical communications and military technology [2]. Different lasing regimes have been realized at present on Cr^{2+} and Fe^{2+} doped II–VI bulk crystal [3]. Compact, low energy consuming and possibly injection pumped microchip laser can be obtained with the use of heterostructures [4]. However, thin films lasing is still not obtained in spite of progress in Cr^{2+}: II–IV epitaxial growth technology [5–7]. Formation of effective waveguide structure can be the key feature to obtain thin film lasing in the mid-infrared.

In this work we present numerical calculations to optimize waveguiding properties of ZnSe/ZnMgSSe/GaAs semiconductor heterostructures (Fig. 1) in 2–3 μm wavelength range for Cr^{2+}:ZnSe waveguide.

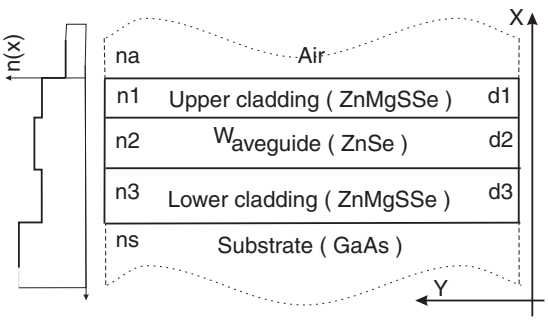

Fig. 1. Planar waveguide structure and refractive index profile.

1. Theory

Three layered planar structure unbounded in the Y direction with semi-infinite upper air layer and substrate are considered in the present paper. If we suppose electric field $E \sim \exp[j(\omega t - \beta z)]$, the solutions of the wave equation for TE-modes propagating in the Z direction can be found in the form:

$$E_{yi} = A_i \exp[-k_i(x - x_{i-1}] + B_i \exp[k_i(x - x_{i-1})],$$
$$k_i = \sqrt{\beta^2 - k_0^2 n_i^2},$$

where β — propagation constant, n_i — refractive index of the i-th layer, k_0 — wave number in vacuum.

Useful way to calculate the physical properties of multilayer waveguide structures is the transfer-matrix method (TMM). TMM gives the amplitudes of forward (A) and backward (B) propagating waves in the air and in the substrate connected by 2×2 matrix:

$$\begin{pmatrix} A_s \\ B_s \end{pmatrix} = (\prod Q_i) \begin{pmatrix} A_a \\ B_a \end{pmatrix} = \begin{pmatrix} q_{11} & q_{12} \\ q_{21} & q_{22} \end{pmatrix} \begin{pmatrix} A_a \\ B_a \end{pmatrix}$$

$$q_{22} = |q_{22}| \exp(j\phi),\ \gamma = \mathrm{Re}(\beta),\ L = \frac{d\phi(\gamma)}{d\gamma},\ \alpha = \mathrm{Im}(\beta).$$

For our calculations we used reflecting pole method [8]. This method is based on the extraction of real and imaginary parts of propagation constant from Lorentzian-type peaks of the reflection coefficient. Propagation constants are determined by monitoring the variation of the reflection coefficient denominator's phase as a function of the effective index. Loss in waveguide structure can be determined as half width at the half maximum of the $L(\gamma)$ curve.

2. Results

Relatively large value of the substrate refractive index is the main drawback of ZnSe/ZnMgSSe/GaAs waveguide structures which leads to a high value of absorption loss. To reduce propagation loss one should increase lower cladding layer thickness or refractive index step between waveguide layer and cladding. Maximal index step that can be achieved with $ZnSe/Zn_{1-x}Mg_xS_ySe_{1-y}$ structure is limited by the value $\sim$0.1 due to the thermodynamical instability in quaternary alloys solid solutions with $x, y > 20\%$ [9]. So, we focus our attention on the search of the minimum cladding layer thickness having fixed maximum available refractive index step.

The results of loss calculations in the waveguide structure are shown in Fig. 2. Firstly, it is seen that waveguide loss has rather large value with cladding thickness of 2 μm. Secondly, losses strongly depend on the wavelength in the wavelength range considered. Thus, great value of the waveguiding losses, can be the cause of Cr^{2+}:ZnSe thin films lasing failure. Our estimations show that the value of waveguiding loss should be less than 1 dB/cm for mid-infrared lasing in the considered structures. To obtain such loss value in the Cr^{2+} emission band 2–3 μm the lower cladding layer thickness should be not less than 3.2 μm.

The application of antiresonant reflecting optical waveguide (ARROW) can be an efficient way to reduce the loss [10].

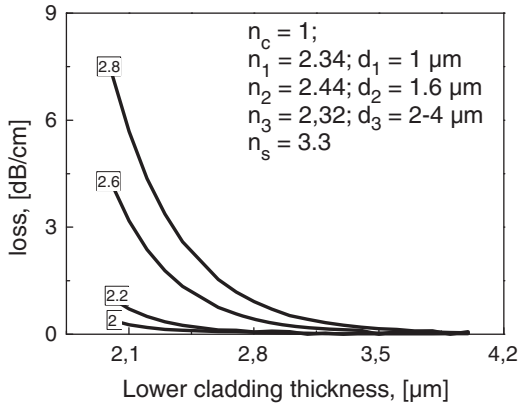

Fig. 2. Loss value in the waveguide as a function of lower cladding layer thickness for four different wavelengths (2; 2.2; 2.6; 2.8 μm). Parameters of waveguide are shown in the inset.

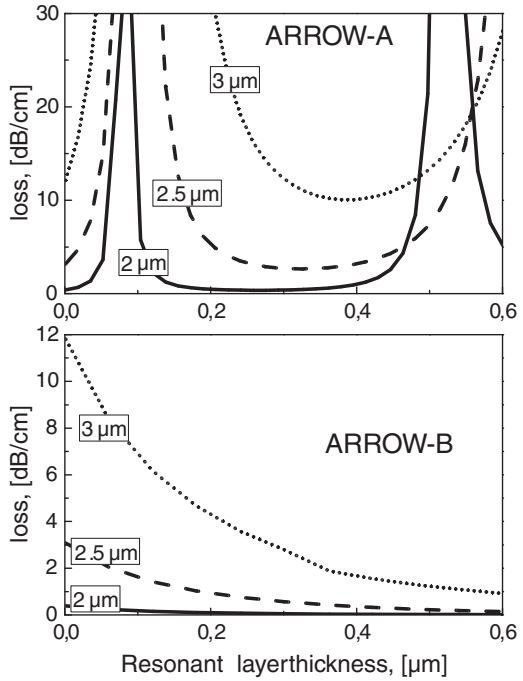

Fig. 3. Loss in ARROW-A and ARROW-B structures for three wavelengths (2; 2.5; 3 μm)

Here we considered ARROW-A with resonant layer of GaAs and ARROW-B with MgS. Technically ARROW-A structure can be realized by using molecular beam epitaxy system with two growth chambers. ARROW-B can be grown with one growth chamber but each MgS epitaxial layer has an upper limitation of thickness of about 0.13 μm [11]. However this thickness limitation can be avoided by using multiple resonant layers.

The results of loss calculations in ARROWs are shown in Fig. 3. For ARROW-A structure the first optimal resonant layer thickness occurred to be 0.2–0.35 μm for 2 μm wavelength with the value of propagation loss of 0.4 dB/cm. With the wavelength increase the optimal resonant layer thickness and propagation loss are increased. Thus, to cover all the emission band of Cr^{2+}: ZnSe one should use two or three resonant layers with different thicknesses.

Such structures are rather difficult to be grown, which makes ARROW-B more preferable because reasoning this case

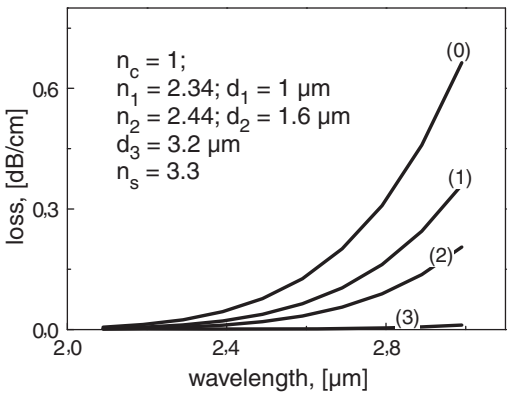

Fig. 4. Loss as a function of wavelength for waveguide with optimal parameters shown in the inset, lower cladding consists of: (0) — ZnMgSSe only ($n = 2.32$); (1),(2),(3) — ZnMgSSe with one, two and three MgS ($n = 1.84$) layers , with thicknesses of 0.1 μm each one.

the thickness and wavelength dependences are flattened (see. Fig. 3). For calculations we assumed that the refractive index of MgS monocrystal is equal to 1.84 in the mid-infrared.

Propagation loss calculations for optimal set of parameters are shown in Fig. 4 for ARROW-B structure without, with one, two and three resonant layers of MgS.

3. Conclusion

In conclusion, it is shown that the high index of GaAs substrate leads to large loss in Cr^{2+}:ZnSe/ZnMgSSe/GaAs based waveguide structures. Thick cladding and ARROW structures can be used to overcome these difficulties. The propagation loss value which is less than 1 dB/cm is suitable for lasing. This value has been obtained with 3.2 μm lower cladding layer thickness. The value of propagation loss of less than 0.4, 0.2 and 0.02 dB/cm is calculated for ARROW-B structure with one, two and three 0.1 μm thickness MgS layers respectively.

Acknowledgements

This work was supported by Russian Foundation of Basic Research Grant 05-07-08176.

References

[1] L. D. DeLoach *et al*, *IEEE J. Quant. El.* **32**, 885 (1996).
[2] I. T. Sorokina, *Opt. Mat.* **26**, 395 (2004).
[3] S. B. Mirov *et al*, *IEEE J. of Sel. Top. In QE.***13**, 810 (2007).
[4] A. Gallian *et al*, *Appl. Phys. Lett.* **86**, 091105 (2005).
[5] I. P. Kazakov *et al*, *Int. J. of Nanoscience* **6**, 448 (2007).
[6] B. L. Vanmil *et al*, *J. Electron. Mater.* **31**, 770 (2002).
[7] Ming Luo *et al*, *J. Appl. Phys.* **97**, 013518 (2005).
[8] E. Anemogiannis *et al*, *J. Light. Tech.* **17**, 939 (1999).
[9] V. S. Sorokin *et al*, *J. Cryst. Growth* **214–215**, 130 (2000).
[10] T. Baba *et al*, *IEEE Quant. El.* **28**, 1689 (1992).
[11] C. Bradford *et al*, *J. Cryst. Growth.* **227–228**, 634 (2001).

16th Int. Symp. "Nanostructures: Physics and Technology"
Vladivostok, Russia, July 14–18, 2008

Collinear interaction between light beams in the nanocomposite with liquid-phase matrix

A. V. Scherbakov, Y. N. Kulchin, V. P. Dzyuba and S. S. Voznesenskiy
Institute for Automation and Control Processes FEB RAS, Vladivostok, Russia

Abstract. The experimental results of the collinear nonlinear optical interaction between light beams with different wavelengths in the heterogeneous liquid-phase composite (HLPC) are shown. The low-threshold optical nonlinearity proved to be obtained by using the HLPC composed of Al_2O_3 wide-band dielectric nanoparticles and matrix of an organic medium with minor refraction index. Such nonlinearity allows one to control the light transmission characteristics in nanocomposite. It is shown that the optical radiation control device of a "photon transistor" type can be developed on the HLPC basis.

Introduction

It is very important today to find out the extra technology to increase a processing power. Parallel optical and quantum technologies are supposed to be the most effective ones. Improving of the light usage possibilities for processing of the huge amount of data is associated with development of the new technologies for optical logical elements.

Thereby, laser induced processes in nanocomposite media composed of organic material matrices [1–7] are being studied widely today. Heterogeneous liquid-phase composites (HLPC) with nanoparticles made of semiconductor and dielectric material are supposed to be successfully applied in such part of optical informational systems as the light control devices.

HLPC are at advantage owing to their ability to change the nonlinear optical characteristics by using the selection of the material and concentration of its components is a great advantage. Realizable low-threshold nonlinear optical processes of self-focusing and light dispersion allow us to use them in the development of functional elements of optical processors [3–7].

The aim of the work is to study such promising approach to the development of light radiation control devices as collinear nonlinear-optical interaction between light beams with different wavelengths.

1. Light beams interaction process

Interaction between light beams and nanoparticles-liquid-phase complex caused by passing the light radiation through HLPC results in effective refractive index and absorption coefficient changes. These changes are strongly depend upon light intensity, characteristics of the matrix material and nanoparticles concentration.

Because of Gaussian profile of the light intensity distribution in the laser beam cross-section the lateral distribution of the effective refractive index of HLPC in the laser wave field will be inhomogeneous and dependable upon the light intensity, the values and the signs of nonlinear optical additions to the refractive index: $n_1(a, N)$ and $n_2(T, t)$ which depend on nanoparticles concentration (N) and temperature of the medium (T). Given $n_1(a, N) > 0$ to the direction of light propagation the positive gradient lens will appear in HLPC, otherwise, lens will be negative. The last case will provide focusing or defocusing of the light in the near axial area.

Since the light propagation in HLPC is mostly concerned with its partial absorption in the nanoparticles and matrix material, heat release into liquid-phase matrix occurs along the beam path. Amount of the released heat depends upon absorption coefficient in the HLPC material and light intensity. It allows us to control medium transmission characteristics which means that it is possible to modulate the passing light radiation intensity.

2. Experimental results

For the purposes of study the collinear interaction between light beams with different wavelengths in the HLPC the next devices were used: He-Ne laser ($\lambda = 632$ nm) with average power about 50 mWt and YAG laser pumped by semiconductor lasers matrix (the second laser harmonic $\lambda = 632$ nm) with average power about 40 mWt.
Immersion oil (refractive index $\sim$1.5) with $\sim 40-50$ nm Al_2O_3 wide band dielectric nanoparticles (refractive index $\sim$1.7) was used as matrix of HLPC. Volume concentration of nanoparticles in HLPC was about $\sim$0.3.

Dependencies of the HLPC passing effectiveness on intensity of the light beams with 532 nm and 633 nm wavelengths incoming into cuvette in cases of their independent passing through medium and their collinear interaction were investigated. Normalized dependencies of amplification and attenuation of light beams with wavelengths 532 and 633 nm (for fixed values of their light intensities) on values of the collinear

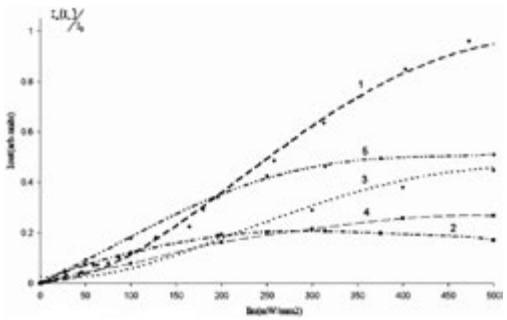

Fig. 1. Dependencies of the HLPC light transmission on the light intensity and combination of the interacted light beams wavelengths. 1 — $\lambda = 630$ nm / ($\lambda = 0.53$ nm, $I = 0$); 2 — $\lambda = 530$ nm /($\lambda = 0.63$ nm, $I = 0$); 3 — $\lambda = 630$ nm / ($\lambda = 0.53$ nm, $I = 250$ mW/mm^2); 4 — $\lambda = 630$ nm / ($\lambda = 0.53$ nm, $I = 500$ mW/mm^2); 5 — $\lambda = 530$ nm /($\lambda = 0.63$ nm, $I = 500$ mW/mm^2).

light beams intensities are shown at Fig. 1. According to these dependencies it is possible to realize the control process of the laser radiation in HLPC by using the intensity changes of the collinearly interacting light beams with different wavelengths. This approach enables the "photon transistor" function. The "amplification" level can be up to 10 dB.

Conducted experiments have shown the possibility to optimize the light radiation control process by using the selection of the energetic and spectral characteristics of the modulating light beam. It seems very promising to develop optically controlled filters for lightwave systems and modulators for information input into optical processors.

3. Conclusions

The collinear interaction between light beams with different wavelengths in a heterogeneous liquid-phase nanocomposite (HLPC) was investigated. It has been shown that low-threshold optical nonlinearity can be obtained in HLPC by using wideband dielectric nanoparticles as sensitizer and organic liquid medium with minor refractive index as a matrix. Such nonlinearity allows us to control the transmission characteristics of HPLC and to develop optical processor elements.

References

[1] M. I. Samojlovich, M. J. Tsvetkov, *Nano- and microsystem technic*, **10**, 8 (2006).
[2] A. A. Afanasjev, A. N. Rubinov, *Optics and spectroscopy* **102**, 116 (2007).
[3] O. P. Mikheeva, A. I. Sidorov, *Journal of Applied Physics*, **74**, 77 (2004).
[4] Y. N. Kulchin, A. V. Scherbakov, V. P. Dzyba, S. S. Voznesenskiy, G. T. Mikaelyan, *Quantum electronics* **38**, 2 (2008).
[5] J. A. Ferrari, E. M. Fins, E. Garbius, M. Korn, *Optical Engineering* **45**, 065001 (1–4) (2006).
[6] V. A. Trofimov, E. B. Tereshin, *Optics and spectroscopy* **99**, 998 (2005).
[7] N. V. Kamanina, A. K. Philipov, Y. M. Voronin, *Optical Journal* **73**, 19 (2006).

16th Int. Symp. "Nanostructures: Physics and Technology"
Vladivostok, Russia, July 14–18, 2008

Self-assembled biosilification processes in animate nature as the base of prospective nanostructures creation technology

Yu. N. Kulchin
Institute for Automation and Control Processes FEB RAS, Vladivostok, Russia

Abstract. An overview of the results of comprehensive investigation into physical and biochemical properties of sea glass sponge spicules is presented. The potential of natural self-organizing process of biosilification has been analyzed as a promising nanotechnology for photonics and nanoelectronics applications.

Introduction

In the course of evolution biological systems have developed unique survival techniques ranging from means of frightening predators and achieving mechanical hardness to complex photosynthesis processes. Skeletons of sea organisms are built from diverse minerals: calcite, aragonite, apatite and silica [1]. The following sea organisms attract particular attention: diatomaceous, radiolarian and sponges, whose skeletons are built form silica [2] by self-organizing process of biosilification (Fig. 1).

Nowadays optical telecommunications based on fused silica optical fibers have become an essential part of our everyday life. However the idea of using glass fibers to transmit light had been realized by Nature long before it created human. *Hexactinellida (Porifera)* glass sponges represent a group of the most ancient multicellular animals using silicon as a biological mineral to build their skeletons from, with their evolution started as long as 525 million years ago. Such organisms commonly occur in nature and are predominantly found in deep water areas of the oceans. The skeleton of such sponges is composed of peculiar thread-like siliceous spicules, with their size ranging drastically depending on the age of the sponge: diameter — 0.01 to 30 mm, length — 0.001 to 5 m [2].

Diatoms which are very common in the oceans and freshwater bodies represent another example of organisms with silica skeletons. Their evolution started somewhat later — 260 million years ago. Those are substantially smaller ones ranging in size from a few to several tens of microns.

Characteristic of all of the above mentioned organisms is that they use self-organizing process of biosilification to form a robust silicon skeleton composed of silicon dioxide nanoparticles 20 to 400 nm in size. The process is governed by a special program recoded in the genetic code of the proteins responsible for the extraction of silicon from the surrounding environment.

As of now silicon metabolism in the live Nature named biosilification is given much attention to by the leading biotechnology and biomedicine scientists. On the one hand it results from common use of silicon in numerous high-tech industries and production processes, e.g. microelectronics, optoelectronics, industrial chemistry, etc. On the other hand this interest is caused by that the bio-catalytic process of silicon extraction from the surrounding media takes place under normal conditions contrary to the standard methods of physical chemistry requiring extreme temperature, pressure or pH values.

Throughout millions of years Nature has been perfecting the mechanism of skeleton formation of biological objects and has made it by now a highly rational one through the utilization of ingenious technical and technological solutions.

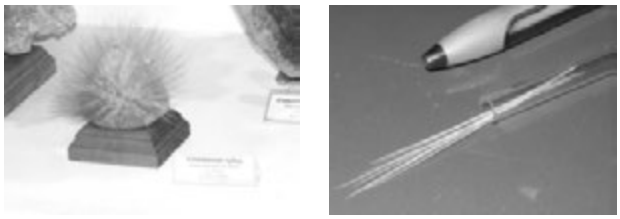

(a) (b)

Fig. 1. *Pheronema sp.* sea sponge photo (a), fragments of its skeleton-forming spicules (b).

The purpose of the present work is to overview the results of the investigation into physical and biochemical specifics of the sea organisms skeletons formed by self-assembly biosilification process, which makes it possible to develop new technologies for realizing functional units of photonics and nanoelectronics.

1. Structural, mechanical and biochemical properties of glass sponge spicules

In practical terms the most attractive object for investigation are the sea sponges whose skeleton is formed of sufficiently long spicules (on the order of centimeters) representing hydrated quartz structures deposited around a protein core. The present work focused on *Hyalonema sieboldi* and *Pheronema* sea sponges dwelling in the Pacific and Indian Oceans at a depth of 30 to 5000 m [2–5].

The study of structural, mechanical, and optical properties of *Hyalonema sieboldi* and *Pheronema* spicules 0.01 to 0.05 m in length and 40 to 1000 μm in diameter proved that depending on their function and position in the sea sponge organism spicules can differ in structure but the principles of spicule formation are always the same.

Spicules are classified into basal (or anchor) and skeleton-forming ones. The basic function of basal spicules seems to consist in the mechanical linkage with the surrounding media and responding to the variations in the environmental conditions. As opposed to basal ones, skeleton-forming spicules present more elaborate structures responsible for shaping skeletons of sponges as well as ensuring their rigidity. Fig. 2 shows cross-section views of basal and skeletal spicules obtained by scanning electron microscopy.

Spicules of both types represent complex thread-like struc-

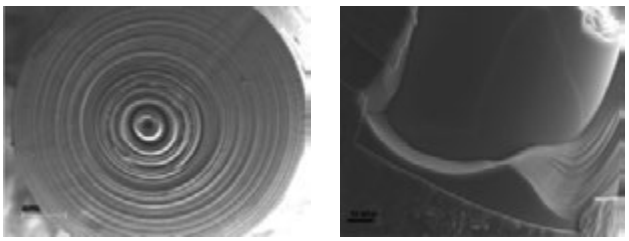

(a) (b)

Fig. 2. Scanning electron microscopy photos of: cross sections of *Hyalonema sielbody* basal spicule (scale 100 μm) (a) and fragment of Pheronema skeleton-forming spicule (scale 10 μm) (b).

tures composed of silicon dioxide nanoparticles and protein components which is verified by X-ray photoelectron spectroscopy.

So as to gain better insight into the regulatory mechanisms of silica polymerization and concentration processes silicatein protein was extracted from spicules, which acts as a hydrolysis catalyst and is responsible for silicon polycondensation, and its genetic structure was analyzed.

In-depth study of microhardness and Young modulus of the spicules proved that though close to those of fused silica they are unequally distributed over spicule cross-section and tend to decrease towards the periphery. The multilayer structure of spicules makes them mechanically strong and flexible.

2. Optical properties of sea sponge spicules

Researches on the light transmission in the spectral range of 400 to 1600 nm indicated a good transparency of spicules at 500 to 1300 nm wavelengths.

Measurements of refractive index distribution over the cross-section of spicules showed the refractive index to be 1.45–1.48 at the center and to decrease to 1.4–1.45 at the periphery.

In the course of the research on white light transmission basal spicules were found to concentrate the light transmitted within the paraxial region with a distinct white-to-red color gradient along the spicule. This is explained by the quasi-periodical layer structure of the spicule. Additional research using femtosecond Ti:sapphire laser proved the spicules under study to be a new kind of natural photonic crystals.

Further research on fluorescence in sea sponge spicules using YAG:Nd laser (the first and second harmonic pulses) revealed a substantial increase in the fluorescence intensity in the long wavelength region together with a saturable maximum at 770 nm. This proves the nonlinear character of light energy transformation in the spicules due to their inherent high concentration of organic complexes. In-depth examination of fluorescence spectra of laser radiation both in the sea sponge body and spicules confirmed the presence of chlorophyll A. A comprehensive research on spicule morphology, absorption and fluorescence spectra as well as fatty acids composition enabled us to assert that the main symbionts of glass sea sponges are photosynthesizing cyanobacteria.

3. Conclusion

The researches carried out demonstrated that natural self-assembly technology of the extraction of silicon dioxide from seawater by silicateine protein allows production under normal conditions of a promising for photonics and nanoelectronics material which combines the elasticity of protein with the strength of fused silica. The material under research potentially has a number of important features, namely, no birefringence, good mechanical properties, as well as simplicity of production and incorporation of additives. Nonlinear character of fluorescence spectrum as well as photonic crystal properties make sea glass sponge spicules a promising material for the development of active photonic devices.

Acknowledgements

The research is supported by RFBR grants No. 06-02-96902-r_ofi, RFBR No. 07-02-01442_a; by the program of basic research of the Department of physics RAS the “Coherent radiation of semiconductor lasers and structures”.

References

[1] C. Vikram *et al*, *Nature* **424**, 899 (2003).
[2] Yu. N. Kulchin, S. S. Voznesensky *et al*, *FEB RAS Bulletin* **1**, 27 (2007).
[3] Yu. N. Kulchin, S. N. Bagaev *et al*, *Opt. Mem. and Neural Networks* **16**, 189 (2007).
[4] Yu. N. Kulchin *et al*, *Nonlinear waves*, Nizhniy Novgorod, (2007).
[5] Yu. N. Kulchin *et al*, *Quantum Electronics* **38**, (2008).

16th Int. Symp. "Nanostructures: Physics and Technology"
Vladivostok, Russia, July 14–18, 2008

Fractal-related assembly of the axial filament in the demosponge *Suberites domuncula:* contribution to the pattern formation of bio-silica

Werner E. G. Müller[1], Xiaohong Wang[2], Ute Schloßmacher[1], Alexandra Boreiko[1] and Heinz C. Schröder[1]

[1] Institut für Physiologische Chemie, Abteilung Angewandte Molekularbiologie, Universität, Duesbergweg 6, D-55099 Mainz, Germany
[2] National Research Center for Geoanalysis, 26 Baiwanzhuang Dajie, CHN-100037 Beijing, China

Biomineralization, biosilicification in particular (i.e. the formation of biogenic silica, SiO_2), has become an exciting source of inspiration for the development of novel bionic approaches following "nature as model". Siliceous sponges are unique among silica forming organisms in their ability to catalyze bio-silica, a material with increasing applied potential in bio-medicine and bio-optics. The sponges (phylum Porifera; diploblasts), as the phylogenetically oldest metazoan phylum, are characterized by a distinct body plan, which is organized — in contrast to that of most other, higher metazoan phyla — along only one body axis. It runs in apical-basal direction, while most triploblastic metazoans are organized along an antero-posterior and a dorso-ventral axis. Surely the form and hence the body plan of sponges is genetically controlled, since the size and shape of a given species are defined. In the last years a bulk of information became available about the genetic basis of cell-cell and cell-tissue interactions in sponges, e.g. about the integrin system, the differentiation of cells, e.g. stem cells, the axis formation of the body, e.g. the Wnt pathway, or the immune system, e.g. cytokines or immunoglobulin. Most of the studies were performed with the demosponge *Suberites domuncula*.

The siliceous spicules of sponges (Porifera) show great variations of sizes, shapes and forms; they constitute the chief supporting framework of these animals; these skeletal elements are synthesized enzymatically by silicatein. Each sponge species synthesizes at least two silicateins, which are termed $-\alpha$ and $-\beta$. In the present study, using the demosponge *Suberites domuncula*, we studied if the silicateins of the axial filament contribute to the shape formation of the spicules. For these experiments native silicateins have been isolated by a new Tris/glycerol extraction procedure. It is shown that the Tris/glycerol extracted silicateins are monomeric (24 kDa), but readily form dimers through non-covalent linkages. The Tris/glycerol extracted silicateins show a considerable proteolytic activity that increases during the polymerization phase of the protein. The assembled silicateins (dimers, tetramers as well as hexamers) can be demonstrated in zymograms. The filament/aggregate formation from disassembled silicatein can be visualized by both light and transmission electron microscopic (TEM) analyses. Since in *S. domuncula* silicatein-α is 4-times more abundant in the axial filament than silicatein-β we propose that four silicateins form a platform with serine clusters directed to the center. These serines of the con-axially arranged silicateins interact with silicatein-β. We conclude that the silicateins re-assemble initially chaotically, and, in the second phase assemble to fractal-like structures, which subsequently form the filaments.

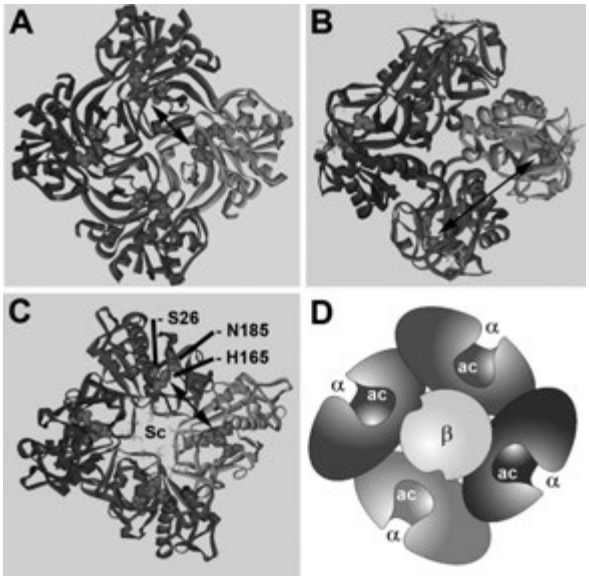

Fig. 1. Schematic representation of one planar silicatein-α tetramer (α; green-grey-blue-pink); with one silicatein-β (β in the center [yellow]). It is proposed that the orientations of the silicatein units are identical in each of the three configurations. The amino acids involved in the active centers of the silicateins (the amino acids are counted within the mature molecule) are marked; serine (S26), histidine (H165) and asparagine (N185). (**A**) The silicatein molecules are oriented with their active centers towards the center of the axis (syn-axial), or (**B**) in the opposite direction of the axis (anti-axial), or, (**C**) the entrances of the con-active centers are located in the plane of the tetramer (con-axial). Only in the axial-orientation the Ser-rich clusters (Sc) are directed towards the center of tetramer. The double arrow is showing the distance between one pair of histidines between two silicatein-α molecules (H165). (**D**) Graphical model of the silicatein-α tetramer with the silicatein-β in the center. The active centers in the silicatein-β molecules are marked (ac). (**D** and **F**) The distortion of the silicatein-β molecules within the tetrameric plane is illustrated.

The data presented will contribute to a controlled enzymatic synthesis of biosilica, applicable for biomedical use.

References

[1] W. E. G. Müller, How was metazoan threshold crossed: the hypothetical Urmetazoa. *Comp. Biochem. Physiol. A* **129**, 433–460 (2001).

[2] W. E. G. Müller, Spatial and temporal expression patterns in animals. In: Meyers R. A. (ed.) *Encyclopedia of Molecular Cell Biology and Molecular Medicine*. WILEY-VCH Press, Weinheim **13**, 269–309 (2005).

[3] W. E. G. Müller, B. Blumbach, and I. M. Müller, Evolution of the innate and adaptive immune systems: Relationships between potential immune molecules in the lowest metazoan phylum [Porifera] and those in vertebrates. *Transplantation* **68**, 1215–1227 (1999).

[4] W. E. G. Müller, A. Krasko, G. Le Pennec, R. Steffen, M. S. A. Ammar, M. Wiens, I. M. Müller, and H. C. Schröder, Molecular mechanism of spicule formation in the demosponge *Suberites domuncula*: Silicatein-collagen-myotrophin. *Progress Molec. Subcell. Biol.* **33**, 195–221 (2003).

[5] W. E. G. Müller, M. Wiens, T. Adell, V. Gamulin, H. C. Schröder, and I. M. Müller, Bauplan of Urmetazoa: Basis for genetic complexity of Metazoa. *Intern. Review of Cytology* **235**, 53–92 (2004).

[6] W. E. G. Müller, M. Rothenberger, A. Boreiko, W. Tremel, A. Reiber, and H. C. Schröder, Formation of siliceous spicules in the marine demosponge *Suberites domuncula*. *Cell & Tissue Res.* **321**, 285–297 (2005).

[7] W. E. G. Müller, A. Borejko, D. Brandt, R. Osinga, H. Ushijima, B. Hamer, A. Krasko, C. Xupeng, I. M. Müller, and H. C. Schröder, Selenium affects biosilica formation in the demosponge *Suberites domuncula*: effect on gene expression and spicule formation. *FEBS Journal* **272**, 3838–3852 (2005).

[8] W. E. G. Müller, S. I. Belikov, W. Tremel, C. C. Perry, W. W. C. Gieskes, A. Boreiko, and H. C. Schröder, Siliceous spicules in marine demosponges (example *Suberites domuncula*). *Micron* **37**, 107–120 (2006).

[9] W. E. G. Müller, O. V. Kaluzhnaya, H. C. Schröder, V. A. Grebenjuk, A. Borejko, I. M. Müller, A. Krasko, and S. I. Belikov, Silicateins, the major biosilica forming enzymes present in demosponges: protein analysis and phylogenetic relationship. *Gene* **395**, 62–71 (2007).

[10] W. E. G. Müller, X. Wang, S. I. Belikov, W. Tremel, U. Schloßmacher, A. Natoli, D. Brandt, A. Boreiko, M. N. Tahir, I. M. Müller, and H. C. Schröder, Formation of siliceous spicules in demosponges: example *Suberites domuncula*. In: Bäuerlein E. (ed.) *Handbook of Biomineralization*. Vol. 1: The Biology of Biominerals Structure Formation. Weinheim: Wiley-VCH, 59–82 (2007).

16th Int. Symp. "Nanostructures: Physics and Technology"
Vladivostok, Russia, July 14–18, 2008

The features of nanostructured biosilica

S. S. Voznesenskiy, *A. N. Galkina* and Yu. N. Kulchin
Institute for Automation and Control Processes of FEB RAS, Vladivostok, Russia

Abstract. The results of the structural, mechanical and biochemical properties comparative analysis of the glass sea sponges *Pheronema sp., Pheronema raphanus, Hyalonema sieboldy* spicules are given. The structural properties of the glass sponge's spicules are investigated by the methods of the optical, scanning electronic (SEM) and atomic force microscopy (AFM). The distribution of chemical elements and generatrix of their compound in the longitudinal and cross section of the spicules of glass sponges is obtained by energy-dispersive X-ray spectroscopy (EDX) analyses. The correlation of these properties with the functional purpose of spicules and their optical characteristics is analyzed.

Introduction

Materials for studies were obtained from the museum collections of Zoological Institute and Institute of Oceanology Russian Academy of Science, and was collected by dredging during expeditions of "Academic Oparin" into the South China sea. Spicules from the skeleton of the sponges were selected: *Pheronema sp.* (South China sea, depth 215 m.), *Pheronema raphanus* (South China sea, depth 300 m.), and also the basal spicules of the sponge *Hyalonema sieboldy* (Philippines sea, depth of approximately 5000 m).

1. Results and discussions

Study of such important operating characteristics of the sponges *Pheronema sp.* and *H. sieboldy* spicules material as microhardness and Young's modulus by the dynamic of the ultramicrohardness gauge method of transverse sections with the use of a Berkovskogo pyramid showed that for the spicules their values were close to the appropriate values for the vitreosil [7]. In this case, the distribution of microhardnesses and Young's modulus they are heterogeneous in the cross section of spicule and have for the *H. sieboldy* basal spicules the tendency of drop from the center toward the periphery, that it is possible to explain by the stratification of the structure of spicule, by the presence of protein connections, and also by thinning the sizes of the layers of silica with their approximation to the periphery. This one of the components of the properties of the spicules composite material ensures their high resistance to bending. In comparison with not basal *Pheronema sp.* spicules the distribution of microhardness and Young's modulus bears more chaotic and these spicules more fragile than in *H. sieboldy* [6].

The scanning electron microscopy (SEM) analyses show that sizes and the geometry of the sponge's spicules varies depending on their designation and locations; however, the principles of the organization of spicules persist [1, 2, 3, 4]. The spicules from the body of the sponges *Pheronema sp.*, *Pheronema raphanus* are the thin extensive fiber formations, which have uniaxial symmetry, extent from 5 to 8 cm and thickness 150–170 m, which is compared with the sizes of the *Euplectella sp.* basal spicules [1]. Each spicule has dense central cylinder and thin siliceous concentric layers around it [1,2,3,4] outside covered with the laminating shell with the developed surface (Fig. 1a–d).

AFM phase imaging of cross section *Pheronema sp.* and *H. sieboldy* spicules revealed the presence of their composite

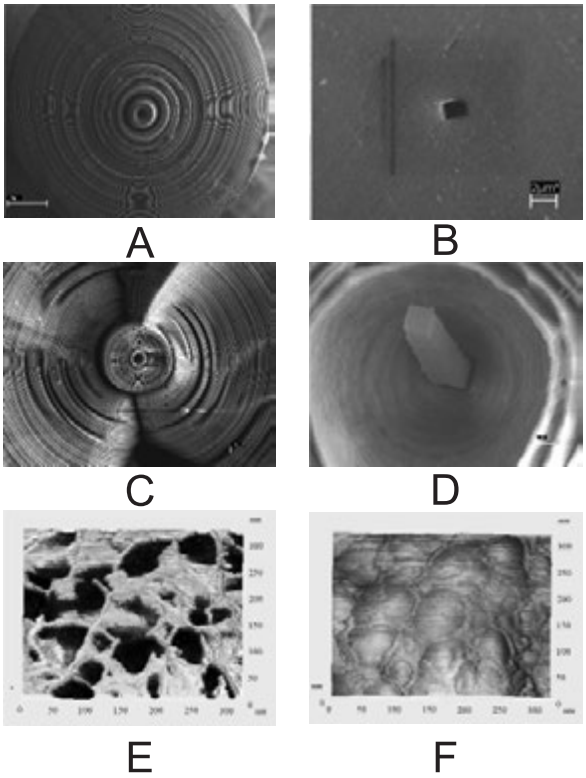

Fig. 1. Morphology of glass sponges skeletal fragments. A–D SEM analyses. A polished and etched cross section, scale 100 μm. B — axial channel of basal spicules from *H. sieboldy*, scale 2 μm. C — polished and etched cross section through a spicule of the sponge *Pheronema raphanus*, scale 10 μm. D — the etched axial channel of the *Pheronema raphanus* spicule, morphology of axial filament are visible, scale 2 μm. E–F AFM analyses. E — AFM phase imaging of fragment the cross section *Pheronema sp.* spicule surface. F — AFM height imaging the the same section of spicule *Pheronema sp.*

regular structure (Fig. 1e). It is distinctly evident that the structure of the spicule of sponge consists of the formations, which resemble flowers with the size of 0.1–1.5 m, which with a great increase more greatly are similar to the channels, supposedly, for the nanofiber of the connecting protein. For the comparison the same section of spicule of AFM height imaging is given (Fig. 1f). With the measurement in the regime of the topography of surface it is obtained that the diameter of the globules, of which are folded the layers of spicules, is 150–250 nm. The size of data of spheres not final and is not critical for the formation of composite material [1, 3]. Supposedly, globules

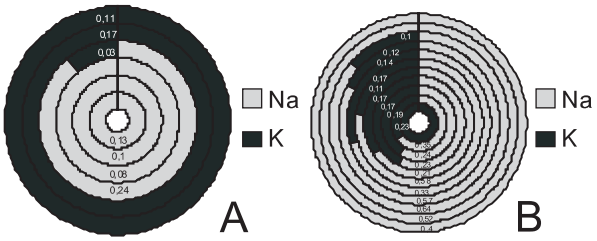

Fig. 2. EDX analysis results of the cross section spicule surface for the content of sodium and potassium: A — *Pheronema sp.*, B — *H. sieboldy*. (The region of spicule being investigated, chemical elements and their atomic content are given (%)).

themselves have complex composite composition, with the size of the component parts of 20–40 nm.

The EDX analysis results of the glass sea sponges spicules testify about their composite structure which confirm the presence in their composition of the high concentrations of the oxide of silicon and protein connections, which correlate with the results, obtained for *Euplectella sp.* [1]. It is shown for the sponges *Pheronema sp.* spicules that the smallest quantity of silicon and a maximum quantity of carbon contain the center section of the spicule (axial filament, central dense cylinder and the first layers around it) (probably organic origin). An increase in the content of silicon and a reduction of carbon content is observed in proportion to removal from the spicule center to its shell. The external laminating shell of spicule consists, predominantly, from the clean oxide of silicon and it does not contain the connections of carbon. Should be focused attention that the presence of the sodium (Fig. 2a) is characteristic for the center section of the spicule with their maximum content in the region 13–20 μm of the spicule center, and a potassium quantity — for the laminar region and the laminating shell.

Results of EDX analysis of cross section surface of basal the spicule *H. sieboldy*, indicate the different nature of chemical elements distribution, which, most likely, tells about different functional designation of spicules. The sponge *H. sieboldy* spicule center section, in contrast to *Pheronema sp.*, does not contain the connections of carbon, and it consists, predominantly from the silica. The silica distribution on the cross section of spicule uniform and composes 26–33%, whereas for the sponge *Pheronema sp.* spicules we see a gradual increase in the content of silicon from the spicule center to its periphery. It should be noted that for the *H. sieboldy* spicules is recorded the joint content of the sodium and potassium (Fig. 2b) on the entire part of the spicule, with exception of axial channel and external of laminar shell, that are been located at a distance 1–5 μm and 290–350 μm of the spicule center respectively. Special attention should be focused on the distribution of the potassium and sodium over the cross section of spicules, since the presence of sodium testifies about the large hydration of material, and consequently, the larger elasticity of this section of spicule. Whereas the presence of potassium in the system testifies about the high degree of material condensed, which is expressed in its increased density [4].

The established in the course of studies presence in spicules of the high concentration of the nonhomogeneously distributed organic starts leads to the nonlinearity of the process of the conversion of luminous energy [5, 6]. The results of the conducted investigations make it possible to make the conclusion that the presence in the glass sea sponges basal spicules of the periodic axial cylindrical layers of nanometer sizes, is capable of leading to control of the emission with the aid of the quantum effects, extended on them, based on the formation of the forbidden photon energy bands. The obtained results allow to assume that observed in the spicules of glass sponges laminar silicon structure it leads to the appearance of periodic three-dimensional modulation of dielectric constant with the period, compared with the wavelength of luminous radiation, which makes with their similar to the known microstructured fiber light guides. Specifically, the presence of translational symmetry in the cross section of the light-conducting region of spicules is capable of leading to the near-axial concentration and to the differential weakening of different regions of the spectrum of emission. In connection with which the glass sponge's spicules can be considered as the new form of natural photon crystals [5].

Acknowledgements

Work is supported by Grants RFBR 06-02-96902 and RFBR 07-02-01442.

References

[1] J. Aizenberg *et al*, *Science* **309**, 275 (2005).
[2] W. Müller *et al*, *Biosensors and Bioelectronics* **21**, 1149 (2006).
[3] W. Müller *et al*, *Journal of Structural Biology* **161**, 188 (2008).
[4] Wang Xiao-Hong *et al*, *Acta Zoologica Sinica* **53**, 557 (2007).
[5] Yu. N. Kulchin *et al*, *Opt. Mem. and Neural Networks* **16**, 189 (2007).
[6] Yu. N. Kulchin *et al*, *Quantum Electronics* **38**, 51 (2008).
[7] G. V. Samsonov *et al*, *Physicochemical properties of oxides* M.: Metallurgy, 1978, 472 pp.

16th Int. Symp. "Nanostructures: Physics and Technology"
Vladivostok, Russia, July 14–18, 2008

Viral particles influence on life systems as nanocontainer design prototype for cellular metabolism regulation

N. G. Plekhova[1], E. V. Pustovalov[2], L. M. Somova[1] and V. S. Plotnikov[2]

[1] Institute of Epidemiology and Microbiology, 1 Selskaya, Vladivostok, 690087, Russia
[2] Far East National University, Shukhanova 8, Vladivostok, 690950, Russia

Abstract. Different RNA and DNA viruses are examined as nanocontainer prototypes for cellular metabolism regulation. We found that Hantavirus and Tick Born encephalitis virus produce new viral particles in the first 24-hous after cell infection while for poliovirus, enteroviruses Coxsackie B1, 71 and ECHO 11 we have got different results. Poliovirus have expresses cytopathogenic effect inhibit cells metabolism and other used enteroviruses on the contrary make more active synthetic processes in different extent.

Introduction

Viruses are belonging to realm Vira are non-cellular form of live and contain a nucleic acid genome (RNA or DNA) and a protective protein coat (called the capsid). The nucleic acid genome plus the protective protein coat is called the nucleocapsid. Nucleocapsids have similar shape as crystals and may have icosahedral, helical or complex symmetry. Lot of virus groups have nucleacapsid covered by lipid capsule — supercapsid with specific structure and contains glicolipids. Such viruses are called "enveloped" while viruses without supercapsid "naked". Viruses can not reproduce on one's own outside the live systems and penetrate into a live system controlling metabolism of cell or bacteria. It able to switch functioning of the enzymes systems of host cell to reproduce new virus particles are intensify one of the synthetical processes and inhibit other. Penetration of virus nucleic acids into a cell is occurring by active or passive way. Lot of viruses infects only cells which it can specifically recognize by their own receptors. Despite the fact of complex origin of virus structure some models and schemes of viruses envelops and nucleocapsids as well as interaction viruses receptors and plasmalemms receptors are developed. Some results of investigation of virus ability to reproduce semiconductor and magnetic nanowires are published recently. Under corresponding conditions genetic modified virus will be able synthesize its own capsule from surrounding nanoparticles of semiconductor or magnetic materials [1,2]. On our opinion detailed investigation of interaction process between "ideal nanobiostructures" — viruses — with the live systems allows to understand of intracellular transference mechanism of different nanostructures and possibility of metabolism control of the live systems. In the future similar investigation can invent methods of address affecting on macroorganism by nanobiostructures will be able to regulate homeostasis in negative ecological condition.

1. Experimental

We determine by cytomorphological and ultrastructure methods that RNA-viruses can penetrate in the host cells and control its metabolism. So we discover that ways of virus entry in the cells do not depend on virus belongings to "enveloped" and "naked" type. Along with this virus particles can activate or inhibit synthesis of different substance in the host cells depending of virus type. The distinction between types of "enveloped" viruses used by us — Hantavirus and Tick Born encephalitis virus besides genome sequence (RNA positive and negative) determine by different nucleocapsid structure — spiral and icosahedral, and surface structure of its supercapsids. Hantavirus glycoproteins have form of a grid and glycoproteins of Tick Born encephalitis virus have shape of thorn 10 nm long. In spite of all specified differences of used "enveloped" viruses they have a similar by grade of intensity influence to the target cells. The exit of the new synthesized viruses in extracellular envelopment take place in first 24-hours after cells inoculation and expression of metabolic cell processes concerned with virus components reproduction was equally expressed. This fact was confirmed by using biochemical methods [3]. In case of cell infection by "naked" viruses of Picornaviridae family — poliovirus, enteroviruses Coxsackie B1, 71 and ECHO 11 we have got different results. It is well known that icosahedral structure surface of its nucleocapsids have 60 equivalent facets which consists of five protomers and used virus differences were only in receptors by means of which viruses connected to the determined type of cells. Nevertheless our investigation shows that poliovirus have expresses cytopathogenic effect inhibit cells metabolism while other used enteroviruses on the contrary make more active synthetic processes in different extent. So virus ENHO 11 shows the most effect as cells metabolism activator in this case we found synthesis of new virus particles. Other viruses were subdivided by influence degree thereby: at first enterovirus Coxsackie B1 than virus 71. We did not register the production of virus particles in the cells. Thus data analysis shows that complex investigation of RNA-virus interaction, which did not activate nuclear synthesis, with live systems allows us to approach in understanding mechanisms of controlling correction of cells processes molecular in accordance with virus structure differences side. This finally allows us to develop new methods for human organism state homeostasis correction in growing aggressive influence of environment conditions.

References

[1] C. Mao, D. J. Solis, B. D. Reiss *et al*, *Science* **303**, 213 (2004).
[2] K. T. Nam, D. -W. Kim, P. J. Yoo *et al*, *Science* **312**, 885 (2006).
[3] N. G. Plekhova, L. M. Somova, E. I. Drobot *et al*, *Biochemistry (Moscow)* **72**, 199 (2007).

16th Int. Symp. "Nanostructures: Physics and Technology"
Vladivostok, Russia, July 14–18, 2008

Study on DNA molecule patterning through dewetting process on microwell structure

C. H. Lin[1], S. W. Chau[1], J. Guan[2] and L. J. Lee[2,3]

[1] Department of Mechanical Engineering, Chung Yuan University, 32023 Jhongli, ROC
[2] Nanoscale Science and Engineering Center for Affordable Nanoengineering of Polymeric Biomedical Devices, The Ohio State University, 43210 Columbus, USA
[3] Department of Chemical and Biomolecular Engineering, The Ohio State University, 43210 Columbus, USA

Abstract. Dewetting a topologically micropatterned surface with DNA solution can generate well-defined arrays of stretched DNA molecules. Simulations of dewetting process on an array of microwells provide information to explain the stretching of DNA. The employed simulation method is validated by experimental results to study the effect of dewetting direction on the pattern of stretched DNA.

Introduction

Single DNA molecules can be stretched and immobilized onto a flat solid surface by a dewetting process called Molecular Combing for various biosensing and nanotechnological applications [1,2]. But the application of this technique is significantly limited by the poorly controlled locations and lengths of the stretched DNA. We developed a novel Molecular Combing approach capable of stretching and patterning DNA into highly-ordered arrays on a surface with an array of microwells or micropillars [3–5]. We also proposed qualitative models to explain the mechanism for stretching/patterning of DNA based on flow patterns of the dewetting solution mediated by the surface microstructures. However, direct experimental verification of the models is difficult due to the small spatial and temporal scales involved. In this paper, we introduce numerical simulation of dewetting flow on an array of microwells to explain the stretching/patterning of DNA. Additionally, DNA stretching/patterning experiments have been conducted to investigate the effect of dewetting direction on the orientation of stretched DNA, which are further validated by our numerical simulations.

1. DNA stretching experiments

λ-DNA (48,502 base-pairs) obtained from New England Biolabs (Ipswich, MA, USA) was diluted in TE buffer solution (10 mM tris-HCl and 1 mM EDTA, pH=8) to 20 μg/ml. DNA was labeled with YOYO-1 fluorescent dye at a dye-base pair ratio of 1:5. PDMS (polydimethylsiloxane) stamps containing microwells of 5 μm in diameter, 10 μm in center-to-center distance and 4 μm in depth were produced by soft lithography [6]. To generate DNA nanostrand arrays, a small droplet of 10 μl DNA solution was dropped on a glass coverslip. A PDMS stamp was placed on the solution. A pressure was applied on the stamp manually, followed by peeling up the stamp from one end with the other end remaining in contact with the glass surface. The peeling was performed manually at a rate of about 90°/sec and in a controlled dewetting angle with respect to the lattice of the microwell pattern. For imaging, the stamp with DNA nanostrands was placed on a glass coverslip with the nanostrands in contact with the coverslip. The stretched DNA nanostrands on the surface of the PDMS stamp between the microwells were transferred onto another solid surface by contact printing. Further experimental details of DNA stretching and printing are described by Guan and Lee [3].

2. Simulation of dewetting process

The dewetting process of DNA solution on microwells is described by the receding water front located between two originally parallel substrates due to the rotation of the upper substrate. The dewetting mediated by microwells is a complicated flow phenomenon, because it involves not only the moving outer boundaries, i.e. the upper substrate, but also the deforming front between two fluids, i.e. the air-water interface. To treat the moving solid boundary properly, a deforming body-fitted grid, regenerated at each time step in order to precisely describe the computational domain defined by the moving outer boundary, is employed in this paper. The fluid-gas interface is then tracked by an interface-capturing approach, where the numerical grid extends over both fluids and the front location is implicitly defined by the volume fraction varying in space. Because the mass and size of DNA is relatively small, its influence on the flow pattern is neglected. As a result, only air and water are considered in the simulation of the dewetting process. In the numerical simulation, the geometrical characteristics of microwell are chosen as those given in the experiments. A hexahedral grid, with about 5 million cells to discretize the computational domain comprising of a 3x3 microwell array, is typically adopted in our numerical simulation. No-slip condition is applied to the solid boundaries, such as the glass cover and PDMS substrate, where the contact angle is as well enforced at those boundaries. The two side boundaries, parallel to the peeling direction, are treated as symmetrical planes, while the atmospheric pressure is applied to the front and back boundaries, where fluid flux across boundaries is allowed. The typical time step adopted in the numerical simulation is 0.1 ns and a vertical velocity $V_G = 5.0$ m/s is assumed as a typical velocity of glass substrate during the dewetting process on microwells. Further details can be referenced in [7].

3. Results and discussion

To validate our simulations, we conducted DNA stretching/patterning experiments at different dewetting directions between 0° and 45° with respect to the lattice of the microwell array as shown in Fig. 1. The results show that dewetting angles of

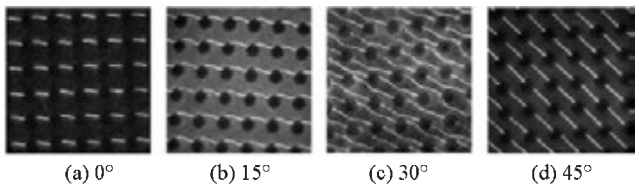

Fig. 1. Fluorescence micrographs of stretched DNA arrays on PDMS stamps formed by controlling the direction of dewetting.

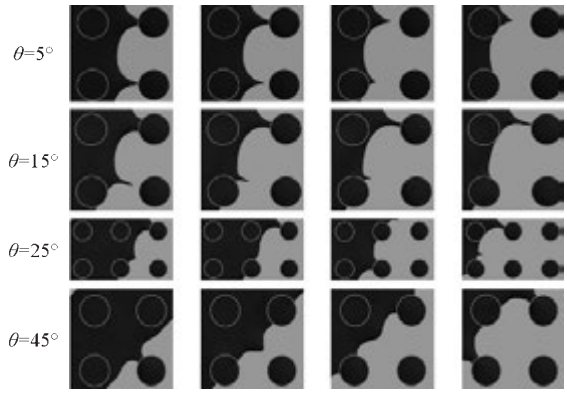

Fig. 2. Time evolutions of water front among successive microwells at different peeling angles (Top view).

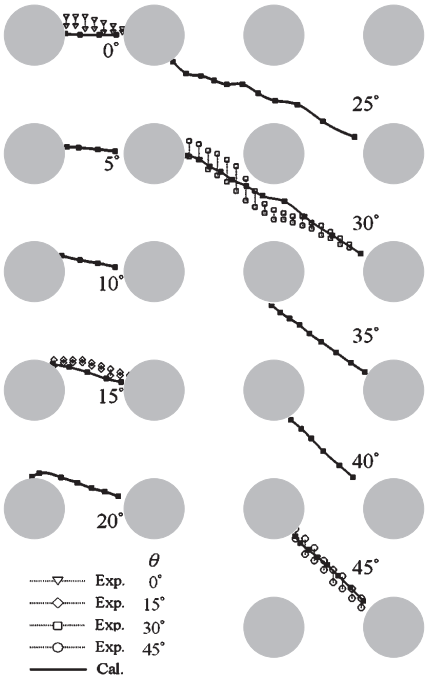

Fig. 3. Comparison of measured and calculated DNA nanostrand trajectory obtained from the dewetting process on microwells at different peeling angles.

0° and 45° produced straight DNA nanostrands in the dewetting direction (Fig. 1(a) and 1(d)), while dewetting angles are close to 15° and 30° generated curved nanostrands mainly in the dewetting direction (Fig. 1(b) and 1(c)). Furthermore, the DNA nanostrands obtained at the peeling angles of Fig. 1(c) seem to have a critical point where the DNA nanostrands change their stretching direction, and the length of DNA nanostrands connecting two microwells is the largest among all the studied peeling angles. Fig. 2 illustrates our simulation results of time evolutions of receding water fronts at different dewetting angles. It is obvious that different dewetting directions lead to different flow patterns. As proposed in our qualitative model [3], a tail-like region of the receding meniscus forms right after it detaches from the previous microwell. This "tail" continuously blunts as it approaches the next microwell presumably due to the high surface tension of water and high surface-to-volume ratio of the tail-like region. Formation and receding of the tail-like front likely contributes to clustering multiple DNA molecules together and stretch them to form a DNA nanostrand, especially for those DNA molecules already having one end immobilized at the left edge of the previous microwell. The DNA nanostrand may also contribute to the formation and maintenance of the "tail" because the nanostrand is hydrophilic and tends to "drag" the receding contact line. We believe that flow pattern of the dewetting solution especially the evolution and movement of the tail-like front plays an important role in determining the orientation and shape of the DNA nanostrands. Fig. 3 provides a comparison between experimentally observed DNA nanostrand trajectories and numerically predicted trajectories of the tip of the tail-like water front at different dewetting angles, where θ denotes the dewetting direction. The results show that our simulation agrees well with the experimental results. Also being consistent with the experimental observation, the simulated trajectory of DNA nanostrands at the dewetting angle of 25° clearly shows a critical point, where the trajectory changes its tangent direction. This is associated with the conversion from a tail-like front to a concave front during the dewetting process. The shape-change of the front occurs between two vertically adjacent microwells at the left side of the starting microwells, corresponding to the curving region of the DNA nanostrands as shown in Fig. 1(c).

4. Conclusions

Numerical simulation has been employed to describe the flow pattern of dewetting water on a surface with an array of microwells and is able to reveal information that is difficult to obtain experimentally. The obtained flow pattern can be used to explain the stretching and patterning DNA molecules by the dewetting process on microwells. Our simulation method is further validated by experiments studying the effect of dewetting direction on the pattern of stretched DNA nanostrands. In short, numerical simulation offers a powerful tool to reproduce the dewetting process on micropatterned surfaces, and holds great potential to reveal the mechanism for stretching/patterning DNA molecules as well as directing the creation of different patterns of stretched DNA for diverse applications.

Acknowledgements

This work has been supported in part by the National Science Council, ROC through NSC 96-2745-E-033-003-URD.

References

[1] R. M. Stoltenberg *et al*, *Biomed. Microdevices* **6**, 105 (2004).
[2] R. Lebofsky *et al*, *Briefings in Functional Genomics and Proteomics* **1**, 385 (2003).
[3] J. Guan *et al*, *Proceedings of National Academy of Science* **102**, 18321 (2005).
[4] J. Guan *et al*, *Advanced Materials* **19**, 1212 (2007).
[5] J. Guan *et al*, *Soft Matter* **2**, 1369 (2007).
[6] Y. Xia *et al*, *Angew. Chem. Int. Ed* **37**, 550 (1998).
[7] S. W. Chau *et al*, *Biosensors and Bioelectronics* **20**, (2004).

16th Int. Symp. "Nanostructures: Physics and Technology"
Vladivostok, Russia, July 14–18, 2008

Morphogenetic activity of silica and bio-silica on the expression of genes, controlling biomineralization using SaOS-2 cells

Heinz C. Schröder[1], Xiaohong Wang[2] and *Werner E. G. Müller*[1]

[1] Institut für Physiologische Chemie, Abteilung Angewandte Molekularbiologie, Universität, Duesbergweg 6, 55099 Mainz, Germany
[2] National Research Center for Geoanalysis, 26 Baiwanzhuang Dajie, CHN-100037 Beijing, China

In general, morphogenesis is one of three fundamental aspects in developmental biology; it requires differential gene expression, cell growth and cellular differentiation. Morphogenesis involves the control of an organized spatial distribution of cells which gives rise to the characteristic forms of tissues/organs/overall body anatomy. The formation of hard tissue from inorganic components present in the extracellular space requires cellular activities that govern nucleation, growth, morphology and final location of the mineral deposits. For biomineralization processes in most metazoans, from the phylogenetically oldest metazoan phylum (Porifera) to the vertebrates, the extracellular structural, filamentous collagen net serves as an organic layer around the skeletal elements. Surely collagen controls the form/shape/size of the mineralization products; but likewise important are the additional organic matrices which exist around and within the extracellularly mineralized deposits.

In a previous study (Schröder *et al* 2005 [J. Biomed Mat. Res. Part B — Applied Biomaterials 75B: 387–392]) we demonstrated that human SaOS-2 cells, when cultivated on bio-silica matrices, respond with an increased hydroxyapatite deposition. In the present contribution we investigate, if silica-based components (Na-silicate, TEOS [tetraethyl orthosilicate], silica-nanoparticles) (i) change the extent of biomineralization *in vitro* (SaOS-2 cells) and (ii) cause an alteration of the expression of the genes *amelogenin*, *ameloblastin* and *enamelin*, which are characteristic for an early stage of osteogenesis. We demonstrate that the viability of SaOS-2 cells is not affected by the silica-based components. If Na-silicate or TEOS is added together with ß-glycerophosphate, an organic phosphate donor, a significant increase of biomineralization is measured. Fi-

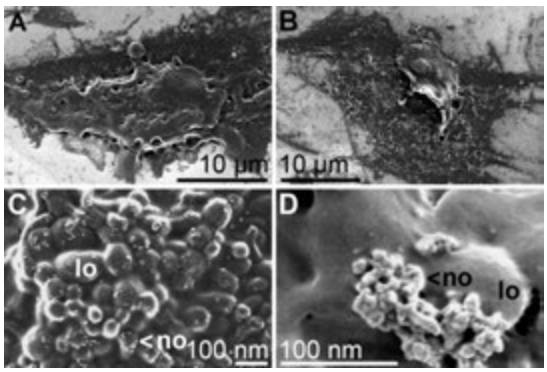

Fig. 1. Formation of rods on the surface of the lobules present on SaOS-2 cells. (**A**) SaOS-2 cells (c) grown in McCOY's medium, supplemented with 10% FCS, antibiotics and 50 μM ascorbic acid for 2 d. (**B**) The cells (c) incubated in the same medium, together with 5 mM ß-glycerophosphate for 2 d. (**C** and **D**) After 5 d in culture with 5 mM ß-glycerophosphate, small rods appear on the lobulated SaOS-2 cells, which represent mineralizing nodules (< no). (**E**) SaOS-2 cells with their lobulated surface (lo) grown for 10 d in cultures without ß-glycerophosphate; no mineralizing nodules are seen. (**F**) Large rods cluster, nodules (< no), are formed during an extensive incubation period (10 d) in the presence of ß-glycerophosphate.

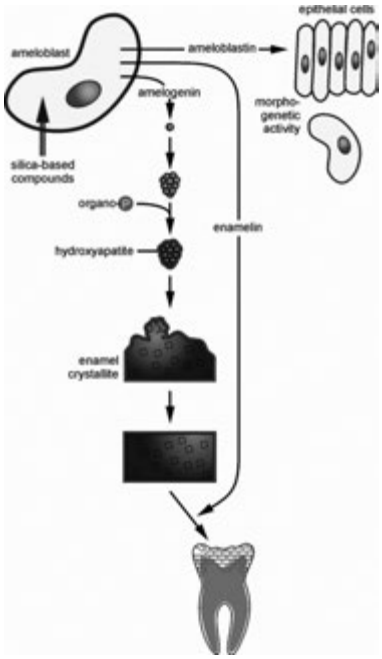

Fig. 2. Schematic outline of the effect of silica-based components (Na-silicate, TEOS, nanoparticles) on the expression of three genes [*amelogenin*, *ameloblastin* and *enamelin*] in ameloblasts. After exposure to the silica-based components, the expression of the *amelogenin* gene is strongly upregulated. After a series of modifications the amelogenin molecules form nanospheres around which hydroxyapatite is deposited (for details, see text). Amelogenin becomes resorbed into the hydroxyapatite crystallites, which aggregate to larger crystallite entities in the presence of enamelin. The gene expression of this second protein is likewise upregulated by the silica-based components. The gene expression of the third protein formed in ameloblasts, and studied here, ameloblastin is not altered by the silica-based components. Ameloblastin displays morphogenetic activity and controls the differentiation state of the ameloblasts.

nally, the expression levels of the *amelogenin*, *ameloblastin* and *enamelin* genes were determined in SaOS-2 cells during exposure to the silica-based components. After exposure for 2 days the expression levels of *amelogenin* and *enamelin* strongly increased in response to the silica-based components, while no significant change was seen for *ameloblastin*. In contrast, exposure of SaOS-2 cells to ß-glycerophosphate resulted in an increased expression of all three genes. We conclude that the levels of the structural molecules of the enamel matrix, amelogenin and enamelin, increase in the presence of silica-based components and substantially contribute to the extent of hydroxyapatite crystallite formation. These results demonstrate that silica-based components augment the hydroxyapatite deposition *in vitro*, and suggest that enzymatically synthesized bio-silica (via silicatein) might be a promising route for tooth reconstruction *in vivo*.

16th Int. Symp. "Nanostructures: Physics and Technology"
Vladivostok, Russia, July 14–18, 2008

Effect of stresses on saturation remanent magnetization of a nanoparticle ensemble

L. L. Afremov[1] and *A. V. Panov*[2]

[1] Physics department, Far-East state university, 8, Sukhanova st., Vladivostok, 690950, Russia
[2] Institute for automation and control processes, 5, Radio st., Vladivostok, 690041, Russia

Abstract. We theoretically study influence of stress on saturation remanent magnetization of single-domain particle ensemble. The increase in the compressive stresses from zero involves a rise in the transverse (or decrease in longitudinal) magnetization. Longitudinal magnetization with the tension and transverse magnetization with the compression reach maximum at the stress, determined by the combined anisotropy (magnetocrystalline and shape), and then at sufficiently large stresses approach the asymptotic values, which depend on the relationships between the magnetostriction constants. The behavior of transverse saturation remanent magnetization at tension (compression) is similar to the manner of the longitudinal remanence at compression (tension).

The research on stress effect on the magnetic properties of natural and artificial magnetic materials has more than half century history. The studies in this field are usually devoted to investigation of remanence of rocks, ferrites or steel samples [1,2,3,4]. Previous theoretical studies were carried out for the cases of small stresses in single-domain ensembles [5] or multidomain samples [6].

In our model of the ensemble of noninteracting magnetic nanoparticles, included into non-magnetic matrix, we use following assumptions: the nanoparticles are single-domain and have the shape of prolate spheroid; the crystallographic symmetry of magnetic material is assumed as the cubic, and the axis isolated by the crystallographic anisotropy (axis of $\langle k_{\rm A}\rangle$) makes the angle α with the long axis of spheroid; the uniaxial stresses σ make the angle β with the axis of $\langle k_{\rm A}\rangle$, if they are applied into the plane, including the long axis of spheroid and axis of $\langle k_{\rm A}\rangle$, or σ are perpendicular to this plane ($k_{\rm A}$, $k_{\rm N}$); the magnetocrystalline anisotropy and shape anisotropy are such that the condition of the magnetic uniaxiality of the particles is satisfied.

The equilibrium states of the magnetic moment of nanoparticle under the assumption of negligible thermal excitations can be determined by minimizing the free energy density, consisting of magnetocrystalline and shape anisotropy, magnetostriction energy and energy of interaction of nanoparticle magnetic moment with external magnetic field.

In the case when stresses are parallel to the plane, containing axis $k_{\rm A}$ and long axis of the ellipsoid the effective anisotropy of the particle K and angle γ, which gives the position of effective axis relative to the axis of $\langle k_{\rm A}\rangle$, can be found as follows:

$$K = \sqrt{k_{\rm N}^2 + 2k_{\rm N}K_1\cos(2\alpha - \psi_0) + K_1^2}, \qquad (1)$$

$$\tan 2\gamma = \frac{k_{\rm N}\sin 2\alpha + \tilde{\lambda}_2\sigma\sin 2\beta}{|k_{\rm A}| + k_{\rm N}\cos 2\alpha + \tilde{\lambda}_1\sigma\cos 2\beta}, \qquad (2)$$

where

$$\tilde{\lambda}_1 = \begin{cases} 3\tilde{\lambda}_{100}, \\ \left(\tilde{\lambda}_{100} + 5\tilde{\lambda}_{111}\right)/2, \end{cases}$$

$$\tilde{\lambda}_2 = \begin{cases} 3\tilde{\lambda}_{111}, & k_A > 0, \\ \sqrt{2}\left(\tilde{\lambda}_{111} - \tilde{\lambda}_{100}\right), & k_A < 0. \end{cases} \qquad (3)$$

$$K_1 = \sqrt{\left(|k_A| + \tilde{\lambda}_1\sigma\cos 2\beta\right)^2 + \left(\tilde{\lambda}_2\sigma\sin 2\beta\right)^2}, \qquad (4)$$

$$\tan\psi_0 = \frac{\tilde{\lambda}_2\sigma\sin 2\beta}{|k_A| + \tilde{\lambda}_1\sigma\cos 2\beta}, \qquad (5)$$

$I_{\rm s}$ is saturation magnetization, $\tilde{\lambda}_{100} = \lambda_{100}/I_{\rm s}^2$, $\tilde{\lambda}_{111} = \lambda_{111}/I_{\rm s}^2$, λ_{100}, λ_{111} are cubic magnetostriction constants, $k_{\rm N}$ is shape anisotropy constant, being equal to a difference in the demagnetizing factors along the short and long spheroid axes, $k_{\rm A}$ is dimensionless constant of magnetocrystalline anisotropy (i.e. divided by $I_{\rm s}^2$).

In the second case (the stresses are applied perpendicularly to the plane, containing axis $k_{\rm A}$ and long axis of ellipsoid):

$$K = \sqrt{k_{\rm N}^2 + 2k_{\rm N}(|k_{\rm A}| + \tilde{\lambda}_1\sigma)\cos 2\alpha + (|k_{\rm A}| + \tilde{\lambda}_1\sigma)^2}, \qquad (6)$$

$$\tan 2\gamma = \frac{k_{\rm N}\sin 2\alpha}{|k_{\rm A}| + k_{\rm N}\cos 2\alpha + \tilde{\lambda}_1\sigma}. \qquad (7)$$

The switching field of the particle H_0 in both cases can be found as $H_0 = I_{\rm s}K$.

Hereinafter we shall assume that the axis of magnetocrystalline anisotropy is parallel to the long axis of ellipsoids. According to equation (2) the position of effective axis relative to the axis of the magnetocrystalline anisotropy of $\langle k_{\rm A}\rangle$ is determined by the following formula:

$$\tan 2\gamma = \frac{\tilde{\lambda}_2\sigma\sin 2\beta}{|k_{\rm A}| + k_{\rm N} + \tilde{\lambda}_1\sigma\cos 2\beta}, \qquad (8)$$

where the positive values of σ correspond to tensile stresses and the negative σ are compressive ones.

If θ and φ are the polar coordinates of the nanoparticle saturation magnetization vector $\mathbf{I}_{\rm s}$ relative to the external field vector $\mathbf{H}$, then the projection of saturation remanence $I_{\rm rs}$ on certain direction $\mathbf{l}$ can be determined as follows:

$$I_{\rm rs}^{(l)} = \int_0^{2\pi} d\varphi \int_0^{\pi/2} 2mc\cos p(\theta,\varphi)F(\theta,\varphi)d\theta, \qquad (9)$$

here $m = I_{\rm s}v$ is the magnetic moment and v is volume of the particle, c is the volume concentration of the particles, $p(\theta,\varphi)$

is the angle between vector **l** and the magnetic moment of the particle, $F(\theta, \varphi)$ is distribution function of magnetic moments with respect to the magnetic field **H**.

Assuming that the distribution of the axes of $\langle k_A \rangle$ is random the distribution function $F(\theta, \varphi)$ can be constructed as follows: $F(\theta, \varphi) = \sin\beta(\theta)/4\pi\ |d\beta(\theta)/d\theta|$, where $\beta(\theta)$ is the angle between the effective axis and the magnetic field determined by the following equation:

$$\theta = \beta - \gamma = \beta - \frac{1}{2}\arctan\frac{\tilde{\lambda}_2\sigma\sin 2\beta}{\left|\,|k_A| + k_N + \tilde{\lambda}_1\sigma\cos 2\beta\right|}. \quad (10)$$

By this means the longitudinal saturation remanence is

$$I_{rs}^{\parallel} = cI_s\int_0^{\pi/2}|\Psi(\theta)|\sin\beta(\theta)\cos\theta\, d\,\theta. \quad (11)$$

Likewise we can calculate transverse magnetization:

$$I_{rs}^{\perp} = \frac{cI_s}{2\pi}\int_0^{2\pi} d\tilde{\varphi}\int_0^{\pi/2}|\Psi(\theta)|\sin\beta(\theta)\cos\tilde{\theta}\, d\tilde{\theta}, \quad (12)$$

where $\theta = \arccos(\sin\tilde{\theta}\cos\tilde{\varphi})$, $\Psi(\theta) = d\beta/d\theta = (d\theta/d\beta)^{-1}$ can be easily obtained analytically.

The equations (11), (12) define theoretical dependences of saturation remanent magnetization on stresses which are shown in Fig. 1.

In the approximation of small stresses ($\tilde{\lambda}_1\sigma$, $\tilde{\lambda}_2\sigma \ll k_A$) equations (11) and (12) can be reduced to the following form:

$$I_{rs}^{\parallel} = \frac{cI_s}{2}\left[1 + \frac{\tilde{\lambda}_2\sigma}{2(|k_A| + k_N)}\right], \quad (13)$$

$$I_{rs}^{\perp} = \frac{cI_s}{2}\left[1 - \frac{\tilde{\lambda}_2\sigma}{4(|k_A| + k_N)}\right]. \quad (14)$$

A growth of the saturation remanence $I_{rs}^{\perp}$ and the decrease in $I_{rs}^{\parallel}$ with an increase in the compressive stresses are connected with the dependence of the orientation of effective axis on σ. According to Eq. (8) the compressing stresses parallel to the magnetic field **H** increase the angle between **H** and effective axis, which leads to the decrease in the projection of magnetic moment on the direction of field, and, therefore, and $I_{rs}^{\parallel}$. Respectively compressive stresses perpendicular to field decrease the angle between the effective axis and the field, which must lead to the experimentally observed with the compression relation between the magnetizations: $I_{rs}^{\parallel} < I_{rs}^{\perp}$.

It should be emphasized that in the approximation $\tilde{\lambda}_1\sigma$, $\tilde{\lambda}_2\sigma \ll k_A$, $I_{rs}^{\perp}$ increases with growth in the compression ($I_{rs}^{\parallel}$ diminishes) linearly with respect to σ, moreover the rate of change of longitudinal remanent saturation magnetization must be twice more than the respective coefficient for $I_{rs}^{\perp}$, see Eqs. (13) and (14). This relation is in accordance with the experimental [1, 2] and previous theoretical [5] results.

With a growth in tensile stresses (see Fig. 1) the longitudinal remanent saturation magnetization $I_{rs}^{\parallel}$ increases, reaching at

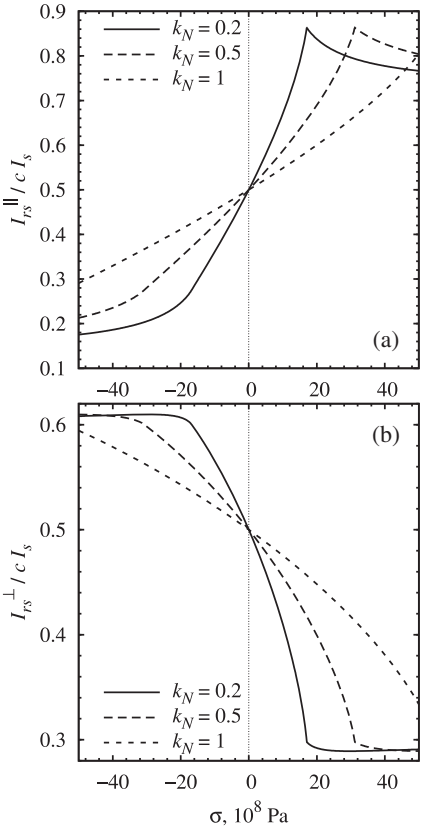

Fig. 1. Dependence of $I_{rs}^{\parallel}$ (a) and $I_{rs}^{\perp}$ (b) on the stress magnitude for various values of the shape anisotropy for ensemble of nanoparticles with $\lambda_{100} \approx \lambda_{111} = 20 \times 10^{-6}$, $k_A = 0.16$, $I_s = 1710$ kA/m.

$\sigma_m = (|k_A| + k_N)/\tilde{\lambda}_1$ the maximum value $I_{rs\,max}^{\parallel} > 0.5cI_s$ and then monotonically decreases to a finite value. This behavior of $I_{rs}^{\parallel}$ is determined by the dependence of the effective axis position on the stresses (see Eq. (8)). While $\sigma \to \sigma_m$ the effective axes of particles with $0 < \beta < \pi/4$ align at an angle to the field **H** $\gamma < \beta$ and for the particles with $\pi/4 < \beta < \pi/2$ are set at the angle $\gamma \to \pi/4$: $I_{rs}^{\parallel}$ reaches maximum. Further rise in the stresses leads to growth in the angle γ ($\gamma > \beta$) for the particles with $\pi/4 < \beta < \pi/2$, that accords with fall in the projection of a magnetization and $I_{rs}^{\parallel}$ respectively.

The decrease of $I_{rs}^{\parallel}$ with the compression is determined by an increase in deflection of the effective axes of all particles about the field **H**. The behavior of transverse saturation remanence $I_{rs}^{\perp}$ is basically reciprocal with respect to $I_{rs}^{\parallel}$.

The results of this theoretical work could be utilized for estimation of stresses by magnetic methods.

References

[1] S. P. Kapitsa, *Izv. Akad. Nauk SSSR: Ser. Geophys.* **6**, 489 (1955).
[2] J. P. Hodych *et al*, *Geophys. J. Int.* **157**, 1017 (2004).
[3] R. Langman, *IEEE Trans. Magn.* **26**, 1246 (1990).
[4] V. G. Kuleev *et al*, *The Physics of Metals and Metallography* **103**, 131 (2007).
[5] J. P. Hodych, *Can. J. Earth Sci.* **14**, 2047 (1977).
[6] M. J. Sablik *et al*, *J. Appl. Phys.* **74**, 480 (1993).

16th Int. Symp. "Nanostructures: Physics and Technology"
Vladivostok, Russia, July 14–18, 2008

Coexistence of superconductivity and ferromagnetism in Sn nanoparticles

W.-H. Li, C.-W. Wang, C.-Y. Li, C. K. Hsu and C.-M. Wu
Department of Physics, National Central University, Jhong-Li, 32001 Taiwan

Abstract. Ferromagnetic spin polarization has been observed in 14 nm and 16 nm Sn nanoparticles. Superconductivity with a noticeable increase in the superconducting transition temperature and a dramatic increase in the critical magnetic field develops below 4.05 K. The presence of a magnetic field in the superconducting phase reveals a regime in which the magnetic susceptibility and magnetization increase with decreasing temperature. We attribute these behaviors to the coexistence of ferromagnetic spin polarization and superconductivity at low temperatures.

Although the microscopic BCS theory for weak coupled superconductivity does not favor the formation of a ferromagnetic superconducting state, the search for ferromagnetic superconductors has continued for several decades. Many magnetic superconductors have been identified. Most of them, however, are associated with antiferromagnetic coupling, where the antiferromagnetic and superconducting electrons being contributed from chemically well separated ions. A ferromagnetic superconductor has yet to be found. It is known that finite size effects can lead to unusual superconducting and magnetic behaviors. Ferromagnetic spin polarization has been observed in many ultra small nanoparticles. This unconventional magnetic behavior is currently understood by assuming that ferromagnetic spin correlations will appear in the surface region of the nanoparticle. One particular feature of nanoparticle superconductivity is then the possible occurrence of ferromagnetic spin polarization near the particle surface that coexists with superconductivity at low temperatures.

Here, we report on the observation of ferromagnetic spin polarization and superconductivity in 14 nm Sn nanoparticles. Ferromagnetic spin polarization, which is characterized by the appearance of Langevin magnetic-field profiles for magnetization, as shown in Fig. 1, persists even at room temperature. The observed Langevin $M(H_a, T)$ curves may be understood as a randomly oriented assembly of non-interacting ferromagnetic Sn nanoparticles of average particle moment μ_p at a temperature that are being aligned by the applied magnetic field H_a. The temperature dependence of μ_p reveals a linear increase with increasing temperature, as shown in Fig. 2. This unusual behavior of μ_p increases with increasing temperature has been

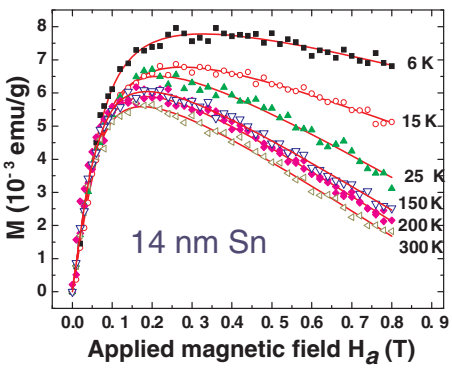

Fig. 1. $M(H_a)$ of the 14 nm Sn particles.

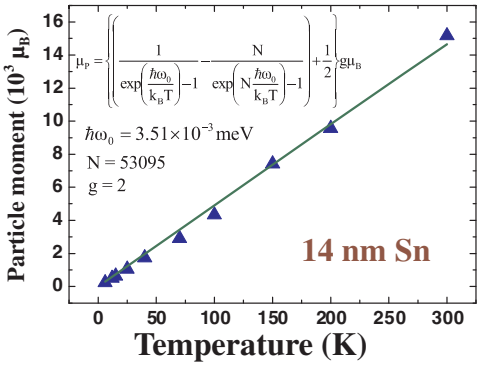

Fig. 2. $\mu_p(T)$ of the 14 nm Sn particles.

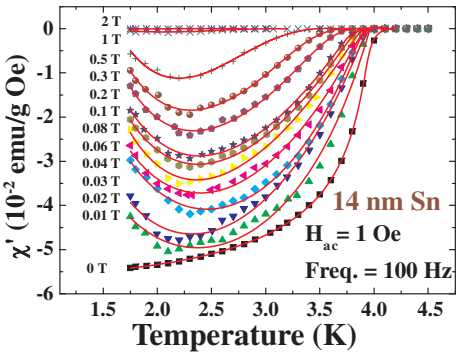

Fig. 3. $\chi(T)$ of the 14 nm Sn particles.

suggested to be associated with the contributions from thermal excitations of magnons and is known as thermoinduced magnetization.

Superconductivity with a noticeable increase in the superconducting transition temperature and a dramatic increase in the critical magnetic field develops below 4.05 K, as shown in Fig. 3. The superconducting transition temperature for the 14 nm Sn particles that we obtained from the fit is $T_C = 4.05(5)$ K, which is ∼9% higher than that of the 3 mm ones. Interestingly, an upturn in $\chi\prime(T)$ appears below ∼2.3 K for the measurement made with a H_a. Similar behaviors are also evident in the temperature dependence of the magnetization $M(T)$, as shown in Fig. 4. These $M(T)$ and $\chi\prime(T)$ curves reveal the existence of a magnetic component below T_C and that superconductivity remains at low temperatures. The upturn in $\chi\prime(T)$ may be described using a Curie T^{-1} profile, as expected for the paramagnetic moments observed at high temperatures.

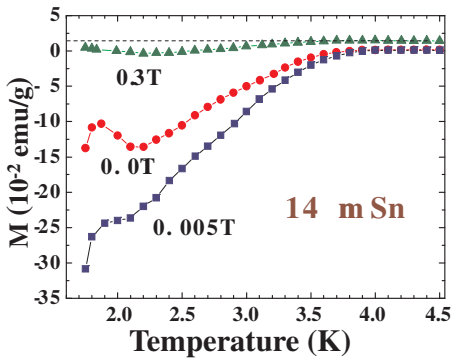

Fig. 4. $M(T)$ of the 14 nm Sn particles.

The solid lines in Fig. 3 indicate the fitted curves of the observed $\chi'(T)$ to a Scalapino term for superconducting screening plus a Curie C/T term for paramagnetic moments, where the Curie constant C is proportional to μ_p^2. They agree very well. Unconventional cross-shaped $M(H_a)$ hysteresis loops can be found at temperatures below T_C. It departs dramatically from the linear $M(H_a)$ profile expected for type-I Sn. A 14 nm particle is far too small to accommodate even a single flux vortex. The type-II-like $M(H_a)$ profile reflects then the characteristic of the penetration of magnetic flux into the particles.

One possible origin for the observed coexistence effect is that the local magnetic field produced by the spin polarized moments is not strong enough to break the enhanced superconducting pairs, so that the spin-singlet superconductivity survives from the local magnetic field. The critical magnetic field H_C of bulk Sn is 309 Oe, showing that the superconducting pairs in bulk Sn can easily be broken by a relatively weak magnetic field. An enhanced superconductivity is then an essential criterion for the superconductivity to survive from the presence of a ferromagnetic moment in extremely space-restricted Sn nanoparticles.

The superconducting parameters may be modulated by interparticle interaction. No sign of superconductivity is found with the temperature is reduced to 1.8 K, when the 3 nm Sn particles are very loosely packed with a mass density that is 3.4% that of bulk Sn. Recovery of superconductivity by interparticle interaction is surprisingly seen, as superconductivity begins to merge when the packing density is raised to reach 18% that of bulk Sn. Possible mechanisms such as breaking of Anderson criterion and interparticle pairing will be presented.

16th Int. Symp. "Nanostructures: Physics and Technology"
Vladivostok, Russia, July 14–18, 2008

Magnetic field oscillation phenomena in multiple asymmetric superconducting rings of 1 μm diameter

V. L. Gurtovoi[1], M. Exarchos[2], R. Shaikhaidarov[2], V. N. Antonov[2], A. V. Nikulov[1] and V. A. Tulin[1]

[1] Institute of Microelectronics Technology, Russian Academy of Sciences, 142432 Chernogolovka, Moscow region, Russia
[2] Physics Department, Royal Holloway University of London, Egham, Surrey TW20 0EX, UK

Abstract. We have studied a structure with 667 asymmetric 1 μm diameter superconducting rings. Little–Parks, rectified voltage and critical current oscillations in magnetic field were measured to characterize the structure. Opposite direction critical current oscillations were symmetric except for narrow region near half-integer of magnetic flux quantum, where we observed formation of sharp peaks of rectified voltage. A high signal to noise ratio, which owes to large number of rings allows us to measure rectification efficiency in the fluctuation region of the superconducting transition and around it by applying calibrated white noise.

It has been demonstrated recently that single [1,2], double [3] and multiple [2,4] superconducting asymmetric ring structures with ring diameters of 4 and 2 μm work as efficient rectifiers of alternating current in magnetic field at temperatures close to superconducting transition. The rectified voltage was periodic in magnetic field like all magnetic field dependent values measured for a ring structures, the period being equal to superconducting magnetic flux quantum $\Phi_0 = h/2e$. Rectification efficiency was dependent on temperature, magnetic field, amplitude of external bias current and geometrical ring parameters (ring diameter, superconductor film thickness and asymmetry degree). Some of these parameters have been investigated in details in [1–4]. Rectification of individual rings can be synchronized and added in a multiple ring structure. The rectified voltage increases proportionally to the number of rings [4]. This allows drastic sensitivity improvement when ring structure is used as small signal or noise detectors. The largest number of rings we studied so far was 110 [4].

In order to optimize operation of multiple ring structure as noise detector, we studied structures with larger number of rings of smaller diameter. We fabricated a structure with 667 asymmetric 1 μm diameter rings (Fig. 1) using e-beam lithography and lift-off process of thermaly evaporated aluminum film. The thickness of aluminum film was 30 nm.

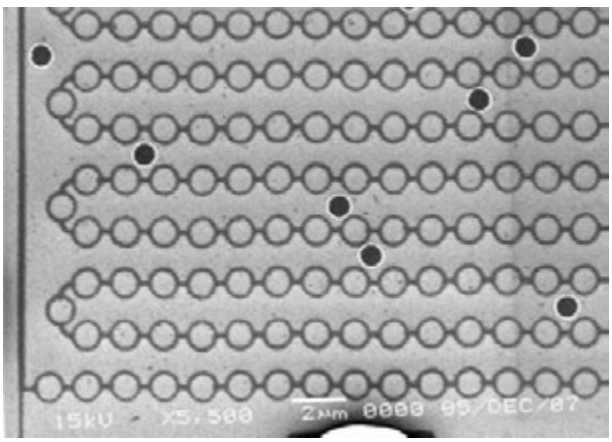

Fig. 1. A fragment of structure consisting of 667 asymmetric rings with diameter of 1 μm.

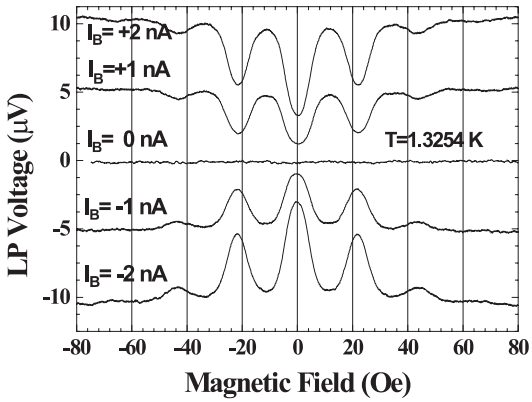

Fig. 2. Little–Parks voltage vs. magnetic field for $I_B = -2, -1, 0, 1, 2$ nA at $T = 1.3254$ K.

Ring arms width was 100 and 125 nm for narrow and wide parts, respectively, which determined the asymmetry of the rings. The main properties of the structures were as followss: the resistance ratio $R(300\ \mathrm{K})/R(4.2\ \mathrm{K}) = 2$, superconducting transition temperature T_c was 1.327 K and the width of resistive transition ΔT_c was 0.01 K.

4-point measurements were carried out in three different regimes: DC bias; sinusoidal bias; white noise (bandwidth from DC to 200 kHz) bias. We used utra-low distortion generator (Stanford Research, Model DS360) with differential output to create bias current across the structure. Voltage corresponding to rectified, Little–Parks, $R(T)$ or IV signal was measured in a frequency band from 0 to 30 Hz by an instrumentation amplifier followed by a low-noise preamplifier SR560. Noise level of the amplification system was 20 nVpp for $f_b = 0$ to 1 Hz. Rectification effects independent of frequency for the bias current at least up to 1 MHz. Magnetic field time scanning was slow enough (∼0.001–0.1 Hz) to avoid distortion of measured voltage spectrum in 30 Hz region.

Fig. 2 shows Little–Parks voltage oscillations in magnetic field at small values of bias current. Oscillations amplitude reaches $0.7R_n$. This can be explained by increased persistent current and narrow width of the superconducting transition, $\Delta T_c = 0.01$ K. We do not see rectified voltage at $I_B = 0$ compared to results in [4], due to careful multistage filtering system of the measurement leads.

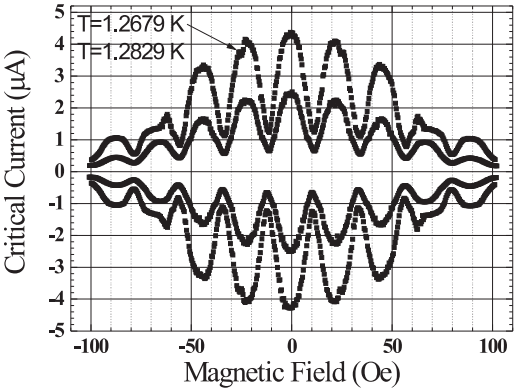

Fig. 3. Critical current oscillations in magnetic field at $T = 1.2679$ and 1.2829 K.

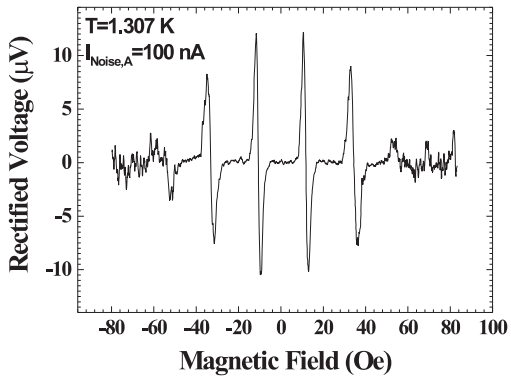

Fig. 4. Rectified voltage oscillations in magnetic field when white noise current is applied.

Critical current oscillations (period is equal to Φ_0) are quite different (Fig. 3) from that we observed before in the rings with diameters of 2 and 4 μm [1–4]. The opposite direction critical current oscillations are symmetric ($I_{c+}(B) = -I_{c-}(B)$) everywhere except for narrow region near half-integer of magnetic flux quantum, which results in formation of sharp peaks of opposite sign rectified voltage near $(n + 1/2)\Phi_0$. These are the points of magnetic field with maximum rectification efficiency, which is verified by the rectified voltage oscillations when white noise current is used as a bias (Fig. 4).We do not see $\Phi_0/2$ shift which has been observed in previous experiments.

To calibrate the structure as noise detector, a white noise current was applied. Rectified voltage amplitude and rectification efficiency as function of noise current amplitude at $T = 1.307\ K = 0.985T_c$ is shown in Fig. 5. From calibration in Fig. 5, we can estimate that nonequilibrium noise power in our system is lower than 2×10^{-15} W.

Thus, we have studied a structure with 667 asymmetric 1 μm diameter superconducting rings using Little–Parks, rectified voltage and critical current oscillation measurements in magnetic field. Opposite direction critical current oscillations were symmetric except for narrow region near half-integer of magnetic flux quantum, where we observed formation of sharp peaks of rectified voltage. A high signal to noise ratio, which owes to large number of rings allows us to measure rectification efficiency in the fluctuation region of the superconducting transition and around it by applying calibrated white noise. Estimated nonequilibrium noise power in our system is lower than 2×10^{-15} W.

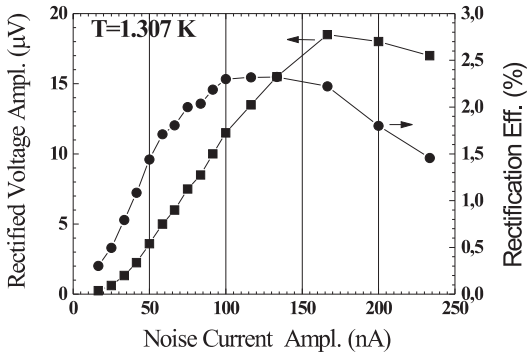

Fig. 5. Rectified voltage amplitude and rectification efficiency as function of noise current amplitude.

Acknowledgements

This work has been supported by grant of the Program "Quantum Nanostructures" of the Presidium of RAS, grant 08-02-99042-r-ofi of the Russian Foundation of Basic Research and grant "Quantum bit on base of micro- and nano-structures with metal conductivity" of the Program "Technology Basis of New Computing Methods" of ITCS department of RAS.

References

[1] V. L. Gurtovoi, S. V. Dubonos, S. V. Karpii, A. V. Nikulov, and V. A. Tulin, *Zh. Eksp. Teor. Fiz.* **132**, 297 (2007) (*JETP* **105**, 257 (2007)).

[2] V. L. Gurtovoi, S. V. Dubonos, A. V. Nikulov, N. N. Osipov, and V. A. Tulin, *Zh. Eksp. Teor. Fiz.* **132**, 1320 (2007) (*JETP* **105**, 1157 (2007)).

[3] V. L. Gurtovoi, S. V. Dubonos, A. V. Nikulov, N. N. Osipov and V. A. Tulin, *Proceedings of SPIE* **6260** (Micro- and nanoelectronics-2005), 62600T (2006).

[4] A. A. Burlakov, V. L. Gurtovoi, S. V. Dubonos, A. V. Nikulov, and V. A. Tulin, *Pisma Zh. Eksp. Teor. Fiz.* **86**, 589 (2007) (*JETP Lett.* **86**, 517 (2007)).

16th Int. Symp. "Nanostructures: Physics and Technology"
Vladivostok, Russia, July 14–18, 2008

Photovoltaic effect in InN films with In clusters

T. A. Komissarova[1], T. V. Shubina[1], V. N. Jmerik[1], M. A. Timofeeva[1], N. A. Pikhtin[1], L. I. Ryabova[2], D. R. Khokhlov[2], P. S. Kop'ev[1] and S. V. Ivanov[1]

[1] Ioffe Physico-Technical Institute, St Petersburg, Russia
[2] Moscow State University, 119991 Moscow, Russia

Abstract. A photovoltaic response in intentionally grown InN:In semiconductor-metal composite structures, as well as InN films with spontaneously formed In clusters was investigated. Temperature and spectral dependences of photocurrent were measured and compared with those of optical absorption. It was found that principal edge in photocurrent spectra is shifted to higher energy, as compared with an optical absorption edge. We consider that as an evidence of the additional optical losses induced by local plasmons excited at the In clusters. Temperature dependence of photocurrent has an activation part at high temperatures and almost does not depend on temperature <100K. This may indicate that charge carriers are localized at low temperatures.

Introduction

InN is a very attractive material for different applications [1]. It may be possible to fabricate high electron mobility transistors and high frequency devices due to predicted extraordinary transport parameters of InN [2,3]. The currently accepted band gap of ∼0.7 eV makes InN seems to be very perspective for formation of solar cells [4], since in solid $In_xGa_{1-x}N$ alloys it is possible to vary the optical gap from 0.7 to 3.4 eV. This energy range coincides with the solar spectrum. However, to the best of our knowledge, there were no published data on the photovoltaic effect at energies below than 1.5 eV in InN-based systems.

It is well known that InN can easily dissociate during the growth process due to few reasons. Among them, small heat of InN formation [5], the low In vapor pressure over the metal phase preventing evaporation of In atoms from a surface, and weak In-N along with strong N-N bonds. The cluster can modify optical properties of the semiconductor. It has been recently shown that local plasmons in such clusters, specified as Mie resonances, induce additional peaks in InN absorption spectra [6]. This can mask the true fundamental edge of InN. The situation is complicated by the possible deviation of a principal optical edge in non-stoichiometrical InN due to strong difference in N and In orbital energies [7].

Spectral dependence of photovoltaic effect in usual semiconductors generally follows the increase of the interband absorption near its fundamental edge [8]. So, comparison of photocurrent (PC) and absorption spectra in InN may help to determine the principal absorption edge and distinguish contribution in absorption induced by the local plasmons within In clusters.

1. Experimental

We investigated the photovoltaic effect and optical absorption in intentionally grown InN:In composite structures along with InN films with spontaneously formed In clusters.

All structures were grown on c-Al_2O_3 substrate with GaN buffer layer by plasma-assisted molecular beam epitaxy. Composite InN:In structures were grown by periodic deposition of pure In separated by 25 nm InN. The nominal In thickness varied from 0 to 48 ML. The number of In insertions was 20, for exception of the 48-ML structure, where they were 6. These structures were intentionally grown in slightly N-rich conditions. The structure with the spontaneously formed In clusters was grown in In-rich conditions. Previous high-resolution TEM measurements have shown that this film contains In clusters with a size about of 20-nm [9].

For measurements of photovoltaic effect electrical contacts were soldered by In on the film surface and the PC flowing between the contacts was recorded. It turns to be that it is not possible to measure reliably the photovoltaic effect in any InN or InN:In structures using the incandescent lamp, because the signal is too small. On the contrary, spectral dependences of photo-response in a GaN film were obtained at illumination by the lamp in similar measurements. They confirm that PC edge coincides perfectly with absorption edge in GaN. To measure the photo-response in InN:In we have used for excitation the power semiconductor lasers (100 mW) of different wavelength. The signal has been normalized to a number of photons impinging the surface. Measurements of photocurrent spectra were performed at 25 K, temperature dependence were measured in temperature range (25–300) K at 1.53 eV excitation.

2. Results and discussion

It was found that the PC principal edge is always shifted to higher energies as compared with absorption edge (Fig. 1). This shift value rises with increasing In amount, while the value of photocurrent decreases. We cannot measure photo-response below ∼ 1.5 eV in InN:In structures with large In amount because the signal was two orders of magnitude weaker.

Generally, it is assumed that photocurrent should be in range of the interband absorption in the matrix and the PC onset can give effective absorption edge of InN. On the other hand, presence of In clusters in InN matrix reduces the area in which photo carriers can generate. The presence of the metallic clusters can disturb the flow of the photo-induced carriers, but not very strongly, because the carrier mobility in InN:In structures is ∼1500 cm^2/Vs [10]. Thus, these effects can explain photocurrent suppression with increasing In amount, but the spectral difference of absorption and PC edges is not clear.

The increasing of the PC edge shift with the In amount may correspond to the deviation from stoichiometry of the InN matrix. These InN:In structures were intentionally grown in N-

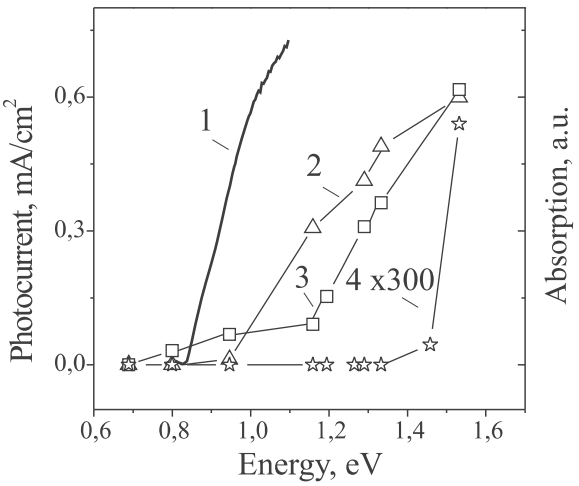

Fig. 1. Spectral dependence of photocurrent at 25 K in different samples (carrier concentration): 2 — the 0-ML sample (1.8×10^{19} cm^{-3}); 3 — the InN film with 20-nm spontaneously formed In clusters (1.5×10^{19} cm^{-3}); 4 — 48-ML sample (4.5×10^{19} cm^{-3}). The curve 1 presents the onset of optical absorption in 0-ML sample at 40K. The thin lines are to guide the eye.

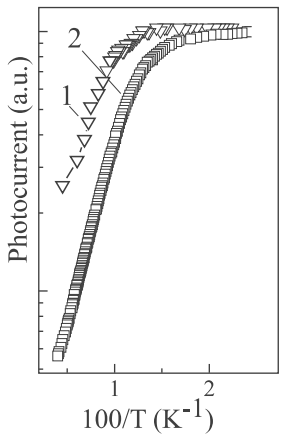

Fig. 2. Temperature dependence of photocurrent in: 1 — 0-ML sample; 2 — the InN film with 20-nm spontaneously formed In clusters.

rich conditions. The additional deviation from stoichiometry can arise as result of depletion of InN matrix due to the coalescence of In atoms into clusters. Early, it has been shown that N-rich conditions should lead to an increase of the optical gap of InN [7]. Note that alternative explanation of the PC edge shift by the Burstein–Moss effect only is not sufficient. The difference between the PC onsets in 0-ML sample (1.8×10^{19} cm^{-3}) and 48-ML sample (4.5×10^{19} cm^{-3}) amounts approximately 400 meV, while the estimated Burstein–Moss shift should be about 100 meV.

Considering the experimental findings, one can conclude that absorption below the PC principal edge is induced by other reason. The local plasmons excited within In clusters are good candidates for that. The additional optical losses appear due to both non-radiative decay of the plasmons and electromagnetic enhancement of absorption due to the increasing electric field in adjusting semiconductor areas. These mechanisms cannot be distinguished in our case.

The temperature dependence of the photocurrent has an activation part at $T > 100$ K (Fig. 2). Activation energy varied for films with different In amount. For instance, it is 30 meV for the InN film with 20-nm spontaneously formed In clusters and 20 meV for the 0-ML sample. At low temperatures PC almost does not depend on temperature. Such behavior of photocurrent with temperature may be associated with localization of charge carriers at low temperatures.

Concluding, we demonstrate that even small amount of metallic inclusions can dramatically suppress a photovoltaic response in InN-based structures in the 0.7–1.5 eV spectral range. The found difference in absorption and photocurrent edges in InN:In is ascribed to an additional optical losses induced by plasmons excited in the clusters. Analysis of temperature dependences of PC allows us to conclude that charge carriers are localized in this system at low temperatures. These findings show the importance of further investigation of photovoltaic effect in InN and InN:In structures for both device application and fundamental issues.

Acknowledgements

This work is supported in part by the RFBR grants and Program of Presidium of RAS.

References

[1] G. Bhuiyan, A. Hashimoto and A. Yamamoto, *J. Appl. Phys.* **94**, 2779 (2003).

[2] B. E. Foutz, S. K. O'Leary, M. S. Shur and L. F. Eastman, *J. Appl. Phys.* **85**, 7727 (1999).

[3] S. Keller, I. Ben-yaacov, S. P. Denvers, and U. K. Mishra, *Proc. the International Workshop on Nitride Semiconductors (Nagoya, Japan, 2000)*, IPAP conference series 1, 233, 2000.

[4] J. Wu, W. Walukiewicz, K. M. Yu, W. Shan, J. W. Ager III, E. E. Haller, H. Lu, W. J. Schaff, W. K. Metzger, and S. Kurtz, *J. Appl. Phys.* **94**, 6477 (2003).

[5] C. Stampfl, and C. G. Van de Walle, *Phys. Rev. B* **59**, 5521 (1999).

[6] T. V. Shubina, S. V. Ivanov, V. N. Jmerik, D. D. Solnyshkov, V. A. Vekshin, P. S. Kop'ev, A. Vasson, J. Leymarie, A. Kavokin, H. Amano, K. Shimono, A. Kasic, and B. Monemar, *Phys. Rev. Lett.* **92**, 117407 (2004). ibid **95**, 209901 (2005).

[7] T. V. Shubina, M. M. Glazov, S. V. Ivanov, A. Vasson, J. Leymarie, B. Monemar, T. Araki, H. Naoi, and Y. Nanishi, *phys. stat. sol. c* **4**, 2474 (2007).

[8] H. B. DeVore, *Phys. Rev.* **102**, 86 (1956).

[9] T. P. Bartel, C. Kiseelowski, P. Specht, T. V. Shubina, V. N. Jmerik, and S. V. Ivanov, *Appl. Phys. Lett.* **91**, 101908 (2007).

[10] T. A. Komissarova, D. S. Plotnikov, V. N. Jmerik, T. V. Shubina, A. M. Mizerov, A. N. Semenov, S. V. Ivanov, L. I. Ryabova, and D. R. Khokhlov, *Phys. Stat. Sol. c* (in press).

16th Int. Symp. "Nanostructures: Physics and Technology"
Vladivostok, Russia, July 14–18, 2008

Fabrication and in situ XPS-diagnostics of a system of isolated silver nanoclusters on silicon surface

V. M. Mikoushkin[1], S. Yu. Nikonov[1], Yu. S. Gordeev[1], S. L. Molodtsov[2] and Yu. S. Dedkov[2]

[1] Ioffe Physico-Technical Institute, St Petersburg, Russia
[2] Institut für Festkorperphysik, Technische Universität Dresden, D-01062 Dresden, Germany

Abstract. Silver nanoclusters were fabricated by ion etching a thin silver film deposited on the oxidized silicon surface. The clusters were electrically separated from the conductive surface by individual SiO_2 isolating layers. Core level Ag $3d_{5/2}$ photoelectron spectra of clusters were measured with using synchrotron radiation. Significant "red" shift of the photoelectron line was observed in the course of ion etching resulted in reduction of the cluster size. This shift was shown to be a result of increase of the capacity of cluster due to reduction of cluster sizes which enlarged the positive charging a cluster due to emission of a photoelectron. The observed effect was used for estimation of the average cluster size.

Introduction

Metallic clusters, nanostructures based on the systems of metallic clusters and the techniques of their fabrication have been intensively studied and developed recently aiming applications in nonlinear optoelectronics, catalysis and single electron memory devices [1, 2]. Electronic properties of clusters are well known to strongly depend on the cluster size. Therefore these applications need both knowledge about regularities in size transformation of cluster properties and technologies of fabrication of structures with designed average size of clusters, especially in the nano- and subnano-scales. However, the progress in these fields is restricted by the difficulties related both to the control of cluster sizes in nanoscale and to the possibility of variation of cluster sizes. The lateral resolution of the Atomic Force Microscopy (AFM) becomes insufficient in this range and Scanning Tunnelling Microscopy (STM) fails in the practically important case of dielectric substrates. The controlled variation of the cluster size in wide range seems also to be a problem. Therefore, designing new technological approaches to fabrication of systems of metallic nanoclusters and development of new ways of cluster size diagnostics are the actual tasks of nanotechnology. We give in this paper an example of possible solution of these tasks by fabrication of silver clusters on silicon. The fabrication technique is based on ion sputtering of thin metallic layer. It enables fabrication of electrically isolated supported nanoclusters of comparable sizes and variation of their average size. Diagnostics of the average cluster size was performed by X-ray photoelectron spectroscopy with using synchrotron radiation (SR). Information about sizes of nanoclusters was obtained despite the fact that photoelectron spectroscopy has no lateral resolution.

1. Fabrication of quasi-isolated supported Ag-clusters and variation of theirs size

Fabrication and ion etching the structure were performed in the high vacuum preparation chamber connected with the photoelectron spectrometer. The technique of fabrication of quasi-isolated supported Ag-clusters is based on the fact that thin metallic films are characterized by a hilly relief even being grown at the room temperature. These hills can be considered as Ag-clusters superimposed on thin Ag-layer. The technique includes fabrication of such a film and the uniform etching the film by ions. This uniform etching makes Ag-clusters smaller and Ag-layer thinner (Fig. 1a). At some stage of the etching, Ag-layer disappears in the area between clusters and a system of separated clusters should be originated on the supporting surface. Further etching diminishes clusters. To reduce the cluster-surface interaction and to electrically isolate clusters, the surface of native silicon oxide was chosen as a supported one. Typical thickness of native silicon oxide layer is known to be 2–3 nm and more. Ion etching this layer should create a system of Ag-clusters on the Si surface. These clusters are separated from the conductive surface by chemically inert SiO_2 isolators in the form of disks (Fig. 1b). Thus, systems of isolated clusters of different average sizes were expected to be available for study.

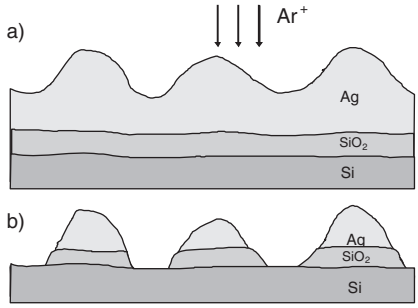

Fig. 1. a) Ag-thin film on the SiO2/Si surface being under Ar+ ion bombardment. b) System of Ag-clusters on Si surface. Clusters are isolated from the conductive Si- surface by individual dielectric SiO_2-layers.

2. Size related Ag3d core photoelectron line shift and the model of charging a cluster by one photoelectron

The prepared structure $Ag/SiO_2/Si$ was studied *in situ* by X-ray photoelectron spectroscopy with using synchrotron radiation just after its fabrication. The photon energy was $h\nu = 502.9$ eV. Fig. 2 shows the sequence of $Ag3d_{5/2}$ photoelectron spectra of the structure measured at different stages of the ion etching. Fig. 2 demonstrates diminishing the kinetic energy E_k of $Ag3d_{5/2}$ photoelectron in the course of reducing the effective thickness d of the silver film due to etching. The effective thickness of the film and the average surface density of silver at-oms in the system were estimated by monitoring the intensity of $Ag3d_{5/2}$ photoelectron line. The thickness was

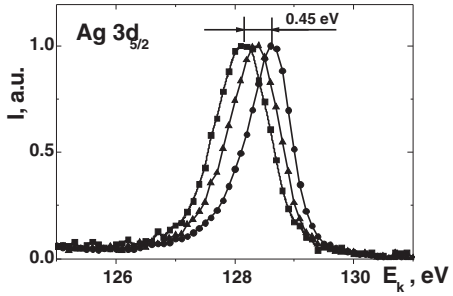

Fig. 2. Ag3d$_5$/2 photoelectron spectra of Ag/SiO_2/Si system at different stages of ion etching. The effective thickness of the film is $d = 0.22\lambda$ (1), $d = 0.1\lambda$ (2), $d = 0.03\lambda$ (3).

measured in terms of the mean free path λ of photoelectron in silver which is the mean length of photoelectron trajectory till the first inelastic collision. The mean free path is $\lambda \sim 0.7$ nm, or of about 3 atomic monolayers, for the photoelectrons of the given kinetic energy. Thus, the photoelectron line shift shown in Fig. 2 was caused by reducing the effective thickness of studied film in submonolayer range: from $d(1) \approx 0.15$ nm to $d(3) \approx 0.02$ nm.

The experimental data enabled obtaining more fundamental characteristics of the material – the binding energy of core-electron: $E_{\rm B} = h\nu - E_k - e\phi$, where $e\phi = 4.7$ eV is the work function of the spectrometer. Fig. 3 displays the dependence $E_{\rm B}(d)$ of the Ag3d$_{5/2}$ electron binding energy on the effective thickness of the layer. It is a monotonously decreasing dependence with some peculiarities probably connected with errors of the measurements. The binding energy of the initial film just after the metal deposition is close to the value $E_{\rm Ag} = 368.3$ eV of the bulk metallic silver. The binding energy increases of about 1 eV when the effective thickness of the layer reaches submonoatomic thickness. According to the assumed model of the cluster system fabrication, the effective thickness of the layer is connected with the average size of clusters created at some stage of the ion etching the deposited silver. Therefore the assumption was made that the observed shift is connected with diminution of the average size of clusters.

We studied transformation of electronic structure of silver clusters supported by conductive surfaces due to size confinement effects earlier and revealed that the corresponding Ag3d$_{5/2}$ binding energy shift does not exceed 0.2 eV in going from the bulk metal to the extreemly small clusters consisting of only two atoms [3,4]. Therefore another hypothesis of the line shift was chosen taking into account that the clusters under consideration are particls electrically isolated by rather thick dielectric layer wich radically deminishes interaction of clusters with the conductive silicon bulk. Isolated clusters of nanometer sizes are characterized by low capacity providing significant positive potential due to charging by one phoelectron. This potential retards photoelectron and results in "red" line shift: the smaller cluster, the larger shift. The model of free (the permittivity $\epsilon = 1$) spheroidal clusters with effective radius R and capacity $C = \epsilon R$ was considered. Fig. 3 shows the dependence of the binding energy on the effective thickness calculated in the frame of the model: $E_{\rm B}(d) = E_{\rm Ag} + e^2/R(d)$. The arrows point at the values of the effective thickness of the silver layer corresponding to the average radii of clusters $R = 5$, 4, 2 nm. One can see a reasonable agreement between the model and the

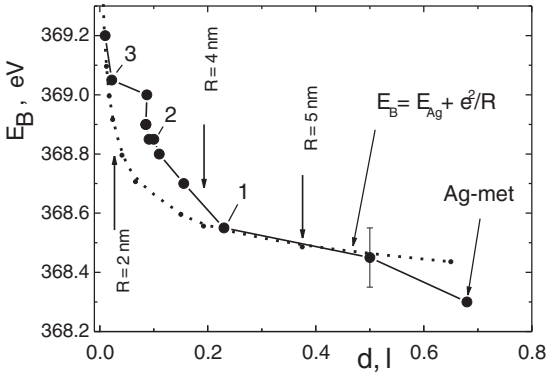

Fig. 3. Dependence of the Ag3d$_5$/2 core level binding energy on the silver amount or on the average number of atoms in the system of silver clusters on the Si/SiO_2 surface.

experimental dependencies both in the shape and values. The observed agreement confirms the assumed model. The suprizing fact is that the capacity of fabricated clusters can be approximated by the capacity of a conductive sphere in vacuum. This fact evidences formation of spheroidal silver nanoclusters on the inert silicon oxide surface due to restructuring the dome-type clusters initially created under ion bombardment. In the case of the flat basis of clusters the effective permittivity should be much larger as well as the capasity, and the agreement of the model and experimental energy dependencies would be hardly possible.

3. Conclusions

Silver nanoclusters in the size range $R = 6$–1 nm were fabricated on silicon surface at high vacuum conditions by ion etching a thin silver film deposited on the oxidized silicon surface. A unique feature of the system is that the metallic clusters are electrically isolated from the surface by individual SiO_2-layers. It was shown that ion etching resulted in reduction of the average cluster size of the system. Transformations of some properties of clusters were studied *in situ* in variation of the cluster size. The 1 eV size related "red" shift of the Ag3d$_{5/2}$ photoelectron line was observed and dependence of Ag3d$_{5/2}$ core level binding energy on the average cluster size was obtained. The model of charging the clusters by one electron in photoemission was suggested. It was shown that the observed "red" shift and the experimental binding energy dependence can be quantitatively described in the frame of this model. The suggested model enabled estimation of the average cluster sizes.

Acknowledgements

The research was supported by the Russian–German Laboratory at BESSY, by the Russian Academy of Sciences ("Quantum nanostructures", 5–22) and by the INTAS grant Ref. No. 06-1000012-8972.

References

[1] K. Okamoto *et al*, *Nature* **3**, 601 (2004).
[2] T. V. Shubina *et al*, *Phys. Rev. Lett.* **92**, 117407 (2004).
[3] V. M. Mikoushkin, *J. Technical Physsics* **44** (1999) 1077.
[4] V. M. Mikoushkin *et al*, *Latest Advances in Atomic Cluster Collisions: Fission, Fusion, Electron, Ion and Photon Impact*, (London: Imperial College Press) 345–354, 2004.

16th Int. Symp. "Nanostructures: Physics and Technology"
Vladivostok, Russia, July 14–18, 2008

Structural characterization of layered martensite structures in copper based shape memory alloys

O. Adiguzel
Firat University, Department of Physics, 23119 Elaziğ, Turkey

Shape memory alloys take place in a class of functional materials by exhibiting a peculiar property called shape memory effect. This property is characterized by the recoverability of desired shape on the material at different conditions. Shape memory alloys are metallic alloys which undergo solid state phase transformations in an appropriate temperature interval, martensitic transition on cooling and austenite transition on heating. Shape memory effect refers to the strain recovery of materials resulting from martensite to austenite transformation when heated above reverse transformation temperature after deforming the material in the martensitic phase. These alloys also cycle between two particular shapes with changing temperature. Copper based shape memory alloys serve as an economical alternative to other alloys, and they are widely used as a shape memory element in devices. These alloys are metastable at β-phase field and undergo two ordered transitions on cooling, and bcc structures turn into B2(CsCl) or DO_3(Fe_3Al)-type ordered structures. These ordered structures martensitically undergo the non-conventional structures on further cooling from high temperatures. The product phases have the unusual complex structures called long period layered structures such as 3R, 9R or 18R depending on the stacking sequences on the close-packed planes of the ordered lattice. In case the parent phase has a B2-type superlattice, the stacking sequence is ABCBCACAB(9R). If the parent phase has a DO_3-type superlattice, the stacking sequence is AB'CB'CA'CA'BA'BC'BC'AC'AB'A (18R). The stacking of $(110)_\beta$-planes in DO_3-type structure and formation of layered structures are shown in Figure 1.

Martensitic transformations occur by two or more lattice invariant shears on a {110}-type plane of austenite matrix which is basal plane or stacking plane for martensite, as a first step, and the transformed region consists of parallel bands containing alternately two different variants. All of these martensite

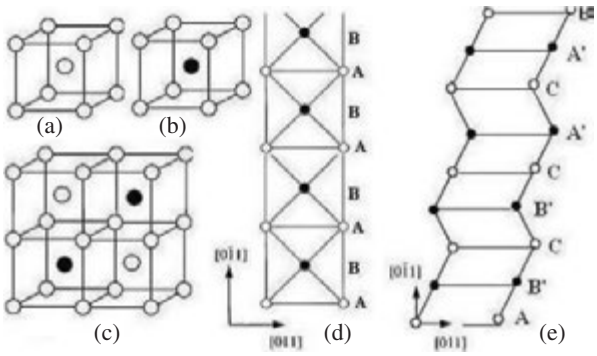

Fig. 1. Basic β-phase structures: (a) — ordinary bcc (A2), (b) — CsCl-type unit cell (B2), (c) — Cu_3Al-type unit cell (DO_3), (d) — stacking of $(110)_\beta$ planes viewed from $[001]_\beta$ direction, (e) — inhomogeneous shear and formation of layered martensite structures.

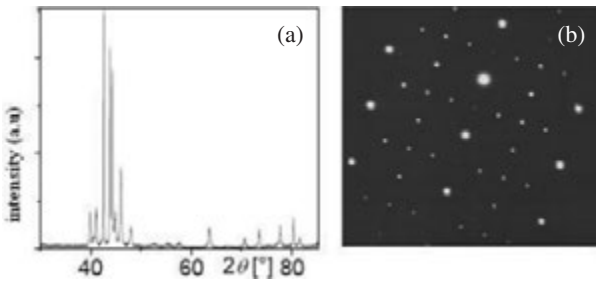

Fig. 2. (a) An x-ray diffractogram, (b) — an electron diffraction pattern taken from the alloy samples.

phases are long-period stacking ordered structures that is the underlying lattice is formed by stacks of close-packed planes. Metastable phases of copper-based shape memory alloys are very sensitive to the ageing effects, and heat treatments can change the relative stability and the configurational order of crystal planes. Also, several types of microscopic deformation involving changes can occur in the stacking sequence of close-packed planes of material with martensite formation, and some defects in the regular sequence of atomic planes can be frequently met. The quantity and sequence of this kind of defects affect the properties and behaviour of the material itself. Atom locations in the lattice sites in the crystal unit cell are also very important for the analysis and process of transformation. In the present contribution, two copper based ternary shape memory alloys were selected for investigation: a CuZnAl alloy with a nominal compositions by weight of 26.1% zink, 4% aluminium, the balance copper, while the other was a CuAlMn alloy with a nominal composition by weight of 11% aluminum, 6% manganese and the balance copper. Powder specimens for X-ray examination were prepared by filling the alloys. Specimens for TEM examination were also prepared from 3mm diameter discs and thinned down mechanically to 0.3 mm thickness. An x-ray powder diffractogram taken from the quenched CuZnAl alloy samples and an electron diffraction pattern taken from the quenched CuAlMn alloy samples are shown in Figure 2(a) and (b), respectively. X-ray powder diffractograms and electron diffraction patterns reveal that this alloys exhibit superlattice reflections.

Metastable phases of copper-based shape memory alloys are very sensitive to the ageing effects, and heat treatments can change the relative stability and the configurational order of crystal planes. Also, several types of microscopic deformation involving changes can occur in the stacking sequence of close-packed planes of material with martensite formation, and some defects in the regular sequence of atomic planes can be frequently met. The quantity and sequence of this kind of defects affect the properties and behaviour of the material itself.

16th Int. Symp. "Nanostructures: Physics and Technology"
Vladivostok, Russia, July 14–18, 2008

Interlayer tunneling spectroscopy of Landau levels in graphite

Yu. I. Latyshev[1], A. P. Orlov[1], V. A. Volkov[1], A. V. Irzhak[2], D. Vignolles[3], J. Marcus[4] and T. Fournier[4]

[1] Institute of Radio-Engineering and Electronics RAS, 125009 Moscow, Russia
[2] Moscow Institute of Steal and Alloys, 119049 Moscow, Russia
[3] Laboratoire National des Champs Magnetiques Pulses, 31432 Toulouse, France
[4] Neel Institute, CNRS, 38042 Grenoble, France

Abstract. New method of interlayer magneto-tunneling spectroscopy is used for study of electron energy spectra in graphite. It is shown that single graphene layer controls the electron tunneling transversely thin graphite sample

We adapted mesa-type structures used recently for interlayer tunneling spectroscopy of layered high temperature superconductors [1] and charge density wave materials [2] for interlayer tunneling spectroscopy of graphite. The structures have been fabricated by focused ion beam technique [3] and had lateral sizes of 1×1 μm and contained 20–30 graphene layers along the c-axis. The interlayer tunneling spectra of graphite mesas under magnetic field oriented across the layers ($B = 0.4-6$ T) show the peaks, which can be identified as transitions between Landau levels (LLs) with numbers $N = 1, 2, 3$ in valence band and $N' = N$ in conduction band. The most pronounced are peaks correspondent to transitions (1,1) (Fig. 1). The higher order peaks become resolved at fields above 2 T. The energy of the peaks and their square root dependence on NB corresponds to relativistic LLs observed in graphene by magneto-transmission experiment [4] (see Fig. 2). Our results are consistent with recent observations of Dirac fermion features in graphite by ARPES [5], STM [6] and magneto-transmission [7] methods.

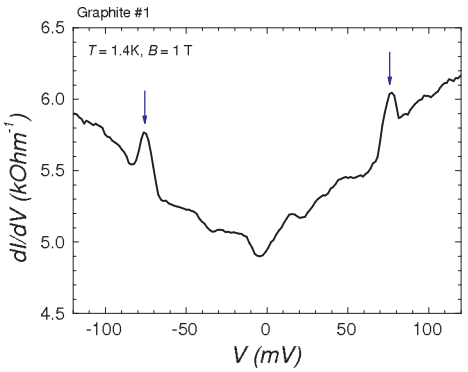

Fig. 1. The interlayer tunneling spectrum $dI/dV(V)$ of the graphite structure No. 1 at 1.4 K and $B = 1$ T, $B||c$. The peaks correspondent to transition (1,1) are marked by arrows.

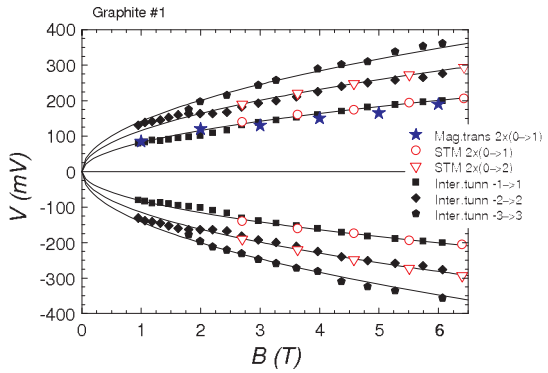

Fig. 2. Dependences of the doubled energy of the first three Landau levels extracted from interlayer tunneling data (full symbols) on magnetic field in comparison with STM data [6] (open symbols) and magneto-transmission data [7] (asterisks). Solid lines correspond to theoretical fit for the first three Landau levels of Dirac fermions with Fermi velocity $V_F = 10^8$ cm/s.

Acknowledgements

The work has been supported by RFBR grants: No. 08-02-01093-a, No. 06-02-72551-a, INTAS grant No. 05-1000008-7972 and Programmes RAS "Quantum nanostructures" and "Strongly correlated electron systems and quantum critical phenomena".

References

[1] V. M. Krasnov *et al*, *Phys. Rev. Lett.* **84**, 5860 (2000).
[2] Yu. I. Latyshev *et al*, *Phys. Rev. Lett.* **95**, 266402 (2005), *ibid.* **96**, 116402 (2006).
[3] Yu. I. Latyshev *et al*, *Supercond. Sci. Technol* **20**, S87 (2007).
[4] Z. Jiang *et al*, *Phys. Rev. Lett.* **98**, 197403 (2007).
[5] S. Y. Zhou *et al*, *Nature Phys.* **2**, 595 (2006).
[6] G. Li and Eva Y. Andrei, *Nature Phys* **3**, 623 (2007).
[7] M. Orlita *et al*, *cond-mat.* **0709**, 2681 (2007).

16th Int. Symp. "Nanostructures: Physics and Technology"
Vladivostok, Russia, July 14–18, 2008

Tunnel Schottky structures with 2D channels and negative differential conductance

I. N. Kotel'nikov[1] and M. N. Feiginov[2]

[1] Institute of Radioengineering and Electronics of the RAS, Moscow 125009, Mokhovaya St. 11/7, Russia
[2] Technische Universität Darmstadt, Merckstr. 25, D-64283 Darmstadt, Germany

Abstract. Experimental data are presented that demonstrate the conductance decrease with bias in the tunnel Al/GaAs Schottky structure with delta-n-doped 2D channel. The conductance is decreasing due to the increase in the tunnel-barrier height and the corresponding drop in the barrier tunnel transparency with bias. Theoretical calculations are in very good agreement with the experimental data, they also show that the mechanism should lead to the negative value of the differential conductance, if the separation between the subbands in the 2D channel is sufficiently large. The Al/InAlGaAs/InAlAs and Ti/GaN/AlGaN heterostructures with tunnel Schottky-barriers are suggested, where negative differential conductance should be achievable.

There are just a couple of tunnel structures with negative differential conductance (NDC): resonant-tunnelling diodes [1], Esaki tunnel diodes [2] and several their modifications. In the existing structures, NDC appears as a consequence of the violation of the elastic-tunnelling condition. Recently [3], we have theoretically described an other mechanism of NDC.

The mechanism of NDC in the tunnel Schottky contact with 2D channel is as follows [3]. At low temperatures, the elastic resonant tunnelling is the predominant mechanism of the electron transport between the metal and 2D channel. For each of the 2D subbands (i is the subband index) with the bottom energies (E_i) lower than the Fermi level in the metal (μ_m), the partial tunnel current (j_i) can be represented in the form:

$$j_i \sim (\mu_\mathrm{m} - \max(\mu_s, E_i))\, T_i, \qquad (1)$$

where μ_s is the Fermi level in the channel and T_i is the tunnel transparency of the barrier for the i-th subband. The Schottky barrier height is fixed with respect to μ_m due to the pinning, but the barrier height for the electrons tunnelling elastically and resonantly into the subbands is increasing with increase of bias; metal is cathode. As a consequence, T_i drops exponentially with bias. At some bias point, the decrease in T_i in (1) overcomes the increase due to the first term, the current starts to decrease and NDC appears. This mechanism does not require violation of the elastic-tunnelling condition. The total tunnel current through the Schottky barrier is the sum of the partial resonant currents of the subbands in the channel. With the onset of tunnelling to the next upper subband, the current and conductance are rapidly increasing. Therefore it is necessary to have the separation between the subbands sufficiently large to achieve NDC.

For the verification of the mechanism which should lead to NDC, we were experimentally investigating MBE-grown Al/δ-GaAs structures with the 2D channel formed by the δ-doped layer (Si) at the distance of 20 nm from Al/GaAs interface [4,5]. The structure was MBE-grown on semi-insulating (100) GaAs substrate and, to achieve high quality of the tunnel Schottky barrier, ≈100 nm thick Al has been grown *in situ* [4,5] in MBE chamber on Ga-stabilized GaAs surface. The Al-gates with the geometry of 10 μm × 1 mm were defined and Au-Ge-Ni ohmic contacts to the 2D channel have been fabricated on the wafers afterwards. The tunnel current has been measured between the

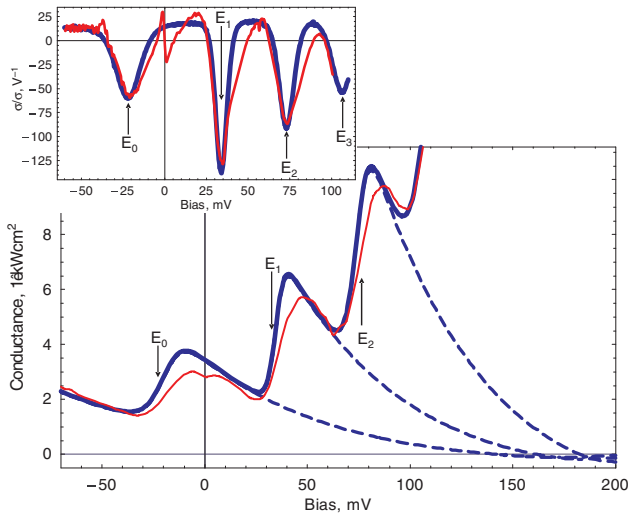

Fig. 1. Differential conductance of Al/GaAs structure with delta-doped 2D channel. The thin and thick lines are the experimental and theoretical curves, respectively. The dashed lines show the extension of the conductance, if one excludes tunnelling to the higher subbands in the calculations. The lines show that NDC would be reachable, if the separation between subbands were larger. The left inset shows the tunnel spectrum of the structure. The band diagram is shown in the right inset.

gate and the ohmic contacts. The 2D-channel is limited by a steep Schottky-barrier on one side and by a relatively mildly sloping on the other one due to the p-doping. As compared to the similar structures we were studying before [4,6], the GaAs p-doping of the present structure has been chosen to be relatively high (∼10^{16} cm^{-3}) to achieve larger separation between 2D subbands (∼50 meV), see inset in Fig. 1. The tunnel spectrum [which is the second derivative of the current, normalized by the conductance (σ)] of the structure measured at 4.2 K is shown in Fig. 1. The minima in the spectrum correspond to the bias points, where the Fermi level in the metal (Al) crosses the bottoms of the 2D-subbands in the channel [7]. The Schottky-barrier height at Al/GaAs interface is 0.86 eV [6]. The levels of delta-n-doping (≈4.1×10^{12} cm^{-2}) and p-doping (≈7.4×10^{15} cm^{-3}) in our structure were determined by fitting of the subband minima in the calculated and measured spectra (see inset on Fig. 1), the values are close to the nomi-

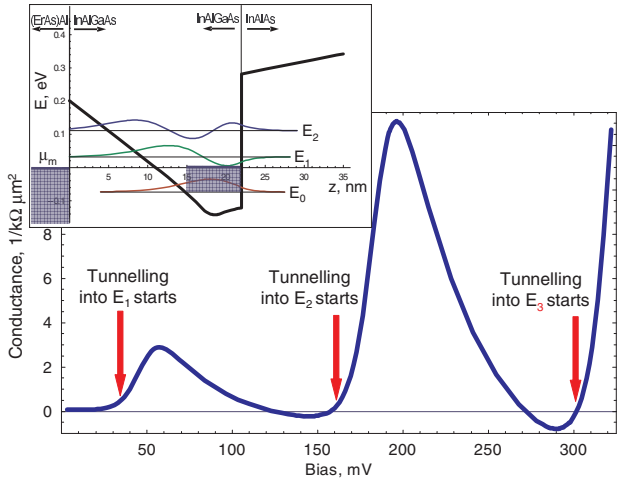

Fig. 2. Calculated differential conductance at 4.2 K of Al/InAlGaAs/InAlAs heterostructure lattice matched to InP. The subband broadening was supposed to be the same as for Al/GaAs structure in Fig. 1. Two regions with NDC are expected in such structures: one is around 150 mV and another one is around 300 mV. The inset shows the band diagram of the structure at zero bias.

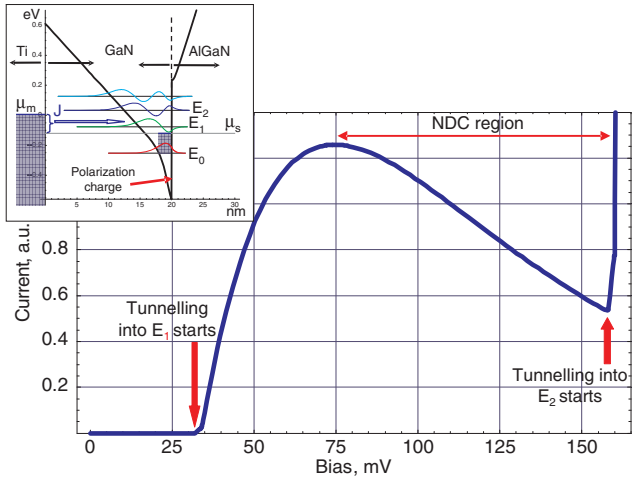

Fig. 3. Calculated I–V curve of Ti/GaN/AlGaN heterostructure. NDC should be observable between 75 and 150 mV. The inset shows the band diagram of the structure at the bias of 100 mV.

nal MBE-growth parameters. The fitting of the minima width in the calculated and measured spectra gives us information about the broadening of the different subbands: $\Delta E_0 \approx 4$ meV (half width) for the ground subband and $\Delta E_i \approx 2$–3 meV for the higher ones. The position of the spectral minimum of the ground subband (E_0) determines the electron concentration in the 2D channel: $N_{2D} \approx 5 \times 10^{11}$ cm^{-2} at zero bias. The tunnel current, conductance and spectra were calculated self-consistently as in [6, 8].

The measured and calculated differential conductances shown in Fig. 1 are in very good agreement with each other. At the voltages of around −20 mV and higher, one can see a series of steps in the differential conductance. The onset of tunnelling to the next subband with increase of bias leads to appearance of stepwise increase in the conductance, marked in the figure with the corresponding subband index. In each step, the conductance is first rapidly increasing with bias and then relatively slowly decreasing till the next step starts. The decrease in conductance is evident both in the measured and calculated characteristics. Our calculations show that the decrease in conductance is due to the drop in tunnel transparency of the barrier and it would have lead to the appearance of NDC in the structure, if not the tunnelling to the higher subbands. The dashed lines in Fig. 1 show the behavior of the conductance, if one excludes tunnelling to the higher subbands in calculations. The plots show that the conductance would have become negative at the biases of around 150 mV.

There are two obstacles to NDC observation. First, the separation between subbands should be sufficiently large, otherwise the tunnelling to the higher subbands prevents observation of NDC. The channel formed by delta-doping alone is rather wide, therefore observation of NDC in such structures is hardly possible. Second, the Schottky-barrier height in GaAs (0.86 eV) is comparable to the band-gap energy (1.52 eV), therefore nonparabolicity has essential influence on the tunnel properties of the barrier. Due to the nonparabolicity effects, the variation of the barrier tunnel transparency with bias slows down and therefore it is required to apply higher voltages to achieve NDC in such structures. It also makes the requirement on separation of the 2D subbands in the channel more stringent.

To overcome these difficulties we suggest two structures of a similar type, but with few modifications. First, the structures have heterointerfaces to make the channel more narrow. The separation of the subbands can be made more than ≈100 meV in this case [8]. Second, the use of (Er)Al/InAlGaAs [9] or Ti/GaN materials for the Schottky barrier allows one to make the barrier height small as compared to the band-gap energy and the nonparabolicity effects become less essential. As it is shown in Fig. 2 and Fig. 3, NDC should be achievable in such structures.

Acknowledgements

The work was supported by RFBR (grants 06-02-16955a, 08-02-00206a, 07-02-92171-PICS-a) and by RAS. We are grateful Yu. V. Fedorov and A. S. Bugaev for preparation of the samples.

References

[1] L. L. Chang *et al*, *Appl. Phys. Lett.* **24**, 593 (1974).
[2] L. Esaki, *Phys. Rev.* **109**, 603 (1958).
[3] M. N. Feiginov, *Appl. Phys. Lett.* **81**, 930 (2002).
[4] I. N. Kotel'nikov *et al*, *JETP Lett.* **71**, 387 (2000).
[5] I. P. Kazakov *et al*, *International Symposium Nanostructures: Physics and Technology*, Novosibirsk, Russia, 25–29 June, 2007, p. 340.
[6] I. N. Kotel'nikov *et al*, *Semiconductors* **40**, 818 (2006).
[7] E. L. Wolf, *Principles of Electron Tunneling Spectroscopy* (Oxford Univ. Press, Oxford) 1985.
[8] M. N. Feiginov *et al*, *Appl. Phys. Lett.* **91**, 083510 (2007).
[9] J. D. Zimmerman *et al*, *J. Vac. Sci. Technol. B* **23**, 1929 (2005).

16th Int. Symp. "Nanostructures: Physics and Technology"
Vladivostok, Russia, July 14–18, 2008

Phonon induced Fano resonances in photocurrent spectra of InP doped with shallow donors

V. Ya. Aleshkin[1], A. V. Antonov[1], L. V. Gavrilenko[1], *V. I. Gavrilenko*[1] and B. N. Zvonkov[2]

[1] Institute for Physics of Microstructures Russian Academy of Sciences, Nizhny Novgorod, GSP-105, 603950, Russia
[2] Pysico-Technical Research Institute of the Nizhny Novgorod State University, Nizhny Novgorod, 603950, Russia

Abstract. The results of theoretical and experimental study of the impurity photocurrent peaks in the spectral region corresponding to the longitudinal optical phonon energy in n-InP are presented. It is shown that the suggested theory adequately describes the impurity photocurrent peaks observed in n-InP.

Introduction

There are the asymmetrical features (peaks or deeps) in the impurity photocurrent spectra of many semiconductors doped with impurities at photon energy corresponding to the longitudinal optical (LO) phonon peculiar to the material. Firstly, analogous features in the photoexcitation spectra were observed in p-Si [1]. Later similar features were observed in the absorption and photocurrent spectra in n-Si, doped with deep donors and n-Ge. The authors of Ref. [2] explained the appearance of the above spectral features by the interaction of carriers with optical phonons. They suggested using the term "Fano resonances" to denote these features. The famous expression from Fano work [3] where the configuration interaction between a resonant level and a continuum was considered, is often used to qualitatively describe these spectral features.

Asymmetric peaks in the impurity photocurrent spectra have been recently observed in GaAs and InP, doped with the shallow donors [4]. Until now the following contradiction was unresolved: from work [4] it is seen that in n-GaAs Fano peak is wider than one in n-InP. It is known that the peak width is proportional to electron-phonon scattering frequency. However in n-InP this frequency is almost twice as that in n-GaAs. So the situation must be opposite.

To clear this contradiction the detailed investigations of n-InP photocurrent spectra were provided in the present work.

1. Experimental results

The measurements was carried out with Fourier-transform spectrometer BOMEM at $T = 4.2$ K. Sample of n-InP was grown by MOCVD epitaxy at atmosphere pressure on semiinsulating InP substrate. Epitaxial layer 5.5 micron wide was not doped on purpose. On Hall measurements data free electron concentration in epilayer was 4.4×10^{15} cm^{-3}. The electron mobility was 3350 cm^2/V s at room temperature. This fact denotes a high level of the material compensation.

On cooling to liquid helium temperature the sample resistance increases in 400 times, so the electrons are frozen on donor states. Measured photocurrent spectrum of n-InP in the spectral range corresponding to transitions between localized donor states is shown on Fig. 1. It is seen that the main peak (1s-2p transition) is situated at 38.7 cm^{-1} (4.8 meV). This value is less than the energy of 1s-2p transition for single donor in InP (5.6 mev) [5]. Evidently, the difference is caused by considerable overlap of 2p state wavefunctions (and higher states) and the rise of the impurity bands, which merge into the conduction band judging from the data [5].

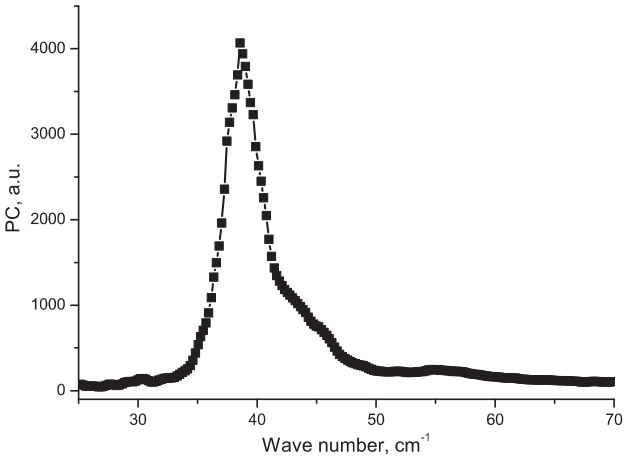

Fig. 1. Measured photocurrent spectra of n-InP (sample #5176) at $T = 4.2$ K in the spectral range corresponding to donor localized states transitions.

The photocurrent spectrum of n-InP in the spectral range corresponding to LO phonon energy is presented in Fig. 2. It is seen from the picture that asymmetrical peak is situated at 350 cm^{-1} which coincides with LO phonon energy in InP.

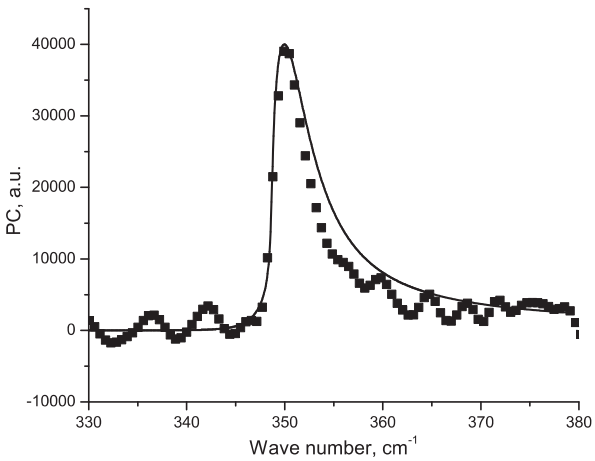

Fig. 2. Calculated (curves) and measured (squares) photocurrent spectra of n-InP (sample #5176) at $T = 4.2$ K in the spectral range corresponding to Fano resonance.

Note, that the Fano peak width insensibility to variation of the impurity ionization energy was shown by the example of Fano resonance in QW [6]. However the width strongly depends on electron-phonon scattering frequency in situ [6]. Calculated photocurrent spectrum is also shown in Fig. 2.

2. Model

To calculate a photocurrent spectrum we need to know the light absorption probability, the lattice absorption and reflectance spectra.

Let us consider the light induced electron transitions from initial donor ground state $|i\rangle = |\varphi_{1s}, N\rangle$ (without additional phonons) to the state $|\varphi_q\rangle = |\varphi_{1s}, N+1\rangle$ (there is one more LO phonon with wave vector q). The Hamiltonian containing electron-phonon interaction and impurity potential is

$$H = \frac{p^2}{2\mu} - \frac{e^2}{\kappa_0 r} + \sum_q V(q)\exp(-iqr)b_q^+ + \sum_q V^*(q)\exp(iqr)b_q + \sum_q \hbar\omega_0\left(b_q^+ b_q + \frac{1}{2}\right), \quad (1)$$

here $V(q) = \frac{ie}{q}\sqrt{\frac{2\pi\hbar\omega_0}{\overline{\kappa}V}}$, e and μ are the electron charge and effective mass, respectively; κ_0 and κ_∞ are low-frequency and high-frequency permittivities; $\overline{\kappa} = \kappa_0\kappa_\infty/(\kappa_0 - \kappa_\infty)$; q, ω_0 are the LO phonon wavevector and frequency; b_q^+, b_q are the creation and annihilation operators; and V is the crystal volume. The asterisk (*) stands for complex conjugation.

Let us consider the resonant state of the system $|\varphi_q\rangle$, where the electron is in the donor ground state and additional LO phonon with wavevector q and impulse moment projection $\hbar$ is present.

Follow Fano work [3] we seek for exact wavefunction corresponding to the energy E in the form

$$|\Psi(E)\rangle = \sum_q a_q(E)|\varphi_q\rangle + \int dE' b(E, E')|\psi(E')\rangle. \quad (2)$$

here $\psi(E')\rangle$ is unperturbed wave function of states with the full momentum and z-projection of momentum equal to $\hbar$. Neglecting the electron state renormalization due to electron-phonon interaction and using [3] we derived expansion coefficients for (2) and light absorption spectrum.

Electron-electromagnetic wave interaction operator is

$$V_{\rm ph}(t) = V_{\rm ph}\left[\exp(-i\omega t) + \exp(i\omega t)\right], \quad (3)$$

where $V_{\rm ph} = e\mathcal{E}r\sqrt{\frac{4\pi}{3}}Y_{1,1}(\theta,\varphi)$, $\mathcal{E}$ is the electric field amplitude, $Y_{1,1}(\theta,\varphi)$ is the spherical function.

The total light absorbtion probability is proportional to the squared modulus of the following matrix element:

$$\langle\Psi(E)|V_{\rm ph}|i\rangle = \frac{\Gamma(E)\langle\psi(E)|V_{\rm ph}|i\rangle}{2\sqrt{(E-E_\varphi)^2 + \Gamma(E)^2/4}} \times\left(Q(E) + \frac{E-E_\varphi}{\Gamma(E)/2}\right), \quad (4)$$

here

$$Q(E) = \frac{1}{\Gamma(E)/2\langle\psi(E)|V_{\rm ph}|i\rangle} \times\left(P\int_{E_f}^{\infty} dE' \frac{\langle\psi(E')|V_{\rm ph}|i\rangle\sum_q V_q(E)V_q^*(E')}{E-E'} + \sum_{n=2}^{\infty}\frac{\langle\psi(E_n)|V_{\rm ph}|i\rangle\sum_q V_q(E)V_q^*(E_n)}{E-E_n}\right),$$

where $V_q(E) = \langle\psi(E), N|V(q)\exp(-iqr)b_q^+|\varphi_q, N+1\rangle$ and $V_q(E_n) = \langle\varphi(E_n), N|V(q)\exp(-iqr)b_q^+|\varphi_q, N+1\rangle$; $\psi(E_n)$ is wave function of donor localized P-states numbered with principal quantum number n; $\Gamma(E)/\hbar$ is the frequency of electron transition between the state in continuum $|\psi(E)\rangle$ and localized state $|\varphi_q\rangle$ due to the spontaneous LO-phonon emission, $\Gamma(E) = 2\pi\sum_q |V_q(E)|^2$. In the vicinity of Fano resonance, the spectrum of the photocurrent is significantly influenced by the the frequency dependencies of the reflection coefficient and of the lattice absorption, which rapidly vary in this region. Taking into account these factors, the photocurrent can be expressed as

$$J(\omega) = BI(\omega)\frac{|\langle\Psi(\hbar\omega - E_{\rm i})|V_{\rm ph}|i\rangle|^2}{|\mathcal{E}|^2}[1-R(\omega)] \times\int_0^d \exp\left[-\eta(\omega)x\right]dx, \quad (5)$$

where B is a frequency-independent constant, $I(\omega)$ is the incident light intensity, $\eta(\omega)$ is the optical absorption coefficient and d is the thickness of the doped region, $R(\omega)$ and $\eta(\omega)$ are light reflection and absorption coefficients, $E_{\rm i}$ is donor ionization energy.

It is seen from Fig. 2 that calculated spectrum is wider only by 15%, so there is a good agreement between theory and experiment.

Acknowledgements

This work has been supported by RFBR (07-02-00549), the Dynasty foundation (grant for L. Gavrilenko).

References

[1] H. J. Hrostowski, R. H. Kaiser, *J. Phys. Chem. Solids* **4**, 148 (1958).
[2] A. Onton *et al*, *Phys. Rev.* **163**, 686 (1967).
[3] U. Fano, *Phys. Rev.* **124**, 1866 (1961).
[4] K. Jin *et al*, *Phys. Rev. B* **64**, 205203 (2001).
[5] A. Dargys, J. Kundrotas, *Handbook on physical properties of Ge, Si, GaAs and InP*, Science and Encyclopedia Publishers, Vilnus (1994) 262 p.
[6] V. Ya. Aleshkin *et al*, *Proc. 8th Russian conf. on physics of semiconductors*, Ekaterinburgh, Russia 2007, p. 345.

16th Int. Symp. "Nanostructures: Physics and Technology"
Vladivostok, Russia, July 14–18, 2008

Picosecond dynamics of transmittance in GaAs/InGaAs quantum well heterostructure

V. Ya. Aleshkin, A. A. Dubinov, L. V. Gavrilenko, *Z. F. Krasilnik*, D. I. Kuritsyn, D. I. Kryzhkov and S. V. Morozov

Institute for Physics of Microstructures Russian Academy of Sciences, Nizhny Novgorod, GSP-105, 603950, Russia

Abstract. Light transmittance changes in GaAs structure with 50 InGaAs quantum wells with subpicosecond temporal resolution have been studied by pump-probe method under strong optical excitation. The transmittance is shown to increase at characteristic photon energies due to the population of quantum well states. Fast negative transmittance changes at 0.25–0.9 ps after excitation pulse have been detected.

Introduction

Nowadays, theoretical and experimental investigations of carrier dynamics in quantum confined structures are widely developing, aiming research of fundamental properties of non-equilibrium carriers [1,2] and nanostructured device design [3]. Femtosecond spectroscopy is one of the basic methods of the investigation of ultrafast phenomena, governed by different carrier scattering mechanisms and subsequent carrier recombination. This technique allows to shed light on physical processes governing carrier dynamics from the moment of their generation till the relaxation to the equillibrium state [4,5].

The paper is devoted to experimental investigations of GaAs/InGaAs heterostructure with multiple quantum wells (QW) by femtosecond pump-probe spectroscopy.

The heterostructure under study has been grown by MOCVD technique on 300 μm thick semiinsulating GaAs substrate. It consists of 50 periods of 60 A wide $In_{0.22}Ga_{0.78}As$ QWs separated by 500 A wide GaAs barriers and GaAs cap layer of 3000 A in thickness. The structure has not been specially doped. Free electron concentration is less than 10^{10} cm^{-2} per QW as it has been obtained from Hall measurements.

The energy-band structure of the sample is schematically shown in Fig. 1. As easy to see there are one electron (e1) and two heavy hole subbands (hh1, hh2) in the QW. The Calculated e1-hh1 and e1-hh2 transition energies between subband edges are 1.255 eV and 1.295 eV, respectively.

Note that calculated transition energy between electron subband (e1) and the top of the valence band (Ev) is 1.328 eV, and between first heavy hole subband (hh1) and electron the conduction band (Ec) bottom is 1.343 eV.

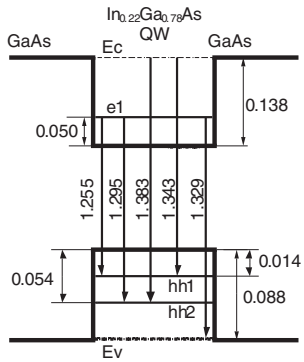

Fig. 1. Band discontinuities and level positions (eV) for QW heterostructure. e1, hh1, hh2 are edges of electron, first and second heavy holes subbands.

1. Experimental technique

Relative transmittance measurements of the QW structure were performed with double-differential technique: the white light probe signal was divided into two beams which were focused on the sample surface in the spots about 0.2 mm in diameter at 10 mm from each other. The pump pulse affected only one above spot. Passed through the structure probe beams were then dispersed by grating monochromator and registered by two linear silicon CCD arrays. Then, the spectrum originated from the pumped spot was weighted by that from the unpumped spot. Thus, all spectral features not responding to the pump pulse influence were eliminated in the resulting curve.

The regenerative amplifier "Spitfire" (Spectra Physics) was used as a pump source (800 nm), providing about 60 μJ pulses (1 kHz repetition rate) of 120 fs in duration. The sample was pumped by 2 μJ pulses, the rest of pulse energy was used for continuous-water-flow white light continuum generator to produce probe pulses with average power about 100 μW per channel. The pump radiation frequency was filtered a narrow band high-reflecting dielectric mirror.

2. Result and discussion

Transmittance spectrum of the investigated sample is shown in Fig. 2 (curve 2 — open circles). The exciton-induced deep is clearly seen close to e1-hh1 transition edge (1.255 eV) in the spectrum. The features related with forbidden e1-hh2 transition and e1-Ev transition are also distinguishable. Note that the high energy transmission cutoff ($\sim$1.40 eV) lies lower than band gap edge in GaAs (1.424 eV at RT) that results from the density-of-states tails in the forbidden gap [6] and rather thick GaAs substrate (300 μm).

Curve 1 in Fig. 2 represents the photoluminescence (PL) spectrum measured under Ar^+ laser pumping. PL peak maximum coincides with exciton-induced deep in transmittance (curve 1 in Fig. 2).

In the same figure the relative transmittance spectra ($\Delta T/T$) for delay time 5 ps, 500 ps, and 1500 ps (curves 3–5, respectively) under femtosecond laser pumping are shown.

One can see from Fig. 2 that in 5 ps after the pump pulse QW states are filled up with carriers that leads to the transmittance

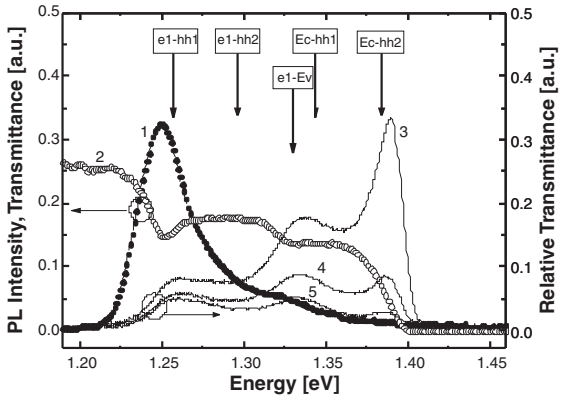

Fig. 2. Curves: 1) PL spectrum, 2) transmittance spectrum, 3–5) relative transmittance spectra for delay times 5 ps, 500 ps and 1500 ps, respectively. Calculated transition energies labeled as e1-hh1, e1-hh2, e1-Ev, Ec-hh1, Ec-hh2.

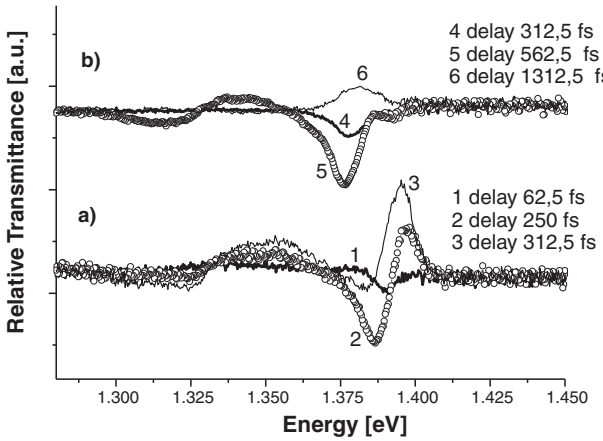

Fig. 3. Relative transmittance spectra of $In_{0.22}Ga_{0.78}As/GaAs$ QW for short delay times (62.5 fs to 1.3 ps) for the cases of a) QW side and b) substrate side excitation.

increase in the spectral range corresponding to the band-gap absorption in QWs.

The photocarrier concentration nearby QWs is estimated as 4×10^{18} cm^{-3} (or $\sim 2 \times 10^{13}$ cm^{-2} per QW). But probably the number of carriers in QWs is one order of magnitude less. Therefore the most carriers just after thermalization remain in GaAs layers. The peak at 1.4 eV in the relative transmittance spectra seems to be caused by these carriers.

The photocarrier concentration in GaAs barriers and in excited QW's subbands decreases rapidly with the time, while the concentration in the ground electron and heavy hole subbands decreases slower (cf. curves 3–5 in Fig. 2). The GaAs layers and QW's excited subbands act as a reservoir of carriers for the lower subbands because the thermalization time is much shorter than recombination time.

An unusual behavior of relative transmittance spectra was observed for a short delay time between 60 fs and 1.3 ps for the pumping from both the QW and the substrate sides of the sample. Corresponding relative transmittance spectra are shown in Fig. 3. It is well seen that induced absorption effect appears in two spectral ranges (1.294–1.330 eV and 1.370–1.390 eV in the case of pumping from QW side, and 1.294–1.330 eV and 1.357–1.385 eV in the case of pumping from the substrate side).

Note that the maximum induced absorption is observed at delay of 0.56 ps and 0.25 ps for the excitation from substrate and QW side, respectively. The origin of the induced absorption is not clear. The possible reason is the surface electric field screening by photocarriers. Similar induced absorption was observed at approximately the same delay time in AlGaAs/GaAs heterostructures [7].

Acknowledgements

This work has been supported by the Program of fundamental research of RAS Presidium "Femtosecond optics and physics of superstrong laser fields" (project 3.8 "Femtosecond spectroscopy of solid state nanostructures") and by the Dynasty foundation (grant for L. Gavrilenko).

References

[1] A. Othonos, *J. Appl. Phys.* **83**, 1789 (1998).
[2] V. M. Axt and T. Kuhn, *Rep. Prog. Phys.* **67**, 433 (2004).
[3] J. Wang and H. C. Schweizer, *IEEE J. Selected Topics in Quatum Electronics* **3**, 218 (1997).
[4] A. R. Vasconcellos, R. Luzzi and J. R. Madureira, *J. Phys.: Condens. Matter.* **12**, 5325 (2000).
[5] F. Rossi and T. Kuhn, *Rev. Mod. Phys* **74**, 895 (2002).
[6] H. C. Casey, D. D. Sell, K. W. Wecht, *J. Appl. Phys.* **46**, 250 (1975).
[7] L. Robledo *et al*, *Physica E* **13**, 708 (2002).

16th Int. Symp. "Nanostructures: Physics and Technology"
Vladivostok, Russia, July 14–18, 2008

Visible photoluminescence from Ge nanocrystals in GeO_2 matrix

D. V. Marin[1,2], V. A. Volodin[1,2], E. B. Gorokhov[1], H. Rinnert[3], P. Miska[3] and M. Vergnat[3]

[1] Institute of Semiconductor Physics of SB RAS, pr. ak. Lavrentjeva 13, Novosibirsk 630090, Russia
[2] Novosibirsk State University, Pirogova street, 2, 630090, Novosibirsk, Russia
[3] Laboratoire de Physique des Materiaux (LPM), Nancy-Universite, CNRS, Boulevard des Aiguillettes B.P. 239, 54506 Vandouvre les Nancy, France

Abstract. GeO_2 films with germanium nanocrystals (NCs) with sizes of 6–8 nm were deposited from supersaturated GeO vapor with subsequent dissociation of metastable in solid state GeO on heterophase system Ge:GeO_2. The broad green-red photoluminescence (PL) peak was detected in Ge:GeO_2 films after thermal annealings in high vacuum up to 600 °C. According to effective mass approach, maximum of PL signal from such relatively big Ge NCs should be in IR region. The experimentally observed PL signal is presumably originated due to direct $L_1 - L_3'$ optical transitions "folded" in germanium NCs. The studied heterostructures can be perspective for using in opto-electronics, or for creation of elements of quasi-nonvolatile MOS memory using Ge NCs as traps for electrons or holes.

The nanometer-sized semiconductor nanocrystals (NCs), embedded in wide-gap insulating matrices, have shown significant promises for a wide range of nanoelectronics and optoelectronics applications. Quantum effects in such heterosystems become brightly apparent at room temperature. As, in some experiments, a single NC reveal delta-function-like energy spectra [1] it can be called quantum dots. A comparison of Si and Ge reveals that, from the technological point of view, Ge has advantages. The melting point of Ge is low (940 °C), causing lower crystallization temperature. The germanium monoxide is volatile and readily sublimates at sufficiently low temperature (∼500 °C), forming the bases for the development of different technologies utilizing the mass-transfer reactions. The energy gap values of Ge and Si NCs become equal when their sizes reach 2.3 nm. Further decrease of sizes down to 1.5 nm causes an abrupt increase in Ge gap up to 3 eV, which exceeds by 0.7 eV the gap of Si NC with the same size. This is the reason for an intensive and useful blue shift of Ge-based light-emitting nanostructures. Ge has a large exciton Bohr radius (24.3 nm). Thus, the quantum-confinement-related positive effects in Ge manifest themselves at large sizes. The disposition of energy bands at the Ge-GeO_2 interface is favorable for the carrier injection. This important feature can increase the efficiency of the injection-type devices produced on the basis of Ge-GeO_2 system. Ge is a high-refractive-index semiconductor, valuable for filling the interstitial voids in opals and producing photonic crystals with a complete photonic bandgap. So, the relatively old obtained Ge:GeO_2 heterostructures [2] attract more attention to researchers recent years [3,4].

The GeO_2 films with Ge NCs were deposited on silicon substrates from supersaturated GeO vapor with subsequent dissociation of meta-stable (in solid state) Ge monoxide on heterophase system Ge:GeO_2. The scheme of reactor and technology is described elsewhere [5].

The obtained films were studied with the use of photoluminescence (PL) spectroscopy, Raman scattering spectroscopy, IR-spectroscopy techniques. Experimental Raman spectra were registered in quasi back-scattering geometry, the 514.5 nm Ar^+ laser lines was used. The normal incidence IR absorption measurements were carried out with a resolution of 4 cm^{-1}. Some samples were annealed in high-vacuum quartz tube. To avoid the evaporation of Ge:GeO_2 films its was covered by cap layer from 50 nm thick SiO_2 deposited at temperature 100 °C and pressure equal to 10^{-8} Torr using electron beam gun evaporation of silica.

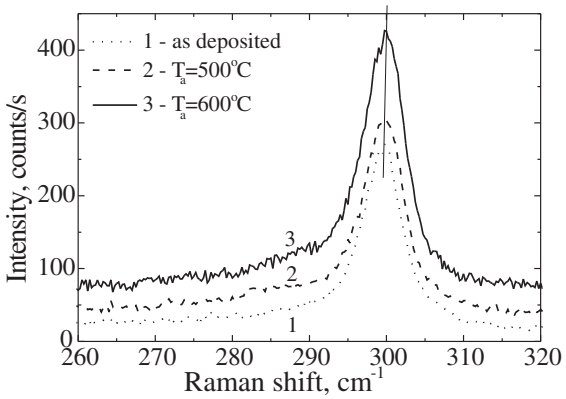

Fig. 1. Raman spectra of as deposited Ge:GeO_2 film (covered by 50 nm thick SiO_2 cap layer) and films annealed at different temperatures (T_a).

According to IR absorption data initial film was totally decomposited on Ge and GeO_2. The Raman spectra of the initial and annealed films are shown in Figure 1. One can see the Raman peak due to scattering on optical phonons confined in Ge NCs in Raman spectra. The confinement effect shifts the position of Raman peak to low frequencies from bulk-Ge Raman peak position (about 300.5 cm^{-1}). In Figure 1 one can see that in initial Ge:GeO_2 film practically all Ge clusters are crystalline. The NCs sizes can be estimated from position of Raman peaks, and the diameter of Ge NCs was estimated as about 6–8 nm. One can see very small shift of Raman peaks with annealing (thin line is drawn for convenient). It can be caused by some ordering of Ge-GeO_2 interface and also by annealing of defects in Ge NCs.

According to theoretical calculations of quantum confinement effects in Ge NCs with the sizes of 6–8 nm, the maximum of PL signal should be in range 1.0–0.8 eV [6]. Our

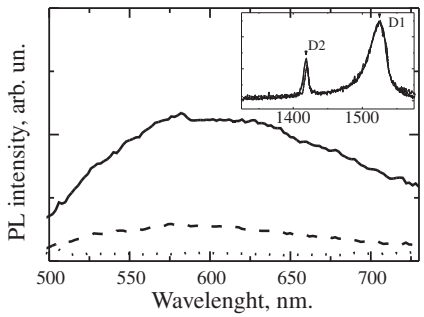

Fig. 2. Room temperature PL spectra in visible diapason of as deposited Ge:GeO_2 film (covered by 50 nm thick SiO_2 cap layer) and films annealed at different temperatures (T_a). Inset — PL spectrum of the as deposited film in IR diapason measured at 4 K.

simple effective-mass approach model also gives similar values. So, to study the PL signal we used IR-region PL setup with monochromator equipped with a 600 grooves/mm grating and InAs cooled photodiode as a detector. HeNe (633 nm) and HeCd (325 nm) cw lasers with power about 30 mW were used for excitation. For study PL in visible diapason we used another PL setup — with Ar^+ and N_2 lasers for excitation and photomultiplier tube as a detector.

The PL spectra of the initial and annealed films are shown in Figure 2. In diapason 0.8–1.0 eV we have observed two peaks (see insert in Figure 2). These peaks are from dislocations in silicon substrate. These are well-known D1 (1523 nm) and D2 (1420 nm) peaks [7]. To grow our film on clear fresh surface we used silicon substrates with thick thermal silicon dioxide (used as a cap layer), which we had removed by HF acid immediately before the film deposition. Obviously, the thermal oxidation of silicon at very high temperatures had created the dislocations in our substrates. The PL signal from dislocations at low temperatures is relatively high, so we could not see PL signal from Ge NCs even if we had any.

According to theoretical calculations, radiative lifetime in Ge NCs of spherical shape with diameter 6–8 nm should be quite large — about 10^{-2} second [6]. So, if we have non-radiative recombination centers with much shorter lifetime, the radiative recombination would be negligible. In Ge NCs such centers can be defects inside NCs, interface defects and molecules of water. It is known that GeO_2 films and low temperature porous SiO_2 films can absorb H_2O molecules and evaporate it during thermal annealings. Using the thermal annealing we have tried to supress defects, to evaporate water and to order the Ge NCs/GeO_2 matrix interface. To avoid the evaporation of Ge:GeO_2 films, the layers was covered by cap layer from 50 nm thick SiO_2. We used Ar^+ laser excitation and results are reported in Figure 2. After annealings, the green-red PL signal appears (the blue-green 488 nm Ar^+ laser line was used for excitation). When we used for excitation UV laser (N_2, wavelength 337 nm) the signals from Ge:GeO_2 films were very low. It is also important to mention that we used Si/SiO_2 sample as reference (the SiO_2 film was deposited on Si substrate without Ge:GeO_2 film in the same process "side-by-side") and that we have no PL signal for this sample.

If the observed PL signal (2–2.4 eV) was from quasi-direct excitons in Ge NCs, the sizes of NCs should be about 2 nm [6]. As it was mentioned above, according to our Raman data and also according to direct electron microscopy data for samples grown in similar conditions [5], average diameter of Ge NCs in our case is of 6–8 nm. So, one can assume, that we have PL assisted with some defects in GeO_2 matrix or Ge-GeO_2 interface, or some other excitations in Ge NCs. However, GeO_2 film obtained by Ge oxidation (without Ge NCs) has no PL in this region. Paying attention to band structure of bulk Ge, one can see that energy of direct transition between L valleys for electrons and holes is about 2.1 eV. From this energy of photons the abrupt increase of light absorbance takes place. In the case of excitation of bulk Ge, the holes relax very fast to Γ-valley emitting acoustical and optical phonons through continuous energy band states. In NCs electron (and phonon) states is discrete, not continuous, and such relaxation can be not very fast, and part of holes can recombine radiatively with electrons through direct transitions in L valleys. Also, because the average quasi-pulse of electron and holes in NCs is zero (localized, standing waves), the 4 L valleys is "folded" and electrons and holes from all that valleys can recombine. So probability of such processes can be compared with probabilities of nonradiative transitions. It can be presumable explanation of observed PL signal in our case. Some shift (compared to bulk Ge $L_1 - L_3'$ transition energy) can be due to quantum-size effects. The broad PL peak can be due to Ge NCs size dispersion, and also due to complex energy structure of discrete electron states in relatively big Ge NCs. It should be noted, that at temperature of 600 °C and higher the intermixing of SiO_2 and GeO_2 films can begin with forming of $Ge_xSi_{(1-x)}O_2$ thin layer and origination of PL signal from this layer can be also possible. In further studies, the proposed mechanism of PL should be tested using the GeO_2 films with bigger and smaller Ge NCs.

Optical properties of GeO_2 films with Ge NCs with average sizes 6–8 nm (according to Raman data) were studied. The visible PL was observed for samples annealed under high vacuum. Annealings can improve the structure of the Ge NCs and the interface. The mechanism of direct radiative transitions for confined electrons and holes (it's wave functions are originated from L valleys of bulk Ge) is proposed for explanation of experimental effect.

Acknowledgements

The RFBR supports this study (projects 07-08-00438).

References

[1] I. Sychugov *et al*, *Phys. Rev. Lett.* **94**, 087405 (2005).
[2] N. N. Ovsyuk *et al*, *JETP Letters* **47**, 298 (1988).
[3] V. A. Volodin *et al*, *JETP Letters* **77**, 485 (2003).
[4] M. Ardyanian *et al*, *Appl. Phys. Lett.* **89**, 011902 (2006).
[5] E. B. Gorokhov *et al*, *Proc. of SPIE.* **6260**, 626010 (2006).
[6] Y. M. Niquet *et al*, *Appl. Phys. Lett.* **77**, 1182 (2000).
[7] N. A. Drozdov *et al*, *JETP Letters.* **23**, 597 (1976).

16th Int. Symp. "Nanostructures: Physics and Technology"
Vladivostok, Russia, July 14–18, 2008

Multi-channel adaptive measurement system for sub-nanometer metrology

R. V. Romashko[1], Yu. N. Kulchin[1], S. Di Girolamo[2], A. A. Kamshilin[2] and J.-C. Launay[3]

[1] Institute of Automation and Control Processes FEB RAS, Vladivostok, Russia
[2] University of Kuopio, FI-70211 Kuopio, Finland
[3] CNRS Bordeaux Institute of Condensed Matter & Chemistry, Bordeaux, France

Abstract. Adaptive interferometer which is based on diffusion holograms recorded in semiconductor photorefractive crystal is developed. The interferometer sensitivity achieved is only 5.7 times less then highest sensitivity which is possible only in non-adaptive lossless classical interferometer. A practical detection limit is equal to 9.3×10^{-7} nm$\sqrt{\text{W/Hz}}$, which allows to reliably detect object's displacement or vibration with amplitude of order 1 pm. Multiplexing of several dynamic holograms in single photorefractive crystal with extremely low crosstalk noises makes possible to create highly effective multi-channel adaptive measurement system for simultaneous measuring vibrations of several nanoobjects.

Introduction

Development, creation and usage of nanostructures require analyzing not only electronic and optical [1] but also mechanical properties of nanostructures. Thus, for example, measured resonance response of a nanoelectromechanical oscillator allows obtaining a mass of nanoobjects, such as viruses, bacteria, DNA molecules etc. [2]. Measurement of a nanoobject eigenfrequencies makes possible to calculate its rigidity [3]. It is clear that amplitude of nanoobjects vibration is quite small, and does not exceed nanometer scale. In order to measure such vibrations an interferometer as a very sensitive instrument for detecting different physical parameters can be used. However high sensitivity of the interferometer makes it open to influence of environment. It is well known that two-wave mixing in photorefractive (PR) crystals allows not only transformation of the interferometer's phase-modulated light into modulation of the output light power but also compensation of any low-frequency modulations caused by change of environmental condition. However, application of a high-voltage electric field to the PR crystal is required for both increasing the efficiency of wave coupling [4] and realization of the linear regime of phase demodulation [5].

In this work we present adaptive interferometer system for nano-scale vibration measurement which is based on diffusion holograms recorded in semiconductor photorefractive crystal without applying electric field.

1. Measurement system

Scheme of the measurement system is shown in Fig. 1. CW radiation of Nd:YAG laser ($\lambda = 1064$ nm) is split into reference and signal waves via beam splitter. Signal wave is launched to multimode optical fiber which guides a light to an object under testing (it can be element of a nanoelectromechanical system, nanoobject or at least AFM probe which is suspended above nanoobject). Light emerged from the fiber is focused on the object surface by means of a microlens having short focal length. Light reflected from the object is collected back to the fiber via the same microlens. Vibrations of the object cause a modulation of phase of signal wave which is guided to a photorefractive crystal where it mixed with reference wave.

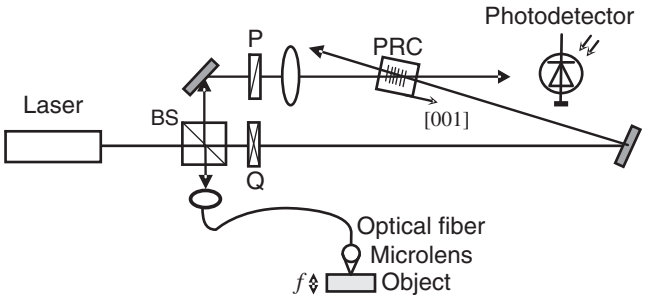

Fig. 1. Adaptive interferometer for ultra-small vibration measurement: PRC — photorefractive crystal, BS — beam splitter, Q — quarter-wave plate, P — polarizer.

Interference of signal and reference waves in the bulk of PR crystal leads to recording of dynamic hologram due to photorefractive effect [6]. Two-wave mixing at the hologram allows transforming phase modulation of the signal wave to its intensity modulation which is registered by photodetector.

Peculiarities of the system proposed are following. The dynamic hologram is recorded in so called reflection geometry when interacting beams are counter propagating. It allows significantly reduce the hologram spatial period (down to $\Lambda \approx 0.19$ μm) and as a result increase wave coupling efficiency without application strong electric field to the crystal. Additionally a vectorial mixing of light waves with different polarization states (linear and elliptical) in geometry of an anisotropic diffraction makes possible to avoid applying electric field to the crystal for realization of linear phase-to-intensity transformation. In reflection geometry we have achieved the sensitivity of adaptive interferometer which is just 5.7 times less (Fig. 2) then highest sensitivity which is possible only in non-adaptive lossless classical interferometer. Obtained sensitivity is correspond to minimal detection limit 1.9×10^{-9} rad$\sqrt{\text{W/Hz}}$ which, however, can be achieved only in case when all measuring system's noises are less then shot noise of the photodetector [7]. For real noises in our system we has achieved a practical detection limit equal to 1.1×10^{-8} rad$\sqrt{\text{W/Hz}}$. Obtained sensitivity of the interferometer allowed reliable broadband ($\Delta f = 50$ MHz) measurement of fiber elongation in the range from 0.09 to 113 nm providing only 10 mW of the object beam's power. At the same time it

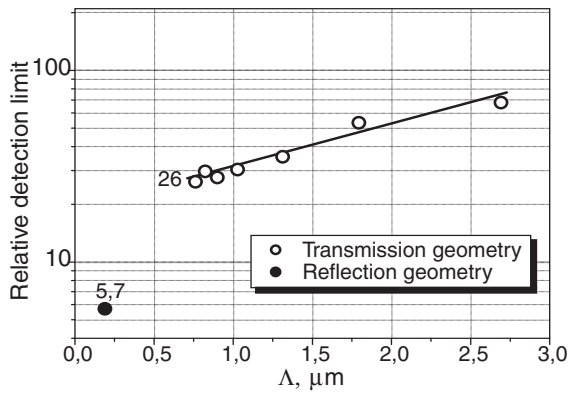

Fig. 2. Relative detection limit of the interferometer as a function of the hologram grating period for two recording geometries.

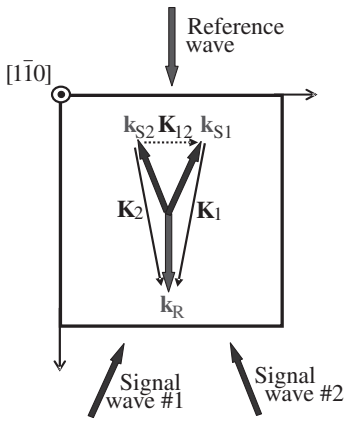

Fig. 3. A geometry of angular multiplexing of reflection holograms in a photorefractive crystal.

is possible to reduce minimal detectable elongation down to 1.2 pm in case of relatively narrow bandwidth $\Delta f = 10$ kHz.

Using of semiconductor CdTe:V with relatively high mobility of charge carriers has made possible to reduce response time of the hologram and as a result increase a cut-of frequency up to 800 Hz with keeping a light intensity at relatively low level (~ 40 W/cm^2). From the other hand, an optimal geometry of beams focusing inside the crystal has been developed in this work. This geometry allows obtaining two extremely narrow beams (with cross-section $\sim$ 0.1 mm) which are overlapped along crystal length ($\sim$5 mm). As a result, highly efficient and simultaneously fast hologram can be recorded by using low power optical sources (3–5 mW) providing noted above light intensity.

2. Multi-channel system

Possibility of angular multiplexing of several reflection holograms in a single crystal with using a single reference beam has been investigated in this work (Fig. 3). It was shown that a reduction of holograms efficiency cased by overlapping of optical fields of different signal waves is insignificant due to low interaction length of this fields inside crystal and low efficiency of "intermediate" hologram which are recorded in transmission geometry at low spatial frequencies (big spatial period $\Lambda \sim 2$ μm). Due to the same reason the crosstalk noises does not exceed -32 dB (see Fig. 4). As a result a highly effective multi-channel adaptive measurement system for simultaneous measuring vibrations of several objects (nanoobjects) can be easily implemented on a base of a single photorefractive crystal.

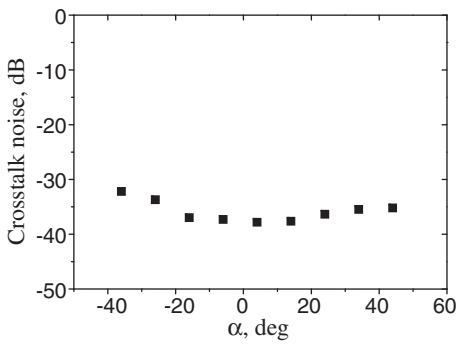

Fig. 4. Cross-talk noise between two channels for different orientation of dynamic holograms multiplexed in the PRC.

3. Summary

We have developed a highly sensitive adaptive interferometer based on a dynamic hologram recorded in semiconductor photorefractive crystal. High sensitivity of the adaptive interferometer approaches the sensitivity of the classical lossless non-adaptive interferometer and allows for the detection of ultra-small vibrations ($\sim$1 pm) while adaptive properties of dynamic hologram eliminate all low-frequency unwanted influences. The hologram is recorded without applying any external electric field to the crystal. This significantly simplifies the measuring system and reduces system's nose which additionally improves it performance (detection limit). Thus the adaptive interferometer measuring system developed holds much promise for monitoring of ultra-small vibrations and dynamic deformations of nonoobjects.

Possibility of holograms multiplexing allows developing more effective multi-channel measurement systems for simultaneous monitoring vibrations of several nanoobjects.

Acknowledgements

RVR and YNK acknowledge partial financial support of the Russian Foundation for Basic Research (grant 07-02-91015) and INTAS (grant 04-78-7227). SDG and AAK thank the Academy of Finland for financial support (project 118487).

References

[1] G. Iadonisi *et al*, *Physica Status Solidi (b)* **237**, 320 (2003).
[2] B. Ilic *et al*, *J. Appl. Phys.* **95**, 3694 (2004).
[3] E. A. Ivanova *et al*, *Doklady Physics* **51**, 569 (2006).
[4] A. A. Kamshilin *et al*, *Appl. Phys. Let.* **81**, 2923 (2002).
[5] P. Delaye *et al*, *J. Opt. Soc. Am. B* **14**, 1723 (1997).
[6] M. P. Petrov *et al*, *Photorefractive Crystals in Coherent Optical Systems*, Berlin, Germany: Springer–Verlag (1991).
[7] S. Di Girolamo *et al*, *Opt. Express* **15**, 545 (2007).

16th Int. Symp. "Nanostructures: Physics and Technology"
Vladivostok, Russia, July 14–18, 2008

The influence of hydrostatic pressure and temperature on photoluminescence spectrum of multilayer-structures planarly ordered quantum dot InAs/GaAs

V. A. Gaisin[1], B. V. Novikov[1], V. G. Talalaev[1,2], M. O. Tagirov[1], N. D. Zakharov[2], G. E. Cirlin[3], Yu. B. Samsonenko[3] A. A. Tonkikh[3] and V. A. Egorov[3]

[1] St Petersburg State University, Faculty of Physics, Ulyanovskaya 1, Petrodvorets, 198504 St Petersburg, Russia
[2] Max-Planck Institute Für Mikrostrukturphysik, 06120, Haale (Saale), Germany
[3] Institute for Analytical Instrumentation, Russian Academy of Science, St Petersburg Russia

Abstract. At pressure $P = 0$, 9, and 16 kBar and in the temperature range 77–300 K, the photoluminescence spectra of InAs/GaAs quantum dot were studied. The InAs quantum dots were grown by the SMEE technology and contained 10 layers separated by the 7.5 nm GaAs spacer layers. The dependences of the activation energies on the value of hydrostatic pressure have been studied. The available scheme of energy levels of quantum dot has been proposed.

Introduction

Quantum dots (QDs) have been intensively studied in recent years. In our previous papers [1], the temperature and pressure behaviors of the photoluminescence spectra (PL) of the 10 layers of InAs separated by GaAs spaces were reported. The PL spectrum at $P = 0$ and $T = 77$ K consists of a wide slightly structured band in the region of 900–1300 meV. The PL band was decomposed into four components, L1, L2, L3, associated with large size QD (AQD) and L4 associated with columns of QDs being in contact with wetting layer (CQD). The sizes of columns of QDs increase monotonously along the direction of growth axis with layer number. For investigated QDs the baric coefficient (BC) have been measured. The numerous calculations (G. G. Zegrya, R. M. Peleschak and O. O. Dankiv) are in good agreement with measured dependence of BC on sizes of QD. The experimental and calculated curves have similar slopes [1]. It was found that the BC energy dependence for L3 and L4 lines have the same anomalies as that for p_+- and d_+-excited molecule states [2]. These results have stimulated further investigation of these objects.

1. Experimental

Studied samples were grown by the molecular beam epitaxy and consist of 10 InAs layers separated by 7.5 nm GaAs spacer layers on the GaAs substrates. The measurements were carried out in the temperature interval $T = 0 - 77$ K and at the hydrostatic pressure $P = 0$, 9, and 16 kBar in the spectral range 1.0–1.4 eV. The PL spectra are excited by He-Ne laser at power 1 W/cm^2. The value of hydrostatic pressure was estimated by shift of the R1 ruby PL line. Ruby crystal was placed in high pressure cell close to the studied sample.

2. Results and discussion

In this paper, we investigate the temperature behavior of the QD PL spectra. The PL bands were decomposed into several components. The best agreement with experiment has been obtained under approximation of the bands by Gaussian contours with various intensities, halfwidths and energies of maxima. For description of the temperature behavior of integral intensities of the components, an Arrenius ratio, $I/I_m = [1 + C\exp(E_a/kT)] - 1$, has been used. Here C is a constant, E_a is the activation energy. In the Figs. 1–3, the $1/T$ dependencies of the $-\ln(I_m/I - 1)$ for different PL lines of QD are present. The value of the activation energies, E_a, for $P = 0$, 9, and 16 kBar has been determined from a slope

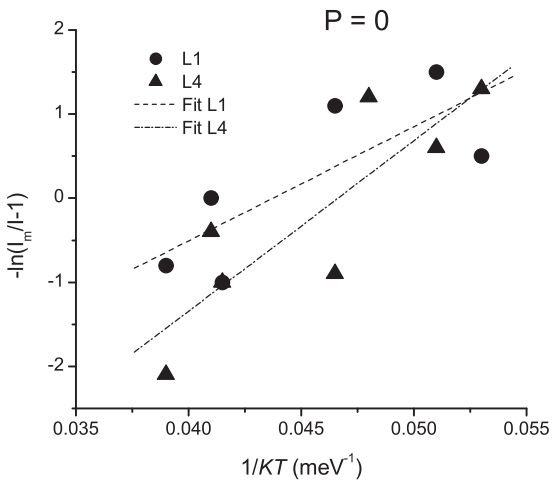

Fig. 1. The 1/T dependences of $-\ln(I_m/I - 1)$ for different emission lines for $P = 0$.

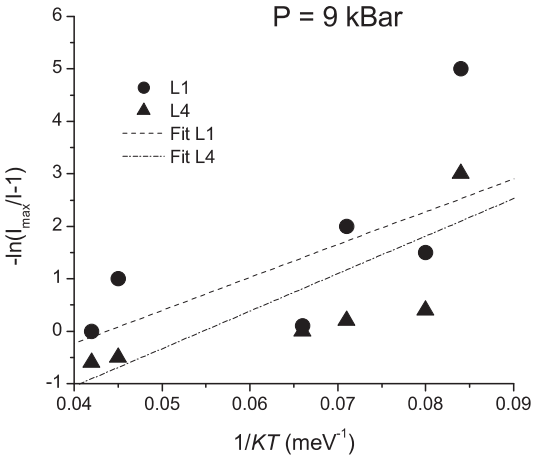

Fig. 2. The same for $P = 9$ kBar.

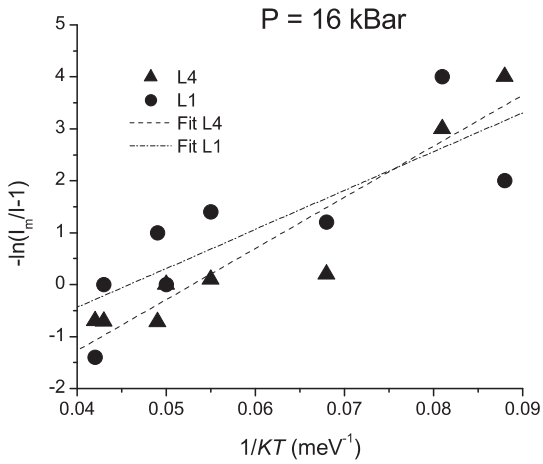

Fig. 3. The same for $P = 16$ kBar.

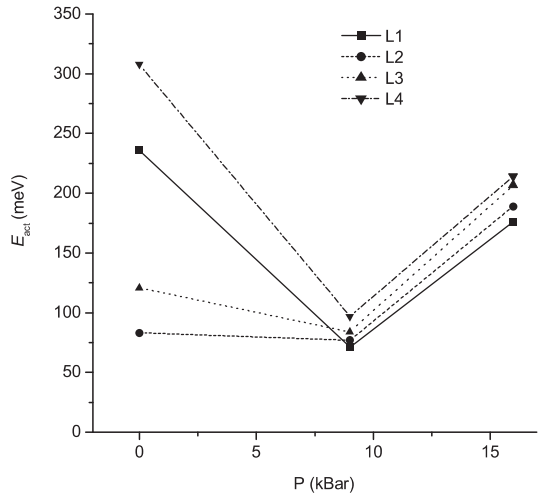

Fig. 4. Dependence of activation energy of different lines on pressure P.

of these dependences. The dependencies of the value E_a for L1–L4 lines on the hydrostatic pressure are shown in Fig. 4.

3. Conclusion

The influence of hydrostatic pressure and temperature on the photoluminescence spectra of InAs/GaAs quantum dots was studied. The InAs quantum dots were grown by the SMEE and contained 10 layers separated by 7.5 nm GaAs spacer layers. The dependencies of the activation energies on the value of hydrostatic pressure have been studied.

Acknowledgements

The work was supported by the Russian Foundation for Basic Research, Grant No. 08-02-00954.

References

[1] V. A. Gaisin *et al*, *Proc. 13th Int. Symp. "Nanostructures: Physics and Technology"*, St Petersburg, p. 352 (2005).

[2] V. A. Gaisin *et al*, Proc. 15th Int. Symp. "Nanostructures: Physics and Technology", St Petersburg, p. 212 (2007).

16th Int. Symp. "Nanostructures: Physics and Technology"
Vladivostok, Russia, July 14–18, 2008

Impurity photoconductivity in strained p-InGaAs/GaAsP heterostructures

V. Ya. Aleshkin[1], A. V. Antonov[1], V. I. Gavrilenko[1], D. V. Kozlov[1] and B. N. Zvonkov[2]

[1] Institute for Physics of Microstructures RAS, 603950, Nizhny Novgorod, Russia
[2] Physico-Technical Research Institute, University of Nizhny Novgorod, 603950 Nizhny Novgorod, Russia

Abstract. The spectrum of far-infrared photoconductivity resulted from excitation of shallow acceptors in strained quantum well of solid solution InGaAs has been observed for the first time. Energies of shallow acceptor levels including resonant ones in strained InGaAs/GaAsP quantum well heterostructure have been calculated. Calculated energies of optical transitions between ground and excited acceptors states are shown to be in a good agreement with those of lines observed in the photoconductivity spectrum.

Introduction

Recently it has been a significant interest to the shallow acceptors in semiconductors heterostructures, in particular to the resonant impurity states due to the observation of the stimulated emission in THz range in uniaxially stressed p-type germanium crystals and strained Si/SiGe:B hetero- structures excited by high electric field [1,2].

Till now the resonant lines of the impurity photoconductivity (PC) quantum well (QW) heterostructures were observed in the quantum wells of pure material (in contrast to a solid solution) only. In far IR photoconductivity spectra in p-type $Si_{1-x}Ge_x$/Si QWs a broad PC band was observed instead of narrow lines in bulk Si already at Ge content of 1% in the solid solution [3]. In another material system InGaAs/GaAs with strained quantum wells of solid solution the shallow acceptor binding energies were probed by band gap photoluminescence technique [4] and by the thermal activation of the conductivity [5]. In the presence work we report on the first observation of optical transitions from the ground shallow acceptor states into excited localized and resonant ones in strained QWs of solid solution InGaAs.

1. Experimental

The sample under study was multiple QW (30 periods) $In_{0.05}Ga_{0.95}As/GaAs_{0.9}P_{0.1}$ heterostructure 5189 grown on semi-insulated GaAs(100) substrate by atmospheric pressure MOCVD technique. Two delta-layers of carbon were introduced into each InGaAs QW 200 Å wide at 50 Å apart from the heterointerface. InGaAs layers were biaxially compressed in the plane of structure growth while GaAsP ones were biaxially stretched. The valence band offset for heavy holes is estimated as 80 meV that is much more than the shallow acceptor binding energy in bulk GaAs (26 meV). Let's note, that biaxial compression of InGaAs layers is equivalent to uniaxial stretching that results in reduction of the acceptor bounding energy due to light and heavy sub-band splitting. The increase on In content in solid solution results in the decrease of acceptor bounding energy as well because of the reduction of effective heavy hole mass.

Photoconductivity spectra were measured at T = 4.2 K with BOMEM DA3.36 Fourier-transform spectrometer. Two strip Ohmic contacts were deposited onto the sample surface 4 mm apart. Two spectra measured at different bias voltage are presented in Fig. 1. A strong PC band at photon energies in between 20 and 30 meV is clearly seen. Within this band two narrow lines at 19.5 meV and 21.5 meV are resolved in the spectrum as well as a broader line corresponding to photon energies 25 to 28 meV. Also the narrow PC line is observed near the GaAs LO-phonon energy 37 meV.

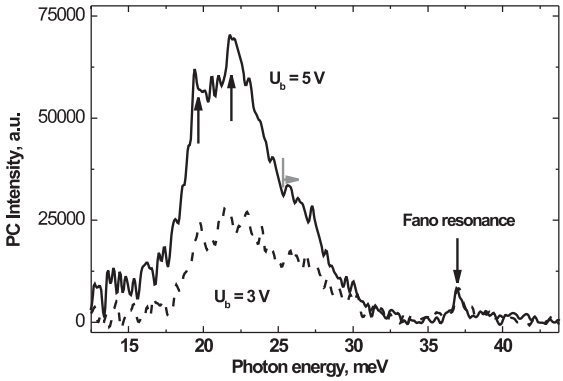

Fig. 1.

2. Method of calculations

Energy spectra of shallow acceptors in QW heterostructure were calculated in the envelope function approximation. The acceptor Hamiltonian used was a 4×4 matrix operator including the Luttinger Hamiltonian, the deformation term, the QW confinement potential due to the valence band discontinuity and the Coulomb potential. Similarly to the work [5] the axial approximation was used, i.e. the Hamiltonian was considered to be invariant by rotation about the $z \parallel [001]$ axis (the axis perpendicular to the growth plane of the structure). In this case the z-component of the total angular mo-mentum J_z is a good quantum number and the acceptor states are two-fold degenerate by the sign of the component of the angular momentum. The acceptor envelope four-dimensional function is expanded in the basis of the free hole envelope functions in QW, which are the eigenstates of the Hamiltonian not containing the Coulomb potential. By substituting this expansion into the Schrödinger equation for the envelope function the integral equations for the above expansion coefficients are obtained.

Using the developed method, the energies and wave functions of the states, which correspond to the values of the total

Table 1.

Acceptor state		Energy (meV) calculated from hh1 subband bottom
1s ($J_z = \pm 3/2$)		-20
1s(2) ($2p_0$, $J_z = \pm 3/2$)		-6.76
Level I ($2p_\pm$, $J_z = \pm 1/2$)		-7.8
Level II	$3p_\pm$, $J_z = \pm 1/2$	-3.8
	$2p_\pm$, $J_z = \pm 5/2$	-4.0
Level III	$4p_\pm$, $J_z = \pm 1/2$	-2.0
	$3p_\pm$, $J_z = \pm 5/2$	-1.9
Level IV ($4p_\pm$, $J_z = \pm 5/2$)		-0.6
hh2		6.46
$2p_\pm(2)$, $J_z = \pm 1/2$		3.46
$2p_\pm(2)$, $J_z = \pm 5/2$		3.98
$3p_\pm(2)$, $J_z = \pm 1/2$		5.0
$3p_\pm(2)$, $J_z = \pm 5/2$		5.6

angular momentum projection $J_z = +3/2$, $J_z = +1/2$ and $J_z = +5/2$ has been calculated. Dipole optical transitions from the acceptor ground state ($J_z = +3/2$) are allowed into the localized excited states and the states of the continuum corresponding to $J_z = +1/2$ and $J_z = +5/2$.

Since the chemical shift of carbon shallow acceptor in bulk GaAs is insignificant in our calculations we neglect the central cell corrections.

3. Discussion

The results on acceptor state calculations are listed in the table. The index (2) indicates the impurity states pertained to the second subband of size quantization hh2. $P_\pm$ — like states bound to the lowest heavy hole subband hh1 are numbered as I–IV levels.

The PC signal is proportional to the intensity of the generation of free holes. A hole can be optically excited in the continuum or into a localized excited state. In the latter case the hole in order to participate in the PC should be thermally excited (by absorbing an acoustic phonon) into the valence band continuum (photothermal ionization). Let's note, that a probability of such ionization at low temperature decreases exponentially with binding energy the excited state. In the work [6] it was shown, that the strongest lines (D and C) in photoconductivity spectra of the pure GaAs, which correspond to transition into states with binding energy of 7 and 5 meV, practically vanish at the temperature decrease down to 4.2 K. In view of this, it is natural to assume, that PC lines resulted with transitions from the ground state into the levels I and II (see the table) should be very weak. Therefore the longwavelength line observed at 19.5 meV may be attributed to the transitions into the closely adjacent states forming the level III. According to our calculations the matrix elements of these transitions are large if compared with those into the higher excited states. Next, the line corresponding to the photon energy 21.5 meV can be formed by transitions into higher excited levels and states of the continuum edge. Let's note that, the gap between two observed longwavelength lines corresponds fairly well to the gap between level III and the continuum edge.

The broad PC line at photon energies 25 to 28 meV can be related with transitions from the ground acceptor state into resonant states pertained with the second subband of size quantization hh2: levels $2p_\pm(2)$ and $3p_\pm(2)$ (see the table). The observed spreading of these transitions could results from fluctuations of QW width that strongly affects the position of subband edges in contrast to the localized state energies.

At last, the shortwavelength line observed in the spectra seems to be Fano resonance, which is asymetric feature in PC spectrum of photoconductivity, observed at energies close to LO phonon one (see, for example, [7]). Let's note, that Fano resonance is not observed in bulk p-GaAs [6].

Acknowledgements

The work has been financially supported by RFBR (grants 07-02-01307, 08-02-01126, 07-02-00549) and RAS.

References

[1] I. V. Altukhov *et al*, *JETF* **101**, 756 (1992).
[2] I. V. Altukhov *et al*, *Appl.Phys.Lett.* **79**, 3909 (2001).
[3] M. Franz *et al*, *J. Appl. Phys.* **84**, 709 (1998).
[4] A. P. Roth *et al*, *Phys. Rev. B* **38**, 7877 (1988).
[5] V. Ya. Aleshkin *et al*, *Proc. of the workshop "Nano-photonics". N. Novgorod*, 274 (1999) (in Russian).
[6] R. F. Kirkman, R. A. Stradling and P. J. Lin-Chung *J. Phys. C: Solid State Phys.* **11** 419 (1978).
[7] V. Ya. Aleshkin *et al*, *JETF* **128**, 822 (2005) (in Russian).

16th Int. Symp. "Nanostructures: Physics and Technology"
Vladivostok, Russia, July 14–18, 2008

Shell electronic structure of unoccupied states of fullerenes and fluorinated fullerenes $C_{60}F_x$ (x = 0, 18, 36)

V. M. Mikoushkin[1], V. V. Shnitov[1], V. V. Bryzgalov[1], Yu. S. Gordeev[1], O. V. Boltalina[2,3], I. V. Gol'dt[2], S. L. Molodtsov[4,5] and D. V. Vyalikh[4]

[1] Ioffe Physico-Technical Institute, St Petersburg, Russia
[2] Chemistry Department, Moscow State University, Moscow, 119899, Russia
[3] Chemistry Department, Colorado State University, Fort Collins, 80523, USA
[4] Institut für Festkorperphysik, Technische Universität Dresden, D-01062 Dresden, Germany
[5] Institute of Physics, St Petersburg State University, 198904 St Petersburg, Russia

Abstract. Comparative study of near edge X-ray absorption fine structure spectra (NEXAFS) of fullerenes and fluorinated fullerenes $C_{60}F_x$ (x = 0, 18, 36) has been implemented. Local density of unoccupied states was obtained and an accurate boundary between π^* and σ^* states was determined. The experimental evidence was found that unoccupied π^*-states of $C_{60}F_x$ are delocalized ones and form cluster shells which sequentially disappear starting from the highest states in reduction of the number of the valence π-electrons caused by fluorination. As a result, the density of the lowest π^*-state (LUMO) was revealed to remain being constant in fluorination despite the π-electron subsystem exhaustion.

Introduction

Fluorination of fullerenes seems to be interesting from the point of view of fundamental properties of carbon molecules and nanoclusters, as this process makes possible to clarify the role of different electron subsystems, π and σ, in forming the electronic structure of the cluster. During the last decade, electronic structure of different fluorinated fullerenes $C_{60}F_x$ have been extensively studied by UV photoemission spectroscopy (UPS) [1] and X-ray photoelectron spectroscopy (XPS) [2,4], by UV-visible absorption spectroscopy [2,5], and by reflection electron-energy-loss (EEL) spectroscopy [6,7]. Of particular interest is the comprehensive research of the dependence of electronic structure of fluorinated fullerenes $C_{60}F_x$ and $C_{70}F_x$ on the number of fluorine atoms in molecule (x = 11–48) which is inversely proportional to the number of the valence π-electrons in molecule [2]. Synchronous reduction of the density of all of the unoccupied π^*-states and enhancement of the density of σ^* conjugated states were reported. This behavior evidences for the local type of the electronic structure of fullerenes typical for molecules and excludes the shell type structure typical for metallic clusters. The aim of this work was searching the signs of the shell structure of unoccupied states in fullerenes and fluorofullerenes using molecules $C_{60}F_x$ with well defined number of fluorine atoms (x = 0, 18, 36) and the method of high resolution near edge X-ray absorption fine structure (NEXAFS) spectroscopy. The experimental evidence was found that unoccupied π^*-states of fullerenes and fluorofullerenes are delocalized ones and form cluster shells.

1. Experimental details

The experiment was performed at the BESSY II storage ring (Berlin) on the Russian–German synchrotron radiation (SR) beamline equipped with the plane-grating monochromator (PGM) and the experimental station of the Russian–German laboratory [8]. NEX[4]AFS spectra were measured with the energy resolution $\Delta E \approx 100$ meV. Thin (∼10 monolayers) films of C_{60}, $C_{60}F_{18}$, and $C_{60}F_{36}$ were grown on SiO_2/Si substrate in preparation [4]chamber of the spectrometer by evaporation of high-purity soot onto substrates just before measurements. Thin SiO_2 layer was used to prevent chemical interaction of adsorbates with substrate. The vacuum during deposition falls up to $P \approx 5 \times 10^{-9}$ Torr. Powders of $C_{60}F_{18}$ and $C_{60}F_{36}$ were synthesized by the technology described earlier [9, 10, 11]. The rate of the film growth was estimated by controlling the weakening of the substrate photoelectron lines. Heating SiO_2/Si substrates up to 700 °C enabled purifying the substrate surface.

2. Results and discussion

Fig. 1 shows the C 1s edge NEXAFS spectra of $C_{60}F_{18}$ and $C_{60}F_{36}$ measured at the photon incidence angle $\alpha \sim 45°$ in comparison with C_{60} spectrum. The spectra correspond to the dependence of probability of photoabsorbtion due to excitation of C1s core-level electron into unoccupied π^* (sharp peaks) or σ^* (broad peak) states on the photon energy. The spectra were corrected to the dependence of the photon flux on the photon energy by normalization of experimental data to the adsorption spectrum of silicon measured in the same photon energy range. In addition, all the spectra were normalized to the intensity of high energy background at $h\nu = 320$ eV. Intensities of broad σ^* peaks of the spectra proved to be close to each other after these normalizations. Positions of the lowest energy π^*-peak (state 1 or lower unoccupied molecular orbital (LUMO) state) of all of the spectra coincide just as in Ref. [2], though the energy of the LUMO (284.5 eV) proved to be 0.4 eV higher. Fig. 1 illustrates transformation of electronic structure of unoccupied states due to fluorination. Creation of C-F bond must modify the bonding states of carbons from sp^2 to sp^3 hybridization type. As a result, the number of π-electrons and the density of π^*-states should diminish in molecule proportional to the fluorine content, and the density of σ^*-states should increase. Such a transformation was reported in Ref. [2] in which increase of σ^*-peak and drastic (more than two times) reduction of all of the relative intensities of the LUMO-peaks were observed.

However, Fig. 1 shows a somewhat different behavior. Rel-

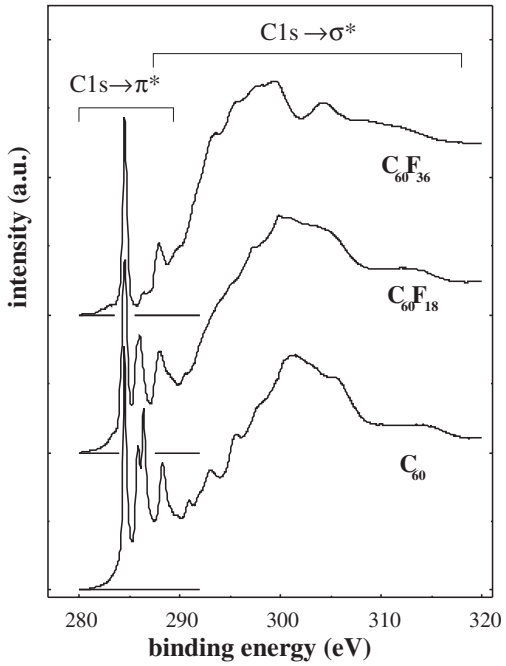

Fig. 1. NEXAFS spectra of ordinary fullerene C_60 and of fluorinated fullerenes C_60F_18 and C_60F_36.

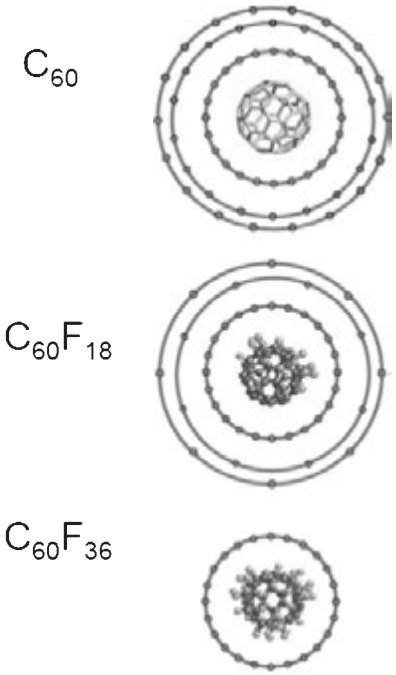

Fig. 2. Scheme of the shell electronic structure of unoccupied states of fullerene C_60 and fluorofullerenes C_60F_18 and C_60F_36.

ative intensity of the LUMO peak (1) diminished only by 20% in attachment of 18 fluorine atoms to C_{60} and remains the same after attachment of additional 18 fluorine atoms which results in 60% exhaustion of the π-conjugated system. To explain the observed NEXAFS spectra transformation, the following assumption was made. The π^*-states of fluorofullerenes are delocalized at large extent and form cluster shells analogous to the shells of metallic clusters according to the scheme drown in Fig. 2. These shells are created in the course of enlargement of the π- electron system starting from low energy states and disappear in the course of the π-electron system exhaustion starting from the high energy states. Indeed, π-high energy states 2 and 3 rapidly disappear when π-electron system is reduced due to fluorination whereas the intensity of low energy state 1 (LUMO) remains practically constant even at high degree of fluorination. Fig. 1 also shows that states 1, 2 and 3 are pure π^*-states and the state 4 is the mixture of π^* and σ^* orbitals because this state weakly depends on the number of π-electrons. The property of fullerene and fluorofullerenes, which makes different these clusters from the metallic ones, is that the adding or removal of π-electrons does not change the energy of the shells because the already existing cluster field is formed by the large number of σ-electrons. The surprising fact is that covering the fullerene surface by the rather dense layer of fluorine atoms does not destroy the shell structure of molecule.

3. Conclusions

In summary, the local density of unoccupied states was measured for fluorinated fullerenes $C_{60}F_x$ ($x = 18, 36$) in comparison with that of ordinary fullerenes C_{60}. Accurate boundary between π^* and σ^* states was determined. The conducted study of fluorinated fullerenes with different content of fluorine atoms evidences for sequential vanishing the π^*-states due to the diminution of the number of π-electrons on fluorination, contrary to the synchronous reduction of the density of all of the unoccupied π^*-states observed in Ref. [2]. The conclusion was made that unoccupied π^*-states of ordinary fullerens C_{60} and of fluorofullerenes $C_{60}F_x$ are delocalized ones and form cluster shells. These shells sequentially disappear due to π-electron subsystem exhaustion in enlargement of the fluorination extent starting from the highest states. This mechanism unexpectedly keeps constant the density of LUMO state in the course of fluorination.

Acknowledgements

The research was supported by the Russian–German Laboratory at BESSY, by the Russian Academy of Sciences (P-03, N2-2-14 and "Quantum nanostructures", 5–22) and by the INTAS grant Ref. No. 06-1000012-8972.

References

[1] P. J. Benning *et al*, *Phys. Rev. B* **47**, 1589 (1993).
[2] R. Mitsumoto *et al*, *J. Phys. Chem. A* **102**, 552 (1998).
[3] D. M. Cox *et al*, *J. Am. Chem. Soc.* **116**, 1115 (1994).
[4] S. Kawasaki *et al*, *Phys. Rev. B* **53**, 16652 (1996).
[5] S. V. Amarantova *et al*, *Nucl. Instr. Meth. A* **470**, 318 (2001).
[6] V. V. Shnitov *et al*, *Fullerenes, Nanotubes and Carbon nanostrucrutes* **14**, 297 (2006).
[7] V. V. Shnitov *et al*, *Nanostructures 2006*, Proceedings, p. 297.
[8] S. I. Fedoseenko *et al*, *Nucl. Instr. Meth. A* **505**, 718 (2003).
[9] O. V. Boltalina *et al*, *J. Fluorine Chem.* **101**, 273 (2000).
[10] O. V. Boltalina *et al*, *J. Chem. Soc. Chem. Commun. 1996*, 529 (1996).
[11] I. V. Goldt *et al*, *Solid State Sciences, 2002* 1395 (2002).

16th Int. Symp. "Nanostructures: Physics and Technology"
Vladivostok, Russia, July 14–18, 2008

Modulus of elasticity and viscosity coefficients of polymeric nanocomposite films with Fe and CdS nanoparticles

B. D. Zaitsev[1], I. E. Kuznetsova [1], A. M. Shikhabudinov [1],V. V. Kolesov[2], A. S. Fionov[2] and I. D. Kosobudskii[1]

[1] Saratov Branch of Institute of Radio Engineering and Electronics of RAS, 410019 Saratov, Russia
[2] Institute of Radio Engineering and Electronics of RAS, 125009 Moscow, Russia

Abstract. The modulus of elasticity and coefficients of viscosity of nanocomposite films with various percentages of nanoparticles of Fe and CdS in the matrix of high-pressure polyethylene are investigated. For measuring we used the appropriate resonators with longitudinal or shear acoustic waves loaded by the film under study. The calculation of resonator impedance was carried out by the method of equivalent circuits. By using the least-squares method and variation of modulus of elasticity and coefficients of viscosity of the nanocomposite film the calculated frequency dependencies of real and imaginary parts of impedance of loaded resonator were fitted to experimental ones.

Introduction

Over the long time the researchers and designers of the electronic devices have given much attention to finding the new physical principles of creation of the artificial electronic media. At present time the new approaches in creation of such media have become to be possible due to the development of nano-technology. One of the important directions of development of nano-technology is the creation and investigation of nanocomposites based on nanoparticles of metals and their compounds, which are stabilized in the volume of polymeric dielectric matrix [1]. The use of the polymeric materials as matrix stabilizer of nanoparticles opened the new scientific direction, namely the plastic electronics.

Earlier [2] it has been shown that the properties of metallized nanocomposite materials depend on the volume concentration of nanoparticles by critical way. The change of the concentration of nanoparticles respectively to polymeric matrix stabilizer significantly influenced on the main parameters of nanocomposite: electric conductivity, complex dielectric permittivity, plasma frequency, etc. The variation of mixture of nanocomposite by the change of type of dielectric matrix, size, composition and concentration of nanoparticles allows to purposefully control the basic physical properties of nanocomposite: electrical, optical, mechanical, etc. But at present time there is not the detailed information about elastic properties of developed polymeric composite nanomaterials. Just recently the paper devoted by the investigation of density, phase velocity, and acoustic impedance of alumina colloidal/polymer composite film has been published. In this connection the paper is devoted to experimental investigation of modulus of elasticity and coefficients of viscosity of some nanomaterials with various concentration of nanoparticles of Fe and CdS in polymeric matrix.

1. Measurements of elastic modulus and viscosity coefficients of nanocomposite films

For measuring the mechanical characteristics of nanocomposite films such as modulus of elasticity and viscosity coefficient one can use the bulk acoustic waves propagating in piezoelectric resonator [3]. From physical reason it was assumed that the nanocomposites under study are isotropic. For measuring the longitudinal and shear components of elastic modulus and viscosity tensor it is necessary to use resonators with longitudinal and shear acoustic wave, respectively.

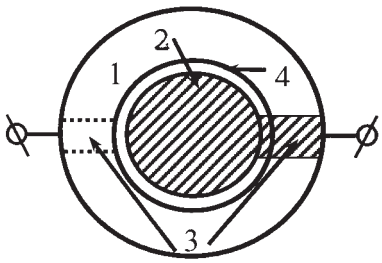

Fig. 1. Measuring resonator: 1 — langasite or quartz plate, 2 — electrodes, 3 — contact area, 4 — nanocomposite film.

For measuring we use the industrial quartz resonators of shear waves and langasite resonators of longitudinal waves (Fig. 1). At first we measured the frequency dependencies of real and imaginary parts of the total impedance of aforementioned resonators without investigated films. For measurements we use the impedance analyzer Agilent 4285A. Then for analysis we used the equivalent circuit of such resonator. By using the Ohm's law for such circuit we determined the real and imaginary parts of the impedance of the resonator as functions of elastic modulus C_{ii}, piezoconstant e_{1i}, permittivity ε_{11}, density ρ and viscosity η_{ii} for given sample of langasite and quartz [3,4]. Then with the help of least-squares method with variation of aforementioned parameters we adjusted the calculated dependencies to experimental ones and determined the necessary parameters of langasite and quartz.

We investigated the nanocomposite films with various concentrations of nanoparticles of Fe and CdS in high pressure polyethylene. The thicknesses of films under study were equal 50–55 microns at diameter 8 mm. For investigation of the mechanical properties the sample of film was set to one side of resonator. For improving the acoustic contact we used thin layer of castor oil. In order to define the viscosity of oil we measured the real and imaginary parts of impedance of resonator immersed into oil. We changed the equivalent circuit by adding the oil load to its mechanical ports. Then by using the least-squares method with variation of oil viscosity and res-

Table 1. The parameters of nanocomposite Fe containing film.

Fe,%	ρ, kg/m^3	C_{11}, 10^8 Pa	η_{11}, Pa × s	C_{66}, 10^8 Pa	η_{66}, Pa × s
0	879.5	16.0	24.0	1.4	2.9
2	884.1	23.2	24.6	2.6	2.2
5	918.6	20.1	6.2	2.8	2.3
7	972.6	17.8	4.0	3.4	2.4
12	993.7	15.1	7.6	3.5	1.1
15	991.3	14.0	4.0	3.4	0.7
17	986.6	12.8	11.3	3.0	1.3
20	1052.0	13.3	22.8	3.5	5.8
25	1186.0	1.49	1.23	0.88	1.0

Table 2. The parameters of nanocomposite CdS containing film.

CdS,%	ρ, kg/m^3	C_{11}, 10^8 Pa	η_{11}, Pa × s	C_{66}, 10^8 Pa	η_{66}, Pa × s
5	1142	41	40.2	1.1	2.9
10	1157	38	19.3	2.4	1.7
30	1277	27	20.05	1.9	1.5

onator parameters we adjusted the calculated dependencies to experimental ones and determined the oil viscosity.

Then we measured the frequency dependencies of real and imaginary parts of impedance of resonator loaded by the film under study. For obtaining the information about parameters of investigated film we analyzed the appropriate equivalent circuit of loaded resonator. By using Ohm's law for such circuit and obtained material constants for langasite and quartz with considering the oil layer we found the frequency dependencies of real and imaginary parts of loaded resonator as function of elastic modulus $^*C_{ii}$ and coefficient of viscosity $^*\eta_{ii}$ of the film. Then with the help of least-squares method by variation of pointed parameters we adjusted the calculated dependencies to experimental ones and determined the sought parameters of nanocomposite film [3]. The Tables 1 and 2 present the measured elastic modulus and viscosity coefficients for the films under study. The Table 1 shows that with increase of the concentration of nanoparticles of Fe the longitudinal elastic modulus and viscosity coefficients decreases, reaches minimum at 17% and then increases. As for film with nanoparticles of CdS the Table 2 shows that with increase of the nanoparticle concentration longitudinal elastic modulus and viscosity coefficients decrease but shear elastic modulus increases reaches the maximum at 10% and then decreases.

2. Conclusion

The modulus of elasticity and coefficients of viscosity of nanocomposite films with various percentages of nanoparticles of Fe and CdS in the matrix of high pressure polyethylene were measured. For measuring we used the appropriate resonators with longitudinal or shear acoustic waves loaded by the film under study. The calculation of resonator impedance was carried out by the method of equivalent circuits. By using the least-squares method and variation of modulus of elasticity and coefficients of viscosity of the nanocomposite film the calculated frequency dependencies of real and imaginary parts of impedance of loaded resonator were fitted to experimental ones. It has been found that with increase of the concentration of nanoparticles of Fe the longitudinal elastic modulus and viscosity coefficients decreases, reaches minimum at 17% and then increases. As for film with nanoparticles of CdS it has been found that with increase of the nanoparticle concentration longitudinal elastic modulus and viscosity coefficients decrease but shear elastic modulus increases reaches the maximum at 10% and then decreases. The behavior of elasticity modulus and viscosity coefficients of films under study points that used technology of nanocomposite film fabrication based on high pressure polyethylene does not provide the acoustical contact between nanoparticles and polyethylene matrix. The obtained results open the way of development of the materials with given value of acoustical impedance for matching the ultrasonic transducer with materials of low acoustical impedance.

Acknowledgements

This work is supported by the grant of Ministry of Education and Science of Russia (grant RNP 2.1.1.8014 and 2007-3-1.3-07-15-036), grant RFBR 06-08-01011. Kuznetsova I. E. thanks Russian Science Support Foundation.

References

[1] G. Y. Yurkov *et al*, *International Journal of Materials and Product Technology* **23**, 3 (2005).
[2] N. M. Ushakov *et al*, *Technical Physics Letters* **29**, 936 (2003).
[3] B. D. Zaitsev *et al*, *Proc. ofIEEE Ultrasonic Symposium (Toronto, Canada, Oct. 5–8, 1997)*, IEEE Inc., 623 (1997).
[4] E. Dieulesaint *et al*, *Elastic waves in solids II*, (New York: Springer) 12 (2000).

16th Int. Symp. "Nanostructures: Physics and Technology"
Vladivostok, Russia, July 14–18, 2008

Thermodielectric and frequency properties of polymer nanocomposites based on oxides and sulphides of transitional metals in low density polyethylene

D. M. Kulbatskii[1], A. N. Ul'zutuev[2], K. A. Razumov[1], *N. M. Ushakov*[1,2], I. D. Kosobudskii[1,2] and G. Yu. Yurkov[3]

[1] Technical State University, Saratov, Russia
[2] V. A. Kotel'nikov Institute of RadioEng.&Electr. of RAS, Saratov Branch, Saratov, Russia
[3] N. S. Kurnakov Institute for General&Inorganic Chemistry of RAS, Moscow, Russia

Abstract. Me(Fe, Cu, Cd, Zn)/MeO & MeS metal-containing polymer nanocomposites in low density polyethylene (LDPE) matrix have been produced by thermal decomposition metal-containing compounds in an argon-oxygen atmosphere. Complex dielectric function and dielectric losses has been measured from 20 to 100 C at 1 MHz, and at the microwave frequency region from 2 GHz to 18 GHz. Optical wave dispersion and absorption has been measured from 400 nm to 1600 nm.

Introduction

Both development and investigation of a new media such as metal-containing polymer nanocomposites (MPNC) are a pair of important fields of nanotechnology. The MPNC consists two-phase system based on metal/metal oxide or metal sulphides nanoparticles (NPs) in polymeric matrix [1]. At present time it is well-known that properties of metal containing nanocomposites are limited by the metallic phase concentration or percolation concentration [2]. However, for MPNC bulk cluster is never formed for percolation concentration NPs more than some the critical one because of mechanic destruction of polymer matrix. The percolation concentration and size of NPs affect on the general parameters of MPNC- complex dielectric function and losses at the wide band from radio to optical frequencies. Thus, the general physical properties of media- electrical, microwave, and optical can be controlled by means concentration and size of NPs in the polymeric matrix. In the present work concentration and size of NPs could were as independent parameters.

1. Experiment

The structure of a polymeric matrix contains both the crystal and the amorphous parts. These parts for one's turn contain a significant number of vacancies clusters. The NPs grow inside these vacancies during the thermodestruction of metal-containing compounds (MCCs). The NPs with size before 4 nm are grown in crystal part, but NPs with size larger then 4 nm are grown in amorphous one. Two sort of nanotechnology as both low and high temperature synthesis based on the well-known technology [1] are developed in the work. The volume type of NPs based on Fe, Cu, Zn and its oxides, and sulphides have been synthesized. Synthesized samples such, as Fe/Fe_2O_3 — LDPE, Cu/Cu_2O(CuO) — LDPE, ZnO — LDPE, CdS(CdSe) — LDPE were prepared as dust, thick films ($d = 50 - 100$ μm) and plates ($d = 400 - 1000$ μm). The great influence on the MPNC properties of NPs size and distribution is shown. The morphology, NPs size and distribution were investigated using a high-resolution electron microscope (TEM). The middle size of NPs for Fe, Cu and Zn is 1–10 nm, 10–25 nm, and 2–10 nm respectively.

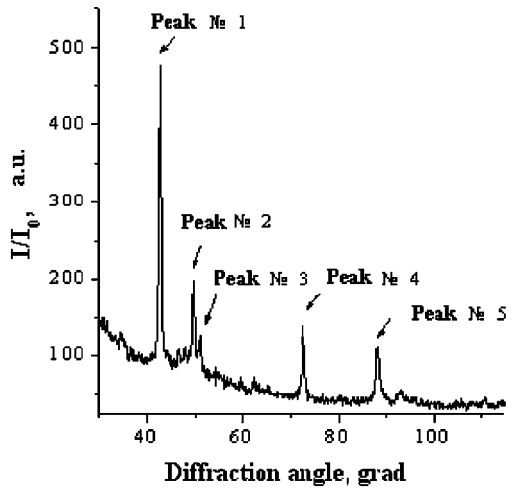

Fig. 1. Difractogram of the 20 mass% Cu/Cu_2O — LDPE composite.

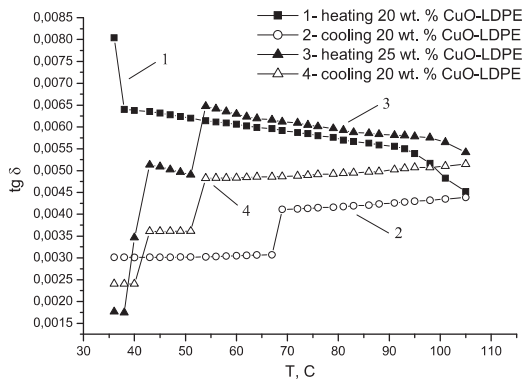

Fig. 2. Temperature behaviour of the dissipation factor for 20 wt.% and 25 wt.% CuO-LDPE at 1 MHz.

The structure of MPNC samples were investigated using X-ray phase analysis method. In Fig. 1 difractogram of the 20 mass% Cu/Cu_2O based on LDPE is presented. Peak No. 1 – Cu_2O (111); peak No. 2 — Cu_2O (200); peak No. 3 — Cu (111); peak No. 4 — Cu_2O (220); and peak No. 5 — Cu_2O (311) are shown. Experimental results were demonstrated that Cu_2O is the general component of the nano composite.

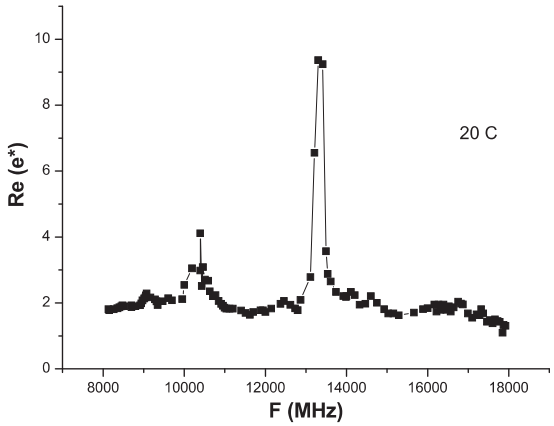

Fig. 3. MW spectra of a real dielectric function for 30 wt.% CuO-LDPE at the room temperature.

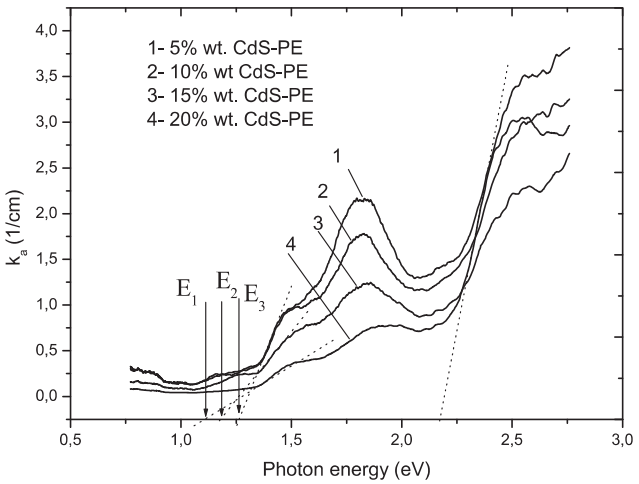

Fig. 4. Optical absorption spectra for the polymer (5–20) wt.% CdS — LDPE nanocomposites at the room temperature.

In the present work the general electro physical and optical properties of MPNC for different percolation concentration (5–30 mass%) and temperature (300–420 K) are measured. Complex dielectric constant, and dissipation factor were measured from 1 MHz to 18000 MHz (see Fig. 2 and Fig. 3).

Under review hysteresis and jumps of the dissipation factor is caused by polarized processes at the NPs-matrix interface and a set of matrix conformers concerned with the flexibility of polymer chains.

The measurements of complex dielectric functionat at the MW band have allowed to find out of the dielectric resonances for the nanomaterials. Two such a resonances are shown in Fig. 3. These results have a good correlation with theoretical model for the diphasic medium in Ref. [3].

Refraction index and absorption coefficient were measured at optical band from 400 nm to 1600 nm.

Acknowledgements

The work was fulfilled with the financial support of Russian Fund Basic Research (RFBR) (# 06-08-01011a) and the Ministries of Education and Sciences of the Russian Federation (# 2.1.1.8014).

References

[1] G. Y. Yurkov *et al*, *Proc. 9th Foresight Conf. on Molekular Nanotechnology.* Santa Clara, USA 2001, pp. 34–36.
[2] A. K. Sarychev *et al*, *Phys. Rev.Lett* **73**, 2895 (1994).
[3] A. V. Turik *et al*, *JETP Lett.* **79**, 512 (2004).

16th Int. Symp. "Nanostructures: Physics and Technology"
Vladivostok, Russia, July 14–18, 2008

Exciton lifetime in SiO_2 layers with embedded silicon nanocrystals as a function of the "dark" fraction of nanocrystals in the system

V. A. Stuchinsky and D. V. Marin
Rzhanov Institute of Semiconductor Physics SD RAS, 630090 Novosibirsk, Russia

Abstract. Previously reported data on photoluminescence (PL) quenching in ion-beam irradiated SiO_2 layers with embedded silicon nanocrystals (Si nc's) were used to analyze the exciton lifetime in such systems versus the quenched fraction of nc's. Estimates of the characteristic time of exciton hopping between adjacent nc grains, the length of excitonic wavefunction decay into the dielectric, and the cross-section of exciton recombination at deep-level centers introduced by the irradiation into the SiO_2 matrix are given.

Introduction

Photoluminescence (PL) from nanostructured (nanocrystalline or porous) Si still attracts interest as it offers promise in possible development of Si-compatible optoelectronics, with silicon nanocrystals (Si nc's) embedded within SiO_2 layers presenting the most interesting system here free of surface effects. A necessary condition making a single nc able to emit light is its defectless structure, i.e., the total absence of deep-level states in the nc [1,2] and, very probably, a low density of band-tail states in the surrounding dielectric matrix. In the cases in which the initial SiO_x layers used for the synthesis of nc's are prepared with a considerable degree ξ of their supersaturation with non-stoichiometric silicon, the density of formed nc's increases, and tunnel excitonic transport between nc's becomes possible, which limits the exciton lifetime τ because of exciton migration from perfect into imperfect nc's [3]. In nanocrystalline (nc-) systems with $\xi = 20$–30% this transport makes the lifetime τ sensitive to the mean imperfectness of the system already at the "natural" fraction of defective nc's [4]. With an additional amount of deep-level centers intentionally introduced into the system (for local control of PL intensity, for instance [1,2]), already in the case of less dense nc's the above migration turns out to be a factor restricting the lifetime τ and, hence, the PL intensity.

For a number of applications it would be highly desirable to have some parametrization of the exciton lifetime τ as a function of the "dark" fraction of nc's f_q in dielectric layers, and also of structural parameters of the system defining the probability of exciton tunnel hopping between nc's.

In the present study we propose such a parametrization for a system of homogeneously distributed spherical nc's of size R_0 in terms of the characteristic time τ^* of exciton localization at an nc.

1. Model

According to the data of [1], we assume here that the relaxation of excitations in imperfect nc's is predominantly due to nonradiative transitions that occur in times shorter than τ^*. In the interval of small values of f_q ($f_q \ll 0.1$) the desired parametrization can therefore be obtained by treating the flow of excitons to defective nc's as a diffusion-limited reaction and by using the well-known expression for the rate constant of this reaction $k = 4\pi D^* R_c$ (see [5], for instance). In this expression, the capture radius R_c should be identified with the nc radius $R_0/2$, and the exciton diffusion coefficient D^*, with the quantity $N_{nc}^{-2/3}/\tau^*$ (here, N_{nc} is the density of nc's in the nc-system). At larger values of f_q ($f_q \geq 0.1$), corresponding to short separations between defective nc's, the above approximation becomes invalid since, in this case, defective nc's appear already among the nearest neighbors of each "bright" nc. In the latter case, an expression for $\tau(f_q)$ can be derived within the framework of a model in which the fraction of defective nc's in the vicinity of each emitting nc is assumed constant, equal to f_q. Within this model, the effective exciton lifetime can be evaluated by averaging performed over the entire ensemble of excitations in the system, with exciton lifetimes being multiples of τ^*. Among all such excitons, excitons with the lifetime $i\tau^*$ ($i = 1, 2, 3, \ldots$) are present in a fraction equal to $f_q(1 - f_q)^{i-1}$ of the total number of excitons. As a result, the proposed parametrization is given by

$$\tau/\tau_{ref} = \left(1 + \frac{\tau_{ref} f_q}{\tau^*} C\right)^{-1}. \quad (1)$$

Here, τ_{ref} is the exciton lifetime in the system of perfect nc's, $C = 2\pi N_{nc}^{-1/3} R_0$ for $f_q \ll 0.1$, and $C = \sum_{i=1}^{\infty} \frac{(1-f_q)^{i-1}}{i}$ for $f_q \geq 0.1$.

2. Discussion

The proposed parametrization well describes the experimental curve of $\tau(f_q)$ obtained in the PL quenching study [1] of ion-beam irradiated SiO_2 layers with Si nc's having sizes $R = 2.9 \pm 1.0$ nm ($\xi = 6\%$, $\tau_{ref} = 54$ μs), and also a similar curve deduced from our analysis of PL quenching data obtained in [6] for an nc-system with $R = 3.8 \pm 1.3$ nm ($\xi = 20\%$, $\tau_{ref} = 65$ μs) (Fig. 1). The best fit of the experimental data with relation (1) yields values $\tau^* = 120$ μs and 15 μs for the time of exciton hopping between adjacent nc's in the nc-systems of [1] and [6], respectively. Thus, while in the nc-system of [1] an exciton hardly does one jump into an adjacent nc, in the nc-system of [6] the mean number of such jumps amounts to four. The abrupt drop of $\tau/\tau_{ref}(f_q)$ in (1) at $f_q > 0.6$ seems to be due to tunnel recombination of excitons at irradiation-induced deep states in the surrounding SiO_2 matrix. Using

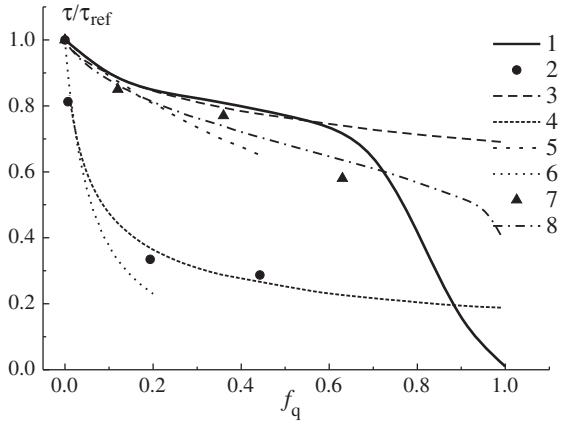

Fig. 1. Normalized PL lifetime versus the damaged fraction of nc's in the nc-systems examined in [1] and [6]. 1 — "universal" (averaged over the various types of ions) curve $\tau/\tau_{\text{ref}}(f_q)$ for the nc-system of [1]; 2 — ratios τ/τ_{ref} calculated for the nc-system of [6] irradiated with 130-keV He^+ ions; 3–6 — curves of $\tau/\tau_{\text{ref}}(f_q)$ calculated by formula (1) with $C = \sum_{i=1}^{\infty} \frac{(1-f_q)^{i-1}}{i}$ (curves 3 and 4) and $C = 2\pi N_{\text{nc}}^{-1/3} R_0$ (curves 5 and 6) for the nc-system of [1] (curves 3 and 5) and for the nc-system of [6] (curves 4 and 6); 7 and 8 — experimental data for the nc-system of [1] irradiated with 2-MeV He^+ ions and the fitting curve calculated by formula (2) with $\sigma_{\text{trap}} = 1\times10^{-14}\,\text{cm}^2$, $l_\Psi = 1.5\,\text{Å}$, $v_q = 4\times10^7$ cm/s, $\tau^* = 120\,\mu$s, and $C = \sum_{i=1}^{\infty} \frac{(1-f_q)^{i-1}}{i}$ on the assumption that the number of recombination centers uniformly introduced by the ion-beam irradiation into the dielectric matrix is equal to the number of atomic displacements produced in SiO_2.

the values of τ^* obtained for the two nc-systems with different tunnel-barrier widths, we obtained an upper estimate for the length l_Ψ of excitonic wavefunction decay into the dielectric matrix ($l_\Psi \leq$ 3–4 Å), and also an estimate of the cross-section of exciton recombination at the deep states introduced by ion-beam irradiation into the matrix ($\sigma_{\text{trap}} \approx 1 \times 10^{-14}$ cm^2). Note that an estimate of l_Ψ from the well-known formula for the tunnel transparency of a rectangular barrier [7] made using the barrier-height data for the Si/SiO_2 interface yields a value of 1–1.5 Å. The estimate of σ_{trap} was obtained by fitting the experimental curve $\tau/\tau_{\text{ref}}(f_q)$ for the nc-system irradiated with 2-MeV He^+ ions [1] with the formula

$$\tau/\tau_{\text{ref}} = \left(1 + \frac{\tau_{\text{ref}} f_q}{\tau^*} C^*\right)^{-1}, \qquad (2)$$

where

$$C^* = C f_q + \sigma_{\text{trap}} N_{\text{trap}} v_q \tau^* \frac{l_\Psi}{R_0}.$$

This formula presents an analogue to formula (1) derived with regard for exciton recombination at deep centers in the matrix. Here, N_{trap} is the concentration of recombination centers in the matrix, assumed spatially uniform and close to the concentration of nonradiative centers introduced by the irradiation into the nc's, and $v_q \approx 10^7$ cm/s is the exciton velocity in nc's. Additionally, the fact was taken into account that in the system of interest irradiated with light He^+ ions we encounter the case of rare random damages, which circumstance makes it possible to calculate f_q as a function of N_{trap} (taken equal to the concentration of atomic displacements estimated from TRIM simulation data) by the formula $f_q = 1 - \exp(-N_{\text{trap}} v^*)$, with $v^* = (\pi/6) R_0^3$ being the nc volume.

The proposed parametrization of the dependence $\tau(f_q)$ can prove useful in analyzing the defect inventory in nanocrystalline systems "nc-Si in SiO_2", and also in analyzing PL quenching curves in such systems under irradiation or after their doping with deep-level impurities.

References

[1] D. Pacifici *et al*, *Phys. Rev. B* **65**, 144109 (2002).
[2] A. N. Tchebotareva *et al*, *Journ. of Luminescence* **114**, 137 (2005).
[3] F. Priolo *et al*, *J. Appl. Phys.* **89**, 264 (2001).
[4] C. Garsia *et al*, *Appl. Phys. Lett.* **82**, 1595 (2003).
[5] A. V. Vasil'ev, A. I. Baranov, *Reaction between Defect and Impurity Species in Semiconductors,* Siberian Division of the Russian Academy of Sciences, Novosibirsk (2001).
[6] G. A. Kachurin *et al*, *to be published in Semiconductors,* (2008).
[7] S. M. Sze *et al*, *Physics of Semiconductor Devices,* New York-Chichester-Brisbain-Toronto-Singapore (1981).

16th Int. Symp. "Nanostructures: Physics and Technology"
Vladivostok, Russia, July 14–18, 2008

Role of the buffer porous layer and dysprosium doping in GaInP:Dy/Por-GaAs/GaAs(100) heterostructures

P. V. Seredin[1], E. P. Domashevskaya[1], N. N. Gordienko[1], A. V. Glotov[1], I. N. Arsentyev[2], I. S. Tarasov[2] and M. V. Shishkov[2]

[1] Voronezh State University, Universitetskaya pl., 1, 394006, Voronezh, Russia,
[2] Ioffe Physico-Technical Institute, St Petersburg, Russia

Abstract. In the samples with porous buffer layer the residual internal stresses caused by the difference in lattice parameters between the surface layer of ternary GaInP alloy and GaAs substrate are redistributed into the porous layer, which in this case plays a role of a "sponge" and completely removes the internal stresses.

Introduction

An interest to heterostructures on the basis of A_3B_5 semiconductor materials is due to their usage in the production of powerful light-emitting devices. Moreover, since rare-earth elements possess strong magnetic properties, their introducing into semiconductors as well as into semiconductor alloys based on A_3B_5 can provide a new degree of freedom into material due to the interaction between free charge carriers and magnetic ions. In its turn, this opens new possibilities for these materials in the electronic industry [1]. The use of porous semiconductor buried layers in such heterostructures as the transition layers allowing to agree lattice parameters between epitaxial layer and substrate seems to be quite perspective.

1. Experimental results

The work is concerned with the study of heterostructures obtained by MOCVD technique. Epitaxial layers of ternary GaInP alloys with a thickness of 0.2 μm, doped with dysprosium were grown either directly on the single-crystalline GaAs (100) substrates or on the buffer porous layer (por-GaAs), formed by anodic etching of GaAs (100) substrate. An agreement of lattice parameters for epitaxial layer and substrate was controlled with X-ray diffractometer. Analysis of the samples cross-section was performed with the use of scanning electron microscope JEOL JSM-6380LV. IR reflection spectra were obtained with Fourier IR-spectrometer Vertex 70 Bruker. Fig. 1 provides the profiles of X-ray diffraction of $K_{\alpha 1,2}$ lines (600) for the samples of GaInP/ GaAs (100) (Fig. 1a), GaInP:Dy/ GaAs(100) (Fig. 1b) and GaInP:Dy/ por -GaAs /GaAs(100) (Fig. 1c).

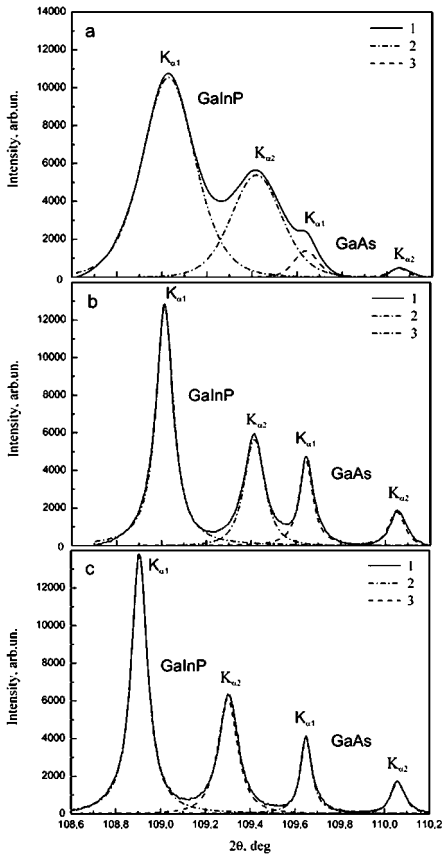

Fig. 1. X-ray diffractograms of Cu K 1,2-lines (600) for heterostructures: a) GaInP/GaAs(100), b) GaInP:Dy/GaAs(100), c) GaInP:Dy/ por-GaAs /GaAs(100).

Two $K_{\alpha 1,2}$ doublets are present in diffractograms: more intensive one (at less angles) from the alloy epitaxial layer and the second one, less intensive, from the substrate. A simple calculation of diffractograms shows that the lattice parameter of the epitaxial layer GaInP ($x0.50$) differs from that one for the substrate of GaAs (100) by $\Delta a = 0.0064$ Å.

Due to a considerable difference of parameters for the film-substrate system in the epitaxial layer of the alloy there appear considerable mechanical stresses, and $K_{\alpha 1,2}$-doublet lines from this strained layer prove to very broad ($\Delta K_{\alpha 1} = 0.28°$) (Fig. 1a). Doping of the epitaxial layer with dysprosium (n_{Dy} 10^{16} cm^{-1}) reduces the stresses in GaInP alloy and almost by three times decreases the width of diffraction lines from the alloy ($\Delta K_{\alpha 1} = 0.1°$, in Fig. 1b. The growth of the same doped alloy on the porous buffer layer in GaInP:Dy/ por-GaAs /GaAs(100) heterostructure results in almost complete elimination of stresses in the epitaxial layer. The lines of $\Delta K_{\alpha 1,2}$ — doublet from this epitaxial layer are the most narrow ones — $\Delta K_{\alpha 1,2} = 0.08°$, in spite of the large disagreement of lattice parameters. Thus, in the samples with porous buffer layer the residual internal stresses caused by the difference in lattice parameters between the surface layer of ternary GaInP alloy and GaAs substrate are redistributed into the porous layer, which in this case plays a role of a "sponge" and completely removes the internal stresses. Data obtained with the use of scanning electron microscope (Fig. 2) demonstrate inhomogeneous dis-

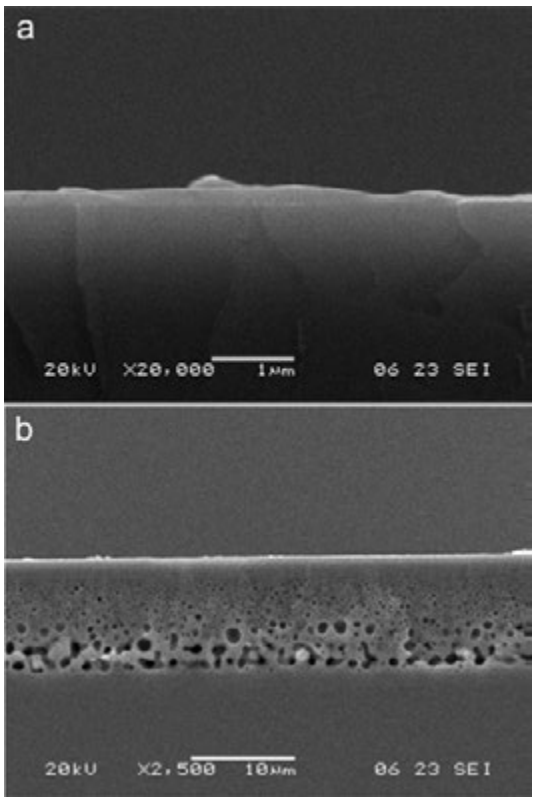

Fig. 2. Scanning electron microscopic image of cross-section for heterostructures of GaInP:Dy/GaAs (a) and GaInP:Dy/ por-GaAs/ GaAs(100) (b).

tribution of pores with different size. It is seen that more large pores are located near the boundary with GaAs (100) substrate while the pores of less size prevail in the upper part of porous layer nearer to the epitaxial layer of GaInP. Analysis of IR reflection spectra shows that under doping of the GaInP epitaxial layers with dysprosium due to a relatively small difference in the radii of Dy and Ga, In atoms dysprosium can penetrate into the alloy as substituting In, Ga atoms as occupying interstitial positions.

Moreover, in heterostructures with por-GaAs the impurity dysprosium atoms penetrate into the buffer layer accumulating in the pores in the form of clusters.

Acknowledgements

We acknowledged RFFI for financial support: grant RFFI 06-02-96313 r-centr-a.

References

[1] H. Föll, Porous III–V compound semiconductors: formation, properties, and comparison to silicon/ H. Föll, J. Carstensen, S. Langa, M. Christophersen, and I. M. Tiginyanu , *Phys. Stat. Sol. (a).* **197**, 61–70 (2003).

16th Int. Symp. "Nanostructures: Physics and Technology"
Vladivostok, Russia, July 14–18, 2008

Composition and parameters of domains formed as a result of spinodal decomposition of quaternary alloys in the epitaxial GaInP/InGaAsP/GaInP/GaAs(001) heterostructures

P. V. Seredin[1], E. P. Domashevskaya[1], N. N. Gordienko[1], N. A. Rumyantseva[1], B. L. Agapov[1], I. N. Arsentyev[2] and I. S. Tarasov[2]

[1] Voronezh State University, Universitetskaya pl. 1, 394006, Voronezh, Russia
[2] Ioffe Physico-Technical Institute, St Petersburg, Russia

Abstract. Two-layer and three-layer epitaxial heterostructures including the layers of quaternary $Ga_x\ In_{1-x}\ As_y\ P_{1-y}$ alloy were investigated in the work. In three-layer heterostructures domains formation was found due to the spinodal decomposition of quaternary alloy. As a result, an additional long-wave band there appears in the photoluminescent spectra and additional Cu $K_{\alpha 1,2}$ doublet line can be observed in X-ray patterns of (006) line. Domains composition was determined basing on Vegards law and Kouphal equation.

Two kinds of epitaxial heterostructures were obtained liquid-phase epitaxy (LPE). For one group of the samples on the substrates of GaAs (001) an intermediate layer of InGaP was grown, and then a quaternary layer of InGaAsP alloy was deposited. For the other group the layer of InGaAsP alloy was covered by a layer of InGaP and thus it appeared to be between two layers of ternary solid solution. InGaAsP epitaxial layers were made employing photoluminescence, scanning electronic microscopy (SEM), atomic force microscopy and X-ray diffractometry methods. In the samples without covering layer only one peak was observed in photoluminescence (PL) spectra from quaternary InGaAsP alloy at the temperature $T = 77$ K. The observation of one peak means that the layer is homogeneous. PL spectra of the samples with a covering layer are characterized by two bands: the main one that is present in all of the samples and an additional low-energy band. At the temperature $T = 300$ K there are also two peaks, but a small shift in the long-wave region is observed. The occurrence of two peaks originating from quaternary InGaAsP alloy indicates at decomposition of solid solution. Short-wave and long-wave peaks correspond to radiation from the recombination in solid phase with various values of the band gap.

SEM investigations show that heterostructures of InGaAsP/InGaP/GaAs (001) with only one PL maximum have a plane, mirror-like surface. Epitaxial layers of this type of heterostructures grow in parallel to a surface of the substrates of GaAs (001). On the surface of heterostructures with two maxima in PL spectra, a microrelief was observed as a statistical distribution of homogeneity — "domains", oriented along the direction of [100] (Fig. 1). Microphotographs of the chips of such samples show a wavy relief (Fig. 2) which is the characteristic for samples in the range of spinodal decomposition. The formation of this relief occurs at decomposition of InGaAsP alloy and it is extended to a to covering layer InGaP.

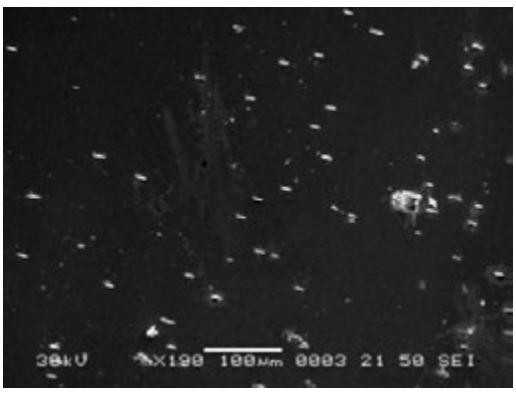

Fig. 1. SEM image of the surface of heterostructure InGaP/InGaAsP/InGaP/GaAs(001).

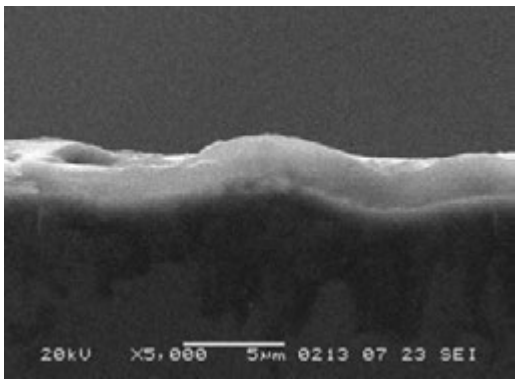

Fig. 2. Microphotography of a chip of heterostructure InGaP/InGaAsP/InGaP/GaAs(001).

Diffractometric investigations were carried out with diffractometer diffraction lines into components and analysis with the use of computer program "New profile" demonstrated, that in samples with one peak PL, one $K\alpha_{1,2}$ doublet in quaternary InGaAsP alloy is observed as is shown in Fig. 3.

Heterostructure with two peaks in PL spectra involve two doublets in diffractograms, one of them with a smaller parameter of crystalline lattice which is a reflection from solid solution of InGaAsP and the second $K\alpha_{1,2}$ doublet originates from domains with a greater lattice parameter (Fig. 4). Interface layer of quaternary InGaAsP alloy with surrounding epitaxial layers of InGaP, with a smaller value of lattice parameter, shows that the film of InGaAsP appears to be compressed in the plane of a layer and expansion along a direction of growth. There is a simultaneous compression and an expansion of the layer for quaternary InGaAsP alloy. The regions of expansion are

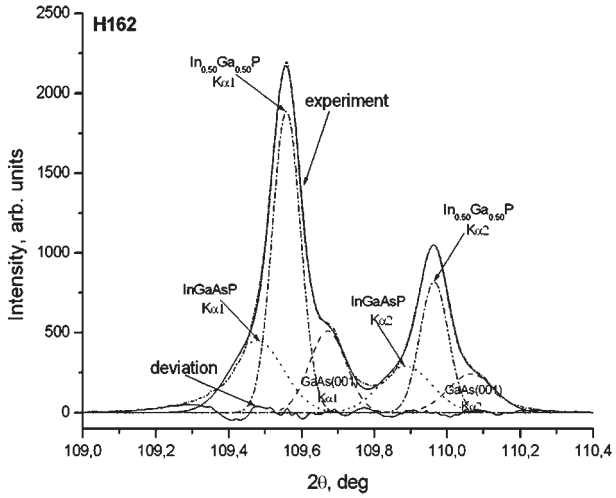

Fig. 3. Decomposition of the diffraction line (006) from heterostructure InGaAsP/InGaP/GaAs (001). The solid line — experiment, shaded and dotted — approximation.

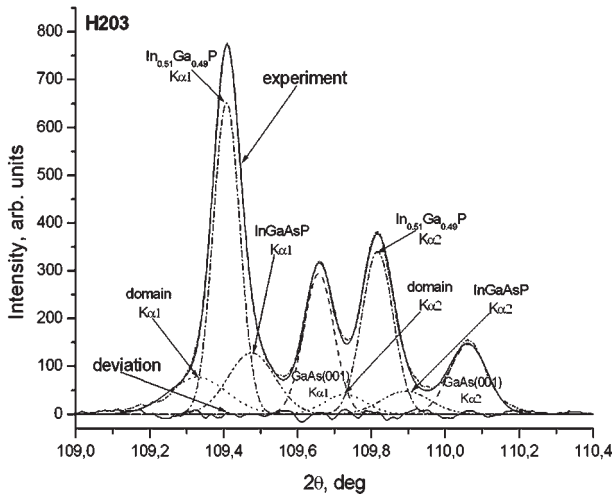

Fig. 4. Line of diffraction (006) heterostructures InGaP/InGaAsP/InGaP/GaAs(001).

formed as domain structures.

For $In_{1-x}Ga_xAs_{1-y}P_y$ alloy a lattice parameter a(x,y) can be obtained, in first-order approximation, through linear interpolation:

$$a(x, y) = a_{\mathrm{InP}}(1-x)y + a_{\mathrm{InAs}}(1-x)(1-y) + a_{\mathrm{GaAs}}(1-y)x + a_{\mathrm{GaP}}xy.$$

However, linear interpolation is not applicable for Eg. At room temperature the expression of In1-xGaxAs1-yPy band gap has the following form:

$$Eg(x, y) = 0.41+0.668x-1.068y+0.758x2+0.078y^2 -0.069xy - 0.0332yx^2 + 0.03xy^2 \text{ (eV)}.$$

The constant of 0.41 eV represents band gap of InAs at 300 K. The determination of composition for the alloys was performed by the experimental values of the band gap from PL spectra and crystal lattice parameter. From system of equations (1) and (2), it is possible to find which fraction of Ga atoms are replaced by atoms of In, and As atoms replace atoms of P in $In_{1-x}Ga_x\ As_{1-y}P_y$ alloy. An distinction for the heterostructures of InGaP/InGaAsP/InGaP/GaAs (001) is that inside the layer of InGaAsP two solid solutions are formed with different compositions due to spinodal decomposition of the strain layer in the quaternary solid solution, compressed between two layer of ternary InGaP.

Dispersion analysis of the IR reflectance spectra showed that due to the spinodal decomposition of the epitaxial InGaAsP alloys a reorganization of the optical phonon subsystem takes place accompanied by the change of the number of the main optical modes and their frequencies. It means a redistribution of the internal stresses for the crystal lattice during formation of the domains.

A set of the performed investigations has shown that in heterostructures of InGaP/InGaAsP/InGaP/GaAs (001) there occurs spinodal decomposition of quaternary alloy. The formation of domains occurs as a result of self-ordering and redistribution of internal pressure in the intermediate epitaxial layer of quaternary solid solution due to compression in the plane layer growth and expansion in a growth direction. The domains consist of the cross layered nanostructure and have a smaller band gap and greater lattice parameter, than rest of quaternary solid solution.

16th Int. Symp. "Nanostructures: Physics and Technology"
Vladivostok, Russia, July 14–18, 2008

Exact finding of optical parameters for real semiconductor heterostructures

A. A. Kovalyov

Institute of Semiconductor Physics, Siberian Division of Russian Academy of Sciences, Academica Lavrentieva prospect, 13, Novosibirsk, 630090, Russia

Abstract. A method to determine optical parameters for real semiconductor heterostructures is proposed. The method is based on the measurements of characteristic angles in spectral reflectivity of a sample. This technique permits to increase the measurement accuracy of refractive index and extinction coefficient spectral dependencies by several orders of magnitude. Abilities of the method are demonstrated by calculated examples for real semiconductor sample containing 10 identical quantum wells.

Introduction

Knowledge of accurate values of optical parameters $n(\lambda)$ and $\kappa(\lambda)$ in semiconductor heterostructures is necessary for design of optoelectronics elements, and in particular the passive saturable absorber mirrors for ultra-short pulse lasers [1]. Conventional approach to control samples containing multiple quantum wells uses transmission of radiation. The total thickness of the sample may comparable with wavelength, that is why spectral distortions because of the interference are inevitable [2]. In many situations like the samples containing quantum wells of type GaAs/Al_xGa_{1-x} As/GaAs [3] the transmission investigation is impossible without removal of the substrate. This procedure can imply mechanical stresses and corresponding changes in spectral characteristics of the samples containing quantum wells. The only one exit in this case is the research of the reflectivity. However, the contribution of heterostructures in the total reflectivity of the sample is rather small, usually of the order of 10^{-5}–10^{-3}. Therefore, the finding of optical parameters of heterostructures become a difficult task, especially by taking into account light interference and possible presence of impurities in the substrate.

This work demonstrates possibility to determine effective values of refractive index $n(\lambda)$ and extinction coefficient $\kappa(\lambda)$ for the structures including identical quantum wells. The quantities ti be measured are two characteristic angles. The first corresponds to the minimum of reflectivity at a fixed wavelength (just the analog of Brewster angle for non-absorbing materials). The second angle corresponds to the minimal slope of the incidence angle dependence of reflectivity. In fact, it concerns the angles, for which the first and second reflectivity derivative over incidence angle are zero in the vicinity of an angle — analog of the Brewster one.

1. Idea of the measurements

The measurements of the substrate reflectivity are to be carried first. As it is clear from our experience, the real values of the substrate characteristics $n_s(\lambda)$ and $\kappa_s(\lambda)$ may differ considerably from their values taken from the handbook [4].

The essence of measurements is as following. The sample is irradiated by p-polarized low intense radiation of a fixed wavelength λ and under an incidence angle θ which is tunable and measurable. The accuracy of the angle determination is not worth than 10^{-2} degree. This angle is modulated at a frequency of about 10–100 Hz. The detection scheme should be organized in such a way that a spatial location of reflected beam would not change under incidence angle modulation. The angle $\theta_1(\lambda)$ responding a minimum of reflectivity $R(\lambda)$ at a fixed wavelength λ of radiation is to be measured first. In this measurement the synchronous detection at the modulation frequency of incident angles takes place. The next measurement is to determine the angle $\theta_2(\lambda)$, which corresponds the minimum of the first derivative of reflectivity over incidence angle $dR/d\theta$. In this case the reference signal for synchronous detection has doubled frequency.

2. Typical functional dependencies

Let's estimate the typical values of $\theta_1(\lambda)$ and $\theta_2(\lambda)$ for the sample containing heterostructure of 10 identical quantum wells of type $In_{0.25}Ga_{0.75}As$ of 8.7 nm thickness surrounded by GaAs barriers of 22.3 nm at the substrate of GaAs. The values of $\theta_1(\lambda)$ and $\theta_2(\lambda)$ are obviously the functions of a st of parameters: refractive index $n_s(\lambda)$ and $\kappa_s(\lambda)$ of the substrate, refractive index $n_w(\lambda)$ and $\kappa_w(\lambda)$ of the quantum wells region, and wavelength λ itself.

The parameter $\kappa_w(\lambda)$ in a spectral region accessible for the measurements can be determined from the transmission of p-polarized light incident under an angle close to the Brewster angle of the substrate GaAs. The component of electric field in

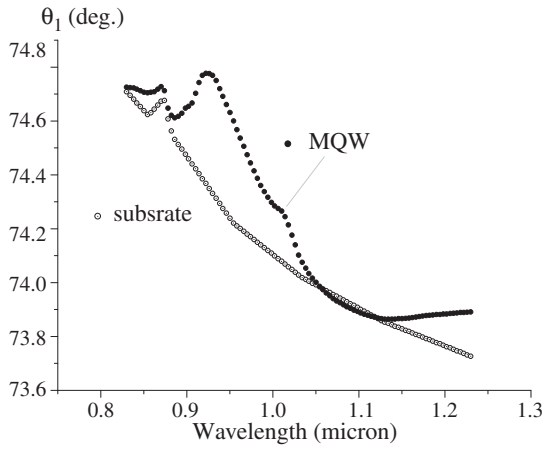

Fig. 1. Angle $\theta_1(\lambda)$ for the substrate (open circles) and for the sample containing 10 MQW on a substrate (black points). The MQW manifestation near 1 μm is of high contrast.

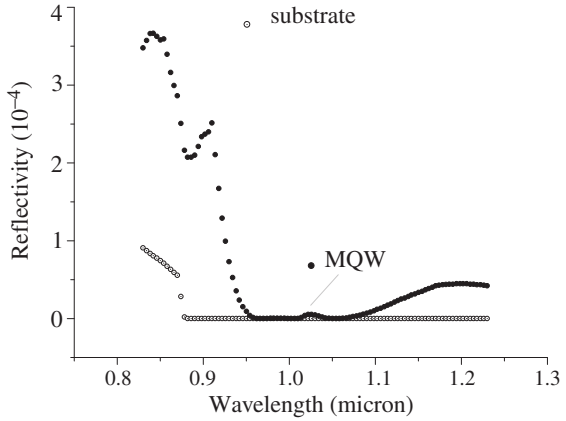

Fig. 2. Reflectivity at an incidence angle close to the Brewster one for the substrate and for the sample containing 10 MQW on a substrate.

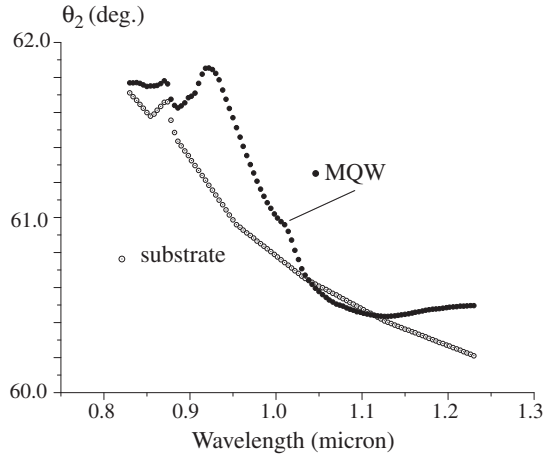

Fig. 3. Angle $\theta_2(\lambda)$ for the substrate MQW on a substrate.

the plane of quantum wells is of about 0.96 from those of the incident wave in this case. so the extracted value of $\kappa_w(\lambda)$ was used in the following calculations as a quantity corresponding to the normal incidence case. Outside the spectral region accessible for the transmission measurements, the $\kappa_w(\lambda)$ data were taken from [4] followed by corresponding recalculations for the composition of quantum well $In_{0.25}Ga_{0.75}As$. Resulting wide spectral range function $\kappa_w(\lambda)$ was then used to determine $n_w(\lambda)$ via Kramers–Kronig relations. The same procedure can be performed for the real substrate.

The calculation of the sample containing heterostructure was carried out without any approximations. The optical matrices technique [5] for the inclined incidence for all layers of the structure by using parameters $n(\lambda)$ and $\kappa(\lambda)$ for each layer was applied to calculate the sample transmission. The variation of wavelength and incidence angle around Brewster angle analog allowed to extract the functional dependencies of $\theta_1(\lambda)$ and $\theta_2(\lambda)$.

Fig. 1 shows $\theta_1(\lambda)$ functions for the substrate GaAs (here the data for $n_s(\lambda)$ and $\kappa_s(\lambda)$ were taken from [4]) and for the sample with 10 quantum wells over this substrate. Qualitative representation of quantum wells can serve the reflectivity signal detected at $\theta_1(\lambda)$ shown in the Fig. 2.

As it is clear from Fig. 1, the contrast structure corresponds to the quantum wells. Since the accuracy of the linear angles measurement by optical methods is enough high, and since the contrast of above indicated structure is not lesser that 0.1 degree, there is possibility to increase considerably the optical parameters of the sample.

The second angle characteristics of reflectivity $\theta_2(\lambda)$ corresponding the minimum of the first derivative of reflectivity over incidence angle is shown in Fig. 3. The same case of the substrate and 10 quantum wells is presented. As it could be expected, the contrast of the structure corresponding the quantum wells is higher that in the Figs. 1, 2 due to reflection at the boundaries "barrier–well". This circumstance should allow to extract separately the contributions from $\kappa_w(\lambda)$ and $n_w(\lambda)$ into the total reflectivity of the sample.

3. Discussion

So, to extract the values of $\kappa_w(\lambda)$ and $n_w(\lambda)$, the numerical calculations of $\theta_1(\kappa_w(\lambda), n_w(\lambda), \kappa_s(\lambda), n_s(\lambda), \lambda)$ and $\theta_2(\kappa_w(\lambda), n_w(\lambda), \kappa_s(\lambda), n_s(\lambda), \lambda)$ are to be used. The parameters $\kappa_s(\lambda)$ and $n_s(\lambda)$ can be found from the measurements of the substrate without heterostructure. From other side, the values of the characteristic angles $\theta_1(\kappa_w, n_w) = S1$ and $\theta_2(\kappa_w, n_w) = S2$ can be found experimentally. So, the complete information concerning optical parameters of heterostructure is a solution of a set of equations:

$$\begin{aligned} \theta_1(\kappa_w, n_w) &= S1, \\ \theta_2(\kappa_w, n_w) &= S2. \end{aligned}$$

The solution of this set of equations can be found by iterations.

Acknowledgements

Financial support of Russian Foundation for Basic Research grant 06-02-16527, Russian–Byelorussian RFBR grant 08-02-90010-Bel, and Integrated Project between Byelorussian National Academy of Sciences and Siberian Branch of Russian Academy of Sciences are acknowledged. Authors are indebted to Dr. M. A. Putyato and Dr. V. V. Preobrazhenski for the samples preparation, stimulating discussions with Dr. N. N. Rubtsova are also acknowledged.

References

[1] Ursula Keller, Anne Q. A. Tropper, Y. Silberberg, D. A. Miller, *Physics Reports* **429**, 67–120 (2006).

[2] V. V. Chaldyshev, A. S. Skolnik, V. P. Evtikhiev, T. Holden, *Fizika i Tekhnika Poluprovodnikov* **39**, No. 6, 729–734 (2005).

[3] A. A. Herasimovich, S. V. Shokovets, G. Gobsch, D. S. Domanevsky, *Fizika i Tekhnika Poluprovodnikov* **40**, No. 12, 1466–1469 (2006).

[4] S. Adachi, *Optical constants of crystalline and amorphous semiconductors: numerical data and graphical information*, Kluwer Academic Publishers, p. 736 (1999).

[5] M. Born, E. Wolf, *Principles of Optics*, 6 ed, Pergamon Press (1986).

16th Int. Symp. "Nanostructures: Physics and Technology"
Vladivostok, Russia, July 14–18, 2008

Electron tomography modelling of nanocluster in amorphous matrix

E. B. Modin, O. V. Voitenko, S. V. Dolzhikov and E. V. Pustovalov
Far Eastern National University, Vladivostok, Russia

Abstract. Electron tomography is a powerful instrument that can probe the three-dimensional structure of material. It can be applied to a wide range of samples that can be prepared for transmission electron microscopy (TEM). This work is devoted to the electron tomography reconstruction and three-dimensional modelling of nano-scale objects by the series of the electron microscopic images received under different angles of an inclination of the sample to electron beam. We made an attempt to apply electron tomography to nanocluster visualization in amorphous matrix.

Introduction

For tomogram reconstruction we used an electron microscopic images of nanocluster Fe_3B in the amorphous matrix FeB_{20}, simulated by the slice-method [2]. There are a lot of software for tomography and three-dimensional modeling of nano-scale objects. For tomography reconstruction the IMOD software package was used. The IMOD [5] software package, includes some tools for image processing and alignments of images series, three-dimensional modelling of various objects, tomography reconstruction, joining of several tomograms, etc. [1] IMOD consists of following basic programs:

1. ETOMO — a tooll for processing a series of images, their alignments and tomogram generation.
2. 3DMOD — a tooll for modelling three-dimensional objects.
3. Tools for graphic files converting to a format necessary for IMOD package.

1. Tomography reconstruction

Once the tilt series has been modeled, the reconstruction procedure can be started. One of the important step in the tomogram reconstruction is alignment of the images within the data set [3]. This can usually be achieved with a cross correlation algotithm available in most software packages like IMOD. However, in some cases, because of geometry of object or absence of typical details (objects) in the image, the given algorithm cannot be used. In that case a series of microscopic images is aligned manually. In our experiment a series of the modelled microscopic images of nanocluster Fe_3B in the amorphous matrix FeB_{20}, received under angles of an inclination to an electronic beam from -30 up to $+30$ degrees with step in 1 degree was used. The size of an amorphous matrix was $15 \times 15 \times 2$ nm, quantity of atoms were 36000. Quantity of atoms in nanocluster were 150–500. Modelling of amorphous matrix atomic structure was made in several steps. First of all FeB_{20} atomic matrix were generated by the method of random density packing. Then in few steps atomic matrix relaxation (energy minimization) was made. Nanocluster was "cut out" from Fe_3B crystal structure of different configuration [4]. Because of absence of typical details in a series of images in our case, algorithm cross correlation could not be applied. The tomogram has been constructed, using manual alignment. There were various series of images examined in experiment. By results of tomogram reconstruction it is possible to make following conclusions:

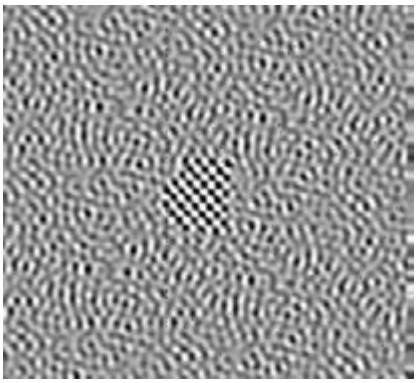

Fig. 1. The frame from tomogramm.

1. For visualization of nanoclaster in an amorphous matrix its thickness should be proportional to thickness of a matrix.
2. It is necessary to use the series of images received under corners not less than -30 up to $+30$ degrees to an electronic beam.
3. As a result of work is the nanocluster Fe_3B tomogram in the amorphous matrix FeB_{20}, shown on Fig. 1.
4. For tomogram reconstruction we use single axis tomography method. As a result generated tomogram can't give enough information for nanocluster three-dimensional modeling. In future experiments we plan to apply dual axis tomography method [3].

References

[1] O. V. Voitenko, E. B. Modin, S. V. Dolzhikov *et al*, *Russian conference of students, postgraduate students and young scientists (Vladivostok,2007)*, Far Eastern National University, **112** (2007).
[2] J. Kauli, *Phisics of difraction*, (Moscow: Mir) **432** 1979.
[3] I. Arslan, J. R. Tong, P. A. Midgley, *Ultra Microscopy* **106**, 994–1000 (2006).
[4] E. V. Pustovalov, N. D. Zakharov, V. S. Plotnikov, *Phys. stat. sol. (a)* **K1**, 135 (1993).
[5] *IMOD Homepage*, http://www.bio3d.colorado.edu.

16th Int. Symp. "Nanostructures: Physics and Technology"
Vladivostok, Russia, July 14–18, 2008

Remote determination of the surface temperature of nanonylon 6 by means of millimeter waves

V. V. Meriakri[3], S. Bourbigot[1], M. Delichatsios[2], I. Nikitin[3], M. Parkhomenko[3] and F. Samyn[1]

[1] Laboratoire des Procdś d'Elaboration de Revetements Fonctionnels Ecole Nationale Supérieure de Chimie de Lilac, BP 90108 59652 Villeneuve d'Ascq Cedex — France
[2] The Institute of Fire Safety Engineering Research & Technology School of the Built Environment, University of Ulster, Newtownabbey, Co Antrim 37 0QB, UK
[3] Institute of Radio Engineering and Electronics, Russian Academy of Sciences, Fryazino Branch, Vvedenski sq. 1, Fryazino, Moscow Region, 141190, Russia

Remote determination of the surface temperature of polymer coverings, including measurements through the flames, is one of important problems of fire safety [1]. This procedure can be carried out by measuring the temperature-dependent reflection coefficient of an electromagnetic wave from the surface of the polymer. The flame is a plasma that shields waves with frequencies $f \leq 3 \times 10^9$ Hz. Therefore, one should use much higher frequencies, namely, millimeter waves ($f\ ge 3 \times 10^{10}$ Hz). In recent years, to reduce the inflammability of polymers, a method of introducing nanoclay particles into polymers has been proposed.

Our task has been to investigate the temperature dependence (first of all, at temperatures close to the melting point) of the complex dielectric permittivity $\epsilon = \epsilon' + j\epsilon''$ of nanonylon 6 with 4% of 30 B, CNa and 20 A clays (samples 1, 2 and 3) at frequencies from 3.0×10^{10} to 3.6×10^{10} Hz and the related variation of the reflection coefficient R.

We have found that at $T = 20$ °C the dielectric permittivities of samples 1, 2 and 3 are equal to $\epsilon' = 2.94$, $\epsilon'' = 10^{-3}$ (sample Nylon 6/30 B), $\epsilon' = 2.86$, $\epsilon'' = 8 \times 10^{-4}$ (sample Nylon 6/CNa), and $\epsilon' = 2.92$, $\epsilon'' = 10^{-3}$ (sample Nylon 6/20 A). These data have been averaged over an area of about 10 cm^2. The accuracy of the measurements is as follows: $\Delta\epsilon'/\epsilon' = 1$–$2\%$ and $\Delta\epsilon''/\epsilon'' = 20\%$.

To determine the surface temperature of nylon 6 samples and its nanocomposites (first of all, at temperatures close to the melting point), we investigated the reflection coefficient R of samples as a function of their temperature at frequencies 30–36 GHz.

We have established that,as temperature increases from 20 to 180 °C, R increases due to the increase of ϵ'. The increase of ϵ' ($\Delta\epsilon'$) for samples 1, 2, and 3 is equal to 0.1, 0.18, and 0.07, respectively. These samples had thickness of 3 mm, and in this case $R_{\min}(T)$ increases by 3, 7, and 4 dB from its minimal value $R_{\min}(20\,°\mathrm{C})$ equal to about -20 or -25; the major part of increase occurs at temperatures $T > 100$ °C. Thus, measuring

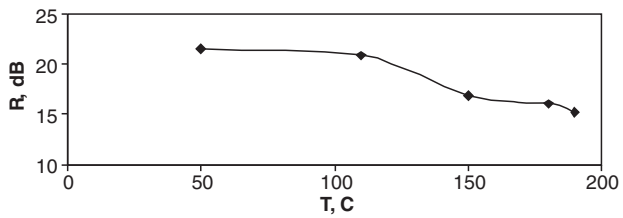

Fig. 1.

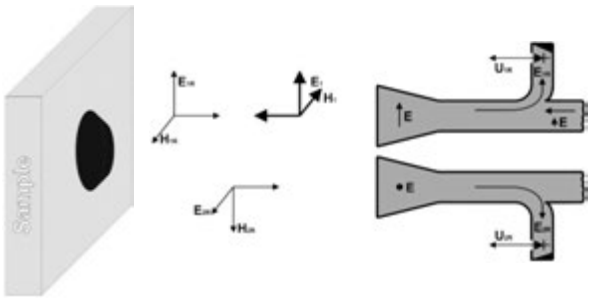

Fig. 2.

the functions $\epsilon'(T)$ and $R_{\min}(T)$, one can determine the surface temperature of a sample. The value of ϵ'' also increases, but its contribution to R is small ($\epsilon'' \ll \epsilon'$). The results of measurements for a PA 5/ 30 B sample are shown in Fig. 1.

The heating of nanopolymer samples may lead to irregularities on their surfaces and give rise to coked regions. We have developed a method for the remote detection of these irregularities through the flames. The method is based on the fact that these irregularities lead to the depolarization of the incident wave; i.e., when a linearly polarized wave is incident on such an irregularity, the reflected wave has a component of orthogonal polarization. The measurement scheme is shown in Fig. 2.

The effect of flame on the measurement of the surface temperature of samples at millimeter wavelengths is very small. For pressure of 760 mm Hg, the flame temperature of 1400 K, electron concentration of 10^{11} cm^{-3}, and the collision rate of 90 GHz, the absorption coefficient in flame is less than 0.1 dB/cm.

These results show that one can carry out remote measurement of the surface temperature of nanonylon, including measurements behind a flame, by means of millimeter waves.

Remote measurement of the surface temperature of samples (including measurement behind the flame) consists in measuring the reflection coefficient of a millimeter wave from a sample of known thickness. The distortions of the plane surface of a sample and the emergence of coked regions are detected by the measurement of the reflected wave of orthogonal polarization.

References

[1] Natsuko Noda *et al*, *Polymer* **46**, 7101 (2005).

16th Int. Symp. "Nanostructures: Physics and Technology"
Vladivostok, Russia, July 14–18, 2008

Theoretical study of the influence of the electric field on the emission from carbon bamboo-like nanotubes

O. E. Glukhova and O. A. Terentev
Saratov State University, 410012 Saratov, Russia

Abstract. The atomic structure and energetics of bamboo-like single-layered carbon nanotubes has been studied by the tight-binding method. It was found, that the optimum step between the crosspiece exists for a tube of the given diameter at which emission properties of a tube improve that is accompanied by decreasing of potential of ionization and as consequence, work function. It was also found, that the bamboo-like nanotubes placed an electrostatic field its work function decreased on 0.05–0.10 eV in comparison with single-layered ideal tubes of similar geometrical parameters.

Introduction

Application of bamboo-like structures as nanoemitters became a reality as well as usual nanotubes. Experimental researches have shown, that bamboo-like carbon tubes (BCNT) possess good emission properties, providing 120 mA/cm^2 at intensity of an external field of 16 V/micron [1]. As a result there is a necessity of studying of an electronic structure and topology of BCNT in strong electric fields.

1. Bases of theoretical research

The single-layered BCNT with the distance of 0.7 nm and 1.37 nm (Fig. 1) between the crosspiece and similar ideal nanotubes in a homogeneous electrostatic field 3–10 V/nm (the direction of field line coincides with an nanotube axis) was ivestigated by the tight-binding method with modified parameters [2,3].

Calculations were spent with help of the package of the computing programs developed by us. This programs allows to model a nanotube of any forms, including nanopeapods, nanotori, bamboo-like nanotubes, Y- and T-shaped tubes. It also allows to modify structure and model deformations. It can obtain nuclear structure by the quantum-chemical tight-binding method and by the molecular dynamics.

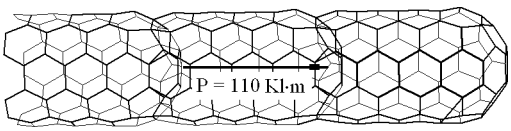

Fig. 1. Three-section bamboo-like nanotube (5,5) and its dipole moment.

2. Results

1) Bamboo-like carbon tubes are stretched 1–3% under action of ponderomotive force of an external electrostatic field. For comparison, there are investigated the ideal single-layered carbon nanotubes. It is revealed, that in an electric field the deformation of ideal tubes more appreciable (2–7%). Small deformation of bamboo-like tubes was revealed because this tube possess greater value of Young's module Y (2–3 TPa [4]) than single-layered ideal tubes (1.3 TPa [2]). Besides, we found that the Young's module increasing with the increasing of number of crosspieces (N) at unit of tube length (Fig. 2).

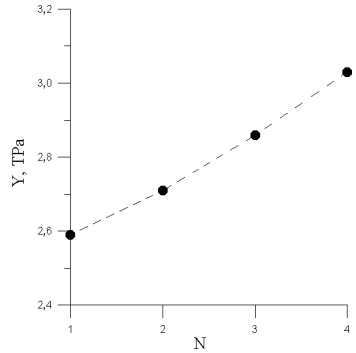

Fig. 2. Dependence of Young's module Y of number of crosspieces N.

2) Bamboo-like tubes possess their own dipole moment that allows us to recommend this tube as filling agent of the composit materials, capable to be guided in one direction, defined by field lines of an external electrostatic field. In an external electrostatic field dipole moment of bamboo-like tubes increases, buf for a tube without crosspieces — it is induced. Here the polarizability of hollow ideal tubes above, than one of bamboo-like tubes because of presence of crosspieces. Electrostatic parameters of BCNT are given in Table 1, where μ — dipole moment, α — polarization tensor.

3) Permittivity of BCNT is greater than one of ideal tubes in 1.6–2 times. In Table 2 are presented obtained data for BCNT of different diameters and with different number of crosspieces (two-section — with one crosspiece, three-section — with two crosspieces): permittivity (ϵ_r), rate of permittance (ϵ). All results are received for intensity of an electrostatic field of 3 V/nm.

4) We found, that the optimum step between the crosspiece exists for a tube of the given diameter at which emission prop-

Table 1. Dipole moment and atomic polarizability of bamboo-like nanotube (Fig. 1) in external electrostatic field $F_z = 3$ V/nm.

crosspieces count	0	1	2	3
$\mu \times 10^3$, Kl × m	291.2	95.40	56.24	47.88
$\mu_x \times 10^3$, Kl × m	41.25	23.80	13.37	-6.46
$\mu_y \times 10^3$, Kl × m	41.20	24.11	10.82	-15.08
$\mu_z \times 10^3$, Kl × m	285.35	89.02	53.55	44.98
$\alpha_x z$, nm^3	1.55	0.87	0.50	-0.24
$\alpha_y z$, nm^3	1.54	0.90	0.41	-0.27
$\alpha_z z$, nm^3	10.73	3.35	2.02	1.69

Table 2. Permittivity of bamboo-like nanotubes.

	three-section BCNT (5,5)	two-section BCNT (10,10)
diameter, nm	0.7	1.37
ϵ_r	301	330
ϵ, μF/m	2.67	2.9

erties of a tube improve that is accompanied by decreasing of potential of ionization and as consequence, work function. It was also found, that the bamboo-like nanotubes placed an electrostatic field its work function decreased on 0.05–0.10 eV in comparison with single-layered ideal tubes of similar geometrical parameters.

5) Bamboo-like tubes can be applied as separate nanoavtoemitter with high field-emission properties, and a film with similar structures can be applied as the cathodes providing a stable current at small voltage in devices of nano- and microelectronics.

Acknowledgement

This work has been supported in part by the Programma Presidiuma RAN P-03 "Kvantovaya Macrofisica" and by the grant RFFI (No. 07-02-00852a).

References

[1] O. E. Glukhova *et al*, *Summaries of lectures of school-seminar " Nanostructures, models, the analysis and management", (Moscow, 2008)*. MIEM, 7 (2008).
[2] O. E. Glukhova *et al*, *Physics of the Solid Stale* **48**, 1329 (2006).
[3] O. E. Glukhova *et al*, *Nanotechnics* **1(9)**, 3 (2007).
[4] O. E. Glukhova *et al*, *J. of Nano and Microsystem Technique* **3**, 2 (2008).

16th Int. Symp. "Nanostructures: Physics and Technology"
Vladivostok, Russia, July 14–18, 2008

Models of absorption cross-section and scattering cross-section of light by dielectric nanoparticles

V. P. Dzyuba and Yu. N. Kulchin
Institute for Automation and Control Processes FEB RAS, Vladivostok, Russia

Abstract. The theoretical model describing of both absorption cross-section and scattering cross-section of light by any shape and small sizes dielectric nanoparticles is presented.

The both absorption cross-section $\sigma_{\rm a}(\omega,a)$ and scattering cross-section $\sigma_{\rm s}(\omega,a)$ of light by nanoparticles are defined of their electronic structure [1–2]. Direct calculation of both $\sigma_{\rm a}(\omega,a)$ and $\sigma_{\rm s}(\omega,a)$ which considering their geometry and localization volume limited of wave functions of quantum states of both excitons and free charges, is impossible now. Nevertheless, using modeling representations about the mechanisms defining of this sections can be obtained of their dependence on both the frequency of the radiation and the size nanoparticle.

Dependence of $\sigma_{\rm a}(\omega,a)$ and $\sigma_{\rm s}(\omega,a)$ on frequency of radiation ω and the size nanoparticle a can be expressed through its polarization $A(\omega,a)$ by expressions [3]

$$\sigma_{\rm a}(\omega,a)=\frac{4\pi\omega}{c}V\,{\rm Im}\,A(\omega,a),$$
$$d\sigma_{\rm s}(\omega,a)=\frac{\omega^4}{c^4}V^2\left|A(\omega,a)\right|^2\sin^2\theta d\Omega, \qquad (1)$$

where V — volume nanoparticle, and θ is corner between vectors of direction of the wave scattered and of the electrostatic intensity of the electromagnetic wave, and c — speed of light in vacuum. If sizes of the dielectric nanoparticle are small, power spectrum of both the holes and the electrons is defined them Coulomb' interaction and volume limited of the area of quantization (volume nanoparticle) in main. It is well known that the polarization $A(\omega,a)$ in approach dipole can be expressed by using the matrix elements of the dipole electric moments $D_{ij}(a)$ of the transitions between quantum states $|i\rangle$ and $|j\rangle$ [4].

$$A(\omega,a)=\frac{2}{V\hbar}\left[\sum_{i,j}\frac{\left|D_{ij}(a)\right|^2\left(\omega_j^2-\omega^2\right)}{\left(\omega^2-\omega_j^2\right)^2+\omega^2\Gamma_j^2}\omega_j\right]$$
$$+i\frac{2}{V\hbar}\left[\sum_{i,j}\frac{\left|D_{ij}(a)\right|^2\Gamma_1}{\left(\omega^2-\omega_i^2\right)^2+\omega^2\Gamma_i^2}\omega\omega_i\right], \qquad (2)$$

where summation is made to all aroused transitions dipole, ω_j is the frequency of transition, Γ_j is width of aroused J-th level, $\hbar$ is Planck's constant. Matrix element $D_{ij}(a)=-\Lambda(\varepsilon_1,\varepsilon_2)\,e\langle j|\vec{r}\vec{\gamma}|i\rangle$, where $\vec{r}$ is radius-vector of a charge, $\vec{\gamma}$ is the direction of the polarization vector of the electromagnetic wave which has realized this transition. Multiplier $\Lambda(\varepsilon_1,\varepsilon_2)$ considers influence of both form and dielectric constants of the nanoparticle ε_1 and environment surrounding ε_2. Using the theorem of an average of the certain integral [5], we can be find what $D=d_{ij}a$, where quantity d_{ij} depends to the form of the nanoparticle. This linear dependence $D_{ij}(a)$ from the size nanoparticle is correct for values a smaller $a_{\rm c}$. If $a\geq a_{\rm c}$, that is to consider interaction between the carriers of charge and the induced on interfaces of environments a charges necessary. In the this case the moment dipole of transitions will be defined by the sizes of area of localization of states and is depended weakly from the size nanoparticles [6]. In the case of transitions in states with a continuous spectrum, $D_{ij}(a)$ will be proportional to area dislocation the carrier of the charge, i.e. is proportional a. Therefore for the momentes dipole of transitions in the bound states and in states with a continuous spectrum of energy it is possible to write accordingly:

$$D_{ij}^{\rm q}(a)=d_{ij}^{\rm q}a,\quad D_{ij}^{\rm ex}(a)=d_{ij}^{\rm ex}a,\quad D_{ij}^{\rm c}(a)=d_{ij}^{\rm c}a, \qquad (3)$$

for transitions in quantum-dimensional $D_{ij}^{\rm q}(a)$, exciton $D_{ij}^{\rm ex}(a)$ and states with a continuous spectrum $D_{ij}^{\rm c}(a)$. To modeling nanoparticle a three-dimensional potential hole with infinitely high walls and with its geometrical form dependence ω_j on a is possible to find as

$$\omega_j=\frac{E_j}{\hbar}=\frac{\hbar\varphi_{[j]}^2}{2m_{\rm e(h)}a^2}\vartheta=\frac{c_j}{a^2}, \qquad (4)$$

where φ_j^2 — roots of the decision of the wave equation for free electrons (holes) in a potential hole with its surface, $m_{\rm e(h)}$ — effective mass of electron or holes, ϑ — a multiplier is defined by the form nanoparticle. The exciton states in nanoparticle are more stability if their sizes there are less than sizes of the nanoparticle. Therefore to assume reasonable, that for transitions in exsiton states the frequency ω_j also as well as Γ_j in a greater degree depends from form of nanoparticle. Expressions (1), (3), (4), allows to define expressions of cross-sections $\sigma_{\rm a}(\omega,a)$ and $\sigma_{\rm s}(\omega,a)$ in following form for transitions in quantum-dimensional states

$$\sigma_{\rm a}^{\rm q}(\omega,a)=\frac{8\pi}{c\hbar}\sum_{i,j}\frac{d_{ij}^{\rm q\,2}c_j\Gamma_j}{\left(a^4\omega^2-c_j^2\right)^2+a^8\omega^2\Gamma_j^2}\omega^2a^8,$$
$$\sigma_{\rm s}^{\rm q}(\omega,a)=\frac{4P\omega^4}{c^4\hbar^2}$$
$$\times\sum_{i,j}\sum_{i,k}\frac{d_{ij}^2d_{ik}^2c_jc_k\left[\left(c_j^2-a^4\omega^2\right)\left(c_k^2-a^4\omega^2\right)+a^8\Gamma_j\Gamma_k\right]}{\left[\left(c_k^2-a^4\omega^2\right)^2+a^8\omega^2\Gamma_k^2\right]\left[\left(c_j^2-a^4\omega^2\right)^2+a^8\omega^2\Gamma_j^2\right]}a^8,$$

where $P = \int\limits_{4\pi} \sin^2\theta d\Omega$, in exciton states

$$\sigma_{\rm a}^{\rm ex}(\omega, a) = \frac{8\pi}{c\hbar}\sum_{i,j}\frac{d_{ij}^{\rm ex\,2}a^2\omega_j\Gamma_j}{\left(\omega^2-\omega_j^2\right)^2+\omega^2\Gamma_j^2}\omega^2,$$

$$\sigma_{\rm s}^{\rm ex}(\omega, a) = \frac{4P\omega^4}{c^4\hbar^2}$$

$$\times\sum_{i,j}\sum_{i,k}\frac{d_{ij}^2d_{ik}^2\omega_j\omega_k\left[\left(\omega_j^2-\omega^2\right)\left(\omega_k^2-\omega^2\right)+\omega^2\Gamma_j\Gamma_k\right]}{\left[\left(\omega_k^2-\omega^2\right)^2+\omega^2\Gamma_k^2\right]\left[\left(\omega_j^2-\omega^2\right)^2+\omega^2\Gamma_j^2\right]}a^4.$$

At transitions in a continuous spectrum, for which $\omega_j = \omega$

$$\sigma_{\rm s}^{\rm ex}(\omega, a) = \frac{4P\omega^4}{c^4\hbar^2}\sum_{i,j}\sum_{i,k}\frac{d_{ij}^2d_{ik}^2}{\Gamma_j^2\Gamma_k^2}a^4.$$

If the value Γ_j is do not depends from both j and the sizes nanoparticle, we have

$$\frac{\sigma_{\rm s}(\omega, a)}{\sigma_{\rm a}(\omega, a)} \approx \frac{P\omega^3}{2\pi c^3\hbar\Gamma}\sum_{i,j}\left|D_{ij}(a)\right|^2 \sim \omega^3a^2.$$

For the sizes of the nanoparticle 10–100 nm and the field with frequencies $\omega = 10^{13} - 10^{16}$ of Hz and $\Gamma = 10^9$ Hz, we have

$$\frac{\sigma_{\rm s}(\omega, a)}{\sigma_{\rm a}(\omega, a)} \leq 10^{-7}.$$

Essential difference in behavior of cross-sections $\sigma_{\rm a}(\omega, a)$ and $\sigma_{\rm s}(\omega, a)$ from the sizes nanoparticle and frequency of radiation enable experimental research of a relative role quantum-dimensional and exsiton states, and also states with the continuous power spectrum of carriers of charge in formation of optical properties of materials on basis of dielectric nanopartiles.

Acknowledgements

The research supported by the program of basic research of the Department of physics RAS the "Coherent radiation of semiconductor lasers and structures".

References

[1] J. I. Alferov, FTT **32**, 3 (1998).
[2] S. I. Pokutnyi, *J. Appl. Phys.* **99 (1)**,323 (2007).
[3] L. D. Landau, E. M. Lifshich, *Elektrodinamika splochnuh sred*, (M.: Fizmatlit) 657, (2001).
[4] V. M. Agranovich, V. L. Ginzburg, *Kristallooptika s uthetom prostranstvenoi dispersii i teorii eksitonov*, (M.: Nauka), 432 (1979).
[5] G. Korn, T. Korn, *Spravochnik po vushei matematiki*, (M.: Nauka) (1973).
[6] S. I. Pokutnyi, *FTT* **35**, 257 (1993).

16th Int. Symp. "Nanostructures: Physics and Technology"
Vladivostok, Russia, July 14–18, 2008

Light-emitting Si nanostructures formed in SiO_2 by pulsed anneals

G. A. Kachurin[1], S. G. Cherkova[1], R. A. Yankov[2] and D. V. Marin[1]

[1] Institute of Semiconductor Physics of SB RAS, pr. ak. Lavrentjeva 13, Novosibirsk 630090, Russia
[2] Forschungszentrum Rossendorf, 01314 Dresden

Thin Si-rich SiO_2 layers have been prepared by implantation of 100 to 190 keV Si ions in thermally grown oxide films. The ion doses provided the excess Si concentration of about 10–15%. KrF excimer laser pulses, flash lamp annealing and rapid thermal annealing were used for the post-implantation heat treatments to form light-emitting Si quantum dots. The pulse durations were 20 ns, 20 ms and 1 s, respectively. Studies were carried out using a spectroscopy of PL excited at room temperature by a nitrogen laser ($\lambda = 337$ nm). The excess Si atoms in SiO_2 are not free to migrate, but are rather incorporated into the oxide network.

For laser pulse duration of 20 ns no formation of nanocrystals occurs, which is evidently associated with the insufficient growth time. However, if one creates in advance amorphous Si nanoprecipitates of the right size, it is possible to form quantum-size Si nanocrystals by pulsed laser processing. This process occurs most likely via melting rather than in a solid phase, favored by the release of latent heat and the reduction in temperature of melting of the nanoparticles. Photoluminescence band near 800 nm, typical to quantum-size Si nanocrystals, was found after laser annealing (Fig. 2).

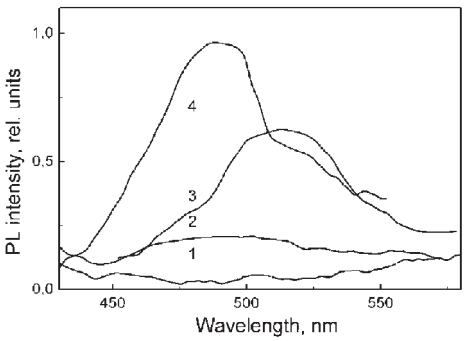

Fig. 1. PL spectra of the Si doped SiO_2 layers after the nanosecond laser annealing. Pulse energy densities, J/cm^2: 1 0.2; 2 0.25; 3 0.3; 4 0.3 × 3 pulses.

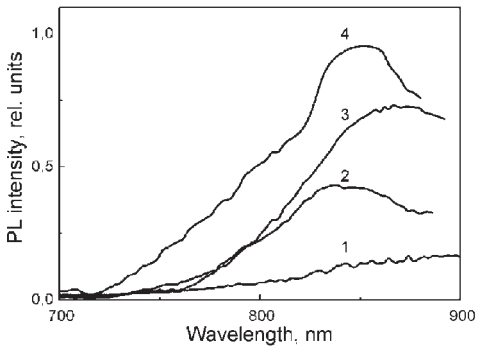

Fig. 2. PL spectra of the SiO_2 layers with the amorphized Si-ncs after the nanosecond laser annealing. Pulse energy densities, J/cm^2: 1 0.2; 2 0.25; 3 0.3; 4 0.3 × 3 pulses.

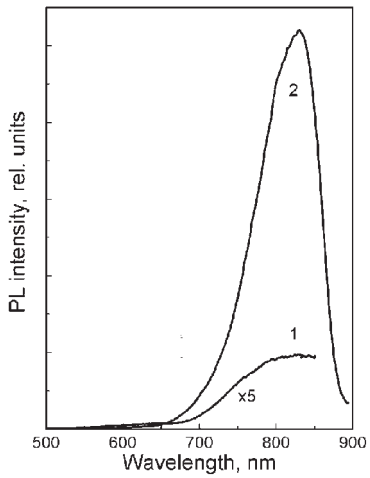

Fig. 3. PL spectra of the Si doped SiO_2 layers after the RTA. 1 — as-annealed; 2 — after annealing in H_2.

Formation of the luminesing Si nanocrystals in Si-rich SiO_2 layers is feasible under the influence of intense light pulses of 20 ms and 1 s duration. In this case the SiO_2 layer has not been heated above the Si melting point. Photoluminescence may be enhanced by the low temperature annealing in H_2 (Fig. 3). Comparison of the nanocrystals formation rate and the estimates of the diffusion-limited growth yields diffusivity of the excess Si in SiO_2 that are substantially larger than the values obtained in experiments using stationary annealing. The discrepancies may be explained by the existence of a transient mechanism of rapid growth at the beginning of the pulsed annealing.

The fabrication of Si-ncs necessitates segregation of the Si atoms, availability of sinks to which these atoms may diffuse, availability of Si-phase nucleation centers, growth of the incipient nanoprecipitates, their crystallization, and, finally, the Ostwald ripening. Due to the high temperatures resulting from intense light pulses, the different stages in the formation of light-emitting Si quantum dots may occur quite rapidly. Treatment for times as short as 20 ns is already sufficient for the segregation of the excess Si in the SiO_2 atomic network and the formation of nanostructures that luminesce in the visible portion of the spectrum 400–600 nm (Fig. 1).

Acknowledgements

This work has been supported by the Grants RUS 01/234 (Federal Ministry of Education and Science, Germany), 05-02-16455 (Russian Foundation for Basic Researches), and 06-02-72003 (Russian Foundation for Basic Researches and Ministry of Science and Technology, Israel).

16th Int. Symp. "Nanostructures: Physics and Technology"
Vladivostok, Russia, July 14–18, 2008

Atomic steps and nanoclusters on silicon surface

A. V. Latyshev
Institute of Semiconductor Physics SB RAS, 630090 Novosibirsk, Russia
Novosibirsk State University, 630090 Novosibirsk, Russia

Abstract. Some brief overview of nanoscale diagnostic of semiconductor surface structures by *in situ* ultrahigh vacuum reflection electron microscopy and atomic force microscopy is presented. Monatomic step pattern and nanoclaster distribution was analysed to be applied for silicon based nanostructure technology. Dynamic structural processes on the stepped silicon surface at the initial stages of epitaxial growth, adsorption, sublimation and gas reactions are under consideration. Obtained results provide new opportunities for better understanding elementary structural acts on semiconductor surfaces during nanostructure fabrication.

Introduction

Evolution of a crystal surface determines by the migration of adsorbed atoms on this surface that explains increasing interest to elementary acts occurring on the crystal surface during epitaxial growth. The main research efforts are concentrated on the study of kinetics of adsorbed atoms and mechanisms of them interaction with the surface sources because that has technologic aspects for crystal growth. Now the progress in development of the nanotechnology demands fabrication the thin films with well-defined chemical composition, structure, level of impurity doping and perfect qualitative properties of the structure of the interface.

In spite of mutual structural investigations of the atomically clean semiconductor surfaces, there are absent the detailed information about morphology, kinetics of adatoms and the mechanisms of them interaction with surface sinks. Preferably that deals with problems of the visualization of the elementary (atomic) acts with a high special resolution at elevated temperatures in spite of high progress in this field during last years. It makes difficult to solve the applied problems: preparation of the perfect surface-substrate with required surface profile and evaluation the data about kinetics of surface rearrangements that is necessary to control the density of the surface sinks for adatoms, determination the mechanism of thin films growth.

1. Experimental

Development of the methods allowing to visualize the structure of a surface makes available to study the structure of surface and kinetics of surface processes with a high spatial resolution sufficient for imaging the single monatomic steps and superstructure domains. One of the sophisticated methods of structurtal diagnostic is ultra-high vacuum reflection electron microscopy (UHV-REM), which meets the following requirements: (i) supplying with the high spatial resolution (equal or less then size of interplane spacing), (ii) providing for the UHV condition around of the sample, (iii) carrying out *in situ* experiments on heating, cooling, epitaxy, adsorption, deformation, gas exposure, etc., and (iv) allowing the real-time registration of dynamic processes.

To demonstrate some benefits of complex structural investigations, *in situ* UHV-REM and *ex situ* atomic force microscopy (AFM) have been applied to investigate stepped silicon surface morphology during thermal annealing, epitaxial growth, sublimation, metal adsorption and gas reactions at the surface. Atomic force microscope, Solver P-47 H (NT-MDT, Zelenograd), at ambient conditions has been applied to investigate stepped surface morphology after lifting from an ultrahigh vacuum chamber of a reflection microscope.

2. Step redistribution

The monatomic step moves in the step-up direction during sublimation due to the atoms detachment from step kinks, diffusion along the surface and desorption from the terrace. This step motion can be observed by REM up to the crystal melting temperature. The step motion depends on the temperature and the distance between neighboring steps. According to competition of two tendencies: free energy minimisations and system entropy increasing, the straight monatomic step is unstable against to step shape meandering. Temporal and amplitude analysis of these fluctuations at thermodynamical equilibrium allows to deduce a number of important parameters of adatoms and steps.

The system of diffusion linked steps was found to be unstable in respect to step fluctuations, which is the reason of rearrangement of regular monatomic steps into step bunches on the Si(111) surface during sublimation. Note that the phenomenon of step bunching is completely reversible and depends strongly on the direction of the electric current used for specimen heating [1]. The step bunching suggests an electromigration effect of silicon adatoms with an effective charge in the applied electric field. Step bunching and electromigration of adatoms are under active discussion in the frames of experimental and theoretical considerations. Also surface instability was discovered on the silicon (111) surface due to step rearrangement during phase transitions at polynucleation of the reconstructed domains on the surface.

To display the role of the effective charge of adatoms in step bunching, a small amount of gold atoms was deposited on the Si(111) surface at bunching temperatures. It was found that, in the case of sample heating by direct current in step-up direction, the regular steps on the clean surface were unstable after sub-monolayer gold adsorption, while step bunches were transformed to the regular steps on the gold adsorbed surface during heating by DC in step-down direction. One can proposes that gold adsorption changes the sign of the effective charge of silicon adatoms from positive to negative one. At this temperature range the value of the adatom effective charge was

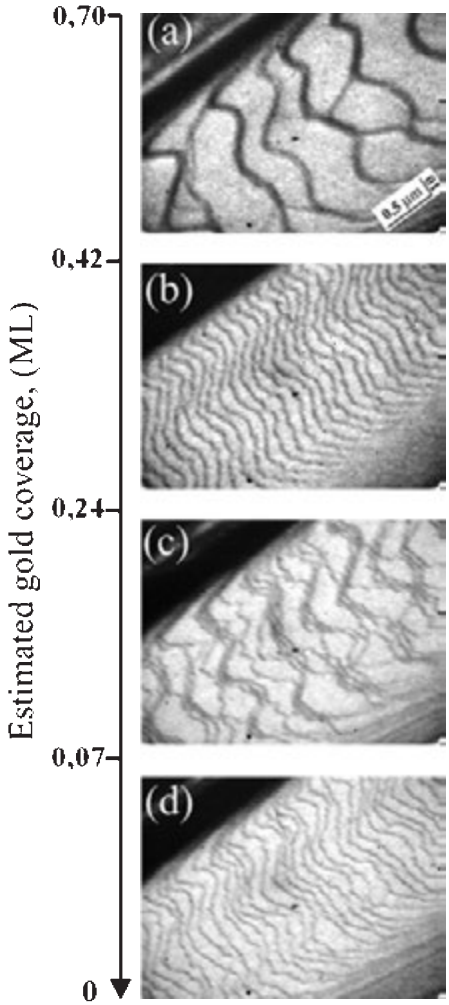

Fig. 1. REM-images of Si(111) surface morphology during thermal annealing at 900 °C after deposition of 0.7 ML of gold (a–d). See details in the text.

evaluated to be 0.004 ± 0.001 in units of the electron charge. Moreover *in situ* UHV REM has been applied to investigate the impact of adsorbed gold atoms on Si(111) surface morphology stability at elevated temperatures (830–1260 °C) in the case of the direct electrical current heating of the sample. New phenomenon of the surface morphology instability was observed on the gold covered surface by means of periodic redistribution of the regular atomic steps (RS) into the step bunches (SB) and vice versa as the gold coverage decreased [2].

Fig. 1 represents series of REM-images illustrated the Si(111) surface morphology transformations after deposition of 0.75 ML of gold and subsequent annealing at 900 °C in the case of step-up current direction. At once no additional reflections corresponding to surface reconstruction were observed at the RHEED pattern at this temperature. During high temperature annealing a decreasing of gold concentration should be due to gold evaporation and gold dissolving into the bulk. After 16 minutes of annealing the step bunched structure (Fig. 1a) was fluently transformed into an array of regular steps (Fig. 1b). Subsequent isothermal annealing at 900 °C in an ultrahigh vacuum chamber during 23 minutes caused step bunching (Fig. 1c). Further annealing during 27 minutes caused the formation of regular steps on the surface (Fig. 1d). Thus, isothermal annealing at 900 °C is accompanied by the following transitions on the silicon surface with predeposited 0.75 monolayer gold coverage: RS (0.72)⇒ SB (0.42) ⇒ RS (0.24) ⇒ SB (0.07) ⇒ RS(0). The numbers given in parentheses are estimated values of the critical gold coverage measured in monolayers at which the morphological transitions are observed.

Decreasing of gold atoms concentration during annealing should be due to both evaporation and dissolving into silicon bulk. Switching the direction of the direct electric current used to sample heating leads to the reversible changes RS ⇒ SB and SB ⇒ RS at the same values of gold coverage [4]. The critical gold concentrations required for changing of the surface relief were determined at different temperatures and directions of DC passing through the sample. The silicon (111) surface was characterised only regular steps for sample heating by an alternative current in the investigated range of gold coverages (0–0.7 ML).

Analysis of REM-images of three-dimensional gold islands nucleated at enough high gold supersaturation showed a dominating migration of the islands on the silicon (111) surface in step-up direction. This migration was independent on the direction of the DC heating of the crystal. The smaller gold islands moved faster than the larger ones due to smaller interaction energy with the silicon substrate. Continued coalescence of small gold particles into the larger one led to an increase of average size of the 3D-islands, but the total amount of the islands was reduced. The 3D-islands showed a tendency to orient along step bunch. No interaction between the gold islands and single monatomic steps was observed at high temperatures.

3. Formation of large step-free area

For investigation of the atomic mechanisms of surface transformations one need to reduce the impact of the atomic steps. It may be achieved by creating wide terraces between steps. There are several ways to produce areas on the silicon surface with extremely small atomic steps density. One of the ways is to use the so-called "mesa"-structured surfaces and another one is based on self-reordering of the atomic steps on the silicon surface.

To form a large step free area, we used phenomenon of a step distribution instability at the silicon surface at the conditions of sample heating by direct electrical current. Step bunching effect allows us to control the spatial distribution of the atomic steps by means of step redistribution. By using step bunching, extra large terraces with maximum width up to 100 μm were achieved [3]. The process of step bunching on silicon surface in the UHV chamber was controlled routinely by REM. After high temperature annealing the sample was cooled down to room temperature and transferred from UHV microscope. The average roughness of the silicon surface with natural oxide measured by AFM was less than one angstrom at the area between monatomic steps.

4. Surface morphology after quenching

Figure 2a represents AFM-image of the silicon surface after quenching from 1100 °C with cooling rate of 400 °C/s. One can see that high density of triangular islands having dark contrast were formed on the terraces after quenching. Shape and

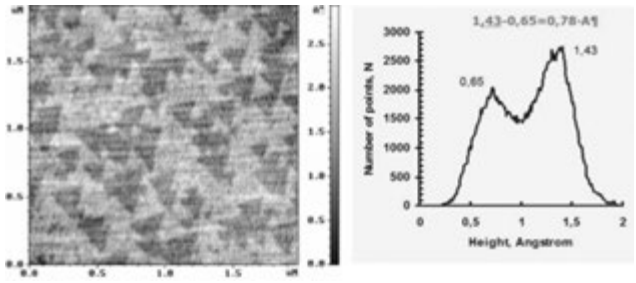

Fig. 2. Typical ACM-image of silicon (111) surface morphology after quenching from 1200 °C (a) and corresponding a height spectrum from the same AFM-image (b).

distribution of the islands follows a three-fold symmetry of the Si(111)-7 × 7 surface structure. Narrow denuded zones, free of islands, were observed along the atomic step on the both terraces. An average width of denuded zone on the upper terrace was measured by AFM to be equalled 0.20 ± 0.02 μm and on the bottom terrace — 0.22 ± 0.04 μm.

Contrast analysis shows that the island depth is less than the height of the monatomic step. Figure 2b shows corresponding height spectra from the area with islands on the terrace. The average depth of these islands is approximately 0.08 nm that is sufficiently smaller than the step height on the Si(111) surface. Similar experiments on the quenching of a silicon surface, performed by means of UHV-STM technique, confirmed the depth measurements by AFM and showed that an area within the negative island has the (7 × 7) surface phase. From the analysis of the temperature dependencies of density of the negative islands it was shown, that the effective activation energy of island growth is 0.35 ± 0.05 eV.

The surface density of negative islands was measured to be dependent on the temperature, whereas the size of the triangular islands did not alter during changing the quenching temperature. The temperature independence of the island shape allows us to conclude that negative island nucleation during quenching is due to accumulation of vacancies during the growth of the (7 × 7) and other surface phases. There are at least three possible sources of vacancies: the adatom sublimation from the surface, transportation of bulk vacancies to the surface and generation of surface vacancies during the (1 × 1) ⇒ (7 × 7) transition. From the velocity of step motion on the Si(111) surface at 1260 °C measured by in situ UHV-REM experiments, a possible step shift during the quenching time is about 50 nm. This corresponds to the density of generated vacancies 8×10^9 cm^{-2} which is much smaller than that one measured experimentally. It means that the role of sublimation on vacancy formation during quenching is negligible.

According to estimations the vacancy concentration near melting point is about 10^{15} cm^{-3} for silicon crystal. The diffusion length of vacancies is 200 μm guessing the quenching time to be equal one second and the diffusion coefficient 5×10^{-4} cm^2/s. Assuming that the whole bulk vacancies drain to the surface during quenching from 1380 °C with the diffusion length, the density of surface vacancies reaches approximately 2×10^{13} cm^{-2}. The changing quenching temperature from 1250 °C, with the bulk vacancy concentration near 10^{13} cm^{-3}, to 1100 °C reduces the density of surface vacancies from 2×10^{11} to 2×10^9 cm^{-2}. These estimations clearly show drastic changing of surface vacancy concentration. Since the area of the negative islands does not depend experimentally on quenching temperature hence, the drain of bulk vacancies to the surface does not influence island formation.

The source of vacancy formation might be the (1 × 1) ⇒ (7 × 7) transition which is supplemented by generation of the additional adatoms on the silicon surface that can change the surface morphology. The structures and energies of adatom vacancies on the Si(111)-(7 × 7) surface were studied by tight-binding molecular dynamics calculation. Adatom vacancies on the edge of the (7 × 7) unit cell were found to have formation energies lower than those of corner of the unit cell by about 0.1 eV. This calculation is in agreement with our result that the negative islands 0.08 nm in depth, are formed at the large step-free areas of Si(111) surface after quenching from high temperature. Thus, while rapid cooling allows to freeze the step distribution on the surface, the significant atomic transformation occurs due to changing of the surface superstructure. Generation of point defects during the (1 × 1) ⇒ (7 × 7) surface phase transition assumes to be responsible for the island formation [5].

5. Conclusion

In conclusion, the in situ observation of monatomic steps behaviour on the silicon surfaces by UHV-REM allows to evaluate a lot of important parameters described the surface processes of sublimation, growth, thermal annealing, adsorption, gas reaction and phase transitions. UHV-REM tolerates to carry out in situ experiments with a high spatial resolution on various physical phenomena on a crystal surface, to optimize the methods of surface cleaning, to study the desorption kinetics of various coverings from a surface, to research the crystal structure and local stress of atomically clean surface in monolayer level, to analyse the superstructural phase transitions on a surface, to examine atomic mechanisms of evaporation and epitaxial growth, to explore processes of reorganization of a surface and to form epitaxial and dielectric films.

Acknowledgements

Author expresses thanks to co-workers of original papers: A. L. Aseev, S. S. Kosolobov, E. E. Rodyakina and D. V. Sheglov. This work was partly supported by Russian Found of Basic Researches, Grant 07-02-10003 and scientific school N3766.2008.8.

References

[1] D. A. Nasimov *et al*, *Phys. Low-Dim. Struct.* **3**, 157 (2003).
[2] A. V. Latyshev *et al*, *Surf. Sci.* **213**, 157 (1989).
[3] A. L. Aseev *et al*, *Phys. Stat. Sol. (a)* **202**, 2344 (2005).
[4] S. S. Kosolobov *et al*, *JETP Lett.* **81**, 149 (2005).
[5] S. S. Kosolobov *et al*, *Phys. Semicon.* **41**, 462 (2007).

16th Int. Symp. "Nanostructures: Physics and Technology"
Vladivostok, Russia, July 14–18, 2008

Multilayer silicon-silicide heteronanostructures with buried semiconductor silicide nanocrystallites: growth, properties and device perspectives

N. G. Galkin
Institute for Automation and Control Processes of FEB RAS, Vladivostok, Russia

Abstract. Studies of nanosize (5–50 nm) island formation of Fe, Cr and Mg silicides on Si(111)7 × 7 and Si(100)2 × 1 surfaces, silicon growth atop nanosize silicide islands and multilayer repetition of developed growth procedure for all silicides have been carried out. Optimization of growth parameters has permitted to create monolithic multilayer heteronanostructures with buried nanocrystallites of iron and chromium disilicides. Only polycrystalline multilayer heteronanostructures with buried Mg_2Si nanocrystallites have been created after optimization of growth procedures. Optical properties and electrical properties of multilayer heteronanostructures have been studied and device perspectives have been discussed.

Introduction

Semiconductor materials created on the basis of buried nanocrystallites, including semiconductor silicide (β-$FeSi_2$, $CrSi_2$ and Mg_2Si) nanocrystallites in silicon matrix, can possess new optical, electrical and thermoelectrical properties, which are important for construction of new kinds of device structures. It is known, that iron disilicide nanocrystallites with large sizes (100–120 nm), which are far from quantum confinement regime, demonstrate electroluminescence [1] in the energy range of 0.80–0.84 eV, when it's buried in the p-layer of silicon p-n mesa-diode.

In this report we compare growth conditions for the formation of multilayer silicon-silicide heteronanostructures with buried semiconductor silicide (β-$FeSi_2$, $CrSi_2$ and Mg_2Si) nanocrystallites (NC's), discuss the structure of buried NC's, optical and thermoelectrical properties of grown heteronanostructures and perspectives of their applications.

1. Results and discussions

1.1. Nanosize island formation

A comparison of nanosize silicide island formation for Fe, Cr and Mg on silicon substrates has shown that minimal sizes of islands depend on initial metal thickness, growth mode, temperature and lattice mismatch of silicon and silicides [2]. For iron and chromium disilicide formation by reactive deposition epitaxy method, small deposition rates and near the same substrate temperatures (475–550) °C have been used. For iron disilicide three types of disilicides (α, β, γ) are known. It was shown that for β-$FeSi_2$ island formation Fe thickness could not be smaller than 0.4–0.5 nm, since at smaller thicknesses metal disilicides are formed on silicon surface. As a result of Fe thickness deposited on Si the formed disilicide islands have big lateral sizes (20–70 nm) and big average height (5 nm). Therefore, both lateral and bulk diffusion processes of Fe and Si atoms are involved in the silicidation process that results in wide distribution of island sizes and heights. However for $CrSi_2$ island formation essential smaller values of Cr thickness (0.06–0.07 nm) have been used, since $CrSi_2$ is a first silicide phase, which is formed at 500–550 °C in Si(111)-Cr system. As compared with Si(111)-Fe system the smaller silicon surface transport has been observed during silicidation process in Si(111)-Cr system. Therefore, Cr atoms mainly react with silicon atoms account for the Si or Cr bulk diffusion. Si(111)-Mg system shows another behaviour during silicidation process as compared with Si-Cr and Si-Fe systems. It is very difficult to obtain nanosize Mg_2Si islands on silicon surface during reactive deposition epitaxy of Mg at temperatures higher than 200 °C because of a zero value of Mg sticking coefficient. Another approach has been developed in this case. This is a solid phase annealing of some Mg thickness (1.0 nm) at temperature of 375 °C, which is enough for partial desorption of Mg and silicidation of residual Mg atoms with silicon atoms in surface layer. But this temperature is small enough for a decomposition of formed Mg_2Si nanosize islands.

1.2. Silicon overgrowth atop nanosize islands

Silicon epitaxial growth atop nanosize semiconductor silicide islands is very important task, since it is desirable to grow smooth silicon layer with buried NC's and obtain a minimal silicon thickness.

Compare a silicon overgrowth above iron and chromium disilicides [3,4]. During a growth of silicon layer above nanosize iron disilicide islands on Si(111) substrate only big (30–70 nm) β-$FeSi_2$ NC's are formed inside silicon matrix. Nanocrystallites have relaxed crystalline form, but in silicon matrix dislocation are usually formed [3]. NC's of smaller sizes (5–15 nm) have not been observed. Therefore, coalescence and crystallization of β-$FeSi_2$ islands on Si(111) surface are more energetically favorable as compared with growth of high-density nanosize islands. A growth of silicon above iron silicide islands on Si (100) substrate brings to a formation of different type of elastically strained iron disilicide nanocrystallites [4]. In this case a formation of small and big islands of iron disilicides has near equal probability from thermodynamic point of view. The size distribution conserves during a silicon overgrowth, so silicon epitaxial growth occurs mainly in 2D mode. A bulk pseudomorphism of small β-$FeSi_2$ nanocrystallites (4–6 nm) inside silicon matrix can lead to strong changes of its electronic structure in the directions of lattice compression. Silicon epitaxial overgrowth above $CrSi_2$ nanosize islands has shown that in Si-Cr system a 2D growth mode is preferentially

conserved owing to the small sizes (10–40 nm) and heights (1–2 nm) of $CrSi_2$ islands and absence of coagulation and coalescence. Decrease of silicide island sizes brings to the decrease of silicon layer thickness, which is necessary for full burying of $CrSi_2$ nanocrystallites in silicon matrix. In both cases monolithic heteronanostructures with buried semiconductor silicide nanocrystallites have been grown.

Comparing the silicon overgrowth above Mg_2Si nanosize islands with silicon overgrowth above β-$FeSi_2$ (or $CrSi_2$) nanosize islands and silicon structures in both cases has shown that 3D mechanism of silicon growth brings to the breaking of epitaxial ordering. An absence of 2D growth mechanism is a consequence of breakdown of silicon surface reconstruction during the formation of Mg_2Si nanosize islands and eliminating of surface diffusion of silicon atoms during solid phase growth. Seemingly the MBE growth mode of silicon above Mg_2Si islands must be chosen, but an optimization of growth temperature and silicon deposition rate must be carried out for a creation of monolithic heteroepitaxial structure Si(111)/NC's Mg_2Si/Si.

1.3. Monolithic silicon-silicide heteronanostructures

Using the obtained parameters for growth of iron silicide islands and epitaxial growth of Si, the monolithic heterostructures with 8 and 10 layers were formed on Si(100) substrates [3]. In 8-layer structure the distance between layers was 100 nm and a growth was controlled by LEED. The sample surface of 8-layer sample is smooth ($\sigma_{\rm rms} = 0.28$ nm) by AFM data and defects are absent. On each growth stage a bright 2×1 LEED pattern was obtained. So, an epitaxial growth was observed on every stage of silicon deposition. In multilayer sample the β-$FeSi_2$ NC's (with Moiré pictures) and γ-$FeSi_2$ NC's (Moiré picture is absent) have been observed by HR TEM data [4].

For a growth of monolithic silicon structures with few buried layers of $CrSi_2$ nanocrystallites the substrate temperature of 750 °C and silicon layer thickness of 35 nm were selected. Three samples with 2, 4 and 6 layers of buried $CrSi_2$ nanocrystallites were grown [5]. Si(111)7×7 patterns were preserved for all cases that corresponds to a formation of monolithic heteronanostructures based on silicon. A study of morphology has shown that a film surface consists of triangle crystallites, which have an increased surface relief. However, crystallite sizes are about 500 nm that permit to observe a Si(111)7×7 LEED pattern from them. Good quality of LEED patterns and small value of rms testifies about creation of monolithic epitaxial multilayer structures on the base of silicon and $CrSi_2$.

An absence of epitaxial ordering in Si(111)/NC's Mg_2Si/Si in each layer of heterostructures brings to surface roughness and increase of an effective thickness of nanocrystallite layer inside silicon matrix at the expense of nanocrystallite moving along surface relief [6]. So, a solid phase growth of multilayer structures with buried Mg_2Si NC's is not appropriate to a creation of monolithic multilayer structures. The growth conditions for molecular beam epitaxial growth must be found and optimized.

1.4. Study of monolithic heteronanostructure properties

A contribution of all studied silicides into the electronic structure of multilayer structures in the 1.5–3.0 eV photon energy range was determined from calculated optical functions. The phonon structure of grown multilayer samples was studied on the basis of an analysis of two-phonon and three-phonon resonances in silicon and semiconductor silicide NC's. The huge increase (in 50–180 times) of a thermoelectric power coefficient for samples with buried semiconductor silicide NC's in comparing with one for the bare p-type silicon substrate has been observed. Perspectives of such silicon-based materials in thermoelectronics are evident.

The photoluminescence (PL) at 5 K was observed at 1.55 micron in the Si(100)/NC's β-$FeSi_2$/Si(100)-epi heteronanostructures grown by solid phase epitaxy method. It was shown that PL line width and its amplitude depends on crystalline quality of β-$FeSi_2$ NC's and it's interface with silicon lattice. Such multilayer heteronanostructures can be used in silicon-based light emitting diodes.

Acknowledgements

An author is grateful to the researchers of IACP FEB RAS, ISP SB RAS and RI TPMS (Hungary) for carrying out the main part of experiments with silicon-silicide heteronanostructures. The work was performed with financial support from the RFBR grant No. 07-02-00958_a.

References

[1] T. Suemasua *et al*, *Appl. Phys. Lett.* **79**, 1804 (2001).
[2] N. G. Galkin, *Thin Solid Films* **515**, 8179 (2007).
[3] N. G. Galkin *et al*, *J. Nanosci. and Nanotechnol.* doi:10.1166/jnn.2007.A093.
[4] N. G. Galkin *et al*, *Thin Solid Film* **515**, 7805 (2007).
[5] N. G. Galkin *et al*, *Technical Physics* **52**, 1079 (2007).
[6] N. G. Galkin *et al*, *e-J. Surf. Sci. and Technol.* **3**, 12 (2005).

16th Int. Symp. "Nanostructures: Physics and Technology"
Vladivostok, Russia, July 14–18, 2008

Si/β-$FeSi_2$/Si heteronanostructures fabricated by ion implantation and Si MBE: growth, structural and luminescence properties

N. G. Galkin[1], *E. A. Chusovitin*[1], D. L. Goroshko[1], R. I. Batalov[2], R. M. Bayazitov[2], T. S. Shamirzaev[3], A. K. Gutakovsky[3], K. S. Zhuravlev[3] and A. V. Latyshev[3]

[1] Institute for Automation and Control Processes of FEB RAS, Vladivostok, Russia
[2] Kazan Physical-Technical Institute of RAS, Kazan, Russia
[3] Institute of Semiconductor Physics of SB RAS, Novosibirsk, Russia

Abstract. The method of ultrahigh vacuum low-temperature ($T = 850$ °C) cleaning of Si(100) and Si(111) samples implanted by iron ions (Fe^+) with different implanted fluencies ($\Phi = 10^{15}$–1.8×10^{17} cm^{-2}) has been applied for the first time. The possibility of the formation of atomically smooth and reconstructed Si surfaces after Fe^+ implantation and nanosecond pulsed ion-beam treatment has been shown. It was found that smooth Si films with thickness up to 1.7 μm and with reconstructed surface grow up to implanted fluence $\Phi = 10^{16}$ cm^{-2}. Preservation of β-$FeSi_2$ nanocrystallites inside silicon matrix after cleaning and formation of a cap epitaxial Si layer has been confirmed by transmission electron microscopy data, optical spectroscopy data and existing of photoluminescence peak at 0.75–0.85 eV during temperature range of 5–150 K.

Introduction

In recent years the considerable attention has been paid to the formation of isolated precipitates and continuous layers of semiconducting iron disilicide (β-$FeSi_2$) in Si due to the possibility of application of β-$FeSi_2$ in optoelectronics as a light emitter in the 1.5–1.6 μm range. The main methods for the formation of β-$FeSi_2$ are Fe^+ implantation of Si [1] and reactive deposition epitaxy of Fe layers followed by molecular beam epitaxy (MBE) of Si layer [2]. Both methods include the high-temperature (up to 900 °C) and long-time (up to 20 hours) furnace annealing undesirable for device structures because their parameters essentially degrade at elevated temperatures. We have demonstrated earlier the formation of β-$FeSi_2$/Si heterostructures by low-energy Fe^+ implantation and pulsed treatments by ion and laser beams [3]. For subsequent fabrication of light-emitting diode the formation of Si/β-$FeSi_2$/Si heterostructures is preferable.

In this paper a new low temperature growth technology including ion implantation and Si MBE is applied for the first time. The structural and optical properties of the grown Si/β-$FeSi_2$/Si heterostructures are studied.

1. Experimental

The implantation of Fe^+ ions into monocrystalline Si wafers with (100) and (111) orientations was carried out at room temperature with ion energy $E = 40$ keV ($R_p = 37$ nm, $\Delta R_p = 13$ nm) and fluencies $\Phi = 10^{15}$–1.8×10^{17} cm^{-2}. The details of sample preparations are given in Table 1. Pulsed ion-beam treatment (PIBT) of the implanted Si layers was carried out using pulsed ion accelerator with high-energy nanosecond carbon ion beams (C^+, $E = 300$ keV, $\tau = 50$ ns). Pulse energy density varied between $W = 1.2$–1.5 J/cm^2 and fluence of C^+ ions implanted into Si during PIBT does not exceed $\approx 10^{13}$ cm^{-2}.

Si overgrowth was performed in two UHV chambers with base pressures $p = 10^{-10}$ Torr and $p = 10^{-9}$ Torr. Both chambers were equipped with sublimation p-type Si sources ($N_p = 10^{-16}$ cm^{-3}) for MBE growth. The first chamber was equipped with Auger electron spectrometer (AES) used for measuring of impurity concentrations on Si surface before and after cleaning procedure, the last one had the low energy electron diffraction (LEED) facility for *in-situ* studying of the structure of the grown Si layers. Si deposition rate was controlled by quartz sensor of thickness. Si samples were annealed by applying of direct current.

Table 1. Parameters of Samples.

Sample	Substrate	Implanted dose, cm^{-2}	Conductivity type	Resistivity (Ohm cm)
A	Si(111)	10^{16}	*p*	20
B	Si(111)	1.8×10^{17}	*p*	20
C	Si(100)	10^{15}	*n*	4.5
D	Si(100)	10^{16}	*n*	4.5
E	Si(100)	1.8×10^{17}	*n*	4.5

Photoluminescence (PL) measurements (5–150 K) were carried out (ISP SB RAS) by means of He-Ne laser ($\lambda = 632.8$ nm, $J = 40$ mW/cm^2). PL spectra were analyzed in spectrometer on the basis of double monochromator and detected by Ge photodiode "Edinburgh Instruments".

2. Results and discussion

According to TEM data [4] an implantation of Fe^+ ions into monocrystalline Si wafers with (100) and (111) orientations leads to nanocrystallites formation in near surface region about 100 nm in size if implanted fluence doesn't exceed 1×10^{16} cm^{-2}. An increase of implanted fluence results in coalescence processes up to continuous layer formation at fluence about 1×10^{17} cm^{-2}.

Sample *A* surface after PIBT (Table 1) represents nearly periodical structure of alternative round or oval shaped areas, 300–500 nm in diameter. These areas are situated 3–4 nm lower

than the rest of the surface and they represent the cellular structure of Si layer which was observed in [3] by TEM. Increase of implanted fluences of Fe^+ ions (by 18 times for the sample B) leads to considerable increase of surface relief; hills and holes were formed with height and depth of 20–30 nm with respect to some mean level. This attributed to higher content of iron impurity in the near-surface Si layer and significant mass transfer during PIBT due to deep melting of Si (up to 1 μm). The formation of cellular structure is related to low solubility of Fe in Si and to Fe segregation on Si cell walls due to instability of the solidifying interface.

The sample C implanted with the lowest fluence $\Phi = 10^{15}$ cm^{-2} has the minimal root-mean square roughness ($\sigma_{\rm rms} =$ 0.23 nm) after PIBT. Si surface implanted with fluence $\Phi = 10^{16}$ cm^{-2} (sample D) is quite smooth ($\sigma_{\rm rms} = 0.4$ nm). Increase of the fluence up to 1.8×10^{17} cm^{-2} (sample E) results in the increase of local surface non-uniformity as well as occurrence of areas with large relief ($\sigma_{\rm rms} = 2.62$ nm) and with iron disilicide crystallites inside that have moved up and occurred on the surface in the form of granular film. The formation of β-$FeSi_2$ phase is confirmed by optical reflectance spectroscopy data, type of absorption coefficient spectra and the presence of interband transitions (2.7 eV) corresponding to β-$FeSi_2$ (2.57 eV, [5]).

A new low-temperature (LT) cleaning procedure suitable for Si overgrowth upon Si layers implanted by Fe^+ ions has been studied. The sample kept at $T = 850$ °C was exposed to the Si atomic flow with small rate of about 0.1 nm/min for 15–20 minutes, which provides decomposition of SiO_2 firstly to SiO and then to Si and O_2 (gas). AES data revealed that all oxide and carbon contaminations were completely removed and clean Si surface was obtained as a result of this procedure. This procedure was successfully applied for the first time for Fe^+ implanted samples.

Si overgrowth on the surface of all samples was performed after LT cleaning. After Si overgrowth ($T_{\rm Si} = 700$ °C) on the sample C a smooth ($\sigma_{\rm rms} = 0.08$ nm) epitaxial film with thickness of 1700 nm was obtained and LEED Si(100)2 × 1 pattern was observed without any additional annealing. Si overgrowth with the same growth parameters on the sample D resulted in the obtaining of an epitaxial film (1700 nm) demonstrating LEED Si(100)2 × 1 pattern although after LT cleaning LEED pattern was not observed. Hence, the annealing of defects on the surface takes place during Si deposition and then the growth goes on epitaxially and surface ordering takes place. The increasing of the fluence up to 1.8×10^{17} cm^{-2} (sample E) results in polycrystalline growth of silicon and the sample surface becomes rougher ($\sigma_{\rm rms} = 86.2$ nm). The pinholes observed in AFM images indicate a 3D growth mechanism and agglomeration of Si crystallites. The similar tendency was observed during Si overgrowth on the samples A and B after LT cleaning; however, the surface roughness was 7.0 nm and 11.8 nm, respectively. The reflection spectroscopy data obtained from all samples after Si overgrowth reveal that in the energy range below 2 eV the behaviour of the reflection coefficient is in line with that for silicon. Hence, β-$FeSi_2$ crystallites do not occur on the surface after Si overgrowth.

The discovered optical interference in p-type Si layers grown onto the surface of Fe-implanted layers in the transparency

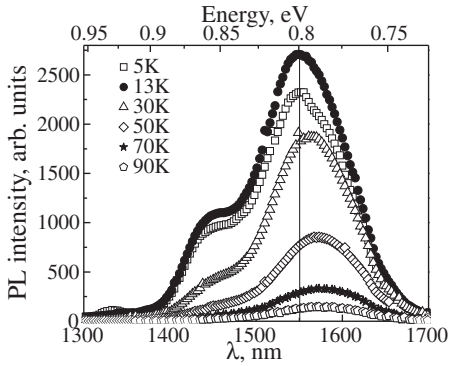

Fig. 1. PL spectra of sample D registered at different temperatures.

wavelength range (higher 1200 nm) proves a formation of abrupt interfaces in grown heteronanostructures.

The study of PL properties of Si/β-$FeSi_2$/Si heteronanostructures obtained by ion implantation, PIBT and MBE has been carried out. It was shown that intensity of PL depends on a dose of implanted iron, crystalline quality of grown epitaxial silicon layer and substrate orientation. From the PL spectrums of sample D obtained at different temperatures (Fig. 1) we plot the temperature dependence of amplitude of the PL band near 0.8 eV and approximated it by the equation follow.

$$I(T) = \frac{I_0}{1 + C_1 \exp\left(\frac{-E_1}{kT}\right) + C_2 \exp\left(\frac{-E_2}{kT}\right)}.$$

Here, C_1 and C_2 are weighting coefficients, E_1 and E_2 are activation energies of the decay process, and I_0 is the PL intensity at a temperature close to absolute zero. The values of activation energies ($E_1 = 41$ meV and $E_2 = 12$ meV) were determined by fitting the theoretical curve to the experimental data. From the comparison of E_1 and E_2 values with activation energy of dislocation line D_1 (≈10 meV) we can conclude that this line makes a contribution to PL signal and E_1 energy apparently relates to PL signal from β-$FeSi_2$ precipitates. Furthermore we observe a red shift of the PL band near 0.8 eV in the temperature range 5–70 K (≈15 meV) whereas energy position of D_1 line in this range almost preserve.

Recently we have obtained planar TEM images of sample D. They showed us a high density of dislocations (5.3×10^9 cm^{-2}), which confirms our PL data for sample D. An origin of these dislocations apparently is the implanted substrate because our AFM and LEED data testifies that cap silicon layer was grown epitaxially. So the dislocations just have come up from the substrate.

Acknowledgements

The work was performed with financial support from the FEB RAS grants No. 06-I-P1-001, No. 06-I-DPS-118, SB RAS grant No. 3.18, RFBR grant No. 08-02-01280-a and Russian Science Support Foundation.

References

[1] K. Oyoshi *et al*, *Thin Solid Films* **381**, 194 (2001).
[2] T. Suemasu *et al*, *Thin Solid Films* **381**, 209 (2001).
[3] R. Bayazitov *et al*, *Nucl. Instr. Meth.* **B24**, 224 (2005).
[4] K. Oyoshi *et al*, *Thin Solid Films* **381**, 202 (2001).
[5] J. Chrost *et al*, *Surf. Sci.* **330**, 34 (1995).

16th Int. Symp. "Nanostructures: Physics and Technology"
Vladivostok, Russia, July 14–18, 2008

Formation, structural and optical properties of two-dimensional silicide phases in Si(111)/Mg system

K. N. Galkin[1], S. A. Dotsenko[1], N. G. Galkin[1], V. V. Korobtsov[1], Mahesh Kumar[2], Govind[2] and S. M. Shivaprasad[2]

[1] Institute for Automation and Control Processes of FEB RAS, Vladivostok, Russia
[2] Surface Physics and Nanostructures Group, National Physical Laboratory, Dr. K. S. Krishnan Road, New Delhi, India

Abstract. Initial stages of the silicide formation process at room and elevated temperatures (100–200 °C) have been studied by electronic spectroscopy methods (AES and EELS) at ultra high vacuum conditions and constant Mg deposition rate. Crystal structure of two-dimensional silicide layers has been determined by LEED. Optical properties of formed Mg silicides have been controlled at 150 °C by differential reflectance spectroscopy (DRS) in the energy range of 1.13–2.5 eV. Different stages of silicide formation have been observed at different substrate temperature due to increase of Mg desorption rate and decrease of real condensation rate. Optical functions of Mg silicides with (1×1) and $(2/3)\sqrt{3} - R30°$ have been calculated by using a method of dynamic standard.

Introduction

Formation of magnesium silicide (Mg_2Si) epitaxial films on silicon substrates is interesting from the point of view of fundamental growth mechanism problems and technological applications as thermoelectrical material. The formation of various ordered two-dimensional magnesium silicide phases like (1×1) and $(2/3)\sqrt{3} \times (2/3)\sqrt{3} - R30°$ have been shown by researchers [1, 2]. The ones can be a precursor of further epitaxial growth of magnesium thick silicide film However, the atomic and electronic structures and optical properties of these epitaxial phases on silicon are unknown today. Therefore researchers can not find optimal growth conditions of thick epitaxial magnesium silicide films on silicon substrates.

In this paper the formation process, structural and optical properties of two-dimensional magnesium silicide phases on Si(111) substrates at elevated temperatures (100–200 °C) are studied.

1. Experimental

The experiments were performed in two ultra high vacuum chambers ($P_b = 5 \times 10^{-11}$ Torr and 1×10^{-10} Torr of VARIAN firm in India and Russia) equipped with in-situ surface characterization probes such as Auger Electron Spectroscopy (AES), Low Energy Electron Diffraction (LEED) and Electron Energy Loss Spectroscopy (EELS). The VARIAN chamber (in Russia) was additionally equipped with a quartz microbalance sensor, in situ optical spectrometer and halogen lamp for differential reflectance spectroscopy (DRS). The sample was cut (size $6 \times 16 \times 0.32$ mm^3) from a commercial p-type Si(111) wafers with a resistivity of $\rho = 10\ \Omega$cm. The samples were heated at 600 °C by direct current for 5 hours and finally cleaned by flashing at 1250 °C for a few seconds. Cleanliness of the silicon surface was confirmed by AES and LEED. The deposition rate of Mg was regulated by controlling the direct current passing through the Ta K-Cell.

In experiments, which carry out in India, the magnesium was evaporated by portions with duration of 1 min with the deposition rate of about 0.5 nm/min onto the Si(111)7×7 substrate surface held at different temperatures: RT, 100, 150 and 200 °C. After each deposition the AES and EELS data were registered and the formation of surface phases was determined by observing the characteristic LEED pattern. The deposition time has been used to calibrate the adsorption coverages. A flux rate of magnesium evaporation and portion thickness was calculated from EELS adsorption curve for experiment at room substrate temperature.

Optical properties of magnesium silicide phases were studied by DRS method during deposition of Mg at 150 °C (in Russia). Deposition rate of Mg at room temperature was 0.6 nm/min. DRS spectra were registered in the energy range of 1.13–2.5 eV. Obtained spectra were analyzed by a method of dynamic standard [3]. EELS spectra were registered at RT before and after Mg deposition and have a good conformance with "Indian" EELS spectra's.

2. Results and discussion

According to AES and EELS data at room temperature the deposition of Mg results in three stages of Mg-Si(111) interface formation. On the first stage (0-0.5 nm) the nucleation and three-dimensional (3D) growth of Mg silicide islands occur. On the second stage a synchronous growth of magnesium silicide islands and metallic Mg atop silicide islands is observed. This stage was finished after full filling of substrate surface by silicide islands. The third stage is characterized only by a growth of metallic Mg.

An increase of substrate temperature during Mg deposition results in increase of Mg diffusion in silicon lattice and partial changing of mechanism of Si(111)-Mg interface formation. According to AES and EELS data at 100 °C the deposition of Mg results in three stages of Mg-Si(111) interface formation. On the first stage the nucleation and growth of Mg silicide islands occur. On the second stage Mg silicide islands coalesce and new ordered Mg silicide film is formed with $(2/3)\sqrt{3} \times (2/3)\sqrt{3} - R30°$ (further $(2/3)\sqrt{3} - R30°$) structure (by LEED data). On the third stage a formation of metallic Mg islands atop $(2/3)\sqrt{3} - R30°$ silicide layer is observed. Since the substrate temperature is not high enough, the Mg condensation

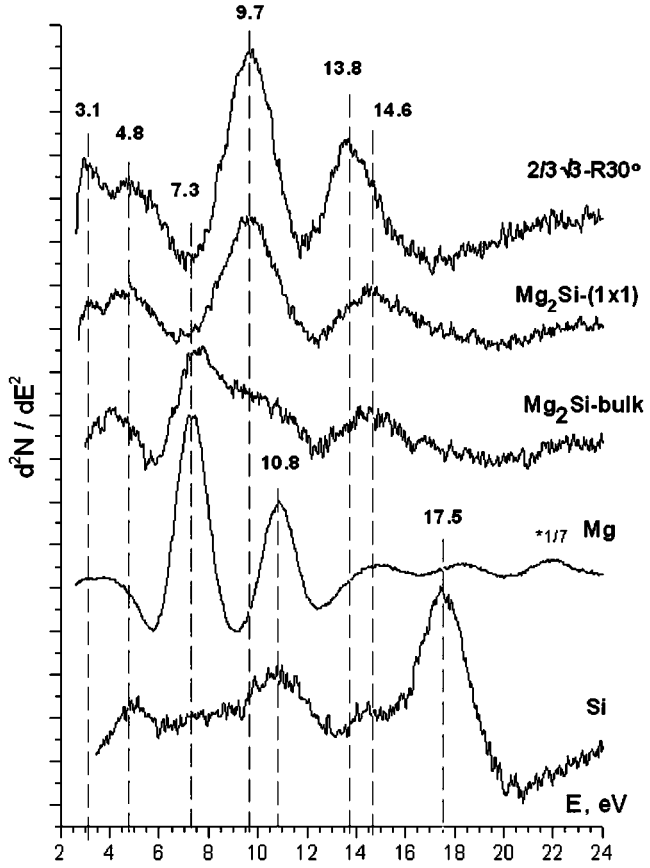

Fig. 1. EELS spectra for Si(111)7 × 7 surface, thick Mg film, Mg_2Si bulk film, Mg_2Si(111)1 × 1 and Mg silicide $(2/3)\sqrt{3} - R30°$.

coefficient to Mg silicide layer is not closed to zero.

At 150 °C the Mg adsorption rate decreases, diffusion of Mg atoms on silicon surface increases, and only two stages of Si(111)-Mg interface formation during Mg deposition are observed. On the first stage a formation of Mg silicide with (1 × 1) LEED structure and strong background is observed. By EELS data (Fig. 1, Mg_2Si-(1 × 1)) this stage is characterized only by plasmon peaks from Mg silicide. Therefore, LEED patterns are mainly determined by a contribution from pseudomorphic Mg silicide film. On the second stage a formation of $(2/3)\sqrt{3} - R30°$ silicide layer is observed by LEED data due to the structural transition. In EELS data a shift of bulk plasmon to 13.8 eV as compared with 14.6 eV for Mg silicide with (1 × 1) LEED structure is observed (Fig. 1). Pseudomorphic film transformed to another ordered 2D Mg silicide film with smaller lattice mismatch (about 1.9%). It is known, that the lattice mismatch between fcc $Mg_2Si(111)$-(1 × 1) ($a = 0.635$ nm) and Si(111)-(1 × 1) ($a = 0.539$ nm) is about 18% [4,5], but lattice mismatch between Mg_2Si(111)-(1 × 1) and Si(111)-$(2/3)\sqrt{3} - R30°$ is about 1.9% [1]. For Mg/Si(111) system K. S. An *et al* [2] was observed the same transfer at room substrate temperature and smaller Mg adsorption rate. Therefore, at 150 °C the sizes of Mg silicide islands are increased on the second growth stage, continuous silicide film is formed, lattice stress relaxes and structural transition to the ordered Mg silicide with $(2/3)\sqrt{3} - R30°$ LEED structure occurs due to the changes in Mg-Si bonds on the Si(111)-Mg interface.

When the substrate temperature was increased to 200 °C another formation mechanism of Si(111)-Mg interface was observed. According to LEED, AES and EELS data only one stage can discriminate from experimental data: formation of Mg silicide islands on Si surface. After third minute of Mg adsorption the saturation of Si and Mg AES-peak intensities and EELS spectra's is observed. This corresponds to the nanosize Mg silicide island formation, the density and form of which are not depended from quantity of deposited Mg atoms. Therefore, Mg accommodation coefficient to the surface is equal to zero.

In the work a new structural model of Mg silicide with $(2/3)\sqrt{3} - R30°$ LEED structure was proposed. It is based on LEED, EELS and AES data and electron beam energy dependence of EELS spectra of Mg silicide film with $(2/3)\sqrt{3} - R30°$ LEED structure. From this analysis a thickness of grown 2D Mg silicide film (about 0.5 nm) was determined. According to the model the Mg silicide with $(2/3)\sqrt{3} - R30°$ LEED structure consists from 3 Mg layers and 2 Si layers with fixed Mg-Si bonds in contradiction with bulk Mg_2Si structure, where Mg-Si bonds are not fixed. It was shown that in proposed model of $(2/3)\sqrt{3} - R30°$ Mg_2Si layer the density of electrons decreases, but effective electron mass increases. Such a model can explain the bulk plasmon shift in EELS spectra.

By DRS data the Mg silicide film grown at 150 °C has the same stages of formation. Since EELS-AES data for both series of experiments had near the same form and grown films were characterised by equal bulk and surface plasmons on the same stages of Mg/Si(111) interface formation. We can determine optical properties of Mg silicide films with (1 × 1) and $(2/3)\sqrt{3} - R30°$ structures from the DRS data. Both silicides are characterised as indirect semiconductors with closed forms of changes of an imaginary part of dielectric functions. But in calculated spectra some shifts of direct interband transitions were observed, which emphasize some changes in the electronic structures of pseudomorphous (1 × 1) structure and partially relaxed $(2/3)\sqrt{3} - R30°$ structure.

Acknowledgements

One of authors (K. N. Galkin) thanks the financial support from Department of Science and Technology, New Delhi, India, to work at National Physical Laboratory, India (NPL) in the year 2006 within the framework of the International Long-Term Program of Scientific and Technical Cooperation between Russia and India. The work executed is also supported by grant of RFBR No. 07-02-00958_a and grant of FEB RAS 06-III-B-02-048.

References

[1] J. Quinn, F. Jona, *Surf. Sci. Lett.* **249**, L307 (1991).
[2] K. S. An *et al*, *J. Appl. Phys.* **78**, 1151 (1995).
[3] N. G. Galkin *et al*, *e-J. Surf. Sci. and Technol.* **3**, 12 (2005).
[4] Peter M. Lee, *Physical Review* **135**, A1110 (1964).
[5] M. Henzler *et al*, *Surface Science* **36**, 109 (1973).

16th Int. Symp. "Nanostructures: Physics and Technology"
Vladivostok, Russia, July 14–18, 2008

Self-organization of $FeSi_2$ nanodots on Si(111)7×7 and Si(111)$\sqrt{3}\times\sqrt{3}$-R30°-B surfaces

M. V. Ivanchenko[1], E. A. Borisenko[1], V. G. Kotlyar[1], O. A. Utas[1], A. V. Zotov[1], A. A. Saranin[1], N. I. Solin[2], L. N. Romashev[2] and V. V. Ustinov[2]

[1] Institute of Automation and Control Processes, Vladivostok, Russia
[2] Institute of Metal Physics, Ekaterinburg, Russia

Abstract. Using scanning tunneling microscopy, solid phase epitaxial (SPE) growth of $FeSi_2$ nanodots on Si(111)7 × 7 and Si(111)$\sqrt{3}$ × $\sqrt{3}$-R30°-B surfaces has been studied in the temperature range of 400–700 °C and Fe coverage of up to 0.5 monolayer. It has been found that the density of the β-$FeSi_2$ nanodots formed on Si(111)$\sqrt{3}$ × $\sqrt{3}$-R30°-B surface is essentially higher than that on Si(111)7 × 7 surface at the same temperature and coverage. The density of the 2 × 2 (γ-$FeSi_2$) islands and structural defects is, in contrast, reduced on Si(111)$\sqrt{3}$ × $\sqrt{3}$-R30°-B surface compared to that on Si(111)7 × 7 surface.

Introduction

The extensive use of optical junctions led to a considerable growth of the interest in direct-band semiconductor silicides. In particular, the wavelength of emission from β-$FeSi_2$ perfectly corresponds to the maximum transmission of fiber-optic structures, which is a necessary pre-requisite for the creation of the effective optical transmitters [1–3]. A promising basis for the development of small-size light-emitting devices is offered by the semiconductor structures involving β-$FeSi_2$ nanoparticles [4–6]. Unfortunately, the emission efficiency drops with increasing temperature and only a few among the numerous papers devoted to such structures have reported on the observation of room-temperature photoluminescence from the β-$FeSi_2$ particles incorporated into *p*-*n* junctions [5]. One of the main factors responsible for the decrease in the emission efficiency is the non-radiative recombination of charge carriers on defects [7].

Although massive β-$FeSi_2$ samples have a stable structure, continuous thin films of this compound are difficult to grow on a Si(111) substrate because the lattice mismatch leads to the island growth. As known, this growth mechanism usually leads to the formation of the islands of several types. In addition to the islands possessing the β-$FeSi_2$ structure (comprising three domains separated by grooves oriented in the [11$\bar{2}$] directions), there appear the γ-$FeSi_2$ islands possessing metallic properties [2] and characterized by a 2 × 2-reconstructed surface [8,9]. Such γ-$FeSi_2$ can play the role of non-radiative recombination centers and together with the surface defects increase the probability of breakdown.

Since an atomic structure of the substrate surface affects the film overgrowth, we have undergone a comparative study of the silicide formation on the Si(111) surfaces of two types, namely atomically-clean Si(111)7 × 7 surface and boron-modified Si(111)$\sqrt{3}$ × $\sqrt{3}$-R30°-B surface. The goal was to find the conditions for the growth of islands with more homogeneous structures and higher density. The growth was conducted in the solid-phase epitaxial (SPE) regime, i.e., using deposition of 0.05–0.50 monolayer (ML) of Fe at room temperature (RT) followed by annealing at 550–770 °C.

Results and Discussion

1. SPE growth on Si(111)7×7 surface

Results of our observations on the growth on Si(111)7 × 7 surface are in general agreement with the known reported data and can be summarized as follows. After SPE growth, the surface typically comprises a mixture of the disordered regions, iron disilicide nanoislands and remaining areas of the pristine 7 × 7 reconstruction. Disordered regions (labeled DR in Fig. 1) nucleate preferentially near the step edges and along the original 7 × 7 domain boundaries, as one can see in Fig. 1(a) showing the surface with 0.2 ML of Fe. With increasing Fe coverage, the disordered regions expand and at 0.5 ML cover the most of the surface area (Fig. 1(b)). Our STM observations have revealed that the structure of the disordered regions is basically similar to that of the so-called "1 × 1"-RC (ring-cluster) phase.

$FeSi_2$ nanoislands are formed at the Si(111)7 × 7 surface upon SPE growth at temperatures above ∼550 °C. They include β-$FeSi_2$ islands, 2×2 (γ-$FeSi_2$) islands and mixed β-$FeSi_2$/2× 2 islands. The typical STM appearance of the islands of the each type is illustrated in Figs. 1(c), (d) and (e). The β-$FeSi_2$ islands have been found to constitute about 3/4 fraction of the total number of islands, while the left 1/4 falls at the 2 × 2 and mixed β-$FeSi_2$/2 × 2 islands. The total number density of all islands does not change noticeably with increasing Fe coverage, the islands only grow in size. The island density is also independent of the annealing temperature, preserving the same value of about 10^{10} cm^{-2} in the whole range of 550 to 700 °C (see Fig. 3).

2. SPE growth on Si(111)$\sqrt{3}\times\sqrt{3}$-B surface

Our STM observations have revealed that SPE growth on the Si(111)$\sqrt{3}$ × $\sqrt{3}$-B surface (Fig. 2) differs from that on the Si(111)7 × 7 surface in many respects [10].

First, no disordered regions (related to the "1 × 1"-RC phase) are formed on the Si(111)$\sqrt{3}$ × $\sqrt{3}$-B surface.

Second, SPE growth on the Si(111)$\sqrt{3}$ × $\sqrt{3}$-B surface results in the almost exclusive formation of only the β-$FeSi_2$ nanoislands, while fraction of the 2 × 2 islands is vanishingly small.

Third, the surface density of the $FeSi_2$ islands on the Si(111) $\sqrt{3}$ × $\sqrt{3}$-B surface demonstrates an apparent dependence on

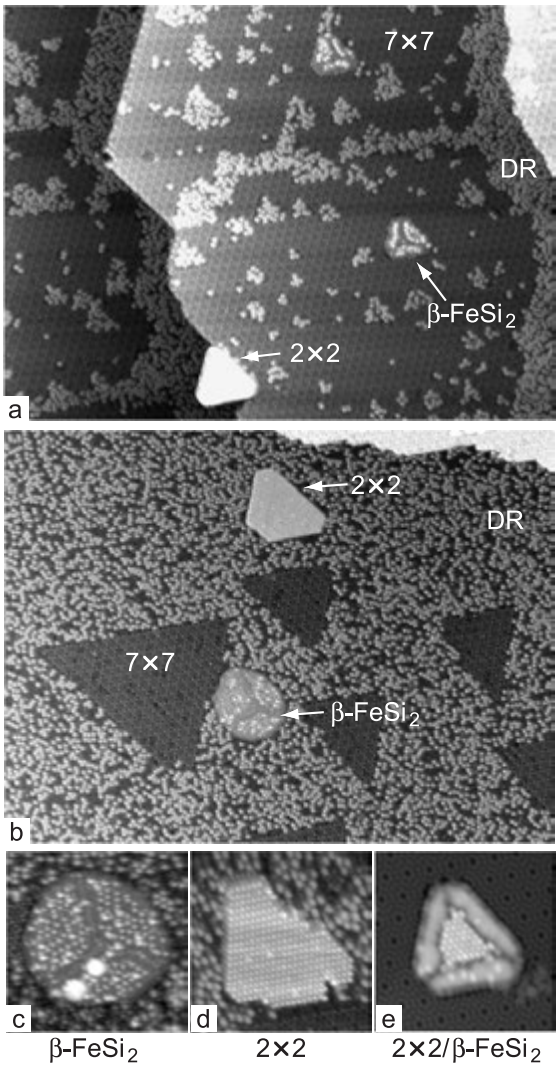

Fig. 1. 1180 × 890 Å^2 STM images of the Si(111)7 × 7 surface after RT deposition of (a) 0.2 ML and (b) 0.5 ML of Fe, followed by annealing at 600 °C for 5 min. Disordered regions (DR), 2 × 2 and β-$FeSi_2$ islands and remaining areas of the 7 × 7 reconstruction are indicated. In the low panel, the typical STM appearance of the islands is shown for: (c) β-$FeSi_2$ island, (d) 2 × 2 (γ-$FeSi_2$) island, (e) mixed 2 × 2/β-$FeSi_2$ island. Scale of (c), (d) and (e) is 200 × 200 Å^2.

the growth temperature and Fe coverage (see Fig. 3). At a given temperature, the island density increases almost linearly with increasing Fe coverage, while the mean size of the islands remains essentially unchanged. At a given Fe coverage, the island density decreases with temperature, while the island size, consequently, increases (e.g., from 30–50 Å at 600 °C to 70–100 Å at 700 °C).

Fourth, in the whole temperature range studied, the density of islands on the Si(111)$\sqrt{3} \times \sqrt{3}$-B surface far exceeds that on the Si(111)7 × 7 surface. The difference is especially great at lower temperatures, where it is more than an order of magnitude (see Fig. 3).

Conclusion

Thus, comparing the SPE growth of $FeSi_2$ nanodots on two surfaces, one can see that the B-modified Si(111)$\sqrt{3} \times \sqrt{3}$-R30°-B surface is more promising. The number density of the β-$FeSi_2$ islands on the Si(111)$\sqrt{3} \times \sqrt{3}$-R30°-B is much greater than that on Si(111)7 × 7 surface, while disordered regions and metallic γ-$FeSi_2$ islands are absent. Therefore, the number of potential emitting centers are significantly increased.

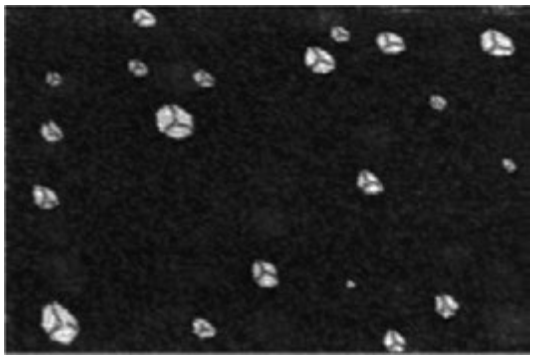

Fig. 2. 1500 × 1000 Å^2 STM image of the array of β-$FeSi_2$ islands grown by depositing 0.5 ML of Fe onto Si(111)$\sqrt{3} \times \sqrt{3}$-B surfaces at RT followed by annealing at 700 °C.

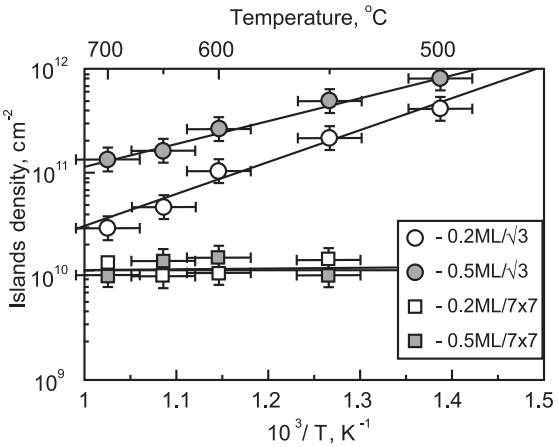

Fig. 3. Temperature dependence of the total number density of islands SPE grown on Si(111)7 × 7 and Si(111)$\sqrt{3} \times \sqrt{3}$-B surfaces after deposition of 0.2 and 0.5 ML of Fe.

References

[1] M. C. Bost and J. E. Mahan, *J. Vac. Sci. Technol. B* **4**, 1336 (1986).
[2] N. E. Christensen, *Phys. Rev. B* **42**, 7148 (1990).
[3] V. Bellani, G. Guizzetti, F. Marabelli, M. Patrini, *Solid State Commun.* **96**, 751 (1995).
[4] T. Suemasu, T. Fujii, K. Takakura, F. Hasegawa, *Thin Solid Films* **381**, 209 (2001).
[5] T. Suemasu, Y. Negishi, K. Takakura and F. Hasegawa, *Jpn. J. Appl. Phys.* **39**, L1013 (2000).
[6] M. A. Lourenco, M. Milosavljevic, R. M. Gwilliam, G. Shao, K. P. Homewood, *Thin Solid Films* **461**, 219 (2004).
[7] M. A. Lourenco, T. M. Butler, A. K. Kewell, R. M. Gwilliam, K. J. Kirkby and K. P. Homewood, *Jpn. J. Appl. Phys.* **40**, 4041 (2001).
[8] Y. Manassen, H. Reaple, R. Shneck, D. Barlam and A. Brokman, *Phys. Rev. B* **68**, 075412 (2003).
[9] M. Krause, F. Blobner, L. Hammer, U. Starke and K. Heinz, *Phys. Rev. B* **68**, 125306 (2003).
[10] M. V. Ivanchenko, E. A. Borisenko, V. G. Kotlyar, O. A. Utas, A. V. Zotov, A. A. Saranin, V. V. Ustinov, N. I. Solin, L. N. Romashev and V. G. Lifshits, *Surf. Sci.* **600**, 2623 (2006).

16th Int. Symp. "Nanostructures: Physics and Technology"
Vladivostok, Russia, July 14–18, 2008

The Hartree–Fock–Slater equation for the planar accumulation layer of n-InN

A. A. Klochikhin[1,2] and *I. Yu. Strashkova*[1]

[1] Ioffe Physico-Technical Institute, St Petersburg, Russia
[2] Nuclear Physics Institute, 188350, St Petersburg, Russia

Abstract. The Hartree–Fock–Slater quantum equation and the Kohn–Sham local density approximation for the exchange interaction are used to describe the nanosize planar accumulation layer of the degenerate n-InN. The magnitude of the exchange potential is corrected according to data on the band gap concentration dependence obtained early from the photoluminescence. The applicability of the solution is demonstrated by using recent experimental data.

InN and InGaN alloys are considered as important materials for optoelectronic devises operating from near IR to near UV regions. Recently the experimental evidences of the existence of an intrinsic electron accumulation layer near the surfaces of the InN- and InGaN-epilayers [1,2,3,4] have been found. In addition, the photoemission studies [5] have shown that electrons of the accumulation layer of the n-type InN populate the strongly confined 2D-bands. This have generated a considerable interest to the quantitative description of the accumulation layer properties. The quantum solution of this problem in the Hartree approximation was found in Ref. [6]. This communication describes the solution of the problems of the planar accumulation layer for the n-type degenerate semiconductor taking into account the exchange interaction in framework of the Kohn–Sham local density formalism.

We assume that the accumulation layer potential is produced by the external positive charge of density Q_s and by the electrons of density $\delta n(z)$ trapped by 2D-bands and inhomogeneously distributed within the crystal. The Hartree–Fock–Slater equation contains an exchange potential in addition to the Coulomb interaction

The local density approximation for the exchange interaction in the Kohn–Sham local density formalism is obtained from the following shift in energy per particle due to exchange interaction $\Delta E_{ex}(n) = -\left[\frac{81}{8\pi}\right]^{1/3} \frac{e^2 n^{1/3}}{2}$. The shift $\Delta E_{ex}(n)$ is usually expressed through the averaged separation of electrons r_s instead of concentration n by substituting the standard relation $n = \frac{3}{4\pi r_s^3}$. Afterwards, the Kohn–Sham exchange potential in the case of 3D-inhomogeneous electron gas is obtained by the substitution of the variable r instead of r_s. In the case of the planar accumulation layer the electrons are distributed homogeneously in two dimensions and the system has the cylindrical symmetry. Therefore, the equation relating the averaged distances between electrons is described by two parameters $n = \frac{1}{\pi R_s^2 \zeta_s}$ where R_s is the averaged separation of electrons in projection on the plane and ζ_s is the averaged separation in the perpendicular direction. The magnitude of R_s can be found from the equation $\pi R_s^2 = \frac{1}{\int dz \delta n(z)} = \frac{1}{Q_s}$, where $\int dz \delta n(z) = Q_s$ is the density of the external surface charge.

Then substituting the variable $\zeta(z)$ instead of ζ_s we obtain the exchange interaction as $eV_{ex}(z) = -\left[\frac{81}{8\pi}\right]^{1/3} \frac{e^2}{2\zeta(z)} = -\left[\frac{81}{8\pi}\right]^{1/3} \frac{e^2 \delta n(z)}{2\int dz \delta n(z)}$. Therefore, the local density approximation gives for systems with cylindrical symmetry the exchange potential depending on the wave functions as $|\psi(z)|^2$ in contrast to the $|\psi(z)|^{2/3}$ dependence for the 3D-inhomogeneity.

It was shown in Ref. [7] that the magnitude of the exchange interaction of a crystal differs from the $\Delta E_{ex}(n)$ for free electron gas and in the case of InN crystal the observed band gap shift consists only about 20 percents of this value. In order to correct $\Delta E_{ex}(n)$ and $eV_{ex}(z)$ we introduce the factor α which takes into account the difference between theoretical and experimental magnitudes of exchange interaction. Then we obtain the Hartree–Fock–Slater equation for the accumulation layer [8] as

$$-\frac{\hbar^2}{2m^*}\frac{d^2\psi_m}{dz^2} - \frac{\lambda e^2}{\varepsilon}\frac{2m^*}{\hbar^2}\left\{\sum_n \hbar\omega_n \int \psi_n^2(z+z')z'dz'\right\}\psi_m(z),$$
$$-\left[\frac{81}{8\pi}\right]^{1/3} \frac{\alpha e^2 \delta n(z)}{2\int dz \delta n(z)}\psi_m(z) = \hbar\omega_m \psi_m(z). \quad (1)$$

Here, n enumerates the energies and wave functions of the confined bands and the Coloumb potential is expressed via $\delta n(z)$ as $\Phi_q(z) = -\frac{2\pi e}{\varepsilon}\int z'dz'\delta n(z+z')$ and ε is the electron dielectric constant. The 2D-confined bands give the quantum electron density in an accumulation layer $\delta n^q(z) = \frac{\lambda}{2\pi}\frac{2m^*}{\hbar^2}\sum_n \hbar\omega_n \psi_n^2(z)$, so that $\Phi_q(z) = -\frac{\lambda e}{\varepsilon}\frac{2m^*}{\hbar^2}\sum_n \hbar\omega_n \int \psi_n^2(z+z')z'dz'$, where λ is the dimensionalless parameter which define the vertex renormalization and $\psi_n(z)$ are the wave functions of confined states which are normalized to unity $\int \psi_n^2(z)dz = 1$.

The theory was applied to calculate the accumulation layer characteristics by using the recent data obtained in the high-resolution angle-resolved photoemission experiment with InN crystals [5]. The photocurrent intensity map presented in Fig. 3 of Ref. [5] was used to estimate the electron band dispersion. Figure 1 demonstrates dispersions of the 2D-bands calculated in the parabolic (for the effective mass $m^* = 0.15m_0$) and nonparabolic band approximations.

We compared the obtained electron densities with the electron density distribution obtained in Ref. [4] for the InN samples with the bulk concentration of the order of 1×10^{18} cm^{-3}. It can be seen in Fig. 2 that the electron densities agree well with experimental data if the experimental data are shifted for 0.5 nm toward $z = 0$.

The shape of the PL band for 650 nm thick InN sample with a pronounced high-energy tail was fitted using the solution [9]

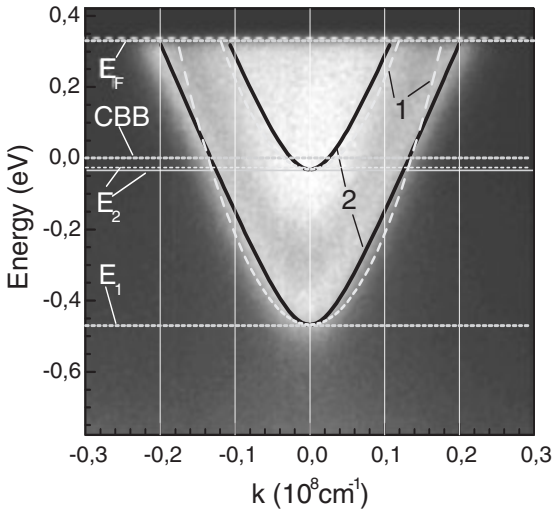

Fig. 1. (Color online).The photocurrent intensity map that reflects the dispersion of quantized states along the ΓΣM direction in the surface plane (Fig. 3 of Ref. [5]) and 2D-band parabolic (at $m^* = 0.15m_0$) and nonparabolic dispersions with the effective mass at Γ-point $m_\Gamma = 0.07m_0$. 2D-electron band energies at zero wave-vector are $E_1 = -0.47$ and $E_2 = -0.034$ or -0.026 eV for parabolic or nonparabolic dispersions, respectively. $E_F = 0.330$ eV is the Fermi energy corresponding to the nonparabolic dispersion at the electron concentration of 4×10^{19} cm^{-3}. The reference point for energies is taken to be at the conduction band bottom (CBB).

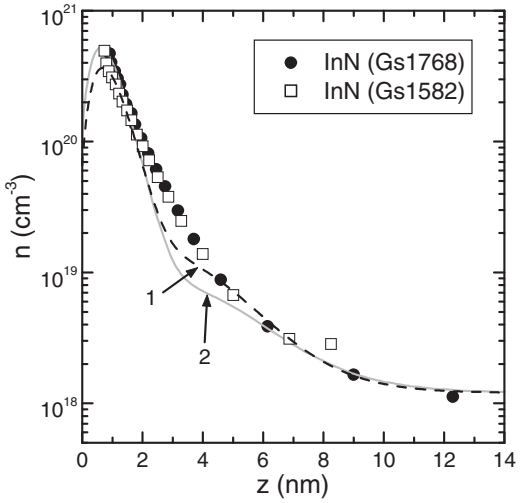

Fig. 2. (Color online). Electrolyte-based CV measurement data of two InN films from Ref. [4] showing electron concentration as a function of depth from the film surface (symbols). Experimental curves are shifted toward $z = 0$ for 0.5 nm as compared with the original data in Fig. 18 of Ref. [4]. Curves 1 and 2 are the full self-consistent inhomogeneous densities $n(z)$ in parabolic (1) and non-parabolic (2) band approximations. The bulk electron density is equal to 1.2×10^{18} cm^{-3}.

of the classical Thomas–Fermi equation for the accumulation layer. The agreement of curve 2 with the experimental spectrum shown in Fig. 3a was obtained under the condition that the PL contribution from the surface accumulation layer (excluding the top 5.7-nm-thick part) is taken into account.

To summarize, we have presented quantum solutions of the planar accumulation layer problem for a degenerate n-type

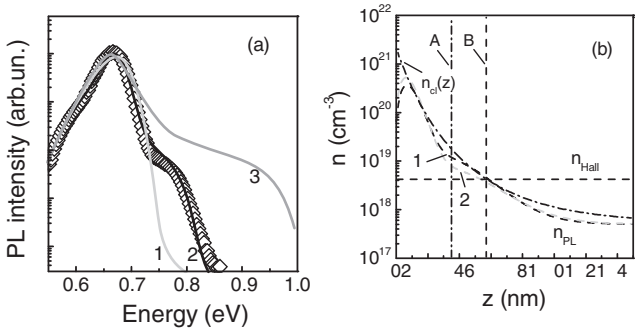

Fig. 3. (Color online). (a) PL band shapes for the 650 nm thick InN sample #050118. The symbols present experimental data. Lines 1 and 2 display the calculated PL band shapes when the accumulation layer is restricted by one of two vertical lines as shown in Fig. 3b. Line 3 shows the calculated PL band shape for the homogeneous electron concentration equal to $n_{PL} = 5 \times 10^{17}$ cm^{-3}. (b) $n_{cl}(z)$ is the classical inhomogeneous electron distribution as it was obtained in Ref. [9]. Curves 1 and 2 are the full self-consistent inhomogeneous densities $n(z)$ in parabolic (1) and non-parabolic (2) band approximations. The bulk electron density is equal to 5×10^{17} cm^{-3}. Vertical lines (A or B) show the boundaries between the sample regions participating or not in the PL formation.

semiconductor within the parabolic effective mass approximation. The role of the electron band nonparabolicity has been estimated by using the nonparabolic dispersion for the in-plane motion. The comparison with experimental data shows that the accumulation layer parameters are only weakly dependent on the sample properties and can be considered as fairly universal characteristics of n-InN semiconductor.

Acknowledgements

This work was supported by NSC-RFBR Project 94WFA0400 128, Russian Foundation for Basic Research (grants 06-02-17240 and 06-02-16218), the Programs "Quantum nanostructures" and "New materials and structures".

References

[1] Hai Lu, W. J. Schaff, L. F. Eastman, and C. E. Stutz, *Appl. Phys. Lett.* **82**, 1736 (2003).
[2] I. Mahboob, T. D. Veal, C. F. McConville, H. Lu, and W. J. Schaff, *Phys. Rev. Lett.* **92**, 036804 (2004).
[3] S. X. Li, K. M. Yu, J. Wu, R. E. Jones, W. Walukiewicz, J. W. Ager III, W. Shan, E. E. Haller, H. Lu, and W. J. Schaff, *Phys. Rev. B* **71**, 161201 (2005).
[4] W. Walukiewicz, J. W. Ager III, K. M. Yu, Z. Liliental-Weber, J. Wu, S. X. Li, R. E. Jones, and J. D. Denlinger, *J. Phys. D: Appl. Phys.* **39**, R83 (2006).
[5] Leyla Colakerol, T. D. Veal, Hae-Kyung Jeong *et al*, *Phys. Rev. Lett.* **97**, 237601 (2006).
[6] A. A. Klochikhin, V. Yu. Davydov, I. Yu. Strashkova, and S. Gwo, *Phys. Rev. B* (2007).
[7] V. Yu. Davydov, A. A. Klochikhin, V. V. Emtsev *et al*, *phys. stat. sol. (b)* **234**, 787 (2002).
[8] A. A. Klochikhin and I. Yu. Strashkova, submitted to *Phys. Rev. B* (2008).
[9] A. A. Klochikhin, V. Yu. Davydov, I. Yu. Strashkova, P. N. Brunkov, A. A. Gutkin, M. E. Rudinsky, H.-Y. Chen, and S. Gwo, *phys. stat. sol. (RRL)* **1**, 159 (2007).

16th Int. Symp. "Nanostructures: Physics and Technology"
Vladivostok, Russia, July 14–18, 2008

Investigation of iron silicide islands grown by solid phase epitaxy on Si(001) surface

V. V. Balashev[1,2], V. V. Korobtsov[1,2], T. A. Pisarenko[1,2] and E. A. Chusovitin[1]

[1] Institute of Automation and Control Processes FEBRAS, Vladivostok, Russia
[2] Far Eastern State University, Vladivostok, Russia

Abstract. Iron silicide islands were grown on Si(001) surface by solid phase epitaxy (SPE). It was found that the annealing of iron layer with thickness less than 1 ML at substrate temperature over 500 °C leads to formation of 3D α-$FeSi_2$ and ε-FeSi islands on Si(001) surface. At increasing of iron film thickness up to ∼2 ML the annealing results in 3D γ-$FeSi_2$ islands growth, preferentially. The transition to 2D β-$FeSi_2$ islands growth was observed for iron film thickness more than ∼4 ML.

Introduction

During the last years the investigation of SPE growth of iron silicides on silicon surface with (001) orientation is of interest of many researchers [1–3]. Data of their works evidence about formation of various types of iron silicides. Recently, a schematic phase diagram for the Fe-Si(001) system was summarized against iron coverage at room temperature and subsequent annealing temperature [4]. It was found, the annealing of iron films with thickness of less than ∼1 nm results in growth both two-dimensional (2D) and three-dimensional (3D) islands of iron silicides on Si(001) surface. Attention of many works was mainly devoted to structural analysis of 2D islands using scanning tunneling microscopy (STM) and low energy electron diffraction (LEED), and investigation of surface by such spectral methods as X-ray/ultra-violet photoelectron spectroscopy (XPS/UPS), energy electron loss spectroscopy (EELS), auger electron spectroscopy (AES) and so forth. On the other hand, crystalline structure of 3D iron silicide islands which begin to form at iron layer thickness equal to ∼1 ML (1 ML=6.8×10^{14} cm^{-2} for Si(001)) and temperature of subsequent annealing higher than ∼500 °C is not quite clear. Furthermore, it is of interest the island structure evolution depending on iron coverage and substrate annealing.

1. Experimental

The experiments were performed in an ultra-high vacuum MBE-system "Katun" equipped with 25 keV reflection high-energy electron diffraction (RHEED) apparatus, an electron gun to evaporate Si, and Knudsen cell to evaporate Fe. The base pressure of the MBE system was 1×10^{-10} Torr and it was kept below 5×10^{-9} Torr during iron evaporation. The substrate was heated radiatively by a Ta resistive heater situated behind the substrate. The p-type Si(001) wafers of 4.5 Ω cm resistivity and $20\times10\times0.5$ mm^3 in size were used. The surface was protected by an ultrathin oxide layer prepared by a wet chemical treatment before loading the substrate into the growth chamber. The protective oxide layer was removed by heating to 910 °C for 10 min and clean Si(001)2×1 surface was formed. The deposition rate of iron was 0.57 ML/min. After Fe deposition on Si(001)2×1 surface at room temperature the sample was heated up to 800 °C with rate of ∼20 °C/min and kept at this temperature for 5 minutes. For checking of iron silicide stability samples were additionally annealed at 850 °C for 1 hour. The structure and composition of grown silicide films were determined from analysis of RHEED patterns taken at sample heating. The morphology of SPE grown films was observed by atomic force microscopy (AFM) after unloading samples from the vacuum chamber.

2. Results and discussion

Observation of RHEED pattern shows that after 0.57 ML iron deposition 2×1 surface sructure remains on the most part of the surface. The heating of deposited layer up to 420 °C leads to appearance of additional reflections as weak and diffuse spots which can be related to nucleation of iron silicide islands. The sharpness and intensity of diffraction spots increased with annealing temperature that evudenced about enlargment of iron silicide islands.

Analysis of these diffraction spots shows that on the surface the growth of iron monosilicide ε-FeSi (B20-structure) and disilicide α-$FeSi_2$ (tetragonal structure) islands occurs, simultaneously. It was found that ε-FeSi islands are formed epitaxially with $(111)_{Si}$: $(111)_\varepsilon \| (111)_{Si}$, where $[11\bar{2}]_\varepsilon \| [1\bar{1}0]_{Si}$. It is worth to note such crystallographic relationship is typical for continuous ε-FeSi film grown on Si(111) substrate at SPE [5]. On the other hand two epitaxial orientations of α-$FeSi_2$ with $(001)_{Si}$ were found: $(111)_\alpha \| (001)_{Si}$, where $[1\bar{1}0]_\alpha \| [1\bar{1}0]_{Si}$ and $(110)_\alpha \| (001)_{Si}$, where $[001]_\alpha \| [1\bar{1}0]_{Si}$. Later relationship $(110)_\alpha \| (001)_{Si}$ was suggested in Ref. [4] for observed 3D islands elongated along $[1\bar{1}0]_{Si}$ direction. Such kind of islands

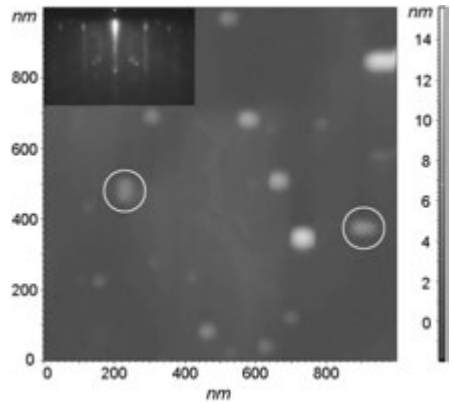

Fig. 1. AFM image of Si(001) surface after 0.57 ML RT deposition of iron followed by annealing at 800 °C for 5 min. The inset shows RHEED pattern along Si[1$\bar{1}$0] direction.

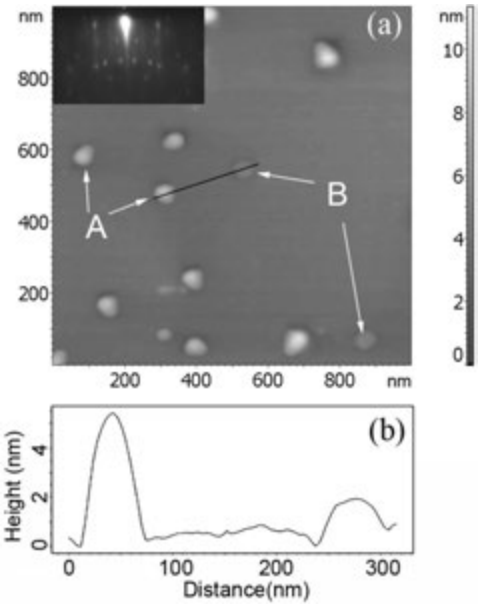

Fig. 2. AFM image of Si(001) surface after RT deposition of ∼2 ML of iron followed by annealing at 850 °C for 1 hour (a) and height profile for islands of A and B type (b). The inset shows RHEED pattern along Si[1$\bar{1}$0] direction.

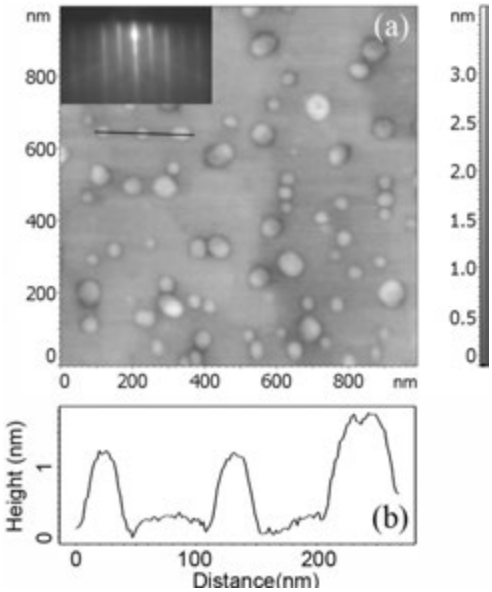

Fig. 3. AFM image of Si(001) surface after RT deposition of 4 ML of iron followed by annealing at 850 °C for 1 hour (a) and height profile for B-type islands (b). The inset shows RHEED pattern along Si[1$\bar{1}$0] direction.

was also observed in our AFM image (marked by circles in Fig. 1).

After RT deposition of ∼2 monolayers of iron and subsequent heating up to 500 °C original 2 × 1 structure remained as for 0.57 ML deposition. At substrate temperature higher than 500 °C complicated transmission RHEED pattern was observed that included both diffraction spots from α-$FeSi_2$ with two epitaxial orientations and ones corresponding to γ-$FeSi_2$ phase (fluorite structure). Further temperature increase up to 700 °C leads to disappearance diffraction spots from α-$FeSi_2$ phase. The temperature range of the existence of α-$FeSi_2$ phase at this iron coverage is an accordance with phase diagram represented in Ref. [4]. On the other hand 3D γ-$FeSi_2$ islands remained stable even at heating up to 850 °C and subsequent annealing for 1 hour. AFM image, RHEED pattern and height profile for this surface after annealing are shown in Fig. 2. As can see from height profile in Fig. 2(b) there are two types of islands: 3D ones 5–8 nm in height (marked by **A**) and practically flat islands 1–1.5 nm in height (marked by **B**). Sharp transmission diffraction spots are only attributed to 3D γ-$FeSi_2$ (A-type) islands epitaxially oriented relatively $(111)_{Si}$: $(11\bar{1})_\gamma \| (111)_{Si}$, where $[1\bar{1}0]_\gamma \| [1\bar{1}0]_{Si}$.

After 4 ML RT deposition of iron the transition from original (2 × 1) to (1 × 1) pattern was observed. Subsequent heating up to 400 °C resulted in only c(2 × 2) RHEED pattern from silicide layer that at temperature higher than 500 °C break up into 3D γ-$FeSi_2$ and 2D islands, preferentially, with c(2 × 2) structure (Fig. 3(a)). The density of 3D γ-$FeSi_2$ islands was significantly less than for 2D islands. 2D island height and shape were practically same as for B-type islands in case of 2 ML deposition (Fig. 2). These islands can be related to β-$FeSi_2$ phase (orthorombic structure). So, in Ref.[6] by medium-energy ion scattering (MEIS) the formation of β-$FeSi_2$ layer at 400 °C for 4.5 ML of iron and lateral disruption of film were also observed at heating up to 800 °C.

At increasing of iron coverage up to 11.5 ML we observed growth of non-oriented ε-FeSi crystallites at temperature higher than 300 °C. At 520 °C structure of crystallites changed to β-$FeSi_2$ in accordance with phase diagram of Nakano *et al* [4]. These non-oriented crystallites were stable at subsequent high-temperature annealing.

3. Conclusion

At iron coverage less than 1 ML it was observed SPE growth of 3D ε-FeSi islands (B20-structure) and 3D α-$FeSi_2$ (tetragonal structure) islands with two epitaxial orientations. For 2 ML coverage substrate annealing results in formation of 3D α-$FeSi_2$ and γ-$FeSi_2$ (fluorite structure) islands. In comparison with α-$FeSi_2$ islands γ-$FeSi_2$ ones were stable at subsequent annealing at 850 °C for 1 hour. The transition to 2D β-$FeSi_2$ layer growth was found for iron coverage more than 4 ML. It was shown the break up of β-$FeSi_2$ layer into 2D islands at substrate temperature increase from 500 to 850 °C.

References

[1] J. Chrost, J. J. Hinarejos, P. Segovia, E. G. Michel, R. Miranda, *Surf. Sci.* **371**, 297 (1997).
[2] S. Hajjar, G. Garreau, S. Pelletier, P. Bertoncini, P. Wetzel, G. Gewinner, M. Imholf, C. Pirri, *Surf. Sci.* **532–535**, 940 (2003).
[3] M. V. Gomoyunova, D. E. Malygin, I. I. Pronin, A. S. Voronchikhin, D. V. Vyalikh, S. L. Molodtsov, *Surf. Sci.* **601**, 5069 (2007).
[4] H. Nakano, K. Maetani, K. Hattori, H. Daimon, *Surf. Sci.* **601**, 5088 (2007).
[5] X. Wallart, J. P. Nys, C. Tetelin, *Phys. Rev. B* **49(8)**, 5714 (1994).
[6] K. Konuma, J. Vrijmoeth, P. M. Zagwijn, J. W. M Frenken, E. Vlieg, J. F. Van der Veen, *J. Appl. Phys.* **73(3)**, 1104 (1993).

16th Int. Symp. "Nanostructures: Physics and Technology"
Vladivostok, Russia, July 14–18, 2008

Electron interaction, film nanophases and nanoheterostructure formation

N. I. Plusnin

Institute of Automation and Control Processes of FEB RAS, Radio 5 Str., 690041, Vladivostok, Russia
Vladivostok State University of Economics and Service, Gogolya 41 Str., 690600, Vladivostok, Russia

Abstract. Film nanophases stabilized by electron interaction have been considerated. The results of investigation series show that they have difference on their properties from the bulk phases and also they have a development in phase transitions during the growth and epitaxy of heterostructures. That discerns them as a new type of low dimensional phases, which directly proceed to bulk phases under the growth. Particular qualities of the film nanophases are modification of their electron and atomic structure due to interaction with the substrate and quantum size limitations and their self-sustaining epitaxial growth due to lowered interface energy. It has been shown that the film nanophases are precursors for the bulk phase nucleation and template formation during heteroepitaxy.

Introduction

Phases as forms of atoms self-organization into a solid, which is homogeneous one on their properties, are basic subjects of investigation of solid state physics. And inasmuch as all the processes of solid nanostructure technology connected with phase transitions and interfaces, then the phases are else basic objects of their technology. The nanostructure formation is connected with the size limitation in any dimension; therefore phases of a new type, that is the low-dimensional phases, take part in these processes. Film phases [1] occupy the separate place among these phases, as bulk phases are nucleated from them. Concept of "film" implies unbroken atomic-homogeneous layer beginning from the thickness of 1 ML and more. That differs the phases from surface structures induced by interaction adsorbat-substrate at submonolayer coverage. Feature of film nanophases is their formation due to interaction of valence electrons with the substrate and due to quantum-size limitation on their electron structure [2,3]. Another reason of their formation is quantum-size interaction between interfaces of film-vacuum and film-substrate [4,5]. Transition metals and their silicides, which are technologically compatible with silicon, have special significance for silicon microelectronics [6,7]. Bellow the review of results on nanostructure formation of transition metals and their silicides on silicon and also for silicon on silicide and silicon is presented. The object of the review is showing different developments of film nanophases in the growth processes and properties of the nanostructures.

1. Electronic structure of transition metal films on silicon at nanosize thickness

Still beginning 80-th years the investigations have evidenced that the electron structure of monolayers of transition metals on silicon was significantly modificated and had difference from bulk phases [8]. So as early as in 1984 we have observed by the method of electron energy loss spectroscopy (EELS) a lowered density of valence electrons in films of Cr on Si(111) and on SiOX/Si(111) at quantum-size thickness in the range of 0.2–0.4 nm [2]. And recently it has been shown by us that an electron redistribution from the film to the substrate take else place [3].

2. The growth of transition metal, silicide and silicon during formation of heterostructures of silicon-metal (silicide)-silicon substrate

A precursor consisted from a metal or a metal-silicon mixture proceeds usually before nucleation and formation of epitaxial film during low-temperature growth of metals or solid-phase epitaxy of silicides on silicon. A number of researches evidence about that the structure [9,10] and even the orientation [10–12] of epitaxial film is other ones, if the thickness of the precursor is lower then several ML. Such precursor behavior is additional argument in favor of the formation of a film phase in it. It has been shown by our investigations that metastable nanophase of Cr is actually a precursor changing orientation of $CrSi_2$ from A-type to B-type [13]. Studies of growth of silicon on silicon [14] and silicide [15,16] have also shown formation of a metastable film nanophase for the silicon case. It is typical that such film nanophase can be overgrown on the thickness under moderate annealing [17,18]. The fact assisting this is that the film of metal or silicide can be self-sustaining in metastable state up to some critical values. The reason of that is a lowered energy of the epitaxial interface (an example of this is formation of FeSiX with the lattice of CaCl [19]).

3. The growth, electron structure and stability of film nanophases of transition metal on silicon

For a trusty extraction of film nanophases it was needed that they had evident differences of their electron structure from that of bulk phases of the film and the substrate. From the point of view, transition metals has been found as most approached, since they have a high chemical activity and at the same time a high atomic density in relation to silicon. But there is an obstacle for formation of the film nanophase on the silicon. It is an intermixing of atoms with the substrate during their deposition and the growth of silicide interlayer. We have found that the deposition rate and the kinetic energy of atoms in the beam influent onto the process [20–22].

As a result, it has been found the growth method not giving intermixing with the substrate. The method gave us an opportunity to grow films of Cr, Co and Fe on the silicon with the thickness from 1 ML up to tens ML and to monitor for changes of their electron structure, composition, morphology

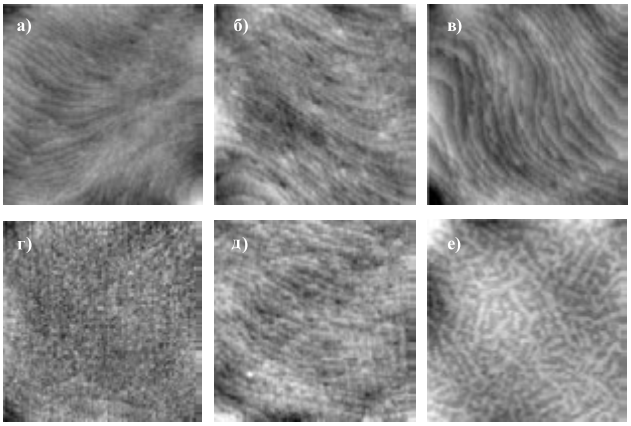

Fig. 1. AFM images of Fe films on Si(100) after annealing at $T = 250\,^{\circ}$C [22]: The film thickness is 0.03, 0.12, 0.3, 0.45, 0.6 and 1.2 nm for a), b), c), d), e) and f), respectively. The image size is 2.5×2.5 μm for $d = 0.12$ nm and 2×2 μm for all the other thicknesses.

and other properties [3,20–23]. We have found direct proofs of film nanophase formation on silicon by means that. In this way it was shown by us that lowering an electron density take place in monolayers of Co on Si(111) and its rising take place in interface ragion of the Si(111) substrate [3]. We have discovered a similar redistribution of electron density also at interfaces of Cr and Fe with Si(111). Moreover, by methods of Auger-electron spectroscopy (AES) and EELS we have studied the composition and the electron density in monolayers of Fe on Si(100) before and after moderate annealing in the range of the thickness from 0.03 up to 1.2 nm. And we have studied the morphology of the films after annealing (see Figure 1) by method of atomic force microscopy (AFM) [23]. The conducted investigations have shown that unlike the thickness of 0.03–0.12 nm and 1.2 nm the electron density in the films had drastic increase at the thickness of 0.3 and 0.45 nm and the composition had enrichment by silicon. In addition, the film at the thickness of 0.45 nm after annealing had not a stepped relief, which is typical for the substrate (see Figure 1 at $d = 0.003$–03 nm), and it had own relief with often pin holes in film and maximal rate of it roughness. The film was smooth one, looked like an epitaxial film with a net of mismatch dislocations (see Figure 1 at $d = 0.6$ nm) and had film composition of $FeSi_2$. All that means that the Fe film with the thickness of 0.3–0.6 nm was in metastable state at $T = 25\,^{\circ}$C and the silicide film was formed from it at $T = 250\,^{\circ}$C. At the same time the Fe film was been a stable bulk phase of Fe at $d > 0.6$ nm and $T = 25\,^{\circ}$C. It was not mixed with Si during annealing and got only a wrinkled relief (see Figure 1 at $d = 1.2$ nm). Obviously that film nanophase of Fe on Si(100) with the thickness of 0.6 nm is a good precursor for formation of an unbroken template during formation of $FeSi_2$-Si heterostructures on the silicon.

References

[1] N. I. Plyusnin *et al*, *Surface (Rus).* **1**, 17 (2005).
[2] V. G. Lifshits *et al*, *Phys. Chem. and Mech. Surf. 3* **3**, 2669 (1985).
[3] N. I. Plusnin *et al*, *Appl. Surf. Sci.* **253**, 7225 (2007).
[4] Z. Y. Zhang *et al*, *Phys. Rev. Lett.* **80**, 5381 (1997).
[5] Z. Y. Zhang *et al*, *Science.* **276**, 377 (1997).
[6] M. Ieong *et al*, *Materials Today.* **9**, 26 (2006).
[7] J. R. Tucker *et al*, *Nanotechnology.* **7**, 275 (1996).
[8] C. Calandra *et al*, *Surf. Sci. Rep.* **4**, 271 (1984).
[9] V. G. Lifshits *et al*, *Phys. Chem. and Mech. Surf.* **2**, 784 (1984).
[10] N. I. Plusnin *et al*, *Surf. Rev. and Lett.* **2**, 439 (1995).
[11] P. A. Bennet *et al*, *Phys. Rev.* **B. 37**, 4268 (1988).
[12] R. T. Tung *et al*, *Phys. Rev. Lett.* **50**, 429 (1983).
[13] N. I. Plyusnin *et al*, *Surface (Rus).* **9**, 55 (1989).
[14] N. I. Plusnin, *Phys. of Low-Dim. Str.* **8/9**, 51 (1997).
[15] N. I. Plyusnin *et al*, *Surf. Investigations.* **14**, 1667 (1999).
[16] N. I. Plyusnin *et al*, *Surf. Investigations.* **16**, 917 (2001).
[17] N. I. Plusnin *et al*, *Surf. Science.* **426**, 38 (1999).
[18] N. I. Plusnin *et al*, *Appl. Surf. Sci.* **166**, 125 (2000).
[19] U. Kafader *et al*, *Europhys. Lett.* **22**, 529 (1993).
[20] N. I. Plusnin *et al*, *Phys. of Low-Dim. Str.* **9/10**, 129 (2002).
[21] N. I. Plusnin *et al*, *Phys. of Low-Dim. Str.* **11/12**, 39 (2002).
[22] N. I. Plyusnin *et al*, *Tech. Phys. Lett.* **33**, 486 (2007).
[23] N. I. Plusnin *et al*, *Proc. 8-th ISMTII, Sendai, JP.* 645 (2007).

16th Int. Symp. "Nanostructures: Physics and Technology"
Vladivostok, Russia, July 14–18, 2008

Morphology and optical properties of Fe-Si film-wise nanophases on Si(111) after exposition to air

S. A. Kitan'[1], V. M. Il'yashenko[1] and *N. I. Plusnin*[1,2]

[1] Institute of Automation and Control Processes of FEB RAS, Vladivostok, Russia
[2] Vladivostok State University of Economics and Service, Vladivostok, Russia

Abstract. Dependencies of the surface relief (obtained by AFM method) and the reflection coefficient on the thickness have been investigated for Fe-Si film nanophases on Si(100) after prolonged exposition to air. The nanophases was obtained by ultra-high vacuum deposition of Fe films (d = 1.2–12 Å) on Si(100) and by annealing at 250 °C. Stability of the nanophases at the thickness of 1.2, 6 Å and 12 Å has been shown in relation to oxidation. Nanophases with the thickness of Fe 3 Å and 4.5 Å had morphological transformation after oxidation due to their lowest stability. Anomalous values of the optical reflection and transmission coefficients (in the range of 0.7–1 eV), which have been explained by metallic properties of Fe film and interface layer of the Si substrate, have been discovered at the thickness of 1.2 Å in the difference from those for other thicknesses.

Introduction

Film nanophases of silicides had been early discovered on the silicon [1,2]. Recently, in the works of [3–8], it has been shown that film nanophases of the transition metals can be also formed on silicon at the quantum-size thickness. Because of possible application in nanoelectronics, the question arises about the long-term stability and the properties of the nanophases in air. In the work new results have been presented on morphological transformation and optical properties of film nanophases of Fe on Si(100), which obtained in ultra-high vacuum conditions (see [8]) and which were in air during several months.

1. Experimental technique

Film nanophases with the Fe thickness of 1.2; 3; 4.5; 6 and 12 Å were obtained by the molecular-beam deposition of Fe on Si(100) at room temperature of the substrate and were annealed after the deposition at temperature of 250 °C under ultra-high vacuum conditions [8]. The phase composition determined by Auger-electron spectroscopy was closed to Fe, Fe_3Si, FeSi, $FeSi_2$ and Fe, respectively [8]. Obtained films were placed in atomic force microscope (AFM) for scanning AFM-images after unloading from the chamber. After that the samples with the films was put to container and saved in it during 5 months up to the moment of carrying out second scanning in AFM and during near 10 months up to the moment of obtaining optical spectra of reflection and transmission. The AFM images were obtained in microscope of the model of Solver-P-47 (NT MDT) and optical spectra were obtained in spectrophotometers of Hitachi-310 (photon's energy range 1.4–6.5 eV) and homemade one on base of monochromator of MDR-3 (photon's energy range 0.7–1.5 eV).

2. Morphological transformations

As investigations by method of AFM and comparisons with early obtained AFM images [8] showed, the surface relief of the films was smoothed after oxidation in air. With this, roughness of the most of the films was decreased approximately on 30%, except for the films at 1.2 Å and 3 Å, where it stayed the same (0%) or slightly decreased (5%), and except for film at 4.5 Å, where it decreased in 2.6 times. Other effect of surface oxidation in air is change of morphology type of film. This effect was most expressively developed at the thickness of 4.5 Å. In this film multiple small voids with diameter near 0.1 μm disappeared after oxidation (see Figure 1). And, at the thickness of 3 Å, the film no longer repeated stepped relief of the substrate and formed its own relief. The relief looked like some net of ring-like structures, which was similar to dislocation's net (see Figure 1). As it follows from this, the film at 1.2 Å was not changed, the film at 3 Å underwent a phase transformation, and void's healing took place in the film at 4.5 Å. Other films were slightly smoothed possibly due to surface oxide formation. Thus, the most changes took place in the films at 3 Å and 4.5 Å. That speaks about their high surface energy and maximal metastability before oxidation. On the whole, the oxidation promoted decrease of the surface energy and increase of the substrate wettability by the film. Apparently, the film at 1.2 Å had a lowest surface energy and a lowest stability to oxidation.

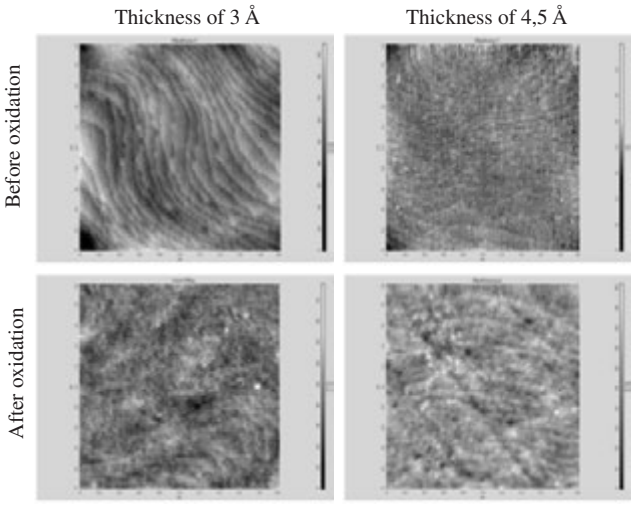

Fig. 1. AFM-images of Fe films on Si(100) with the thickness of 3 Å and 4.5 Å before and after oxidation: image size is 2 × 2 μm.

3. Optical spectra of reflection

The measurements of reflection in the range of photon's energy of 1.4–6.5 eV showed that the films lift up the reflection spectra in IR range (1.4 eV) and lift down them in UV range (6.5 eV), unchanging the form of the spectra as the whole. Figure 2 show the dependencies of reflection (R) and transmission (T) coefficient on the film thickness at energies of 0.85 eV, 1.4 eV and 6.5 eV.

In case of a pure Si, values of R(6.5 eV) and R(1.4 eV), R(0.85 eV) are obviously caused by interband p-p transitions over the bulk and surface p-states, respectively, which are located lower (4 eV and 1 eV) and higher (2.5 eV and 0.4 eV) than Fermi level [9]. In case of Fe films, we see significant (on 7%) and slow (<3%) increase of R(1.4 eV) for $d = 1.2$ Å and $d > 3$ Å, respectively. The dependence of R(0.85 eV) correlated with the dependence of R(1.4 eV), but the increase of R was significantly bigger (21% at $d = 0.3$–1.2 Å and 29% at $d > 3$ Å). Therefore, it is reasonably to connect the behavior of R(1.4 eV) with formation of metallic phases (Fe, Fe_3Si, FeSi, $FeSi_2$ and Fe, at $d = 1.2$, 3, 4.5, 6 Å and 12 Å, respectively — see [8]). Anomalous high values of R(1.4 eV) and R(0.85 eV) at 1.2 Å can be explained by formation of pd-bands in interface region of Si due to redistribution of part of d-electrons from metallic Fe film into the substrate (by analogy with Co on Si [7]). As for reflection from the film ($d = 1.2$ Å) at 6.5 eV, the decrease of R(6.5 eV) down to 19% can mean a resonance absorption by d-band of Fe. At the thickness of 3 and 4.5 Å, wider pd-band of Fe_3Si and FeSi forms [10]. Therefore, absorption decreases and it lead to increase of R(6.5 eV). At the thickness of 6 Å, pd-band converges to narrow band of $FeSi_2$. Therefore absorption increases again, and reflection decreases. Finally, at the thickness of 12 Å, absorption in the film increases, and R(6.5 eV) decreases due to formation of d-band Fe. The suppositions corresponds to dependence of electron structure of Fe silicides [10] and other silicides [11] on their composition. As the whole, the dependencies of R(6.5 eV) and R(1.4 eV), shown in the Figure 2, lead themselves in opposition to each other up to $d = 4.5$ Å, and they are correlated after $d = 4.5$ Å. With all this, the dependence of R(6.5 eV) correlates with IR-transmission of T (0.7–1 eV) (see Figure 2). For reasons given, we have came to conclusion that the reflection from the substrate plays the main role at photon's energy of 6.5 eV in the spectra of reflection, and film modulates this reflection due to its absorption. Anomalous high absorption in film at 1.2 Å for IR and UV ranges of spectra, and also high reflection for IR range of spectra can be explained by absorption and reflections on conductivity electrons of Fe film and interface Si region.

4. Discussion

Oxidation and structure transformation. Obviously, that films obtained under vacuum conditions and room temperature of substrate have a high surface energy and a tension as the result of bonds energy minimization at interface and in film itself. Some balance sets between the tension's energy and minimized energies of bonds of film-substrate system. The balance is disturbed, when the film surface is oxidized. As the result of oxidation, the free energy of the surface decreases and film changes its structure or form in such a way, that contribution of bulk energy of film itself would be minimal. This leads to relaxation of tensions, structure reconstruction (at 3 Å) and void's healing (at 4.5 Å).

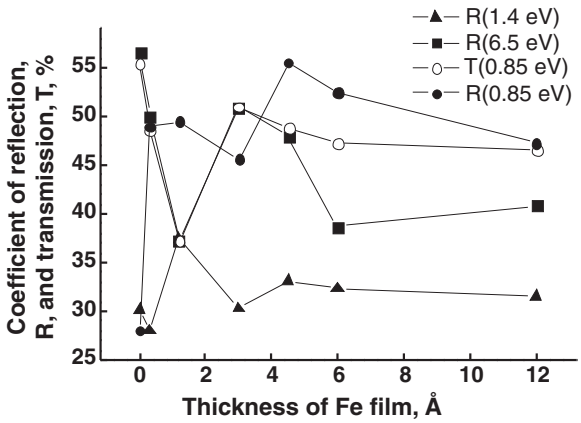

Fig. 2. Dependencies of reflection (R) and transmission (T) coefficient on the film thickness at energies of 0.85 eV, 1.4 eV and 6.5 eV for Fe films on Si(100).

Properties of nanophase at 1.2 Å. Stability of nanophase at 1.2 Å in relation to oxidation and also existence of its metallic properties is evidence of its similarity to noble metal. The effect is quite possible, supposing hybridization of Fe d-electron bands with Si p-electron bands and redistribution of d and p electrons at interface. The formed pd-band of metal is completely turned out filled one and does not take part in reaction with oxygen.

5. Conclusion

In addition to early discovered metastability of nanophase composition, surface relief changes brought to light the metastability of their structure-phase state at 3 Å and morphological state at 4.5 Å in the process of oxidation of the Fe film nanophase. Fe nanophase stability at 1.2 Å and comparison of its optical properties with electron properties of bulk phases of Si and Fe, and also analysis of behavior of its properties with the thickness allowed making conclusion about formation of electron structure similar to noble metal in it.

References

[1] N. I. Plusnin *et al*, *Surf. Rev. and Lett.* **2**, 439 (1995).
[2] N. I. Plusnin *et al*, *Surface (Rus).* **1**, 17 (2005).
[3] N. I. Plusnin *et al*, *Phys. of Low-Dim. Str.* **9/10**, 129 (2002).
[4] N. I. Plusnin *et al*, *Phys. of Low-Dim. Str.* **11/12**, 39 (2002).
[5] V. M. Il'yashenko *et al*, *Phys. Low-Dim. Struct.* **2**, 42 (2006).
[6] N. I. Plyusnin *et al*, *Tech. Phys. Lett.* **33**, 486 (2007).
[7] N. I. Plusnin *et al*, *Appl. Surf. Sci.* **253**, 7225 (2007).
[8] N. I. Plusnin *et al*, *Proc. 8-th ISMTII*, Sendai, JP, 645 (2007).
[9] F. J. Himpsel *et al*, *J. Vac. Sci. Technol.* **A2**, 815 (1984).
[10] F. Sirotti *et al*, *Appl. Surf. Sci.* **65/66** 800 (1993).
[11] C. Calandra *et al*, *Surf. Sci. Rep.* **4** 271 (1984).

16th Int. Symp. "Nanostructures: Physics and Technology"
Vladivostok, Russia, July 14–18, 2008

In situ optical method for calculation of desorption parameters of easily melted thin metal films

S. A. Dotsenko, N. G. Galkin and K. N. Galkin
Institute for Automation and Control Processes of FEB RAS, Vladivostok, Russia

Abstract. The method for calculation of desorption parameters and its simplified variant for metals are described in the article. Spectra of change of imaginary part of dielectric function of the film are initial data for the method. The simplified variant of the method was used for Mg/Si(111) system. The desorption parameters for bulk Mg film were calculated and limitations of the simplified variant were found.

Introduction

Nanoelectronic is perspective way for development of microelectronic. Therefore many scientists are finding new nanostructures in different systems. However a lot of low desorption temperature systems are poorly studied and desorption parameters influencing on film growth strongly are not calculated. The latter is reason for the former. Traditional methods were destined to investigation of thick films desorption. It is difficult to grow thick films in low desorption temperature systems and so using of these methods seems useless in this case. Therefore aim of the article was to devise method for calculation of desorption parameters for any film thickness and use it for Mg/Si(111) system. Formation of nanocrystals of semiconductor magnesium silicide (Mg_2Si) occurs in this low desorption temperature system. When Mg_2Si nanocrystals were embedded in Si substrate, high value of relative thermoelectromotive for film was observed [1]. Therefore investigation of Mg/Si(111) system is actual problem.

1. Experimental

The experiments were carried out in ultrahigh vacuum (UHV) chamber "Varian" (base pressure 1×10^{-10} Torr) equipped with electron energy loss spectroscopy (EELS) and differential reflectance spectroscopy (DRS) techniques. The samples ($19.5\times 9\times 0.35$ mm) were cut from n-type Si wafer (0.3 Ohm cm). Surface phase of clean Si(111) surface (phase (7×7)) was prepared by several flash heating at 1250 °C in UHV chamber. Magnesium was evaporated from tantalum tube and was deposited on Si sample at different temperatures (20–350 °C). To reduce sample heating by evaporation unit the distance between unit and sample was 8 cm. The rate of Mg atom deposition ($v_{\text{ad}}(\text{RT}) = 0.6$ nm/min) was calibrated by quartz sensor at room temperature (RT). EELS spectra were recorded for clean surface of sample and for film grown at certain temperature. DRS spectra were recoded in photon energy range 1.13–2.5 eV during Mg deposition on Si(111) at constant temperature and processed by method of dynamic standard (MDS). Detailed description of techniques and MDS presented in [2,3].

2. Method for calculation of desorption parameters

The main recorded value for DRS is differential reflection coefficient

$$\frac{\Delta R}{R}(h) = \frac{R(h) - R_0}{R_0}, \tag{1}$$

where $R(h)$ and R_0 — reflectance for thickness h film and for standard (in our case phase 7×7), respectively. According to MDS

$$\Delta\epsilon''_{\text{S}}(T) = \frac{\lambda}{8\pi}\frac{\left(\epsilon'_{\text{b}} - 1\right)}{v_{\text{ad}}(T)}K(T), \tag{2}$$

where K(T) — slope of linear region of $\Delta R/R(t)$ dependence, t — deposition time, T — temperature, λ — wave length, $K_h(T) = K(T)/v_{\text{ad}}(T)$ — slope of linear region of $\Delta R/R(h)$ dependence, ϵ'_b — real part of dielectric function of substrate (Si), $\Delta\epsilon''_{\text{S}}(T) = \epsilon''_{AxBy}(T)/C_x$ — change of imaginary part of dielectric function of film, $C_x = x\mu_A\rho_{AxBy}/(\rho_A(x\mu_A + y\mu_B))$, μ and ρ — molar mass and density, respectively (in our case A-Mg, B-Si) [2,3].

The adsorption rate

$$v_{\text{ad}}(T) = v_{\text{dep}} - v_{\text{des}}(T), \tag{3}$$

where v_{dep} and $v_{\text{des}}(T) = v_0\exp(-E_{\text{des}}/(kT))$ — desorption rate, v_0 and E_{des} — desorption parameters, k — Boltzmann constant. For low desorption systems $v_{\text{ad}}(T) = v_{\text{ad}}(\text{RT})$, and so relative change of imaginary part of dielectric function of film

$$\Delta\epsilon''(T) = \frac{\lambda}{8\pi}\frac{\left(\epsilon'_{\text{b}} - 1\right)}{v_{\text{ad}}(\text{RT})}K(T) \tag{4}$$

equals change of imaginary part of dielectric function of film: $\Delta\epsilon''(T) = \Delta\epsilon''_{\text{S}}(T)$. However for low desorption temperature systems $v_{\text{ad}}(T) < v_{\text{ad}}(\text{RT})$ and so

$$\Delta\epsilon''(T) = \Delta\epsilon''_{\text{S}}(T)\, v_{\text{ad}}(T)/v_{\text{ad}}(\text{RT}) \tag{5}$$

was lower than $\Delta\epsilon''_{\text{S}}(T)$. Having substituted expression (3) in (5), one obtained equation for desorption parameters

$$v_0\exp\left(-E_{\text{des}}/(kT)\right) - v_{\text{des}}(\text{RT}) = v_{\text{ad}}(\text{RT})\left(1 - \frac{\Delta\epsilon''(T)}{\Delta\epsilon''_{\text{S}}(T)}\right). \tag{6}$$

To solve equation (6), $\Delta\epsilon''_{\text{S}}(T)$ values should be known. One can find them in reference book.

If AxBy substance is metal, equation (6) can be simplified. It is known that imaginary part of dielectric function of metal $\epsilon''_{AxBy}(T) = \epsilon''_1 + \epsilon''_2(T)$, where ϵ''_1 and $\epsilon''_2(T)$ — losses due to intraband conductance and interband transitions, respectively [4]. If $\epsilon''_1 \gg \epsilon''_2(T)$, $\epsilon''_{AxBy}(T) = \epsilon''_1$, and it does not depend on temperature. Therefore

$$\Delta\epsilon''_{\text{S}}(T) = \Delta\epsilon''_{\text{S}}(\text{RT}) = \Delta\epsilon''(\text{RT}). \tag{7}$$

After substituting expression (7) in equation (6) the equation for desorption parameters

$$v_0 \exp\left(-E_{\text{des}}/\left(kT\right)\right) - v_{\text{des}}\left(\text{RT}\right) = v_{\text{ad}}\left(\text{RT}\right)\left(1 - \frac{\Delta\epsilon''\left(T\right)}{\Delta\epsilon''\left(\text{RT}\right)}\right) \quad (8)$$

contains only experimental data ($\Delta\epsilon''$ and v_{ad}(RT)). The left part of equation (8) does not depend on photon energy E and so the right one does not. Therefore $\Delta\epsilon''(T)/\Delta\epsilon''$(RT) value must not depend on photon energy. It is a criterion of correctness of expression (7) and a solution of equation (8).

3. Calculation of desorption parameters for Mg in Mg/Si(111) system

Fig. 1 contains $\Delta\epsilon''(T)$ spectra obtained for last stage of Mg film growth on Si(111) at different temperatures. Shape of spectra implies the metallic film formation at this stage. Therefore simplified variant of the method (equation (8)) can be applied. According to plasmon peak positions in EELS spectra, the film is continuous bulk Mg film. Therefore the solution of equation (8) will describe Mg desorption from bulk Mg film.

To find region of correctness of expression (7), $\Delta\epsilon''(T)/\Delta\epsilon''$(RT) dependence versus photon energy at 250 °C presented in Fig. 2. The shape of this dependence is not greatly changed at different temperatures and so these curves are not shown in Fig. 2. According to Fig. 2, photon energy range 1.13–1.4 eV is the region of correctness of expression (7). For equation (8) to solve, $\Delta\epsilon''(T)/\Delta\epsilon''$(RT) values were used from this region. The calculated desorption parameters for bulk Mg film are: $v_0 = 1571$ nm/min, $E_{\text{des}} = 0.409 \pm 0.006$ eV.

To estimate the variation of E_{des}, if expression (7) is not correct, E_{des} value was calculated in the range used (1.13–2.5 eV) and presented in Fig. 2. E_{des} value is seen to be invariable in region of correctness of expression (7), i.e. 1.13–1.4 eV. When expression (7) is not correct (range 1.4–2.5 eV), E_{des} value is noticeably reduced.

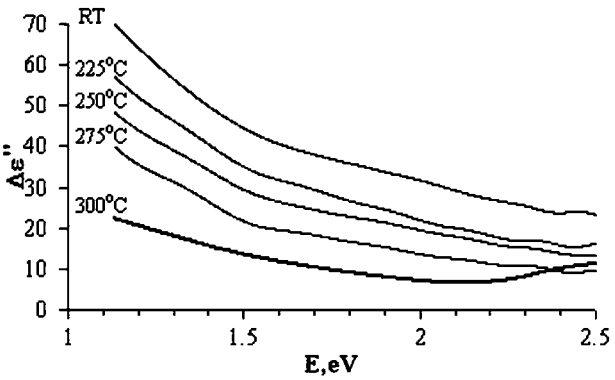

Fig. 1. Relative change of imaginary part of dielectric function of film obtained for last stage of Mg film growth on Si(111) at different temperatures.

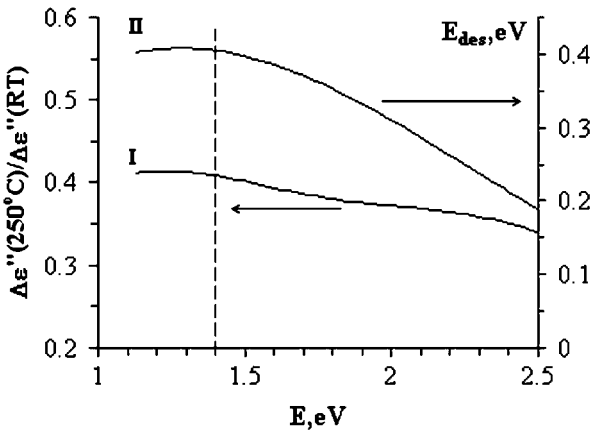

Fig. 2. Ratio of change of imaginary part of dielectric function of film at 250 °C to the same variable at RT (I) and activation energy of desorption E_{des} (II) obtained in the range used.

Acknowledgements

The work was supported by RFBR (grant No. 07-02-00958a), FEB RAS (grant No. 06-III-B-02-048), the Department of Physical Sciences of the Russian Academy of Science (grant No. 06-I-DPS-118) and Russian Science Support Foundation.

References

[1] N. G. Galkin *et al*, *e-J. Surf. Sci. Nanotechnol.* **3**, 12 (2005).
[2] S. A. Dotsenko, *Doctor Thesis*, Vladivostok, Far Eastern State University, 2006 (in Russian).
[3] S. A. Dotsenko *et al*, *e-J. Surf. Sci. Nanotechnol.* **3**, 113 (2005).
[4] V. A. Kizel', *Light Reflection*, (Moscow: Nauka) 351, 1973 (in Russian).

16th Int. Symp. "Nanostructures: Physics and Technology"
Vladivostok, Russia, July 14–18, 2008

MNOS memory structures with embedded silicon nanocrystals

Zs. J. Horváth[1], P. Basa[1], T. Jászi[1], A. E. Pap[1], A. I. Kovalev[2], D. L. Wainstein[2] and L. Dózsa[1]

[1] Hungarian Academy of Sciences, Research Institute for Technical Physics and Materials Science, Budapest, Hungary

[2] Surface Phenomena Researches Group (SPRG), 9/23, 2nd Baumanskaya Street, CNIICHERMET, 105005 Moscow, Russia

Abstract. Non-volatile metal-silicon nitride-silicon dioxide-silicon (MNOS) memory structures with an embedded sheet of Si nanocrystals were prepared by low pressure chemical vapour deposition using chemical SiO_2 tunnel layers. The duration of Si nanocrystal deposition was studied. It was obtained that Si nanocrystals improved the charging behaviour of the MNOS structures, but increased the rate of charge loss. Nevertheless, the performance of a part of the MNOS structures with embedded nanocrystals were better, than that of the structures without nanocrystals.

Introduction

It is well known that current non-volatile floating gate memory arrays face difficulties with technology scale-down. Both the tunnel and control layers in these arrays are usually SiO_2 layers. The main problem is that through defects or weak points of tunnel oxide with reduced thickness the whole amount of stored charge carrying the information can be lost. One of the possible solutions is to replace floating gate with separated semiconductor nanocrystals (ncs), which are electrically isolated [1].

But, in metal-nitride-oxide-silicon (MNOS) devices, which were the first realized memory structures, the charge is stored in traps located in the Si_3N_4 layer close to the Si_3N_4/SiO_2 interface. In these structures traps are isolated a'priori. So, difficulties mentioned above can also be solved by replacing the SiO_2 control layer with a Si_3N_4 layer. However, it is expected that formation of semiconductor nanocrystals in MNOS structures can enhance their charging and/or retention behaviour.

Further on, if using Si_3N_4, as a control layer, due to its higher dielectric constant, higher electric field will be developed in the tunnel oxide for the same layer thicknesses and voltage pulses, than for a SiO_2 control layer. The higher electric field enhances the charge injection. This is another advantage of using Si_3N_4, as a control layer.

Si ncs can be formed in Si-rich SiN_x layers by different CVD deposition techniques even without postdeposition annealing [2]. However, in this case Si ncs are distributed along the whole layer, while memory structures require a thin nc layer just near the tunnel layer.

In this work our goal has been to create memory structures with a thin Si nc layer by low pressure chemical vapour deposition (LPCVD) using a chemical SiO_2 tunnel layer and a Si_3N_4 control layer, i.e. to prepare MNOS structures with an embedded Si nc layer.

1. Experimental

For tunnel layer a SiO_2 layer was prepared after cleaning the wafers in 1 wt% HF. The SiO_2 layer was prepared using a HNO_3 treatment [3]. n-type Si wafers were immersed in 68 wt% HNO_3 at the boiling temperature (121 °C) for 60 minutes. This method yielded a SiO_2 layer with a tickness of 2.5 nm, as obtained by cross-sectional transmission electron microscopy (XTEM) [4]. The Si nc layer and the Si_3N_4 control layer were deposited by LPCVD on n-type Si substrates at 830 °C at a pressure of 30 Pa using SiH_2Cl_2 and NH_3. The Si_3N_4 layers were grown at gas flow rates of SiH_2Cl_2 and NH_3 of 21 and 90 sccm, respectively, while the Si nc layer with a gas flow rate of SiH_2Cl_2 of 100 sccm. The duration of deposition for the Si nc layer was 30 s and 60 s. Reference structures without Si nc layer were also prepared. Si_3N_4 control layer for MNOS structures was grown during 15 min, which yielded a layer thickness of 37–40 nm, obtained by ellipsometry. For electrical and memory measurements Al capacitors were formed with dimensions of 0.8 mm by 0.8 mm by evaporation after an appropriate chemical surface treatment [5].

The crystal structure of the layers was studied by X-ray photoelectron spectroscoy (XPS). Memory window measurements were performed using voltage pulses with amplitude in range ± 3 to ± 17 V and width in range 10 ms to 400 ms. To enhance the development of inversion layer, and so to avoid high voltage drop on the deep depletion layer during negative voltage pulses, the structures were illuminated with white light during the measurements. Retention measurements were carried out in dark.

2. Results and discussion

XPS results obtained on the MNOS structures after removing the upper part of the control silicon nitride layer clearly indicate the presence of Si ncs at the oxide/nitride interface, as it is presented in Fig. 1. for the structure with Si nc deposition

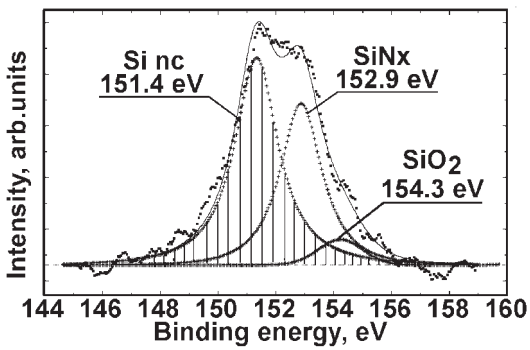

Fig. 1. Si 2s photoelectron spectrum of MNOS structure with Si nanocrystal deposition duration of 60 s after Ar ion etching at depth of 38 nm.

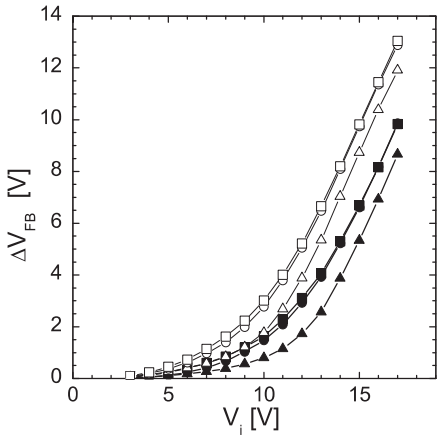

Fig. 2. The memory window width as a function of writing/erasing pulse amplitude with pulse width of 10 ms (filled dots) and 150 ms (open dots) for the studied MNOS structures with Si nanocrystal deposition duration of 0 s (triangles), 30 s (circles), and 60 s (squares).

duration of 60 s.

The results of memory window measurements as a function of writing/erasing pulse amplitude with pulse width of 10 and 150 ms are presented in Fig. 2 for MNOS structures with Si nanocrystal deposition duration of 30 s and 60 s, and without middle nc layer deposition (indicated as 0 s duration). The structures with Si ncs exhibited wider memory window, than the reference structure for the whole studied voltage pulse width range.

Results concerning the retention behaviour of all the studied structures are presented in Table 1. Although the rate of charge loss is higher for the structures with embedded Si nanocrystals, the memory behaviour of structures with Si nc deposition duration of 30 s is better, because its memory window width is higher up to 1 year, and than it is comparable with the reference structure.

Table 1. Retention behaviour of the studied MNOS structures as a function of Si nanocrystal deposition duration: the initial memory window width after applying a charging pulse of ± 15 V, 10 ms, and its extrapolated values for 1 and 10 years.

Duration (s)	Initial MW	MW after 1 year (V)	MW after 10 years (V)
0	5.34	0.87	0.46
30	6.61	0.85	0.32
60	6.68	0.47	0

3. Conclusions

Non-volatile MNOS memory structures with an embedded sheet of separated Si nanocrystals have been prepared by low pressure chemical vapour deposition using a Si_3N_4 control layer and chemical SiO_2 tunnel layers. The memory behaviour have been studied by memory window and retention measurements. It has been obtained that Si nanocrystals improve the charging behaviour of the MNOS structures. However, the presence of Si nanocrystals increased the rate of charge loss. Nevertheless, the performance of a part of the MNOS structures with embedded nanocrystals were better, than that of the structures without nanocrystals.

Acknowledgements

This work has been partially supported by the European Commission through project called SEMINANO under the contract NMP4-CT-2004-505285, and by the Hungarian Scientific Research Fund under Grant No. T048696.

References

[1] Zs. J. Horváth *et al*, *Current Appl. Phys.* **6**, 145 (2006).
[2] K. S. Cho *et al*, *Appl. Phys. Lett.* **86**, 071909 (2005).
[3] H. Kobayashi *et al*, *J. Appl. Phys.* **94**, 7328 (2003).
[4] L. Dobos *et al*, *unpublished*.
[5] P. Basa *et al*, *Physica E* **38**, 71 (2007).

16th Int. Symp. "Nanostructures: Physics and Technology"
Vladivostok, Russia, July 14–18, 2008

Quantum dot nanodevice with electron-phonon interaction

K. Král
Institute of Physics, Academy of Sciences of Czech Republic, Na Slovance 2, 18221 Praha 8, Czech Republic

The multiple scattering of electrons on LO phonons in quantum dots, included in the electronic quantum kinetic equation in the self-consistent Born approximation to the electronic self-energy, leads not only to the fast electronic energy relaxation [1,2] in these nanostructures, but also to the effect of the upconversion of electronic level occupation in quantum dots [1]. From the experimental point of view the upconversion theoretical mechanism can give an alternative explanation of the lasing of the quantum dot lasers from the higher excited electronic states. Recently the self-consistent Born approximation has also been shown to provide an explanation of the shape of the luminescence spectral line of individual quantum dots, namely the form of a very narrow peak with a shoulder at the low-energy side.

The mechanism of the up-conversion is likely to play an important role in the open nanostructures like those of a quantum dot connected to two electrodes, or in similar structures. We present some theoretical results on the electronic transport in such a zero-dimensional nanostructure, or a nanotransistor, in which we demonstrate the influence of the multiple-phonon scattering of electrons. Upon using the simple well-known Toy Model of Supprio Datta, or alternatively upon using the Meir and Wingreen formulation of the electronic transport in nanodevices, we are going to show that in an asymmetric nanodevice we can meet an effect of a spontaneous electric potential step generation between the two electric contacts of such a device. This will be documented numerically on a model of the active region of the nanotransistor having two electronic bound states. The presently discussed approximation uses the Toy Model for the electronic transport between the electric wires and the quantum dot, while the electron-LO-phonon interaction effect is included as a mechanism added to the mechanism based on the Toy Model. The electron-phonon coupling is included in the self-consistent Born approximation to the electronic self-energy. The relation of the presented theoretical results to some measurements of current-voltage characteristics of nanodevices will be discussed.

Acknowledgements

The work was supported by the grant ME 866 OS of MSMT.

References

[1] K. Král, P. Zdenek, Z. Khás, *Surface Science* **566–568**, p. 1, 321–326 (2004).
[2] K. Král, *Czech. J. Phys.* **56**, 33–40 (2006).

16th Int. Symp. "Nanostructures: Physics and Technology"
Vladivostok, Russia, July 14–18, 2008

Self-sensitive torsional microresonators based on a charge-density wave system

V. V. Koledov, V. Ya. Pokrovskii and S. G. Zybtsev
Institute of Radioengineering and Electronics, Moscow 125009, Russia

Abstract. Constructing of efficient actuators, especially working in resonance modes, is one of the most developing directions in the NEMS area. The more intriguing could be involving of new physical forces for the actuation. Here we demonstrate electrically driven torsional resonators based on whiskers of the quasi one-dimensional conductor with CDW, TaS_3. The driving force for the torsional deformation is peculiar to the CDW systems and reflects the transmission of the CDW deformation to the crystalline lattice. In comparison with the piezoelectrics, the effect of electric field on the crystal deformation is 3–4 orders of magnitude larger. The resonator is found to provide also a torsion-induced electrical feed-back (output signal) from the oscillations. We discuss the CDW systems as promising elements for NEMS.

Introduction

Most of the micro- and nanoelectromechanical systems (MEMS-NEMS) operate in the resonant modes [1]. Such devices are driven usually by electrostatic or piezoelectric forces; scaling down the dimensions of the electromechanical systems into submicron range makes these ways of actuation low effective. Still, piezoelectric nanoresonators can be highly efficient [2].

Apart from actuation, an objective of NEMS is getting the output signal characterizing the oscillations [1], so, actuators sensing their own motion are rather topical (see [3] for example).

Not long ago, several works appeared demonstrating high sensitivity of the sizes [4,5] and form [5,6] of quasi one-dimensional conductors to the deformations of the charge-density wave (CDW). The CDW deformation under electric field is well studied [8,9], however its mechanical effects on the crystal are in the early stage of understanding. The CDW forms in quasi one-dimensional conductors below the Peierls transition temperature T_P, which is typically hundreds of Kelvin and can even exceed the room temperature [8,9]. Recently it has been found [6,7] that the CDW depinning at threshold field E_t is accompanied by torsional strain of the whiskers of TaS_3, a typical CDW conductor from the chalcogenide group [8] with $T_P = 220$ K.

1. Current results

Here we report high-frequency torsional oscillations. In contrast to [6,7], the strain starts at low voltages, without a threshold. For observation of torsional oscillations we developed three variants of sample arrangement (Fig. 1). In the variant **a)** the electric contact to the elevated end is supplied by a thin low-Ohmic wire [6,7] — here a HTSC whisker of $Ba_2Sr_2CaCu_2O$ (BSCCO). Our optical scheme [10] allows to get signal from the photodiode proportional to the deflection of the beam reflected from the mirror(s) (also BSCCO whiskers) stuck to the sample. Variant **b)** exploits the orientation of the polar axis [6,7]: the two samples connected in the center are parts of one whisker cut crosswise. One of the pieces is turned upside down. Electric field $\geq E_t$ forces the adjacent (the soldered) whiskers ends to turn in the same direction [6,7]. No additional wire is needed,

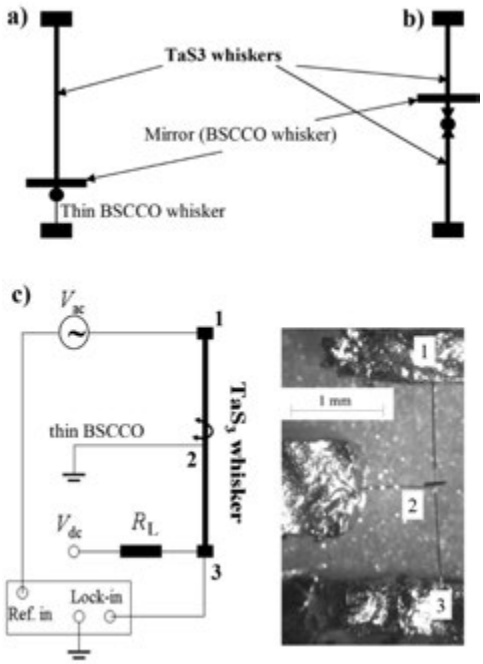

Fig. 1. Arrangements for observation of torsional oscillations. In (b) the arrows point out opposite directions of the polar axes, (c) is supplied with the electric scheme providing the feedback.

so the parasitic elasticity is completely excluded. The highest quality factor, Q, has been achieved in this arrangement. Variant **c)**, the central one for this Report, has allowed obtaining a feedback signal from the resonator. Both ends (contacts 1 and 3) of the suspended TaS_3 whisker are fixed, while a flexible thin whisker (BSCCO or $NbSe_3$) forms an additional contact (No. 2) near the center. Voltage 1–2, V_{12}, results in the torsional strain of the upper part of the whisker. The strain is transmitted to the lower part, which acts as a receiver. Measuring the 2–3 resistance we observe its torsional modulation.

Fig. 2a shows the frequency dependence of the signal from the photodiode for the sample in the 2nd arrangement (Fig. 1b), detected by a lock-in. One can see a narrow maximum at $f_0 = 4.03$ kHz. Here the AC voltage is below the threshold value, the amplitude at the maximum is about 0.2°. For higher voltages the Q-factor drops [11]. Q and f_0 grow notably with lowering temperature, the highest values of Q exceeding 104.

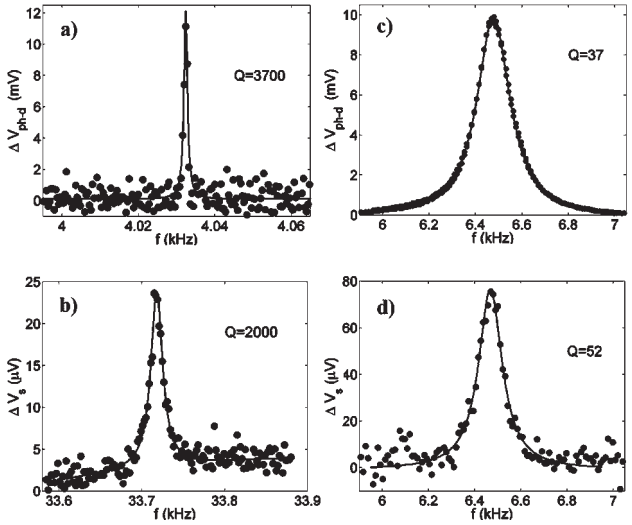

Fig. 2. Resonance peaks detected with the lock-in technique. (a) — signal from the photodiode (Fig. 1b). (b) — AC voltage across the contacts 3–2 (Fig. 1c). (c,d) — signal from the photodiode and V_{32} under identical conditions [10].

The resonant frequencies observed fall in the range 1–200 kHz.

Figures 2b and d show the signal directly from the TaS_3 samples in the configuration shown in Fig. 1c. A constant current is passed through contacts 3–2, I_{32}. The modulated (AC) component of the voltage across the sector 3–2, V_{32}, detected by a lock-in is shown in Figures 3b and d. Figures 3c and 3d show the signals detected by the photodiode and as V_{32} under identical conditions. Both methods reveal a torsional resonance at the same frequency. Thus, the TaS_3 whisker works here as a torsional piezoresistor (a "torsistor"). Up to our knowledge, this is the first indication of the effect. For all the samples we estimate the ratio between the resistance modulation and the shear deformation to be of the order of unity.

The result in Figs. 3b,d is a demonstration of a self-sensitive resonator based on the effects peculiar to the CDW. The closest parallel is piezoelectric effect. In terms of piezo-moduli, the CDW-based actuators are at least 3-4 orders of magnitude "stronger" [6,7]. However, the difference from the piezoelectric effect is not only quantitative: the torsional strain is fundamentally non-uniform, the shear growing from the center to the surfaces. Meanwhile, it develops under uniform electric field. Here the deformation reveals the non-local properties and surface pinning of the CDW [6,10].

For the present demonstration we did not make special efforts for miniaturization of the devices. However, we do not see principal complications in reducing the length below 1 μm, and the thickness below 0.1 μm. At such dimensions the whiskers retain their CDW properties [12,13]. In principle, such devices could be fabricated even manually [12,13], without involving special nanotechnology. Note, the thinner is a whisker, the higher is the torsional angle [6]. The dimensions of such a device would be defined by the whisker sizes, as it does not require external macro-parts, such as gates, solenoids or lasers.

Thus, we demonstrate a resonator based on the CDW system. The CDW provides both the actuation and the output signal. Driven like a piezoelectric, it provides a tensoresistive-like response. The particular MEMS-NEMS based on the CDW actuators could be mechanical processors of electrical signal, optical modulators and commutators, mass and moment-of-inertia detectors, nanomanipulators. In the free-end (single-clamped) mode [6] the whiskers can work as nano-screwdrivers or nano-perforators. In the present state the resonator is a nearly ready self-sensitive cantilever for an AFM.

References

[1] K. L. Ekinci, M. L. Roukes, *Rev. Sci. Instr.* **76**, 061101 (2005); H. B. Peng *et al*, *Phys. Rev. Lett.* **97**, 087203 (2006).
[2] S. C. Masmanidis *et al*, *Science* **317**, 780 (2007).
[3] V. Sazonova *et al*, *Nature* **431**, 284 (2004).
[4] S. Hoen *et al*, *Phys. Rev. B* **46**, 1874 (1992).
[5] V. Ya. Pokrovskii, A. V. Golovnya and P. M. Shadrin, *Phys. Rev. Lett.* **88**, 246401 (2002).
[6] V. Ya. Pokrovskii, S. G. Zybtsev and I. G. Gorlova, *Phys. Rev. Lett.* **98**, 206404 (2007).
[7] C. Day, *Physics Today* **60**, 24 (2007).
[8] P. Monceau, in *Electronic Properties of Inorganic Quasi-1-dimensional Conductors* Part 2. Ed. by P. Monceau. (Dortrecht: D. Reidel Publ. Comp., 1985).
[9] G. Gruner, *Density Waves in Solids* (Addison-Wesley Reading, Massachusetts, 1994).
[10] V. Ya. Pokrovskii and S. G. Zybtsev, arXiv:0708.2694v1.
[11] J. W. Brill, in *Handbook of Elastic Properties of Solids, Liquids, and Gases* (eds M. Levy, H. E. Bass and R. R. Stern) vol. II, 143–162 (Academic Press, New York, 2001).
[12] S. V. Zaitsev-Zotov, *Physics — Uspekhi* **47**, 533 (2004).
[13] A. McCarten *et al*, *Phys. Rev. B* **46**, 4456 (1992).

16th Int. Symp. "Nanostructures: Physics and Technology"
Vladivostok, Russia, July 14–18, 2008

Efficient light absorption in high-speed metal-semiconductor-metal nanostructures

St. Collin[1], F. Pardo[1], *St. Averin*[2], N. Bardou[1] and J.-L. Pelouard[1]

[1] Laboratoire de Photonique et de Nanostructures CNRS, Route de Nozay, 91460 Marcoussis, France
[2] Institute of Radioengineering and Electronics, Russian Academy of Sciences, square acad. Vvedensky 1, 141190, Fryazino, Moscow region, Russia

High speed and efficient photodetectors are of great interest for optical communication, terahertz generation and scientific instrumentation. Both the absorption length in bulk semiconductor and diffraction effects reduces drastically light conversion efficiency in nanoscale photodiode structures. As a result, conventional high-speed photodetectors (PIN-diodes, MSM-detectors etc.) are subjected to a trade-off between response speed and quantum efficiency. The highest response speed measured to-date (FWHM = 0.58 ps) had been achieved in LT-MSM-detector with 100 nm finger spacing but with very low quantum efficiency of ∼2% due to low-temperature-grown GaAs active layer and opacity of the detector metallic contacts [1]. Another approach for considerable shortening detector response time (FWHM = 0.63 ps) was in use of MSM-heterobarrier diode structure [2] and again has resulted in poor quantum efficiency of ∼8%. The achievement of quantum efficiencies greater than 50% with cut-off frequencies above 300 GHz requires new solutions to confine efficiently the absorption of light in nanoscale, low capacitance structures.

We report on the resonance cavity enhanced sub-wavelength MSM-photodiode structures (RCE SMSM) based on nanoscale (feature dimensions smaller than $\lambda/8$) metallic gratings which are used both as a tool for efficient light confinement and the photocarriers collection [3]. Fig. 1a shows the schematic cross-section of detector structure. The bottom mirror is a quarter wave stack multilayer Bragg reflector. The resonance cavity is made of a thin absorbing layer on top of nonabsorbing "spacing" layer. The thickness of the absorbing layer can be only a few tens of nanometers and the thickness of the spacing layer is adjusted to satisfy the Fabry–Perot condition. The subwavelength metallic grating is a partially reflecting mirror whose electromagnetic properties depend on the light polarization and must be tuned precisely. Light transmission through the metallic grating occurs via a coupling of the incident light with the optical modes into the slits. This coupling mechanism depends strongly on TE and TM polarization, resulting in different spatial distribution of the electric field intensity (Fig. 1a).

The RCE SMSM photodetector has been realized on a semi-insulating GaAs substrate. The semiconductor layer structure was grown by molecular beam epitaxy. The multilayer Bragg reflector is composed of 16 periods of quarter waves AlAs/$Al_{0.2}Ga_{0.8}As$ layers. The GaAs absorption layer thickness is 40 nm. For a resonance at ∼800 nm wavelength in the center of the stop band of the Bragg mirror the $Al_{0.35}Ga_{0.65}As$ spacing layer thickness was chosen to be 300 nm. We have fabricated these RCE SMSM-photodetectors on GaAs substrates

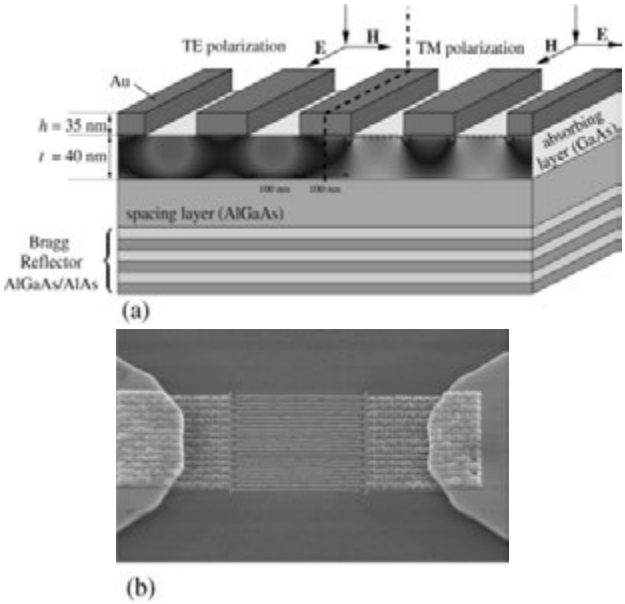

Fig. 1. Spatial distribution of the electric-field intensity in the absorbing layer of an RCE SMSM photodetector was calculated for TE ((a) left) and TM ((a) right) polarization. Most of the incident light is absorbed in the red regions. A Ti/Au grating deposited on GaAs-based layers forms a 5 × 5 μm RCE SMSM ((b), scanning-electron micrograph).

with Ti/Au gratings and 100 nm finger width/ spacing, Fig. 1b. The grating was defined by electron-beam assisted evaporation and lifted off in trichloroethylene. The 2–5 nm thick titanium layer has been used to improve the metal adhesion to the GaAs layer. The measured reflectivity of fabricated devices 3 × 3, 5 × 5, 10 × 10 μm^2 in size for TE and TM polarization matched well with theory confirming the resonance mechanism.

The RCE SMSM-diodes have nearly symmetrical I–V characteristics with typical dc dark current of 100 pA at 2 V for the $5 \times 5\ \mu m^2$ device with 100 nm finger gap and width. I–V curves were examining by taking into account the barrier height dependence on the electric field and tunneling through the barrier [4]. Following this analysis we have extracted the Schottky barrier height $\Phi = 0.6$ eV and diode ideality coefficient $n = 1.05$ for the RCE SMSM-diode structure.

The spectral dependence of the RCE SMSM-detector responsivity has been measured using tunable laser source and high resolution Jvon–Yobin spectrometer. The spectrometer was calibrated with Ar-lamp as a reference. The spectral dependence of the laser power and all optical components were evaluated using calibrated detector Newport 818-ST. A laser

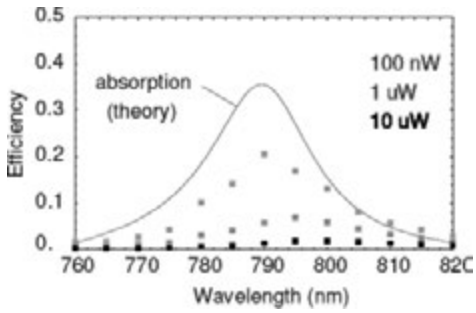

Fig. 2. Measurements of the external quantum efficiency and calculations (solid lines) for RCE SMSM-photodiode.

spot diameter smaller than the MSM active detector area has been focused on the detector with an objective and traced on the screen with CCD camera. Subsequent measurements of the RCE SMSM-detector and reference Newport detector against the calibration detector yielded absolute detector responsivity at a particular laser wavelength. The final MSM-detector spectral responsivity curves were then obtained using this calibration points, Fig. 2. These measurements have demonstrated detector resonance behavior with good agreement with calculations. High density of photogenerated carriers shifts the optimum detector efficiency for longer wavelengths.

Our devices have reached an experimental external efficiency of 22% at 790 nm in TE polarization for low level of optical excitation, Fig. 2. This is considerable efficiency improvement by more than order of magnitude in comparison with conventional MSM photodetector with a similar geometry of 100 nm finger spacing [1]. The efficient collection of photocarriers through a high and homogeneous electric field in RCE SMSM diode structures with only 50 nm mean collection path along with low diode capacitance (8 fF) should allow theoretical cut-off frequencies as high as 500 GHz. Response time measurements are now in progress.

In summary, we have shown experimentally how light absorption can be confined efficiently in nanoscale metal-semiconductor-metal nanostructures. Sub-wavelength metallic gratings were used as a tool for both the light confinement and the photocarriers collection. In the resonant-cavity-enhanced subwavelength metal-semiconductor photodetector absorption is achieved through 100 nm finger widths and finger spacing in a 40 nm thick absorption GaAs layer. External quantum efficiency as high as 22% has been obtained. These detectors constitute a step ahead towards the realization of highly efficient and ultrafast photodetectors.

References

[1] S. Y. Chou, Y. Liu, Khalil, T. Y. Hsiang *et al*, *Appl. Phys. Lett.* **61(7)**, 819–821 (1992).

[2] S. V. Averin, E. Stein von Kaminski, H. G. Roskos *et al*, *Quantum Electronics* **24 (9)**, 814–818 (1994).

[3] St. Collin , F. Pardo, R. Teissier, J.-L. Pelouard, *Appl. Phys. Lett.* **85(2)**, 194–196 (2004).

[4] S. V. Averin, Y. C. Chan, Y. L. Lam, *Appl. Phys. Lett.* **77(2)**, 274–276 (2000).

16th Int. Symp. "Nanostructures: Physics and Technology"
Vladivostok, Russia, July 14–18, 2008

Quantum point contacts in disordered Si-MNOS mesoscopic structures with inversion n-channel: Percolation path locality and magneto-transport peculiarities

A. S. Vedeneev[1], B. A. Aronzon[2], A. B. Davydov[2], A. M. Kozlov[1], P. E. Ruzanov[1], A. S. Bugaev[1], J. Galibert[3] and J. Leotine[3]

[1] Institute of Radioengineering and Electronics, RAS, Fryazino, Moscow distr.,141190, Russia
[2] RSC "Kurchatov Institute", Moscow, 123182, Russia
[3] LNCMP, Toulouse, France

Abstract. For mesoscopic Si-MNOS structures with inversion n-channel and high ($N_t \approx 7 \times 10^{12}$ cm^{-2}) built-in charge concentration, and thus strong fluctuation potential (FP) the longitudinal conductance G has been studied in dependence on the gate voltage V_g and magnetic field at the temperature 4.2 K. The $2e^2/h$ conductance quantization characterizes the $G(V_g)$ dependence. The mesoscopic percolation path reconstruction, i.e. variation of the number N ($1 < N < 10$) for series connected point quantum contacts (the FP saddle regions) along the path with the V_g variation, has been observed there.

At $G > 2e^2/h$ the structures manifest the Shubnikov–de Haas oscillations, while in case of the percolation path reconstruction ($G \leq e2/h$) the structures show anormal strong negative magneto-resistance, up to 40% in magnetic fields of 10–20 T.

The effect is discussed in terms of the mesoscopic percolation path reconstruction when the quantum point contact transparency and filling of Landau levels in the FP wells are both dependent on the V_g and magnetic field.

Interest to insulator-metal transition properties for usual Si-based MIS structures [1,2,3] disordered by a high ($N_t > 10^{12}$ cm^{-2}) built-in charge concentration (ionized impurities), when the charges act themselves as sources of strong fluctuation potential (FP) with the amplitude $\Delta \propto N_t^{1/2}$ [4] ($\Delta > kT$ at $T > 200$ K), improves present study of the percolation conductance [3] in mesoscopic systems. The electron transport there is carried out by electron tunneling between the FP wells across the FP saddle regions acting as the quantum point contacts in the considered case [5,6]. In the mesoscopic case, when the structure length L is smaller then the percolation cluster correlation radius L_c, the electron transport is dominantly carried out along a single percolation path which resistance is mainly controlled by the most resistive element, alone FP saddle constriction acting as the quantum point contact at a high N_s by the requirement [5,6] $h\omega_x \sim (N_t \Delta/D)^{1/2} > kT$, where the $D = 2m/\pi h^2$ is the electron state density at the lower subband.

The discussed scenario has been previously realized for the case of Si-MNOS (metal-nitride-oxide) structures and Si-MOS structures with inversion n- and p-channel, and high ($N_t \leq 3 \times 10^{13}$ cm^{-2}) concentration of built-in charge at the Si-SiO_2 interface. By analyses of the G vs. V_g, the temperature T (4.2–300 K), and longitudinal voltage dependence [7,8,9] the $h\omega_x$ and $h\omega_y$ parameters have been estimated in frames of [5,6] as effective characteristics of the saddle point constriction in longitudinal and transverse direction. Reciprocal assent for experiment estimations have been arrived at [7,8,9].

In the work we continue study of the G vs. V_g and magnetic field for estimation the hwx and hwy parameters for understanding the mechanism of the structure magneto-transport.

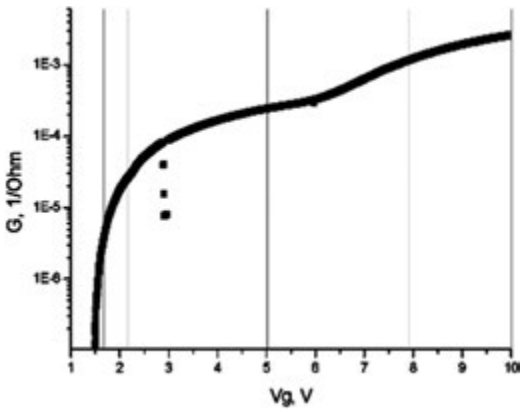

Fig. 1.

Studied Si-MNOS structures have been fabricated as planar FETs with inversion n-channel and the gate length and width of 50 and 500 nm. Thickness of the under-gate SiO_2 and Si_3N_4 layers was 2.5 and 35 nm respectively. Built-in charge concentration N_t has been set by the field injection of electrons from silicon onto traps at the Si-SiO_2 interface and then controlled by the threshold voltage removal [1]. As previously shown [7], the L_c well restricts 100 nm at the G threshold, thus studied structures are considered as mesoscopic ones. Static conductance G has been measured by the modulation method at longitudinal voltage $\leq$1 mV and the structure magneto-transport has studied in pulsed magnetic fields up to 50 T.

Fig. 1 illustrates the G vs. V_g dependence. The $2e^2/h$ conductance quantization is qualitatively confirmed by presence of a quasi-plateau at $G \approx 2e^2/h$. The G vs. V_g analyses by [7] has shown that the mesoscopic percolation path connects more then one active quantum contact along the path, and the number of this contacts N varies with the V_g variation in frames of $1 \leq N \leq L/R_s$ [8], where R_s is the FP non-linear screening radius [4] and $L/R_s \sim 10$ in the considered case. By the Fig. 1 data the built-in charge concentration $N_t \approx 7 \times 10^{12}$ cm^{-2} and $h\omega_x \sim 100$ meV have been estimated.

Fig. 2 illustrates magneto-transport characteristics for the structures. At $G \geq 2e^2/h$ the $G(B)$ has an oscillation character

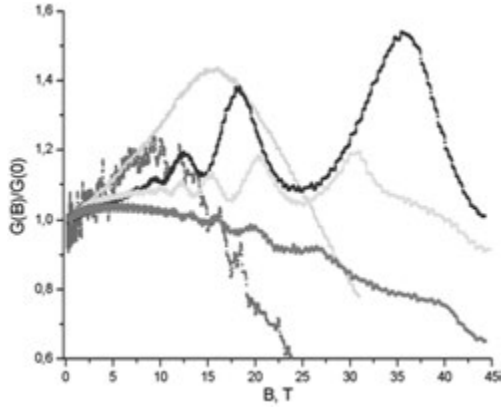

Fig. 2.

when position of the G maxima is the linear function of $1/B$. It corresponds to variation of Landau level number in frames of 1 to $\approx$5. The electron concentration estimated by Shubnikov–de Haas oscillations is found to be by the order smaller then the concentration estimated by the field effect data. The result qualitatively illustrates the case of strong electron localization in considered structures.

Effect of strong negative magneto-resistance at $G < e^2/h$ we associate with the percolation path reconstruction because of the quantum contact transparency dependence on the V_g and magnetic field in frames of [5,9].

Acknowledgements

The work has been supported by RFBR (# 06-02-17529) and RNP (# 2.1.1.4639).

References

[1] T. Ando, A. Fowler, and F. Stern, Rev. Mod. Phys. **54**, 437 (1982).
[2] Y. Imry, *Introduction to Mesoscopic Physics*, Oxford, University Press (2002).
[3] B. I. Shklovskii and A. L. Efros, *Electron Properties of Doped Semiconductors* (Nauka, Moscow, 1979; Springer, New York, 1984).
[4] V. A. Gergel and R. A. Suris, *Sov. Phys. JETP* **57**, 415 (1983).
[5] M. Buttiker, *Phys. Rev. B* **41**, 906 (1990).
[6] Y. Meir, *Phys. Rev. Lett.* **83**, 3506 (1999).
[7] B. A. Aronzon, A. S. Vedeneev *et al*, *Semiconductance* **35**, 448 (2001); **36**, 1241 (2002).
[8] A. S. Vedeneev, M. A. Feklisov, *Semiconductors* **40**, 1069 (2006).
[9] M. E. Raikh and L. I. Glazman, *Phys. Rev. Lett.* **75**, 128 (1995).

16th Int. Symp. "Nanostructures: Physics and Technology"
Vladivostok, Russia, July 14–18, 2008

New shape memory nanoactuator

V. Shavrov[1], V. Koledov[1], A. Kirilin[1], V. Khovaylo[1], G. Lebedev[2], V. Pushin[3] and A. Tulaikova[1]

[1] Institute of Radioengineering and Electronics, Moscow 125009, Russia
[2] Moscow State Institute of Steel and Alloys, Technological University, Moscow 119049, Russia
[3] Institute of Metal Physics Ural Division of RAS, Ekaterinburg 620219, Russia

Abstract. The aim of the present work is to propose the new composite functional material on the basis of shape memory effect (SME) alloy which permits the much higher reversible change of the bending strain. This change can be attained under the action of thermal field in case of SME alloys or SME polymers and moreover under the action of magnetic field in case of ferromagnetic shape memory alloys. The composite includes a SME element in the form of ribbon, film or plate and an elastic layer of usual metal. Elements are connected rigidly to each other. The pseudo plastic tensile deformation is given to the SME layer before connecting to the elastic element. The result is the reversible giant bending strain (up to 10%) of composite, though only the "one-way" shape memory effect of the SME element is used. We discuss the new composite system as promising elements for NEMS.

Introduction

In the recent years much effort has been directed to the development of new functional materials. Under functional or intellectual materials those ones are usually understood, which change their shape and/or size in response to the actions of external fields: thermal, magnetic, electric. Such materials are of great importance in the development of microelectromechanical systems, because in this case the usual mechanical scheme, comprising an engine, a transmission and an executive element is often not applicable. Functional materials which exhibit Shape Memory Effect (SME) are thought to solve this problem and have already found a great number of applications, for example in electronics, space technology and medicine. However the SME alloys demonstrate the inherent drawback, particularly, a change of the form of an SME actuator is irreversible on temperature ("one-way shape memory effect"), or demands the preliminary non-technological operation of training of the alloy ("two-way shape memory effect").

The bimorph layered structures of different materials are used in several works in order to attain the reversible bending deformation in response to heat, current or electric field [1–3]. The bimorph structures using NiTi SME alloy films deposited on Si substrate have been studied and showed the reversible heat controlled actuation [4]. Unfortunately all of these schemes demonstrate comparatively low controlled bending due to small change of layer length in response to external field (not higher then 0.1%).

The aim of the present work is to propose and to study the new composite functional material on the basis of SME alloy which permits much higher reversible change of the bending strain under the action of the external thermal field or under the action of electric current. Fig. 1 gives the schematic view of the composite. The composite includes a SME element in the form of ribbon, film or plate (1) and an elastic layer of usual metal (2) connected rigidly to each other. Before connecting to the elastic element the SME layer is given the pseudo plastic deformation for example the tensile one, during the process of composite preparation. The result is the reversible giant bending strain (up to several %) of composite in response to heating, using only "one way shape memory effect" of the SME element.

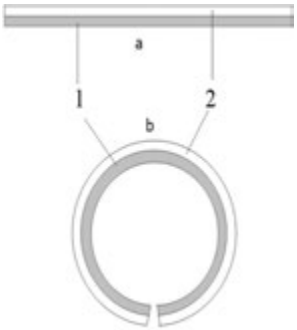

Fig. 1. A layered composite on the basis of SME melt spun ribbon after preparation (a) and after heating upper then martensit — austenite transition temperature (b). 1 — SME alloy element, 2 — usual elastic metal element.

1. Composite preparation and performance

On the first stage of the process of composite preparation the preliminary tensile pseudo elastic deformation of SME alloy element has been accomplished as follows. The 30 μm thick TiNiCu melt spin ribbon, demonstrating perfect SME, has been loaded with the tensile force of about 3 N. Then the electric current of about 1 A has been supplied to it. After that the current has been turned off. The deformation of the ribbon due to changing of the temperature caused by current flow was measured by optical microscope. The dependence of the SME ribbon elongation $\Delta l/l$ versus current I is hysteretic type dependence obtained is typical for the SME alloys.

At decreasing of the current the ribbon is stretched for about 1%, at increasing of the current it restores the initial length.

For the composite preparation the ribbon has been left in the cooled stretched state. The stretched ribbon has been glued to 30 microns thick amorphous steel elastic ribbon at room temperature. The resulting bimorph composites lengths are 4–6 cm and thickness — 60 μm.

The electric current controlled composites have been prepared by gluing of the isolated 30 μm thick nichrome wire on the surface of bimorph composite. The test of temperature

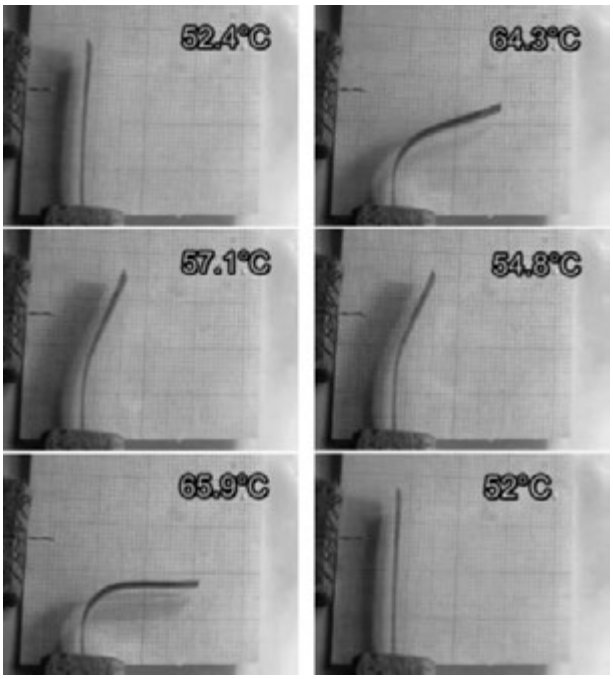

Fig. 2. Reversible strain of TiNiCu based composite.

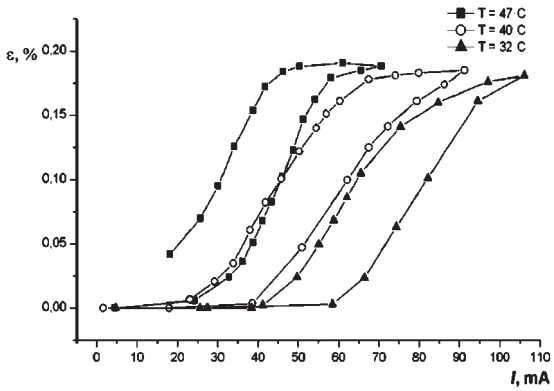

Fig. 3. The composite bending deformation of versus current at different temperatures.

controlled operation of the composite is illustrated by Fig. 2. The composite bending strains versus current curves show hysteretic dependence (Fig. 3). The controlling current appears to be strongly temperature dependant.

2. Conclusions and outlook

We can conclude that in the present work the new functional material scheme has been proposed and preliminary tested in the model experiments. The reversible bending deformation of the composite using only "one way" SME have been demonstrated under thermal and current control. We think that it is possible to apply the various technologies for creating of the elastic and SME layers for composites manufacturing, including vacuum and galvanic deposition. The resulting composites can be applied in a large variety of fields, such as micromanipulators, micro tools, various actuators, medicine etc. The minimal size of actuator on the basis of a composite is determined by the size of crystallite which can be about 10 nanometers in nanocrystalline SME alloys films. The ferromagnetic SME alloys can also be used in order to provide magnetic field controlled composites on micrometer and probably on nanometer scale [5–6].

Acknowledgements

This work was supported by the RFBR (projects Nos. 06-02-16266, 06-02-16984 and 06-02-39030).

References

[1] J. H. Yoo *et al*, *Sensors and Actuators A* **79**, 8 (2000).
[2] A. Cozma Lapadatu *et al*, *Sensors and Actuators A* **82**, 69 (2000).
[3] H. Sehr *et al*, *J.Micromech. Microeng.* **11**, 306 (2001).
[4] A. Composeo *et al*, *Appl. Surf. Sci.* **208–209**, 518 (2003).
[5] A. A. Cherechukin *et al*, *Phys. Let. A* **291**, 175 (2002).
[6] M. Kohl *et al*, *Sensors and Actuators A* **114**, 445 (2004).

16th Int. Symp. "Nanostructures: Physics and Technology"
Vladivostok, Russia, July 14–18, 2008

Peculiarities of current-voltage tunnel characteristics of Al-SiO_2-n-Si structures with the ultrathin oxide in a state of the Si surface depletion

G. V. Chucheva, E. I. Goldman, Yu. V. Gulyaev and A. G. Zhdan

Institute of Radio Engineering and Electronics Russian Academy of Sciences, 141190 Fryazino, Moscow Region, Russia

The use of gate dielectrics at most small (before 2 nm) of the thickness is one of the main of the nanoscaling conditions of the element base of integrated circuits, based on metal-oxide-semiconductor field effect-transistors (MOSFET). Tunneling currents across an insulator layer are a characteristic feature of modern nanoscale metal-oxide-semiconductor (MOS) structures. In this context, the studies of electron tunneling through ultrathin SiO_2 layers (5 nm and under) became more intensive.

The conductivity of ultrathin ($h < 5$ nm) oxide in the metal-oxide-semiconductor (MOS) structure is defined by electron direct tunneling through the potential barrier, formed by a gate insulator [1]. At the same time the transparency of the barrier already at the zero-voltage between a field electrode (FE) and a semiconductor ($V_g = 0$) is so great, that tunneling current becomes measured practically all at once after breaking of the detailed balance. Within the range of not too greater voltage drops on oxide V_i, corresponding to the depletion of the semiconductor, electrons on the Fermi level of the FE for the tunnel transition in a semiconductor, in addition to the barrier-oxide it is necessary to overcome else and the classically forbidden region in Si (the additional potential barrier $\Delta\varphi$, the Fig. 1). This region appears therefore that the bottom of the conduction band of the semiconductor at the Si-Si[41e]$_2$ interface (IF) under $V_g = 0$ is situated above the Fermi level of the FE. With growing V_i the bottom of the conduction band of the silicon is lowered under the Fermi level of the FE, and indicated range disappears. Thereby, the current-voltage (I–V)-characteristic of the circuit of the FE-Si must to contain to features, connected

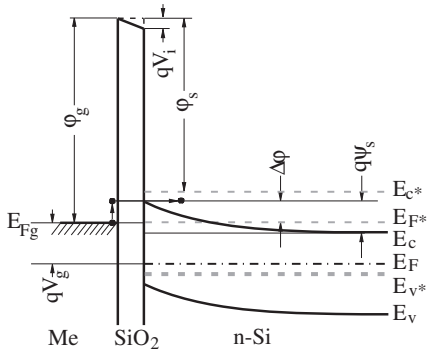

Fig. 1. The band diagram of the MOS-structure in a state of the depletion. φ_g, φ_s — contact potential barriers at the oxide heterointerfaces, E_c — the bottom of the conduction band, E_v — the top of the valence band, E_F, E_{Fg} — the Fermi energy, E_{c*}, E_{v*}, E_{F*} — the position of bands and the Fermi energy at the $V_g = 0$, ψ_s — the semiconductor surface potential, V_g — the potential of metal electrode, V_i — the voltage drop across the oxide.

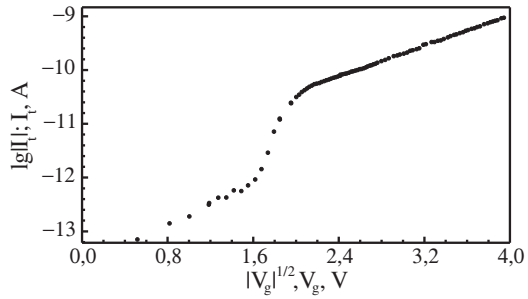

Fig. 2. The experimental I–V-characteristic of the investigated Si-MOS-structure.

with the limitation of the electronic flow by the forbidden region in a semiconductor, as well as with its disappearance under the certain V_g.

Exactly, under small values $|V_g|$ the tunnel current will be defined by the thermoautoemission with the FE, growing with the increase $|V_g|$ on the typical thermoautoemission law, taking into account the reduction and following disappearance of the additional barrier. Further, with growing $|V_g|$ the tunnel current will be defined by the classical law of the direct tunneling through the barrier, created by the gate insulator. Thereby, between the initial region of the tunnel I–V-characteristic and the region of the I–V-characteristic, appearing after the disappearance of the additional barrier must to exist the region of the sharp growth of the current.

Calculations of the tunnel I–V-characteristic, taking into account considered circumstance, show that the initial and the final (after the disappearance of the additional barrier) of regions of dependencies of the tunnel current I_t from V_g must to follow of the law: $\lg I_t \propto |V_g|^{1/2}$.

In Fig. 2 the experimental I–V-characteristic of the tunnel conductivity of the Al-SiO_2-n-Si structure with the oxide thickness of 4[43d][43c] is presented. I–V-characteristics are measured under the room temperature; steps of the depletion voltage with the amplitude before — 16 V are applied on the structure. Initial values of the tunnel current are registered under each voltage step. This current has the step form before the moment of the time $t \leq 1$ s. As is seen from the Fig. 2, observed I–V-characteristics agree well with above stated presentations.

Acknowledgement

Work was supported party by the Russian Foundation for Basic Research (grant 06-08-01649-a).

References

[1] S. M. Sze, *Physics of Semiconductor Devices*, John Willey and Sons, New York (1981).

16th Int. Symp. "Nanostructures: Physics and Technology"
Vladivostok, Russia, July 14–18, 2008

Synthesis, properties, and applications of III–V nanowires

Jonas Johansson
Solid State Physics and the Nanometer Structure Consortium, Lund University
P.O. Box 118, SE-221 00 Lund, Sweden

Abstract. In this paper, some important aspects of the nanowire research in Lund are presented. Freestanding, epitaxial nanowires in most of the common III–V materials are routinely being grown by metal-organic vapor phase epitaxy. The growth is seeded by aerosol fabricated metal particles, typically of gold. A mass-transport model describing the length growth rate of the nanowires is described. The morphology and the crystalline quality of the wires are also discussed. A few state-of-the art applications are high-lighted: nanowire array guided cell growth, wrap-gate field effect transistors, and solar cells.

Introduction

During the last decade there has been a tremendous research interest in semiconductor nanowires. These structures can be described as quasi-one-dimensional crystallites — a few micrometers in length and about 5–100 nm in diameter. Nanowires have made a significant impact in several applications in physics, electronics and photonics, as well as in life sciences.

Metal particle-seeded III–V nanowires represent one of the most thoroughly investigated categories of nano-wires. In general, the first step is to arrange metal particles on a semiconductor substrate surface. The next step is to insert this sample into a crystal growth chamber. The temperature is then elevated and the metal particle may form an equilibrium alloy with the substrate. When the growth species are introduced, the metal particle becomes supersaturated and crystallization of material at the interface between the particle and the substrate initiates. Thus, the nanowire lifts the particle as it grows, with the size of the particle dictating the diameter of the nanowire. The growth continues as long as the concentration of growth species in the ambient phase is high enough to supersaturate the particle. This supersaturation is the driving force for growth. A recent review article on nanowire growth mechanisms has been written by Kolasinski [1].

In this paper we discuss a mass-transport based model for the overall growth rate of nanowires in connection with the Gibbs–Thomson effect, which has to be included when the seeding metal particles are small or when the supersaturation is low. We describe the morphology of nanowires and the amount of planar defects in them based on classical nucleation theory. We will also show a few state-of-the-art applications, reflecting the research in Lund.

1. Synthesis

As mentioned in the introduction, the first step in nanowire synthesis is to arrange metal particles on a semiconductor substrate surface. There are several routes to this. Heating a deposited thin metal film can cause the film to "roll up" and form balls under non-wetting conditions. Other methods are deposition of commercially available colloidal particles, lithographic definition of particles, or formation of particles in the aerosol phase.

When requirements on the positions of the particles have to be met, the most practical way is to lithographically define the particles. In this case a resist is deposited and the desired patterned is defined by means of electron beam or nanoimprint lithography. In the next step, the desired metal is deposited by evaporation or sputtering. Finally the lift-off process is used to remove the excess metal together with the resist.

When it comes to the particles, one of the most versatile fabrication routes is to produce the particles in the aerosol phase just before depositing them on the substrate surface. In this process, which has been developed in Lund, metal source material is evaporated and condensated in a carrier gas that transports the particles to a size selection device, the differential mobility analyzer, and a series if sintering steps before deposition on a substrate surface. The method is suitable for most metals and metal alloys. Since the condensation process takes place far from equilibrium, even thermodynamically unstable alloy particles can be formed. As a final result, size homogeneous particles of a chosen diameter can be deposited at a desired areal density.

The next step is the nanowire crystal growth step. In Lund we have equipment for both chemical beam epitaxy (CBE) and metal-organic vapor phase epitaxy (MOVPE). In this paper we will mainly focus on MOVPE growth but also show some results related to CBE. We routinely grow gold particle seeded nanowires in GaAs, GaP, InAs, InP, and InSb. In many of these materials we also fabricate radial and axial heterostructures, alloys, such as $Al_xGa_{1-x}As$, and intentionally doped segments.

After aerosol deposition (or lithographical definition of particles) the substrate is transferred to the MOVPE reactor. Before growth under low-pressure conditions, the gold particles are annealed at the surface for around 10 min in a hydrogen/group V (phosphine or arsine) atmosphere at elevated temperature (typically 580 °C for GaAs, InAs, and InP substrates and 650 °C for GaP substrates). During the annealing step, any surface oxides will be desorbed and the gold will be alloyed with the substrate material, primarily by an uptake of Ga or In by the Au particles. After annealing the temperature is ramped down to growth temperature. Wire growth starts when group III precursors (trimethyl gallium or trimethyl indium) are supplied to the reactor cell.

For wire growth we use a lower growth temperature as compared to epitaxial film growth. Typical growth temperatures for III–V nanowires are 400–500 °C, whereas optimum 2D epitaxial film growth generally occurs at about 200 °C above this. At these lower temperatures, 2D film growth is kinetically suppressed but the nanowires grow, with minimal competition from substrate growth. We have not been able to find a minimum temperature below which nanowires no longer grow.

However it is unfeasible to grow at too low temperatures, since the growth rate becomes extremely low.

2. Properties

Here, some important properties of nanowire growth will be discussed. We have developed a mass-transport model for nanowire growth. The model is based on two coupled deposition-diffusion equations, one for adatom diffusion on the substrate and one for diffusion along the wire. The gold alloy particle is approximated as a hemisphere of radius r, identical to the radius of the wire. The diffusive flux of material on the substrate and the wire side walls is directed to the gold particle, which acts as a collector of material. There is no accumulation of material in the particle, but a steady-state flow (not rate limiting) of material to the wire growth interface. At late stage, when the wire length $L > \lambda$, where λ is the diffusion length along the wire, the wire length growth rate is given by,

$$\frac{dL}{dt} = 2R\left(1 + \frac{\lambda}{r}\right). \tag{1}$$

Here R is the arrival rate of reactant species per surface site. The full derivation has been done by Johansson *et al* for MOVPE [2] and by Dubrovskii *et al* for MBE [3].

For thin wires or for low supersaturation, the Gibbs–Thomson effect has to be included in the growth rate. For a reactant pressure P surrounding the wire and a pressure P_r of the same reactant in a metal particle of radius r, the net arrival rate is proportional to the pressure difference $R \propto P - P_r$. According to the Gibbs–Thomson effect, P_r increases with decreasing r as $P_r = P_\infty \exp(2\sigma\Omega/rk_\mathrm{B}T)$, where P_∞ is the reactant pressure in a particle with infinite radius, σ is the surface energy of the particle, and Ω is the molecular volume of the reactant specie. Combining these expressions, we arrive at

$$\frac{dL}{dt} \propto \left[P - P_\infty \exp\left(\frac{2\sigma\Omega}{rk_\mathrm{B}T}\right)\right]\left(1 + \frac{\lambda}{r}\right). \tag{2}$$

This proportionality has two interesting limiting cases.

For nanowire growth with typical particle sizes (20–100 nm) and under high supersaturation, the Gibbs–Thomson effect can be neglected. This leads to a case where thinner wires grow faster than thicker ones. This is the common case, observed in most experiments and illustrated in Fig. 1 for MOVPE grown, Au seeded, GaP nanowires.

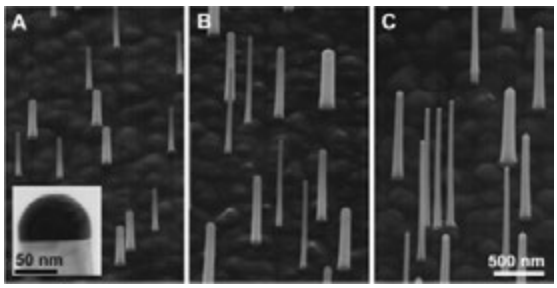

Fig. 1. Scanning electron micrographs of GaP nanowires grown with MOVPE at different temperatures: (A) 440, (B) 470, and (C) 500 °C. The transmission electron micrograph inset shows the top region of one of the GaP nanowires grown at 440 °C with its roughly hemispherical gold particle.

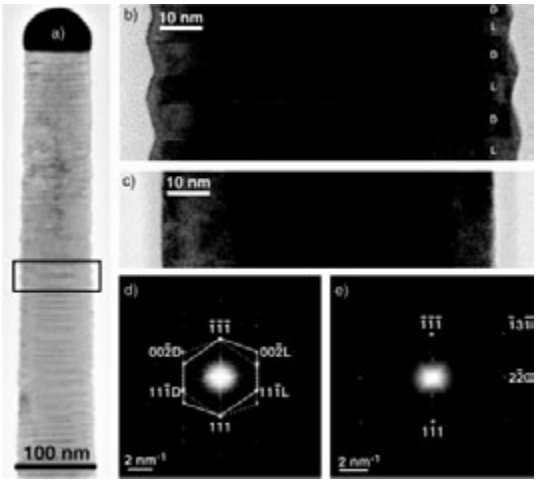

Fig. 2. The crystalline structure of ⟨111⟩B GaP nanowires as determined from HR-TEM. In a) an overview image of a nanowire with a gold particle on its top is shown. The dominating structure is cubic zinc blende with repeated {111} twinning resulting in a geometric feature where the twinning planes are clearly visible in b) the $\langle\bar{1}10\rangle$ directions but completely aligns in c) $\langle 11\bar{2}\rangle$. The respective segments are seen as dark (D) and light (L) bands in $\langle\bar{1}10\rangle$ as a result of the refracting conditions in the TEM. The corresponding fast Fourier transforms (FFTs) show a splitting in d) $\langle\bar{1}10\rangle$, originating from D- and L-segments respectively, but not in e) $\langle 11\bar{2}\rangle$.

For nanowire growth with small particles and working close to equilibrium, the r dependent term P_r is dominating. The consequence is that thicker wires grow faster than thinner ones and, in the extreme case, wires can not grow below a certain minimum radius, corresponding to $P - P_r = 0$. We have recently observed this effect for CBE grown, Au seeded, InAs nanowires. The minimum radius below which wires did not grow could be tuned between 11 and 18 nm, by changing the supersaturation [4].

Concerning the internal structure of the wires, we have shown that the dominating crystal structure of the nano-wires is zinc blende. By carefully rotating single nanowires in the transmission electron microscope (TEM) we could conclude that the wires consist of twin lamellae, shaped as truncated octahedra and thus terminated by {111} facets only, see Fig. 2. The thickness of the lamellae is 3–5 mono-molecular layers, depending on growth temperature. The alternating orientation of the twin lamellae gives rise to a microfaceting of the {112} overall oriented nanowire side walls into {111}A and {111}B microfacets [5].

By pulsing the group III source (trimethyl gallium for GaP), we have shown that it is possible to reach extremely low supersaturations. In these cases we get wires with very long zinc blende segments, limited by {112} side facets. With our classical nucleation model we have shown that it is possible to qualitatively relate the density of planar defects in a nanowire to the growth conditions. For low supersaturations, we predict a low twin plane density, consistent with our experimental observations of pulsed nanowire growth. In addition, for a specific interval of supersaturations and under certain conditions, our model suggests that it might be possible to grow almost perfect wurtzite wires (in materials where zinc blende is the

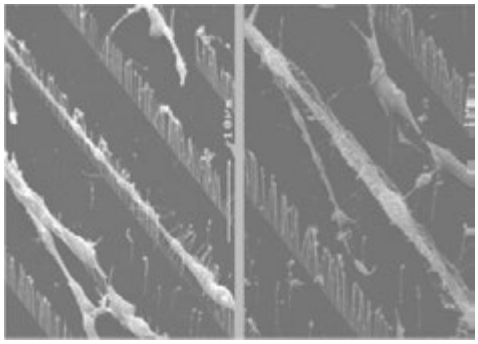

Fig. 3. SEM images of axon guidance. The two images show how nerve cell fibres are guided by the nanowire row pattern.

stable bulk crystal structure).

Although the experimental results shown here are limited to GaP, our results are of a general nature and should also apply to nanowires of other III–V materials with zinc blende bulk crystal structure, such as InP and GaAs. Indeed, preliminary results show that gold-particle-seeded GaAs nano-wires grown under pulsed conditions have significantly longer zinc blende segments than those grown under normal conditions.

3. Applications

As mentioned in the introduction, there are several promising applications for nanowires. Among these we will highligt a few, reflecting important parts of the reserach in Lund: (i) nanowires for guidance of cell growth, (ii) nanowires for FET devices, and (iii) nanowires for solar cells.

(i) Cells grow well with functioning cell processes on surfaces patterned with nanowires. However their growth behavior is altered when the growth takes place on nanowire patterned surfaces. The wires seem to hinder, or redirect, cell growth. This property can be used to effectively control the growth of axons (nerve fibres) and other cellular structures. EBL defined nanowire patterns in the form of fences can be used. Cell structures can grow, either along the fences or in the middle of the channel between adjacent fences [6]. In Fig. 3, two examples of axon growth along nanowire rows are displayed.

Nanowire aided cell guidance can be extremely accurate. Compared to biological methods, physical structures are much more stable over time and are not critically affected by diffusive loss or spontaneous absorption of other molecules. Apart from fundamental insights in cellular biology, a natural long-term application could be man/machine interfacing, such as advanced prosthetics technology.

(ii) III–V nanowires offer a few important design benefits for FETs. Current design ideas to prevent short channel effects include gates that wrap around the channel in connection with high-k gate dielectrics. Nanowires, with epitaxial contact with the underlying substrate is ideal for realization of this. In Fig. 4, an InAs nanowire FET, with wrap-gate is shown. The gate dielectric is HfO_2 (deposited with atomic layer deposition), the gate metal is Cr, and SiO_x is used as insulator. The gate length is 50 nm, and further down-scaling should be possible [7].

These nanowire FETs show very good figures of merit and are a considerable improvement compared to previously reported vertical InAs devices.

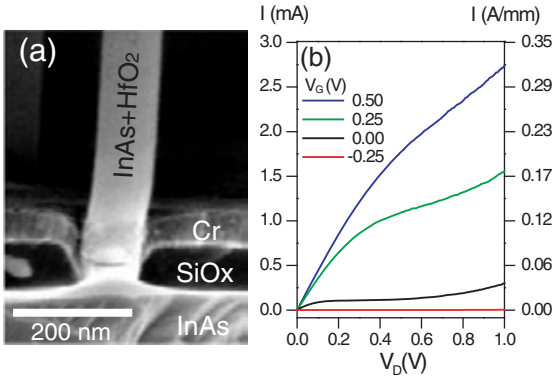

Fig. 4. Characteristics of an InAs nanowire wrap-gate FET. Side view of a cleaved sample where a SiO_x layer lifts the gate pad from the InAs source contact (substrate) (a). I–V_{drain} characteristics at different wrap-gate voltages (b).

(iii) Solar cell applications is an emerging field where nanowires can offer important benefits. These include their high surface to volume ratio and the possibility to fabricate both axial and radial heterostructures, which is of high importance for device fabrication. It is also important to be able to make well controlled *p-n* junctions in the nanowires.

We have recently got funding to develop a tandem photovoltaic cell with embedded, nanowire based, Esaki tunneling diodes as the active components.

Apart from the above mentioned applications, we also carry out research on nanowires for single electron memories, light emitting diodes, and nanoelectromechanical systems.

Acknowledgements

I want to thank the scientists at the Nanometer Structure Consortium in Lund for valuable discussions and input. The work was financed by the Knut and Alice Wallenberg foundation, the Swedish research council (VR), the Swedish Foundation for Strategic Research (SSF), and the IP NODE (EU contract nr 015783 NODE).

References

[1] K. W. Kolasinski, *Curr. Opin. Solid State Mater. Sci.* **10**, 182 (2006).
[2] J. Johansson *et al*, *J. Phys. Chem. B* **109**, 13567 (2005).
[3] V. G. Dubrovskii *et al*, *Phys. Rev. B* **71**, 205325 (2005).
[4] L. E. Fröberg *et al*, *Phys. Rev. B* **76**, 153401 (2007).
[5] J. Johansson *et al*, *Nature Mater.* **5**, 578 (2006).
[6] C. Prinz *et al*, *SMALL*, submitted (2007).
[7] C. Thelander *et al*, *IEEE Electron Device Lett.* **29**, 206 (2008).

16th Int. Symp. "Nanostructures: Physics and Technology"
Vladivostok, Russia, July 14–18, 2008

Critical diameter of A_3B_5 nanowires grown on lattice mismatched substrates by molecular beam epitaxy

G. E. Cirlin[1,2,3], Yu. B. Samsonenko[1,2,3], V. A. Egorov[1,2], I. P. Soshnikov[2,3], V. G. Dubrovskii[2,3], N. V. Sibirev[2], V. P. Ulin[3], V. M. Ustinov[2,3] and F. Glas[4]

[1] Institute for Analytical Instrumentation RAS, 190103 St Petersburg, Russia
[2] Physics and Technology Centre for Research and Education RAS, 194021 St Petersburg, Russia
[3] Ioffe Physico-Technical Institute, St Petersburg, Russia
[4] CNRS-LPN, Route de Nozay, 91460 Marcoussis, France

Abstract. Threshold behaviour of A_3B_5 nanowires grown on different lattice mismatched substrates during molecular beam epitaxy is observed. Dependently on the lattice mismatch, the wires can be grown at the diameters smaller that the critical value which is inversely proportional to the lattice mismatch value.

During the recent years one of main trend in the fundamental and applied surface science is an investigation of nanowire (NW) formation processes via exploring the vapor-liquid-solid (VLS) growth. These NW reveal new ways in designing of new micro- and optoelectronic devices. In particular, the dream of many researchers during several decades is to combine optoelectronic highly-efficient A_3B_5 emitters with traditional Si-based microelectronic parts. It was recently theoretically shown [1] that NW can be grown on mismatched surfaces without formation of the structural prolonged defects (e.g., dislocations) formation and there exists a radius dependent critical NW height below which no interfacial dislocation should be introduced. This critical thickness becomes infinite for radii less than some critical value, below which arbitrarily high coherent NW can be grown. In this work we experimentally show that during the MBE growth, A_3B_5 NW (GaAs, InAs) can be coherently fabricated on the substrates having significant lattice mismatch (GaAs and Si) reaching 11.6% in the InAs/Si(111) heteroepitaxial system. We also compare experimental data with theoretical calculations.

Growth experiments are carried out using EP1203 and Riber 32P setups equipped with effusion Au cell to get Au-metal droplets at the high vacuum conditions. During the growth we used GaAs(100), GaAs(111)B, Si(100), Si(111) and InAs(111) B substrates. After the desorption of an oxide layer in the growth chamber GaAs or InAs, depending on the substrate, the buffer layer having 1000Åthickness is grown by conventional MBE, for silicon substrates the buffer layer was not grown. After that, the deposition of Au layer (0.1–1 nm) was applied. The substrate temperature was then set to be sure the formation of Au-metal eutectic droplets. After this stage the grown of

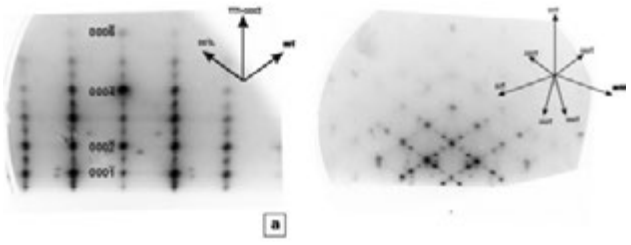

Fig. 1. RHEED patterns of GaAs NW grown on Si(111) (a) and Si(100) (b) substrates after deposition of ∼100 nm of GaAs.

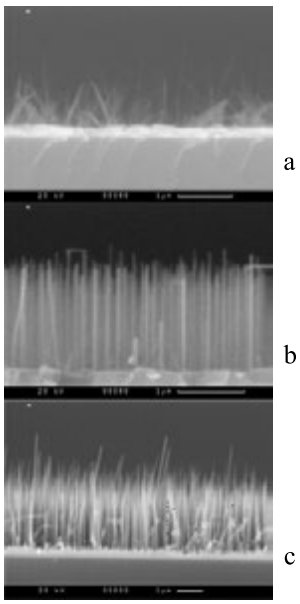

Fig. 2. SEM images of different A_3B_5 NW grown on lattice mismatched substrates. a) — InAs/Si(111), b) — InAs/GaAs(111)B, c) — GaAs/Si(111).

NW with desirable chemical composition was initiated. The growth temperature of NW, annealing substrate temperature, V/III flux ratio and growth rate were varied during our experiments depending on the material. The process of NW appearance and development was monitored *in situ* by reflection high energy electron diffraction (RHEED) patterns. Formation of cubic, polytype or wurzite crystal phases at different stages was clearly observed from RHEED patterns. After the growth the samples were examined by scanning electron microscopy (SEM) method.

It was found that the InAs/Si(111), InAs/GaAs(111)B, GaAs/Si(111) and GaAs/Si(100) NW can be grown within different technological parameters windows. As an example, in Fig. 1 typical RHEED patterns after the deposition of ∼100 nm GaAs on Si(111) and Si(100) substrates are presented.

In Fig. 2 a–c we present typical SEM images of these NWs. In a case of InAs/Si(111) heterostructure (11.6% mismatch (Fig. 2a), the NWs are very thin (10–20 nm in diameter) and can be grown up to several microns in length. Maximum di-

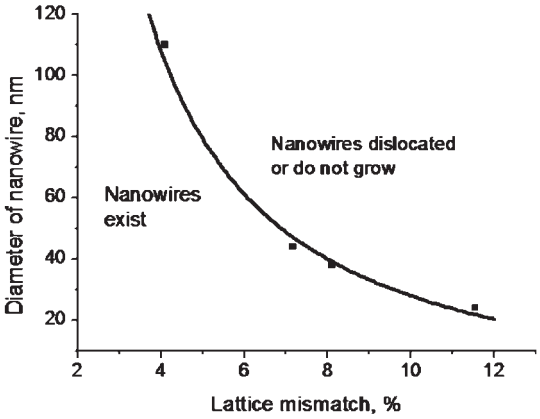

Fig. 3. Experimental data (squares) and theoretical curve for the critical diameter of different NWs grown on mismatched substrates.

ameter for coherent NW does not exceed 24 nm. If the size of the droplet larger than 24 nm, the NW grew with dislocation formation of did not erected at all. Other interesting observation consist in the very narrow substrate temperature range where the NWs can be formed, namely (320–340 °C), which is smaller that the growth of the same materials during MOCVD [2]. If the density of the NWs increases they become higher (up to 5–6 μm) keeping the same diameters. In the latter case due to extremely high length/diameter ratio they tend to bend.

In Fig. 2b typical SEM image for InAs/GaAs(111)B NWs which corresponds to 7.1% lattice mismatch is presented. The critical diameter at which the wires can me grown coherently, become larger in comparison to previous case and reaches 44 nm. The substrate temperature range increases, typically within (370–420 °C).

The largest temperature range (380–540 °C) corresponds to the case of GaAs/Si(111) NWs having 4% lattice mismatch. For this case we observe largest critical diameter, ∼110 nm (Fig. 2b).

In Fig. 3. we summarize the data obtained for different NWs grown on mismatched substrates. One of the data point is taken from the [2] on the growth of InP NWs on Si(111) substrate. To fit the experimental data, we used the equation of [1] for the critical radius r_c:

$$\frac{2\pi}{A_\nu}\left(\frac{\alpha^2 b_{\text{eff}}^2}{4} - \alpha b_{\text{eff}}\varepsilon_0 r_c\right) + C\left(\ln\frac{\beta r_c}{b}\right) = 0.$$

Here, ε_0 is the misfit parameter, $b_{\text{eff}} = b\sin\theta$, b is the dislocation length, $\alpha = 4/\pi$, $\beta = 2/\pi$ are the geometrical coefficients, θ is the dislocation angle, $A_\nu = 27.3$ at Poisson ratio $\nu = 1/3$ and $C = (1 - \nu\cos^2\theta)b^2/[2/\pi(1+\nu)]$. The parameters were adjusted to the material systems considered. Our results demonstrate a good quantitative correlation between theory and experiment.

Acknowledgements

The authors acknowledge V. V. Busov and S. I. Troshkov for SEM studying of NWs morphology. The financial support of SANDiE European project, RAS scientific programs (“Quantum macrophysics” and “Quantum nanostructures”) and that of RFBR grants is acknowledged.

References

[1] F. Glas *Phys. Rev. B* **74**, 121302 (2006).
[2] L. C. Chung *et al*, *Appl. Phys. Lett.* **90**, 043115 (2007).

16th Int. Symp. "Nanostructures: Physics and Technology"
Vladivostok, Russia, July 14–18, 2008

Formation of hexagonal crystal structure in nanowires of cubic semiconductor materials

V. G. Dubrovskii[1,2], *N. V. Sibirev*[1], I. P. Soshnikov[1,2], G. E. Cirlin[1,2,3], J.-C. Harmand[3], G. Patriarche[3] and F. Glas[3]

[1] St Petersburg Physics and Technology Centre for Research and Education of the RAS , Khlopina 8/3, 195220, St Petersburg, Russia
[2] Ioffe Physico-Technical Institute, St Petersburg, Russia
[3] CNRS-LPN, Route de Nozay, 91460 Marcoussis, France

Abstract. The formation of hexagonal (HEX) crystal phase in nanowires (NWs) with a stable cubic (CUB) structure under the bulk form, among which zinc blende (ZB) III–V and Si semiconductor materials are of paramount importance, is studied theoretically and experimentally. Recent experimental findings concerning the influence of NW radius, surface energy and supersaturation on the crystal structure in different material systems are considered. The model of NW growth via the vapor-liquid-solid (VLS) mechanism under the influence of the Gibbs–Thomson effect, surface diffusion and nucleation is presented and analyzed. Structural phase diagrams and probabilities of CUB and HEX phase formation are constructed and compared to the experimental data on GaAs NWs grown by Au-assisted molecular beam epitaxy (MBE). It is demonstrated that the fabrication of pure HEX NWs generally requires high liquid supersaturation and small radius of growth seeds, which gives a key for the control over the phase purity of NWs in different epitaxy techniques.

A rapidly growing interest in self-standing semiconductor NWs ranges from fundamental physics of their growth, transport and optical phenomena to many promising applications in nanoelectronics, nanophotonics and nanosensors. Using modern epitaxy techniques, NWs with radii of order of ten nanometers and lengths up to several tens of micrometers can be obtained. One of the most surprising features of these NWs is that their crystal structure may differ from that in bulk form. Recent studies demonstrate that III–V NWs of CUB ZB materials often adopt HEX wurtzite (WZ) structure. This phenomenon has been reported for most ZB compounds, both for Au-assisted [1–4] and selective area [5] growth. Recently, HEX diamond lattice was experimentally observed in Si NWs [6]. In many cases, the structure of NWs is not stable and exhibits a spontaneous switching between different phases, creating rotational twins and stacking faults. This clearly impedes material properties, so the control over the phase purity is now considered as one of the main challenges in NW technology.

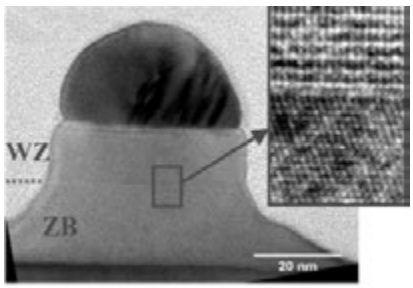

Fig. 1. TEM image of a short GaAs NW with high resolution close-up of transition zone between CUB ZB and HEX WZ.

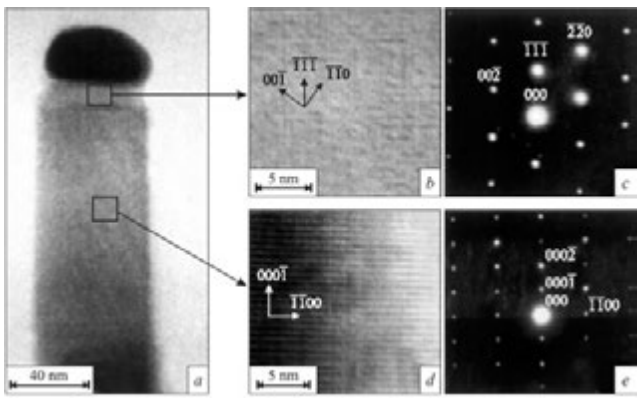

Fig. 2. TEM image of top section of GaAs NW (a,b,d) and electron diffraction patterns (c,e), showing the HEX (d,e) to CUB (b,c) transition at the NW neck.

Given the prominence of HEX phase in the majority of III–V NWs, it is interesting to find two instances where CUB ZB phase systematically appears in our GaAs NWs grown by Au-assisted MBE. The first one corresponds to the initial stage of growth [7]. By growing NWs for short times, we ensured that the foot of each NW could be observed clearly before being buried by the 2D layer. The cross-sectional images obtained ex situ by transmission electron microscopy (TEM) prove that the whole NW is initially pure ZB. Growth then switches abruptly to WZ stacking (Fig. 1). Second, when we terminate MBE growth by switching off the Ga flux while maintaining an As flux, we systematically observe a section of NW that adopts the ZB structure (Fig. 2). This effect, consistent with previously reported facts [1,3], is interpreted as a partial consumption of the Ga dissolved in the Au particle to form the terminal section of NW. These two situations where ZB forms have in common to be transient growth phases during which the supersaturation of Ga in the liquid is less than during steady growth. This strongly suggests that CUB phase forms when the supersaturation is less than some critical value and that HEX formation requires a *high supersaturation*. We therefore conclude that the growth kinetics plays an important role in crystal structure. The CUB to HEX transition can not be entirely determined by a lower surface energy of HEX NWs [8,9]. While the latter should be indeed smaller in HEX than in CUB phase, the estimates of Refs. [8] and [9] provide the values of critical radii of transition in order of magnitude smaller than the experimentally observed HEX NWs.

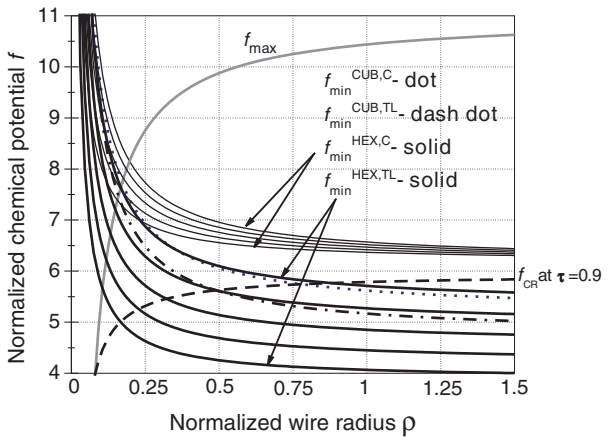

Fig. 3. Structural diagrams at different $\tau = 0.75$, 0.8, 0.85, 0.9 and 0.95. Minimum chemical potentials in HEX phase $f_{\min}^{\mathrm{HEX,C}}$ (C nucleation) and $f_{\min}^{\mathrm{HEX,TL}}$ (TL nucleation) are uplifted at increasing τ. The dotted line is the critical curve of CUB to HEX transformation at $\tau = 0.9$.

To explain and analyze the peculiarities of CUB to HEX transformation in different materials, we have developed the model of NW growth and crystal structure. The model accounts for the following verified facts: (i) formation of NWs is strongly influenced by the Gibbs–Thomson effect of elevation of chemical potential in the drop and in the NW with a curved surface [9]; (ii) growth of Si and III–V NWs is controlled by the diffusion of adatoms from the substrate surface to the NW top [2,10]; (iii) VLS growth on the NW top is mediated by 2D nucleation, which often takes place at the triple line (TL) rather than in the centre of the liquid-solid interface [7]. We also allow for the formation of NWs in CUB and HEX phase with different surface energies of lateral facets, characterized by coefficient $\tau \equiv \gamma_{\mathrm{HEX}}/\gamma_{\mathrm{CUB}}$. In view of fact (i), the chemical potentials of semiconductor material in the liquid and in the NW are modified by the radius-dependent corrections. Fact (ii) gives the upper limit for the supersaturation of liquid phase, $\Delta\mu_{\mathrm{LS}}$, below which the diffusion flux is directed from the surface to the NW top. Fact (iii) provides the lower limit for $\Delta\mu_{\mathrm{LS}}$, above which the NW growth rate is larger than that of a non-activated surface. This lower limit is different, however, for CUB and HEX NWs as well as for nucleation at TL and C position. Structural diagrams of NWs in normalized coordinated of liquid supersaturation, $f = \Delta\mu_{\mathrm{LS}}/\psi$, and NW radius, $\rho \equiv R/R_0$, are

Table 1. Radius R_0 in different semiconductor NWs.

Material	Lateral facets	γ_{CUB}, J/m^2	ψ, meV	R_0, nm
AlSb	{110}	1.3	19.0–27.5	34–49
GaSb	{110}	1.1	19.8–28.6	27–39
InSb	{110}	0.75	16.4–23.7	27–39
AlAs	{110}	1.8	16.4–23.7	43–62
GaAs	{110}	1.5	16.6–24	35–51
InAs	{110}	1	10.6–15.3	46–67
AlP	{110}	2.4	11.4–16.5	72–105
GaP	{110}	2	11.6–16.8	60–87
InP	{110}	1.3	6.8–9.8	84–121
Si	{110}	1.43–1.7	10–11.72	30–42
Si	{211}	1.31	10–11.72	28–33

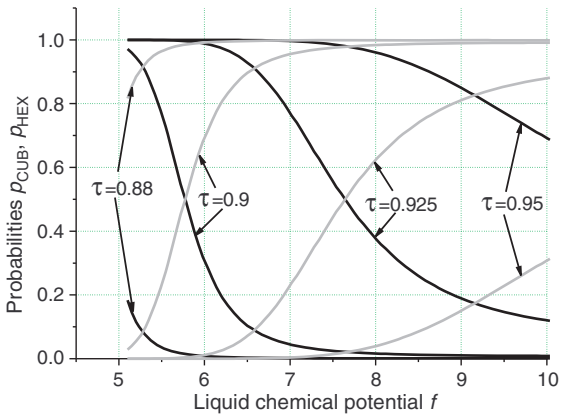

Fig. 4. Probabilities of CUB (decreasing curves) and HEX (increasing curves) phase formation as functions at different τ.

presented in Fig. 3, for typical MBE growth conditions and τ ranging from 0.75 [9] to 0.95. In the latter, ψ stands for the difference of bulk cohesive energies of HEX and CUB phase (16.6–24 meV per pair in GaAs [7–9]). Material-related parameter $R_0 = 2\gamma_{\mathrm{CUB}}\Omega_{\mathrm{S}}/\psi$ (Ω_{S} is the volume per pair in solid phase) determines the characteristic radius of CUB to HEX transition. Numerical estimates for R_0 in different materials are given in Table 1. The obtained results demonstrate that (i) CUB to HEX structural transition onsets in the nanometer range for all materials considered; (ii) TL nucleation is favorable in the most cases and (iii) the formation of HEX phase generally requires high supersaturations. For the parameters of Fig. 3, HEX phase is predominant in the growth domain between f_{CR} and $f_{\max}$, while CUB phase is prevalent between $f_{\min}^{\mathrm{CUB,TL}}$ and f_{CR}.

From the analysis of different scenarios of nucleation, we have also calculated the probabilities of NW formation in HEX and CUB phase. In Fig. 4, the probabilities are plotted as functions of liquid supersaturation at fixed $\rho = 1.14$, relating to $R = 40$ nm in the case of GaAs NWs, and different τ. Calculations show that NWs adopt the HEX phase in the whole growth domain at $\tau < 0.85$. The curves at $\tau = 0.9$–0.925 relate to phase mixing at intermediate values of supersaturation, where the observation of rotational twin layers and stacking faults is most likely. Lower supersaturations correspond to the pure CUB phase, and higher supersaturations to the pure HEX phase. Increase of τ to 0.95 leads to the domination of CUB phase in the whole growth region.

To conclude, we have demonstrated experimentally and modeled theoretically the effect of CUB to HEX transformation in NWs, and described the domains of phase purity and phase mixing.

References

[1] A. I. Persson *et al*, *Nature Mater.* **3**, 678 (2004).
[2] J. C. Harmand *et al*, *Appl. Phys. Lett.* **87**, 203101 (2005).
[3] I. P. Soshnikov *et al*, *Phys. Sol. State* **47**, 2213 (2005).
[4] L. C. Chuang *et al*, *Appl. Phys. Lett.* **92**, 013121 (2008).
[5] P. Mohan *et al*, *Nanotechnology* **16**, 2903 (2005).
[6] A. Fontcuberta i Morral *et al*, *Adv. Mater.* **19**, 1347 (2007).
[7] F. Glas *et al*, *Phys. Rev. Lett.* **99**, 146101 (2007).
[8] T. Akiyama *et al*, *Jpn. J. Appl. Phys.* **45**, L275 (2006).
[9] V. G. Dubrovskii and N. V. Sibirev, *Phys. Rev. B* **77**, 035414 (2008).
[10] V. G. Dubrovskii *et al*, *Phys. Rev. B* **71**, 205325 (2005).

16th Int. Symp. "Nanostructures: Physics and Technology"
Vladivostok, Russia, July 14–18, 2008

Some calculations related to the growth of GaAs nanowires

N. V. Sibirev[1], *V. G. Dubrovskii*[1,2], G. E. Cirlin[1,2,3], V. A. Egorov[1], Yu. B. Samsonenko[1,2,3], I. P. Soshnikov[1,2] and V. M. Ustinov[1,2]

[1] St Petersburg Physical Technological Center for Research and Education RAS, 194021 St Petersburg, Russia
[2] Ioffe Physico-Technical Institute, St Petersburg, Russia
[3] Institute for Analytical Instrumentation RAS, 190103 St Petersburg, Russia

Abstract. The model of catalyst-assisted nanowire growth by the generalized vapor-liquid-solid mechanism is developed. The experimental study of the dependence of nanowire height on the deposition rate during the Au-assisted MBE of GaAs nanowires on the GaAs(111)B substrates is performed. Theoretical and experimental results are compared to each other and a good quantitative between them is demonstrated. It is shown that the nanowire height has a maximum at a certain growth rate, which position depends on the growth conditions and the nanowire radius. In the case of Au-assisted MBE of GaAs nanowires with the mean radius of 20 nm, this maximum is reached at the growth rate of GaAs of 0.5–0.6 monolayers per second. Also the model of nanowire growth allows us to measure the diffusion length of atom. Comparing of two samples of nanowire arrays showed that diffusion length of Ga on the GaAs(111) is about 400 nm and on the AlAs(111) is about 250 nm.

Many recent investigations have been devoted to studying the growth mechanisms of different III–V NWs. This work is devoted to the investigation of the dependence of nanowire height on the deposition rate during the Au-assisted MBE of GaAs nanowires on the GaAs(111)B substrates. The model of catalyst-assisted nanowire growth by the generalized vapor-liquid-solid mechanism [1] is developed. The experimental study is performed.

In our growth experiments, the NW formation procedure consisted of three stages: (i) the substrate [GaAs(111)B or GaAs(100)] surface preparation; (ii) the Au film deposition; (iii) the Au-Ga drop formation by heating the surface above the eutectic melting point and GaAs deposition (again in MBE growth chamber). The effective thickness of deposited GaAs was varied from 270 to 320 nm. The substrate temperature T was about 560 °C. The deposition rate was varied from 0.2 to 0.8.

Theoretical and experimental results are compared to each other and a good quantitative between them is demonstrated see Fig. 2.

Theoretical model takes into account the Gibbs–Thomson effect and diffusion from the substrate throw nanowire sidewalls to the tip of nanowire. In terms of our model we obtain the equation (1) on the nanowire growth rate.

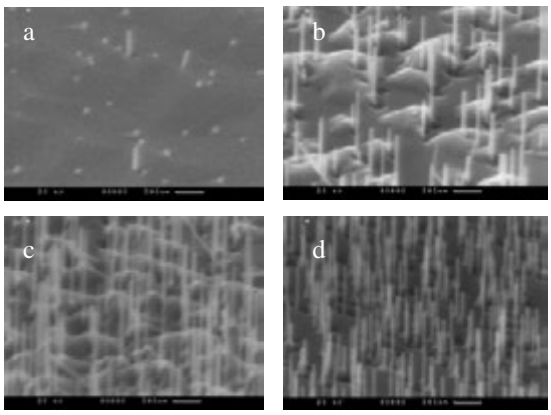

Fig. 1. SEM images of a sample with GaAs NWs grown on a GaAs(111)B surface: a) 0.2 ML/s; b) 0.4 ML/s; c) 0.6 ML/s; d) 0.8 ML/s. Tilted angle is 30°.

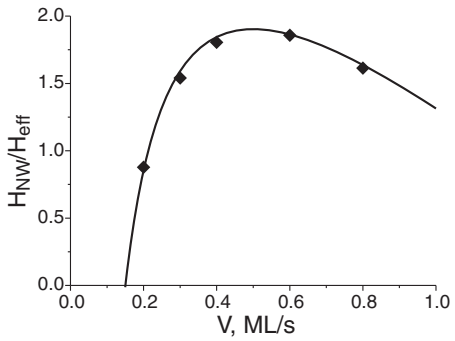

Fig. 2. Experiment — squares and theory — line calculated for V_e = 0.48 ML/s, R_e = 0.4 nm, R = 20 nm, R_{diff} = 3200 nm, Q = 1.217×10^{-4}, $\Gamma = 1.5 \times 10^{-2}$ s/ML.

$$V_{NW} = -V_e \exp\left(\frac{R_e}{R}\right) + V\left(1 + \frac{R_{diff}}{R}\right)(1 - Q) - V^2 Q \Gamma \left(1 + \frac{R_{diff}}{R}\right). \quad (1)$$

Here V_e evaporation rate from flat liquid surface, R_e — the characteristic size of the Gibbs–Thomson effect, R_{diff} — the characteristic radius of the diffusion, Q — is the coefficient characterized the growth rate of non-activated surface and Γ — is parameter which we obtain from linearization of the dependence of substrate growth rate on deposition rate. All this parameters fully defined by experimental conditions and properties of material.

It is shown that the nanowire height has a maximum at a certain growth rate, which position depends on the growth conditions and the nanowire radius. In the case of Au-assisted MBE of GaAs nanowires with the mean radius of 20 nm, this maximum is reached at the growth rate of GaAs of 0.5–0.6 ML/s.

Processes of the substrate growth and the evaporation appoint the life time of atom on the surface τ_s. So, the diffusion length $\lambda_s = (D_s \tau_s)^{1/2}$ on substrate surface is appointed by the probability of the evaporation and nucleation. Here D_s — is

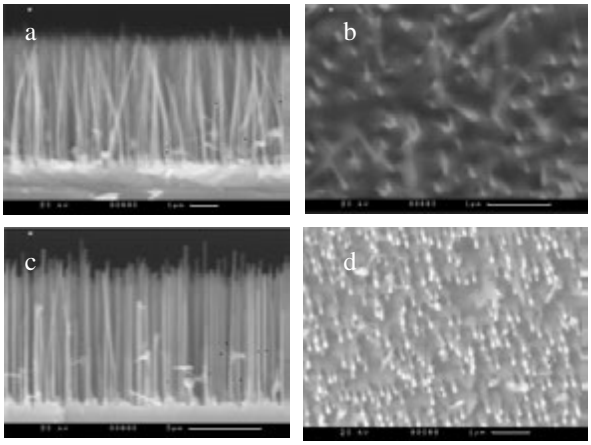

Fig. 3. SEM images of a sample with GaAs NWs grown on a GaAs(111)B surface (a) cross-sectional and (b) planar geometry and SEM images of a sample with GaAs NWs grown on a AlAs(111)B surface (c) cross-sectional and (d) planar geometry.

coefficient of diffusion on the substrate.

In terms of our model we obtain the equation (2) on the diffusion length. This equation allows us to get the diffusion length on the substrate surface from the growth of nanowire.

$$\frac{D_\mathrm{s}}{D_f}\frac{\sigma_f}{\sigma_\mathrm{s}}\frac{L^2}{2\lambda^2} - \frac{L}{\lambda}\frac{R}{\lambda}\ln\left(\frac{R}{\lambda}\right) = 2\frac{H_\mathrm{eff}}{R}. \qquad (2)$$

Here D_f is coefficient of diffusion on the sidewalls, L is length of the nanowire, R is radius of the nanowire and $\sigma_{\mathrm{s},f}$ denote the areas of adsorption site on the nanowire sidewalls (f) and on the substrate surface (s).

Two experiments were held of the growth of GaAs nanowires on AlAs(111) and GaAs(111) substrate see Fig. 3. In terms of given approximation (1) was shown that the diffusion length in typically growth conditions deposition rate 1 ML/s substrate temperature 560 °C is not defined by the evaporation but the substrate growth. Comparing of two samples of nanowire arrays showed that diffusion length of Ga on the GaAs(111) is about 400 nm and on the AlAs(111) is about 250 nm.

Acknowledgements

This work has been supported by the Russian Foundation for Basic Research. One of the authors (N. V. S.) gratefully acknowledges support from the Dynasty Foundation.

References

[1] V. G. Dubrovskii, N. V. Sibirev, R. A. Suris, G. E. Cirlin, V. M. Ustinov, M. Tchernysheva, J. C. Harmand, *Semiconductors* **40(9)**, 1075–1082 (2006).

16th Int. Symp. "Nanostructures: Physics and Technology"
Vladivostok, Russia, July 14–18, 2008

Periodically corrugated nanostructures

A. V. Prinz and V. Ya. Prinz
Insitute of Semiconductor Physics, SD RAS, Novosibirsk, Russia

Abstract. In the present work the phenomenon of spontaneous self-formation of periodically corrugated structures from thin molecular beam epitaxy grown films locally detached from substrate edges is described. Synchronized corrugated structures and corrugations confined between substrate and cap layer were fabricated. The corrugated structures are easily scalable to nanometer range. Transformation of corrugated structures by application of an external force was demonstrated.

Introduction

Forming regular arrays of small structures on semiconductor substrates offers outstanding possibilities both in studying quantum phenomena and in using these phenomena in practical applications. The most important prerequisite for experimental studies and device applications of quantum structures is availability of well-controllable procedures for their fabrication. One possible way to the fabrication of 3D micro- and nanostructures is the approach that uses stress-driven fabrication of precise micro- and nanoshells (tubes, helixes, etc.) [1]. In this approach, by releasing strained epitaxial layers from their substrates the film can be rolled up in nanotubes or bent to other shells. In the present work, we draw attention to the phenomenon, spontaneous self-formation of periodically corrugated structures of thin molecular beam epitaxy grown films locally detached from substrate.

1. Experimental

The technology is applicable to a wide range of lattice-mismatched materials and precise permits control over the shape and parameters of the resultant corrugation both on micro- and nanometer scales. The corrugated structures are easily scalable because film properties determined by epitaxy process [2].

To detach the film from substrate, either selective etching of the substrate itself or selective etching of a sacrificial layer underlying the film may be used. The method is illustrated by an example of epiaxial-grown InGaAs and SiGe films. As a simplest case, we report some results that were obtained on samples grown on Si substrates. On an undoped Si buffer layer, was grown a 11 nm thick strained SiGe film, with 30% Ge content, doped with boron to a concentration of 10^{20} cm^{-3}. The high doping level of the film retarded its dissolution in a 3% aqueous ammonia solution. On the contrary, both the undoped buffer layer and the n-type silicon substrate could be rapidly etched in this etchant. Selectively etching the buffer layer and the substrate in the lateral direction, we obtained a freely protruding SiGe strip, laterally attached to the substrate with one of its edge (see Fig. 1). At the free edge, the material of the freely protruding SiGe strip tends to acquire its inherent lattice constant, i.e., to expand. The planar state of the freely protruding strip is unstable, and its free edge readily forms a hill-and valley structure, thus bringing about a sine-corrugation of the freely protruding areal part of the layer.

Similar experiments have also been carried out on pseudomorphic InGaAs/AlAs/GaAs heterostructures containing a compressively strained InGaAs working layer, an AlAs sacrificial layer, and a GaAs substrate. In this structure, the sacrificial layer could be selectively etched using an HF-based etchant. Selectively etching the AlAs sacrificial layer over the lateral distance, we obtained a strip, the shape of which obeyed the regularities described above.

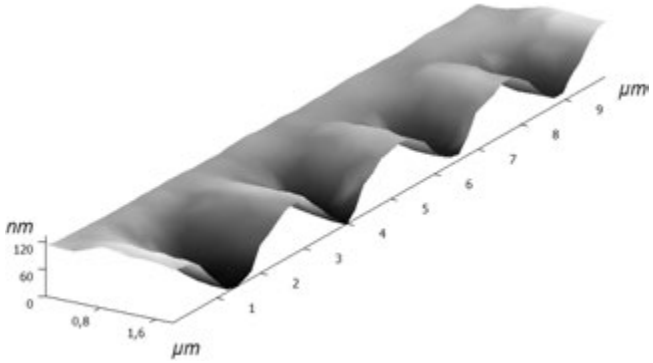

Fig. 1. 3D image of SiGe/Si corrugated film obtained using AFM (Solver-P47, NT-MDT).

2. Results and discussion

From the electrical point of view, periodically corrugated films with a 2D-electron gas may be expected to display the properties of superlattices. Indeed, the bandgap in a freely protruding semiconductor layer may be substantially narrower than the bandgap in the compressed film rigidly attached to substrate, which gives rise to some extra-conductivity. Equally, the bandgap width of a regularly corrugated strip turns out to be periodically modulated along the strip, which results in a spatial redistribution of charge carriers along the strip length and, hence, in formation of an array of quantum wires [3].

The possibility of using well-ordered structures obtainable by the above method for encapsulating polymers and metals shows much potential in fabrication of diffraction gratings suitable for application in a wide spectral range. By analogy with well-ordered arrays of quantum dots, it may be expected that the resultant corrugated surfaces may be of use in production of solid-state memory elements.

Considerable promise is the possibility of forming corrugated film edges/rims elastically interacting with each other. The interaction between two corrugations formed at the opposite edges of a strip-shaped mesa-structure allows one to synchronize the corrugations self-forming at the two edges in space and opens an avenue to fabrication of two- and three-dimensional superlattices (Fig. 2). To demonstrate the above possibilities, we used 5 μm-wide strip-patterned mesa-structu-

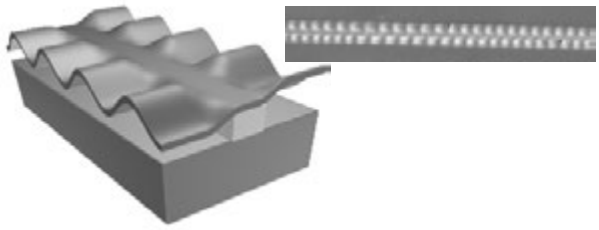

Fig. 2. 3D scheme and optical image of SiGe/Si strip with synchronized corrugations. The wide of strip is 5 μm.

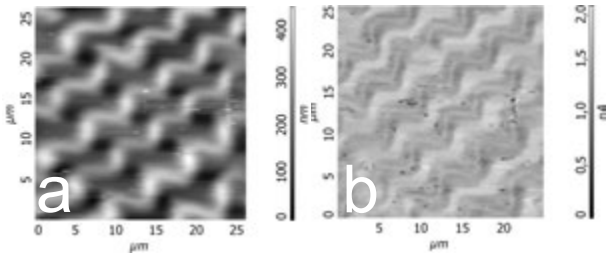

Fig. 3. Corrugated film obtained from structure $In_{0.25}Ga_{0.75}As$-7.5 nm/GaAs-30 nm/$In_{0.2}Ga_{0.8}As$-10 nm/AlAs-15 nm on GaAs (100) substrate. a) AFM image, b) image obtained by force modulation method (lighter areas correspond to more rigid surface).

res prepared on SiGe/Si. The substrate and the Si buffer layer were etched simultaneously from the two edges of the film strip toward its centerline. As the strip edges were detaching from the substrate, they became sine-corrugated. Interestingly, the periodic corrugations arising on either sides of the strip were found to be synchronized in space, being shifted with respect to each other by half a period.

Precision and periodicity of location of corrugated structures is provided by extreme precision of control over thicknesses and strains in epitaxial films. The amplitude and period of corrugations is determined by energy-optimal shape. When the film is bound to the substrate the worm-like buckling structures are formed, which can cover the whole area of the sample in case of certain etching conditions. Local elasticity in such structures was estimated by means of atomic force microscopy (force modulation method), maximal rigidity is reached on crests of corrugations (Fig. 3).

Molecular beam epitaxy permits production of even more complicated precise structures in which layers are precisely spaced. In such structures, buckling emerges in a self-formed manner, resulting in a corrugated structure with a precise corrugation period. Fig. 4 depicts a structure in which a strained InGaAs film was grown between two AlAs sacrificial layers. The structure was grown on GaAs substrates and contains a GaAs cap layer. Selective removal of the sacrificial layers results in the formation of a corrugated structure. With decreasing distance between the cap layer and the substrate, both corrugation amplitude and corrugation period also decrease. Since distance between layers can be predefined with high accuracy in the epitaxy process, the resultant corrugated structure has precise amplitude and period [2,4].

It's possible to adjust the corrugation period continuously by application of an external force to the planes among which the corrugated layers are sandwiched results in variation of distance (the separation between the planes).

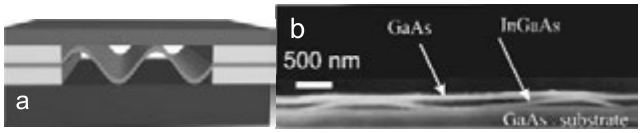

Fig. 4. a) Schematic view and b) SEM image of corrugated InGaAs film sandwiched between the native GaAs substrate and GaAs cap layer (initial structure: GaAs/AlAs/InGaAs/AlAs/GaAs).

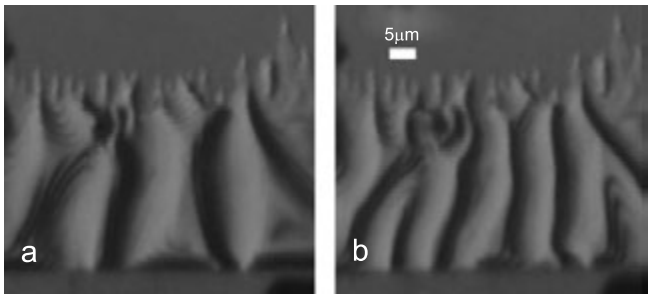

Fig. 5. Corrugated edge of structure (GaAs-200 nm/$In_{0.3}Ga_{0.6}As$-2 nm/AlAs-4 nm); a) free corrugation, b) after applying of pressure.

The possibility was demonstrated for relatively big corrugated structures. Sapphire glass was put on the corrugated structure to exert pressure on it. With increase of pressure the corrugation period changes stepwise, the deformation of the structure is elastic, after pressure relief the structure recovers initial period (Fig. 5). Thus, convertibility of corrugated structures is demonstrated, that opens up the possibility of creation of transformable nanosystems.

It is important that we were able to controllably fabricate micro- and nanocorrugated structures that show much promise for many practical applications. Nanocorrugated systems may find applications in nanoelectronics, nanomechanics, cellular automata, and dynamic quantum devices.

Acknowledgements

This work has been supported by the Russian Foundation for Basic Research.

References

[1] V. Ya. Prinz, V. A. Seleznev, A. K. Gutakovsky, A. V. Chekhovskiy, V. V. Preobrazhenskii, M. A. Putyato, and T. A. Gavrilova, *Physica E* **6**, 829 (2000).
[2] A. V. Prinz and V. Ya. Prinz, *Patent of Russia* **2267832**, (2006).
[3] V. M. Osadchii and V. Ya. Prinz, *Phys. Rev. B* **72**, 033313 (2005).
[4] V. Ya. Prinz, *Physica E* **24**, 54 (2004).

16th Int. Symp. "Nanostructures: Physics and Technology"
Vladivostok, Russia, July 14–18, 2008

Mathematical simulation and experimental investigation of the formation of powder nanocomposites

A. V. Vakhrouchev, A. Y. Fedotov, L. L. Vakhroucheva and A. A. Shushkov

Institute of Applied Mechanics, Ural Branch of Russian Academy of Sciences,
34, T. Baramzinoy St., Izhevsk, 426069, Russia

The problem of the formation of uniform nanodispersed mixtures from nanoparticles and other nanoelements and the preparation of nanocomposites based on them, which have characteristics that are uniform and stable over the entire bulk of a material, attracts more and more attention. It is explained by the fact that physicochemical, chemical and other properties of nanoparticles are very different and, as a rule, depend nonlinearly on the sizes of nanoparticles. Nanocomposites are used as specifically strong materials applied in many fields of engineering. Even the slightest variation in the composition in any local region of these materials can lead to a sharp reduction in the mechanical characteristics of a nanocomposite, cause the appearance of nanodefects at operating loads and decrease considerably the reliability of items prepared from nanocomposites. The goal of the work is the construction of a mathematical tool for studying the regularities of the formation of nanoparticles and their merging in nanocomposites, and the development of a method for obtaining uniform nanocomposites.

The formation of nanoparticles takes place, as a rule, in liquid and gaseous media, which allow avoiding their agglomeration. The problem of the formation of nanoparticles of the composite mixture is usually solved with the use of molecular dynamics. However, the solution of such problem within the framework of molecular dynamics requires a large amount of time and large computational capabilities. Thus, for example, due to a small mass of the interacting atoms, it is necessary to choose the integration step of 10^{-15} seconds in order to provide the stability of the integration scheme, which leads to a process that is slow in time. In addition, at different steps of the nanocomposite formation, a collective behavior of atoms, molecules and nanoparticles is observed. This causes a multi scales character of the problems of the nanocomposite formation process simulation, to which different physical and mathematical approaches correspond. The main problems associated with such simulation are as follows:

— multi scales problems;
— a large number of variables;
— scales changing in space and in time;
— characteristic times of processes at different steps differ from one another by orders of magnitude;
— changes of variables of the problem at different simulation levels;
— coordination of boundary conditions while going from one simulation level to another at the change in the problem variables;
— the stochastic behavior of nanosystems.

To different steps of the nanocomposite formation, different mathematical models are applied. The calculation of the configuration of molecular formations, which form nanoparticles, requires first principles calculations, i.e. quantum-chemical methods of simulation. The calculation of the process of molecule merging in nanoparticles can be carried out with the use of molecular dynamics methods. The calculation of nanoparticles movement in a gaseous mixture and their merging is a mesodynamics problem [1,2]. The specific feature of mesodynamics is simultaneous use of the methods of molecular dynamics and classical dynamics. It also should be noted that a number of processes, especially the ones which take place at final steps of nanocomposite formation, can be considered within the framework of continuum mechanics as well.

The main reasons for changing the simulation method at different steps of nanocomposite formation are as follows:

— the number of nanosystem variables decreases due to going from the calculation of movement of individual atoms to the analysis of the movement of nanoparticles or their groups;
— the number of bonds between the individual elements of a nanosystem reduces as the result of the decrease in a number of "the nearest neighbors", which get to the region of the interaction of the nanosystem unit cells;
— the overall calculated sizes of a nanosystem increase due to the enlargement of the calculation unit cell;
— the scale of the analysis of the nanosystem calculation extends in time due to the increasing time step of the integration of equations.

In the present work, the calculations are performed and the experimental investigations are carried out using the apparatus Nanotest 600 for the formation of nanocomposites based on single-component and composite nanoparticles of different metals.

References

[1] A. V. Vakhrouchev, Simulation of nano-elements interactions and self-assembling, *Modelling and Simulation in Materials Science and Engineering* **14**, 975–991 (2006).
[2] A. V. Vakhrouchev, Computer simulation of nanoparticles formation, moving, interaction and self-organization, *Journal of Physics: Conference Series* **61**, 26–30 (2007).

16th Int. Symp. "Nanostructures: Physics and Technology"
Vladivostok, Russia, July 14–18, 2008

Growth of GaAs nanowhiskers in mesa

I. P. Soshnikov[1,2], G. E. Cirlin[1,2,3], Yu. B. Samsonenko[1,2,3], N. D. Il'inskaya[1], Yu. Zadiranov[1] and V. M. Ustinov[1,2]

[1] St Petersburg Physical Technological Center for Science and Education
[2] Ioffe Physico-Technical Institute, St Petersburg, Russia
[3] Institute for Analytical Instruments of RAS

Abstract. In the work the growth of GaAs nanowhiskers in strip line mesa is studied. It is demonstrated the compatibility of the processes with standard MBE technology of nanowhiskers formation. Possible applications in the design of interconnections between elements are proposed.

Introduction

Nanowires in the nearest future may serve as a base of new micro-, optoelectronic and analytical devices and could be a good candidate for the interconnection between different elements on a chip [1–3]. Additionally, semiconductor NWs are interested for investigation of new processes and phenomena related to unique object [4–6]. During the last years, the processes of NW growth mechanisms are actively studied. In particular, in [5,6] it was experimentally found and theoretically explained the role of the diffusion mechanism during NWs growth. It was also demonstrated the appearance of wurzite and polytypics phases in III–V NWs [7–10].

Important application in NW technology is the the growth of NWs in mesa structures which is the aim of the present work. This is not trivial task because of the technological problems due to the non-ideality of the mesa formation on submicron and nano level.

1. Experimental

As the first step, microlithography and ion beam etching of GaAs (100) wafers were used to produce strip line mesas with width and depth about 5 and 2–3 μm, correspondently. As the result, the inclination angle is in the range 55–60°. The main reason to choose the mesa direction is the appearance of crystal surface (111)B which is the surface well studied for NWs growth.

On the next step, Au film having the thickness about 1 nm is deposited by electron beam evaporaion in VUP-5 in glazing geometry. This evaporation geometry was used to ensure the deposition of Au film on one of the mesa side facet. Then, final lift-off of the rest of resist is carried out using oxygen plasma.

At the last stage, GaAs NWs are grown by molecular beam epitaxy in EP1203 growth chamber equipped with Ga and As effusion cells using the growth parameters described early [5,6]. The monitoring of NWs formation *in situ* is realized by reflection high energy electron diffraction RHEED [11].

After the growth the surface morphology with NWs is studied by scanning electron microscopy CamScan 4-90FE.

2. Results and discussion

Fig. 1 demonstrates the typical morphology with NWs grown in mesa. The formation of NWs is observed predominantly only on facet activated by Au. The NWs growth axis corresponds to the crystal axis of (111)B direction. The density of NWs

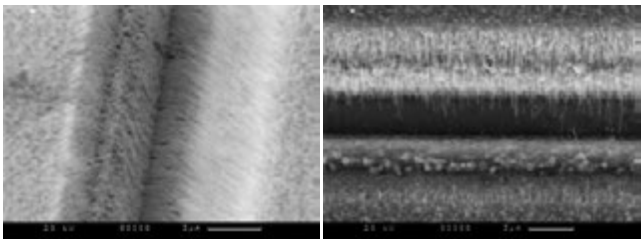

Fig. 1. SEM images of GaAs NWs grown on side facet of mesa in isometric (left) and in plan view (right).

can reach up to 10^9 cm^{-2} and dependent on Au film thickness, quality of facet fabrication and peculiarities of the growth process. At the same time, the growth of NWs on the opposite facet and the upper part of the mesa is suppressed (the NWs density as low as $\leq 10^2$ cm^{-2} was detected). The diameter and length of NWs on the sidewall is 10–50 nm and 1000–3000 nm, correspondently. The comparison sizes of NWs grown on mesa facet and reference sample without mesa shows that diameter and length in mesa NWs are bigger probably due to the incidence of the beams difference geometry.

Habitués of the NWs is defined as hexagonal prism with length/diameter ration 100 and more. We do not observe the formation of dendrite NWs in mesa. The facets of the prism are defined by $(1\bar{1}0)$ planes. According to our data, the NWs length is anytime larger then the total thickness of GaAs deposited and proportional to the effective thickness of deposition layer. The dependence of NW length is inversely proportional to their diameter which can be explained by predominantly diffusion mechanism of NWs growth during MBE [5,6] (Fig. 2).

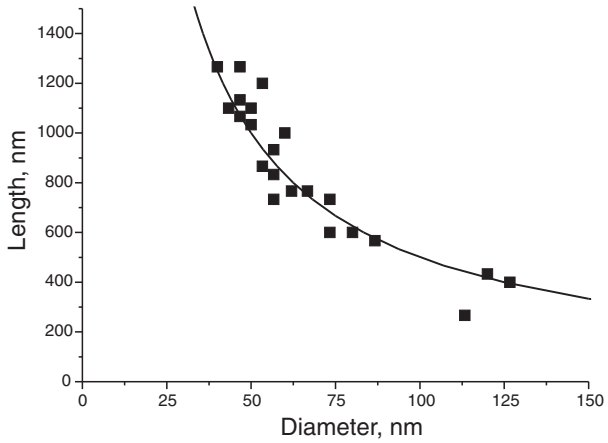

Fig. 2. Size distribution of GaAs NWs grown on mesa side facet.

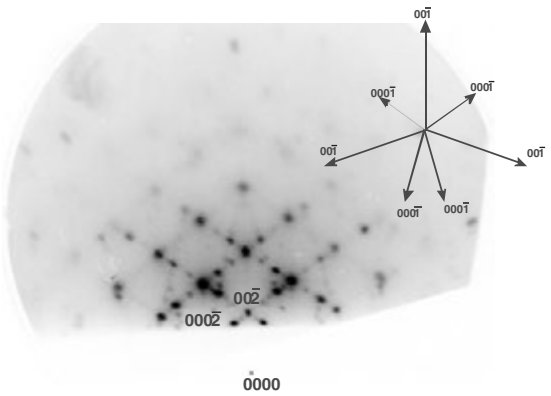

Fig. 3. RHEED image for the satellite sample with GaAs NWs grown in strip line mesas.

Example of RHEED image obtained from the sample having GaAs NWs in mesa is shown on Fig. 3. Analysis of RHEED images demonstrates that the NWs exhibit wurzite and/or polytypic phases. The special investigation of this phenomenon is given in [11].

3. Conclusion

There possibility of NWs growth in strip mesa is demonstrated. The result shows that using the geometry proposed the NWs can be fabricated and may serve as contacts between two parts on a chip.

Acknowledgements

Authors are acknowledgement V. V. Busov and S. I. Troshkov for SEM studying of NWs morphology.

The financial support of SANDiE European project, RAS scientific programs (“Quantum macrophysics” and “Quantum nanostructures”) and that of RFBR grants is acknowledged.

References

[1] R. B. Marcus *et al*, *APL* **56**, 236 (1990).
[2] Y. Cui and C. M. Lieber, *Science* **291**, 851 (2000).
[3] Q. Wan *et al*, *Appl. Phys. Lett.* **84**, 3654 (2004).
[4] E. I. Givargizov, *J. Cryst. Growth* **31**, 20 (1975).
[5] V. G. Dubrovskii, G. E. Cirlin, I. P. Soshnikov, N. V. Sibirev, A. A. Tonkikh, Yu. B. Samsonenko, and V. M. Ustinov, *Phys. Rev. B* **71**, 205325 (2005).
[6] G. E. Cirlin, V. G. Dubrovskii, I. P. Soshnikov, N. V. Sibirev, A. A. Tonkikh, Yu. B. Samsonenko, and V. M. Ustinov, *Semiconductors* **47** (2005).
[7] K. Hiruma, M. Yazawa, K. Haraguchi, K. Ogawa, T. Katsuyama, M. Koguchi, and H. Kakibayashi, *J. Appl. Phys.* **74** No. 5, 3162–71 (1993).
[8] B. J. Ohlsson, M. T. Bjork, M. H. Magnusson, K. Deppert, L. Samuelson L. R. Wallenberg, *Appl. Phys. Lett.* **79** No. 20, 3335–37 (2001).
[9] I. P. Soshnikov, G. E. Cirlin, V. G. Dubrovskii, A. A. Tonkikh, Yu. B. Samsonenko, V. M. Ustinov, O. M. Gorbenko, D. Litvinov, D. Gerthsen, *Solid State Phys.* **47** 2121–2126 (2005).
[10] I. P. Soshnikov, G. E. Cirlin, A. A. Tonkikh, Yu. B. Samsonenko, V. V. Nevedomskii and V. M. Ustinov, *Solid State Phys.* **49** No. 8, 1373–1378 (2007).
[11] I. P. Soshnikov, G. E. Cirlin, N. V. Sibierev, V. G. Dubrovskii, Yu. B. Samsonenko, V. M. Ustinov, D. Litvinov, D. Gerthsen, *Tech. Phys. Lett.* (2008).

16th Int. Symp. "Nanostructures: Physics and Technology"
Vladivostok, Russia, July 14–18, 2008

Molecular beam epitaxial growth of thermodynamically metastable GaInAsSb alloys for mid-IR photodetectors

A. N. Semenov, B. Ya. Meltser, Ya. V. Terent'ev, V. A. Solov'ev, T. B. Popova, I. A. Andreev, E. V. Kunitsyna and S. V. Ivanov

Ioffe Physico-Technical Institute, St Petersburg, Russia

Abstract. $Ga_xIn_{1-x}As_ySb_{1-y}$ alloys lattice matched to GaSb with In content up to the 25%, which are highly requested for active region of mid-IR photodetectors in the 2.5–3.0 μm range, have been grown by molecular beam epitaxy on GaSb and GaAs substrates and studied by double-crystal X-ray diffraction, scanning electron microscopy and photoluminescence spectroscopy. It has been found that $Ga_xIn_{1-x}As_ySb_{1-y}$ alloys with $x \leq 80\%$ grown at 500 °C exhibit degradation of structural and optical properties as the layer thickness increases. The thick layer with a thickness above critical ones demonstrates a tendency to spinodal decomposition in a good agreement with the calculated chemical instability gap boundary. The optimization of growth conditions for such GaInAsSb alloys to suppress their degradation has been discussed.

Introduction

$Ga_xIn_{1-x}As_ySb_{1-y}$ alloys are widely used in a large variety of applications, such as lasers or light-emitting diodes and photodetectors operating without cooling in the mid-IR spectral range [1]. The main disadvantage of $Ga_xIn_{1-x}As_ySb_{1-y}$ alloys is an extended immiscibility gap which restricts application of these materials and limits cut-off wavelength of photodetectors around 2.5 μm. Determination of the boundaries of instability and immiscibility regions in GaInAsSb was carried out both experimentally [2,3] and theoretically [4,5]. The results of these calculations depend both on the model and initial thermodynamic parameters, while experimental data on GaInAsSb miscibility gaps are contradictory.

Although molecular beam epitaxy (MBE) is generally accepted as a nonequilibrium growth technique, it reveals some difficulties in yielding GaInAsSb alloys with high optical and structural quality and good enough composition control at compositions inside the thermodynamically defined immiscibility region [6,7]

In this paper we will present our results on growth by MBE, optical and structural characterization of GaInAsSb alloy with different alloy compositions inside the instability gap from a GaSb side.

1. Experiment

The $Ga_xIn_{1-x}As_ySb_{1-y}$ alloys were grown by MBE on GaSb (001) (lattice matched) and GaAs (001) (mismatch around 7%) substrates using a RIBER 32P setup equipped with conventional solid source effusion cells for group III elements and antimony and a VAC-500 valved cracking cell for As_4. Substrate temperature T_{sub} was fixed at 500 °C and measured by an IR pyrometer calibrated via different surface reconstruction transitions on GaAs and GaSb surface, monitored *in situ* by reflection high energy electron diffraction (RHEED). The thickness of GaInAsSb layers varied from 0.5 to 2 μm. The In concentration was changed from 12% up to 25%, the As/Sb concentration ratio was chosen to provide lattice matched condition to GaSb. The Ga flux was kept constant, while In flux was varied to obtain necessary In molar concentration. For the composition control in anion sub-lattice the Sb flux value was set below that of the total group III flux to provide necessary antimony concentration, whereas the As flux ensured the resulting V/III flux ratio to be above 1, typically V/III ∼3.

The structural and optical properties of the GaInAsSb alloys were analyzed using double-crystal X-ray diffraction (XRD), scanning electron microscopy (SEM) and photoluminescence (PL) spectroscopy. The composition of the alloys was determined using a CAMEBAX x-ray spectral microanalyzer. The microanalysis data on the composition of the metal components were used in simulation of the XRD rocking curves for more accurate determination of the lattice mismatch between the GaInAsSb alloys and substrate. The simulation was performed under the assumption of pseudomorphic phase matching or complete relaxation of elastic stress, depending on the ratio between the real alloy layer thickness and the critical one for a given lattice mismatch, that was calculated using the equilibrium-strain model [8] and corrected in accordance with the published experimental data.

The X-ray measurements were performed in the ω and $\Theta - 2\Theta$ scan mode. A copper tube ($K_{\alpha 1} = 1.5406$ Å) served as the X-ray source, and a high-quality germanium crystal was used as the monochromator. PL spectra were measured under a chopped diode laser excitation ($\lambda_{ex} = 809$ nm) at the excitation power density of ~ 1.5 W/cm^2 at the sample surface. Emitted light was detected with a nitrogen-cooled InSb photodiode and a standard lock-in amplification technique.

2. Results and discussion

We have found that in accordance with the theoretical prediction [5] MBE allows one to growth GaInAsSb alloys lattice matched to the GaSb with In molar concentration up to 18–20%. Note, that this compositions fall inside the metastable region and such alloys cannot be grown under equilibrium conditions. These alloys demonstrate high structural quality, smooth and atomically flat surface and bright PL up to the room temperature. The photodetector device performance based on GaInAsSb alloys lattice matched to the GaSb with In content less than 20% have been published elsewhere [9,10].

The GaInAsSb alloys with higher In concentration (but still inside the metastable region) grown on GaSb substrate under similar condition demonstrate worse structural quality, more

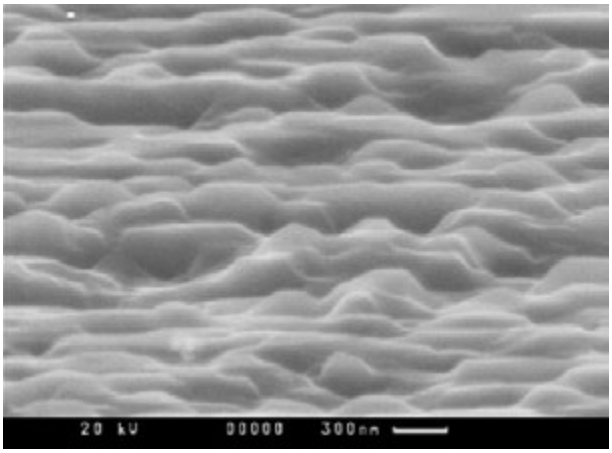

Fig. 1. SEM image of the $Ga_{0.75}In_{0.25}As_{0.21}Sb_{0.79}$ alloy surface with a thickness around 2 μm.

appreciably in thick layer (thickness above 0.6 μm). In these samples the RHEED pattern during growth becomes fuzzy and almost disappears in case the layer thickness exceeds 1.5 μm. As a results a hazy surface morphology is observed at SEM image (Fig. 1). Although XRD and PL studies do not reveal any signs of decomposition, the full width at half maximum (FWHM >700 arcsec.) of XRD peak corresponding to the GaInAsSb layers indicates their poor structural quality.

The GaInAsSb alloys grown on GaSb substrate are nearly lattice matched to the GaSb, but if the thickness increases partial relaxation is possible. It was shown for AlInAsSb solid alloys [11] that residual strain plays crucial role in preventing decomposition. We believe that in the case of GaInAsSb alloys (In >20%) we observed similar situation. Thin strained layers demonstrate high quality and bright PL, but in thick layers composition fluctuations and surface roughness increase. Probably in very thick layers the decomposition occurs in accordance with theoretical predictions. But the low growth rate in MBE does not allow us to check this assumption directly. Another way to clarify this assumption is the employing of lattice mismatched substrates, like GaAs. The very high mismatch (∼7%) leads to the strain relaxation during growth of first several monolayers. Thereafter the GaInAsSb alloy layers grow with only minor residual stress. The XRD curve for this sample is presented in Fig. 2. Three peaks are clearly resolved, attributed to a GaAs-substrate (at 0 point), to the GaInAs-rich phase (at −4000 arcsec), and to the GaInSb-rich phase (−10 000 arcsec). This result clearly indicates the spinodal decomposition of the solid alloy.

A clear tendency in improving structural quality of the thick metastable GaInAsSb layers was found with the V/III ratio going down to 1. In our opinion, the high V/III flux ratio (excessive As flux) facilitates the local composition fluctuations at the alloy layer surface and leads to precipitation of GaInAs-rich phase that serves as initial nucleation centers for decomposition.

The optimization of growth conditions for the thick solid GaInAsSb alloys with In content well above 20%, their structural and PL properties, as well as characteristics of mid-IR photodetectors based on these alloys will be discussed.

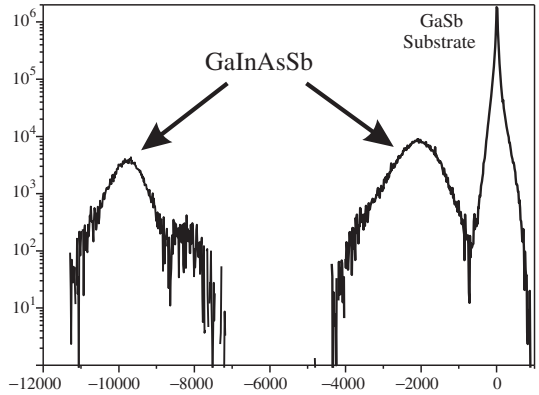

Fig. 2. XRD curves of the $Ga_{0.75}In_{0.25}As_{0.21}Sb_{0.79}$ alloy grown on GaAs substrate.

3. Conclusions

The influence of miscibility gap on structural and optical properties of GaInAsSb alloys is investigated. It is found that both the quality degradation and decomposition of these solid alloys are strongly suppressed by the residual elastic stress. Thin strain GaInAsSb layers (<0.6 μm) of high quality with compositions inside the metastable region can be grown by MBE without additional efforts. Thicker GaInAsSb layers require optimized growth condition with V/III flux ratio slightly above unity.

Acknowledgements

The authors are thankful to S. Troshkov and V. Busov for the SEM measurements. The work was supported partly by RFBR.

References

[1] A. A. Toropov, O. G. Lyublinskaya, V. A. Solov'ev, and S. V. Ivanov, *in III–V Semiconductor Heterostructures: Physics and Devices*, ed. by W. Z. Cai, Research Signpost (Keraia, 2003), p. 169.
[2] K. Nakajima *et al*, *J. Crystal Growth* **41**, 87 (1977).
[3] A. N. Baranov *et al*, *Sov. Tech. Phys. Lett.* **16**, 177 (1990).
[4] G. B. Stringfellow, *J. Crystal Growth* **58**, 194 (1982).
[5] V. S. Sorokin *et al*, *J. Crystal Growth* **216**, 97 (2000).
[6] H. -R. Blank *et al*, *J. Crystal Growth* **187**, 18 (1998).
[7] H. Miyoshi, Y. Horikoshi, *J. Crystal Growth* **227–228**, 571 (2001).
[8] J. W. Matthews, A. E. Blakeslee, *J. Crystal Growth* **27**, 118 (1974).
[9] O. V. Sulima *et al*, *Electron. Lett* **42**, 55 (2006).
[10] I. A. Andreev *et al*, *Abs. of 8th Int. Conf. MIOMD*, Bad Ischl, 2007, p. 94.
[11] A. N. Semenov *et al*, *J. Crystal Growth* **278**, 203 (2005).

16th Int. Symp. "Nanostructures: Physics and Technology"
Vladivostok, Russia, July 14–18, 2008

Castle-like quantum dot complexes formed by indium droplet epitaxy on (001)GaAs substrate

A. A. Lyamkina[1,2], D. V. Dmitriev[1] , S. P. Moshchenko[1], V. A. Haisler[1], Yu. G. Galitsyn[1] and A. I. Toropov[1]

[1] Institute of Semiconductor Physics SB RAS, Novosibirsk, Russia
[2] Novosibirsk State University, Novosibirsk, Russia

Abstract. Castle-like quantum dot InAs/GaAs complexes grown by droplet epitaxy are studied. Typical QD complex consists of 30 nm high center dot and about 12 separate 10 nm dots around with total structure diameter 300 nm. Average density of castle-like complexes with high center dot is 10^8 cm^{-2}. The part of spectrum corresponded to QD is shifted toward long wavelength compared with spectrum of usual Stranski–Krastanov QD sample. Analysis of kinetics of formation QD reveals a destruction tendency which can be used to low QD density.

Introduction

Self-assembled InAs quantum dots (QD) have been extensively investigated for the past decade because of perspective of their applications in advanced devices such as lasers, infrared detectors and quantum computers. Evident rise of interest to fabrication of nanostructures has lead to great diversity of geometrical shapes of QD complexes [1,2]. Morphology of such QD molecules depends on growth technique, conditions such as temperature, layer's thickness etc. Choice of temperature is disputable because there are two opposite arguments. To minimize the effects of anisotropic surface diffusion on substrate during crystallization the temperature should be lowered. However, the migration length of In atoms is longer when there is no excess As and increases with temperature's growth. So using of high temperature can provide low density and high quality of QD as it is desired for a single-photon source [3]. Additional ways of density control can be found out by analyzing of growth kinetics.

1. Experimental

In this work we fabricated InAs/GaAs QD using droplet epitaxy at high temperature (∼500 °C). Before QD forming proper amount of Ga was deposited to saturate excess arsenic atoms on the substrate surface.

The nanostructures studied were grown by molecular beam epitaxy on semi-insulating (001)-oriented GaAs substrates using a Riber32P system with gate arsenic source. 1.5 ML of Ga was applied to the GaAs surface, then 2.1 ML of In was deposited without As_4 flux and the sample was exposed to a beam equivalent pressure of 1.5×10^{-5} Torr of As_4. Necessary gallium deposition time was tuned in preliminary test on working substrate to obtain exactly 1.5 oscillations of SB after closing arsenic source and opening gallium source just before main experiment.

Two layers of QD were grown — capped one between AlGaAs/GaAs layers for photoluminescence (PL) measurements and uncapped. The morphology of the surfaces was studied ex-situ by the atomic force microscopy (AFM), using the scanning probe microscope Solver-P47H (NT-MDT). Standard silicon cantilevers were used. AFM image is shown on Fig. 1.

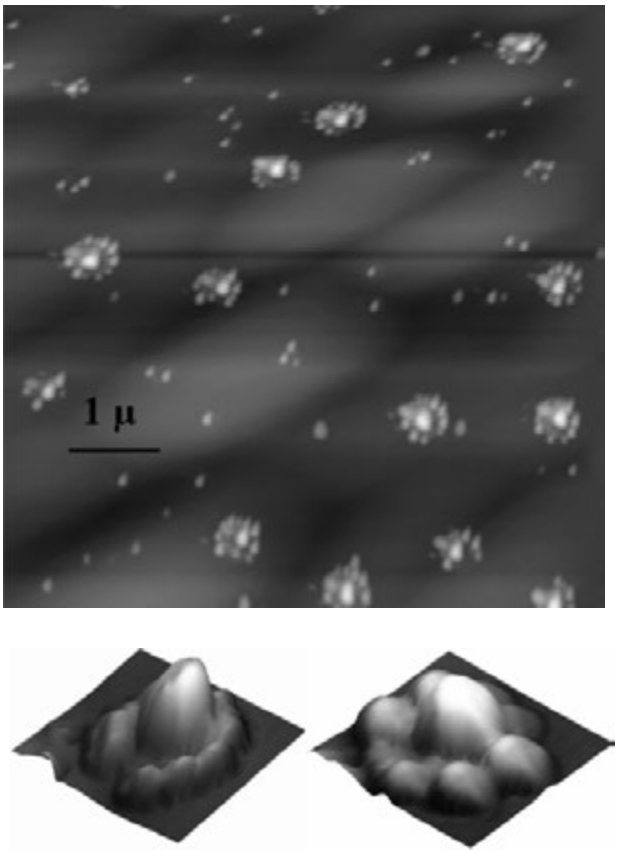

Fig. 1. AFM image of grown nanostructure. Inserted enlarged 3D AFM images are the typical structures for the given sample. Figure is 5×5 μm, insertions are 530×530 nm.

2. Results and discussion

For growth control and kinetics analysis high-energy electron diffraction was used. Fig. 2 shows typical diffraction pattern for formed QD. This data accumulates information about phases of progress of QD. Profile of intensity represented on Fig. 3 demonstrates some of such important phases. Two profiles shown are specular beam (SB) and 3D InAs spots respectively. Enlarged profile demonstrates an oscillation of specular signal which can be corresponded to deposition of InAs monolayer coverage — formation of wetting layer (WL).

This process is rather rapid comparing with formation of QD and occurs immediately after arsenic source opening. Ki-

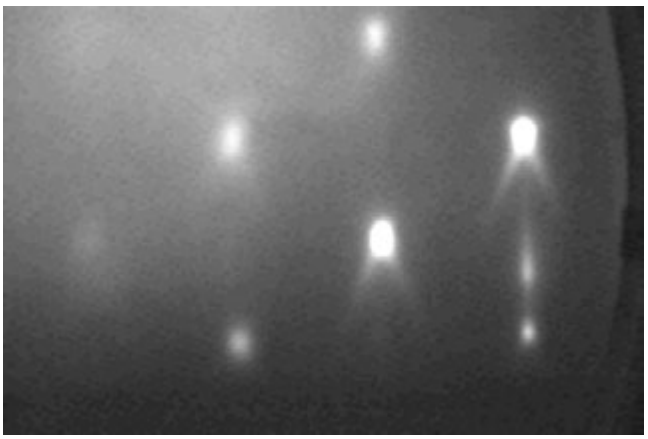

Fig. 2. RHEED picture with formed QD.

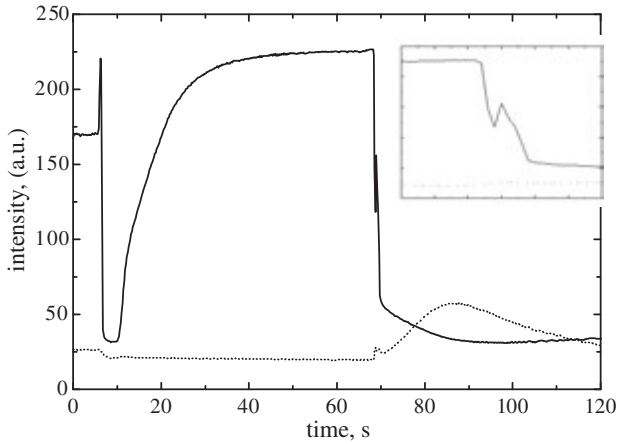

Fig. 3. RHEED intensity growth kinetics (SB — line, 3D InAs — spot-line). Insert shows SB growth oscillation after arsenic source was open.

netics of QD growth is slower and changes to destruction after passing throw its maximum. Position and magnitude of this maximum depend on In amount deposited on the substrate, the less In the lower maximum and slower the raising. It concerns to kinetics of destruction as well, so it can be used to regulate QD density. Usually attention concentrates on kinetics of QD formations, assuming that process of formation of QD arrays on it comes to an end and they further exist stably.

PL spectrum of the structure with QD was measured at room temperature and is shown on Fig. 4. The excitation power of laser with wavelength of 533 nm was 0.1 kW/mm^2. It is seen that the part of spectrum corresponded to QD is shifted toward long wavelength compared with spectrum of usual Stranski–Krastanov (SK) QD sample. There is a peak clearly corresponded to WL, in spite of in paper [4] method of growth with similar parameters was used and no WL was observed. A presence of WL allows to interpret SB oscillation seen on insert in Fig. 3 as formation of InAs monolayer coverage as it was mentioned above. After that self-organization by SK growth mode takes place immediately that accords to SB and 3D spot behavior: SB strongly decreases and simultaneously the 3D spot increases.

Structure of distinctive QD complexes is rather complicated: high (∼30 nm) center dot and about 12 separate lesser (∼10 nm) dots around (castle-like) with total structure diameter ∼300 nm. Furthermore, there are isolated dots which can be supposed to be the remains of such complexes. So we can assume that complexes with defects were almost destroyed as affected high temperature, then the rest might be high-quality crystalline nanostructures. Average density of castle-like complexes with high center dot is 10^8 cm^{-2}.

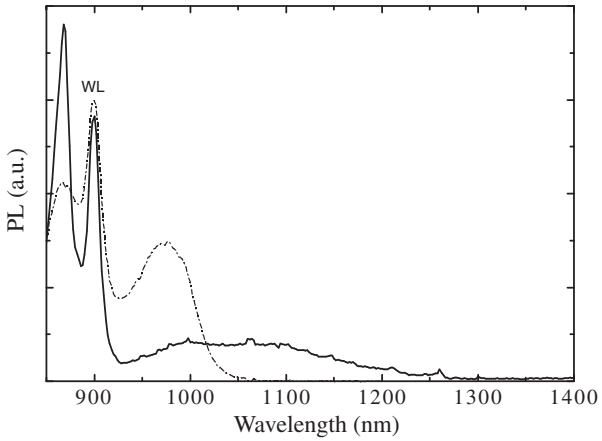

Fig. 4. Room temperature PL spectrum of the sample with castle-like structures (solid line) compared with spectrum of usual SK QD sample with density 10^8 cm^{-2} (dashed line).

Acknowledgements

We are grateful to V. A. Seleznev and A. V. Prinz for the help with AFM measurements.

References

[1] J. H. Lee, Zh. M. Wang, N. W. Strom, Yu. I. Mazur and G. J. Salamo, *Appl. Phys. Lett.* **89**, 202101 (2006).

[2] T. Mano, T. Kuroda, S. Sanguinetti, T. Ochiai, T. Tateno, J. Kim, T. Noda, M. Kawabe, K. Sakoda, G. Kido and N. Koguchi, *Nano Lett.* **5**, 425 (2005).

[3] M. Scholz, S. Buttner, O. Benson, A. I. Toropov, A. K. Bakarov, A. K. Kalagin, A. Lochmann, E. Stock, O. Schulz, F. Hopfer, V. A. Haisler, D. Bimberg, *Optics Express* **15**, 9107 (2007).

[4] S.-S. Huang, Z.-C. Niu, H.-Q. Ni, F. Zhan, H. Zhao, Z. Sun and J.-B. Xia, *Chin. Phys. Lett.* **24**, 1025 (2007).

16th Int. Symp. "Nanostructures: Physics and Technology"
Vladivostok, Russia, July 14–18, 2008

Self-assembly formation of adsorbate nanostructures on semiconductor surfaces with atomic precision

A. A. Saranin and A. V. Zotov
Institute of Automation and Control Processes, Vladivostok, Russia

Abstract. Self-organization of atoms adsorbed on atomically-clean semiconductor surfaces in ultra-high vacuum has been used to fabricate the main principal nanostructures, including nanofilms, nanowires and nanodots. The most principal results obtained with this technique and prospects of its development are discussed in detail.

Introduction

Recent progress, achieved in the nanostructure formation using self-organization of atoms adsorbed on semiconductor surfaces in ultra-high vacuum (UHV), allows to consider this technique as a prototype technology for fabrication of nanoelectronic devices. Combination of the extra-clean UHV conditions and surface monitoring with scanning tunneling microscopy (STM) ensures controlling the growth processes on atomic scale. In the present report, we review the recent results obtained in this field in the Department of Surface Science in the Institute of Automation and Control Processes. We consider how using self-assembly of adsorbate atoms on semiconductor surfaces one can fabricate the main principal nanostructures, including nanofilms, nanowires and nanodots.

1. Nanofilms

Nanofilms having thickness on atomic scale are represented by a wide set of surface phases (reconstructions) formed in monolayer and submonolayer adsorbate/silicon and adsorbate/germanium systems. Surface phases have been an object of extensive researches for more than 40 years. As a result, a considerable body of manifold information has been accumulated by scientific community: for many systems the phase diagrams have been constructed; for the phases of the greatest interest the phase composition, atomic structure and electronic properties have been elucidated (Fig. 1) [1]. Nowadays more than 300 different reconstructions are known on Si and more than 100 on Ge surfaces. Current researches are directed towards reaching the greater structural perfection of the surface phases, as well as controlling their properties. As an example, we can refer to the results of our recent work on Au/Si(111) system, which demonstrate that adding the second adsorbate (In) alters the domain wall structure, which in turn affects electronic properties of the surface phase [2]. Plausible mechanism of stabilization of the domain-wall-free Si(111)$\sqrt{3}\times\sqrt{3}$-(Au,In) surface is the stress relieving caused by In adsorption.

Another example is related with an attempt to modify Si(111) 4×1-In surface by the varying averaged lattice constant of the substrate. In the experiment, the lattice constant of Si(111) substrate has been increased by forming a thin alloying Ge_xSi_{1-x} layer on Si(111) [3]. It has been found that this action results in removing the 4×1 reconstruction and developing a new 7×3 reconstruction, the transformation being completed when more than 0.3 ML of Ge have been incorporated into the substrate. The 7×3 reconstruction is not observed in "pure" In/Si(111)

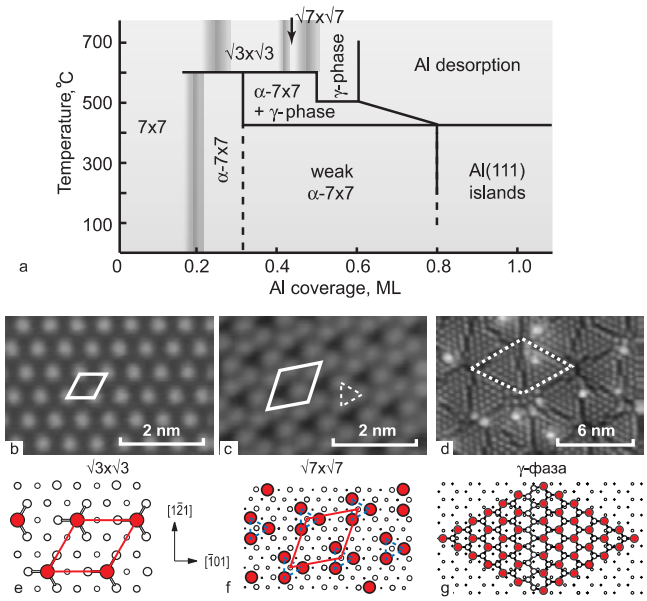

Fig. 1. (a) Structural phase diagram of the Al/Si(111) system obtained based on the Auger-electron spectroscopy and low-energy electron diffraction data. (b)–(d) Scanning tunneling microscopy images and (e)–(g) atomic structural models of the $\sqrt{3}\times\sqrt{3}$, $\sqrt{7}\times\sqrt{7}$ and γ-phase.

and In/Ge(111) systems. We believe that the artificial variation of substrate lattice constant not only provides a possibility to examine the role of surface stress in reconstructions, but also opens a new degree of freedom for engineering new types of reconstructions.

2. Nanowires

For self-assembly formation of the nanowires, one can use highly anisotropic growth, say, as in the case of growing nanowires made of silicides of metals (e.g., Er, Dy, Sm) on Si(100) surface. To reach the same goal, we have used alternative approach, namely preferential metal island nucleation at the atomic steps, which takes place, for example, in the Cu/Si(111) system.

Upon room-temperature deposition onto the Cu/Si(111) '5×5' surface in ultra-high vacuum, Cu atoms migrate over extended distances to become trapped at the step edges, where they form Cu nanowires [4]. The forming nanowires are 20–80 nm wide, 1–3 nm high and characterized by the resistivity of $\sim8\ \mu\Omega$ cm. The surface conductance of the nanowire array is anisotropic with the conductivity along the nanowires being

about three times greater than that in the perpendicular direction. Using a similar growth technique, not only the straight nanowires but also other types of the NW-based structures (e.g., nanorings) can be fabricated [5].

3. Nanodots and clusters

Nanodots, which are represented by various nanocluster arrays, attract currently a great interest and a number of the vivid results have been obtained in this field. In particular, highly-ordered arrays of the identical-size nanoclusters (i.e., magic-cluster 2D crystals) have been successfully fabricated with Group-III adsorbates on Si surfaces.

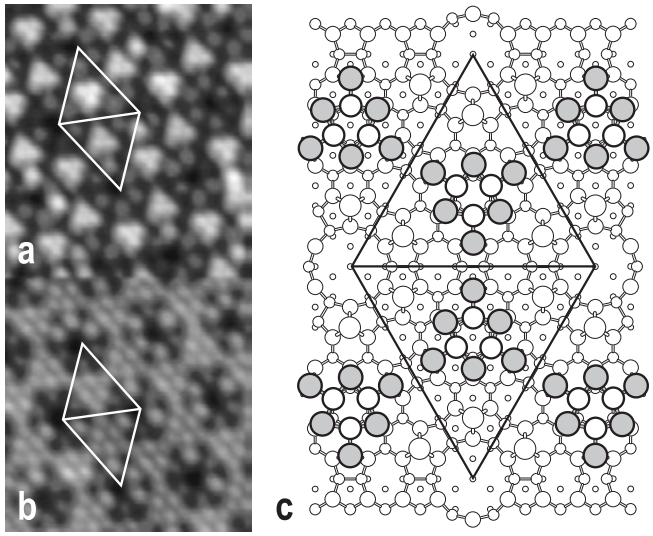

Fig. 2. (a) Filled state (+2.0 V) and (b) empty state (−2.0 V) STM appearance of the Al magic clusters. (c) Atomic structure of the magic cluster of the Group III metals, as established in Refs. [7,8,9]. The magic cluster is built of six metal atoms (grey circles) linked through three top Si atoms. The protrusions seen in filled states correspond to the location of the top Si atoms, the protrusions seen in empty states to that of the metal atoms. The 7 × 7 unit cell is outlined.

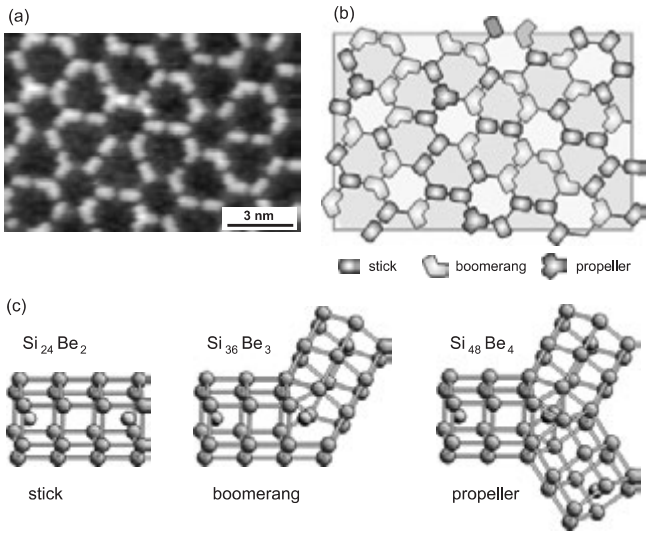

Fig. 3. Building blocks of nanostructure array. (a) Filled-state STM image of the 13.5 × 9.0 nm^2 fragment of the nanostructure array and (b) its schematic diagram. The array is built of elements of three types, labelled "stick", "boomerang" and "propeller". (c) Hypothetic structure of the array building blocks: $Si_{24}Be_2$ for stick, $Si_{36}Be_3$ for boomerang and $Si_{48}Be_4$ for propeller.

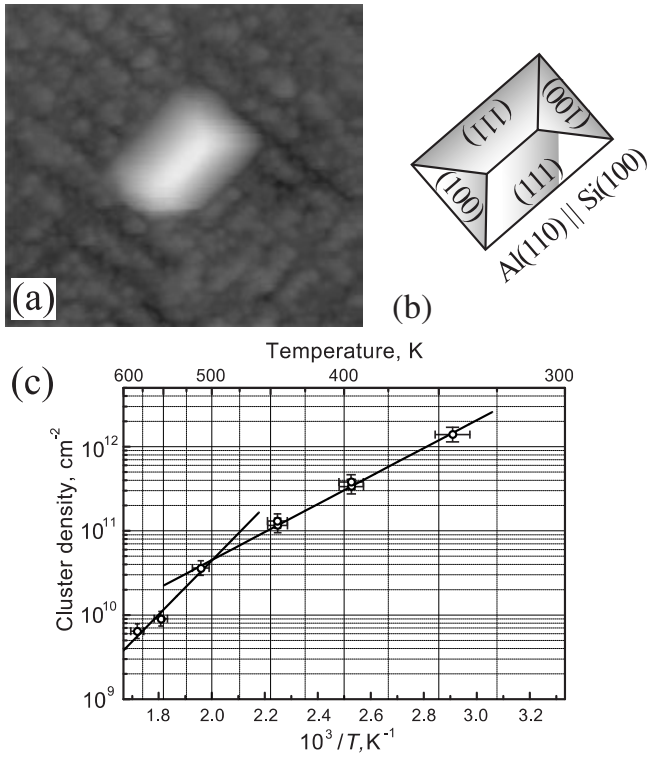

Fig. 4. Crystalline structure of the Al hut-cluster grown on the Si(100)c(4 × 12)-Al surface. (a) STM image and (b) schematic illustration of its shape. (c) Arrhenius plot of the number density of Al nanoclusters formed upon deposition of 0.12 ML of Al. Deposition rate is 0.25 ML/min.

Deposition of Al onto the Si(111)7 × 7 surface held at temperatures ranging from 475 to 600 °C has been found to result in the formation of a superlattice of the magic atomic clusters [6]. Each Al magic cluster contains six metal atoms linked by three Si atoms (see Fig. 2).

Recently it has been found that such magic cluster lattice has potential application as a catalyst [10]. The surface with the Al surface magic clusters lattice had the highest activity for the dissociation of CH_3OH while the bulk Al film showed the lowest activity.

Modification of the magic-cluster composition leading to the changeover of its electronic properties (i.e., cluster doping) has been demonstrated [11]. It has been found that dynamic behavior of the doped cluster in In/Si(100) system opens a prospect for using the cluster as an atomic-scale memory cell [12]. Nanocluster growth on the various modified Si surfaces has also been studied.

Carbon has a number of nano forms like fullerenes and nanotubes but this is not the case for silicon though carbon and silicon are both Group IV elements. In particular, Si nanotubes remain the subject of merely theoretical consideration which predicts that metal (e.g., Be) encapsulation stabilizes Si nanotubes [13]. Following this hint, we have examined Be interaction with the heated Si(111) substrate under ultra-high-vacuum conditions and found formation of the ordered nanostructure arrays with the building blocks which have composition, size and properties similar to those theoretically predicted for the

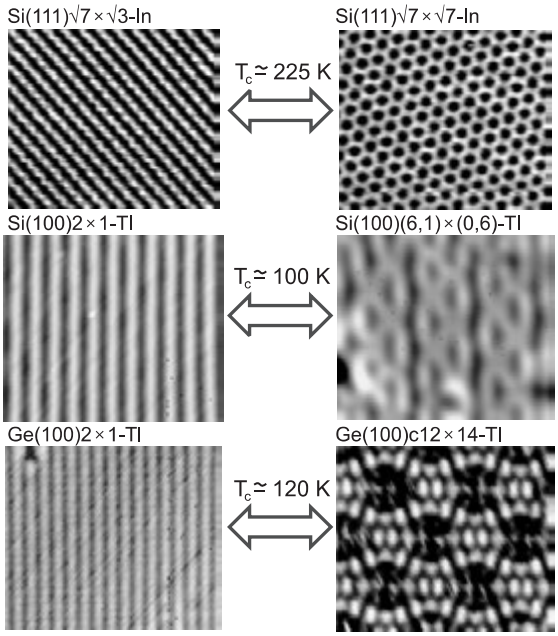

Fig. 5. Low-temperature reversible phase transitions in the metal (In, Tl) monolayers on Si(111), Si(100) and Ge(100) surfaces.

short Be-encapsulated Si nanotubes (Fig. 3) [14].

To control the growth mode of a number of metals on semiconductor surfaces we have investigated the growth on modified surface when the "stable" surface phase is formed on the surface which changes the interaction strength between adatoms and the surface. It turns out that the Si(100)c(4 × 12)-Al surface reconstruction has a desired property i.e. it "passivates" the surface leading to the formation of three-dimensional adatom clusters or nano islands, thus changing Stranski–Krastanov and/or Frank-van der Merwe growth modes typical for the most elements on silicon surfaces to the Volmer–Weber one. The formation of monocrystalline nanoclusters of several metals (Al, Au, Cu, and In) has been found. In all cases the growth is well described by classical nucleation rate theory (Fig. 4).

4. Structural phase transitions

Self-assembly of adsorbates can be used in the fundamental studies of the critical phenomena in the low-dimensional systems. For example, Fig. 5 shows STM images of the unusual reversible phase transitions that have recently been found in the surface phases developed in the Tl/Si(100) [15], Tl/Ge(100) [16] and In/Si(111) [17] systems.

5. Perspectives

Further development of the above directions are believed to be associated with expansion of the adsorbate types, with various modifications of the substrate surfaces, as well as with developing of the STM technique, say, with using STM tips made of carbon nanotubes covered by thin layers of the functional (e.g., metallic, magnetic or superconducting) materials.

References

[1] V. G. Lifshits, A. A. Saranin, and A. V. Zotov, *Surface Phases on Silicon*, John Wiley & Sons, Chichester, 448 (1994).

[2] D. V. Gruznev, I. N. Filippov, D. A. Olyanich, D. N. Chubenko, I. A. Kuyanov, A. A. Saranin, A. V. Zotov, and V. G. Lifshits, *Phys. Rev. B* **73**, 115335 (2006).

[3] D. V. Gruznev, D. A. Olyanich, D. N. Chubenko, A. V. Zotov, and A. A. Saranin, *Phys. Rev. B* **76**, 073307 (2007).

[4] A. V. Zotov, D. V. Gruznev, O.A. Utas, V. G. Kotlyar, and A. A. Saranin, *Surf. Sci.* **602**, 391 (2008).

[5] D. A. Tsukanov, M. V. Ryzhkova, D. V. Gruznev, O. A. Utas, V. G. Kotlyar, A. V. Zotov, and A. A. Saranin, *Nanotechnology* (2008), (submitted).

[6] V. G. Kotlyar, A. V. Zotov, A. A. Saranin, T. V. Kasyanova, M. A. Cherevik, I. V. Pisarenko, and V. G. Lifshits, *Phys. Rev. B* **66**, 165401 (2002).

[7] M. Y. Lai and Y. L. Wang, *Phys. Rev. B* **64**, 241404 (2001).

[8] J. L. Li, J. F. Jia, X. J. Liang, X. Liu, J. Z. Wang, Q. K. Xue, Z. Q. Li, J. S. Tse, Z. Zhang, and S. B. Zhang, *Phys. Rev. Lett.* **88**, 066101 (2002).

[9] M. Y. Lai and Y. L. Wang, *Phys. Rev. Lett.* **81**, 164 (1998).

[10] Z. Zhang, Q. Fu, H. Zhang, Y. Li, Y. Yao, D. Tan, and X. Bao, *J. Phys. Chem.* **111**, 13524 (2007).

[11] V. G. Kotlyar, A. V. Zotov, A. A. Saranin, E. N. Chukurov, T. V. Kasyanova, M. A. Cherevik, I. V. Pisarenko, H. Okado, M. Katayama, K. Oura, and V. G. Lifshits, *Phys. Rev. Lett.* **91**, 026104 (2003).

[12] M. Hashimoto, Y. Fukaya, A. Kawasuso, and A. Ichimiya, *Surf. Sci.* **601**, 5192 (2007).

[13] A. K. Singh, V. Kumar, T. M. Briere, and Y. Kawazoe, *Nano Lett.* **2**, 1243 (2002).

[14] A. A. Saranin, A. V. Zotov, V. G. Kotlyar, T. V. Kasyanova, O. A. Utas, H. Okado, M. Katayama, and K. Oura, *Nano Lett.* **4**, 1469 (2004).

[15] A. A. Saranin, A. V. Zotov, I. A. Kuyanov, V. G. Kotlyar, M. Kishida, Y. Murata, H. Okado, I. Matsuda, H. Morikawa, N. Miyata, S. Hasegawa, M. Katayama, and Oura, *Phys. Rev. B* **71**, 165307 (2005).

[16] A. A. Saranin, A. V. Zotov, M. Kishida, Y. Murata, S. Honda, M. Katayama, and K. Oura, *Surf. Sci.* **601**, 595 (2007).

[17] A. A. Saranin, A. V. Zotov, M. Kishida, Y. Murata, S. Honda, M. Katayama, K. Oura, D. V. Gruznev, A. Viskovskiy, and H. Tochihara, *Phys. Rev. B* **74**, 035436 (2006).

16th Int. Symp. "Nanostructures: Physics and Technology"
Vladivostok, Russia, July 14–18, 2008

Surface magic clusters on silicon

A. V. Zotov[1], A. A. Saranin[1], Y. L. Wang[2] and M. Y. Lai[2]

[1] Institute of Automation and Control Processes, Vladivostok, Russia
[2] Institute of Atomic and Molecular Sciences, Academia Sinica, Taipei, Taiwan

Abstract. Surface magic clusters (SMCs) are clusters exhibiting enhanced stability at certain sizes on a particular surface. Through the formation of SMCs, it is possible to grow an ensemble of nanostructures on a surface with extremely small or essentially zero size dispersion. Such an ensemble of nanostructures with identical size and atomic structure is highly desirable for certain nanotechnology that relies on the homogeneity in the physical and chemical properties of the constituent nanostructures. This report summarizes current experimental observations and understanding of SMCs and discusses the most recent progress in the formation of two dimensional lattices of SMCs.

Introduction

Magic clusters are defined as clusters with enhanced stability at certain sizes. Here, for clarity and consistency, the size of a nanocluster is defiend as its total number of atoms rather than its characteristic linear dimension. Magic clusters in a free space were discovered by mass spectrometry more than two decades ago [1]. Numerous researches have been devoted to the subject; and it has been known for sometime that the enhanced stability at certain sizes originates from either the electronic or atomic shell closure of a cluster with magic number of constituent atoms. A vivid example of the magic clusters is the family of the carbon fullerenes [2]. Intuitively, such clusters with enhanced stability could be exploited for the growth of nanostructures on surfaces with very narrow size dispersion. However, the shell closure and corresponding enhanced stability of a magic cluster could be destroyed by the cluster-surface interaction when it is brought into contact with certain surface. Surface magic clusters (SMCs), i.e., clusters with enhanced stability at certain sizes on a particular surface, have caught the attention of the scientific community since their first discovery of SMCs on the $\sqrt{3} \times \sqrt{3}$R30°-reconstructed Ga/Si(111) surface in 1998 [3]. A considerable progress has been achieved in this field during the last decade. In the present report, we provide a brief review of our recent experimental and theoretical results on the formation and characterization of SMC arrays, including the growth of the high-quality SMC lattices, controlled modification of SMC structure and composition (SMC doping) and elucidation of the dynamic behavior of atoms within a SMC.

1. Lattices of surface magic clusters

Consideration of the random SMC formation leads us to the conclusion that not only the closed-shell atomic arrangement of the cluster itself, but also the closed arrangement of its surrounding shell controls the preference for selecting SMC of a certain type and size. Thus, it is possible to find a surface whose unit cell structure provides conditions for the formation of the SMC with a closed surrounding shell and their periodic repetition produces a lattice of SMCs. The Si(111)7 × 7 surface appears to be the most suitable substrate. In this highly stable surface, the attractive basin inside each 7 × 7 half unit cell (HUC) is bordered by Si-dimer rows, which act as barriers for the deposited adsorbate atoms. These atoms, if being accumulated in a given HUC up to the required amount, have a chance to build a magic cluster there. This, indeed, have been found for a wide set of adsorbates and to date many examples of the SMC lattice formation are known. However, it should be remarked that the structural perfection of the forming SMC lattices varies in a wide range for various material systems. The most vivid examples of the SMC lattice formation are associated with the Group-III metals, Ga [4], Al [5] and In [6], in which case the Me_6Si_3 cluster is nicely built into the 7 × 7 HUC utilizing Si adatoms already present there. As an example, Fig. 1 shows an array of Al_6Si_3 SMCs on Si(111)7 × 7.

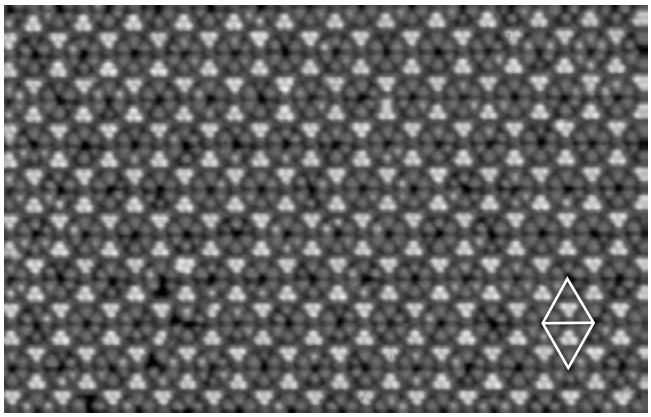

Fig. 1. STM image (340 × 210 Å^2) of the 2D lattice of Al-induced SMCs on Si(111)7 × 7 surface.

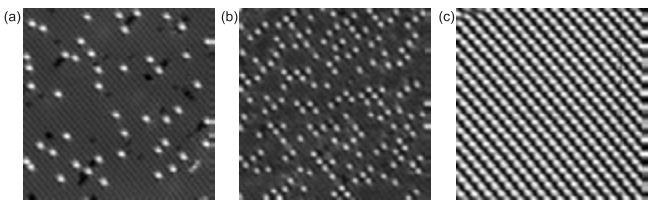

Fig. 2. 290 × 290 Å^2 STM images of the In/Si(100) surface formed upon adsorption of (a) 0.05 ML, (b) 0.18 ML and (c) 0.50 ML of In at 500 °C. In/Si(100) SMCs are distributed randomly at the low coverages, but become aligned into the superlattice at saturating coverage.

Formation of the SMC lattice is not limited to template-constrained self-organization of adsorbates on Si(111)7 × 7 surface. The case of the the 4 × 3-In clusters on Si(100) [7] (Fig. 2) gives an example of the SMC lattice formation which is not controlled by a template constraining effect. Here, the

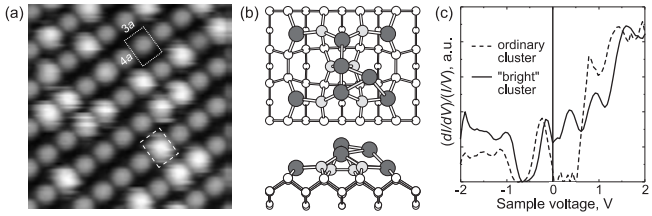

Fig. 3. a) Filled-state STM image (100×100 Å^2) of the In/Si(100)4×3 SMC lattice with In-modified clusters. The ordinary cluster is outlined by a dotted frame, the modified cluster by a dashed frame. (b) Structural model of the modified In_8Si_6 cluster. (c) $(dI/dV)/(I/V)$-versus-I STS spectra from the ordinary In_6Si_7 SMC (dashed line) and modified In_8Si_6 SMC (solid line).

original substrate reconstruction is lifted locally by the SMC formation and the SMC spatial ordering takes place to reduce the number of dangling bonds that are created by the lifting of the original reconstruction.

The material system of Tl on Si(111)7 × 7 provides a special example of magic nanoclustering [8]. Here, the ordered arrays of Tl-clusters of three various structural types are formed depending on growth conditions. Such an interesting phenomenon of diverse magic clustering might be associated with the so-called "inert pair effect" of Tl atom's $6s^2$ electron configuration, which allows Tl to exhibit either one or three valences and therefore to bond with Si atoms in various configurations.

2. Modification of surface magic clusters

Here, we review the cases where the properties of a SMC were studied by changing some its constituent atoms and the linkage between the structure/composition of the SMC with its properties was established. In retrospect, this seemingly natural way to explore the properties of a SMC by studying its response to cluster modification is not as easy as might be thought at a glance. There were several attempts of SMC modification by depositing foreign atoms onto the pre-formed SMC arrays, however there are only two researches, where the goal was reliably achieved. These investigations were devoted to elucidate the modification and the corresponding property change of the In_6Si_7 SMCs on Si(100) surface by the adsorption of In [9,10] and Pb [11].

In particular, In-induced modification results in substituting of a central Si atom in the In_6Si_7 SMC by a pair of In atoms leading to the formation of the asymmetric In_8Si_6 cluster (Fig. 3b). Results of STS demonstrated that the modification of the cluster altered its electronic properties (Fig. 3c). While the original In_6Si_7 SMC's STS spectrum exhibited a semiconductor behavior with a band gap of 0.6 eV, the modified cluster had an extra density of states within the band gap. The phenomenon is very similar to the doping of semiconductor crystals, and therefore could be referred to it as SMC doping and coined the name of the doped-SMC [9].

3. Atomic dynamics within surface magic clusters

One can see in Fig. 3b that in the asymmetric In_8Si_6 cluster one of the additional In atoms is located in the cluster center and the second In atom occupies the off-centered position. Note that there are four equivalent sites within the cluster, which

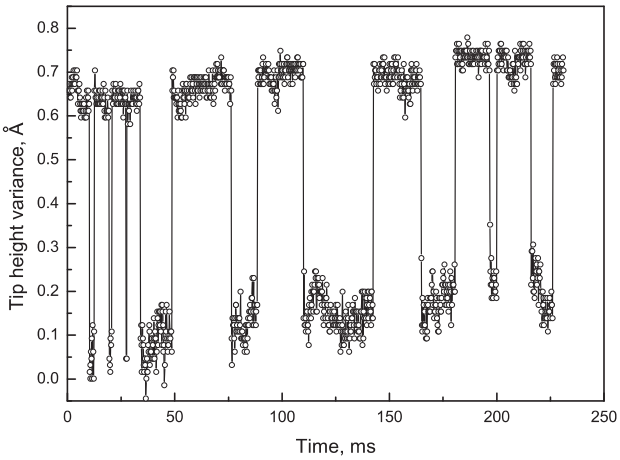

Fig. 4. Tracking of the In-atom hopping between the 2a×3a halves by measuring the time dependence of the apparent tip height in the off-centered point within the Si_6In_8 cluster.

off-centered In atoms can reside in. Total-energy calculations showed that In atom has to surmount barrier of 0.07 eV to visit the neighboring site within the same half unit cell and that of 0.7 eV to visit the sites in the other half unit cell. At room temperature, the cluster appears fuzzy due to hopping of In atom between neighboring half unit cells. The dynamics of the hopping was directly detected by placing the STM tip off the center of the cluster and monitoring the tip height (or tunneling current) as a function of time (Fig. 4). When the mobile In atom was in the same half unit cell as the tip, the STM signal reached its high state, when it hoped to another half the signal dropped to the low state. This interesting properties of the asymmetric In_8Si_6 cluster provided a conceptual starting point for the design of atomic switch, memory cell, or logic gate that can be used in the future nanoelectronics.

References

[1] W. D. Knight, K. Clemenger, A. Walt de Heer, W. A. Saunders, M. Y. Chou, and M. L. Cohen, *Phys. Rev. Lett.* **52**, (1984) 2141.
[2] H. W. Kroto, J. R. Heath, S. C. O'Brien, R. F. Curl, and R. E. Smalley, *Nature* **318**, (1985) 162.
[3] M. Y. Lai and Y. L. Wang, *Phys. Rev. Lett.* **81**, (1998) 164.
[4] M. Y. Lai and Y. L. Wang, *Phys. Rev. B* **64**, (2001) 241404.
[5] V. G. Kotlyar, A. V. Zotov, A. A. Saranin *et al*, *Phys. Rev. B* **66**, (2002) 165401.
[6] J.-L. Li, J.-F. Jia, X.-J. Liang *et al*, *Phys. Rev. Lett.* **88**, (2002) 066101.
[7] V. G. Kotlyar, A. V. Zotov, A. A. Saranin *et al*, *e-J. Surf. Sci. Nanotech.* **1**, (2003) 33.
[8] A. V. Zotov, A. A. Saranin, V. G. Kotlyar, O. A. Utas, Y. L. Wang, *Surf. Sci.* **600**, (2006) 1936.
[9] V. G. Kotlyar, A. V. Zotov, A. A. Saranin *et al*, *Phys. Rev. Lett.* **91**, (2003) 026104.
[10] A. A. Saranin, A. V. Zotov, I. A. Kuyanov *et al*, *Phys. Rev. B* **74**, (2006) 125304.
[11] A. V. Zotov, O. A. Utas, I. A. Kuyanov, and A. A. Saranin, *Phys. Rev. B* **76**, (2007) 115310.

16th Int. Symp. "Nanostructures: Physics and Technology"
Vladivostok, Russia, July 14–18, 2008

Fabrication of nanostructures on the surface by laser induced quantum adsorption

A. E. Afanasiev, *P. N. Melentiev* and V. I. Balykin
Institute of Spectroscopy Russian Academy of Sciences, 142190, Troitsk, Moscow reg., Russia

Abstract. We report new approach to control adsorption of atoms on to dielectric surface by laser light. The approach used is based on the atom energy-pooling collisions in a near resonant laser field. Our results show a possibility of production of the atom micro- and nanostructures on the surfaces.

Introduction

Fabrication of nanostructures of a given arbitrary shape on the solid surface is a key problem of modern nanotechnology. The fabrication of structures at scales smaller than the current limits is a technological goal of great practical and fundamental interest.

Adsorption of atom (molecule or cluster) on the surface is intrinsic process to capture atom (molecule or cluster) by a surface potential well (van der Waals interaction or creation of a chemical bounds). Besides of clear physical interest to the process of atom adsorption on to the surface [1] it forms the basis of current micro and nanotechnology industry, based on the use of molecular beam epitaxy and gas phase epitaxy techniques [2,3]. That's why to control elementary processes of particles adsorption on the surface has fundamental and great practical importance.

To date there is one proposal how to control atom adsorption on to the surface by the laser light (quantum adsorption). It is based on the phenomenon of atom photoassociation with a surface [4]. This process is analogues to atom photoassociation process-collision of two atoms with absorbing a photon leads to formation of a molecule. The use of this process became possible after development of methods of laser cooling of atoms which allow considerably increase phase density of atomic ensembles [5] and accordingly increase the probability of a triple atom-atom-photon collision which is proportional to the phase density $\rho\lambda_B^3$ where ρ is the density of atoms and λ_B is the de Broglie wavelength. The probability of the photo-association process can be considerably increased if one of the colliding bodies posses a macroscopic size. Such a situation happens in the process of atom collision with a surface in the presence of the laser field. In this case the rate of photo-association of the atom with the surface can be increased by many orders of magnitude, typically in the ratio $S/\lambda_B^2 \gg 1$ where S is the square of the surface illuminated by the laser light. Nevertheless, according to theoretical estimations the loading of atoms in the surface trap with the use of the photo-association process is also practically possible only for ultracold atoms since even for ultracold atoms the efficiency of the process is relatively low.

In this report we propose new approach of atom loading in the surface potential well by use of laser light (atom quantum adsorption) and describe experimental realization of such a trap for neutral Rb atoms [6]. Proposed method of the atom loading in the surface trap is based on the energy-pooling collisions effect. The effect consists in inelastic collision of two excited atoms followed by transition of one of the atoms in the ground state and the other one in the highly excited state. In such a process the shortage of the internal atomic energy is compensated for by the kinetic energy of colliding atoms. When such a collision happens inside the surface potential well the ground-state atom can be trapped inside the potential well. We also describe formation of the microstructures of arbitrary shape produced by the atoms localized on the dielectric surface and propose a possibility of formation of nanostructures on the surface.

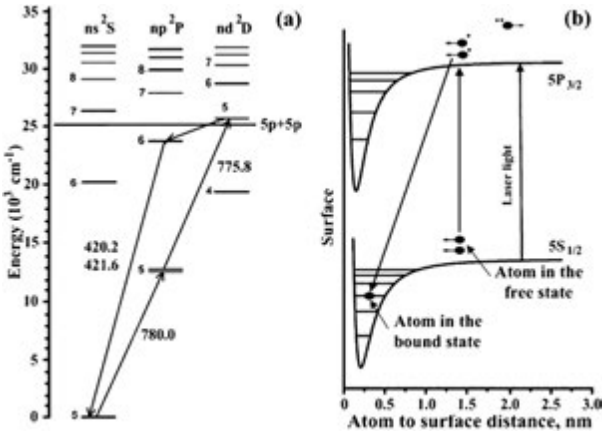

Fig. 1. The energy level diagram for Rb atom (a). The mechanism of loading of Rb atom in the surface trap (b).

1. Idea

Proposed method to control atom adsorption is based on the energy-pooling collisions effect. The effect consists in inelastic collision of two excited atoms followed by transition of one of the atoms in the ground state and the other one in the highly excited state. In such a process the shortage of the internal atomic energy is compensated for by the kinetic energy of colliding atoms. When such a collision happens inside the surface potential well the ground-state atom can be trapped inside the potential well.

Figure 1(a) shows the energy level diagram for lowest levels of Rb atoms. The $5^2P_{3/2}$ level of Rb atom is populated by absorption of a laser light at wavelength of 780 nm. The levels 6P, 5D and 7S are close to the 5P+5P state of Rb_2 molecular asymptotes, and therefore they may become populated through the following "energy-pooling" processes:

$$\mathrm{Rb}(5P) + \mathrm{Rb}(5P) + \Delta E_1 \rightarrow \mathrm{Rb}(6P) + \mathrm{Rb}(5S), \quad (1)$$

$$\mathrm{Rb}(5P) + \mathrm{Rb}(5P) + \Delta E_2 \rightarrow \mathrm{Rb}(5D) + \mathrm{Rb}(5S), \quad (2)$$

$$\mathrm{Rb}(5P) + \mathrm{Rb}(5P) + \Delta E_3 \rightarrow \mathrm{Rb}(7S) + \mathrm{Rb}(5S), \quad (3)$$

here the difference between the total kinetic energy before and after collision, i.e. the energy defects are as $\Delta E_1 = -2753$ K, $\Delta E_2 = 94$ K, and $\Delta E_3 = 942$ K. Collisional processes (1)–(3) result in transition of one atom into the ground state 5S and excitation of the other atom in one of the states 6P, 5D and 7S. The most probable is the process (2) since in this process the shortage of the internal atomic energy is minimal being about $\Delta E_2 = 94$ K. This energy shortage is compensated for by the energy of the translational atomic motion, accordingly in the process (2) kinetic energy of the two atoms decreases in a single collision by the value of 94 K. The energy-pooling process is easily observable though the atomic emission lines from upper excited states. In the processes (2) the atom in 5D state makes a transition into 6P state and then decays into the ground 5s state. This transition is followed by a blue photon emission with wavelength 420.2 or 421.6 nm. When the above process occurs near the bottom of the surface potential well the loss of the atomic kinetic energy in the collisional process may lead to localization of atoms in the surface potential as shown in Fig. 1(b).

2. Experiment

Experimental scheme to study laser induced quantum adsorption of atoms is shown in Fig. 2. Basic element of the scheme is the glass cell filled with Rb vapor. Windows of the cell are made of a crystalline dielectric YAG. The cell was maintained at the temperature which could be changed from the room temperature up to 240 °C. The temperature of the cell windows maintained at value 30 °C above the cell temperature. Such temperature regime allowed us to keep the cell windows free of the Rb atoms in the absence of the laser light. Laser light with wavelength $\lambda = 780$ nm was tuned to a resonance with atomic transition $5^2S_{1/2} \rightarrow 5^2P_{3/2}$. Laser light propagated though the vapor cell along the axis orthogonal to the cell windows. Laser beam diameter could be changed in the region between 0.5 and 2 mm, laser power could be changed up to the maximum value 40 mW. Existence of the energy-pooling process was observed by detecting the blue emission from the inner part of the cell illuminated by the laser beam. Blue emission was registered with the use of the monochromator (not shown in Fig. 2) and photodiode.

The adsorption of Rb atoms onto the surface was achieved by proper choice of the laser light intensity and frequency,

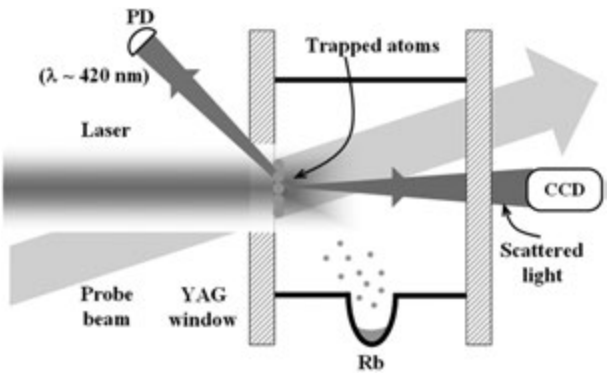

Fig. 2. Scheme of the experimental setup.

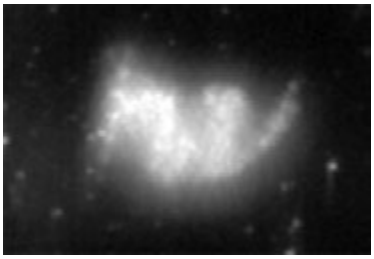

Fig. 3. The microstructure of Rb atoms in the form of two letters h and ν that are obtained by the laser induced quantum adsorption.

density of Rb vapor, and temperature of the cell windows. The laser light intensity and frequency define the relative fraction of the excited Rb atoms, the vapor density defines the probability of collision of the excited atoms and, accordingly, efficiency of the energy-pooling process, temperature of the cell windows defines the life time of the atom in the surface potential. Experimentally, the optimal parameters of the laser light and atomic density were determined by observing the intensity of the blue emission. Maximum intensity of the blue emission corresponded to the maximum rate of atomic loading into the surface potential well. The loading of Rb atoms into the surface potential followed by a growth of a thin layer of the atoms adsorbed on the incoming window of the cell in the region shined by the laser beam.

3. Results

Above described technique of laser controlled atom adsorption on a surface opens a way of producing micro and nanostructures of arbitrary shape. Such a possibility is illustrated in Fig. 3 on the example of creation of letters h and ν on the dielectric surface. Atomic structure of the shape $h\nu$ was produced in a following way: (1) 29 openings in a metal foil were done to produce a mask for these letters; (2) the mask was illuminated by the laser light; (3) the image of the mask was projected onto the dielectric surface and during the time interval $t = 5$ min were produced 29 microtraps on the surface reproducing the letters h and ν of size about 50 μm.

In conclusion, we have proposed and realized new approach to control adsorption of atoms on to dielectric surface by laser light. The approach used is based on the atom energy-pooling collisions in a near resonant laser field. We have also demonstrated a possibility of production of atomic microstructures on the surfaces with the use of the surface traps. Finally, we note that the use of the laser nanofields for formation of the surface traps may open the way for production of atomic nanostructures on the surfaces.

References

[1] Z. Zang and M. G. Lagally, *Science* **276**, 377 (1997).
[2] Special issue of Phys. Today, *Physics of Quantum Electronic Devices*, edited by F. Capasso, Springer-Verlag 1990.
[3] A. L. Aseev, *Russian nanotechnologies* **1**, 97 (2006).
[4] T. Passerat de Silans, B. Farias, M. Oriá and M. Chevrollier, *Appl. Phys. B* **82**, 367 (2006).
[5] M. Mackie and J. Javanainen, *Phys. Rev. A* **60**, 3174 (1999).
[6] A. E. Afanasiev, P. N. Melentiev, V. I. Balykin, *JETP Letters* **86**, 172 (2007).

16th Int. Symp. "Nanostructures: Physics and Technology"
Vladivostok, Russia, July 14–18, 2008

Controllable modification of surface reconstructions

D. V. Gruznev[1], D. A. Olyanich[1], D. N. Chubenko[1], I. A. Kuyanov[1,2], A. V. Zotov[1,3] and A. A. Saranin[1,2]

[1] Institute of Automation and Control Processes, 690041 Vladivostok, Russia
[2] Faculty of Physics and Engineering, Far Eastern State University, 690000 Vladivostok, Russia
[3] Department of Electronics, Vladivostok State University of Economics and Service, 690600 Vladivostok, Russia

Abstract. We have examined the possibility to modify adsorbate-induced reconstructions by adding atoms of another adsorbate and by varying averaged lattice constant of the substrate. We review several effects experimentally observed such as elimination of domain walls and development of a highly-ordered defect-free surface, changes in crystal structures of surface reconstructions accompanied by changes of their electronic properties, and increase of the thermal stability of an array of magic clusters. We believe that artificial modification of surface reconstructions is an important step on the way to the creation of nanostructures with desirable properties.

Introduction

Starting from the early 1960s and till now, adsorbate-induced reconstructions on the semiconductor surfaces have been objects of numerous investigations and a great body of information has been accumulated about them by scientific community [1]. However the question of which specific parameters of the substrate surface and adsorbate overlayer control the structure and properties of a given reconstruction still demands a thorough consideration. Finding the answer to this question opens possibility for the controllable modification of the reconstructions in a desired way.

It is generally accepted that formation of a particular reconstruction is basically a result of the interplay of two trends, (i) reducing the number of dangling (unsaturated) bonds due to rearrangement of atoms at the surface (this trend acts towards minimizing surface energy) and (ii) increasing lattice stress induced by atom displacements (this trend acts towards increasing surface energy). Changing the balance between these two trends it becomes possible to alter the crystal structure and properties of a reconstruction.

In the present investigation, by means of scanning tunneling microscopy (STM) we studied controllable modifications of surface reconstructions on the Si(111) surface. Two approaches have been used, adding atoms of another adsorbate and changing averaged lattice constant of the substrate.

1. Modification of reconstructions by surface stress relief

One possible way to alter the structure and properties of a reconstruction is to add atoms of another adsorbate. This action can affect both trends, thus leading to various types of effects. As a prototype reconstruction we have chosen the Si(111)-α-$\sqrt{3} \times \sqrt{3}$-Au surface that stands apart for its peculiar domain-wall structure [2]. In STM images domain walls appear as a network of bright zigzag chains (Fig. 1) breaking the perfect $\sqrt{3} \times \sqrt{3}$ periodicity of commensurate domains. According to total-energy calculations, this reconstruction as described by CHCT model [3] is characterized by a stress of $+20.4$ eV/nm^2 [4].

In our experiments we have found that adding about 0.15 ML of In onto this reconstruction leads to the elimination of domain walls and development of highly-ordered defect-free homogeneous $\sqrt{3} \times \sqrt{3}$-(Au,In) surface. It displays in the RT-STM

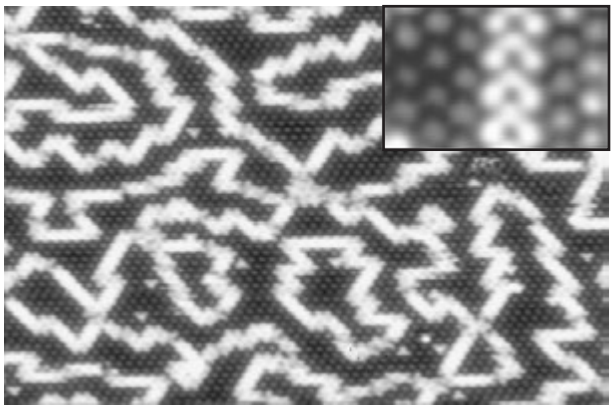

Fig. 1. 522 × 346 Å^2 empty-state STM image of the $\alpha - \sqrt{3} \times \sqrt{3}$-Au surface. Inset shows the high resolution image of both the commensurate domain and the domain wall.

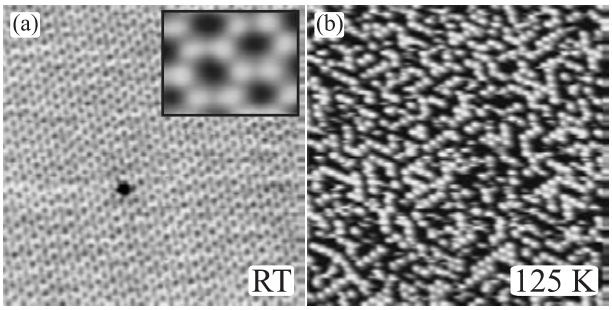

Fig. 2. 250 × 250 Å^2 empty-state STM images of the the α-$\sqrt{3} \times \sqrt{3}$-Au surface after adsorption of about 0.4 ML of In, followed by annealing at 600 °C. Images were obtained at (a) room temperature and (b) 125 K.

images a honeycomb structure (Fig. 2(a)) due to the In atoms hopping among the T_4 adsorption sites in between Au trimers. The In atom motion is frozen at 125 K (Fig. 2(b)). The plausible mechanism of the stabilization of the domain-wall-free Si(111)$\sqrt{3} \times \sqrt{3}$-(Au,In) surface is the stress relief caused by In adsorption. Indeed, calculations revealed that addition of one In atom per $\sqrt{3} \times \sqrt{3}$ unit cell reduces the surface stress to $+3.9$ eV/nm^2. Thus, the obtained results present the procedure to convert the surface with a high density of domain walls to the homogeneous surface free of domain walls. This conversion is believed to have a common nature and can affect electronic properties of a surface.

2. Modification of reconstructions by changing the substrate lattice constant

Another possibility to modify a reconstruction is to do this by changing averaged lattice constant of the substrate. This action is concentrated towards changing surface stress. In this work, varying the substrate lattice constant were done by adding Ge atoms to the Si substrate, since Ge has the 4% larger lattice constant compared to Si and initial deposition of Ge on Si is displacive, leading to the formation of the homogeneously mixed Ge_xSi_{1-x} alloying layer on Si substrates [5].

We observed that changing the lattice constant of the substrate induces a dramatic alteration in atomic arrangement of a 4 × 1-In reconstruction. Addition of about 0.3 ML of Ge (i.e., changing the substrate lattice constant by about 0.07%, assuming that the Ge is dissolved in the top Si(111) bilayer), the 4 × 1-In reconstruction is removed and a new 7 × 3 reconstruction develops at the surface. Figure 3 shows the STM image of the surface with coexisting domains of original 4 × 1 and new 7 × 3 reconstructions prepared by 0.25 ML Ge adsorption. High-resolution STM observations (insert in the Fig. 3) reveal that features constituting 7 × 3 reconstruction show up as features of three types, namely single, double and triple protrusions. The modification of crystal structure is accompanied by certain changes in the electronic structure of the surface as detected by STS measurements.

Varying the averaged lattice constant of the substrate can affect not only the crystal structure, but some physical properties as well. We demonstrate this with the famous array of Al magic clusters [6].

The array of identical-size Al nanoclusters is formed at the early stages of Al deposition onto the clean Si(111) surface in the temperature range of 475 to 600 °C. Upon annealing above 600 °C, the array of Al clusters becomes thermally unstable and the irreversible transition to $\sqrt{3} \times \sqrt{3}$-Al reconstruction takes place [6].

Changing the top layer from Si(111) to Ge_xSi_{1-x}(111) does not affect the atomic structure of the Al clusters. However, the temperature of the "array $\rightarrow\sqrt{3}$" transition gradually increases as a function of Ge coverage (Fig. 4). When Ge coverage reaches about 0.5 ML, the transition is completely suppressed and array of Al clusters preserves under annealing at the temperatures close to the Al desorption temperature (∼800 °C).

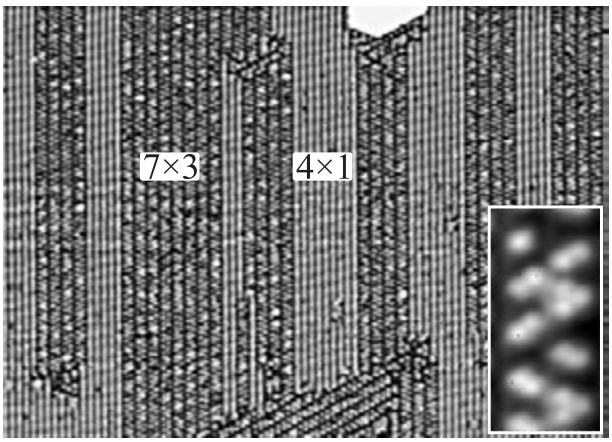

Fig. 3. 1150 × 900 Å^2 filled-state STM image of the surface with coexisting domains of 4 × 1-In and 7 × 3-In reconstructions.

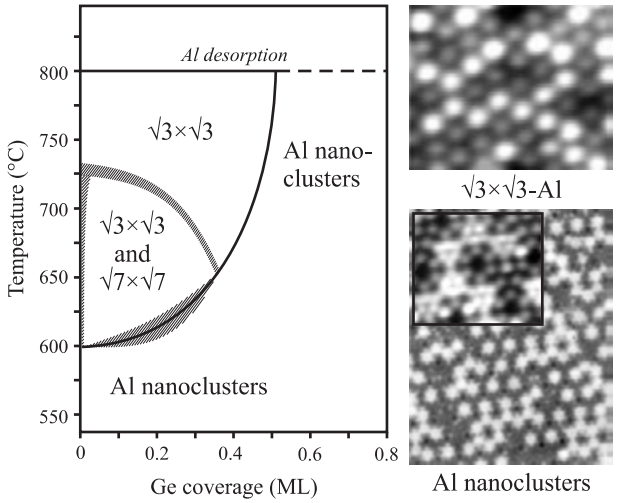

Fig. 4. Phase diagram for the 1/3-ML-Al/Ge_xSi_{1-x}(111) system as a function of Ge coverage. STM images on the right panel correspond to the $\sqrt{3} \times \sqrt{3}$-Al and the array of Al nanoclusters.

3. Conclusion

In summary, we have demonstrated possibility for modifying adsorbate-induced reconstructions by adding atoms of another adsorbate and by varying average lattice constant of the substrate. It was shown that adding neglible amount of In onto the Si(111)-α-$\sqrt{3} \times \sqrt{3}$-Au reconstruction converts the surface with a high density of domain walls to the homogeneous surface free of domain walls. This effect has been explained by the In-induced relief of the surface stress.

Varying substrate lattice constant may induce changes in both crystal structure and some physical properties of the system. Thus, by increasing the constant by only 0.07% the 4 × 1-In reconstruction is transformed into the 7 × 3. The same alteration of substrate applied to the array of Al magic clusters leads to the drastic rise of their thermal stability.

Acknowledgements

Part of this work was supported by Russian Foundation for Basic Research (Grants No. 07-02-00650-p) and Russian Federation Ministry of Education and Science (Grant No. 2007-3-1.3-07-01-352).

References

[1] V. G. Lifshits, A. A. Saranin, and A. V. Zotov, *Surface Phases on Silicon*, John Wiley & Sons, Chichester, 1994.
[2] T. Nagao, S. Hasegawa, K. Tsuchie, S. Ino, C. Voges, G. Klos, H. Pfnür, and M. Henzler, *Phys. Rev. B* **57**, 10100 (1998).
[3] Y. G. Ding, C. T. Chan, and K. M. Ho, *Surf. Sci.* **275**, L691 (1992).
[4] D. V. Gruznev *et al*, *Phys. Rev. B* **73**, 115335 (2006).
[5] R. M. Tromp, *Phys. Rev. B* **47**, 7125 (1993).
[6] V. G. Kotlyar, A. V. Zotov, A. A. Saranin, T. V. Kasyanova, M. A. Cherevik, I. V. Pisarenko, and V. G. Lifshits, *Phys. Rev. B* **66**, 165401 (2002).

16th Int. Symp. "Nanostructures: Physics and Technology"
Vladivostok, Russia, July 14–18, 2008

The synthesis, micromorphology and structure of germanium oxide (IV) nanocrystals

I. B. Troitskaia[1], T. A. Gavrilova[1], V. G. Kostrovsky[2], L. D. Pokrovsky[1] and V. V. Atuchin[1]

[1] Institute of Semiconductors Physics SB RAS, Novosibirsk, Russia
[2] Institute of Solid State Chemistry and Mechanochemistry SB RAS, Novosibirsk, Russia

Abstract. The nanocrystals of GeO_2 with good crystallinity and sizes up to 500 nm have been obtained by precipitation from water solution of ammonium germanate. The final product was characterized by X-ray diffraction (XRD), scanning electron microscopy (SEM), transmission electron microscopy (TEM), IR- and Raman spectroscopy.

Introduction

Fabrication of nanocrystal materials is a paramount task in modern materials science because of unusual properties appeared due to particle dimension decreasing to nano range. Creation of nanoscale functional oxides open a way for creation new electronic devices and sensors.

There are several polymorph modifications of GeO_2 such as α-phase with rutile type structure stable up to 1035 °C, β-phase with α-quartz type stable above 1035 °C, α- and β-cristobalite types of glassy GeO_2. The germanium dioxide with α-quartz type is a blue photoluminescence material with peak energies around 3.1 eV and 2.2 eV. It may have a potential using in such fields as non-linear optics, luminescence, optoelectronics and integrated optics.

Most popular ways for creation of GeO_2 nanoparticles are physical evaporation and thermal oxidation. A crystallization through evaporation leads to one dimensional structures [1,2,3]. The nanorods were grown with thermal oxidation method [4]. In present study the low-temperature way ($T = 105$ °C) for preparation of β-phase GeO_2 with α-quartz type is suggested and structural and morphologic characteristics of the nanocrystals have been evaluated.

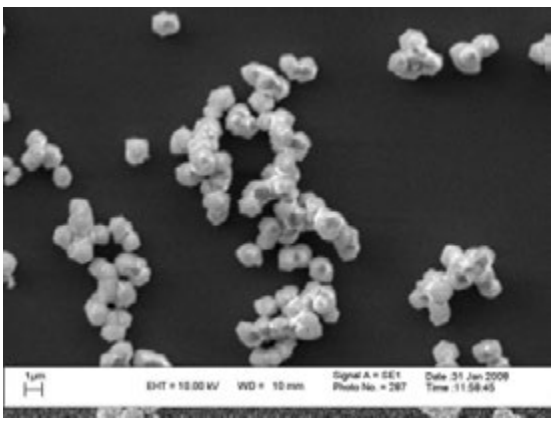

Fig. 1.

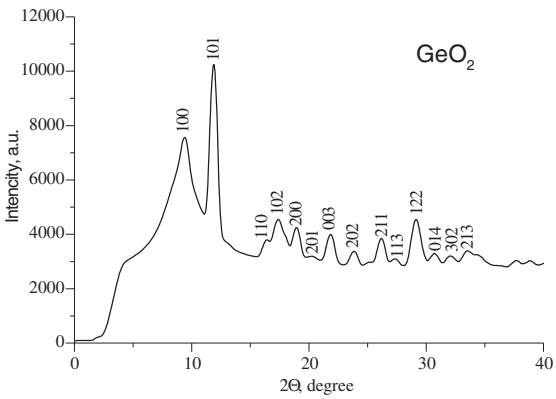

Fig. 2.

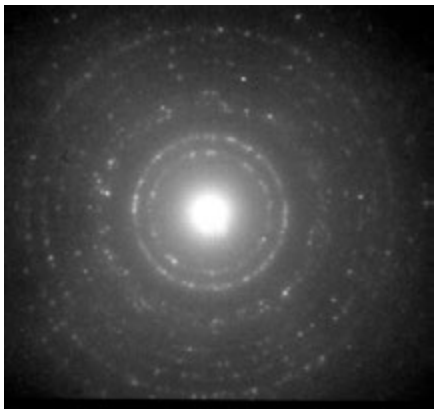

Fig. 3.

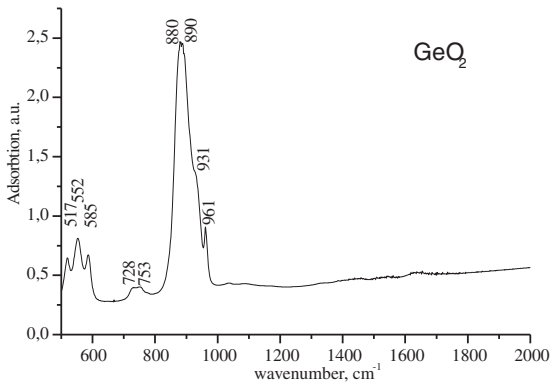

Fig. 4.

1. Experimental

Samples of GeO_2 nanocrystals were made by precipitation of germanium dioxide from ammonium germanate water solution with nitric acid. The ammonium germanate water solution was prepared by dissolving germanium dioxide in the ammonia water solution under (90 ± 5) °C heating. The final deposit was washed by distilled water to pH=6 of wash water and dried in air at room temperature. As a result, white crystals with typical

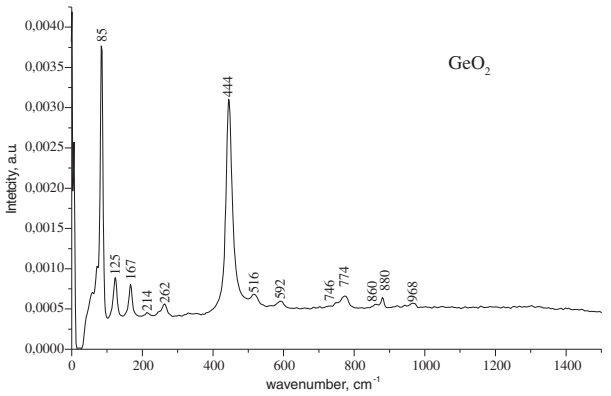

Fig. 5.

diameter ∼500 nm were fabricated (Fig. 1).

Phase composition of the precipitate as β-phase GeO_2 with α-quartz type has been confirmed by XRD analysis. In Fig. 2 the X-ray diffraction pattern recorded for germanium dioxide deposit is shown. All diffraction peaks were successfully indexed.

Typical transmission electron diffraction pattern is shown in Fig. 3. The results of TEM analysis confirm the presence of only β-phase of GeO_2. The IR spectrum measured for as-prepared deposit of GeO_2 (Fig. 4) demonstrates the spectral components consistent with that of β-phase of GeO_2 [5].

The Raman spectra obtained for as-prepared sample (Fig. 5) closely agree with that of β-GeO_2 [6].

References

[1] H. Y. Kim, P. Viswanathamurthi, N. Bhattarai, D. R. Lee, *Rev. Adv. Mater. Sci.* **5**, 220 (2003).

[2] Z. G. Bai, D. P. Yu, H. Z. Zhang, Y. Ding, Y. P. Wang, X. Z. Gai, Q. L. Hang, G. C. Xiong, S. Q. Feng, *Chem. Phys. Lett* **303**, 311 (1999).

[3] Y. H. Tang, Y. F. Zhang, N. Wang, I. Bello, C. S. Lee, S. T. Lee, *Appl. Phys. Lett.* **74**, 3824 (1999).

[4] J. Q. Hu, Q. Li, X. M. Meng, C. S. Lee, S. T. Lee. *Adv. Mater.* **14**, 1396 (2002).

[5] A. V. Shvets, N. V. Kas'yan, E. M. Bezuglaya, G. M. Tel'biz, V. G. Il'in, *Theoretical and Experimental Chemistry* **37**, 372 (2001).

[6] T. P. Mernagh, L.-G. Liu, *Phys. Chem. Minerals* **24**, 7 (1997).

16th Int. Symp. "Nanostructures: Physics and Technology"
Vladivostok, Russia, July 14–18, 2008

Growth of metal nanoislands on the Si(100)-c(4×12)-Al template reconstruction

D. A. Olyanich[1], D. V. Gruznev[1], D. N. Chubenko[1], A. V. Zotov[1,2] and A. A. Saranin[1,3]

[1] Institute of Automation and Control Processes, 690041 Vladivostok, Russia
[2] Department of Electronics, Vladivostok State University of Economics and Service, 690600 Vladivostok, Russia
[3] Faculty of Physics and Engineering, Far Eastern State University, 690000 Vladivostok, Russia

Abstract. Growth of In, Cu and Au nanoislands on the Si(100)-c(4 × 12)-Al template surface has been studied using scanning tunneling microscopy (STM). Comparing to the growth of these elements on the clean Si(100) surface, formation of elongated island with well-defined faceting has been observed. Orientation of the islands is mediated by the relief of the template reconstruction. Within the framework of nucleation rate theory the diffusion activation energies of the adatoms along the c(4 × 12)-Al surface have been evaluated.

Introduction

Small metal particles with a size of the nanometer scale — nanoclusters — attract much interest nowadays due to their properties different from those of the corresponding bulk counterparts [1, 2]. Among other methods, using extrinsic self-organization on strain-relief patterns [3] and "template" reconstructions [4] is considered as promising. The main features, which such reconstruction should possess, are high stability, long-period structure and high amplitude of atomic corrugations. Search of new template surfaces for the controlled nanoisland growth is a current challenge for material scientists.

The Si(100)-c(4 × 12)-Al (denoted as c(4 × 12)-Al) is the one which nicely fits the above requirements. This surface consists of "clusters" arranged in rows along the ⟨011⟩ direction and separated by zigzag "trenches" [5]. It is highly corrugated with amplitude of about 4 Å due to the fact that several atomic layers are involved in the reconstruction [5]. The c(4 × 12)-Al surface structure remains stable up to ∼650 °C, i.e., the temperature when Al desorption becomes significant. The template effect of the c(4 × 12)-Al reconstruction has already been proved for self-organized Al island growth [6].

In the present work, we discuss the scanning tunneling microscopy (STM) study of the nanoisland growth upon In, Cu and Au deposition onto the Si(100)-c(4 × 12)-Al surface in the wide range of substrate temperatures and adsorbate coverage.

1. Experimental

Experiments were performed in the UHV chamber STM-VT25 by "Omicron Nanotechnology GmbH" with a base pressure better than 2×10^{10} Torr. Atomically-clean Si(111)-7 × 7 surfaces were prepared in situ by flash-annealing process at 1280 °C after the samples were first outgassed at 600 °C for several hours. Initial c(4 × 12)-Al reconstruction used as a substrate for further metals adsorption was prepared by about 0.5 ML of Al deposition onto a clean Si(100) substrate held at 600 °C. In, Cu and Au adsorbate elements were deposited onto the c(4 × 12)-Al surface at a rate of about 0.1, 1 and 0.5 ML/min, respectively. The STM images have been acquired in a constant-current mode at room temperature.

2. Results and discussions

Consider first the growth of indium islands. In contrast to In deposition onto the clean Si(100) surfaces [7], incorporation of the c(4 × 12)-Al reconstruction into the In/Si(100) interface changes the growth mode of In from 2D to 3D type, thus displaying a vivid example of the Volmer–Weber growth mode. Fig. 1 shows STM images obtained after In deposition onto the c(4 × 12)-Al surface at two substrate temperatures, 50 and 100 °C. As can be seen, In atoms agglomerate into small islands randomly distributed over the surface. The clusters extend more along the rows of c(4 × 12)-Al domains than across them due to the anisotropy of the surface mobility of In adatoms. Close examination of the c(4 × 12)-Al surface after In deposition reveals that the initial surface does not undergo any significant changes. Rising of the growth temperature results in the enlargement of In islands and decreasing their number density due to the increase in surface mobility of In adatoms.

The nucleation ability of the c(4 × 12)-Al reconstruction is not limited by the Group-III elements. Fig. 2 represents the STM images of nanoisland arrays induced by adsorption of transition metals, Cu and Au, at 400 °C. Growth kinetics of these elements differ essentially as can be noticed from size and number density of the islands. In the both cases, the destruction of the initial c(4 × 12)-Al reconstruction was not detected at such relatively high temperature. It implies the suppression of intermixing with substrate atoms that is typical for transition metals. However, the destruction of the template surface was observed for the case of Au growth above ∼600 °C.

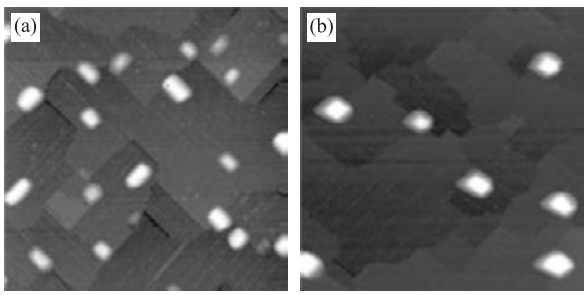

Fig. 1. 2000 × 2000 Å^2 filled state STM images of the surface after 0.7 ML In adsorption onto the c(4 × 12)-Al reconstruction at (a) 50 °C and (b) 100 °C.

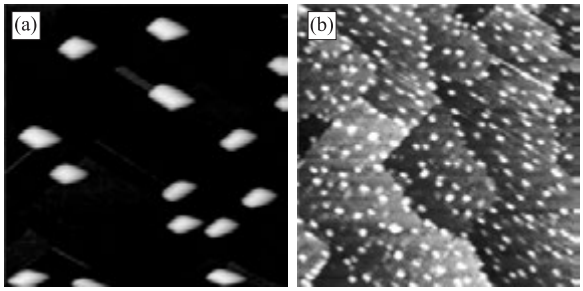

Fig. 2. (a) 2000 × 2000 Å^2 filled state STM images of (a) Cu and (b) Au nanoislands grown on the c(4 × 12)-Al surface at 400 °C.

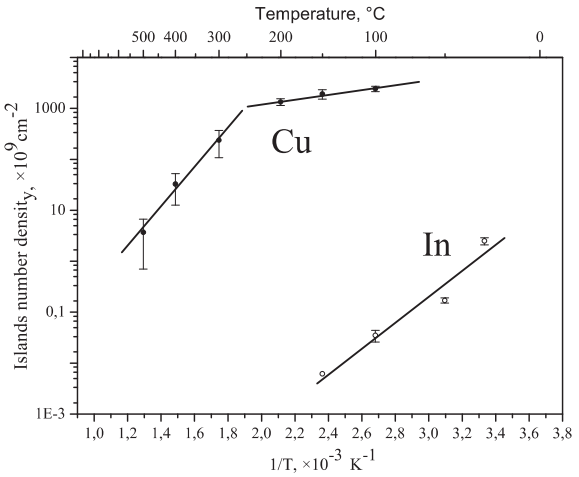

Fig. 3. Temperature dependence (Arrhenius plot) of In (open circles) and Cu (solid circles) island number densities.

Using the nucleation rate theory, activation energies of In, Cu and Au atoms diffusion have been estimated. Recall that the saturation density of islands N is given by

$$N \propto \exp\left[\frac{i E_{\text{diff}} + E_i}{(i+2)k_{\text{B}}T}\right], \qquad (1)$$

where i is the critical cluster size, E_i denotes the binding energy of the critical cluster (given approximately by the number of nearest-neighbor atom bonds within the cluster), E_{diff} is the activation energy of the adatom diffusion, k_{B} is the Boltzmann's constant and T is the growth temperature.

From the slopes of the Arrhenius plot shown in the Fig. 3, upper limits for the diffusion activation energies have been estimated as summarized in Tab. 1. These values are on the order of magnitude of migration energies determined for many metals on the Si surface [8].

Fig. 4 shows the quasi-3D STM images of the In, Cu and Au islands. The islands are elongated crystallites bounded by well-defined facets. Orientation of the nanocrystallites relative to the surface is imposed by corrugations of the underlying c(4 × 12)-Al reconstruction. Both sides of the rectangular island base are aligned along the main crystallographic directions, namely [0$\bar{1}$1] and [011].

Table 1.

Element	E_{diff}
In	0.64 ± 0.08 eV
Cu	0.26 ± 0.09 eV
Au	0.31 ± 0.06 eV

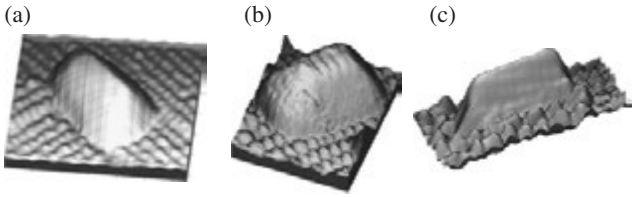

Fig. 4. Quasi-3D STM image of (a) In, (b) Cu and (c) Au nanoislands on the c(4 × 12)-Al reconstruction.

3. Conclusion

Using STM, the growth of In, Cu and Au crystalline nanoislands on the Si(100)-c(4 × 12)-Al template reconstruction was studied in a wide range of the substrate temperatures. Presence of the c(4 × 12)-Al reconstruction changes the growth mode from 2D to 3D type. Orientation of the metal crystallites is dictated by the corrugations of the template surface. From the temperature dependence of island density, the upper limits of diffusion activation energies along the c(4 × 12)-Al surface have been estimated. These experimental results can be used for fabricating arrays of In, Cu and Au nanoislands with desired size and density.

Acknowledgements

Part of this work was supported by Russian Foundation for Basic Research (Grants No. 07-02-00650-a) and Russian Federation Ministry of Education and Science (Grant No. 2007-3-1.3-07-01-352).

References

[1] W. Eberhardt, *Surf. Sci.* **500**, 242 (2002).
[2] S. N. Rashkeev, A. R. Lupini, S. H. Overbury, S. J. Pennycook, and S. T. Pantelides, *Phys. Rev. B* **76**, 035438 (2007).
[3] H. Brune, M. Giovannini, K. Bromann, and K. Kern, *Nature* **394**, 451 (1998).
[4] M. Hupalo and M. C. Tringides, *Phys. Rev. B* **73**, 041405 (2006).
[5] N. Shimizu, H. Kitada, and O. Ueda, *Phys. Rev. B* **51**, 5550 (1995).
[6] S. Itou, A. Nishida, Y. Murata, O. Kubo, H. Okado, M. Katayama, A. A. Saranin, A. V. Zotov, and K. Oura, *Surf. Sci.* **565**, 121 (2004).
[7] M. M. R. Evans, J. C. Glueckstein, and J. Nogami, *Surf. Sci.* **406**, 246 (1998).
[8] E. G. Seebauer and M. Y. L. Jung, Surface diffusion on metals, semiconductors and insulators, in *Physics of Covered Solid Surfaces*, edited by H. P. Bonzel, volume III/42 of Landolt-Börnstein (New Series), pages 455–530, Springer-Verlag, Berlin, Heidelberg, New York, 2001.

16th Int. Symp. "Nanostructures: Physics and Technology"
Vladivostok, Russia, July 14–18, 2008

Multi-mode growth in Cu/Si(111) system: Magic nanoclustering, layer-by-layer epitaxy and nanowire formation

V. G. Kotlyar, O. A. Utas, D. V. Gruznev, B. K. Churusov, A. N. Kamenev, A. V. Zotov and A. A. Saranin
Institute of Automation and Control Processes, Vladivostok, Russia

Abstract. Using scanning tunneling microscopy and low-energy electron-diffraction observations, it has been demonstrated that by varying growth conditions nanostructures of various types can be fabricated in the Cu/Si(111) system, including ordered two-dimensional lattices of the identical-size Cu nanoclusters (magic clusters), arrays of Cu nanowires, atomically-flat Cu nanofilms and three-dimensional Cu nanoislands having a shape of truncated pyramides.

Introduction

Growth of Cu on Si(111) has been a subject of extensive research not only due to basic scientific interest but also due to its technological significance as one of the most relevant metal-semiconductor interfaces for modern device technology. Peculiar feature of the Cu/Si(111) interface is the large lattice misfit of about 15%. At the interface, silicide layer is known to be formed which plays a key role in overcoming the large lattice mismatch. The interlayer thickness varies from a few to a dozen monolayers depending on the growth temperature [1,2,3]. On top of the silicide interlayer, epitaxial Cu(111) film grows in the layer-by-layer-like fashion, albeit not ideal. Thus, quality of the extra-thin epitaxial Cu(111) films grown on the Si(111)7×7 surface suffer from both the presence of the silicide layer at the interface and the roughness of the outer surface [4].

In the present work, besides studying the growth of Cu on the "traditional" atomically-clean Si(111)7 × 7 surface, we have explored Cu growth on the Si(111)'5 × 5'-Cu surface phase, which is essentially an epitaxial Cu_2Si monolayer. Experiments were conducted with growth temperatures ranging from room temperature (RT) down to about 100 K. In the latter case, the samples were placed into the specially designed stage, cooled by liquid nitrogen [5]. Results of the present study demonstrate that depending on the growth conditions nanostructures of all principal types can be fabricated in this system , including 0D nanoclusters, 1D nanowires and 2D nanofilms, as well as 3D truncated pyramides.

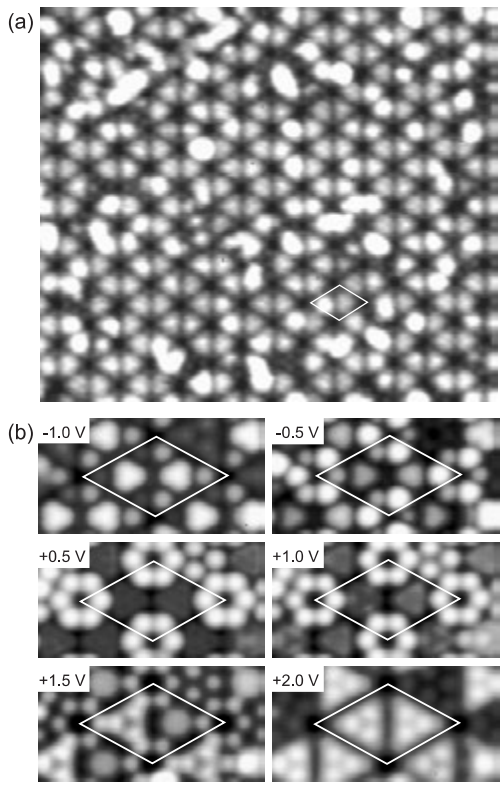

Fig. 1. (a) 420 × 420 Å^2 empty-state (+2.0 V) STM image of the magic cluster array prepared by depositing 0.4 ML of Cu onto the Si(111)7 × 7 surface held at RT. (b) Bias-dependent STM appearance of the magic clusters. STM images were acquired from the same clusters with different sample voltages. 7 × 7 unit cell is outlined.

1. Cu/Si(111) magic nanocluster arrays

Deposition of Cu submonolayers onto Si(111)7×7 surface held at RT results in the formation of the ordered arrays of *nanoclusters* (Fig. 1a). The nanoclusters have identical size and shape (i.e., these are surface magic clusters) and each nanocluster occupies a single 7 × 7 unit cell half, hence their ordered arrangement. Basing on their bias-dependent STM appearance (Fig. 1b), one can conclude that the atomic structure of the Cu magic clusters differs from the known structure of the magic clusters formed by Group-III metals [6,7] or by sodium [8].

The next nanostructures have been fabricated using the Si(111)'5 × 5'-Cu surface phase (Fig. 2) as a template for Cu overgrowth. The Si(111)'5 × 5'-Cu phase (which has been proved in this study to have a Cu_2Si composition [9]) is typically prepared by depositing 2–3 ML of Cu onto Si(111)7 × 7 surface held at 550 °C. At a large scale the surface shows up as a hexagonal-like array of domains formed by the regular dislocation network (Fig. 2a), while at the atomic scale its char-

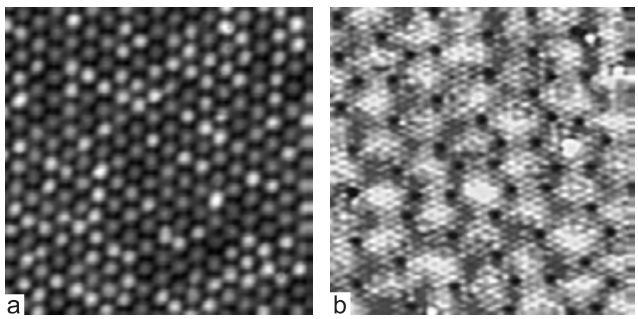

Fig. 2. (a) 330 × 330 Å^2 and (b) 100 × 100 Å^2 STM images of the Si(111)'5 × 5'-Cu surface phase.

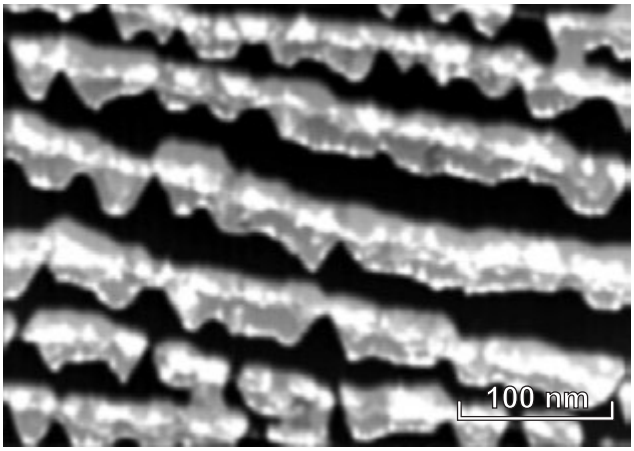

Fig. 3. STM image of the Cu-nanowire array prepared by depositing 12 ML of Cu onto the Si(111)‘5 × 5’-Cu surface held at RT.

acteristic features are the 1 × 1-like structure in the interior of the domains and the random crater defects at the domain boundaries (Fig. 2b).

2. Cu-nanowire arrays on Si(111)‘5×5’-Cu phase

Si(111)‘5 × 5’-Cu phase acts as a buffer layer which blocks direct contact of the deposited Cu with a Si substrate, thus preventing silicide formation. Cu atoms adsorbed onto the Si(111)‘5 × 5’-Cu surface at RT are free to migrate over terraces but are trapped at step edges, where they agglomerate into islands. Interconnected islands decorating steps form the *nanowires*. These nanowire arrays display a considerable anisotropy of the electrical conductivity.

3. Atomically-flat epitaxial Cu(111) nanofilms

When Cu is deposited onto Si(111)‘5 × 5’-Cu surface held at low temperature of about 100 K, formation of the epitaxial Cu(111) *nanofilms* takes place. Nanofilm growth proceeds in a layer-by-layer fashion up to about five Cu(111) monolayers with a first layer having double Cu(111) monolayer thickness. Thus, one can fabricate uniform atomically-flat epitaxial Cu(111) nanofilms on Si(111) having thickness ranging from two to five Cu(111) monolayers and with an extremely sharp film/substrate interface (Fig. 4). Such a samples are believed to be a promising object for observing quantum-size effects.

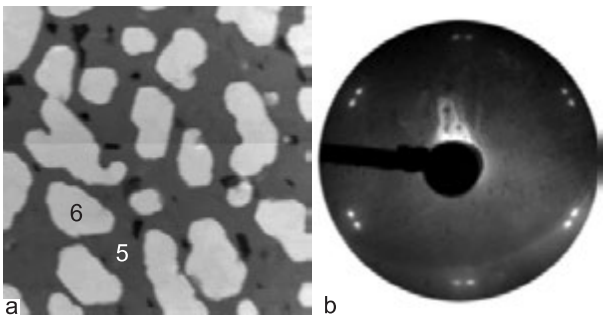

Fig. 4. (a) 1000 × 1000 Å^2 STM image and (b) LEED pattern (E = 65 eV) from epitaxial Cu(111) film grown by depositing 12.0 ML of Cu onto Si(111)‘5×5’-Cu surface held at 100 K. Surface resembles the 2D islands of the 6th Cu layer (indicated as 6) on top of the completed 5th layer (indicated as 5).

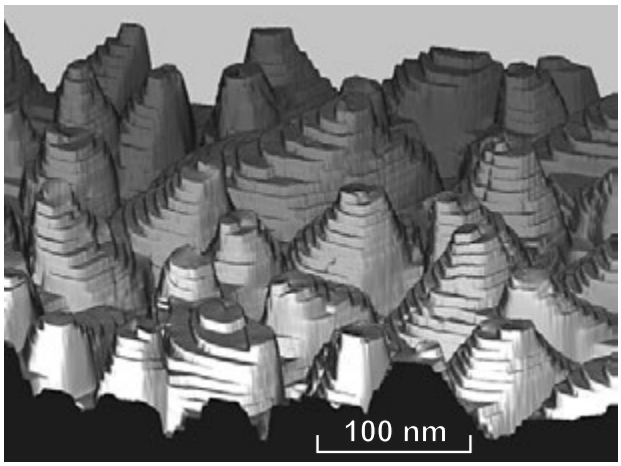

Fig. 5. Qusi-3D STM image of the arra of the Cu truncated pyramides fabricated on the Si(111)‘5 × 5’-Cu surface.

4. Arrays of Cu truncated pyramides

When the first double Cu(111) layer grown on Si(111)‘5 × 5’-Cu surface at about 100 K is completed, the next three-four layers grow in a layer-by-layer fashion, each layer having single Cu(111) layer thickness. Then, the 2D growth changes gradually to the 3D growth. With developing screw dislocations, the 3D islands obtain the shape of the truncated pyramids with a flat top (Fig. 5). This type of growth becomes especially pronounced if Cu deposition is continued at room temperature.

Acknowledgements

Using scanning tunneling microscopy and low-energy electron diffraction, formation of the Cu/Si(111) interface has been studied. It has been found that depending on the growth conditions (i.e., Si(111)7 × 7 or Si(111)‘5 × 5’-Cu substrate, room temperature or 100 K) various types of nanostructures can be formed.

References

[1] T. I. M. Bootsma and T. Hibma, *Surf. Sci.* **331/334**, 636 (1995).
[2] S. Tomimatsu, T. Hasegcwa, M. Kohno, and S. Hosoki, *Jpn. J. Appl. Phys.* **35**, 3730 (1996).
[3] Z. H. Zhang, S. Hasegawa, and S. Ino, *Surf. Sci.* **415**, 363 (1998).
[4] D. V. Fedorov, G. Fahsold, A. Pucci, P. Zahn, and I. Mertig, *Phys. Rev. B* **75**, 245427 (2007).
[5] B. K. Churusov, A. N. Kamenev, O. A. Utas, A. A. Saranin, A. V. Zotov, and V. G. Kotlyar, *Instruments and Experimental Techniques* **49**, 141 (2006).
[6] V. G. Kotlyar, A. V. Zotov, A. A. Saranin, T. V. Kasyanova, M. A. Cherevik, I. V. Pisarenko, and V. G. Lifshits, *Phys. Rev. B* **66**, 165401 (2002).
[7] H. H. Chang, M. Y. Lai, J. H. Wei, C. M. Wei, and Y. L. Wang, *Phys. Rev. Lett.* **92**, 066103 (2004).
[8] K. Wu, Y. Fujikawa, T. Nagao, Y. Hasegawa, K. S. Nakayama, Q. K. Xue, E. G. Wang, T. Briere, V. Kumar, Y. Kawazoe, S. B. Zhang, and T. Sakurai, *Phys. Rev. Lett.* **91**, 126101 (2003).
[9] A. V. Zotov, D. V. Gruznev, O. A. Utas, V. G. Kotlyar, and A. A. Saranin, *Surf. Sci.* **602**, 391 (2008).

16th Int. Symp. "Nanostructures: Physics and Technology"
Vladivostok, Russia, July 14–18, 2008

Initial stages of homoepitaxial growth on flat silicon (111) 7×7 surface

E. E. Rodyakina[1], S. S. Kosolobov[1] and A. V. Latyshev[1,2]

[1] Institute of Semiconductor Physics, SB RAS, 630090 Novosibirsk, Russia
[2] Novosibirsk State University, 630090, Novosibirsk, Russia

Abstract. Analysis of the structural elementary (atomic) processes on large flat silicon surface during initial stage of homoepitaxial growth at 500–700 °C has been presented. The experiments have been carried out by means of *in situ* ultrahigh vacuum reflection electron microscopy and *ex situ* atomic force microscopy. Formation dendrite-shape island has been found under homoepitaxial growth on Si(111) 7×7 surface. One, two and three monolayer in height island growth has been observed.

Introduction

Epitaxy of thin semiconductor films is a key process in modern microelectronics technology. Since the dimensions of semiconductor devices are shrinking constantly, detailed knowledge of the fundamental processes on atomic scale in Si homoepitaxy is desirable. Besides the role of small defects on the surface and surface reconstruction become important on nanometer level. Initial clean silicon surface consist of regularly distributed atomic steps with small distance between them (several dozens or hundreds nanometer). It would be interesting to investigate the epitaxial processes without influence of such linear defect as atomic step. It has been well known about redistribution of atomic steps (step bunching) on Si(111) surface under heating by passing direct electric current [1]. In result, large flat area (more then 10×10 μm^2) could be formed on surface between atomic steps. This work is aimed to investigate the homoepitaxial growth on Si(111) 7×7 surface after steps redistribution.

1. Experimental

The samples, $8 \times 1 \times 0.3$ mm^3 in size, were cut from Si(111) wafer (miscuts angle less then 0.5°) with the along edge near perpendicular to atomic steps line. After standard chemical treatment samples were fixed in tantalum holder and placed into an ultrahigh vacuum chamber of reflection electron microscope (REM) (with base pressure less then 10^{-9} Torr) [2]. The substrates were heated by passing electric current (resistive heating). The investigated sample was flashed to 1250 °C to clean the surface from silicon dioxide and contaminations. Then large step step-free areas was formed using the phenomenon mentioned above. Then sample was slowly cooled to temperature less than temperature of superstructure reconstruction $1 \times 1 \rightarrow 7 \times 7$ (approximately 830 °C). When the whole of surface has had 7×7 reconstruction (was controlled by in situ REM images and RHEED pattern), the sample temperature was decreased to 500–700 °C and about 0.25 monolayer (ML) of silicon atoms was deposited. Finally, the sample was quenched to room temperature, evacuated to atmosphere conditions and investigated *ex situ* by atomic force microscope (AFM, Solver P-47H) with using semicontact and phase contrast regimes. Thin silicon dioxide cover silicon surface uniformly and don't influence on AFM resolution [3].

2. Results and discussion

It was observed 2D islands growth on step-free areas. The shape of the one is polygon consisting of triangles replicating unit cell of 7×7 superstructure. But diffusion of atoms or clusters and their coalescence may sometimes give ramified islands with distinct fractal dimension. Fig. 1 present AFM-image of step-free silicon surface after deposition about 0.25 monolayer (ML) of silicon atoms at 620 °C. The mean distance between triangle-like islands larger at higher temperatures due to exponential temperature dependence of diffusion length of adsorbed silicon atoms. The fractal-like homoepitaxial growth at 0.5 ML coverage has been discussed in [4], but their simulation at 0.25 ML coverage have not predicted such big fractal structures as we have observed. We speculate the fractal structure has grown on domain another superstructure initiated by the dopants which have gone to the surface at elevated temperature. However, no new diffraction reflections have appeared on RHEED pattern from the clean Si(111) 7×7 surface before growth. Thus it is necessary to carry out more detail experiments to recognize a nature of this fractal structures. It should be mentioned, the island chains are seen on image, in which mean distance between islands smaller than on other part of the surface. This chains marked 7×7 superstructures domain boundaries, the atom diffusion length along which is small [5]. This phenomenon is seen clearer on Fig. 2.

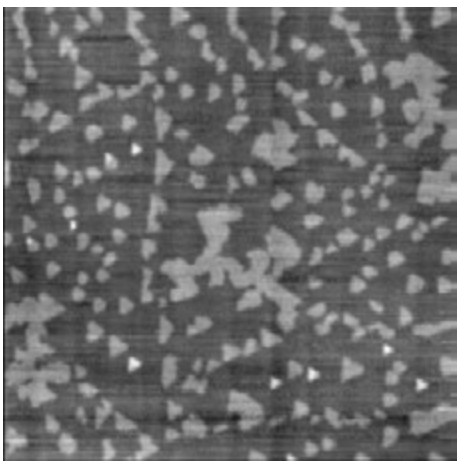

Fig. 1. AFM-image (5×5 μm^2) of Si(111) 7×7 surface with dendrite-shape islands grown after about 0.25 ML silicon atom deposition at 620 °C.

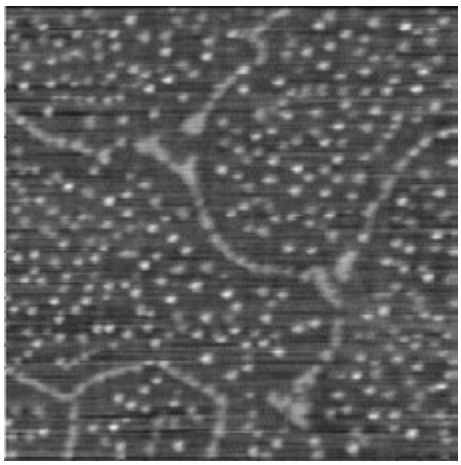

Fig. 2. AFM-image ($2 \times 2\ \mu m^2$) Si(111) surface with silicon islands one, two and three monolayer in height grown at 570 °C.

Also one, two and three monolayer in height islands formation has been observed. AFM-images Si(111) surface with silicon islands grown at 570 °C is presented on Fig. 2. At smaller temperature approximately 30 percent of islands have multilayer structure, whereas at higher one only single islands are not monolayer in height (see Fig. 1). In addition no multilayer growth are seen on island chains, even at lower temperature. This multilayer growth can be explain as follows. A diffusing atoms approaching a island edge can be reflected, incorporated into the edge or jump onto the next higher layer. Probabilities of the processes are dependent on the corresponding energy barriers. In [5] was shown that the lateral growth of an island is associated with a high energy barrier to overgrow the faulted part of substrate reconstruction. So, the rate of multilayer growth is higher than lateral growth of island. However, multilayer island structure is metastable, so when the substrate temperature increased, the value of energy barrier ceased critical role on growth, and diffusing atoms attached to more stable position in edge of the island. Eventually, at sufficient temperature no 2D islands form, and layer-by-layer growth occur.

In conclusion, we have studied the initial stages of homoepitaxial growth on step-free Si(111) 7×7 surface at different temperatures. Formation dendrite-shape islands have been observed. The multilayer growth have been found at lower substrate temperature.

Acknowledgements

This work has been supported in part by the Russian Foundation of basic Research (grant 07-02-01003, 07-08-00434).

References

[1] See for review A. V. Latyshev *et al*, *Surf. Sci.* **213**, 157 (1989), Y. Homma *Phys. Rev. B* **62**, 8323 (2000).
[2] A. V. Latyshev *et al*, *Microsc. Res. Technique* **20**, 341 (1992).
[3] D. Sheglov*et al*, *Microscopy and Analysis* **19/5**, 9 (2005).
[4] Z. Olami*et al*, *Surf. Sci.* **520**, 35 (2002).
[5] B. Voigtlander, *Surf. Sci. Rep.* **43**, 127 (2001).

16th Int. Symp. "Nanostructures: Physics and Technology"
Vladivostok, Russia, July 14–18, 2008

Electronic states induced by antimony and cesium on atomically flat GaAs(001) surface

A. G. Zhuravlev[1,2] and V. L. Alperovich[1,2]

[1] Institute of Semiconductor Physics, 630090 Novosibirsk, Russia
[2] Novosibirsk State University, 630090 Novosibirsk, Russia

Abstract. The evolution of the surface band bending is studied by photoreflectance spectroscopy under the formation of Sb/GaAs(001) and Cs/Sb/GaAs(001) interfaces. A nonmonotonic dependence of the band bending as a function of coverage was observed under antimony deposition on the Ga-rich surface, in distinction with a monotonic dependence on the As-rich surface. Cesium deposition on the Sb-stabilized GaAs(001) surface yielded the band bending evolution similar to that on the As-stabilized surface. This behavior is typical for the anion-terminated surfaces.

Introduction

The development of ultra-high vacuum (UHV) techniques for the preparation and control of atomically flat III–V semiconductor surfaces with certain superstructures and electronic properties is an important task for nanotechnology. Only a semiconductor surface with smooth morphology and well-defined atomic structure can serve both as a playground for fabrication of nanoscale structures for scientific research and as a basis for the production of UHV semiconductor devices. An important example of such a device is a negative electron affinity photoemitter, which contains (Cs,O) activation layer of monolayer thickness deposited on p-GaAs or another III–V semiconductor. One of the effective tools for controlling the surface atomic structure consists in the isoelectronic substitution of the top atomic layer with group III or group V element different from those constituting the semiconductor. In Ref. [1] this opportunity was realized for the Sb/GaAs(001) surface. By studying the surface atomic structure it was shown that a submonolayer amount of antimony, which isoelectronically replaces arsenic in the topmost atomic layer at the GaAs(001) surface, substantially extends the temperature range for the stability of the main anion-terminated (2×4) surface reconstruction [1]. While antimony-induced transformations of the GaAs(001) atomic structure are relatively well-known, the evolution of electronic properties, which accompanies these transformations, was not studied in detail. The goal of this work is to study experimentally electronic properties of the Sb/GaAs(001) and Cs/Sb/GaAs(001) interfaces. The results are compared with the evolution of surface electronic properties under Cs deposition on the As- and Ga-stabilized GaAs(001) surfaces studied earlier in [2,3].

1. Experimental

Atomically clean GaAs(001) surfaces with various reconstructions were prepared by chemical removal of oxides in inert atmosphere and subsequent annealing in UHV [4,5]. Surface electronic properties were studied by means of photoreflectance (PR) spectroscopy, which enabled us to measure the evolution of the surface band bending and surface photovoltage under the adsorption and thermodesorption of Sb and Cs. The surface electric field was determined by Fourier transform of Franz–Keldysh oscillations, and the band bending was calculated from the magnitude of the field. To provide uniform electric field near the surface, epitaxial UP^+ structures with thin (∼100 nm) undoped surface layers were used [3]. The amplitude of PR spectra is proportional to the surface photovoltage. This allowed us to study the evolution of the photovoltage, which reflects the processes of photoelectron trapping and recombination. A modification of the PR spectroscopy technique to a "real-time" version allowed us to measure the band bending evolution during the process of adsorption with a high precision. The atomic force microscopy measurements proved that the surface relief consists of atomically flat terraces of about 200 nm width separated by steps of monatomic height [6].

2. Results and discussion

Figure 1a shows the evolution of the band bending φ_S under Sb deposition on the As- and Ga-rich GaAs(001) surfaces. It is seen that Sb adsorption on the As-rich surface leads to a monotonic increase of the band bending with subsequent saturation at Sb coverage θ_{Sb} of about 1 monolayer (ML). This saturation is due to the formation of surface states induced by an amorphous antimony overlayer. On the contrary, under Sb adsorption on the Ga-rich GaAs(001) surface a non-monotonic evolution of the band bending was observed: φ_S went through a peak at small $\theta_{Sb} \leq 0.1$ ML, then through a broad minimum at $\theta_{Sb} \sim 0.2$–0.3 ML and only after that monotonically increased up to the saturation at the same value of $\varphi_S \approx 0.65$ eV. The peak of φ_S observed at small θ_{Sb} is probably due to a surface state density built-up under Sb-induced disorder of the cation-stabilized reconstruction, while the minimum is due presumably to the formation of the anion-terminated surface. As seen from Fig. 1b, the amplitude of the PR signal, which is proportional to the surface photovoltage, decreased at small θ_{Sb} by almost one order of magnitude and then monotonically increased under Sb deposition on both As- and Ga-rich surfaces. The nonmonotonic evolution of the photovoltage and antibate behavior of the photovoltage and band bending observed at small Sb coverages reflect complicated antimony-induced transformations of the interface electronic states and of the trapping and recombination rates of photoelectrons at the interface. The mechanisms of these transformations are not yet clear.

In order to obtain the Sb-stabilized GaAs(001)-(2×4) sur-

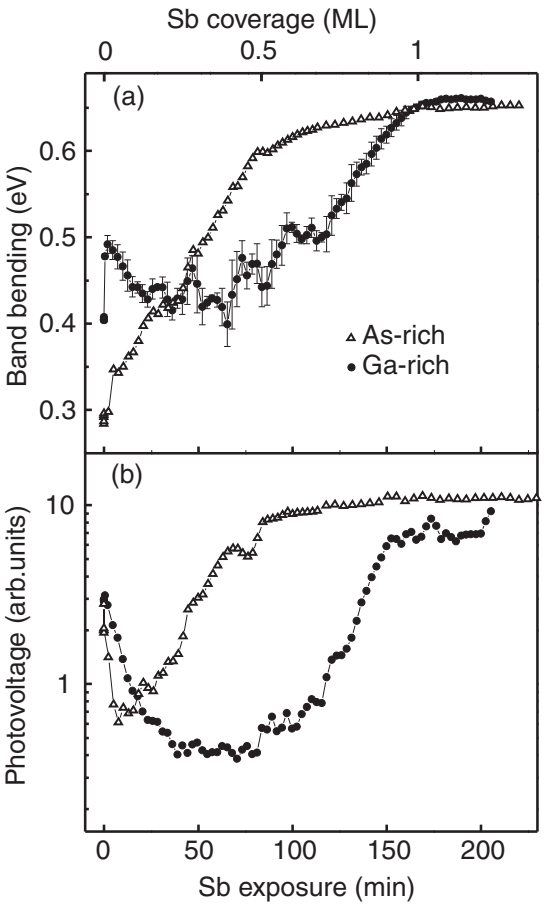

Fig. 1. Band bending (a) and photovoltage (b) evolution under deposition of antimony on the As-rich and Ga-rich GaAs(001) surfaces.

face, the sample with a monolayer of antimony deposited at room temperature was annealed in vacuum at 460 °C [1]. Then cesium was deposited in order to study the Cs-induced electronic states on the Cs/Sb/GaAs(001) interface. The band bending as a function of Cs coverage θ_{Cs} is shown in Fig. 2. It is seen that on the Sb-stabilized surface a steep increase of φ_S at small $\theta_{Cs} < 0.05$ ML is followed by a maximum at $\theta_{Cs} \sim 0.1$ ML and saturation at $\theta_{Cs} > 0.3$ ML. The dependences $\varphi_S(\theta_{Cs})$ measured under Cs deposition on the As-stabilized and Ga-stabilized GaAs(001) surfaces are shown in Fig. 2 for comparison. One can see that the dependences $\varphi_S(\theta_{Cs})$ measured under Cs deposition on the Sb- and As-stabilized surfaces are similar and supposedly typical for the Cs deposition on the anion-stabilized surfaces. On the contrary, Cs deposition on the Ga-stabilized surface leads to a qualitatively different shape of $\varphi_S(\theta_{Cs})$ which contains a number of distinct maxima and minima [2]. The reasons for such a complicated dependence are still unclear. The results obtained in the present study indicate that along with the consecutive filling of different quasi-discrete Cs-induced donor-like surface states corresponding to various adsorption sites under ordered adsorption on the GaAs(001) surface [2], this dependence is related to a specific interaction of Cs adatoms with a certain Ga-stabilized superstructure.

In conclusion, we studied experimentally the evolution of the band bending φ_S, which accompanied transformations of the surface composition and atomic structure under the formation

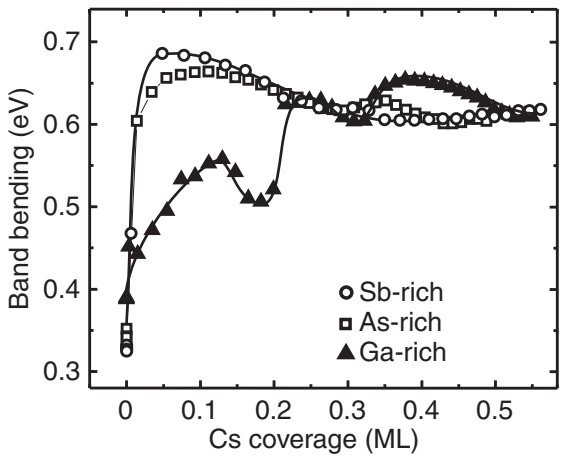

Fig. 2. Band bending evolution under cesium adsorption on the Sb-rich, As-rich, and Ga-rich GaAs(001) surfaces.

of the Sb-stabilized GaAs(001) surface and subsequent adsorption of cesium. Qualitatively different dependences $\varphi_S(\theta_{Sb})$ are observed under Sb deposition on the As- and Ga-rich GaAs (001) surfaces. On the Ga-rich surface the behavior of φ_S is nonmonotonic. Cesium deposition on the Sb-stabilized surface yielded the dependence $\varphi_S(\theta_{Cs})$ which is typical for the Cs adsorption on the anion-terminated (001) surfaces.

Acknowledgements

This work was supported by the Russian Foundation for Basic Research (grant No. 08-02-01236) and by the Russian Academy of Sciences (program "Spin-dependent phenomena and spintronics").

References

[1] F. Maeda, Y. Watanabe, M. Oshima, *Phys. Rev. B* **48**, 14733 (1993).

[2] V. L. Alperovich, A. G. Zhuravlev, O. E. Tereshchenko, H. E. Scheibler, and A. S. Terekhov, *Proc. 28th Intern. Conf. on Physics of Semiconductors*, edited by W. Jantsch and F. Schaffler, p. 12–13 (2007).

[3] O. E. Tereshchenko, V. L. Alperovich, A. G. Zhuravlev, A. S. Terekhov and D. Paget, *Phys. Rev. B* **71**, 155315(7) (2005).

[4] O. E. Tereshchenko, S. I. Chikichev and A. S. Terekhov, *J. Vac. Sci. Technol. A* **17**, 2655 (1999).

[5] V. L. Alperovich, O. E. Tereshchenko, N. S. Rudaya, D. V. Sheglov, A. V. Latyshev and A. S. Terekhov, *Appl. Surf. Sci.* **235**, 249 (2004).

[6] V. L. Alperovich, A. G. Zhuravlev, I. O. Akhundov, N. S. Rudaya, D. V. Sheglov, A. V. Latyshev, and A. S. Terekhov, *Proceedings 15th Int. Symp. Nanostructure: Physics and Technology, Novosibirsk*, p. 166–167 (2007).

16th Int. Symp. "Nanostructures: Physics and Technology"
Vladivostok, Russia, July 14–18, 2008

Monte Carlo simulation of silicon surface active and passive oxidation by O_2 and nc-Si aggregation in SiO_x layers

A. N. Karpov[1,2], I. G. Neizvestny[1], *N. L. Shwartz*[1] and Z. Sh. Yanovitskaya[1]

[1] Institute of Semiconductor Physics RAS SB, Novosibirsk, 630090, Russia
[2] Novosibirsk State University, Novosibirsk, 630090, Russia

Abstract. A lattice kinetic Monte Carlo model for active and passive oxidation of Si-SiO_2 system was developed. Regular short-range order, typical for amorphous silicon dioxide, was self-organized in model SiO_2 layers. Chemical reactions that occur in Si-SiO_2 system at high temperatures were taken into consideration. Influence of SiO generation and decomposition rates on the processes of silicon surface etching and oxide growth was investigated. Simulation of nc-Si formation during SiO_x layers annealing was carried out.

Introduction

Formation of nc-Si light-emitted in visible region 700–900 nm after long-run high temperature annealing of SiO_x layers resumes interest to these layers [1]. Interrelation between nc-Si and photoluminescence was surely established, but mechanism of nc-Si formation is until insufficiently clear. In spite of long history of Si-SiO_2 system investigation, problems concerning solid-phase diffusion as well as the carriers of silicon and oxygen through silicon dioxide film remained unexplained up to now [2].

1. Simulation results and discussion

The kinetic Monte Carlo model of silicon dioxide on the base of diamond-like lattice [3] was used for simulation high temperature processes in Si-SiO_2 system. Partially filled diamond-like crystal lattice enables to arrange SiO_4 tetrahedrons with silicon atom in the centre. Chains of SiO_4 tetrahedrons connected with each other by oxygen give rise to short-range order in any silicon dioxide type. Program algorithm allows atoms organize neighborhood according to their own and neighbors valences.

As the first step simulation of regular short-range order organization in stochiometric SiO_2 layer due to atom diffusion hops at high temperature was caried out. Then phase separation process with nc-Si formation during SiO_x-layers annealing was simulated. The initial state of the model layer was the random distribution of silicon and oxygen atoms at given part of lattice sites (50%) with ratio Si:O equal 1:x ($1 \le x \le 2$). Chosen parameters of interatomic interaction ensure transition from chaotic atom distribution to SiO_2 matrix formation due to atom random walk and the system tendency to the minimum of free energy. Basic ordering of chaotic system occurs during short time ($\sim 2 \times 10^{-5}$ s), corresponding to pulsed laser annealing of thermaly grown silicon dioxide layers enriched with silicon by ion implantation. Perfection of silicon dioxide matrix during SiO_x layers annealing stimulates Si islands growth that indicates presence of phase separation. It was found that silicon precipitation in the model layers was accompanied by voids formation in the places most enriched with silicon where nanoclusters were created (Fig. 1). These silicon islands had considerable number of broken bonds. Taking into account only diffusion transport of silicon atoms we failed to create compact Si clusters with continuous border with SiO_2 matrix.

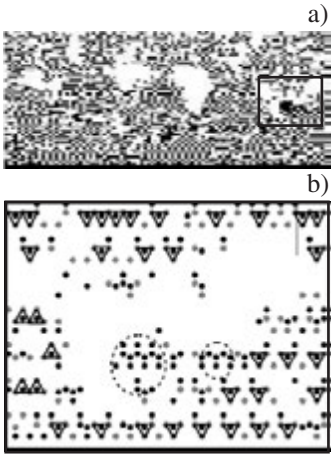

Fig. 1. Model $SiO_{1.54}$ layer after annealing at $T = 1473$ K: a) cross-section (at the bottom is silicon substrate), b) enlarged fragment marked in Fig. 1a by black rectangular. SiO_4 tetrahedrons are indicated by triangles, only atoms located in two nearest atomic planes are shown. Beside nanopores are seen silicon clusters marked by dotted circles, black points — silicon, grey — oxygen.

Possibly chemical reactions at interface Si-SiO_2 play the important role in nanocluster formation.

Silicon diffusion is not the only one mechanism of silicon transport in Si-SiO_2 system. As is known SiO molecules created at Si/SiO_2 interface migrate through thin SiO_2 layers [4,5]. Theoretical calculations revealed that clusters consisted of SiO molecules were converted into precipitating silicon core within oxide shell [6].

Chemical reactions including SiO molecules generation and dissociation were introduced in the Monte Carlo model. Each i-th chemical reaction was characterized by activation energy E_{ri}. Agreement between experimental [7,8] and model ($P - T$) dependencies defining transition from silicon etching to oxide growth (critical conditions) served as a criterion for E_{ri} fitting. According to [8] reaction of silicon monoxide creation O_2+Si→SiO+O is characterized by low energy $E_{\mathrm{r1}} = 0.3$ eV. SiO molecule can be also generated due to chemical reaction between silicon and atomic oxygen, but this reaction is improbable ($E_{\mathrm{r2}} = 2.7$ eV). Volatile components in the system are O_2 and SiO molecules. Silicon monoxide molecule can easily evaporate or decay with low probability into oxygen and silicon forming fragment of SiO_4 tetrahedron. Activation energy of reaction SiO→Si+O ($E_{\mathrm{r3}} = 2.5 - 2.8$ eV) determines

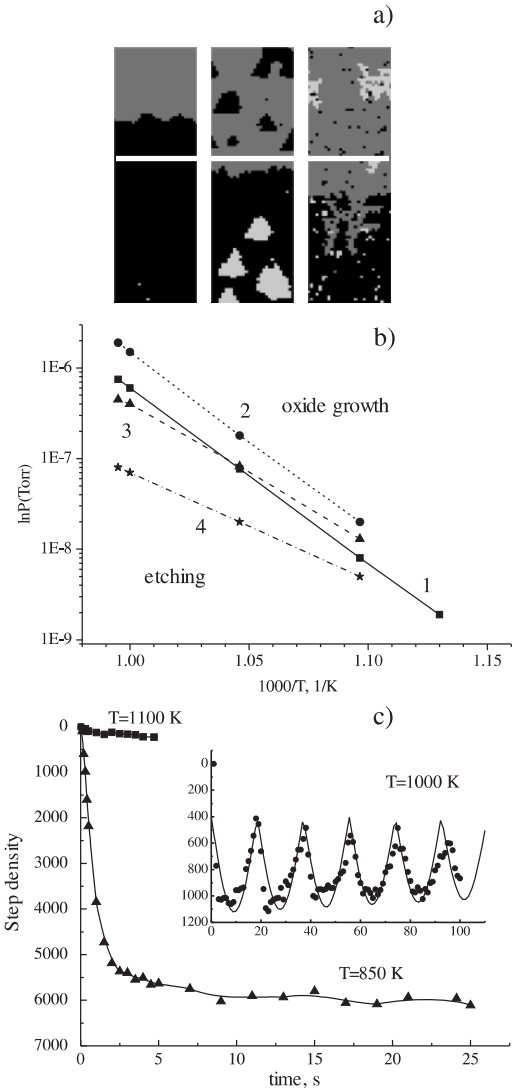

Fig. 2. Critical conditions simulation: a) Fragments of model surfaces (top view) at oxygen pressure $P = 8.4 \times 10^{-7}$ Torr and different temperatures: left) $T = 1100$ K — step flow etching; central) $T = 1000$ K — etching by vacancy island creation; right) $T = 850$ K — oxide active growth. White solid line indicates initial bilayer step position, upper terrace — over the line, lower terrace — under the line; b) Experimental (1) [7] and model (2–4) critical conditions for the interaction of oxygen with Si(111) surface: 2 — $E_{r2} = 2.6$ eV, 3 — $E_{r2} = 2.7$ eV, 4 — $E_{r2} = 2.8$ eV; c) Step density during thermal etching of silicon surface at different temperatures near critical conditions, oxygen pressure $P = 8.4 \times 10^{-7}$ Torr.

oxide growth rate and thickness of transition layer at Si/SiO_2 interface. In the model SiO molecule can migrate within the layer due to re-evaporation inside the voids in dioxide matrix, diffusion through empty lattice sites and exchange diffusion: SiO+O→O+SiO.

The validity of chemical reactions schemes and energies choice was proved by matching calculated and experimental [9,10] critical condition for transition from etching to active oxidation of Si(111) surface by dry oxygen. Fig. 2 illustrates good agreement between experimental [9,10] and model results. Transition from etching to oxide growth with decreasing temperature is shown in Fig. 2a. In Fig. 2b are presented model and experimental critical conditions. In Fig. 2c are demonstrated step density oscillations corresponding to bilayer vacancy islands formation. Such mode of surface etching exists in narrow temperature range close to critical conditions. As in experiment [10], with increasing temperature etching is realized due to steps movement and with temperature decrease relief evolves on the surface. In both cases oscillations disappear.

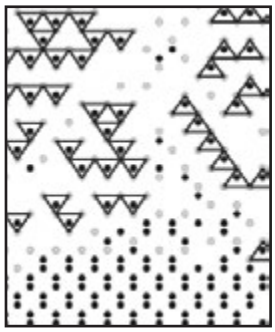

Fig. 3. Fragment of grown SiO_2 layer cross section, $T = 1100$ K, $P = 4.2 \times 10^{-2}$ Torr (passive oxidation). Black circles — silicon atoms, grey circles — oxygen atoms. SiO_4 tetrahedrons are indicated by triangles (4-th oxygen atom is not shown).

Chosen chemical reactions allow obtaining high-quality structure of model oxide (Fig. 3) and kinetic characteristics of initial stage of passive oxidation consistent with known experimental data. Later on it is proposed to use found schemes of reaction for study phase separation in SiO_x layers and SiO influence on oxide shell formation around nc-Si.

2. Summary

Examination of excess silicon aggregation in islands during SiO_x layers annealing was carried out using lattice Monte Carlo model. Taking into account only diffusion mechanism of transport it was possible to obtain silicon nanoclusters, but these nanoclusters had a lot of broken bonds and there was no tendency to decrease their number. Additional mechanism of silicon and oxygen transport was included in the model by taking into consideration chemical reactions of generation and decomposition of mobile SiO molecules. Schemes and energy parameters of reactions were fitted according to known experimental data on initial stages of silicon surface oxidation by dry oxygen. Improved Monte Carlo model is suitable for study processes in SiO_x layers.

Acknowledgements

This work was supported by the RFBR (08-02-00068, MNTI 06-02-72003).

References

[1] M. Dovrat *et al*, *Phys. Rev. B* **69**, 155311 (2004).
[2] E. P. Gusev *et al*, *Phys. Rev. B* **52**, 1759 (1995).
[3] A. V. Zverev *et al*, *Thesis of 8-th Russian conference "Semiconductors 2007"*, Ekaterinburg, 30 Sep.–5 Oct. 2007, p. 113.
[4] S. T. Ahn *et al*, *J. Appl. Phys.* **65**, 2957 (1989).
[5] M. Uematsu *et al*, *Appl. Phys. Lett.* **84**, 876 (2000).
[6] R. Q. Zhang *et al*, *Phys. Rev. Lett.* **93**, 095503 (2004).
[7] A. A. Shklyaev, T. Suzuki, *Phys. Rev. Lett.* **75**, 272 (1995).
[8] J. V. Seiple *et al*, *Phys. Rev. B* **53**, 15432 (1996).
[9] A. Feltz *et al*, *Surf. Sci.* **314**, 34 (1994).
[10] S. S. Kosolobov *et al*, *Semiconductors* **35**, 1038 (2001).

16th Int. Symp. "Nanostructures: Physics and Technology"
Vladivostok, Russia, July 14–18, 2008

The first principle simulation of structure and stability of Al magic clusters on the Ge-modified Si(111)77×7 surfaces

Yu. V. Luniakov
Institute of Automation and Control Processes FEB RAS, Vladivostok, 690041, Russia

Abstract. The energy of formation of the Ge-substituted six-atom Al nanoclusters on the Si(111)7 × 7 surfaces have been determined using the *ab-initio* approach. Several possible positions of the location of substituting Ge atoms have been considered and the most preferable ones have been proposed. The most possible mechanism of the Ge→ Si atoms substitution based on the energy minimization considerations has been established.

Introduction

Self-organized formation of the ordered arrays of the identical-size nanoclusters (i.e. magic clusters) on the metal deposition onto the Si(100)7 × 7 surface has been attracted much attention at the last years [1,2]. A mean of controlling the structure and properties of a given reconstruction is to add atoms of another adsorbate. There is an evidence approved from the recent scanning tunneling microscopy (STM) observations that the small doses of Ge deposition onto the so called α-7 × 7 Al/Si(111) phase [3,4] results in the remarkable improvement of the stability of this structure [5]. A possible mechanism of this is the decreasing the surface energy due to rearrangement of surface atoms. It is generally accepted that the formation of a particular reconstruction is basically a result of the interplay of two trends: (i) reducing the number of dangling (unsaturated) bonds due to rearrangement of atoms at the surface (this trend acts toward decreasing surface energy) and (ii) increasing lattice stress induced by atom displacements (this trend acts toward increasing surface energy). In order to elucidate what is responsible for the stabilization α-7 × 7 Al/Si(111) phase upon Ge exposition we performed the first principle simulations of the Ge modification of the α-7 × 7 Al/Si(111) phase using the optimized triangular M_6 model (see Fig. 1) demonstrated to be the most favorable model of α-7 × 7 Al/Si(111) in respect to the energy [6].

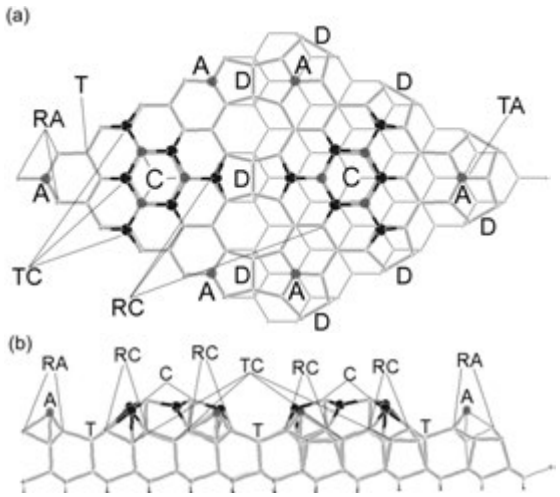

Fig. 1. (a) Top view and (b) side view of the six-atom Al cluster M_6 model [6] unit cell. The Al atoms are shown as the dark circles, the Ge atoms are shown as the gray circles. Si adatoms at the sidecenters of the triangle formed by Al adatoms are marked as C, Si edge adatoms are marked as A, Si atoms bonded with Si edge adatoms A are marked as RA, Si rest atoms bonded with Al atoms are marked as RC, Si T_4 atoms located under Al atoms are marked as TC. Si dimers atoms are marked as D and underlying rest Si atoms in T_4 position are marked as T.

1. Details of calculations

In the ab-initio total-energy calculations we have used the FHI96MD code [7], in which the Car–Parrinello type of electronic structure calculations [8] were used. The local density approximation after Ceperley–Alder [9] in the Perdew–Zunger parametrization [10] for the exchange and correlation functional and fully separable Troullier–Martins [11] pseudopotentials has been employed. The pseudopotentials have been constructed using the FHI98PP code [12].

The surface has been simulated by a periodic slab geometry with the bare 7×7 unit cell containing four silicon atomic layers as is shown on Fig. 1. Six thteefold-coordinated Al atoms form a triangle on the top reconstructed layer in accordance to [6]. The dangling bonds of the bottom slab layer have been saturated by hydrogen atoms. The hydrogen atoms and bottom layer silicon atoms have been fixed and the rest atoms have been set free to move. A vacuum region of approximately 10 Å atomic units has been incorporated within each periodic unit cell to prevent interaction between the adjacent surfaces. An energy cut-off of ≈130 eV has been applied in all calculations presented and one special k point in the Brilloium zone sum has been used.

2. Results and discussions

The results of our calculations in agreement with those in [6] have shown that the stability of Si(111)7 × 7 structures is considerably improved after six-atom Al cluster formation due to appreciable shift of the three Si adatoms and the following removing six dangling bonds from each 7 × 7 unit cell. The energy gain due to Si(111)7 × 7-Al formation is about 0.6 eV per Al atom taking into account the corresponding chemical potential differences. Fig. 2 shows the dependence of energy gain upon the substitution of the different Si atoms on the increasing Ge coverages. The different configurations of Fig. 2 are marked as the letter corresponding to substitution place according to Fig. 1 following by the number of the replacing Si atoms. We see that when six Ge atoms replace six Si adatioms

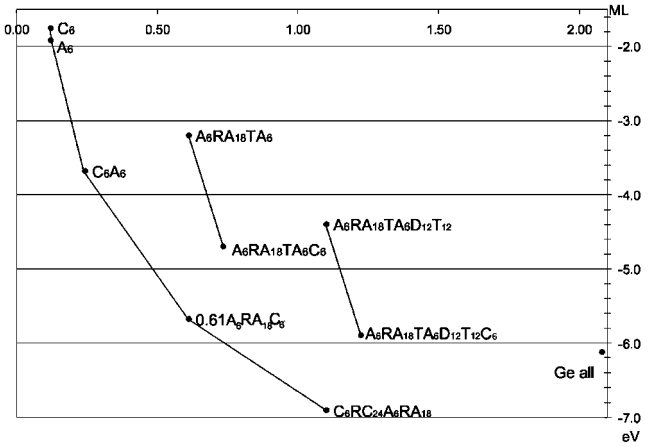

Fig. 2. (a) The energy gain acquired due to the substitution of the Si substrate atoms in the different positions. The chemical potential difference due to Ge→ Si substitution has been taken into account.

in A or C position the energy gain is about 1.8–1.9 eV. The replacement of 12 Si adatoms in A and C position both results in the accumulation of the energy gains almost additively. We assumed that next stage of Si atoms substitution is the replacement of 18 RA Si restatoms that result in the additive energy gain of 2.0 eV. The last stage of this process is the replacement of 24 Si restatoms RC bonded with Al atoms that gives the additive energy gain more than 1 eV. Note that the last configuration is more preferable than those one where all 102 Si double layer atoms are replaced by Ge ones. According to the experimental data [5] α-7 $\times$ 7 Al/Si(111) phase is followed by Al/Si(111) γ-phase at Al coverage over 0.5 ML. That why we did not considered models that correspond to coverages well above one monolayer.

To compare the models considered above with another possible models let's discuss the different mechanisms of the Si atoms substitution that corresponded by four additional points on Fig. 2 connected by pairs. The first pair $A_6RA_{18}TA_6$–$A_6RA_{18}TA_6C_6$ corresponds to the situation where the substitution of Si adations starts from the edges of the 7 $\times$ 7 cell. As we see on the Fig. 2 at the coverage of $\approx$0.61 ML the point $A_6RA_{18}TA_6$ is about by 2.5 eV higher than the point $A_6RA_{18}C_6$ corresponding to the first mechanism that we have proposed. The another pair $A_6RA_{18}TA_6D_{12}T_{12}$–$A_6RA_{18}TA_6D_{12}T_{12}C_{12}$ corresponds to the situation where the substitution of Si dimers atoms D and underlying rest Si atoms T in T_4 position occurs. This possibility is obversely less favorable than the substitution of the all 102 Si reconstructed atoms. In addition we investigate about five more reasonable configurations corresponding to the different places of Ge→ Si substitution, but all of them give the energy gain well above the bottom curve on Fig. 2. That why we conclude that the most favorable mechanism of Ge→ Si substitution is the consecutive layer-by-layer replacement of Si adatoms and restatoms from the topmost surface layer to the bottom.

To summarize the results of our simulations have unambiguously shown that the substitution of the top Si adatoms does favour the stability of the Al/Si(111)7 $\times$ 7 unit cell, moreover the substitution of the considerable share of Si adatoms by Ge ones in layer by layer fashion seems to give an appreciable energy gain for coverages up to 1.1 ML. That agrees with the experimental data proving that the stability of the α-7 $\times$ 7 Al/Si(111) phase is remarkably improved upon Ge deposition.

Acknowledgements

This work was supported by the Russian Foundation for Basic Research (Grant No. 07-02-00650), Russian Federation Ministry of Education and Science (Grant No. 2007-3-1.3-07-01-352), and Far Eastern Department of the Russian Academy of Sciences (FEB RAS). Part of this work was supported by the Russian Foundation for Basic Research (Grant No. 07-02-00650) and the Russian Federation Ministry of Education and Science (Grant No. 2007-3-1.3-07-01-352). Computational facilities were provided by supercomputer resources of Institute of Automation and Control Processes and Institute of Chemistry FEB RAS.

References

[1] J. L. Li, J. F. Jia *et al*, *Phys. Rev. Lett.* **88**, 066101 (2002).
[2] V. G. Kotlyar, A. V. Zotov *et al*, *Phys. Rev. B* **66**, 165401 (2002).
[3] M. Yoshimura, K. Takaoka *et al*, *J. Vac. Sci. Technol B* **12**, 2434 (1994).
[4] M. Yoshimura, K. Takaoka *et al*, *Phys. Rev. B* **47**, 13930 (1993).
[5] D. V. Gruznev, D. A. Olyanich *et al*, *to be published*.
[6] J.-F. Jia, X. Liu *et al*, *Phys. Rev. B* **66**, 165412 (2002).
[7] M. Beckstedte, A. Kley *et al*, *Comp. Phys. Commun.* **107**, 187 (1997).
[8] R. Car and M. Parrinello, *Phys. Rev. Lett.* **55**, 2471 (1985).
[9] D. M. Ceperley and B. J. Alder, *Phys. Rev. Lett.* **45**, 566 (1980).
[10] J. P. Perdew and A. Zunger, *Phys. Rev. B* **23**, 5048 (1981).
[11] N. Troullier and J. L. Martins, *Phys. Rev. B* **43**, 1993 (1991).
[12] M. Fuchs and M. Scheffler, *Comp. Phys. Commun.* **119**, 67 (1999).

16th Int. Symp. "Nanostructures: Physics and Technology"
Vladivostok, Russia, July 14–18, 2008

Antiphase-boundary formation in monolayer Tl /Ge(100) system: Scanning tunneling microscopy and total-energy calculations

Yu. V. Luniakov[1], I. A. Kuyanov[1], A. V. Zotov[1], A. A. Saranin[1], M. Katayama[2] and K. Oura[2]
[1] Institute of Automation and Control Processes, Vladivostok, Russia
[2] Osaka University, Osaka, Japan

Abstract. Using scanning tunneling microscopy observations and total-energy calculations we have examined structural properties of the one-monolayer Tl/Ge(100)2 × 1 phase. The most fascinating finding is that the Tl overlayer facilitates the re-bonding of underlying Ge-dimers, which leads to the formation of the antiphase boundaries (APBs). This phenomenon might be responsible for long-period superstructures developing at Tl/Ge(100) interface upon cooling to low temperatures or exceeding one-monolayer Tl coverage.

Introduction

Motivated by technological importance for nanoengineering, superstructures self-assembled by adsorbate monolayers and submonolayers on semiconductor surfaces are of increasing interest. From scientific point of view, these superstructures have attracted much attention due to the possibility of observing new low-dimensional phenomena. In this respect, exotic systems with unusual structure and properties are of a special interest. Thallium (Tl), the heaviest group III metal, adsorbed on Si and Ge surfaces can serve as an example, since a set of various peculiar effects have been detected in these systems, including diverse magic nanoclustering [1,2] and temperature-induced reversible phase transitions [3,4].

In the present work, using scanning tunneling microscopy (STM) and total-energy calculations we have examined a fascinating possibility of the one-monolayer Tl/Ge(100)2 × 1 surface to form antiphase boundaries (APBs) by re-bonding underlying Ge dimers. This behavior is in contrast to the adsorbate-free Si(100) and Ge(100) surfaces, as well as one-monolayer Tl/Si(100) system, where APB formation does not occur.

1. Atomic structure of one-monolayer Tl/Ge(100) surface

Figure 1a shows a high-resolution filled-state STM image of the Ge(100)2 × 1-Tl surface formed upon adsorption of about 1 monolayer (ML) of Tl. Room-temperature STM appearance of the Ge(100)2 × 1-Tl surface is very similar to that of the Si(100)2 × 1-Tl surface, namely, both surfaces display rows of oval-shaped protrusions [5]. Total-energy calculations conducted in the present study confirm that the surfaces indeed have a similar atomic arrangement being described by the so-called double-layer model proposed earlier by Abukawa and Kono [6] for an alkali-metal monolayer on a Si(100) substrate. In this model shown in Fig. 1b the dimer-row structure of the substrate is preserved, while metal atoms are arranged in chains of two types. In the first type of chain metal atoms reside in the pedestal sites above the dimer rows, and in the second type of chain they occupy the valley-bridge sites in the troughs between the dimer rows.

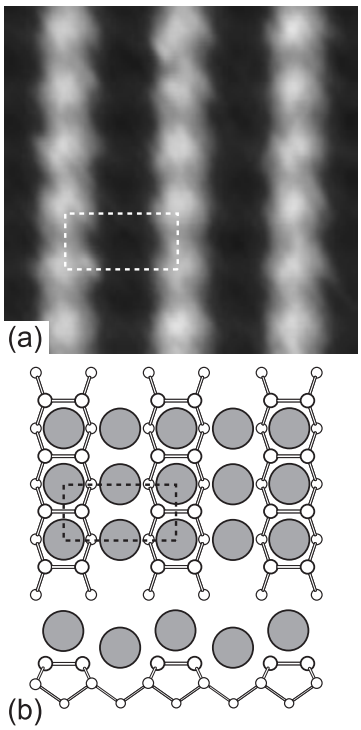

Fig. 1. High-resolution (23 × 23 Å^2) filled-state STM image of the one-monolayer Tl/Ge(100)2 × 1 surface. (b) Double-layer structural model of the surface. Tl atoms are shown by large gray circles, Si atoms by small white circles.

2. STM observation of APBs in Tl/Ge(100) system

In spite of this structural similarity, Ge(100)2 × 1-Tl differs from Si(100)2 × 1-Tl by the presence of antiphase boundaries (indicated APB in Fig. 2a). This is a peculiar feature of only Ge(100)2 × 1-Tl. APBs have never been observed on the Si(100)2 × 1-Tl surface and they never occur at the original atomically-clean Ge(100)2 × 1 and Si(100)2 × 1 substrate surfaces. Figure 1b shows an APB on the Ge(100)2 × 1-Tl surface with atomic resolution. The optimized structural model of the APB derived using total-energy calculations and a simulated STM image of APB corresponding to it are shown in Figs. 2d and c, respectively. According to the model, when passing the APB the dimer rows become shifted by 1a (a = 4.0 Å,

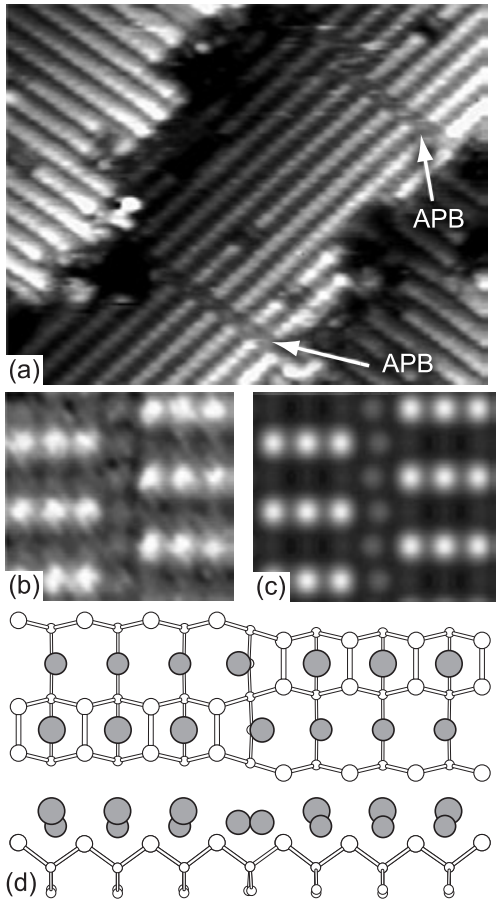

Fig. 2. 165 × 130 Å^2 filled-state STM image of the Tl/Ge(100)2 × 1 surface area containing two antiphase boundaries (indicated APB). (b) Experimental and (c) simulated high-resolution STM images of the APB region. (d) Optimized structural model of the APB region.

lattice constant of the Ge(100)1 × 1 surface) in the direction normal to the row. The shift is naturally caused by Ge-dimer re-bonding. Thus, Tl atoms within the same atomic chain occupy valley-bridge sites on one side of the APB and pedestal sites on the other. Tl atoms residing exactly at the APB form an atomic chain having a zigzag-like shape. These Tl atoms are 0.4 Å higher than those in the valley-bridge sites (for comparison, the height difference between Tl atoms in the pedestal and valley-bridge sites is 1.8 Å) and they are shifted laterally from the ideal valley-bridge positions towards neighboring Tl atoms in the valley-bridge sites by 1.3 Å, hence the zigzag shape of the chain. All the above features are clearly seen in the STM image of the APB (Fig. 2b), which supports greatly the APB model suggested.

Table 1. Calculated formation energies of the structures with APBs for different types of surfaces. Formation energies of the corresponding APB-free surfaces are taken as zero.

Surface	2×4	2×8
Si(100)	+0.35 eV	+0.30 eV
Ge(100)	+0.31 eV	+0.27 eV
Tl/Si(100)	+0.14 eV	+0.13 eV
Tl/Ge(100)	−0.05 eV	−0.15 eV

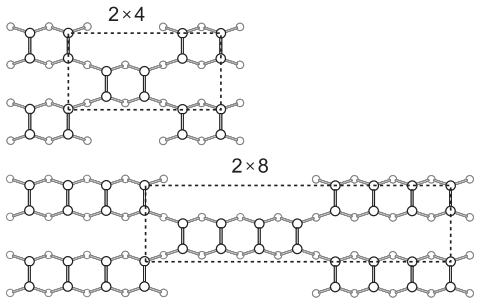

Fig. 3. Surface configurations with APBs for which formation energies have been calculated (see Table 1).

3. Energetics of APB formation

Summarizing experimental results, one can conclude that the capping of a Ge(100)2 × 1 surface by a Tl overlayer facilitates Ge-dimer re-bonding. As a result, in the Tl/Ge(100) system APBs develop which were not present on the original Ge(100)2 × 1 surface. To see if the energetics of APB formation is really different for different surfaces, we have evaluated APB formation energies for adsorbate-free Si(100) and Ge(100) surfaces and Tl/Si(100) and Tl/Ge(100) monolayer systems [7]. As model structures, surface configurations with APB's having 2 × 4 and 2 × 8 periodicity (Fig. 3) have been considered. Calculated formation energies of the configurations are listed in Table 1. Note that each configuration contains two APBs in a unit cell. The formation energy of the corresponding APB-free surfaces was taken as zero.

One can see in Table 1 that APB energies for adsorbate-free Si(100) surface lie in the 0.30–0.35 eV range and decrease with growing separation between neighboring APB's. Formation energies for the adsorbate-free Ge(100) surface are somewhat lower being in the 0.27–0.31 eV range. For a 1-ML Tl/Si(100) system, the energy values are more than twice lower (0.13–0.14 eV). It is believed to be the sequence of lifting dimer buckling in this system as compared to the adsorbate-free Si(100) and Ge(100) surfaces, which are built of buckled dimers. However, APB energies are still positive. The 1-ML Tl/Ge(100) system is the only one for which APB energy becomes negative (−0.05 and −0.15 eV for 2 × 4 and 2 × 8 configurations, respectively). It means that only in this system APB formation is an energetically favorable process.

References

[1] L. Vitali, M. G. Ramsey, and F. P. Netzer, *Phys. Rev. Lett.* **83**, 316 (1999).
[2] A. V. Zotov, A. A. Saranin, V. G. Kotlyar, O. A. Utas, and Y. L. Wang, *Surf. Sci.* **600**, 1936 (2006).
[3] A. A. Saranin, A. V. Zotov, I. A. Kuyanov, V. G. Kotlyar, M. Kishida, Y. Murata, H. Okado, I. Matsuda, H. Morikawa, N. Miyata, and S. Hasegawa, *Phys. Rev. B* **71**, 165307 (2005).
[4] A. A. Saranin, A. V. Zotov, M. Kishida, Y. Murata, S. Honda, M. Katayama, and K. Oura, *Surf. Sci.* **601**, 595 (2007).
[5] A. A. Saranin, A. V. Zotov, V. G. Kotlyar, I. A. Kuyanov, T. V. Kasyanova, A. Nishida, M. Kishida, Y. Murata, H. Okado, M. Katayama, and K. Oura, *Phys. Rev. B* **71**, 035312 (2005).
[6] T. Abukawa and S. Kono, *Phys. Rev. B* **37**, R9097 (1988).
[7] A. A. Saranin, A. V. Zotov, I. A. Kuyanov, Yu. V. Luniakov, M. Katayama, and K. Oura, *Phys. Rev. B* **76**, 193302 (2007).

16th Int. Symp. "Nanostructures: Physics and Technology"
Vladivostok, Russia, July 14–18, 2008

Scanning probe induced local decomposition of solid germanium monoxide films: the nano-patterning possibilities

D. V. Sheglov[1,2], E. B. Gorokhov[1], V. A. Volodin[1,2], K. N. Astankova[3] and A. V. Latyshev[1,2]

[1] Institute of Semiconductor Physics SB RAS, 630090 Novosibirsk, Russia
[2] Novosibirsk State University, 630090, Novosibirsk, Russia
[3] Novosibirsk State Technical University, 630092, Novosibirsk, Russia

Abstract. The possibility of formation of Ge-based wires with nano-scale lateral resolution using modification of GeO films by scanning probe microscope was demonstrated for the first time. The main advantage of used solid germanium monoxide films is its meta-stability and decomposition on Ge and GeO_2 under impact of atomic force microscope probe via solid state chemical reaction. The proposed method can be used in nano-lithography.

Introduction

Semiconductor nanostructures like quantum dots (QDs) and quantum wires (QWs) attract a lot of interest due to its new properties that can be artificially modified [1]. The quantum size effects in QDs lead to possibility of application of semiconductors with indirect band structure (Si and Ge) in optoelectronics [2–4]. Germanium has several advantages. First, the melting point of Ge is sufficiently low as compared to Si (940 ° versus 1420 °C), causing lower crystallization temperature of Ge. Second, Ge has a larger exciton Bohr radius (4.9 nm for Si and 24.3 nm for Ge). Thus, the quantum-confinement-related positive effects in Ge manifest themselves at larger sizes, which can be reached with less difficulty. The energy gap values of Ge and Si QDs become equal when their sizes reach 2.3 nm. Further decrease of sizes down to 1.5 nm causes an abrupt increase in Ge gap up to 3 eV, which exceeds by 0.7 eV the gap of Si NC with the same size. This is the reasons for study of Ge-based nanostructures.

The past decade a lot of interest has been centered on patterning with the scanning probe microscope, which is capable for fabrication of nanostructures [5–7]. In this paper we offer a new perspective method of atomic force microscopy (AFM) lithography for fabrication nanometer-scale structures of Ge-clusters on the solid-state substrates, which is simple, effective, and provides the patterning of features with dimensions below 100 nm.

1. Experimental

The initial films were deposited on silicon substrates from supersaturated GeO vapor with subsequent dissociation of metastable (in solid state) Ge monoxide on heterophase system Ge:GeO_2. The reactor contains evaporation zone and deposition zone. The growth rate depend on GeO vapor pressure and temperature of substrates. The bearing gas is Ar with impurities of O_2 and H_2O. Oxygen and water reacts with Ge plates in evaporation zone with formation of GeO gas. The pressure of GeO gas in deposition zone is higher than saturation pressure, and GeO precipitate on substrate. Depending on growth condition one can obtain Ge:GeO_2 films with amorphous Ge nanoclusters or Ge nanocrystals. More detailed the growth procedure is described elsewhere [8]. It should be noted, that the molar ratio of Ge and GeO_2 in the films is always 1:1. Further, the germanium monoxide film was deposited onto specially prepared clean silicon substrate by thermally evaporating of initial heterolayers Ge:GeO_2 (400–500 nm) from Si-sample at 550–600 °C in a oil-diffusion pump evaporator at a pressure of 5×10^{-5} Pa. In accordance with the reaction $GeO_2+Ge \Rightarrow 2GeO_{(}$gas) vapor of gas GeO condense onto virgin wafer being at room temperature. We have developed a mode that allows growing of 10 nm GeO films for 5 min. The obtained films were studied with the use of Raman scattering spectroscopy and IR-spectroscopy techniques. Experimental Raman spectra were registered in quasi back-scattering geometry, the 514.5 nm Ar^+ laser lines was used. The normal incidence IR absorption measurements were carried out with a resolution of 4 cm^{-1}.

The modification of GeO solid films was carried out using AFM (Solver P-47H, NT-MDT, Russia). The main idea of this work is next. Using germanium monoxide as a resist we can fabricate lines from Ge-nanoclusters, which are subsequence of GeO decomposition: $2GeO \Rightarrow GeO_2+Ge$. Decomposition of germanium monoxide is initiated with a low voltage applied between the atomic force microscope conductive tip and the silicon substrate. As a result of local heating of the film or electrochemically stimulated reaction decomposition of metastable (in solid state) GeO should occur across pass of the tip.

2. Results and discussion

The IR absorption spectrum of initial GeO film in range from 700 to 1200 cm^{-1} is shown in Fig. 1a. The observed peak is assigned to Ge-O-Ge stretching vibration mode. The peak position is about 820 cm^{-1}, so, one can assume, that the initial film (re-deposited from evaporation of Ge:GeO_2 film on room temperature Si substrate) is not dissociated on Ge and GeO_2. It is known, that in GeO_x films this peaks approximately linearly shift from about 820 cm^{-1} for $x \approx 1$ to about 870–880 cm^{-1} for $x = 2$ [4]. One can conclude, that our thin film had not oxidized essentially being kept on air atmosphere. According to ellipsometry data, the film had thickness about 10 nm and refractive index 1.78–1.8 (wavelength 633 nm).

The Raman spectra of the initial GeO film, annealed films and totally decomposited Ge:GeO_2 film are shown in Fig. 1b. In the spectrum of Ge:GeO_2 film with Ge nanocrystals one can see the Raman peak due to scattering on optical phonons confined in Ge NCs (curve 3). It is known, that Raman signal from amorphous Ge is a broad peak with maximum at 270–

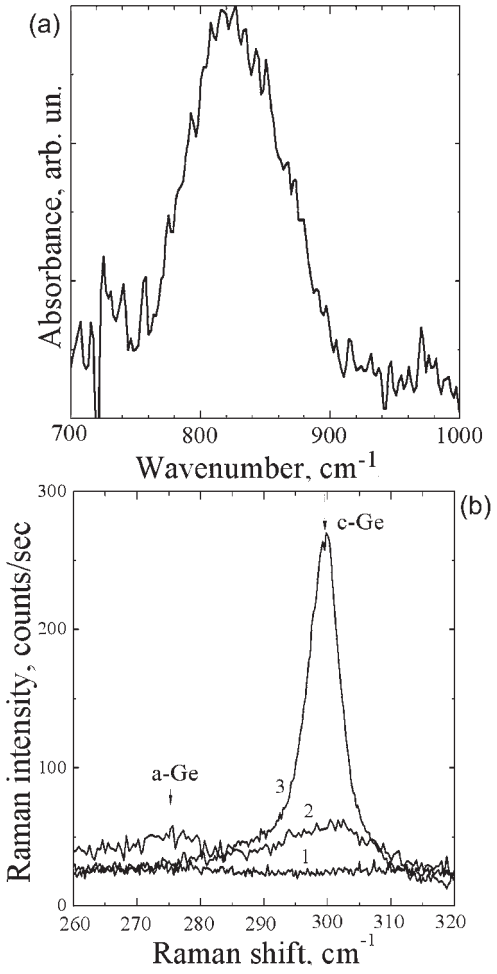

Fig. 1. IR absorption spectrum of the initial GeO film (a) and Raman spectra of as deposited GeO film (curve 1), partly decomposited film (annealing 2 minutes $T = 380\,^{\circ}\mathrm{C}$ — curve 2) and fully decomposited Ge:GeO_2 film (curve 3) (b).

280 cm^{-1}. The Raman signal from crystalline Ge is narrower peak with position depending on NCs sizes. The confinement effect shifts the position of Raman peak to low frequencies from bulk-Ge Raman peak position (about 300.3–300.5 cm^{-1}). The NCs sizes can be estimated from position of Raman peaks [8,9]. It should be noted, that in Raman spectrum of initial GeO film there is no peaks related to vibration of Ge-Ge bonds. So, Raman data confirm the IR spectroscopy data that the initial film had not contain Ge clusters. These clusters can appear as result of annealing of metastable films. One can see it from curve 2. As a result of annealing the initial GeO film partly decompose into Ge clusters in GeO_2 matrix. Because GeO films are thin ($\sim$10 nm), the size of Ge-NC's dispersed into the GeO_2 matrix is thought to be on the order of 1/3 of film thickness after full decomposition of germanium monoxide. The presence of Ge nanoclusters with sizes down to 2–3 nm in decomposed films was confirmed by direct data of electron microscopy [8,9]. The initial GeO films were deposited on special cleaned Si substrate.

The sample was studied using AFM. Then film of germanium monoxide was exposed with a voltage applied between the AFM conductive tip (positive) and the silicon substrate (negative) with the tapping mode. Figure 2 shows an AFM

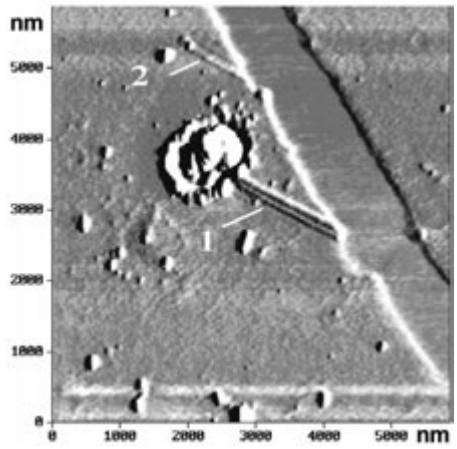

Fig. 2. Phase AFM- image of Ge-lines on Si substrate.

micrograph of Ge-lines after sample was rinsed in deionized water to remove GeO_2 and not decomposed GeO. The patterns were written with a 10 V and 30 V bias and with a writing speed of 6 nm/s and 2 nm/s, respectively. The line (1) has a width of 150 nm and height of 2 nm, but the linewidth of line (2) is 185 nm and height is near 8 nm. Optimizing the GeO film thickness and the regimes of AFM treatments one can enhance the lateral resolution of nano-patterning.

In summary, nanometer-scale AFM lithography of GeO films has been demonstrated. We have patterned as narrow as nanometer-scale-wide nanowires of germanium.

Acknowledgements

The work was supported by Russian Fund for Basic Research – grants No. 07-08-00438.

References

[1] A. P. Alivisatos, *Science* **271**, 933 (1996).
[2] Y. M. Niquet *et al*, *Appl. Phys. Lett.* **77**, 1182 (2000).
[3] N. Myung *et al*, *Neno Lett.* **4**, 183 (2004).
[4] M. Ardyanian *et al*, *Appl. Phys. Lett.* **89**, 011902 (2006).
[5] D. V. Sheglov *et al*, *Int. Journ. of Nanosci.* **3**, 1 (2004).
[6] D. V. Sheglov *et al*, *Appl. Surf. Sci.* **243**, 138 (2005).
[7] S. W. Park *et al*, *Appl. Phys. Lett.* **67**, 2415 (1995).
[8] V. A. Volodin *et al*, *Solid State Phenomena* **84**, 108 (2005).
[9] E. B. Gorokhov *et al*, *Semiconductors* **39**, 1168 (2005).

16th Int. Symp. "Nanostructures: Physics and Technology"
Vladivostok, Russia, July 14–18, 2008

Electronic states in 3D dense array of Ge/Si quantum dots

A. V. Dvurechenskii and A. I. Yakimov
Institute of Semiconductor Physics, 630090 Novosibirsk, Russia

Abstract. The results of strain modification of the electron energy spectrum in dense array of Ge/Si quantum dots (QDs) are presented. The electron binding energy in a strain induced potential well enlarges vastly in multilayer Ge/Si structures with vertical stacking of Ge islands due to accumulation of strain energy from different dot layers in a stack and increase of the potential well depth. For holes confined in Ge double dot molecule there are some intermediate interdot distances of vertical correlated Ge QDs where two phenomena have been observed: 1) the reduction of the binding energy below the value of the binding energy of single dot and 2) molecular bond breaking for and localization of the hole in the one of the two dots.

Introduction

Quantum dot nanostructures have emerged many nanoscale phenomena and promising devices for nano- and optoelectronics [1]. Among the problems which are in focus of scientists there are the most universal ones: a) the homogeneity of quantum dot array in size, shape and composition; b) the quantum dot density tuning from rare one to dense array and the long range ordering in matrix space; c) the decreasing the density of point and extended defects. The atomic-like density of electronic states in ensembles of quantum dots (QDs) is the crucial issue when QDs are considered for both device applications and fundamental physical studies. In this work we present the results of the electron/hole energy spectrum modification in dense array of QDs. A few electron small sizes (about 10 nm) QDs are of particular interest due to discrete energy level separation big enough to provide room temperature device operation. Together with additional requirement on high density of QDs needed for device application the sheet density is estimated to be about 10^{12} cm^{-2}. Elastic deformations in epitaxial films and 3D Ge island on Si are the key factors that not only causes the morphological planar-to-island film transition but also affects the further stages of island evolution, including the shape, the size and the spatial distribution of the Ge nanocrystals especially for multilayer QDs structure. The strain induced nucleation leads to vertically correlation of Ge QDs growth in multilayer structure. With QDs layers space separation about 10 nm 3D densities are estimated to be near 10^{18} cm^{-3}.

1. Localization of electrons in multiple layers of self-assembled quantum dot

For type-II QDs, the localization inside the dot occurs only for one of the charge carriers, whereas the dot forms a potential barrier for the other particle. A system like this is that of Ge/Si(001) dots formed by strain epitaxy, in which the holes are strongly confined in the Ge region and the electrons are free in the Si conduction band. The above consideration disregards possible modification of the band structure due to inhomogeneous strain in the dots and the surrounding matrix. Tensile strain in the nearby Si causes splitting of the sixfold degenerate delta valleys into the fourfold-degenerate in plane Δ_4 valleys and the twofold-degenerate Δ_2 valleys along the [001] growth direction [2,3]. The lowest conduction band edge just above and below the Ge pyramidal shape nanocrystal is formed by the Δ_2 valleys yielding the triangle potential well for electrons in Si near the Si/Ge boundary. Thus the expected three-dimensional localization of electrons in the strained Si near the Ge dots takes place. The electron binding energy in a strain induced potential well in a single Ge/Si quantum dot was found to be small (less then 10 meV). This value was found to enlarge vastly in multilayer Ge/Si structures with vertical stacking of Ge islands due to accumulation of strain energy from different dot layers in a stack and increase of the potential well depth [3]. Space-charge spectroscopy was used to look for the evidence of the electron accumulation in samples with a single layer of GeSi islands and with a stack of four layers of GeSi QDs embedded in a n-type Si(001) matrix. The strain distribution was found in terms of atomic positions using valence-force-field model with a Keating interatomic potential. The electronic energy levels were calculated by solving three-dimensional effective-mass Schrodinger equation by means of a free relaxation method. The carrier confinement potential in this equation is modified by the strain distribution. A three-dimensional potential well for electrons emerging due to the strain in Si nearby a Ge QDs is formed near the apex and under the bottom of the dot, with the binding energy being smaller in the latter case. The direct evidence on electron localization in three-dimensional potential well has been made with ESR measurements on Ge/Si heterostructures with self-assembled QDs [4]. It was demonstrated that the QDs size dispersion has no significance for line width of ESR signal from electrons in the Ge/Si QDs heterostructure in contrast to other semiconductor systems with a stronger spin-orbit interaction. It has been shown that in the Ge/Si QDs structures the strain has a crucial effect on the g-factor of the localized electrons. On the contrary, the electron binding energy plays a negligible role in line width of ESR signal. A well pronounced anisotropy of the line width was found and explained in terms of an effective magnetic field, lying in the plane of the quantum dot array. This magnetic field arises during the tunneling of electrons between quantum dots and leads to an acceleration of the spin relaxation. The origin of the field is the asymmetry of Ge/Si quantum dot structures. In two-dimensional structures an analogue of considered field is the Bychkov–Rashba field. The magnitude of effective magnetic field can be estimated to be about 30 Oe in tunnel coupled array of Ge QDs in Si.

2. Hole states in quantum dot molecules induced by strain driven self-assembly

Space-charge spectroscopy was employed to study the emission of holes from the ground (bonding) state of vertically self-aligned double Ge quantum dots separated by a Si barrier [5]. The dots have a shape of hut clusters with lateral dimensions of about 10 nm. From the temperature- and frequency-dependent measurements, the hole binding energy was determined as a function of the separation between the dots. To analyze the experiment the electronic structure of two vertically coupled pyramidal shape Ge quantum dots embedded in Si was investigated by a nearest neighbor tight-binding single-particle Hamiltonian with the sp3 basis. The elastic strain due to the lattice mismatch between Ge and Si was included into the problem. The three-dimensional spatial strain distribution was found in terms of atomic positions using a valence-force-field theory with a Keating interatomic potential. For pure Ge dots (no mixing with matrix material), it is found that, when the thickness of the Si barrier between Ge dots exceeds 2.5 nm, the two effects are observed, contrasting with a conventional quantum-mechanical molecular model. The first is reduction of the binding energy of a hole in bonding state below the value of the single dot with increasing dot separation. The second represents molecular bond breaking for intermediate interdot distances and localization of the hole in the bottom dot. Both phenomena disappear upon Ge-Si intermixing. Analysis of the biaxial strain distribution showed that anomalous decreasing of the hole binding energy below the value of the single dot with increasing interdot separation is caused by the partial strain relaxation upon dot stacking accompanied by the strain-induced reduction of the hole confinement potential. The second effect originates from asymmetry of the strain field distribution within the top and bottom dots due to the lack of inversion symmetry with respect to the medium plane between the dots.

Acknowledgements

This work was supported by RFBR (Grants 08-02-00121) and State Contract 02.513.11.3156.

References

[1] Handbook of Semiconductor Nanostructures and Nanodevices V.1, *Quantum dots, Nanovires and Self-Assemblies.* Ed. Balandin A. A. and Wang K. American Scientific Publishers, New York (2006).
[2] O. G. Schmidt, K. Eberl, and Y. Rau, *Phys. Rev. B* **62**, 16715 (2000).
[3] A. I. Yakimov *et al*, *Appl. Phys. Lett.* **80**, 163126 (2006).
[4] A. F. Zinovieva *et al*, *Phys. Rev. B* **77**, 115319 (2008).
[5] A. I. Yakimov *et al*, J. Appl. Phys. **102**, 093714 (2007).

16th Int. Symp. "Nanostructures: Physics and Technology"
Vladivostok, Russia, July 14–18, 2008

Optical properties of InAs quantum dots in InP quantum wires

Mats-Erik Pistol[1], Niklas Sköld[1], Craig Pryor[2] and Lars Samuelson[1]
[1] Lund University, Lund, 221 00, Sweden
[2] University of Iowa, Iowa, USA

We have grown InP quantum wires using the vapor-liquid-solid method. In this method metal particles, gold in our case, are deposited on a substrate, followed by a growth step at low temperature in an MOCVD-reactor [1]. The gold catalyses growth of wires and by changing precursors it is possible to grow short segments of e.g. InAs in the wires. The wires were subsequently capped with InP and we have thus strained small InAs dots inside the wires. The wires were investigated by transmission electon microscopy, showing dots having sharp interfaces. Figure 1 shows a TEM micrograph of a wire and a set of InAs dots can be seen. The growth is not strictly one-dimensional and there is a small tapering of the wires and the dots are thus capped with InP. This is advantageous since surface states are removed from the dots allowing photoluminescence studies to be performed, also on individual dots.

Figure 2 shows photoluminescence spectra from dots having different sizes indicatd in the figure. Clear confinement effects an be seen where the smalles dots have the highest transition energy. In addition, it can be seen that the emission consists of two closely spaced lines. The linewidth of these lines is about 400 μeV. This linewidth is larger than the corresponding linewidth from Stranski–Krastanow grown dots (typically 100 μeV [2]), but can still be considered to be comparatively narrow. We attribute the two emission lines to excitons and bi-excitons. Figure 3 shows in more detail the evolution of the emission spectra as a function of excitation power density. At low excitation power density we observe one emission line, which we attribute to the exciton. At a higher excitation power density we observe the emergence of an additional line which we attribute to the biexciton, and at the highest excitation power density we also observe emission from the tri-exciton. At the same time as we observe emission from the tri-exciton we also observe emission from single particle excited states, as can be seen in Figure 3. This is expected since when the tri-exciton state is created there must be one electron in an excited state in the conduction band (and similarly for the hole). We furthermore calculated the single particle transition energies of the dots using a full three dimensional calculation within the k.p-approximation including strain and mixing among six bands. We find for dots having a size of 10 nm in widht and a height of 5 nm that the calculated transition energy is 0.89 eV while the experimental transition energy is 1.05 eV. For a dot size of 15 nm in width and a height of 7 nm we find a calculated energy of 0.72 eV while the experimental transition energy is 0.95 eV. Our calculated energies are systematically lower than the experimental energies. Our calculations assume a zinc-blende crystal structure while the actual structure is in fact wurtzite. Wurtzite III–V semiconductors tend to have a higher band-gap than the corresponding zinc-blende structure [3] and we attribute the difference between theory and experiment to this fact.

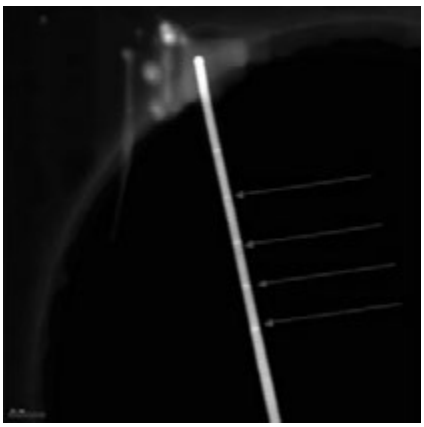

Fig. 1. A transmission electron micrograph of an InP wire containing several InAs quantum dots. At the top of the wire the gold particle is visible. The InAs dots are indicated by arrows.

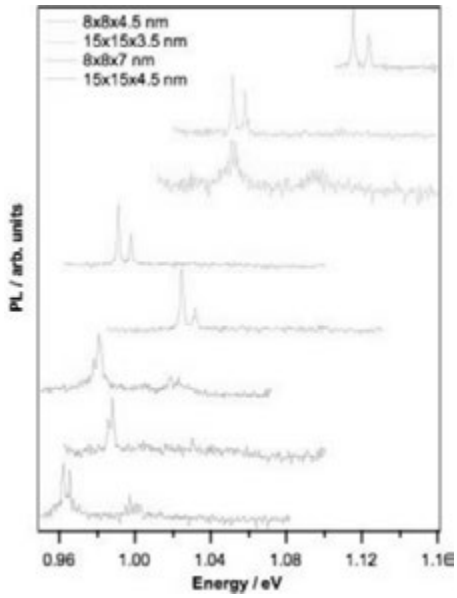

Fig. 2. Photoluminescence spectra of different individual wires containing InAs dots. The dimensions of the dots are indicated in the figure. The largest dots emit at about 0.98 eV and smaller dots emit at higher energy. The spectra of several wires from each growth are displayed, showing the dispersion in emission energies. Two sharp lines are typically seen from each dot at these excitation power densities.

Acknowledgements

This work was supported by VR and SSF and was performed within the nanometer consortium in Lund.

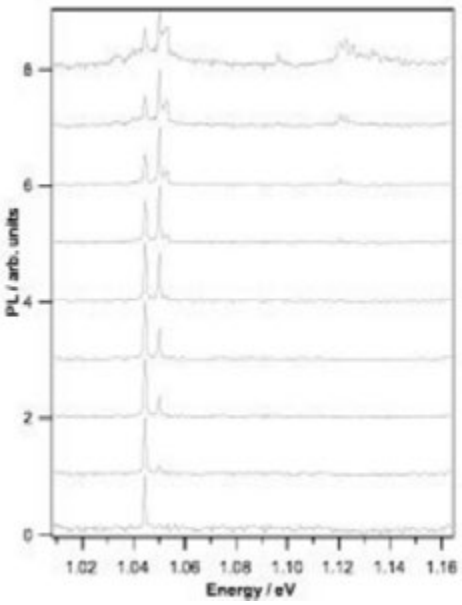

Fig. 3. Spectra of one InAs dot for different excitation power densities. At the lowest power, bottom trace in the figure, only one emission line is seen. At higher excitation power densities we observe initially two lines and then three lines. The extra lines are due to biexciton emission and triexciton emission. At the highest excitation power density we also observe emission from excited single particle states at an energy of about 1.12 eV.

References

[1] W. Seifert *et al*, *J. Cryst. Growth* **272**, 211 (2004).
[2] L. Landin *et al*, *Science* **280**, 262 (1998).
[3] J. Jagadish *et al*, *Appl. Phys. Lett* **91**, 263104 (2007).

16th Int. Symp. "Nanostructures: Physics and Technology"
Vladivostok, Russia, July 14–18, 2008

Carrier transfer and light emission in hybrid nanostructures including InGaAs quantum well and quantum dots array

V. G. Talalaev[1,2,3], J. W. Tomm[1], N. D. Zakharov[2], P. Werner[2], U. Gösele[2], B. V. Novikov[3], Yu. B. Samsonenko[4,5,6], V. A. Egorov[5,6] and G. E. Cirlin[4,5,6]

[1] Max-Born-Institut für Nichtlineare Optik und Kurzzeitspektroskopie, 12489 Berlin, Germany
[2] Max-Planck-Institut für Mikrostrukturphysik, 06120 Halle (Saale), Germany
[3] Fock Institute of Physics, St Petersburg State University, 198504 St Petersburg, Russia
[4] Ioffe Physico-Technical Institute, St Petersburg, Russia
[5] Physics and Technology Centre for Research and Education RAS, 195220 St Petersburg, Russia
[6] Institute for Analytical Instrumentation RAS, 190103 St Petersburg, Russia

Abstract. The transport and emission properties of semiconductor nanostructures are investigated including two closely spaced InGaAs layers with quantum dots (QDs) in the first, and a quantum well (QW) in the second layer. Such hybrid structures are grown by molecular beam epitaxy and measured by time resolved spectroscopy and transmission electron microscopy. By tuning the energy of the excitation photons through the ground state of the QW we observed a distinct different response from hybrid structure. This result is explained by an inverted energy offset as well as the electron tunneling between QW and QDs layers. The pathways of carrier transfer from the QW to the QDs are analyzed. The dependence of the tunneling time on the barrier thickness was found to deviate from the semi-classical approximation for thin barriers (<6 nm). Significant reduction (more than 6 times) of the transfer time is explained by the formation of a point contact (nano-bridge) between the QW and some QDs.

Among the quantum dot (QD) based semiconductor lasers a special place belongs to the device design with vertically coupled dot-in-well structures, in which InAs QDs are capped with an InGaAs quantum well (QW), providing low-threshold and high modal gain at 1.3 μm with high characteristic temperature. Preliminary studies have shown a possibility of several advantages, if the QDs array is separated from the QW layer by a barrier spacer, which remains still tunnel-transparent for carriers [1]. Due to a larger capture cross-section the QW can serve as accumulator of injected carriers, and the QDs can act as light emitter in the hybrid active region. However, the carrier transfer between QW and QDs has not yet been studied in detail.

In the current work we present the results of time resolved photoluminescence (TRPL) and transmission electron microscopy (TEM) of the InGaAs hybrid nanostructure (HnS) grown by molecular beam epitaxy and having the following sequence of layers: InAs QDs (2 monolayers)–GaAs spacer (3–13 nm)–$In_{0.15}Ga_{0.85}As$ QW (11 nm) embedded into a GaAs matrix (Figure 1). A barier thickness is taken as a value B of the

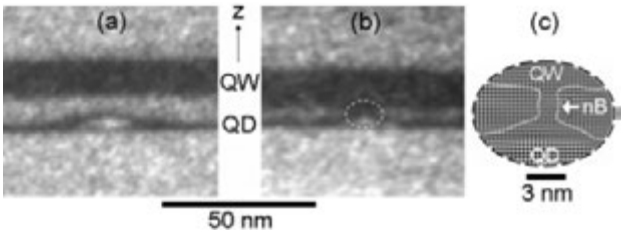

Fig. 1. TEM cross-section images of two HnS with different GaAs barrier thickness (B) between QDs and QW $In_xGa_{1-x}As$ layers: (a) $B = 6.5$ nm; (b) $B = 3.1$ nm and (c) high-resolved TEM of this HnS. The dashed oval shows the area of a nano-bridge (nB) formation. The doted contour was drawn over the contrast disappearance corresponding to $x \sim 0.15$. z — growth direction.

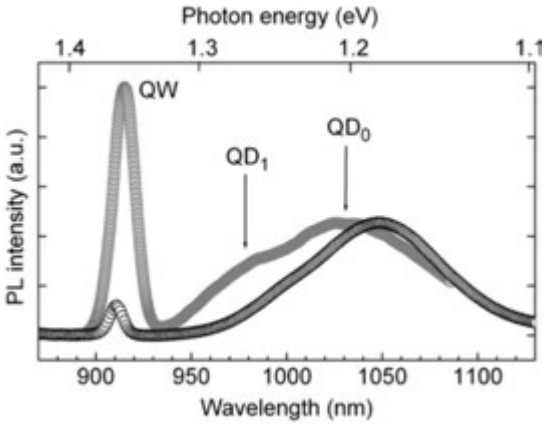

Fig. 2. Normalized PL spectra of HnS with 6.5-nm GaAs barrier for two modes of above-GaAs-barrier excitation with average density of 50 W cm^{-2}: black circles — cw-excitation; gray circles — pulse excitation (10^{12}ph cm^{-2}). $T = 10$ K.

GaAs spacer between QW and the apex of QD. The study is aimed to investigate the interaction between electronic states and pathways of carrier transfer in HnS depending on barrier thickness B.

Figure 2 shows typical PL spectra of the HnS for two excitation modes above the GaAs barrier. For cw-excitation two PL bands are clearly observed: a first one at ∼1.355 eV is narrow (FWHM ∼20 meV) and a second one at ∼1.2 eV is rather broad (∼90 meV). They are attributed to the recombination between ground states of electron and hole (e0-h0) in the QW and the QDs, respectively. For high power pulse excitation a new PL component (QD1) appears. Its spectral position (∼1.27 eV) and power dependence allow to assign it to a transition between excited states of electron and hole (e1-h1) within the QDs.

The statistical analysis of TEM images indicates the following average parameters of the HnS components: lateral size of QD ∼18 nm, height ∼4 nm, array density ∼10^{11} cm^{-2}, QD in-

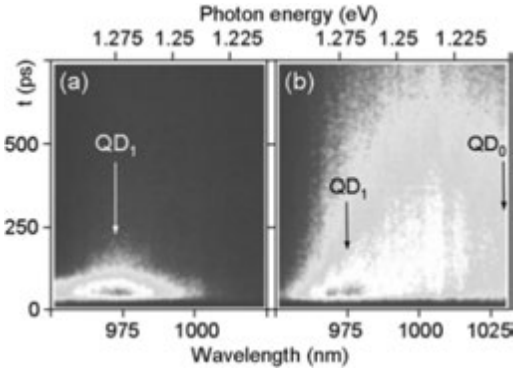

Fig. 3. Gray scale image of streak camera screens of HnS with 6.5-nm barrier for two excitation energies ($h\nu$): (a) $h\nu = 1.333$ eV (below $E_{QW} = 1.355$ eV); (b) $h\nu = 1.425$ eV (above E_{QW}). Excitation density is 10^{12} photons cm^{-2} per pulse. $T = 10$ K.

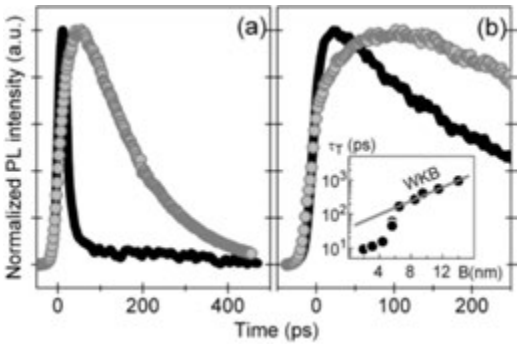

Fig. 4. TRPL profiles for two HnS with barrier thickness $B = 6.5$ nm (gray circles) and $B = 3.1$ nm (black) at 10 K: a) for QW band (excitation $h\nu = 1.6$ eV); b) for QD_0 band ($h\nu = 1.355$ eV). The excitation density was fixed at 10^{12} ph $\times$ cm^{-2} in pulse. Time zero corresponds to a maximum of laser pulse with time FWHM about 10 ps and spectral FWHM about 10 meV. Inset in Fig. 4b shows $\tau_T(B)$ dependence. The values of tunneling time τ_T were obtained from fitting TRPL profile as described in the text.

dium content $x \sim 0.6$, QW thickness ~11 nm and $x \sim 0.15$.

Using the TEM data we can tentatively describe the electronic structure of the HnS within the framework of effective mass approximation. The calculation gives for electrons in QW a barrier height of 55 meV. The calculated energy for the electron excited level in QDs with disc-like shape was found to be 20 meV higher than for electron ground state in QW, although the relationship for transition energies ($E_{QW} > E_{QD1} > E_{QD0}$) remains valid. Below we show the effect that is produced by such inverted energy offset' for the optical pumping of the active region in HnS operating the ground transition in QDs.

TRPL data of HnS with 6.5-nm GaAs barrier are presented in Figure 3 in the original form of streak camera screen-shots. The time-lambda-integrated PL signals (J) from the ground and excited states of QDs is strongly dependent on the excitation photon energy $h\nu$. The tuning of the photon energy from $h\nu < E_{QW}$ to $h\nu > E_{QW}$ (1.333 and 1.425 eV in Fig. 3a and 3b, repectively) increased the $J_0 : J_1$ ratio from 1:4 to 4:1. Taking into account the fix value of the excitation density (10^{12} photons $\times$ cm^{-2} per pulse) we come to next conclusions. Under direct pulse excitation of QDs the radiative recombination goes mainly via short-living excited states of QDs (150 ps), and the pumping of ground states is suppressed. If in tunnel proximity to the QDs lies the QW (HnS), and the light pulses generate there free carriers, an effective pumping of the QD ground state becomes possible. In that case the recombination goes mainly via QD0 with a radiative lifetime of about 750 ps. This is possible for two conditions. 1) The ground level for electrons in QW lies below the excited state of QD (inverted energy offset). 2) The tunneling of electrons from this QW level goes faster than their radiative recombination with holes in QW (420 ps). Thus we have effectively studied the tunnel transfer of electrons between QW and QDs layers in HnS.

A dependence of tunneling time (τ_T) on the barrier thickness (B) is investigated. The values of τ_T are derived from the analysis of profiles of transient PL (Figure 4). The finger-prints of the tunneling are detected, on the one hand, from decay portions of QW PL and, on the other hand, from rise portions of the QDs PL (Figures 4a and 4b, respectively). In both cases the transient PL profile is formed by two processes: radiative recombination with time τ_R and tunneling with time constant τ_T. The values of τ_R were defined from TRPL of referent samples. The values of τ_T were extracted from fitting the TRPL profile to a certain expression. In case of QW PL decay, it was the expression including two competing transitions depleting the ground states in QW. In case of QD_0 PL rise, it was the expression with two noncompeting processes.

The dependence of tunneling time on the barrier thickness for thin barriers was found to deviate from semiclassic Wentzel–Kramers–Brillouin (WKB) approximation, which was developed for the tunnel processes in coupled QWs and which remains valid for the tunneling between two QDs layers [2,3]. The deviation from the WKB approximation is observed for the barrier thickness less than 6 nm (inset in Figure 4b). In particular, for $B = 4$ nm, whereas the WKB approximation predicts a value of T about 100 ps, the tunneling time in HnS approaches to the system resolution limit ($tau_T \sim 15$ ps). Within the framework of WKB approximation for such value of τ_T in HnS the barrier in QW would be vanished. We assume that a significant reduction of the transfer time is explained by the formation of a point-contact-like channel between some QDs and QW (nano-bridges). High resolved TEM image of HnS with $B = 3.1$ nm (Figure 1c) shows such an expected contact nano-bridge with the variable indium content x and the width about 1 nm. These nano-bridges form channels of rapid carrier exchange between QDs and QW layers. Previously we observed similar contact by coalescence of two stacked InAs QDs [3]. The physical model of the carrier transfer through nano-bridge will be developed and discussed. This will pave the ways for novel HnS.

Acknowledgements

This work has been supported by the Russian Foundation for Basic Research, Program RAS "Quantum Nanostructures" and the EU Project SANDiE.

References

[1] V. P. Evtikhiev *et al*, *Semiconductors* **36**, 74 (2002).
[2] Yu. I. Mazur *et al*, *Phys. Rev. B* **71**, 235313 (2005).
[3] V. G. Talalaev *et al*, *J. Appl. Phys.* **100**, 083704 (2006).

16th Int. Symp. "Nanostructures: Physics and Technology"
Vladivostok, Russia, July 14–18, 2008

Exciton recombination in ZnMnTe quantum well structures

V. N. Katz[1], V. P. Kochereshko[1], V. F. Agekyan[2], L. Besombes[3] and G. Karczewski[4]

[1] Ioffe Physico-Technical Institute, St Petersburg, Russia
[2] V. A. Fock Institute of Physics of St Petersburg State University, St Petersburg, Russia
[3] Institut Neel,CNRS, Grenoble, France
[4] Institute of Physics Polish Academy of Sciences, Warsaw, Poland

Abstract. Photoluminescence spectra were studied from $Zn_{1-x}Mn_x$ Te/$Zn_{1-y}Mg_y$Te quantum wells structures with magnetic well and nonmagnetic barriers. A very unusual character of the Zeeman splitting of the heavy hole exciton has been found. We observed that both σ^+ and σ^- spin components are shifted to low energies with increase of magnetic field. We perform calculation of the exciton Zeeman splitting taking into account inbuilt strain in the samples. The obtained results allow us to extract some band parameters of the $Zn_{1-x}Mn_x$Te and $Zn_{1-y}Mg_y$Te with high precision.

Introduction

Optical properties of A_2B_6 semiconductor nanostructures and particularly ZnTe based nanos-tructures are a subject of recent intensive studies. Magnetic nanostructures are especially interesting because of their possible applications in spintronics. Despite that there are a lot of publications devoted to ZnTe properties there are only few papers devoted to properties of bulk semimagnetic ZnMnTe semiconductors.

Very interesting to applications objects are ZnMnTe/ZnMgTe quantum wells that have specific magnetic properties. The magnetic properties of such semiconductors as ZnMnTe are defined by *sp-d* exchange interaction between *sp* carriers and d electrons of magnetic ions. Due to the strong magnetic properties of these structures it is possible to change their bands structure in a wide range by the applied of an external magnetic field, up to transition from type-I to type-II band alignment that can represent significant interest for spin electronics. However, the properties of such structures are investigated rather weakly, and there are many ambiguities in interpretation of their optical spectra. In the present paper we study exciton radiative recombination in quantum wells ZnMgTe/ZnMnTe in magnetic fields to specify the material parameters of the band structure and characteristics of the exciton recombination.

1. Experiment and discussion

Periodic structures with magnetic quantum wells (QW) and nonmagnetic barriers $Zn_{1-x}Mn_x$Te / $Zn_{1-y}Mg_y$Te with Mn concentration in the wells of 3 and 20 percents, and Mg concentration in barriers of 35 percents were investigated. The QW width was 7.8 nm, the barrier thickness was 14 nm, the number of the periods was 100. The structures were grown by MBE method on GaAs [100] substrates. To reduce mechanical strain caused by a lattice mismatch, a ZnTe buffer layer of 3 μ thicknesses is grown directly on the substrate followed by a second layer $Zn_{0.65}Mg_{0.35}$Te of 1.5 μ thicknesses.

The spectra of circular polarized photoluminescence (PL) were studied. The PL was excited by He-Cd 442 nm laser with power density of 10 W/cm^2. The spectra were registered at temperature 4.2 K in magnetic fields up to 11 T in Faraday geometry.

Fig. 1A presents PL spectra taken from the sample with Mn concentration 3 percent in zero magnetic fields. There are

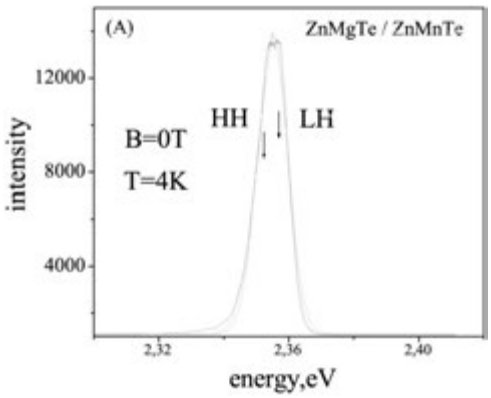

Fig. 1. Photoluminescence exciton line in zero magnetic field. HH- heavy hole exciton line, LH- light hole exciton line. Dotted lines are the result of the deconvolution of these lines into Gaussian lines.

two PL lines in the spectra. The most intensive line at 2.36 eV corre-sponds to the exciton recombination. The exciton PL line is of strongly non-Gaussian shape and contains two Gaussian components of heavy hole exciton (HH) and light hole exciton (LH). In magnetic fields each of these lines splits into (σ^+) and (σ^-) Zeeman components (Fig. 1C and Fig. 1D).

Fig. 2 shows the energy positions of HH and LH lines as a function of magnetic fields. It is clearly seen that the sign of the Zeeman splitting of the HH and LH lines is opposite. The Zeeman components for LH exciton split symmetrically to high and to low energies but the Zeeman components of the HH exciton shifts both to low energy. This looks very unusual and need special explanation.

The opposite sign of the HH and LH splitting can be explained if the value of the electron Zeeman slitting is bigger the hole Zeeman splitting because the HH exciton state with momentum $|\pm 1\rangle$ forms by hole $|\pm 3/2\rangle$ state and $|\mp 1/2\rangle$ electron state as: $|\pm 1\rangle = |\pm 3/2, \mp 1/2\rangle$ and the $|\pm 1\rangle$ LH exciton forms by $|\pm 1/2\rangle$ hole state and $|\pm 1/2\rangle$ electron state: $|\pm 1\rangle = |\pm 1/2, \pm 1/2\rangle$. To explain the same sign of the HH magnetic field shift we should have in mine that in QW the exciton Zeeman splitting depends on the fraction of the carrier wave function in the magnetic well and non-magnetic barrier.

$$E_{\pm} = \pm N_0 \widetilde{\chi} \langle S_z \rangle (\frac{1}{3} \beta J \gamma_h^{\pm} + \alpha I \gamma_l^{\pm}),$$

here:γ_l and γ_h are the probabilities to fined electron (hole) in

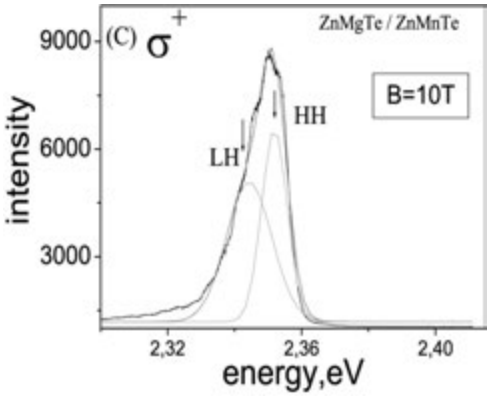

Fig. 2. Photoluminescence C) Exciton line in magnetic field of 10 T in polarization (σ^-). HH- heavy hole exciton line, LH- light hole exciton line. Dotted lines are the result of the deconvolution of these lines into Gaussian lines.

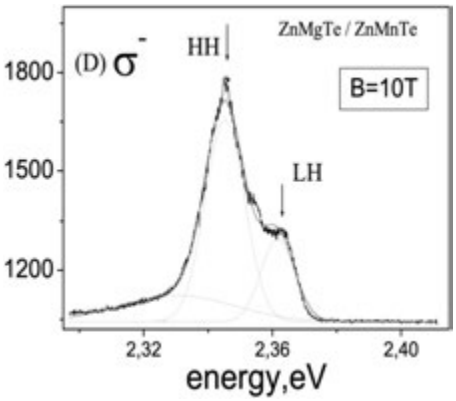

Fig. 3. Photoluminescence D) Exciton line in magnetic field of 10 T in polarization (σ^+). HH — heavy hole exciton line, LH — light hole exciton line. Dotted lines are the result of the deconvolution of these lines into Gaussian lines.

the magnetic layer. Signs + and − correspond to the opposite directions of magnetic field.

In the case if the ZnMnTe layer contains nearly 100% of the electron wave-function and less than 20% of the hole wave-function the exciton Zeeman splitting will be defined by the electron splitting. In this case the LH and HH Zeeman splitting will be of the opposite sign. This is possible in the case if our OW structure is of the type-II. We have calculate precisely the strain induced effects in our structure caused by the lattice mismatch and found that the studied structure is of type-I QW for LH and type-II QW for HH. The HH state is concentrated in the non-magnetic ZnMgTe layer with barrier height of 18 meV.

We also performed calculation of the Zeeman splitting for HH and LH excitons as a function of magnetic fields as shown in the Fig. 2 by solid line which shows a good correspondence to the experiment.

2. Conclusions

Photoluminescence spectra were studied from the structures with quantum wells based on magnetic semiconductors ZnMnTe: $Zn_{1-x}Mn_xTe$ / $Zn_{1-y}Mg_yTe$. It was found that both spin components of heavy hole exciton shift with magnetic field increase to low energies. We per-form calculations of the exciton Zeeman splitting in magnetic fields. It was established,

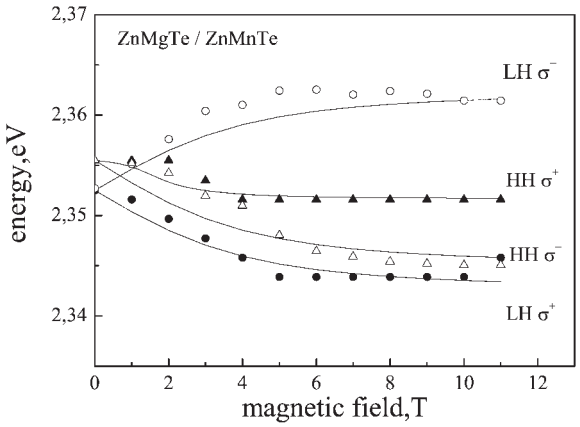

Fig. 4. Magnetic field splitting of LH and HH excitons. Symbols are experimental data, lines are calculation.

that: 1) owing to strain the investigated system has type-II band structure for heavy hole, 2) the ratio of the band offsets between conductivity and valence band is 4 to 1, 3) the exchange constants were specified for holes: $\beta N_0 = -1.16$ and for electrons $\alpha N_0 = 0.13$. Acknowledgement This work was supported in part by grants of RFBR and Presidium RAS.

References

[1] L. Ward, in *Handbook of Optical Constants of Solids II, ed. E. Palik, Academic*, New York, 737 (1991).
[2] V. F. Agekyan, I. Akai, N. G. Filosofov, T. Karasawa, G. Karczewski, A. Yu. Serov and N. N. Vasiliev, *Phys. Stat. Sol. (b)*, 1–6 (2007).
[3] E. L. Ivchenko, A. V. Kavokin, V. P. Kochereshko, G. R. Posina, I. N. Uraltsev, D. R. Yakovlev, R. N. Bicknell-Tassius, A. Waag, and G. Landwehr, *Phys. Rev. B* **46**, 7713 (1992).
[4] A. V. Kavokin, V. P. Kochereshko, G. R. Posina, I. N. Uraltsev, D. R. Yakovlev, G. Landwehr, R. N. Bicknell-Tassius, and A. Waag, *Phys. Rev. B* **46**, 9788 (1992).
[5] Landolt-Buornstein, *Numerical Data and Functional Relationships in Science and Technology*, Group III, vol. 22, ed. O. Madelung, Springer-Verlag, Berlin (1987).

16th Int. Symp. "Nanostructures: Physics and Technology"
Vladivostok, Russia, July 14–18, 2008

Evidence of Mn^{2+} fine structure in CdMnSe/ZnSe quantum dots caused by their low dimensionality

N. G. Romanov, *D. O. Tolmachev*, P. G. Baranov, R. A. Babunts, B. R. Namozov, Yu. G. Kusrayev, I. V. Sedova, S. V. Sorokin and S. V. Ivanov

Ioffe Physico-Technical Institute, St Petersburg, Russia

Abstract. Optically detected EPR of Mn^{2+} ions was measured as a variation of photoluminescence intensity of CdSe:Mn/ZnSe quantum dots under 35.2 GHz microwave irradiation. In spite of isotropic g-factor of Mn^{2+}, the anisotropic behavior of the center of gravity of EPR spectra has been observed. It was found that the EPR lines corresponding to the lowest $M_S = -5/2 \leftrightarrow M_S = -3/2$ transition dominate the spectrum because of the high Boltzmann factor at 35.2 GHz and 2 K. The axial fine structure with positive zero-field splitting in CdSe:Mn/ZnSe quantum dots is concluded to be caused by their low dimensionality.

Introduction

The most extensively studied semimagnetic semiconductors are II–VI compounds in which a fraction of the group II sublattice is replaced at random by Mn [1]. The exciting recent development in the field of semimagnetic II–VI semiconductors, presenting an entirely new physics, is the preparation of low-dimensional structures: quantum wells, superlattices and quantum dots.

The two crystal structures (zinc blende and wurtzite) are closely related, in spite of the difference in symmetry, since they are both formed with tetragonal sp^3 bonding, involving the two valence s electrons of the group II element and the six valence p electrons of the group VI elements. The ease with which Mn atoms substitute for the group II elements results from the fact that the free Mn atom has the $3d^5 4s^2$ configuration and that the $3d$ orbitals of Mn are exactly half-filled. By Hund's rule all five $3d$ spins are parallel, and considerable energy is required to add an electron with opposite spin. In this sense the $3d^5$ orbit acts as a completed shell (like $3d^{10}$ or $4d^{10}$ shells in Zn or Cd), and the Mn atoms are thus more likely to resemble a group II element. Mn can contribute its $4s^2$ electrons to the sp^3 bonding, and can therefore substitutionally replace the group II elements in tetrahedral structures. The ground state $6S$ ($S = 5/2$, $L = 0$) is spherically symmetrical and orbitally non-degenerate.

The band structure of II–VI semiconductors is modified by the exchange interaction of the localized Mn^{2+} magnetic moment (i.e. the $3d^5$ electrons) with band (i.e., sp) electrons. The sp-d exchange interaction influences physical phenomena which involve electrons in the conduction and valence bands, e.g., the giant Zeeman splitting of both the conduction and valence bands [2–4]. Electron paramagnetic resonance (EPR) is a method of choice for the study of transition ions [5]. However, direct measurements of EPR in nanostructures are difficult because of the small total number of spins, therefore optically detected magnetic resonance (ODMR) is much better suited for such systems [6].

1. Results and discussion

The samples were CdMnSe/ZnSe self assembled QD's grown by molecular-beam epitaxy on a semi-insulated GaAs(001) substrate. The concentration of Mn in the QD's was about 10%.

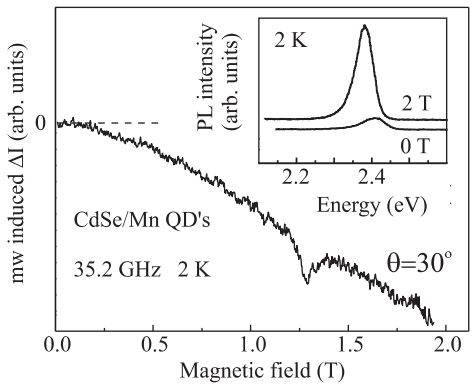

Fig. 1. PL spectra of CdSe:Mn/ZnSe QD's at zero-magnetic field and $B = 2$ T directed along the growth axis [001] (insert) and microwave-induced variations of the PL intensity plotted as a function of the magnetic field. $T = 2$ K, $\nu = 35.2$ GHz.

The QD's have a pancake shape with a lateral size much exceeding their thickness (nominally 2.1 monolayers). ODMR was investigated with the 35 GHz spectrometer operating at 1.6–2 K and providing the magnetic field up to 4.5 T. Photoluminescence (PL) was excited far above the band gap with an argon-ion laser and detected with a grating monochromator and a photomultiplier.

The PL originates from the recombination of excitons localized in CdSe:Mn QD's. The intensity of the emission strongly depends on magnetic field and temperature. At liquid helium temperatures a large increase of the integrated PL intensity with magnetic field was observed following a shift of PL maximum [7,8]. The energy of excitons in QD's varies because of sp-d interaction and finally depends on the thermal average value of the Mn^{2+} spin in the direction of the magnetic field. The PL is extremely sensitive to the state of polarization of the Mn^{2+} ions. The increase of the PL intensity with magnetic field was explained to be evoked by a spin-dependent Auger process in individual Mn^{2+} ion [8,9]. Figure 1 presents the PL spectra for zero magnetic field and $B = 2$ T (insert) and the microwave-induced variations of the PL intensity for CdSe:Mn QD's measured as a function of magnetic field at $T = 2$ K under 35.2 GHz microwave irradiation. As can be seen, the PL line shifts toward lower energies and strongly increases in intensity when magnetic field is applied. An ODMR signal corresponding to a decrease in the PL intensity was found. Figure 2

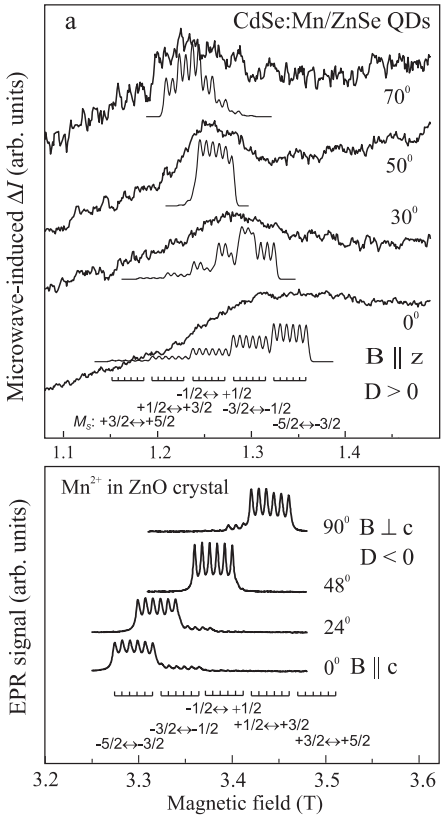

Fig. 2. (a) ODMR spectra of the CdSe:Mn QD's measured as variations of PL intensity for different orientations of the magnetic field. $T = 2$ K, $\nu = 35.2$ GHz, $P = 100$ mW, 10 kHz on-off microwave modulation. (b) The high-frequency (95 GHz) EPR spectra of Mn^{2+} ions in ZnO single crystals measured at 2 K.

(a) shows ODMR spectra of the CdSe:Mn QD's measured at different orientations of the magnetic field. The obvious angle dependence of a broad and featureless signal is observed. The signal is definitely connected with individual Mn^{2+} ions, however, g-factor of Mn^{2+} ions is known to be practically isotropic and can not give rise to an anisotropy of the ODMR signal. EPR of Mn^{2+} was measured in hexagonal CdSe single crystals [10] and was analyzed in terms of a spin Hamiltonian (without cubic terms)

$$\mathcal{H} = \mu_\beta g \mathbf{B}\mathbf{S} + A\mathbf{S}\mathbf{I} + D[S_Z - (1/3)S(S+1)]$$

with the following parameters: $g = 2.003$, $A = -62.7 \times 10^{-4}$ cm^{-1}, $D = 15.2 \times 10^{-4}$ cm^{-1}. The value of D in wurtzite crystals is dependent on the triganal (axial) distortion in these compounds. The low value of D in CdSe compared with the values found in other wurtzite crystals (e.g., $D = -240 \times 10^{-4}$ cm^{-1} in ZnO) and its positive sign were explained by an amount of covalency since the crystal fields are comparable in the wurtzite crystals. All these parameters would give the EPR spectra with an isotropic center of gravity corresponding to $g = 2$. The only case when anisotropy could be observed is low temperatures and high microwave frequencies. An example of such anisotropic behavior which could be useful for understanding of our ODMR results is presented in Fig. 2(b) where 95 GHz EPR spectra of Mn^{2+} in hexagonal ZnO crystals at 2 K are shown. One can clearly see very anisotropic behavior of the center of gravity of EPR spectra in spite of the isotropic g-factor. The spectrum exhibits the characteristic fine structure of the $S = 5/2$ electron spin and hyperfine (HF) structure due to isotropic HF interaction with the $I = 5/2$ nuclear spin of ^{55}Mn. The bars in the upper part of the Fig. 2(b) mark all EPR transitions which should be observed at high temperature in the orientation $B \parallel c$. However the set of six strong lines corresponding to the lowest $M_S = -5/2 \leftrightarrow M_S = -3/2$ transition dominates the spectrum because of the high Boltzmann factor.

The similar angular variation is observed for ODMR signals in CdSe:Mn QD's shown in Fig. 2a). In the ODMR spectra recorded at 2 K the intensities of the fine-structure components differ strongly due to the extreme difference in the populations of the spin sublevels. This result allows us to estimate the D parameter of the Mn^{2+} centers as being about 200×10^{-4} cm^{-1}. Contrary to negative sign of D in ZnO D is positive in CdSe:Mn QDs and much larger that for hexagonal CdSe bulk crystals. Since our experiments were performed at 2 K we can exclude the influence of the exchange coupled antiferromagnetic Mn^{2+}-Mn^{2+} pairs and believe that we are dealing with the high-spin ground state of individual Mn^{2+} ions. The EPR spectra of Mn^{2+} calculated with taking into account the Boltzmann distribution are shown in Fig. 2(a) below the experimental spectra. We observe mainly the transitions between the lowest energy sublevels $M_S = -5/2 \leftrightarrow M_S = -3/2$ and $M_S = -3/2 \leftrightarrow M_S = -1/2$ which positions strongly depend on the value of D. The HF structure is not resolved due to a size distribution of QD's and, as a result, a distribution of the D values. It is to be noted that a 5% dispersion of D values would be sufficient to smooth completely the HF structure. Misorientation of QDs [11] also leads to broadening of the spectra. The resonance depolarization of Mn ions at EPR transitions results in a decrease of the PL which is detected as ODMR. The effect of non-resonant microwaves on the PL intensity corresponds to the heating of the system.

The dominant property of nanostructures is their low dimensionality. To our knowledge, until now no low-symmetry effects caused by low dimensionality were observed in EPR of transition metals. We conclude that the observation of Mn^{2+} fine structure in CdSe:Mn quantum dots is caused by their low dimensionality.

Acknowledgements

This work was supported by the Programs of RAS: Spin-Dependent Effects in Solids and Spintronics, P-03 Quantum Macrophysics, Support of Innovations and Elaborations, and by St Petersburg Scientific Center.

References

[1] J. K. Furdyna, *J. Appl. Phys.* **64**, R29 (1988).
[2] A. V. Komarov *et al*, *Sov. Phys. JETP* **46**, 318 (1977).
[3] T. Wojtovich *et al*, *Phys. Rev. B* **59**, R10437 (1999).
[4] S. J. C. H. M. van Gisbergen *et al*, *Phys. Rev. B* **48**, 11767 (1993).
[5] A. Abragam, B. Bleaney, *Electron Paramagnetic Resonance of Transition Ions*, Oxford University Press, Oxford, 1970.
[6] P. G. Baranov *et al*, *Appl. Magn. Reson.* **21**, 165–193 (2001).
[7] P. R. Kratzert *et al*, Appl. *Phys. Lett.* **79**, 2814 (2001).
[8] A. V. Chernenko *et al*, *Phys. Rev. B* **72**, R2241 (2005).
[9] M. Nawroski *et al*,*Phys. Rev. B* **52**, 045302 (1995).
[10] R. S. Title, *Phys. Rev.* **130**, 17 (1963); **131**, 2503 (1963).
[11] Yu. G. Kusrayev *et al*, *Phys. Rev.* **76**, 153307 (2007).

16th Int. Symp. "Nanostructures: Physics and Technology"
Vladivostok, Russia, July 14–18, 2008

Direct-indirect transition of conduction band structure in type-I InAs/AlAs quantum dots

T. S. Shamirzaev, A. V. Nenashev and K. S. Zhuravlev
Institute of Semiconductor Physics, pr. Lavrentieva 13, 630090 Novosibirsk, Russia

Abstract. Energy structure of InAs self-assembled quantum dots (QDs) embedded in AlAs have been studied by stationary and transient photoluminescence (PL) and calculations. Stationary PL spectrum of the QDs manifests itself superposition of a low-energy (LE) and a high-energy (HE) luminescence bands related to carries recombination in QDs of different size. Transient PL demonstrates drastic decrease in the PL decay time from HE to LE bands. The experimental results evidence direct-indirect transition of conduction band structure of QDs with decreasing QD size.

Introduction

Self-assembly of semiconductor quantum dot (QDs) heterostructures with strong three-dimensional confinement is currently considered for fabrication of novel devices [1]. The majority of the studies reported so far have concentrated on In(Ga)As/GaAs material system, while the technologically similar systems of InAs/AlGaAs received much less attention. The energy structure of InAs/AlAs QDs has been scarcely studied yet. Dawson *et al* [2] propose that QDs have band alignment of type II with electrons localized in the AlAs matrix and holes localized inside the QDs. However, we demonstrate recently that even InAs/AlAs QW with nominal thickness of 1.5 monolayers has band alignment of type I with the lowest electronic state belonging to the X minimum of the conduction band [3]. Here the energy structure of InAs/AlAs QDs has been studied by stationary and transient photoluminescence (PL) and calculation.

1. Experimental

The samples of InAs QDs in an AlAs matrix studied in this work were grown by molecular beam epitaxy in a Riber-32P system. The samples consisted of one layer of the QDs sandwiched between two 25 nm thick layers of AlAs grown on top of a 200 nm buffer GaAs layer. The nominal amount of deposited InAs was equal to 2.5 monolayers. A 20 nm GaAs cap layer was grown on top of the sandwich in order to prevent oxidation of AlAs. The cw PL was excited by a He-Cd laser

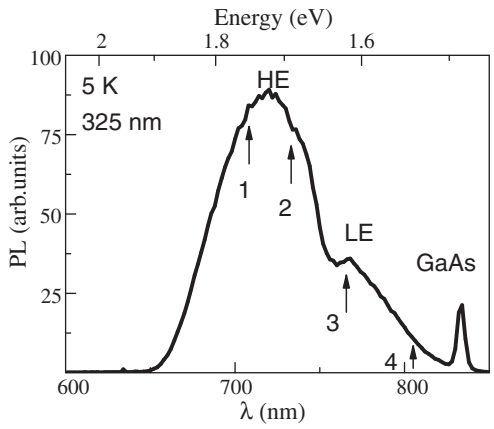

Fig. 1. Low-temperature PL spectra of InAs/AlAs QDs. Arrows mark spectral points where PL kinetics presented in Fig. 2 were measured.

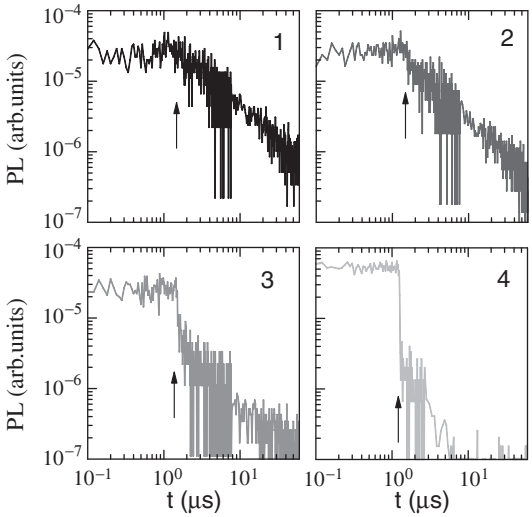

Fig. 2. PL kinetics measured at spectral points marked by arrows in Fig. 1. The arrows in this figure mark the end of a laser pulse.

($h\nu = 3.81$ eV) with a power density of 100 W/cm^2. The excitation of transient PL was accomplished by a 2-ms pulse of semiconductor laser ($h\nu = 1.87$ eV). The detection of cw and transient PL was performed by a double diffraction grating spectrometer equipped with a cooled photomultiplier operated in the photon counting mode.

2. Results

Figure 1 shows spectrum of stationary PL of InAs/AlAs QDs measured at 5 K. The spectrum contains three bands with energy 1.51 eV, 1.61 eV, and 1.73 eV marked in the figure as GaAs, LE, and HE, respectively. The band GaAs related to recombination in GaAs buffer layer, while bands LE and HE connected with recombination in QDs. Two QDs related PL bands in spectra of InAs/AlAs QDs were observed by many groups [4–7]. However, origin of these bands was not established finally. Interpretation given by authors of Ref. 5 connects the high energy PL band with excited electronic states contradicts to experimental observation of high energy band at a low excitation density [4] and appearance of low energy band at high excitation density [6]. We found that the PL kinetics of these LE and HE bands is considerably different. Actually, one can see in Fig. 2. that in spectral points across HE band the PL kinetics demonstrates a long-time decay similar to observed

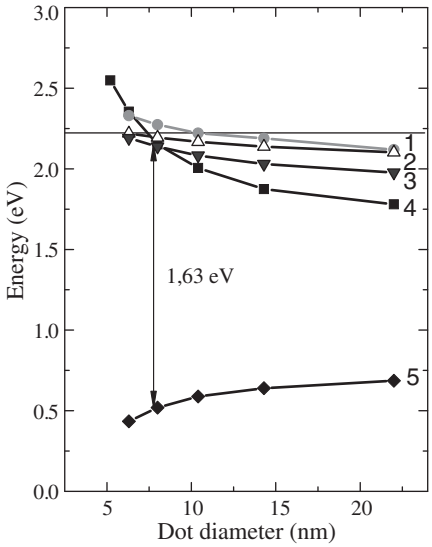

Fig. 3. Band energy structure of InAs/AlAs QDs as a function of the QD size. The line marks edge of AlAs conduction band. Energy related to: 1 — L, 2 — X_Z, 3 — X_{XY}, 4 — Γ, electronic levels and 5 — heavy hole level.

early in Ref. 2 and Ref. 4, whereas the PL intensity of LE band fast decays immediately after end of the excitation pulse with decay time being shorter than the time-resolution of our registration system (<20 ns) and then demonstrates long-time decay. This fast decay appears as a step on the kinetics curve, the amplitude of this step increases with decreasing energy of PL measurement.

In order to explain the experimental data we calculate energy structure of InAs/AlAs QDs as a function of dot size and composition using the nanodevice simulation tool NEXT NANO3 [8]. The direct and indirect minima of QD conduction band and intermixing InAs and AlAs taken into account at the calculation. The result of the calculation for QDs with composition of $In_{0.9}A_{0.1}As$ and aspect ratio of 4:1 typical for QDs grown at condition used in this study [9] presents in Fig. 3. One can see that the QDs have band alignment of type I. With decrease in QDs size a direct-indirect transition in band energy structure occurs. The calculated energy of this transition agrees with energy of crossover between LE and HE bands in the PL spectrum. The results of calculation allow us to conclude that long-time and fast PL kinetics are a result of recombination in indirect and direct band gap QDs, respectively.

Calculation demonstrates also that the energy of direct-indirect transition is a function of composition and aspect ration. Due to dispersion in size, composition and shape of QDs we have a distribution of QDs, which have different band energy structure but radiate at the same spectral point. Increase of the step in PL kinetic curves with decreasing energy of PL measurement is a result of increase in the fraction of direct band gap QDs with QD size increasing.

Acknowledgements

This work was supported by the RFBR (grants Nos. 07-02-00134, 06-02-16988) and by Dynasty Foundation.

References

[1] D. Bimberg, M. Grundmann, and N. N. Ledentsov, *Quantum Dot Heterostructures* Wiley, New York, 1999.
[2] P. Dawson *et al*, *J. Appl. Phys.* **98**, 013541 (2005).
[3] T. S. Shamirzaev *et al*, *Phys. Rev. B* **76**, 155309 (2007).
[4] T. S. Shamirzaev *et al*, *JETP Lett.* **77**, 389 (2003).
[5] Z. Ma *et al*, *Appl. Phys. Lett.* **79**, 2564 (2001).
[6] Z. Ma *et al*, *Physica E* **17**, 117 (2003).
[7] S. I. Jung *et al*, *Physica E* **26**, 100 (2005).
[8] The NEXTNANO3 software package can be downloaded from www.wsi.tum.de/nextnano3 and www.nextnano.de
[9] T. S. Shamirzaev *et al*, *Phys. Rev. B* to be published.

16th Int. Symp. "Nanostructures: Physics and Technology"
Vladivostok, Russia, July 14–18, 2008

2D-superlattices based on the adsorbed hydrogen molecules: the structure and properties

L. A. Chernozatonskii[1] and P. B. Sorokin[1,2,3]

[1] Emanuel Institute of Biochemical Physics, Russian Academy of Sciences, Kosygin st. 4, Moscow, 119334 Russia
[2] Siberian Federal University, 79 Svobodny av., Krasnoyarsk, 660041 Russia
[3] Kirensky Institute of Physics, Siberian Division, Russian Academy of Sciences, Akademgorodok, Krasnoyarsk, 660049 Russia

Abstract. The two-dimensional (2D) superlattices based on graphene with chemically adsorbed 2H arrays have been investigated. Increasing distance between hydrogen pairs in superlattices lead to semiconductor-semimetal transition. Interesting feature of such transition is the different changing of band gaps which strongly depends from the configuration of the superlattice.

Introduction

The emergence of graphene as a stable pure two-dimensional system has been one of the most important events in electronic condensed matter physics over the last years [1,2]. Until recently, the 2D paradigm was limited mostly to electrons confined to quantum wells or inversion layers in semiconductor heterostructures. The situation changed four years ago when it was found that individual atomic planes could be pulled from a graphite crystal. Despite being only one atom thick the 2D crystals remained stable and proved to be nearly high perfectly crystalline and highly conductive.

One of the many interesting properties of graphene is Dirac type of electronic band structure and the drastic changes of the conductivity of graphene-based structures with the confinement of electrons. Such confinement can be realized in graphene by introducing new boundary conditions for wavevector of electrons: periodic boundary conditions in the case of carbon nanotubes [3] and zero boundary conditions in the case of finite-width graphene strips (graphene ribbons) [4]. Also the periodical arrangement of defects (superlattice) on the graphene surface can lead to significant change of graphene's conductivity. For example, periodically closely spaced vacancies on a graphite sheet cause a significant rearrangement of its electronic spectrum. In the direction perpendicular to the vacancy lines, the spectrum exhibits a semimetal or semiconductor character [5]. The adatom defects periodically arrangement also changes the electronics structure of graphene [6].

It was shown in the papers [7,8] that the free-standing graphene ruled by lines of covalently bonded pairs of hydrogen atoms has electronic properties similar to graphene ribbons. The "zigzag" superlattice structures are semiconductors. Changing of width strip, i.e. period of such superlattice, leads to changing of the energy gap width of the 2H-line graphene-based superlattice (2HG-SL).

The possibility of forming of superlattice on graphene has been confirmed by experiments (the quasi periodical hydrogen molecule adsorption during annealing on the pyrographite surface [9]).

The two-dimensional superlattices based on graphene with chemically adsorbed 2H arrays have been investigated in this work. We have investigated the different 2H pairs arrangement on graphene surface and studied their electronic properties.

1. Method and model

Our calculations were performed using density functional theory [10,11] within the local density approximation for the exchange-correlation functional [12]. Finite-range numerical pseudoatomic wave functions were used as an atomic-orbital basis set. The geometry of the structures was optimized until residual forces became less than 0.04 eV/Å. The real-space mesh cutoff was set to at least 175 Ry. The Monkhorst–Pack [13] special k-point scheme was used with 0.08 $Å^{-1}$ k-point spacing.

We used the SIESTA package [14,15] in all calculations.

2. Results and discussion

We consider rectangular $(n, 0, k)$ 2HG-SLs. The geometric scheme of these structures is shown on Fig. 1.

Hydrogen atoms, shown in black, are covalently bound to C atoms, shown in light, forming lines perpendicular to the $(n, 0)$ direction in graphene. The H-atoms form local sp^3-hybridization between hydrogen and carbon atoms, which

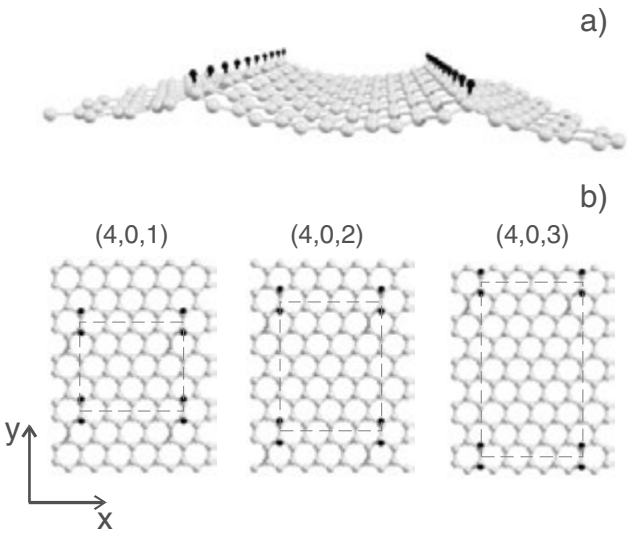

Fig. 1. a) the view of 2HG-SL; b) the schemes of hydrogen superlattice $(4, 0, k)$ — 2HG-SLs ($k = 1, 2, 3$) (the unit cell is marked by dashed rectangular).

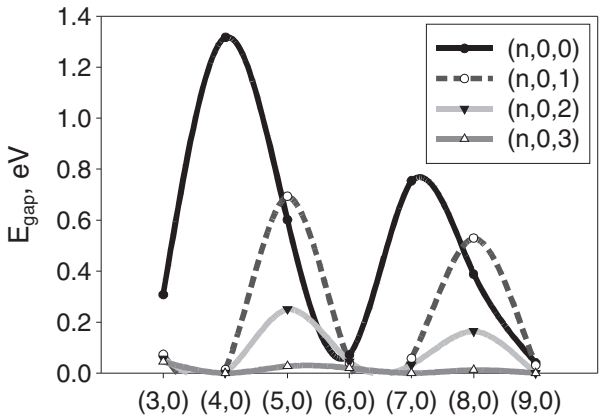

Fig. 2. The variation of band gaps of $(n, 0, k)$ — 2HG-SLs for different n number (black line with filled circles corresponds to $(n, 0, 0)$ case, dashed black line with empty circles — $(n, 0, 1)$, gray line with filled triangles — $(n, 0, 2)$ and gray with empty triangles — $(n, 0, 3)$).

causes a local geometrical distortion of the graphene sheet, as if forming diamond-like lines.

We consider rectangular $(n, 0, k)$ 2HG-SLs which have two periods: one is equal $3^{1/2}d_{\mathrm{C-C}}$ (n hexagons along x-axis, $d_{\mathrm{C-C}}$ — distance between nearest carbon atoms 1.42 Å), another is equal $3(k + 1)d_{\mathrm{C-C}}$.

The band gaps behavior with increasing SL period along x-axis is shown in the Fig. 2. Calculations have been performed for a set of $(n, 0, k)$ 2HG-SLs with $n = 3$–12 for different k ($k = 0, 1, 2, 3$). We have found that band gaps oscillate with increasing superlattice width and vanish in the infinite limit of pure, semimetallic graphene similar to carbon nanotubes [3] or graphene ribbons [4]. Also the band gaps width decreases with increasing space between hydrogen pairs (SL period along y-axis).

Interesting fact that the band gap decreases nonmonotonically for $(3n - 1, 0, k)$ 2HG-SL. The $(3n - 1, 0, k)$ 2HG-SLs have the semiconducting properties when $k < 3$ whereas superlattices with another indexes became a semimetals for any non-zero k value. The $(3n-1, 0, 1)$ 2HG-SL have bigger band gap then the $(3n - 1, 0, 0)$ 2HG-SL.

The effect of nonmonotonically decreasing of band gap of 2HG-SL with increasing k can be useful in nanoelectronics application.

The superlattices described above can be prepared by annealing hydrogen molecules on graphite surface [9] after that superlattices can be transferred over preliminarily prepared grooves, e.g., on the surface of SiO_2 [16]. Also can be used the technique proposed in the [8].

Acknowledgements

We are grateful to the Joint Supercomputer Center of the Russian Academy of Sciences for the possibility of using a cluster computer for quantum-chemical calculations, to I. V. Stankevich, L. Biro and J. Bruening for fruitful discussions. The geometry of all presented structures was visualized by ChemCraft software (http://www.chemcraftprog.com). This work was supported by the Russian Foundation for Basic Research (grant No. 08-02-01096).

References

[1] K. S. Novoselov *et al*, *Science* **306**, 666 (2004).
[2] K. S. Novoselov *et al*, *Nature* **438**, 197 (2005).
[3] *Carbon Nanotubes: Synthesis, Structure, Properties,and Applications*, Ed. by M. S. Dresselhaus, G. Dresselhaus, and Ph. Avouris (Springer, Berlin), Topics in Applied Physics, **80** 2001.
[4] Y. W. Son *et al*, *Phys. Rev. Lett*, **97**, 216803 (2006).
[5] L. A. Chernozatonskii *et al*, *Pis'ma Zh. Eksp. Teor. Fiz.* **84**, 141 (2006) [*JETP Lett.* **84**, 115 (2006)], cond-mat/0611334.
[6] E. J. Duplock *et al*, *Phys. Rev. Lett.* **92**, 225502 (2004).
[7] L. A. Chernozatonskii *et al*, *Pis'ma Zh. Eksp. Teor. Fiz.* **85**, 84 (2007) [*JETP Lett.* **85**, 77 (2007)], cond-mat/0703253.
[8] L. A. Chernozatonskii *et al*, *Appl. Phys. Letters* **91**, (2007), arXiv:0709.1015.
[9] L. Horneker *et al*, *Phys. Rev. Lett.* **96**, 156104 (2006).
[10] P. Hohenberg and W. Kohn, *Phys. Rev.* **136**, B864 (1964).
[11] W. Kohn and L. J. Sham, *Phys. Rev.* **140**, A1133 (1965).
[12] J. P. Perdew, A. Zunger, *Phys. Rev. B* **23**, 5048 (1981).
[13] H. J. Monkhorst and J. D. Pack, *Phys. Rev. B* **13**, 5188 (1976).
[14] P. Ordejon *et al*, *Phys. Rev. B* **53**, R10441 (1996).
[15] J. M. Soler *et al*, *J. Phys.: Condens. Matt.* **14**, 2745 (2002).
[16] J. S. Bunch *et al*, *Science* **315**, 490 (2007).

16th Int. Symp. "Nanostructures: Physics and Technology"
Vladivostok, Russia, July 14–18, 2008

Elastic anisotropy in quantum dots and wires: analytical treatment

A. V. Nenashev, E. A. Duljaninova and A. V. Dvurechenskii
Institute of Semiconductor Physics, Novosibirsk, Russia

Abstract. An analytical approach for strain distribution calculation in quantum dots and quantum wires, taking elastic anisotropy into account, is suggested. The approach is based on our previous method, relating to an isotropic case [1,2], and on anisotropic elastic Green's functions by Faux and Pearson [3]. The structure under study is an two-dimensional (quantum wire) or a three-dimensional (quantum dot) inclusion buried in infinite lattice-mismatched media (a matrix). The shape of the inclusion is an arbitrary polygon (in 2D) or polyhedron (in 3D). The elastic moduli of the inclusion are the same as ones of matrix. Lattice mismatch is an origin of built-in elastic strain. Our goal is to develop an analytical expression for the strain tensor, as a function of position vector.

We found the strain distribution in a structure with small anisotropy, with accuracy to the first-order correction. For simplicity, we restrict ourselves to the case of cubic anisotropy. Our solution has a simple structure: it is a sum of contributions related to faces and edges of the inclusion surface. A contribution of each face is proportional to the solid angle at which the face is seen from the point where the strain is calculated. Edge contributions are more complicated, and we present them only for the case of quantum-wire-like inclusion.

Our results provide an extremely fast method for calculation of strain distribution, in comparison with commonly used finite-element and finite-difference methods.

Introduction

From a point of view of elasticity theory self-assembled quantum dots are three-dimensional lattice-mismatched inclusions of one material in another one (matrix). The lattice mismatch is an origin of a built-in strain field. Knowledge of the strain distribution has a crucial importance for analysis of electronic structure of quantum dots (especially of type-II dots).

There are a lot of theoretical works considering the strain distribution in quantum-dot and quantum-wire structures (see review [4,5]). But an analytical closed form solutions, taking into account an elastic anisotropy, was not found so far, except a trivial case of 2D layer.

The aim of our paper is to develop an approach that allows of constructing the solutions for strain distribution in an anisotropic media.

The problem considered in our paper is the following. There is an infinite elastically anisotropic medium (a matrix) with a finite polyhedron-shaped inclusion. Cubic anisotropy is assumed. The crystal lattice of the inclusion matches the lattice of the matrix without any defects. Elastic moduli of the inclusion are assumed to be equal to that of the matrix, but the inclusion has a different lattice constant. This produces an elastic strain in both the inclusion and the matrix, and the task is to determine the strain tensor as a function of coordinates, $\varepsilon_{ij}(\mathbf{r})$.

1. The method

Our approach starts from expression of strain tensor via Green's tensor G_{ij} by Faux and Pearson [3]:

$$\varepsilon_{ij}(\mathbf{r}) = \varepsilon_0 \int_V G_{ij}\left(\mathbf{r}-\mathbf{r}'\right) d\mathbf{r}',$$

where V is the inclusion volume, and ε_0 is lattice mismatch. These authors found a series expansion for Green's tensor

$$G_{ij} = G_{ij}^{(0)} + \Delta G_{ij}^{(1)} + \Delta^2 G_{ij}^{(2)} + \ldots,$$

where expansion coefficient $\Delta = (C_{11} - C_{12} - 2C_{44})/(C_{12} + 2C_{44})$ is a measure of anisotropy ($\Delta \approx -1/3$ for typical semiconductors), C_{11}, C_{12} and C_{44} are elastic moduli. Each term of this expansion can be presented as a combination of partial derivatives of expressions like $1/r$, x^2/r, etc. For example, isotropic term is

$$G_{ij}^{(0)}(\mathbf{r}) = -\frac{\varepsilon_0}{4\pi}\,\frac{3C_{12}+2C_{44}}{C_{12}+2C_{44}}\,\frac{\partial^2}{\partial x_i \partial x_j}\,\frac{1}{r},$$

xx-component of first-order correction, $G_{xx}^{(1)}$ is a linear combination of the following terms:

$$\frac{\partial^2}{\partial x^2}\,\frac{1}{r}, \quad \frac{\partial^3}{\partial x^3}\,\frac{x}{r}, \quad \frac{\partial^4}{\partial x^4}\,\frac{x^2}{r}, \quad \frac{\partial^4}{\partial x^2 \partial y^2}\,\frac{y^2}{r}, \quad \frac{\partial^4}{\partial x^2 \partial z^2}\,\frac{z^2}{r}.$$

As a result, strain tensor $\varepsilon_{ij}(\mathbf{r})$ expresses as a combination of integrals like these:

$$\frac{\partial^2}{\partial x^2}\int_V \frac{1}{\mathbf{r}-\mathbf{r}'}\,d\mathbf{r}', \quad \frac{\partial^3}{\partial x^3}\int_V \frac{x'}{\mathbf{r}-\mathbf{r}'}\,d\mathbf{r}', \quad \ldots \qquad (1)$$

Our previous work [1] provides an effective method of evaluation of integrals like (1). The method utilizes an analogy between the elastic problem and some electrostatic problems. Namely, the integrals (1) ourselves can be regarded as electrostatic potentials induced by an uniformly or non-uniformly charged inclusion. Taking the derivatives in (1), one proceeds from "volume charge" to "surface dipoles" on faces of the inclusion surfaces, and to "linear charges" on its edges. Thus, our method allows to split the strain tensor into contributions of faces and edges of inclusion surface (assuming that inclusion shape is a polyhedron):

$$\varepsilon_{ij}(\mathbf{r}) = \sum_f A_{ij}^{(\mathrm{f})}(\mathbf{r}) + \sum_{\mathrm{e}} B_{ij}^{(\mathrm{e})}(\mathbf{r}), \qquad (2)$$

where indices f and e run over all feces and edges, correspondingly. Some explicit formulas for contributions $A_{ij}^{(\mathrm{f})}$ and $B_{ij}^{(\mathrm{e})}$ in (2) will be presented in the next section.

Quantum wires can be considered as special cases of polyhedral-shaped inclusions. So, the solution in the form (2) is valid not only for quantum dots, but also for quantum wires.

2. Results

The strain tensor in an *isotropic* case was obtained (in the form (2)) in our previous papers [1, 2]. Now we focus on *anisotropic* first-order corrections to the strain tensor.

A correction for the face-related term $A_{ij}^{(\mathrm{f})}$ is proportional to the solid angle $\Omega_f(\mathbf{r})$ at which the face f is seen from the point $\mathbf{r}$:

$$A_{xx}^{(\mathrm{f})} = -\frac{\varepsilon_0\Delta}{4\pi}\Omega_f(\mathbf{r})\left(1+\frac{(n_x^4+n_y^4+n_z^4)(2\mu^2+5\mu\lambda+3\lambda^2)}{\mu(2\mu+\lambda)} - \frac{n_x^2(4\mu^2+8\mu\lambda+3\lambda^2)}{\mu(2\mu+\lambda)}\right)n_x^2,$$

$$A_{xy}^{(\mathrm{f})} = -\frac{\varepsilon_0\Delta}{4\pi}\Omega_f(\mathbf{r})\left(1+\frac{(n_x^4+n_y^4+n_z^4)(2\mu^2+5\mu\lambda+3\lambda^2)}{\mu(2\mu+\lambda)} - \frac{(n_x^2+n_y^2)(4\mu^2+8\mu\lambda+3\lambda^2)}{2\mu(2\mu+\lambda)}\right)n_x n_y,$$

the other components $A_{yy}^{(\mathrm{f})}$, $A_{zz}^{(\mathrm{f})}$, $A_{xz}^{(\mathrm{f})}$, and $A_{yz}^{(\mathrm{f})}$ have an analogous form. There n_x, n_y and n_z are components of the normal vector to the face f; $\lambda \equiv C_{12}$, $\mu \equiv C_{44}$. The solid angle $\Omega_f(\mathbf{r})$ is taken with positive sign if the point $\mathbf{r}$ is at the outer side of the face f, and with negative sign otherwise.

Expressions for edge-related corrections are cumbersome in the general form. We present there only corrections for quantum-wire-like inclusion oriented along the axis z:

$$B_{ij}^{(\mathrm{e})} = \frac{\varepsilon_0\Delta}{4\pi}\left(\Phi_{ij}(\mathbf{r}-\mathbf{r}_\mathrm{e},\theta_{\mathrm{e}1}) - \Phi_{ij}(\mathbf{r}-\mathbf{r}_\mathrm{e},\theta_{\mathrm{e}2})\right),$$

where $\theta_{\mathrm{e}1}$ and $\theta_{\mathrm{e}2}$ are angles between the axis x and directions of two faces which intersect at the edge e (see Fig. 1);

$$\begin{aligned}
\Phi_{xx}(\mathbf{r},\theta) &= \log r\left(-2a_1+\frac{a_2}{2}\cos 2\theta+\frac{a_3}{4}\cos 4\theta\right)\sin 2\theta \\
&\quad -\left(\frac{a_2}{2}+\frac{a_3}{4}\right)\cos\varphi\cos(\theta+\varphi) \\
&\quad +a_3\left(2\cos(3\theta+\varphi)+\cos(\theta+3\varphi)\right)\sin\theta, \\
\Phi_{yy}(\mathbf{r},\theta) &= \log r\left(2a_1+\frac{a_2}{2}\cos 2\theta-\frac{a_3}{4}\cos 4\theta\right)\sin 2\theta \\
&\quad -\left(-\frac{a_2}{2}+\frac{a_3}{4}\right)\cos\varphi\cos(\theta+\varphi) \\
&\quad +a_3\left(2\cos(3\theta+\varphi)+\cos(\theta+3\varphi)\right)\sin\theta, \\
\Phi_{xy}(\mathbf{r},\theta) &= \log r\left(-2a_1+\frac{a_2}{2}+\frac{a_3}{4}+\left(2a_1-\frac{a_2}{2}-\frac{a_3}{8}\right)\cos 2\theta\right. \\
&\quad \left.-\frac{a_3}{8}\cos 6\theta\right)-\frac{a_3}{4}\left(\sin(\theta+\varphi)+2\sin(3\theta+\varphi)\right. \\
&\quad \left.+\sin(\theta+3\varphi)\right)\cos\varphi\sin\theta, \\
\Phi_{xz} &= \Phi_{yz} = \Phi_{zz} = 0,
\end{aligned}$$

$$a_1 = \frac{\lambda}{\lambda+2\mu}, \quad a_2 = \frac{3\lambda+2\mu}{\lambda+2\mu}, \quad a_3 = \frac{(\lambda+\mu)(3\lambda+2\mu)}{\mu(\lambda+2\mu)},$$

φ and r are polar coordinates of a vector joining the edge e with the point $\mathbf{r}$ (see Fig. 1).

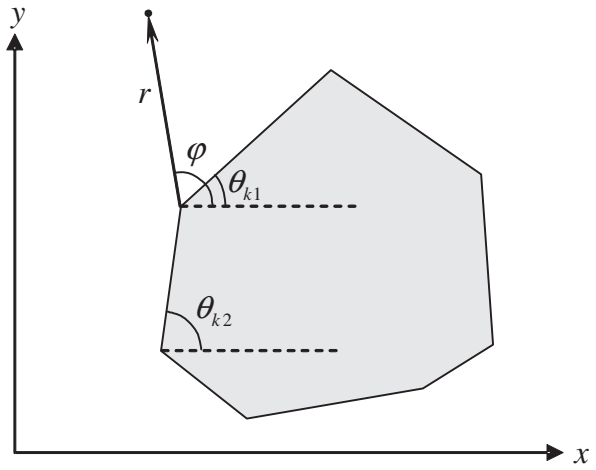

Fig. 1. Schematic sketch of a quantum-wire-like inclusion.

3. Summary

We propose an analytical method for evaluation the strain field inside and around an inclusion in an infinite *anisotropic* medium. We believe that this method will be an useful tool for electronic structure calculation, because analytical calculations take much less computer resources (CPU time and memory) than numerical ones.

Acknowledgements

The authors thank A. F. Zinovieva for fruitful discussions. This work was supported by RFBR (grant 06-02-16988) and the Dynasty foundation.

References

[1] A. V. Nenashev and A. V. Dvurechenskii, arXiv:0707.2183 (2007).
[2] A. V. Nenashev and A. V. Dvurechenskii, Proc. 15-th Int. Symp. "Nanostructures: Physics and Technology", p. 226 (2007).
[3] D. A. Faux and G. S. Pearson, *Phys. Rev. B* **62**, 4798 (2000).
[4] J. Stangl, V. Holý, and G. Bauer, *Rev. Mod. Phys.* **76**, 725 (2004).
[5] R. Maranganti and P. Sharma, *Handbook of Theoretical and Computational Nanotechnology*, Chapter 118 (2006).

16th Int. Symp. "Nanostructures: Physics and Technology"
Vladivostok, Russia, July 14–18, 2008

Effect of interdiffusion and quantum confinement on Raman spectra of the Ge/Si(100) heterostructures with quantum dots

I. V. Kucherenko[1], V. S. Vinogradov[1], N. N. Melnik[1], L. V. Arapkina[2], V. A. Chapnin[2], K. V. Chizh[2] and V. A. Yur'ev[2]

[1] Lebedev Physical Institute RAS, 119991 Moscow, Leninsky pr. 53, Russia
[2] Prokhorov General Physics Institute RAS, 119991 Moscow Vavilova str. 38, Russia

Abstract. We used Raman scattering for study the phonon modes of self-organized Ge/Si quantum dots, grown by a molecular-beam-epitaxy method. It is revealed, that Ge-Ge and Si-Ge vibrational modes considerably intensify at excitation of exciton between the Λ_3 valence and Λ_1 conduction bands (transitions E_1 and $E_1 + \Delta_1$), that allows to observe Raman scattering spectrum from extremely small volumes of Ge, even from one layer of quantum dots with the layer thickness of ~10 A. It is shown that Si diffuses into the Ge quantum dots from the Si spacer layers forming Ge_xSi_{1-x} solid solution, and Si concentration was estimated. It is revealed, that the frequency of Ge-Ge mode decreases in 10 cm^{-1} at decreasing the Ge layer thickness from 10 up to 6 A as a result of phonon size confinement effect.

We have utilize Raman scattering (RS) to study the phonon modes in Ge/Si structures with self-organized Ge quantum dots (QDs). These structures consisting of 5 periods were grown by molecular-beam epitaxy (MBE) on a (001) p-type Si substrate with a residual gas pressure of 5×10^{-10} Torr. The growth chamber was integrated with a scanning tunneling microscope (STM) GPI-300 for analysis of QD shape and size. The Ge layers with an effective thickness in the range of 4–18 A were grown at 350 °C. Each Ge layer was covered with a 50 nm undoped Si layer deposited at 530 °C. According to STM-investigations hut-clusters are forming on Si (100) surface for the Ge layer thicknesses of 6–12 A. Varying the thickness of the Ge layer we can obtain structures with quantum dots of different size with height (h) of 0.6–1.5 nm and dimensions in the growth plane (l) of 6–15 nm.

The QD density is $\sim 5 \times 10^{11}$ cm^{-2}. Typical STM-image of the sample with $h_{Ge} = 10$ A is presented in Fig. 1. STM-image is obtained for the tunneling current $I_t = 0.1$ nA and voltage $V_t = +2.1$ V.

Raman spectra were exited by an Ar-ion laser with the wavelength $\lambda = 514.5$; 488 nm and He-Cd laser with $\lambda = 441.6$ nm. The scattered spectra were analyzed at room temperature with U-1000 spectrometer with resolution of 1 cm^{-1}.

It is well known that in Ge/Si nanostructures with Ge QDs three main peaks are dominated: peak at $f = 520$ cm^{-1}, peak near $f = 300$ cm^{-1}, and the band in the vicinity of 400 cm^{-1}. These frequencies are related to Si-Si, Ge-Ge and Ge-Si vibrations. Frequency dependences of Ge-Ge and Ge-Si modes and their line widths on the effective thickness of Ge layers (h_{Ge}) are studied in this paper. Frequencies of Ge-Ge modes in the samples with $h_{Ge} \geq 10$ A exceed frequency of the same mode of bulk Ge crystals by ~12 cm^{-1} due to elastic strains in the growth plane. But we observed decrease of Ge-Ge mode frequencies from 312 to 301 cm^{-1} while h_{Ge} decreases from 10 to 6 A (Fig. 2). The smallest line width (8 cm^{-1}) corresponds to $h_{Ge} = 9$ and 10 A. In these samples hut cluster size dispersion is minimal.

We studied influence of wetting and spacer layers on the RS spectra of the structures. For this purpose Ge/Si structure with 4 A Ge layers but before formation of QDs (similar to

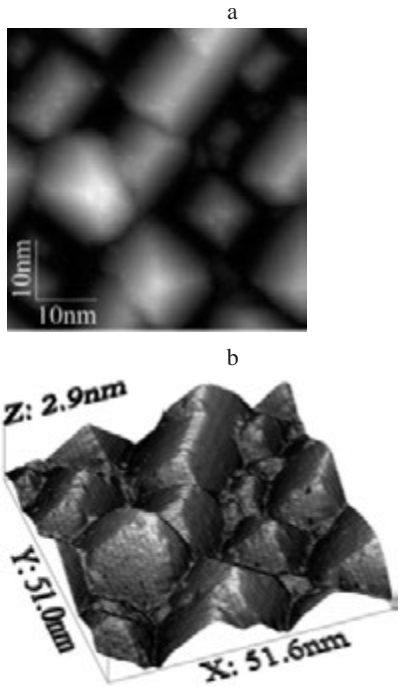

Fig. 1. Two-dimensional (a) and three-dimensional (b) STM-images of Ge hut-clusters on Si (001) surface; effective thickness of the Ge layers is 10 A.

wetting layers) were grown. It is shown that contribution from Ge layers of this sample into Raman spectrum can be ignored. Comparison of Raman spectra of two samples consisting of one 10 A Ge dot layer, uncapped and caped with 50 nm Si layer (spacer), clearly shows that interdiffusion between Si spacer layer and Ge dots takes place during growth. Both Ge-Ge and Ge-Si phonon modes are found to exhibit strong enhancement in capped sample, and the width of their lines is narrow (7–8 cm^{-1}). We relate this enhancement to strong interaction between these modes and E_1 exciton. Energy of E_1 transition ranges up to about 2.6 eV in Ge_xSi_{1-x} solid solution at $x = 0.65$ [1]. This energy is in resonance with the laser excitation energy $E = 2.54$ eV ($\lambda = 488$ nm). According to our estimations the amount of Si in Ge QDs is about 35% due to

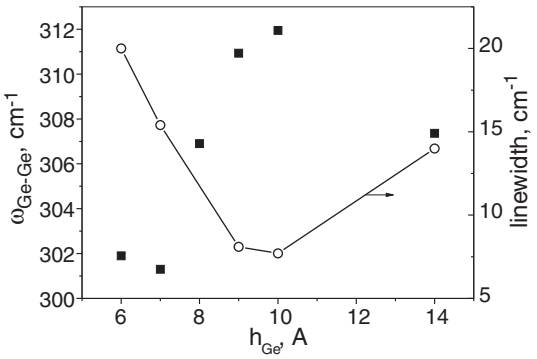

Fig. 2. Dependences of frequency and line width of Ge-Ge mode on the effective thickness of Ge layer. Full squares designate frequencies of Ge-Ge mode.

strong Si-Ge intermixing. The dependence of the Ge-Ge mode intensity on the laser wavelength also proves a resonant character of RS, the highest intensity of this mode corresponds to $\lambda = 488$ nm. Due to resonance Raman scattering it is possible to obtain spectra even from one dot layer. It is shown that Raman spectra have resonance character in the Ge/Si structures with $h_{\mathrm{Ge}} = 9$ and 10 A at Si concentration inside dots about 34%. Concentration of Si inside the dots was obtained from the integral intensity ratio of Ge-Ge and Ge-Si modes [2]. Si concentration remains $\sim$34% in the range of $h_{\mathrm{Ge}} = 6 - 10$ A.

We observed decrease of Ge-Ge mode frequency up to 5 cm^{-1} with decrease of the laser wave length (514.5, 488 and 441.6 nm). This result correlates with [3]. We explain this phenomenon by size dispersion of QDs in our samples. At high excitation energy ($\lambda = 441.6$ nm) small QDs give resonant contribution into RS spectra, and according to Fig. 2 small QDs have less Ge-Ge mode frequency.

Nonmonotonic dependence of Si-Si mode intensity on the effective Ge layer thickness is observed at excitation by Ar^+ laser with $\lambda = 488$ nm: line intensity is the smallest in the samples in which resonance Raman scattering of Ge-Ge and Ge-Si modes occurs and absorption in Ge layers is high ($h_{\mathrm{Ge}} =$ 8, 9 and 10 A).

In conclusion, the effect of different factors on RS spectra in Ge/Si structures with QDs of hut shape is analyzed: interdiffusion, elastic strain and phonon quantum confinement. It is shown that Si diffuses into Ge quantum dot from the lying above Si spacer through faces and edges of pyramid where elastic strains and concentration gradient are highest. As the concentration of Si in QDs remains approximately constant in the samples with $h_{\mathrm{Ge}} =$ 6–10 A, and elastic strains do not depend on the size of QD [4], we came to the conclusion that reduction of the Ge-Ge mode frequency (by about 10 cm^{-1}) with decrease of h_{Ge} in the range of 10–6 A is due to the phonon confinement effect. Using approximation of LO [100] dispersion relation of Ge [5] in the range of wave vectors $q/q_{\max} = 0-1/2$ by the expression $\omega = \omega_0[1 - \alpha(q/q_{\max})^2]$, where $q = \pi/d$, $q_{\max} = \pi/a_{\mathrm{Ge}}$, a_{Ge} is Ge lattice constant, $\alpha = 8/15$ we obtained for our data $\omega_0 = 312$ cm^{-1} and $\Delta\omega = -10$ cm^{-1} the size of the confinement region $d = 23$ A. This value is close to the length of cube which volume equal to pyramidal volume with $h = 6$ A and $l = 100$ A.

Acknowledgements

The work was supported by the Basic Research Foundation (grant No. 07-02-00899-a), by the Basic Research Program "Quantum Nanostructures" RAS (N5.4 Vin) and by the Federal Agency on Science and Innovations of the Ministry of Education and Science of RF (state contract No. 02.513.11.3130).

References

[1] U. Schmid, N. E. Christensen, and M. Cardona, *Phys. Rev. B* **41**, 5919 (1990).
[2] V. A. Volodin, A. I. Yakimov, A. V. Dvurechenskii *et al*, *Semiconductors* **40**, 207 (2006).
[3] A. G. Milekhin, A. I. Nikiforov, O. P. Pchelyakov, S. Schulze, and D. R. T. Zahn, *Nanotechnology* **13**, 55 (2002).
[4] A. V. Nenashev, A. V. Dvurechenskii, *JETF* **118**, 570 (2000).
[5] B. N. Brockhouse and P. K. Iyengar, *Phys. Rev. B* **111**, 747 (1958).

16th Int. Symp. "Nanostructures: Physics and Technology"
Vladivostok, Russia, July 14–18, 2008

Nonlinear optical properties of solutions and films of CdSe nanoparticles with ZnS shell

K. V. Zakharchenko[1], A. A. Chystyakov[1], V. A. Karavanskii[2], V. I. Krasovskii[2] and *A. V. Kulikovskiy*[2]

[1] Moscow institute of Engineering and Physics (Technical University), Solid-state physics department
[2] A. M. Prokhorov General Physics Institute of the Russian Academy of Sciences

Abstract. We present the results of nonlinear optical properties investigation of solutions and naturally deposited films of CdSe/ZnS nanoparticles [1] using z-scan technique [2] on wavelength $\lambda = 532$ nm and pulse duration $\tau = 350$ ps. Nonlinear optical absorption and refraction coefficients and saturation intensity were calculated in terms of model [2]. The values of nonlinear optical susceptibilities $\chi^{(3)} \sim 10^{-11}$ esu under volume fraction of nanoparticles $\sim 10^{-3}$ and $\chi^{(3)} \sim 10^{-6}$ esu were obtained in solutions and films, respectively. Obtained values are explained by enhanced lifetimes of initiated careers due to defects correction by ZnS shell. Nonlinear optical properties of measured films show the extremely high values of third-order nonlinear optical susceptibility ($\sim 10^{-5}$ esu), which can be explained by enhanced effective concentration of nanoparticles and dipole interaction of nanoparticles in film.

CdSe nanoparticles with ZnS shell show the unique properties due to the careers quantum confinement. There are currently receiving technology monodisperse ensembles of nanoparticles CdSe/ZnS. Nanoparticles are promising material for producing a fluorescent tags and sensors that can compete with conventional organic dyes. However, the study of nanoparticles condensates CdSe/ZnS is of the growing interest. In terms of basic science, film nanoparticles are solid body of artificial atoms, and study their properties is interesting and urgent task. Furthermore, the establishment of nanoparticles film opens prospects for the development of tunable lasers, new optoelectronic devices for different areas of science and technology.

Experimental samples 1 and 2 were prepared from CdSe/ZnS nanoparticle powder in water solution with volume concentration 1×10^{15} cm^{-3}. Sample 3 was prepared by deposition of nanoparticles with 4 nm diameter on glass plate from chloroform solution [1]. Film thickness calculated from interference peaks in absorption spectrum was 100 nm. Absorption spectra of experimental samples are presented on Fig. 1.

Mean radii of nanoparticles obtained from absorption spectra energy level structure using expression (1) [3] was 3.2 and 4 nm for samples 1 and 2. The absorption peaks position for nanoparticles with 3.2 nm diameter are 528 nm and 538 nm, and

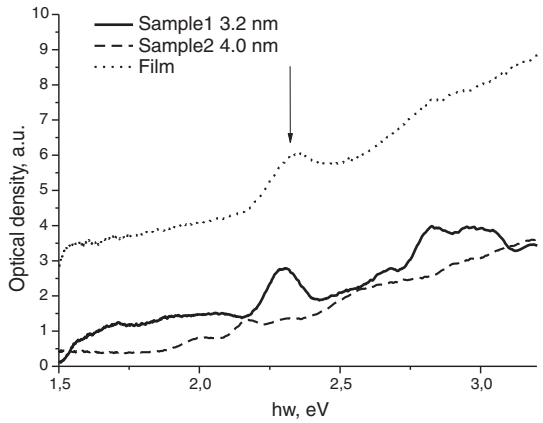

Fig. 1. Optical density spectra of CdSe/ZnS nanoparticles in chloroform solutions and film.

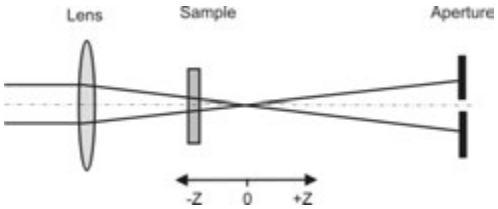

Fig. 2. Z-scan schematic.

for nanoparticles with 4 nm diameter — 562 nm and 470 nm, correspond to optical transitions between quantum confinement levels.

$$\hbar\omega = E_g + \frac{\hbar^2}{2a^2}\left(\frac{\alpha^2_{(n_e,l_e)}}{m^*_e} + \frac{\alpha^2_{(n_h,l_h)}}{m^*_h}\right) - \frac{e^2}{\varepsilon a}, \qquad (1)$$

where $\hbar\omega$ — energy of excited state, equal to photon energy, E_g — band gap energy of CdSe, $E_g = 1.78$ eV; a — nanoparticle radius; n_e, l_e, n_h, l_h — quantum numbers for electron an hole; $\alpha_{n,l}$ — n-th root of Bessel function $J_l(x)$; ε — dielectric constant of CdSe, $\varepsilon = 5.8$.

Nonlinear optical properties were measured by z-scan technique [2]. Experimental geometry is presented on Fig. 2. Second harmonic of Q-switched Nd laser was used with pulse duration $\tau = 350$ ps and pulse energy $E_0 = 24$ μJ with 20 Hz repetition rate. Gaussian beam waist radius $w_0 = 34$ μm. In accordance to [3], the transmittance of sample in z-scan geometry is given by:

$$T(z) = 1 + \Delta T_{\Delta\Phi_0}(z) + \Delta T_{\Delta\Psi_0}(z), \qquad (2)$$

where $\Delta\Phi_0$ — beam phase modification in focal plane,

$$T_{\Delta\Psi_0}(z) = -\left[(z/z_0)^2 + 3\right] \times \left[(z/z_0)^2 + 9\right]^{-1}\left[(z/z_0)^2 + 1\right]^{-1}\Delta\Psi_0, \qquad (3)$$

$\Delta\Psi_0$ — beam amplitude modification in focal plane,

$$T_{\Delta\Phi_0}(z) = 2(z/z_0)\left[(z/z_0)^2 + 9\right]^{-1}\left[(z/z_0)^2 + 1\right]^{-1}\Delta\Phi_0, \qquad (4)$$

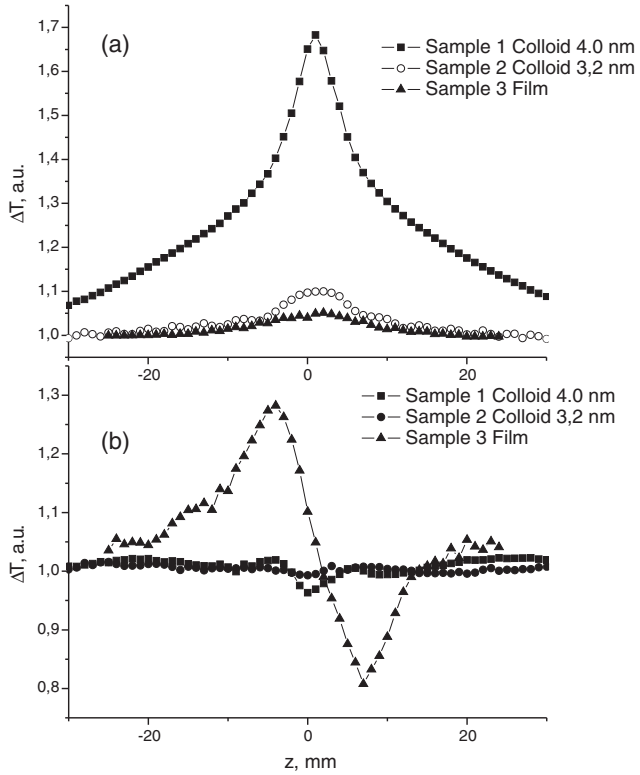

Fig. 3. Measured z-scan curves: without aperture (a), with aperture (b).

$L_{\text{eff}} = \frac{1-e^{-\alpha L}}{\alpha}$ — effective sample thickness, $\alpha = \alpha_0 + \frac{\alpha_2}{2} I$, $n = n_0 + \frac{n_2}{2} I$, $\chi^{(3)} = \chi_{\text{R}}^{(3)} + i\chi_{\text{I}}^{(3)}$, $\chi_{\text{I}}^{(3)} = \frac{n_0^2 \varepsilon_0 c^2}{\omega}\alpha_2$, $\chi_{\text{R}}^{(3)} = 2n_0^2\varepsilon_0 c n_2$, $\Delta\Psi_0 = \alpha_2 I_0 f(t) L_{\text{eff}}$, $\Delta\Phi_0 = k n_2 I_0 L_{\text{eff}} f(t)\alpha$ — linear absorption coefficient, L — sample thickness, n_0 — linear refraction coefficient, k — wave number, I_0 — intensity of laser beam in focal plane, z_0 — diffraction beam length.

Measured z-scan curves are shown on Fig 3. Using (2)-(4) real and imaginary parts of nonlinear optical susceptibilities were calculated as parameters. Obtained values of $\chi^{(3)}$ module was 2–6 $\times 10^{-11}$ esu for colloids and 2–6 $\times 10^{-6}$ esu for films. The absolute values of $\chi^{(3)}$ are determined by Re $\chi^{(3)}$ in colloids and Im $\chi^{(3)}$ in film. The sign change of imaginary part of nonlinear optical susceptibility depended on excitation pulse and first energy level predicted by 2-level model. Obtained values can be explained by enhanced lifetimes of initiated careers due to defects correction by ZnS shell. The nonlinear optical properties of measured films show the extremely high values of third-order nonlinear optical susceptibility ($\sim 10^{-6}$ esu), which can be explained by enhanced effective concentration of nanoparticles and dipole interaction of nanoparticles in film.

The results of nonlinear optical properties investigation of solutions and naturally deposited films of CdSe/ZnS nanoparticles using z-scan technique on wavelength $\lambda = 532$ nm and pulse duration $\tau = 350$ ps. The values of nonlinear optical susceptibilities $\sim 10^{-11}$ esu, under nanopatricles volume fraction of $\sim 10^{-3}$ obtained in solutions. Nonlinear optical absorption and refraction coefficients and saturation intensity calculated in terms of two-level model with saturation. Obtained values explained by enhanced lifetimes of initiated careers due to defects correction by ZnS shell. The nonlinear optical properties of measured films shows the extremely high values of third-order nonlinear optical susceptibility ($\sim 10^{-6}$ esu), which can be explained by enhanced effective concentration of nanoparticles and dipole interaction of nanoparticles in film.

Acknowledgements

This work supported by RFFI grant No. 07-02-12116-OFI.

References

[1] A. Chistyakov *et al*, *Laser Physics* **16**, 1625 (2006).
[2] M. Sheik-Bahae *et al*, *IEEE Journal of Quantum Electronics* **26**, 760 (1990).
[3] M. Yin *et al*, *Appl.Phys. B* **70**, 587 (2000).

16th Int. Symp. "Nanostructures: Physics and Technology"
Vladivostok, Russia, July 14–18, 2008

Shining silicon nanopowder with photoluminescence in blue-red region of light emission

M. D. Efremov[1], V. A. Volodin[1], D. V. Marin[1], S. A. Arzannikova[1] and S. P. Bardakhanov[2]

[1] Institute of Semiconductor Physics of SB RAS, pr. ak. Lavrentjeva 13, Novosibirsk 630090, Russia
[2] Institute of Theoretical and Applied Mechanics SB RAS, Institutskaya str. 4/1, Novosibirsk 630090, Russia

Abstract. Silicon nanopowder was manufactured using electron beam, melting of silicon ingots and following gathering of silicon into spherical balls in a flow of a gas [1]. Different gas atmosphere was used in experiment: oxygen, nitrogen and argon. In oxygen atmosphere full oxidation of silicon occurs usually, whereas in argon and nitrogen atmosphere silicon balls remain partially not oxidised. Raman spectra proved presence of silicon in crystalline form, giving estimation of size for silicon nuclei about 2 nm. High-resolution electron microscopy reveals quite abrupt boundary between crystalline silicon and silicon dioxide within 2 nm range. In spite of displaying very broad dispersion for some series of nanopowder, additional efforts were applied for filtering of fractions with small dimensions. Most surprising was detection of photoluminescence at room temperature in a range of 400–640 nm for silicon nanopowder, whereas fully oxidised samples didn't demonstrate comparative photoluminescence.

Introduction

Silicon nanopowder attracts recent scientific attention because of general interest to silicon nanocrystals. Potential possibility of selection of particle on size looks like benefit in comparison with clusters directly formed in the process of deposition or thermal treatments. Of course, separation of nanoparticles with size about several nanometers represents quite complicated problem. Nevertheless, solving the problem of selection makes a promise to apply silicon nanopowder for creation of high density memory or effective light emitting devices within silicon nanoelectronics. From scientific point of view, investigation of separate silicon nanoparticle could give experimental answer on question concerning electronic spectra of silicon nanocrystals. In this paper an attempt to obtain separate silicon nanoparticles and to examine their properties is presented.

1. Experimental

Silicon nanopowder was obtained utilizing silicon atoms coagulation in gas flow. Injection of silicon atoms was provided by evaporation of silicon ingot by means of power electron beam. Electron beam accelerator ELV-6 with energy of electrons of 1.4 MeV was used as a pumping. Coagulated silicon atoms were gathered through special filters in the form of powder, which properties were examined by means of electron microscopy, Raman and photoluminescence spectroscopies. Photoluminescence spectra were registered at room temperature using pulse N_2 gas laser as a source. Raman spectra were taken at room temperatures in backscattering geometry with Ar gas laser as a pumping (wavelength 514 nm). Both DFS-52 and Dylor Raman spectrometers were used in measurements.

2. Results and comments

Depending on gas atmosphere in the flow silicon or silicon oxide nanocrystals were obtained. Electron microscopy revealed spherical form of nanocrystals. The size of nanoparticles varied from several nanometers to hundreds of nanometers depending on the filter been used (Fig. 1). In the case of silicon nanopowder a visible photoluminescence was detected at room temperature (Fig. 2). Most surprising was photoluminescence of silicon nanopowder in blue region of spectra in addition to room temperature detection of the light emission. Raman spectra for initial silicon ingot and obtained silicon nanopowder were measured. Optical phonon peak is shifted to lower energies due to localization of phonons inside of silicon nanocrystals. The position of the peak corresponds to crystalline form of silicon nanoparticles. Evaluation of the peak position gave an estimation of average nanoparticles size about 2 nm (Fig. 3, Fig. 4). For such small silicon nanoparticles band gap could

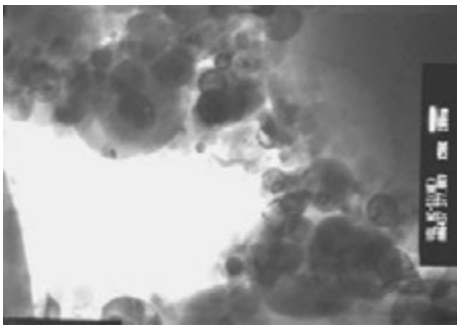

Fig. 1. Electron photograph for silicon nanopowder, displaying different sizes been obtained.

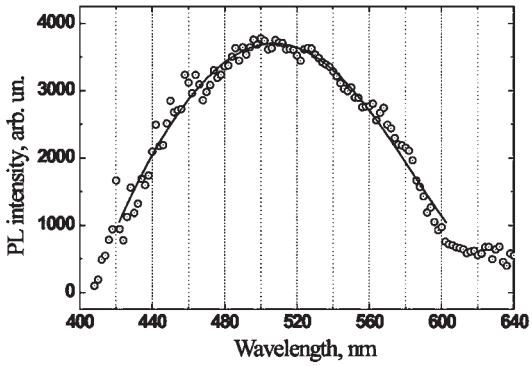

Fig. 2. Photoluminescence spectrum from crystalline silicon nanopowder, for which Raman spectroscopy gave estimation of average size about 2 nm (Fig. 3, Fig. 4).

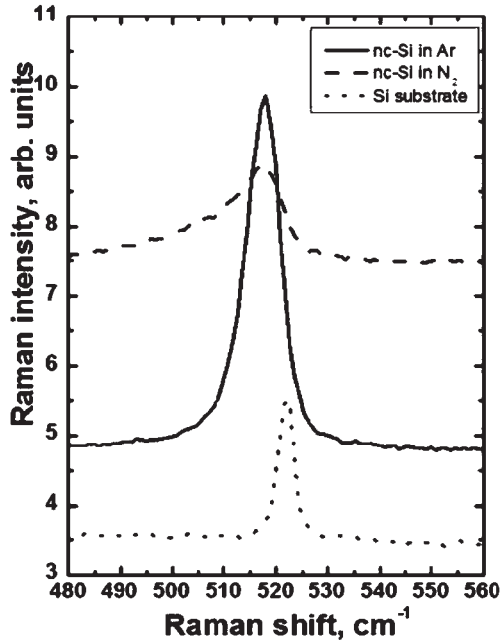

Fig. 3. Raman spectra for silicon substrate and for silicon nanopowder obtained in argon and in nitrogen gas flow. Position of the peaks corresponds to crystalline silicon with average size about 2 nm.

be high enough to provide visible photoluminescence due to direct recombination of electron-hole pair, localized inside of nanoparticle. Taking into account keeping of nanopowder in air atmosphere after preparation and possibility of capping by silicon dioxide, possibility of recombination trough environment electronic state should be considered also. Estimation of optical gap in silicon nanopowder capped with silicon oxide was done in effective mass approximation. Calculations were made in proposition that silicon balls are surrounded by silicon dioxide. The range of observed photoluminescence corresponds quite well to Raman estimation of the size of nanocrystals. For samples with quite thin SiO_2 covering it is possible to assume, that tunneling of carriers could be essential through barriers. So, some correction should be introduced if electron spectrum, moreover estimated in one-electron approximation. Taking into account the tunneling shift the model closer to abinitia calculation where hydrogen passivation of the surface often considered. The electronic spectrum of nanocrystals still interesting for the authors of the paper, owing to the literature data concerning strong variation of the bang gap from metallic kind up to 5 eV depending on surface conditions. Study of electronic spectrum of both conduction and valence band were carried out using deep electron transitions providing exchange with L2, L3 levels and exploring X-Ray emission and absorption. Thin dioxide layer may lead to changing of carrier lifetime in Si nanocrystals, what especially could be important when multi-electron effects will be considered.

Preliminary experiments were provided aimed on forming suspension of silicon powders using different inorganic and silicon-organic mixtures. As was demonstrated in (Fig. 1) silicon balls have almost ideal spherical form. But after preparation of silicon nanopowder, exposure in laboratory conditions leads to some gluing of separate particles may be due to SiO_2 covering. Dissolution of SiO_2 was treated in HF acid, and putting after that on silicon substrate using spin off method.

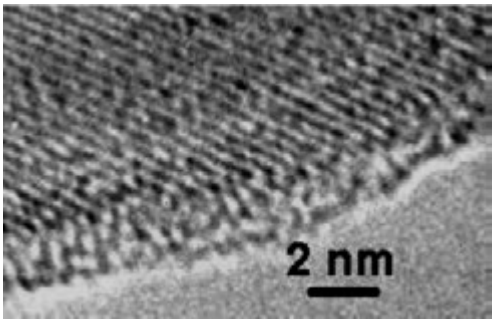

Fig. 4. HREM image of the boundary with SiO_2 layer with transition layer with about 2 nm length. Crystalline structure of silicon is evident from the figure.

The experiment was quite successful, in spite of precautions for full oxidations of silicon nanoballs. After deposition of silicon powder onto substrate Raman spectroscopy detected signal from nanoparticles due to shifting of the crystalline peak.

Other experiment was aimed on obtaining of liquid mixture of silicon nanoballs with silicon-organic materials, which widely used for deposition of silicon films, their nitrides and oxides. Preliminary plasma-chemical method for deposition was tested, and regimes were established for deposition of a-Si, SiO_2, Si_3N_4 films using reactor of induction type. Also plasma treatment of silicon surface for obtaining of very thin films in the range of 3–20 nm was elaborated. Mixtures of hexamethyldisilosan, hexamethyldisiloxane with addends of fractions of silicon nanopowder preliminary selected using microelectronic filters were prepared. Films of mixtures were obtained owing spin off technique. The films are undergoing plasma treatments to form layer of nanocrystals onto preliminary prepared thin dielectric layer. The properties of as obtained films are investigating using optical methods, such as photoluminescence, Raman spectroscopy. Electrical methods are applying to the structures after plasma treatments.

3. Conclusion

So, fractions of silicon nanopowder were manufactured using electron beam heating of pure silicon ingots and blue-red photoluminescence from silicon nanopowder was observed. Raman investigation and HREM observation of single nanocrystal reveal crystalline structure of silicon nanoballs with very thin transition layer with SiO_2. Attempts to form layer containing silicon nanocrystals are undergoing exploitations.

Acknowledgements

Special thanks for Russian Fund of Basic Researches for supporting this theme through grant 07-02-01122.

References

[1] M. D. Efremov *et al*, *Solid State Phenomena* **108–109**, 65–70 (2005).

16th Int. Symp. "Nanostructures: Physics and Technology"
Vladivostok, Russia, July 14–18, 2008

Thermally and infrared stimulated luminescence in beta-irradiated CdS-CdSe doped borosilicate glasses

V. Chernov, T. Piters, R. Meléndrez and M. Barboza-Flores
Departamento de Investigación en Física, Universidad de Sonora, A. P. 5-088. Hermosillo, Sonora 83190, México

Abstract. The behavior of TL and OSL in beta irradiated borosilicate glasses doped with CdS-CdSe nanoparticles has been studied. After irradiation the samples exhibit persistent luminescence due to thermal emptying of shallow traps. Stimulation with infrared light creates OSL due to additional emptying of traps. The TL glow curve consists of a very broad peak with a maximum at about 120 °C. The change of the TL peak shape under the thermal cleaning procedure reveals a monotonous increase of the activation energy that can be explained by the continuous distribution of traps. The results obtained are discussed with respect to a model based on trapping and detrapping of electrons in the glass matrix.

Introduction

Semiconductor nanoparticles or quantum dots represent an emerging area of research in nanomaterials. The CdS-CdSe nanocrystals embedded in glass matrices exhibit quantum confinement, which leads to numerous technological applications. In particular, such composites are used as commercial long pass filters and are promising materials for non-linear optical devices. Although glasses with embedded nanoparticles dots have been investigated for a long time, the effect of ionizing radiation on their properties have been scarcely studied. Thermally and optically stimulated luminescence (TL and OSL, respectively) created by radiation can provide important information about intrinsic and impurity defects and are widely used for determination of kinetic parameters of electron and hole traps. To the best of our knowledge, there are only few works dealing with TL [1,2] and no works devoted to the study of OSL in glasses with embedded CdS-CdSe nanoparticles.

In this work we present the behavior of TL and OSL in beta irradiated borosilicate glasses doped with CdS-CdSe nanoparticles.

1. Experimental

The investigated samples were sliced from a commercially available OG570 Schott glass filter. The filter glasses consist of CdS-CdSe nanocrystallites with diameters of a few nanometers embedded in a borosilicate glass matrix. Beta irradiation (with a 40 mCi ^{90}Sr-^{90}Y source) and luminescence measurements were performed with a RISØ TL/OSL reader (model TL/OSL-DA-15). This device allows to carry out a set of measurements on one sample (fixed position on a holder) with various subsequences of irradiation at room temperature (RT) along with TL or OSL readouts. Stimulated luminescence was measured in the 300–600 nm range (Schott BG-39 detection filter) for all data sets in this study. The heating rate of TL readouts was 2 K/s. The infra red (IR) stimulated luminescence readouts were performed at RT by illumination with an IR laser (830 nm, about 0.4 W at 100% power).

2. Results

Fig. 1a shows a set of TL curves of the glass sample recorded immediately after beta irradiation with doses from 0.33 to 167 Gy. The initial parts of the curves (up to 30 °C) correspond to afterglow (AG) at RT (see below). The glow curves reveal a very broad peak with a maximum at about 120 °C. The shape of the curves does not change with the dose. The integrated TL signal between 50 and 400 °C (sumlight) depends linearly on the dose. The glow curves are similar to those obtained by Miyoshi *et al* [1,2] for Asahi Y-44 filter glass, but with minor differences in the shape and peak position.

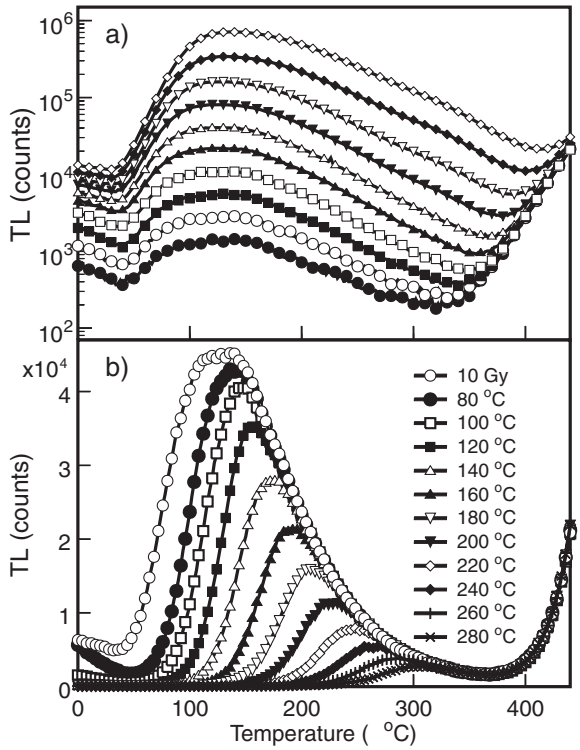

Fig. 1. TL glow curves of the glass sample recorded a) immediately after beta irradiation with 0.33, 0.67, 1.33, 2.67, 5.33, 10, 20, 40, 83 and 167 Gy, respectively; b) after beta irradiation with 10 Gy and after preheats up to indicated temperatures (thermal cleaning).

To clarify the structure of the TL glow curves the thermal cleaning procedure (subsequent TL readouts after irradiation and preliminary heating up to increasing end temperatures) was carried out. Fig. 1b shows the initial and preheated TL glow curves. The preheated glow curves are typical for the thermal cleaning procedure and show subsequent destruction of the low

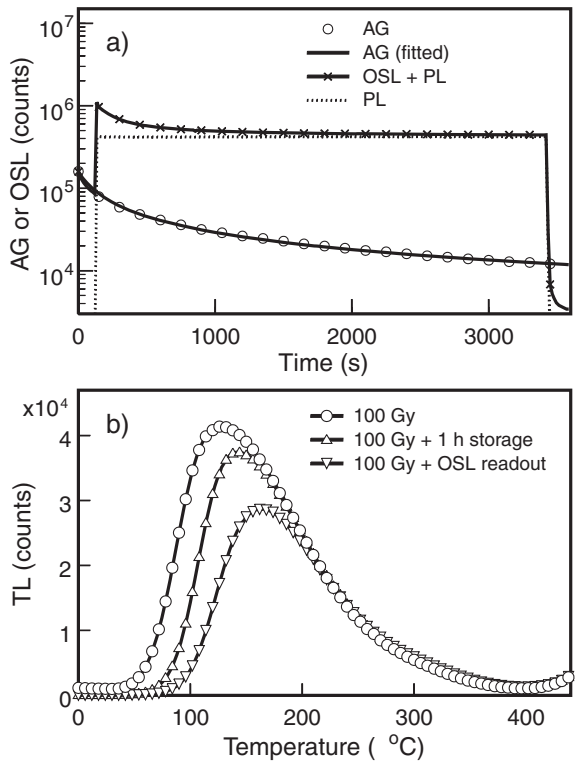

Fig. 2. a) AG and OSL decay curves of the glass sample recorded after beta irradiation with 100 Gy. The solid line passing through the AG points is the fitting with Eq. 1. PL denotes the steady state level of light accompanying OSL readout; b) TL glow curves recorded immediately after beta irradiation and after beta irradiation followed by dark storage at RT during 1 h or OSL readout.

temperature part of the peak. The peak maximum is shifted to the high temperature region when the preheat temperature is increased. The initial parts of the glow curves are well described by straight lines in the logarithm of intensity vs reciprocal temperature scale, which gives a good possibility to determine the activation energy by the initial rise method [3]. The evaluated activation energies increase monotonously from 0.5 to 1.2 eV with the increasing of the maximal preheat temperatures. This indicates that only one trapping level is not enough to explain the shape of the TL peak. The continuous exponential trap distributions was proposed for the TL peak in Brown microcline [4], whose shape is similar to the one measured by us. So, the continuous distribution of trap can be also used to explain the shape of the TL peak in the CdS-CdSe doped glass.

After beta irradiation the samples exhibit persistent luminescence or afterglow (AG) during storage at RT. The AG decay curve is presented on Fig. 2a. The AG intensity increases linearly with the beta radiation dose increasing but the shape of the AG decay curves does not change. The decay curve is fitted well by the phenomenological Becquerel's law [5]:

$$I_{\mathrm{AG}}(t) = \frac{I_0}{(1 + t/\tau)^a}, \qquad (1)$$

where the exponent a is equal to 0.7 and the decay time τ is about of 115 s.

To our knowledge, no investigation has been carried out on OSL in glasses with embedded CdS-CdSe nanoparticles. Fig. 2a shows the effect of stimulation with 830 nm light on the luminescence of the preliminary beta irradiated sample. After irradiation at RT the sample exhibits intense AG due to thermal emptying of traps. When the IR stimulation is switched on, the luminescence intensity increases sharply due to additional emptying of the traps by light. Further stimulation decreases monotonously the luminescence to steady state level. This level is determined by light that is measured by a photomultiplier during IR stimulation of the unirradiated sample (maybe photoluminescence) and corresponds to the full emptying of traps preliminary filled after beta irradiation. Once the stimulation light is switched off, the luminescence intensity drops down rapidly to about 20 percent of AG intensity at the same time. This evidences that IR stimulation destroys the traps responsible for AG.

Fig. 2b shows the effect of the dark storage at RT and IR stimulation on the TL of the beta irradiated sample. The dark storage (fading) and IR stimulation destroy only the low temperature part of the glow curve that corresponds to the thermal or optical emptying of the traps with the activation energy less than about 0.6 and 0.7 eV, respectively.

The behavior of AG, TL and OSL in the beta irradiated CdS-CdSe doped glasses can be interpreted within the frame of a simple model proposed by Miyoshi *et al* [6]. Ionising radiation creates free electrons and hole in a host glass, which are trapped by electron and hole traps. The electron traps have continuous energy distribution. The further behaviour of the irradiated sample is determined by the detrapping of electrons from the filled traps by heat or light and radiative recombination of detrapped electrons with holes leads to observed stimulated luminescence. If the irradiated sample is stored at RT, electrons are released mainly from low energy traps creating long persistence luminescence, which can be detected during 1 h and more after irradiation. Linear heating from RT to high temperature subsequently frees electrons from traps of increasing depth creating the broad TL peak, whose position is determined by the initial distribution of trapped electrons. IR stimulation releases electrons only from low energy traps. It can be explained by the excitation of electrons to some level, from which they are thermally excited to the conduction band.

Acknowledgements

This work has been supported in part by the CONACyT through grant No. 60553.

References

[1] T. Miyoshi *et al*, *Jpn. J. Appl. Phys.* **40**, 2327 (2001).
[2] T. Miyoshi *et al*, *J. Mater. Sci.* **43**, 203 (2008).
[3] C. Furetta and P. Weng, *Operational Thermoluminescence Dosimetry* (Singapore: World Scientific), pp. 252, (1998).
[4] T. Sakurai and R. K. Gartia, *J. Appl. Phys.* **82**, 5722 (1997).
[5] M. N. Berberan-Santos *et al*, *Chem. Phys.* **317**, 57 (2005).
[6] T. Miyoshi *et al*, *J. Lumin.* **102–103**, 614 (2003).

16th Int. Symp. "Nanostructures: Physics and Technology"
Vladivostok, Russia, July 14–18, 2008

Temperature and particle number oscillations of the electron canonical heat capacity

N. K. Kuzmenko[1] and V. M. Mikhajlov[2]

[1] V. G. Khlopin Radium Institute, 194021 St Petersburg, Russia
[2] Institute of Physics, St Petersburg State University, 198904, Russia

Abstract. The low temperature heat capacity (C) is studied by using the spectral distribution of C for mesoscopic fermion systems with a fixed particle number N treated as a canonical ensemble of independent particles confined in a spatial area. It is shown that a concentration of levels near the Fermi level (its extreme case is a high degenerated level) can cause local maxima in C vs T and the temperature of these maxima gives information concerning the level spacings in the immediate proximity of the Fermi level. We predict N-oscillations in C reflecting periodicities in single-particle energy spectra.

Introduction

Among many experiments performed to the present time on mesoscopic systems there are only several investigations of their thermal properties ([1] and references therein) though studying the electron heat capacity (C) of normal (nonsuperconducting) mesoscopic systems could give valuable information concerning the electron level structure in the vicinity of the Fermi energy ($\varepsilon_{\rm F}$).

As opposed to bulk metals in which the electron heat capacity C linearly increases with T in finite electron systems C can reveal the low temperature oscillations caused by the quantized single-particle spectrum. The term "low temperatures" implies that $T < \delta_{\rm F} \sim \varepsilon_{\rm F}/N$, the mean level spacing near $\varepsilon_{\rm F}$. Since $\varepsilon_{\rm F}$ is material dependent the absolute values of "low temperatures" for systems with identical N can differ by orders of magnitude.

The appearance of local low temperature maxima in C of systems with high degenerated electron levels was predicted by Frölich as far back as 1937 in his pioneering investigation of the mesoscopic heat capacity [2]. The low temperature variations of the canonical C were theoretically investigated in Ref. [3] for the equidistant spectrum model in which single-particle levels only spin degenerated and in Ref. [4] for spherical alkali clusters with closed shells. Analysis of the results of [3] and [4] shows that in the equidistant spectrum model [3] with spin degenerated levels local maximum in C is absent while for systems with closed degenerated shells [4] this maximum is present.

Thus one could infer that low temperature maximum in C is caused by the high degeneration of single-particle levels. However the results of our investigations presented here indicate that the low temperature variations of C have a rather complicated dependence on T, the level structure and N.

All our calculations are performed for systems of noninteracting fermions with a fixed N treated as a canonical ensemble by using the polynomial method [5].

1. The spectral distribution of the heat capacity

To investigate variations of C vs T and N we introduce into consideration the spectral heat capacity $\varphi(\varepsilon)$

$$C/k_{\rm B} = \int_0^\infty \rho(\varepsilon)\varphi(\varepsilon)d\varepsilon, \quad \varphi(\varepsilon) = (\varepsilon - \varepsilon_0)\frac{\partial n(\varepsilon)}{\partial T}, \quad (1)$$

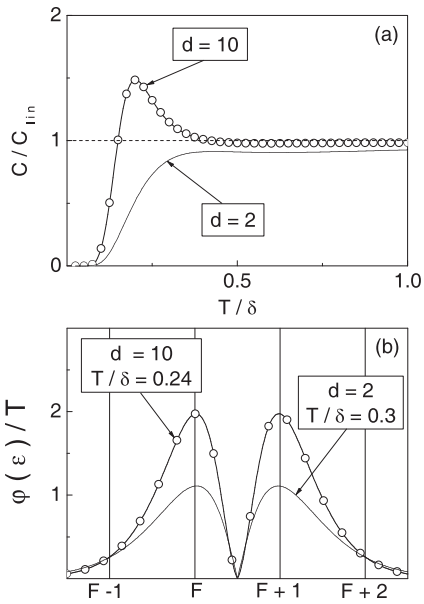

Fig. 1. (a) The low temperature heat capacity $C/C_{\rm lin} \sim C/NT$ in the model system with equal level spacing δ and the completely filled (at $T = 0$) Fermi level. (b) The spectral heat capacity $\varphi(\varepsilon)/T$. The vertical lines mark the positions of the levels.

which plays the role of an averager of the exact state density $\rho(\varepsilon) = \sum_t \delta(\varepsilon - \varepsilon_t)d_t$ (ε_t, $d_t \geq 1$ are respectively the energy and degeneration of the single-particle level t). $\varphi(\varepsilon_t)$ is the contribution to C from one electron on level t; $n(\varepsilon)$ is the canonical distribution of occupation numbers [5], ε_0 is a constant which does not affect the values of C.

In the effective grand canonical approximation $n(\varepsilon)$ is replaced by the Fermi–Dirac function $f(\varepsilon)$ with the temperature dependent chemical potential λ providing the particle number conservation at any T.

Functions $\varphi(\varepsilon)$ and $\varphi_{\rm eff}(\varepsilon) = \varphi(\varepsilon; n(\varepsilon) \to f(\varepsilon))$ have two peaks divided by a minimum in which both functions are equal to zero if $\varepsilon_0 = \lambda + \beta\partial\lambda/\partial\beta$, ($\beta = 1/T$). The energy distance $\Delta\varepsilon$ between two peaks of $\varphi_{\rm eff}(\varepsilon)$ is always equal $\approx$5 T while for $\varphi(\varepsilon)\Delta\varepsilon$ is of the order of or less than 5 T and depends on the level structure.

At some temperature T_0 the positions of two peaks of $\varphi(\varepsilon)$ coincide with the energies of levels F and $F+1$ that can cause

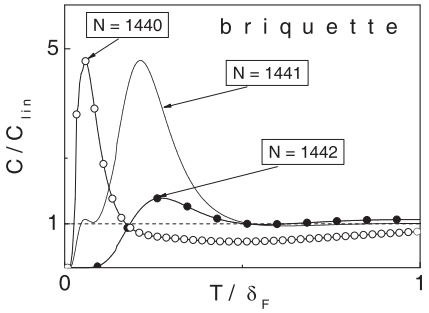

Fig. 2. The low temperature heat capacity $C/C_{\rm lin}$ of a briquette. The ratio of lateral lengths $L_x : L_y : L_z = 1 : 0.6e : \pi$ provides only the spin degeneration of the single-particle levels ($d = 2$). $\delta_{\rm F} = 4\varepsilon_{\rm F}/3N$.

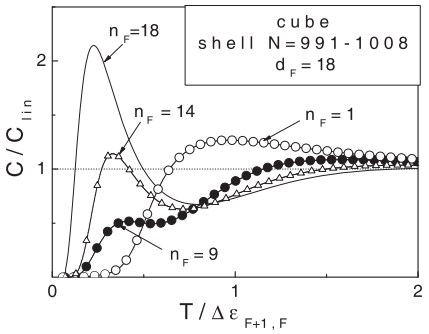

Fig. 3. The low temperature oscillations of $C/C_{\rm lin}$ in the degenerate shell of a cube with $N \sim 10^3$ at different values of $n_{\rm F}$. $n_{\rm F}$ is the number of electrons in the Fermi shell at $T = 0$, $d_{\rm F}$ is the shell degeneration. $\Delta\varepsilon_{\rm F,F+1} = \varepsilon_{\rm F+1} - \varepsilon_{\rm F}$.

the appearance of the local maximum in C/T at

$$T_0 = \xi(\varepsilon_{\rm F+1} - \varepsilon_{\rm F}), \quad \xi \sim 0.2 - 0.5, \tag{2}$$

if the contribution of other levels to C is significantly less i.e. at this temperature $\varphi(\varepsilon)$ cuts out from the single-particle spectrum practically only two these levels.

To show how the spectral heat capacity $\varphi(\varepsilon)$ forms the peak in $C/C_{\rm lin} \sim C/NT$, ($C_{\rm lin}$ is the Zommerfeld heat capacity) we use the equidistant spectrum model with degenerated levels (the level spacing is equal to δ). Fig. 1a shows that the low temperature peak arises in the model with the high level degeneration ($d = 10$) as at $T = 0.24\delta$ the positions of two peaks of $\varphi(\varepsilon)$ coincide with energies of levels F and $F + 1$, Fig. 1b. Although at $T = 0.3\delta$ for $d = 2$ the positions of two peaks of $\varphi(\varepsilon)$ coincide with energies of levels F and $F + 1$ too, the peak is absent because for $d = 2$ the contributions in C from $(F - 1)$-, and $(F + 2)$-levels are comparable with those of F-, and $F + 1$-levels contrary to the case with $d = 10$ where the contributions of F-, and $(F + 1)$-levels to C are nearly twice as large as the case with the small level degeneration ($d = 2$), Fig. 1b. It should be mentioned that at $d \gg 1$ the canonical and effective grand canonical heat capacities practically coincide.

However the small level degeneration does not generally except the local maxima. If near $\varepsilon_{\rm F}$ a group of doubly degenerated levels is concentrated so that spacings between them are much smaller then the distance from this group to other levels the appearance of local maxima are also possible as it occurs e.g. for briquettes with $N = 1440$–1442, Fig. 2.

Fig. 3 shows the low temperature oscillations of $C/C_{\rm lin}$ in a system of cubic symmetry for different occupation numbers $n_{\rm F}$ (at $T = 0$) of the high degenerated Fermi level. These examples demonstrate that measuring the heat capacity of a mesoscopic sample can give information concerning distributions of single-particle levels near the Fermi level.

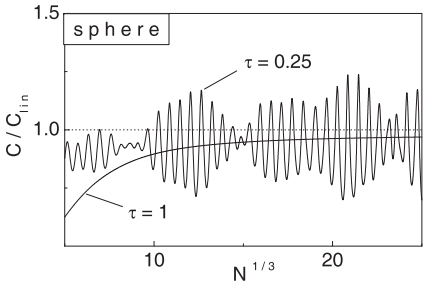

Fig. 4. N-oscillations of the heat capacity in spheres, $\tau = N^{1/3}(T/\varepsilon_{\rm F})$.

2. The particle number oscillations of C

As Figs. 2,3 indicate increasing N (i.e. increasing the volume of the system) at an invariable shape can reveal oscillations in C vs N. At $T > \delta_{\rm F}$ under peaks of $\varphi(\varepsilon)$ there are many levels that results in temperature averaging the state density $\rho(\varepsilon)$, Eq.(1), and in damping high frequency oscillations in C. Therefore in symmetric cavities the N-oscillations of C created by shell and supershell structures can be observed at an optimal temperature (for spheres it is $\sim 0.25\varepsilon_{\rm F}N^{-1/3}$).

Acknowledgements

This work is supported by the ISTC under grant No. 3492.

References

[1] O. Burgeois, S. E. Skipetrov, F. Ong, and J. Chaussy, *Phys. Rev. Lett.* **94**, 057007 (2005).
[2] H. Frölich, *Physica (Utr.)* **4**, 406 (1937).
[3] R. Denton, B. Mühlschlegel, and O. J. Scalpino, *Phys. Rev. Lett.* **26**, 707 (1971); *Phys. Rev.* **B7**, 3589 (1973).
[4] M. Brack, O. Genzken, and K. Hansen, *Z. Phys.* **D21**, 65 (1991).
[5] N. K. Kuzmenko, and V. M. Mikhajlov, *Physica* **A373**, 283 (2007).

16th Int. Symp. "Nanostructures: Physics and Technology"
Vladivostok, Russia, July 14–18, 2008

Electrical control of spin-orbit splitting in GaAs/AlGaAs coupled quantum wells

A. V. Larionov[1] and L. E. Golub[2]

[1] Institute of Solid State Physics, Russian Academy of Sciences, 142432 Chernogolovka, Russia
[2] Ioffe Physico-Technical Institute, St Petersburg, Russia

Abstract. Electron spin dynamics is investigated in n-i-n GaAs/AlGaAs coupled quantum wells. The electron spin dephasing time is measured as a function of an external electrical bias under resonant excitation of the 1sHH intrawell exciton using a time-resolved Kerr rotation technique. It is found a strong electron spin dephasing time anisotropy caused by an interference of the structure inversion asymmetry and the bulk inversion asymmetry. This anisotropy is shown to be controlled by an electrical bias. A theoretical analysis of electron spin dephasing time anisotropy is developed. The ratio of Rashba and Dresselhaus spin splittings is studied as a function of applied bias.

Introduction

Critical point of spintronics investigations is a control of spin degrees of freedom by electrical means. Especially interesting for both fundamental physics and applications is spin-orbit interaction caused by lack of inversion center in the system. There are two main sources for lacking inversion symmetry in low-dimensional semiconductors: Bulk Inversion Asymmetry (BIA) and Structure Inversion Asymmetry (SIA). New interesting effects appear in spin dynamics if both SIA and BIA are present [1].

Among the quasi-two-dimensional objects based on semiconductor heterostructures, Coupled Quantum Wells (CQWs) are of special interest. Electrical bias in such structures does not produce carriers but has dramatic effects on both SIA and BIA. This allows for direct manipulation by spin-orbit interaction even in undoped structures.

In our work we demonstrate via spin relaxation times measurements that spin-orbit interaction can be controlled by means of electric field in n-i-n GaAs/AlGaAs CQWs.

1. Experimental

The studied CQWs system consists of two GaAs quantum wells (width ≈120 Å) separated by a narrow (4 monolayers) AlAs barrier. The QWs were separated from the Si-doped (10^{18} cm^{-3}) GaAs layers by 0.15 μ thick $Al_{0.33}Ga_{0.67}As$ barriers. The upper part of the structure was covered with a 100 Å GaAs layer.

The electron spin dephasing time has been measured by means of the time resolved Kerr rotation (TRKR) technique with using femtosecond Ti-Sapphire laser (Tsunami). Set of time-resolved spin quantum beats in CQWs detected in a magnetic field of 1 T (Voigt configuration) is given in Fig. 1a for the different bias. The energy of pump and probe Ti-Sapphire pulsed laser beams was the same and has been set to the maximum of the photoluminescence line contour corresponding to radiative annihilation of the 1sHH exciton. The observed periodic oscillations are due to Larmor precession of coherently excited electron spins around the external magnetic field.

The set of experimental data can be fitted by an exponentially damped oscillation containing the beating frequency Ω and a single decay time:

$$I = I_0 \exp(-t/T)\cos\Omega t, \qquad (1)$$

where $\Omega = \mu_B g_e B/\hbar$, g_e is the in-plane electron g-factor. The decay rate is a sum of radiative recombination and spin dephasing rates: $1/T = 1/\tau_s + 1/\tau_0$. The dependence of electron spin dephasing time τ_s and the interwell radiative electron-hole annihilation time τ_0 on the applied bias obtained as a result of such fitting are shown in Fig. 1b.

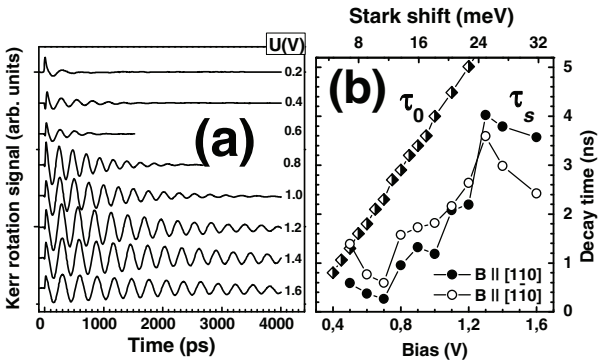

Fig. 1. (a) Kerr rotation signal depending on applied bias. Experimental curves have been received at temperature ≈2 K and photoexcitation power density $P \approx 2 \times 10^3$ W/cm^2. (b) Electric field dependence of the photoluminescence decay time τ_0 and the electron spin dephasing time τ_s (circular symbols) at two magnetic field orientations. The Stark shift is given for the indirect exciton photoluminescence line.

As it has been already shown experimentally [2] two dimensional GaAs heterostructures give a good opportunity for the spin relaxation anisotropy studies. In the present work we have suggested to use CQWs structures with bias for smooth change of spin relaxation anisotropy. For such investigation it is necessary to rotate the sample with a good accuracy relative to the direction of applied magnetic field.

Figure 2a demonstrates the spin dephasing time measured at different angles between the magnetic field direction and the axis [110] in polar coordinates for two applied biases. Experimentally we have measured the data for angles from 0 to 90° only (black points). Open points have been received by inversion extrapolation to next three quadrants. One can see that application of an electric field to CQWs gives good opportunity for change of spin relaxation anisotropy.

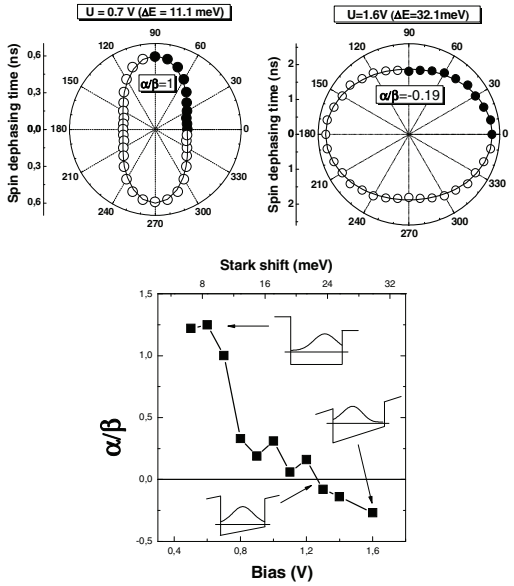

Fig. 2. (a) Spin dephasing time measured at different angles between magnetic field and axis [110] at two applied bias. Experimental data are shown by points, solid lines is the theoretical description. The values ΔE represent the Stark shifts for the given biases. (b) The ratio of Rashba and Dresselhaus constants α/β as a function of applied bias.

2. Theoretical description of electron spin dephasing anisotropy

For the D'yakonov–Perel' spin relaxation mechanism the following expressions exist for the anisotropic spin relaxation rates [1]:

$$\frac{1}{\tau_z} = C(\alpha^2 + \beta^2), \quad \frac{1}{\tau_{x,y}} = \frac{C}{2}(\alpha \pm \beta)^2. \tag{2}$$

Here the times $\tau_{x,y,z}$ are the relaxation times of the spin oriented along $x \parallel [1\bar{1}0]$, $y \parallel [110]$, and $z \parallel [001]$, α and β are Rashba and Dresselhaus electron constants, respectively, which determine the spin-orbit splittings of free electrons, and C is a constant.

Electron spin dynamics in the presence of external magnetic field and anisotropic spin relaxation is described by the following equation

$$\frac{\partial \mathbf{S}}{\partial t} + \mathbf{S} \times \mathbf{\Omega} + \hat{\mathbf{\Gamma}}\mathbf{S} + \frac{\mathbf{S}}{\tau_0} = 0. \tag{3}$$

Here $\mathbf{S}$ is the electron spin density, $\mathbf{\Omega}$ is the Larmor frequency vector, and $\hat{\mathbf{\Gamma}}$ is the tensor of spin relaxation rates. The solution corresponding to our experimental conditions is given by

$$S_z(t) = A \exp(-t/\tau_0 - t/\tau_s) \cos(\Omega t + \varphi), \tag{4}$$

which leads to the dependence (1).

If a magnetic field is strong enough: $\Omega\tau_{x,y,z} \gg 1$ then one can derive an analytical expression for the spin dephasing time τ_s:

$$\frac{1}{\tau_s} = \frac{1}{2}\left(\frac{1}{\tau_z} + \frac{\sin^2\theta}{\tau_x} + \frac{\cos^2\theta}{\tau_y}\right), \tag{5}$$

where θ is the angle between magnetic field $\mathbf{B}$ and the axis $x \parallel [1\bar{1}0]$.

3. Discussion

In our experiments the quantum beats are well pronounced, see Fig. 1. Therefore the relation $\Omega\tau_{x,y,z} \gg 1$ is true for our measurements, and we can use Eq. (5) for description of the spin dephasing time angular dependence which yields:

$$\tau_s(\theta) = \frac{D}{1 + b\cos 2\theta}, \tag{6}$$

where D and b are the fitting parameters ($b < 1/3$). Results of the experimental data fitting according to Eqs. (6) are shown in Fig. 2a by solid lines. One can see a good agreement between experiment and theory.

The performed quantitative description of the spin relaxation anisotropy allows one to derive the ratio of SIA and BIA spin-orbit splittings. For the D'yakonov–Perel' spin relaxation the fitting parameter b in Eq. (6) determines the ratio of the Rashba and Dresselhaus constants:

$$\left(\frac{\alpha}{\beta}\right)^{\pm 1} = \frac{3b}{1 + \sqrt{1 - (3b)^2}}. \tag{7}$$

We used this expression for derivation of the ratio α/β and plotted the result in Fig. 2b. One can see strong variations of this parameter by the electric field.

Experimentally observed electron spin dephasing time anisotropy is an unambiguous indication of variation of the of the Rashba and Dresselhaus constants ratio by means of electric field. Strong variations of the value and change of the sign of this ratio can be explained only by change of the Rashba constant. The observed disappearance of the spin dephasing anisotropy means that at this particular bias an external electric field totally cancelled SIA present in the unbiased structure.

To summarize, electron spin dephasing time anisotropy is observed in the [001] grown n-i-n CQWs with bias. The anisotropy is measured by means of time-resolved Kerr rotation effect at magnetic field differently orientated in the structure plane. The anisotropy is caused by interference of SIA and BIA spin-splittings in the electron spin relaxation via the D'yakonov–Perel' mechanism. It is demonstrated that SIA is changed by bias according to the Rashba effect in the studied structure. It is shown that spin-orbit splitting can be controlled by electrical means in n-i-n GaAs/AlGaAs coupled quantum wells.

Acknowledgements

The authors thank M. M. Glazov for fruitful discussions, and J. Hvam and K. Soerensen for preparation of the samples. This research is supported by RFBR, "Dynasty" Foundation — ICFPM, and President grant for young russian scientists.

References

[1] N. S. Averkiev, L. E. Golub and M. Willander, *J. Phys.: Condens. Matter* **14**, R271 (2002).

[2] N. S. Averkiev, L. E. Golub, A. S. Gurevich *et al*, *Phys. Rev. B* **74**, 033305 (2006).

16th Int. Symp. "Nanostructures: Physics and Technology"
Vladivostok, Russia, July 14–18, 2008

Carrier spin dynamics in quantum wells GaAs under lateral localizing electric potential

R. V. Cherbunin[1], M. S. Kuznetsova[1], S. V. Potavtsev[1], I. Ya. Gerlovin[1], I. V. Ignatiev[1], Yu. K. Dolgikh[1], Yu. P. Efimov[1], S. A. Eliseev[1], V. V. Petrov[1], A. V. Larionov[2] and A. I. Il'in[3]

[1] St Petersburg State University, Faculty of Physics, Ulyanovskaya 1, Petrodvorets, 198504 St Petersburg, Russia
[2] Institute of Solid State Physics RAS, Chernogolovka, Moscow region, Russia
[3] Institute of Microelectronics Technology RAS, Chernogolovka, Moscow region, Russia

Abstract. The dynamics of spin orientation of the electron localized in the potential quantum dot created by mosaic electrode in GaAs/AlGaAs quantum well has been studied experimentally using pump-probe Kerr rotation method.

Introduction

The recent interest to spin dynamics of carriers in semiconductor quantum dots is primarily related to possible prospects of using these structures for implementation of the long-term spin memory. Due to spatial localization of the carriers, suppressing the main mechanism of the spin relaxation, the electron spin lifetime in the quantum dots (QDs) may reach hundreds of microseconds or, even, units of milliseconds [1]. The drawbacks of the QDs created by methods of self-organization are the spread of the QD parameters over the ensemble and imperfections of hetero-interfaces related to considerable mismatch of the lattice constants of the QD and barrier layer materials. The spread of the QD properties, in particular, does not allow one to obtain the same charge state of all the dots needed for implementation of the spin memory. The presence of defects (including paramagnetic ones) shortens the electron spin lifetime, thus limiting the possibility of long-term information storage.

In this paper, we study spin dynamics of electrons placed into an array of potential QDs, created by applying an electric bias to the electrode with a regular structure of nanoholes, deposited onto the surface of the structure. Regular character of the sizes and arrangement of the holes excludes possibility of spread of parameters of the QD ensemble created in this way. An important advantage of the field-induced QDs is virtually complete absence of defects on the hetero-interfaces, which makes it possible to suppress one of the essential spin relaxation channels.

1. Experimental

As an object for the study, we used a sample with a quantum well GaAs, about 9 nm thick, sandwiched between the $Al_{0.25}Ga_{0.75}As$ barriers. The sample was grown on the doped GaAs:Si substrate. The top surface of the heterostructure was coated by a golden electrode with submicron holes (mosaic electrode). The mosaic electrode was fabricated using the electron-beam nanolithography technique. Two resist layers (copolimer and electron resist) were deposited onto the chips. Resists were exposured using JSEM-850 electron microscope supplied by electron lithography complex Nanomaker. After resist development the processed surface was coated by the Cr/Au (10/100 nm) layer and was etched in acetone. The typical size of the mosaic electrode was 150×150 μm with hole diameters varied from 500 to 1000 nm.

The sample thus prepared was placed into a closed-cycle optical helium cryostat, which provided cooling down to 8 K. An electric bias varied between $+1$ and -5 V was applied between the electrode and the back surface of the sample. The cryostat with the sample was placed between the coils of an electromagnet that allowed us to create a relatively small (-0.01–$+0.01$ T) magnetic field.

Dynamics of the spin orientation in the sample under study was detected in the pump-probe mode using the photoinduced Kerr-rotation signal. As the light source we used a Ti:sapphire laser generating 150-fs light pulses with the repetition rate 80 MHz. The measurements were performed in the spectrally nondegenerate mode, when the wavelengths of the pump and probe beams could be varied independently. The signal was detected using double lock-in amplification which allowed us to efficiently suppress the background signal produced by the pump beam reflected from the mosaic electrode.

2. Experimental results and discussion

Figure 1 shows dynamics of the spin polarization for different bias voltages applied to the mosaic electrode. We measured dependence of the rotation signal amplitude on time delay between the probe and pump pulses. For the bias $+0.7$ V, the signal reproduces the one from the free surface. When moving towards negative bias, the decay time of the signal increases and, at the bias about -2 V, a noticeable signal in the region of negative time delay arises. The latter means that the decay time of the signal is comparable with the laser pulse repetition period ($\sim$12.5 ns).

The conclusion that the signal at negative delays is indeed related to the long electron-spin lifetime is supported by the results of studying this signal in a transverse magnetic field (see Fig. 2). Precession of the electron spin in the transverse field reduces the degree of polarization at negative time delays and, in the simplest case, the field dependence of the signal should be described by the equation [2]:

$$\rho = \rho_0 \exp\left[-\frac{\Delta t + T}{\tau_s}\right] \cos\left[g_e \mu_B B \frac{\Delta t + T}{\hbar}\right], \qquad (1)$$

where Δt is the time delay, T is the laser pulse repetition period, τ_s is the electron spin relaxation time, g_e is the electron g-factor, μ_B is the Bohr magneton, and B is the magnetic field strength. As seen from Fig. 2, the field dependence of the long-lived

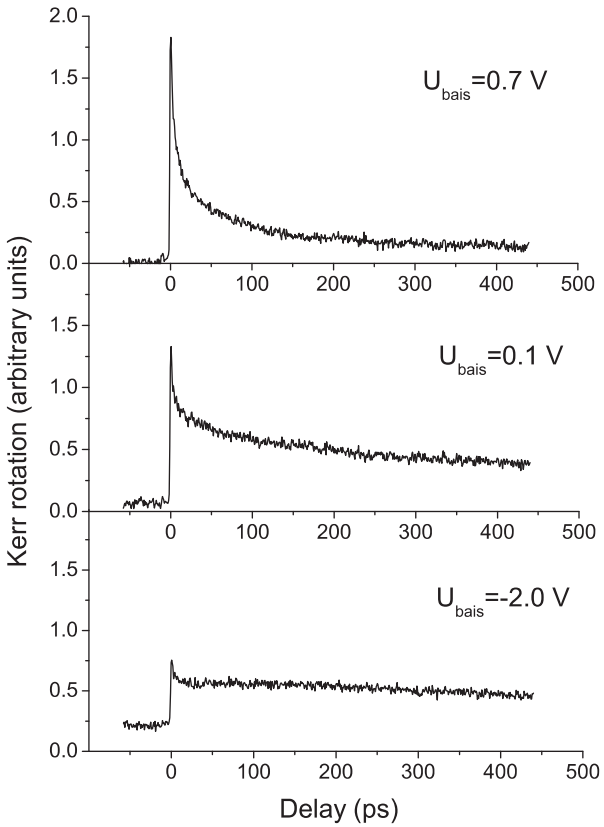

Fig. 1. Dependence of the shape of the detected signal on voltage at the mosaic electrode.

component of the signal can be well approximated by such a function with the parameter g_e close to that found in Ref. [3] for similar quantum wells.

The data thus obtained unambiguously show that the inhomogeneous electric field created by the mosaic electrode substantially affects spin dynamics of the carriers in a quantum well. According to the results of theoretical treatment presented in Ref. [4], application of a negative electric bias to the mosaic electrode should produce an inhomogeneous lateral potential profile in the quantum well, capable of localizing electrons under the holes in the electrode, i.e., in fact, should form quantum dots for the electrons. The calculations show that the depth of the potential well may be as deep as 100 mV for the realistic values of the field between the electrodes ∼100 kV/cm. At $T \sim 8$ K, this potential should be sufficient to reliably localize the electron.

For a positively charged hole, the electric potential has the opposite sign, and, under the negativebias, the hole should be pushed out from the region under the aperture in the electrode. As a result, the overlap of the electron and hole wave functions will substantially decrease, i.e., the photogenerated exciton will prove to be spatially indirect. A consequence of small overlap is virtually complete break down of the exchange coupling between the electron and hole. As a result, the spin of the hole rapidly relaxes, while the electron spin may retain its orientation for a sufficiently long time.

The decay of the signal related to electron-hole pairs is contributed not only by the spin relaxation processes, but also by the recombination of the pairs. In this case, the decay time of the detected signal should be smaller than the time of the

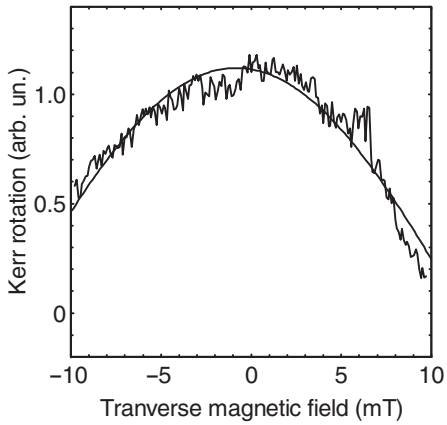

Fig. 2. Dependence of the long-lived Kerr signal on the transverse magnetic field. The noisy curve are experimental results; smooth curve is fitting by Eq. (1) at $g_e = 0.12$.

fastest of these processes. The radiative recombination time of the exciton in the GaAs quantum wells of similar width does not exceed a few tenths of nanosecond [5]. This value is almost by two orders of magnitude smaller than the decay time of the signal, measured by us, at negative bias on the mosaic electrode. We suppose that the reason for such a slow decay of the signal is related to the decrease of the radiative decay rate of the exciton caused by the inhomogeneous electric field and resulted from the strong decrease of overlap of the electron and hole wavefunctions.

Positive bias of 0.7 V practically compensates for the action of the Schottky barrier formed in the contact with the golden electrode. As a result, the quantum well appears to be at zero potential. Under these conditions, the absorption of a photon is accompanied by creation of a free exciton, with its radiative recombination time lying in the range of fractions of nanoseconds. A combined action of radiative recombination and anisotropic component of the electron-hole exchange interaction is the reason for fast decay of the rotation signal.

In conclusion, the above studies have shown fundamental possibility of using mosaic electrodes for considerable lengthening of relaxation time of electron spin in the GaAs quantum wells.

Acknowledgements

The work was supported by the Russian Foundation for Basic Research.

References

[1] A. V. Khaetskii, and Yu. V. Nazarov, *Phys. Rev. B* **61**, 12639 (2000).

[2] J. M. Kikkawa, and D. D. Awschalom, *Phys. Rev. Lett.* **80**, 4313 (1998).

[3] I. A. Yugova, A. Greilich, D. R. Yakovlev, A. A. Kiselev, M. Bayer, V. V. Petrov, Yu. K. Dolgikh, D. Reuter, and A. D. Wieck, *Phys. Rev. B* **75**, 245302 (2007).

[4] V. A. Nikoluk, and I. V. Ignatiev, *FTP* **41**, 1443 (2007).

[5] I. Ya. Gerlovin, Yu. K. Dolgikh, S. A. Eliseev, V. V. Ovsyankin, Yu. P. Efimov, I. V. Ignatiev, V. V. Petrov, S. Yu. Verbin, and Y. Masumoto, *Phys. Rev. B* **69**, 035329 (2004).

16th Int. Symp. "Nanostructures: Physics and Technology"
Vladivostok, Russia, July 14–18, 2008

Dynamics of nuclear spin polarization in InGaAs quantum dots

S. Yu. Verbin[1,3], R. V. Cherbunin[1,3], T. Auer[1], D. R. Yakovlev[1], M. Bayer[1], D. Reuter[2], A. D. Wieck[2], I. Ya. Gerlovin[3] and I. V. Ignatiev[3]

[1] Experimentelle Physik II, Technische Universität Dortmund, 44221 Dortmund, Germany
[2] Angewandte Festkörperphysik, Ruhr-Universität Bochum, 44780 Bochum, Germany
[3] St Petersburg State University, Faculty of Physics, Ulyanovskaya 1, Petrodvorets, 198504 St Petersburg, Russia

Abstract. Dynamics of the nuclear spin polarization in ensemble of the InGaAs quantum dots is studied experimentally in the large time scale from fractions of millisecond to second. Nontrivial time behaviour of the polarization is found.

Introduction

Dynamics of the nuclear spin polarization in semiconductor quantum dots (QDs) attracts considerable attention of researchers at present time. The polarization is created by means of optical orientation of an electron spin which forms with nuclear spin a coupled quantum-mechanical system due to enhanced hyperfine interaction in the QDs. Because of the large number of the degree of freedom, the exact solution of the dynamical problem for such a system is impossible. Results of calculations performed in framework of some approximate models [1, 2] show that the dynamics of the nuclear spin polarization should be nontrivial: the fast rise to the comparable small values at the first moment followed by a successive slow rise of the dynamical nuclear polarization (DNP) is expected. The only experimental data on the DNP in the QDs available now [3] does not confirm this assumption. According to the data, increase of the DNP in the InGaAs QDs is well described by an exponential law with the millisecond-range characteristic time.

In present work, results of the detailed experimental investigation of the DNP in the InGaAs QDs performed in a wide time range from tens of microseconds to fractions of a second is reported. Our experiments confirm nontrivial behaviour of the nuclear spin dynamics predicted by the theory.

1. Experimental

As an object of the study, we use a heterostructure containing 20 layers of self-assembled InAs QDs sandwiched between doped GaAs barriers. The donor ionisation supplies every QD with one resident electron per dot on average. Rapid thermal annealing of the QDs was used to shift the lowest optical transition in the QDs to the energy range of about 1.34 eV. The sample was mounted in a cryostat with a superconductive magnet. The magnetic field was aligned along the axis of the optical excitation and detection of signal (Faraday geometry). The DNP was determined from the position of a dip in the magnetic field dependence of the resident electron spin polarization measured by means of the negative circular polarization (NCP) of the luminescence of the sample [4]. The dip observable in the NCP at small magnetic fields is related to depolarization of the electron spins by the transverse components of nuclear spin fluctuations [4]. In absence of the DNP, the dip is centred at zero external magnetic field. The effective magnetic field of the DNP created by the circularly polarized excitation is parallel or anti-parallel to the external field depending on helicity of the polarization. In the case of anti-parallel mutual orientation, the nuclear field compensates the external one which results in the shift of the dip in the electron spinpolarization to the value of the DNP field. Experiments show that the field of the DNP linearly depends on excitation at the power densities less than 5 W/cm2.

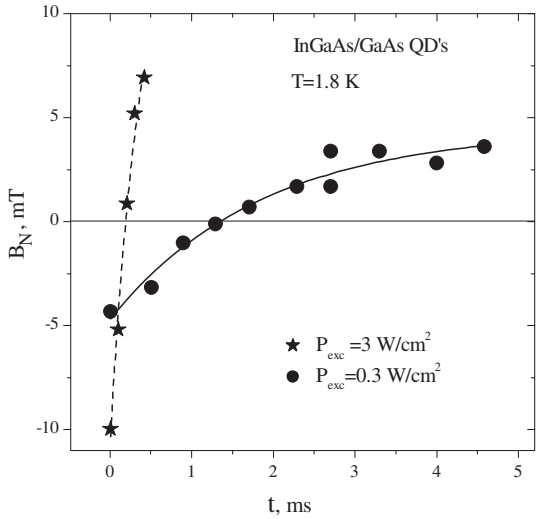

Fig. 1. Kinetics of the DNP rise for different pump power densities P. Symbols are the experimental data, curves are the fits by function $B_N = B_N^0[0.5\exp(-t/\tau)]$ with parameters $B_N^0 = 9.2$ mT, $\tau = 2.0$ ms for $P = 0.3$ mW/cm^2 and $B_N^0 = 23$ mT, $\tau = 0.26$ ms for $P = 3$ mW/cm^2.

For study of the dynamics of nuclear polarization, the sample was excited with a circularly polarized light which helicity was periodically changed so that the duration of the illumination with every helicity of the polarization was half of the period T. Under these conditions, the DNP field is continuously changed from its value $-B_{N_{\max}}$ achieved in the end of the preceding half-period to the same absolute value but with another sign, $B_{N_{\max}}$, in the end of the current period. Photoluminescence of the sample was detected in the narrow time window of about 0.05 T which time position could be changed within the period. We measured the magnetic field dependences of the NCP in different time moments within of the half-periods and thus detected the dynamics of the nuclear polarization. Results of such measurements are shown in Fig. 1.

As seen from the figure, the DNP rise in the time scale of units of milliseconds is well approximated by an exponential function with the amplitude growing with increase of the pump power. Simultaneously, a shortening of the DNP rise time

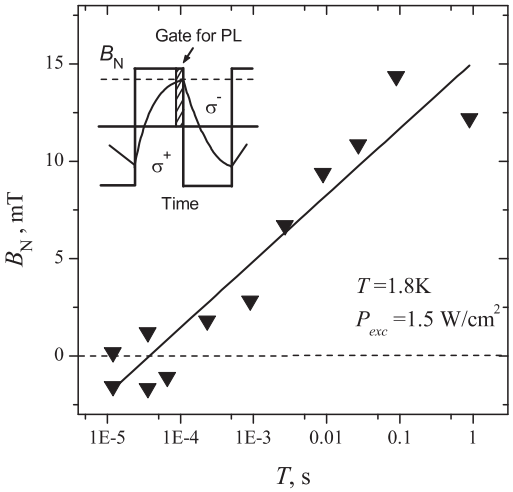

Fig. 2. Dependence of the DNP field on the duration $t_{\text{pump}} \approx T/2$ of the optical excitation with one helicity of polarization (symbols). Solid line is the linear fit. Pump power density is 1.5 W/cm^2. Inset schematically shows the time dependence of the excitation polarization and of the nuclear field.

occurs.

To study the DNP dynamics in the considerably larger time scale, we changed the experimental conditions of the DNP detection. Namely, we measured dependence of the DNP on the period of the polarization modulation. The DNP was detected at the end of the half-period. The time interval of the signal detection was kept 0.05 T for all the periods T that allowed us to get the signal with acceptable signal-to-noise ratio. Results of these experiments are shown in figure 2. As seen, the nuclear field is approximately proportional to ln (t_{pump}) in the large time range from 10^{-5} to 1 s, i.e., overlapping five decimal orders.

2. Conclusion

The experiments performed show that, according to the theoretical predictions, the dynamics of the nuclear polarization in the InGaAs QDs is really nontrivial. The first period of the polarization rise can be described by an exponential function. However further increase of the polarization occurs according to approximately logarithmic dependence on time.

Acknowledgements

The work was supported by the Russian Foundation for Basic Research.

References

[1] H. Christ, J. I. Cirac, and G. Giedke, *Phys. Rev. B* **75**, 155324 (2007).

[2] G. G. Kozlov, JETP 105, 803 (2007) [Zh. Eksp. Teor. Fiz. 132, 918 (2007)].

[3] P. Malenitsky, A. Badolato, and A. Imamoglu, *Phys. Rev. Lett.* **99**, 056804 (2007).

[4] B. Pal, S. Yu. Verbin, I. V. Ignatiev, M. Ikezawa, Y. Masumoto, *Phys. Rev. B* **75**, 125322 (2007).

16th Int. Symp. "Nanostructures: Physics and Technology"
Vladivostok, Russia, July 14–18, 2008

Spin-echo measurements of electrons localized on Ge quantum dots

A. F. Zinovieva[1], A. V. Dvurechenskii[1], N. P. Stepina[1], A. I. Nikiforov[1], L. V. Kulik[2] and A. S. Lyubin[3]

[1] Institute of Semiconductor Physics, 630090 Novosibirsk, Russia
[2] Institute of Chemical Kinetics and Combustion, 630090 Novosibirsk, Russia
[3] Novosibirsk State University, 630090 Novosibirsk, Russia

Abstract. Using a pulsed electron paramagnetic resonance spectrometer, we measure spin echoes and deduce a spin coherence time (T_2) of up to 20 μs for electrons confined in strain-induced Si potential wells in the vicinity of the Ge quantum dots. The decoherence can be understood in terms of an effective magnetic field, lying in the plane of the quantum dot array. This magnetic field arises during the tunneling of electrons between quantum dots and leads to an acceleration of the spin relaxation. The origin of the field is the structure-induced asymmetry of electron potential wells. Two ways of increasing the spin lifetime are suggested: 1) the creation of a higher symmetry confinement potential for electrons; 2) the growth of a well-separated quantum dot array.

Introduction

Spin effects in nanostructures are considered as a basis for realization of new semiconductor devices. Recent investigations showed that the symmetry of nanostructure have a crucial impact on the spin dynamics. The spin-orbit (SO) coupling in asymmetrical quantum well structures gives the possibility to manipulate with spins of carriers [1,2], but it serves as main source of spin relaxation. The direct spin coherence measurements of quantum well structures gives the coherence time $T_2 \sim 3$ μs for electrons at a heterointerface, with longitudinal (spin population) time $T_1 \sim 2.3$ μs ($T_2 > T_1$) [3]. These results are consistent with the suggestion, based on extensive continuous wave (cw) EPR experiments [4], that the longitudinal relaxation time and coherence time are controlled by effective in-plane fluctuating magnetic field, or Rashba field [5], arising from the SO interaction and the broken inversion symmetry at the heterostructure interface. The results of cw EPR experiments on the quantum dot(QD) structures [6] allows to make conclusion about existence of fluctuating Rashba field in the plane of QD array. This field arises during tunneling of carriers between quantum dots and leads to an anisotropy of spin relaxation processes in the dense QD array. The cw EPR experiments on QD array can not provide the exact information about values of T_2 and T_1, and the direct spin coherence measurements of QD structures are needed. Here we report the spin-echo measurements of the spin relaxation times (T_2) and (T_1) of electrons localized on Ge/Si quantum dots. The confinement potential for electrons are formed due to local strain in Si surrounding Ge QDs. Microwave pulses in a pulsed-EPR spectrometer produce the necessary spin rotations (which can be viewed as elementary single-qubit operations) with two- and three-pulse sequences being used to measure the transverse relaxation (decoherence or phase memory) time, T_2, and the longitudinal relaxation time, T_1.

1. Samples and experiment

Samples were grown by molecular-beam epitaxy on n-Si(001) substrates with a resistivity of 1000 Ω cm. The QD structure was optimized with the aim to enlarge the electron binding energy E_b in the Si potential well near a QD, as E_b in a sample with a single Ge QD layer is very small ($E_b \approx 10$ meV) [6]. One way to enlarge E_b is the growth of a vertical stack of Ge islands. The accumulation of the strain from different QD layers in the stack leads to an increase of the potential well depth. A fourfold stack of Ge islands was inserted into the 0.6 μm epitaxial n-Si layer (Sb concentration 4×10^{16} cm^{-3}) at a distance of 0.3 μm from the substrate. In order to reduce distortion of the electron confining potential by the potential of ionized impurities, a 10-nm thick undoped Si spacer was introduced between the topmost Ge layer and the n-type Si cover layer. The Ge QD's formation was controlled by reflection high energy electron diffraction (RHEED).The density of QDs is $\sim 10^{11}$ cm^{-2}. According to the numerical calculations using the effective-mass approximation [7] the electron localization occurs between the second and the third QD layers at the apices of the Ge dots, and the electron binding energy amounts to 60 meV.

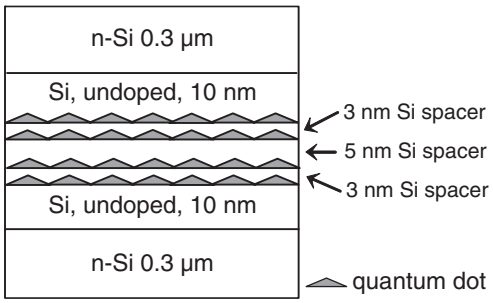

Fig. 1. The structure of the sample.

Measurements were performed with a Bruker Elexsys580 X-band EPR spectrometer using a dielectric cavity Bruker ER-4118 X-MD-5. The samples were glued on a quartz holder, and the entire cavity and sample maintained at low temperature (4–5 K) with a helium flow cryostat (Oxford CF935). The spin echo measurements carried out for the magnetic field $\mathbf{H} \parallel Z$, where Z is the [001] growth direction of the structure. A two-pulse Hahn echo experiment ($\pi/2-\tau-\pi-\tau-$echo) was used to measure T_2 (a detailed explanation can be found in Ref. [8]). In order to observe longitudinal (T_1) relaxation, a different pulse sequence is applied ($\pi - T - \pi/2 - \tau - \pi - \tau -$echo).

A π-pulse rotates the magnetization opposite to its thermal equilibrium orientation, where interaction with the environment causes the spins to relax back to the orientation parallel to $\mathbf{H}_0$ (longitudinal relaxation). After a time T, a $\pi/2$-pulse followed by another π-pulse is used to observe a Hahn echo.

2. Results and discussion

In cw EPR experiments on the quantum dot structures, a single EPR-line with the principal values $g_{zz} = 1.9995$ and $g_{xx} = g_{yy} = 1.9984$ is observed [6]. An analysis of the obtained g-tensor values confirms an electron localization in the strain-induced potential wells in Si in the vicinity of the Ge dots. The observed EPR-line exhibits an inhomogeneous broadening. The linewidth ΔH_{pp} is about 0.8 Oe for the magnetic field $\mathbf{H} \parallel Z$, where Z is the [001] growth direction of the structure. On the deviation of the magnetic field from the Z-axis the ESR line becomes broader and weaker. The well pronounced anisotropy of the ESR linewidth can be explained in terms of an effective magnetic field lying in the plane of the QD array. Spin relaxation comes from the precession of the electron spin in the effective magnetic field during certain tunneling events. Such a mechanism of spin relaxation has been discussed in details in the Ref. [6]. Since the observed ESR line exhibits an inhomogeneous broadening, one can only estimate the lower limit of the spin relaxation time from cw EPR measurements. The linewidth $\Delta H_{pp} = 0.8$ Oe gives the value of $T_2 \sim 10^{-7}$ s.

The measurements of spin echoes give the more exact information about relaxation processes in QD structures. According to results of two-pulse Hahn echo experiment the spin echo behavior can be described by a superposition of two exponentially decaying functions, that can be explained by existing of two groups of carriers with different T_2. The transverse relaxation times for these groups are given in the inset of Fig. 2. The first group (two times larger) has the transverse time $T_2 \approx 0.9$ μs, while the second group of electrons has longer dephasing time $T_2 \approx 20$ μs. According to the model of the anisotropic spin relaxation [6,9], one can expected that the longitudinal time measurements will give two times higher spin relaxation rates ($T_2 = 2T_1$) for the magnetic field $\mathbf{H} \parallel Z$. However, the inversion-recovery experiment gives only one value of spin relaxation $T_1 \approx 8.2$ μs. We refer this time only to the second group of electrons, thinking that electrons in the first group ought to have the longitudinal time shorter than 1 μs. To deduce the longitudinal time for the first group of electrons the more careful measurements with short values of T are needed.

We suppose that the second group with slower spin relaxation rate consists of electrons being in ground states of QDs with smaller probability of tunneling between QDs. The electrons of the first group with faster spin relaxation rate can be attributed to the excited states (first two excited states with s-like wave functions [7]) in our fourfold Ge layers system. They have practically the same g-factor [6], but the higher probability of tunneling between QDs.

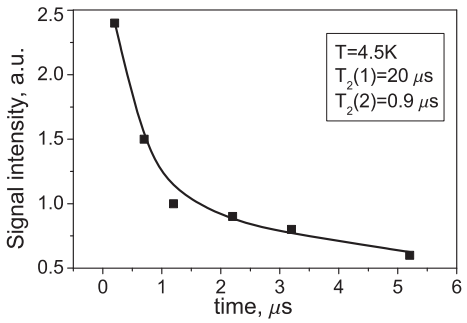

Fig. 2. Two-pulse spin-echo intensity versus delay time τ.

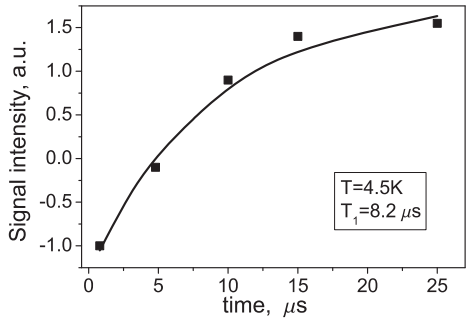

Fig. 3. Inversion recovery signal vs interpulse delay T.

An alternative model explaining the spin echo behavior is based on the existence of QD pairs or small closed clusters of QDs with strong tunneling coupling. These QD groups can be formed due to spontaneous nucleation of QDs during epitaxial growth. The electron hops between QDs in these clusters are exponentially fast as compared with typical hops and can give the high spin relaxation rate. In our experiments this provides the one order high spin relaxation rate in first groups of electrons $T_2 \approx 0.9$ μs. The second group electrons can be related to typical hops between QDs with lower spin relaxation rate $T_2 \approx 20$ μs.

Both models demonstrate that the spin relaxation rate in investigated structure strongly depends on the probability of tunneling between quantum dots. Then the creation of well-separated QD array will provide an increase of spin relaxation time in QD structures.

Using the experimental values of T_1 and T_2 we estimate a Rashba field of 10–20 G, orders of magnitude smaller than in some III–V systems [3]. These results suggest several ways in which the spin decoherence may be reduced: formation of more symmetric potential wells for electrons and suppression of tunneling transitions between QDs providing the appearance of Rashba field.

Acknowledgements

This work was supported by RFBR (Grants 08-02-00121, 06-02-16988), State Contract 02.513.11.3156.

References

[1] S. Datta and B. Das, *Appl. Phys. Lett.* **56**, 665 (1990).
[2] J. Schliemann, J. C. Egues, and D. Loss, *Phys. Rev. Lett.* **90**, 146801 (2003).
[3] A. M. Tyryshkin *et al*, *Phys. Rev. Lett.* **94**, 126802 (2005).
[4] Z. Wilamowski *et al*, *Phys. Rev. B* **66**, 195315 (2002).
[5] A. Bychkov and E. I. Rashba, *J. Phys. C* **17**, 6039 (1984).
[6] A. F. Zinovieva *et al*, *Phys. Rev. B* **77**, (2008).
[7] A. I. Yakimov *et al*, *Phys. Rev. B* **73**, 115333 (2006).
[8] A. Schweiger and G. Jeschke, *Principles of Pulse Electron Paramagnetic Resonance* (Oxford University Press, Oxford, 2001).
[9] Y. Yafet, *in Solid State Physics* (Academic Press, New York, 1963), **14**, 1 (1963).

16th Int. Symp. "Nanostructures: Physics and Technology"
Vladivostok, Russia, July 14–18, 2008

Silicon spintronics

Biqin Huang and Ian Appelbaum
Electrical and Computer Engineering Department, University of Delaware, Newark, Delaware, USA, 19716

Abstract. Although silicon is an excellent candidate for semiconductor spintronics from the perspective of engineering and physics, spin transport in silicon was not achieved until our realization of the vertical silicon spintronic device based upon the hot electron spin filtering effect. The details of the operating principle and measurements will be discussed. With this unique design, coherent spin transport through long distances — 350 μm — was demonstrated, showing the long spin lifetime in silicon. The spin injection efficiency, electric field-controlled spin precession and dephasing effect in silicon have also been explored, paving the way toward practical silicon spintronic applications.

Introduction

Nowadays, the modern semiconductor industry faces a formi dable challenge: continuously improve the performance of the electronic device while decreasing the power consumption and cost. With the size of semiconductor devices approaching the nanometer scale, more fundamental physical challenges need to be resolved to sustain this development trend. It is becoming clear that at a certain point, the fundamentals of present-day devices should be amended or even completely redesigned, which would need the advances of material research and device physics. Instead of constructing semiconductor devices based on the spatial distribution of electron charges, spintronic devices aim to utilize the orientation of electron spin (the intrinsic angular momentum of the electron) for information storage and manipulation, potentially providing power efficient, high speed, nonvolatile and more functional devices [1,2]. The great success of *metal*-based spintronic devices such as Giant Magnetoresistance and Tunneling Magnetoresistance devices has stimulated large-scale research in *semiconductor*-based spintronic devices, which is primarily motivated by our ability to control electron transport in semiconductors with e.g. doping, and the much larger spin *lifetime* in semiconductors as compared to metals, allowing coherent spin transport of non-equilibrium spin polarized electrons. Success in this field could possibly lead to next generation logic circuits, an excellent successor to conventional semiconductor microelectronics.

The other apparent advantage of building spintronic devices with semiconductors is the seamless integration with conventional semiconductor devices, providing a more functional system and advancing the whole industry transition. Silicon, as the workhorse material of the modern semiconductor industry, would be a logical choice for semiconductor spintronics, not only from the perspective of engineering but also from the considerations of fundamental physics, e.g. the long spin lifetime due to lack of bulk crystal asymmetry, low spin-orbit coupling, and small hyperfine interaction in silicon. The critical step to realize silicon spintronics is spin detection. However, normally the indirect bandgap of silicon prevents the application of the prevailing optical spin detection in direct-bandgap semiconductors such as GaAs, except recently one group has demonstrated spin detection in silicon based on this weak light emission process [3].

To overcome this difficulty, a vertical silicon spintronic device [4] based on the ballistic hot electron spin filtering effect was constructed, realizing all electrical spin injection, transport and detection in silicon. This unique spin detection scheme enables further explorations of electron spin transport in silicon, including the spin injection efficiency and dephasing analysis.

1. Device principle

Fig. 1(a) shows the operating principle and schematic band diagram of this device and (b) is the schematic side-view of the device. Hot spin polarized electrons are injected into silicon through a tunnel junction with a ferromagnetic metal (CoFe) as emitter. When electrons arrive at the other side of the Si transport layer and if the electron spins are parallel to the magnetization of the NiFe detector metal layer, some of them will survive inelastic scattering in the metal and couple to silicon's conduction band of the collector, forming the collector current I_{C2}. If the electron spin is antiparallel to the magnetization of the detector after transporting through the ferromag-

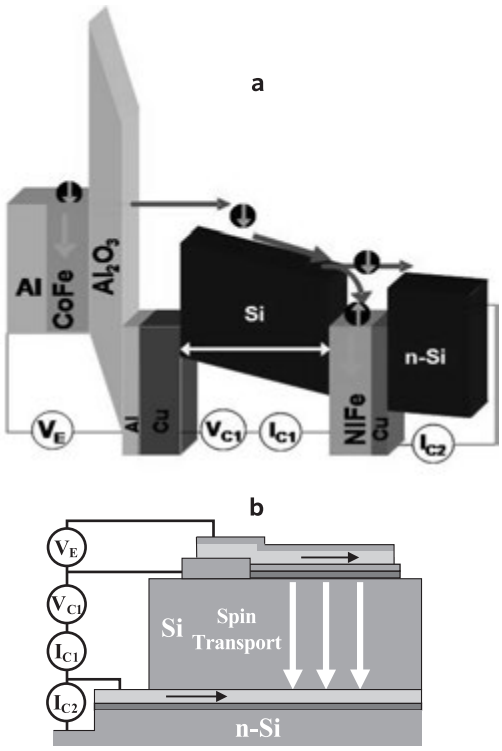

Fig. 1. (a) The schematic illustration of vertical silicon spintronic device composed of spin injector, spin transport layer, and spin detector. (b) Side-view of the device with electrical configuration.

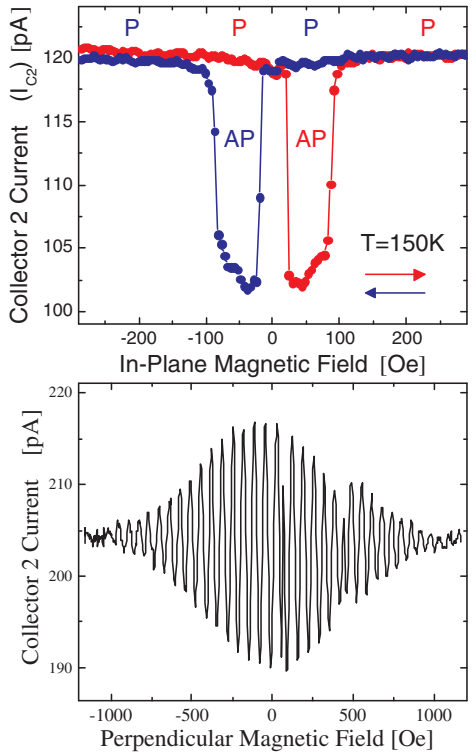

Fig. 2. (a) In-plane magnetic hysteresis measurement of second collector current I_{C2} at constant emitter voltage bias $V_E = -1.3$ V and constant accelerating voltage $V_{C1} = 20$ V, showing ≈18% spin-valve effect at 150 K. The labels "P" and "AP" refer to parallel and antiparallel injector/detector magnetization configuration, respectively. Injected current I_{C1} is 6.6 μA. (b) Spin precession and dephasing (Hanle effect) of Si conduction-band electrons in a perpendicular magnetic field at 150 K with $V_{C1} = 80$ V.

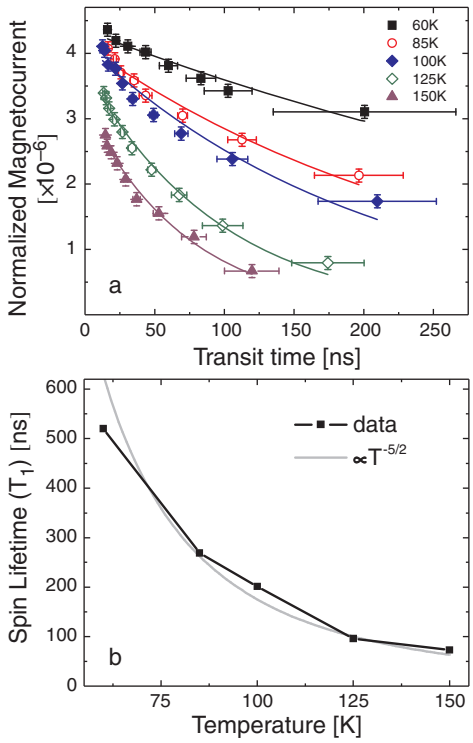

Fig. 3. (a) Fitting the normalized magnetocurrent ($\Delta I_{C2}/I_{C1}$) to an exponential decay model using transit times derived from spin precession measurements at variable internal electric field yields measurement of longitudinal spin lifetimes (T_1) in undoped bulk Si. (b) The experimental T_1 values obtained as a function of temperature are compared to Yafet's $T^{-5/2}$ power law for indirect-bandgap semiconductors [8].

netic layer, ideally all of them will be inelastically scattered and will not have enough energy to surmount the Schottky barrier formed between Cu and Silicon, resulting in reduced collector current I_{C2}. Thus, this spin dependent current change enables an effective, universal, and electrical spin detection, which theoretically could be applied to any other semiconductor. In this device, the hot electron spin filtering effect of ferromagnetic metals plays a vital role in spin detection. Essentially, this device is the combination of a tunnel junction transistor and metal base transistor which requires a special processing technique-metal thin film ultrahigh vacuum wafer bonding [5].

To experimentally confirm spin transport in silicon, two different measurements — in-plane spin valve effect and perpendicular Hanle effect (as shown in Fig. 2) — should be implemented [6]. Similar to an experiment where optical light intensity modulation is achieved by changing the relative optical axis orientation of optical polarizer and analyzer, the in-plane spin valve effect demonstrates collector current (I_{C2}) modulation, as shown in Fig. 2(a), through the magnetization switching in those two ferromagnetic metals in the injector and detector controlled by the external in-plane magnetic field. To confirm that this spin valve phenomenon indicates coherent spin transport, spin precession and dephasing measurement under an external magnetic field (perpendicular to the injected spin orientation) was carried out, whose result is shown in Fig. 2(b). The applied perpendicular magnetic field causes the injected spins to precess at a frequency proportional to magnetic field magnitude, controlling the final precession angle for electron spins arriving at the detector. Hence, varying the external magnetic field will lead to collector current oscillation. At least 15 full spin rotations are evident by the number of oscillation extrema, clearly demonstrating coherent spin transport through 350 μm, the longest distance spin has been transported in the solid-state.

2. Spin life time in silicon

To build a spintronic circuit, long spin lifetime is an extremely important criteria. The longer the spin lifetime, the more logic operations would be allowed before decoherence, and enable a functional system. To determine the spin lifetime, the time dependent spin polarization could be measured, based on the combination of the in-plane spin valve effect and Hanle effect measurements. From the oscillation period of Hanle effect, the transit time τ of electrons from the injector to the detector can be calculated according to $\tau = h/(2g\mu_B B_\pi)$, where B_π is the magnetic field corresponding to π precession extremum, h is Planck constant, g is electron spin g-factor, and μ_B is the Bohr magneton. With the normalized magnetocurrent $\Delta I_{C2}/I_{C1}$ determined by spin-valve measurements like those in Fig. 2(a), a quantity $\mathcal{P}$ that is proportional to conduction electron current spin polarization could be obtained. Fitting these data at different accelerating voltages with an exponential model ($\mathcal{P} \propto \exp(-\tau/T_1)$) will provide the estimation of the spin lifetime as shown in Fig. 3(a). The spin lifetime estimated with this

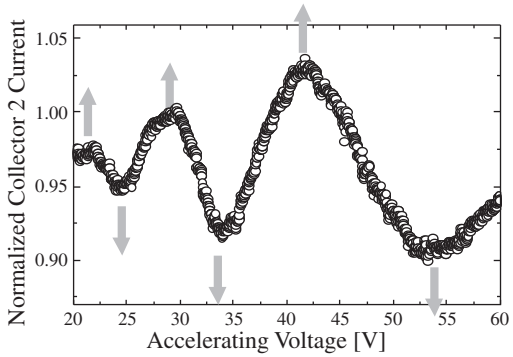

Fig. 4. Normalized collector 2 current as a function of the acceleration voltage with 200 Oe perpendicular magnetic field, indicating electric field controlled spin precession. The arrows indicate spin polarization.

technique at 60 K, 85 K, 100 K, 125 K and 150 K is 520 ns, 269 ns, 201 ns, 96 ns, and 73 ns, respectively. Fitting this temperature dependent spin lifetime gives excellent agreement with the Yafet theory ($\propto T^{-5/2}$) [8].

3. Spin injection and transport

To facilitate the spin transport study in silicon, high spin injection efficiency is absolutely necessary. With the unique design of our spin detector, 37% spin polarization silicon has been demonstrated. This was enabled in part by eliminating the interface formed between ferromagnetic metal and silicon, which causes a nonmagnetic silicide having large, randomly oriented magnetic moments which can cause strong spin scattering [7].

With the optimized spin injector, electric field controlled spin precession has been realized [9]. In the Hanle effect, control over spin orientation is achieved by changing the external perpendicular magnetic field in a constant electric field, causing spin precession at varying frequency. However, if, instead, the acceleration voltage is changed in a constant magnetic field, the electron transit time is altered and the precession angle of spins arriving at the detector would be controlled, also resulting in current modulation as shown in Fig. 4, where current under 200 Oe magnetic field is normalized by collector current at zero magnetic field.

As shown in Fig. 2(b), the suppressed magnitude of oscillations at high magnetic field indicates the dephasing effect which originates from the spin precession angle distribution of the electron spins after transport in the presence of diffusion. Eventually this inherent spin dephasing effect has to be taken into account for device design. However, further study of this effect has to be examined first. It has been shown dephasing is inversely dependent on the square-root of the voltage drop that drives the drift of the electron spin, both theoretically and experimentally [10, 11]. More importantly, we demonstrated that the relative spin dephasing is independent on the transport length under a certain accelerating voltage, which is significant for semiconductor device integration. Furthermore, with the spin drift and diffusion model, the effect of a non-perpendicular (oblique) magnetic field on the Hanle effect has been demonstrated, providing a reliable means to examine the spin transport through semiconductors [10].

4. Conclusion

Although good progress has been made in silicon spintronics, there are certainly a lot of unknowns to be explored. Whether silicon spintronics will eventually make its way to the center stage of the semiconductor industry is still not quite clear. However, silicon spintronic devices' ability to integrate seamlessly with conventional charge-based silicon devices and its inherent long spin lifetime qualify silicon as the most feasible base for continuous development of semiconductor spintronics.

Acknowledgements

This work was supported by DARPA/MTO and ONR. We thank coauthors D. Monsma and J. Li. Figures 1(b) and 2–3 are copyright AIP and APS.

References

[1] D. D. Awschalom and M. E. Flatte, *Nature Physics* **3**, 153 (2007).
[2] S. A. Wolf, D. D. Awschalom, R. A. Buhrman, J. M. Daughton, S. VonMolar, M. L. Roukes, A. Y. Chtchelkanova, and D. M. Treger, *Science* **294**, 1488 (2001).
[3] Berend T. Jonker, George Kioseoglou, Aubrey T. Hanbicki, Connie H. Li, and Phillip E. Thompson, *Nature Physics* **3**, 542 (2007).
[4] I. Appelbaum, B. Q. Huang, and D. J. Monsma, *Nature* **447** (7142), 298 (2007).
[5] D. J. Monsma, J. C. Lodder, Th. J. A. Popma, B. Dieny, *Phys. Rev. Lett.* **74**, 5260 (1995).
[6] Biqin Huang, Douwe J. Monsma, and Ian Appelbaum, *Phys. Rev. Lett.* **99**, 177209 (2007).
[7] Biqin Huang, Lai Zhao, Douwe J. Monsma, and Ian Appelbaum, *Appl. Phys. Lett.* **91**, 052501 (2007).
[8] Y. Yafet, in *Solid State Physics*, Vol. 14, ed. Seitz and Turnbull, (Academic, New York, 1963).
[9] Biqin Huang, Douwe J. Monsma, and Ian Appelbaum, *Appl. Phys. Lett.* **91**, 072501 (2007).
[10] Jing Li, Biqin Huang, and Ian Appelbaum, *Appl. Phys. Lett.* **92**, 142507 (2008).
[11] Biqin Huang and Ian Appelbaum, *Phys. Rev. B* **77**, 165331 (2008).

16th Int. Symp. "Nanostructures: Physics and Technology"
Vladivostok, Russia, July 14–18, 2008

Optical orientation and spin dynamics in quantum wells with large spin-orbit splitting

N. S. Averkiev and M. M. Glazov
Ioffe Physico-Technical Institute, St Petersburg, Russia

Abstract. We address theoretically the processes of optical orientation and spin relaxation in the semiconductor quantum wells. The spin-spitting arising due to the lack of spatial inversion is assumed to be comparable with the characteristic energy of the carriers. It is shown that the significant degree of the spin polarization of the carriers at the photoexcitation can be achieved in the pulse regime only where the pulse duration is comparable with the spin precession period. The total spin of the electron gas is demonstrated to undergo damped oscillations. Their shape and damping time are sensitive to the photoexcitation parameters and spin splitting value.

Introduction

Fundamental problems of electron spin orientation and spin relaxation attract a lot of interest recently. Spin-orbit interaction splits valence band states in III–V semiconductors and allows the transfer of an angular momentum of a photon to the electron system in semiconductor. It is the same interaction which splits conduction band states in non-centrosymmetric structures and leads to an efficient channel of spin relaxation [1].

Here we address a situation where the linear in the electron wavevector $\mathbf{k}$ splitting of the conduction band states in a quantum well is comparable with the characteristic energy of the electrons. In such a case the spin splitting dramatically modifies the processes of optical orientation and spin relaxation [2]. In general situation the optical orientation processes and spin relaxation processes can not be considered independently because the spin-orbit interaction modifies both the electron spectrum and optical selection rules.

1. Model

We consider a two-dimensional electron gas confined in a quantum well grown along $z \parallel [001]$. The conduction band effective Hamiltonian has a form [3]

$$\mathcal{H}_c = \frac{\hbar^2 k^2}{2m} + \frac{\hbar}{2}\left(\boldsymbol{\sigma} \times \boldsymbol{\Omega}_{\mathbf{k}}\right), \tag{1}$$

where the first term is a kinetic energy with m being an effective mass, and the second term is described by the spin-orbit interaction, $\boldsymbol{\sigma}$ is the Pauli matrix vector. The spin-splitting is assumed to be caused by the Rashba term. An effective spin precession frequency $\boldsymbol{\Omega}_{\mathbf{k}}$ can be written as

$$\boldsymbol{\Omega}_{\mathbf{k}} = \Omega_k[\sin\varphi_{\mathbf{k}}, -\cos\varphi_{\mathbf{k}}, 0]. \tag{2}$$

Here $\Omega_k = 2\alpha k/\hbar$, with α being a constant which determines the spin splitting of the carrier energy spectrum, $\varphi_{\mathbf{k}}$ is an angle between $\mathbf{k}$ and an in-plane axis. At a given $\mathbf{k}$ there are two eigenstates, see Fig. 1, which in the basis of the states with definite spin-z projection have a form

$$\begin{aligned} \psi_{\mathbf{k},-} &= \tfrac{1}{\sqrt{2}}\left[-ie^{-i\varphi_{\mathbf{k}}}, 1\right]^{\mathrm{T}}, \quad \mathcal{E}_{\mathbf{k},-} = \frac{\hbar^2 k^2}{2m} - \frac{\hbar\Omega_k}{2}, \\ \psi_{\mathbf{k},+} &= \tfrac{1}{\sqrt{2}}\left[ie^{-i\varphi_{\mathbf{k}}}, 1\right]^{\mathrm{T}}, \quad \mathcal{E}_{\mathbf{k},+} = \frac{\hbar^2 k^2}{2m} + \frac{\hbar\Omega_k}{2}. \end{aligned} \tag{3}$$

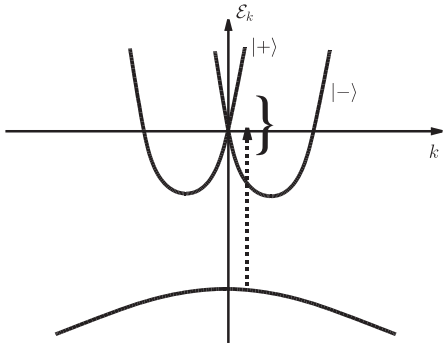

Fig. 1. Schematic illustration of the electron energy spectrum. Symbols $|+\rangle$ and $|-\rangle$ denote two branches of the spectrum. Dotted vertical arrow shows an optical transition. Curly bracket shows the spectral width of the excitation pulse.

In each of the eigenstates the average spin of electron $\mathbf{s}_{\mathbf{k},\pm} = \langle\psi_{\mathbf{k},\pm}|\boldsymbol{\sigma}|\psi_{\mathbf{k},\pm}\rangle$ lies in the (x, y) plane perpendicular to the wavevector $\mathbf{k}$. According to Eqs. (2) and (3) spin splitting linearly increases as a function of k according to $\hbar\Omega_k = 2\alpha k$.

2. Optical orientation

For the sake of simplicity we assume that the upper branch of a valence band is a heavy-hole branch with the z projection of an angular momentum being $\pm 3/2$. Its spin splitting is neglected. Therefore valence band states $|\mathbf{k}, \pm 3/2\rangle_{\mathrm{v}}$ are two-fold degenerate.

An absorption of a circularly polarized (say, σ^+) photon induces the transitions accompanied with the change of the angular momentum of an electron by 1. If the spin splitting is neglected, the σ^+ polarized light causes the transitions from the valence band state $|\mathbf{k}, -3/2\rangle_{\mathrm{v}}$ to the conduction band state $|\mathbf{k}, -1/2\rangle_{\mathrm{c}}$. The allowance for the spin splitting results in the transitions from $|\mathbf{k}, -3/2\rangle_{\mathrm{v}}$ both to $\psi_{\mathbf{k},-}$ and to $\psi_{\mathbf{k},+}$ eigenstates of the conduction band.

The theory of optical orientation is developed in the framework of the density matrix approach [4]. In the interaction representation an operator describing interband transitions can be written as

$$\widehat{V} = \frac{V_0(t)e^{iE_g t/\hbar}}{\sqrt{2}} \sum_{\mathbf{k},s=\pm} e^{i\mathcal{E}_{\mathbf{k},s}t/\hbar} c^{\dagger}_{\mathbf{k},s} c_{\mathbf{k},-3/2} + \mathrm{h.c.} \tag{4}$$

Here $V_0(t)$ describes temporal dependence of the incident field, E_g is the band gap calculated with the allowance for the size

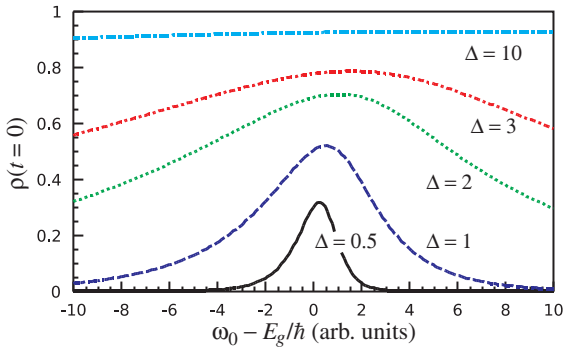

Fig. 2. The polarization degree of photoexcited electrons as a function of the incident light frequency $\omega_0 - E_g/\hbar$ calculated for different pulse widths Δ. The frequency is measured in the units of $\hbar k_R^2/2m$ where $k_R = \alpha m/2\hbar$.

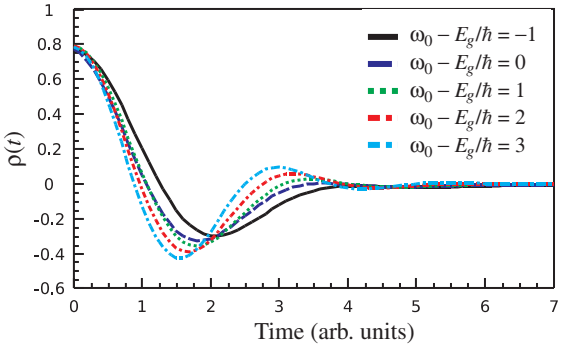

Fig. 3. The dependence of the polarization degree of photoexcited electrons on time calculated for different frequencies of incident light. The spectral width of the excitation pulse is $\Delta = 3$. Frequency is measured in units of $\hbar k_R^2/2m$, time is measured in units of $\hbar/(2\alpha k_R)$ where $k_R = \alpha m/2\hbar$.

quantization of the electrons and holes. Operators $c^\dagger_{\mathbf{k},\pm}$ ($c_{\mathbf{k},\pm}$) describe creation (annihilation) of electrons in states $\psi_{\mathbf{k},\pm}$ in the conduction band, operators $c^\dagger_{\mathbf{k},\pm 3/2}$ ($c_{\mathbf{k},\pm 3/2}$) describe the creation (annihilation) of an electron in the valence band. The resonant transitions are taken into account in Eq. (4) only. We have also neglected the energy dispersion in a valence band.

Eq. (4) clearly shows that the monochromatic excitation can not lead to the efficient optical orientation because only eigenstates can be populated (provided that the electron scattering is inefficient). Therefore the significant degree of optical orientation can be achieved only for the pulsed excitation where the energy uncertainty due to the finite pulse time is comparable with the spin splitting.

Figure 2 shows the dependence of the polarization of the photoexcited carriers right after the photoexcitation pulse as a function of light frequency for different spectral widths of the excitation pulse. The latter is assumed to have a Gaussian shape. The initial occupation of the conduction band is neglected. Fig. 2 shows that the polarization degree decreases with a decrease of the pulse width Δ and depends non-monotonously on the incident light frequency. The polarization degree is non-zero in the frequency range where $\Omega_k \leq \Delta$ ($k = \sqrt{2m(\omega_0 - E_g)/\hbar}$), i.e. where the eigenstates are most efficiently intermixed. Note that for $\Delta/(\hbar k_R^2/2m) \leq 1$ the pulse width is not short as compared with the spin precession period. Here $k_R = \alpha m/2\hbar$. Therefore optical orientation and the spin relaxation can not be treated independently. These curves demonstrate that at $\Delta/(\hbar k_R^2/2m) \leq 1$ the polarization degree is much smaller as compared with the case of $\Delta/(\hbar k_R^2/2m) \gg 1$.

3. Spin relaxation

The kinetic theory of spin relaxation in the case of large spin splitting is developed under the assumption that $E_F\tau/\hbar \gg 1$, where E_F is the Fermi energy, τ is the scattering time. This condition allows to use the kinetic equation in order to describe spin relaxation [4]. In a general case of an arbitrary relation between the pulse spectral width Δ and the characteristic spin splitting $\delta\Omega \sim \alpha \max\{k_R, \sqrt{2m\Delta/\hbar}\}$ the spin generation and spin relaxation can not be separated. However if the condition $\Delta \gg \delta\Omega$ is satisfied the spin precession and optical orientation take place on different time scales and can be considered independently.

The spin polarization in a given state $\mathbf{k}$ as a function of time can be written at $\hbar\Omega_k \sim E_F$ as

$$s_z(k,t) = s_z^0(k)\cos(\Omega_k t)e^{-t/\tau_k}, \qquad (5)$$

where τ_k is the total scattering time of electron in the state k calculated with allowance for the spin splitting. Note that $\hbar\Omega_k \sim E_F$ dictates $\Omega_k\tau_k \gg 1$ and out scattering processes should be taken into account only. cf. Ref. [2]. The total spin of electron ensemble can be found by averaging Eq. (5) over the initial spin distribution.

Figure 3 shows the time dependence of the polarization degree of the photoexcited electrons calculated in the case of pulsed excitation. The electron scattering and initial occupation of the conduction band states are neglected. The excitation pulse parameters are given in the caption to the figure. Fig. 3 clearly demonstrates that the spin beats decay on the same time scale as a spin precession due to the distribution of spin precession frequencies. It differs present situation from the considered earlier, Ref. [5]. The allowance for the scattering does not affect strongly spin dynamics if $\hbar\Omega_k \sim E_F$ and $E_F\tau/\hbar \gg 1$.

4. Conclusions

Optical orientation and spin relaxation in the structures with large spin splitting has several features as compared with the conventional case of $\hbar\Omega_k \ll E_F$. First, an effective optical orientation is achievable by short laser pulses. Second, the damping of spin beats is caused by the spread of the spin precession frequencies. Third, electron scattering leads to a complete loss of spin polarization.

Acknowledgements

Financial support from RFBR, programmes of RAS and "Dynasty" foundation — ICFPM is gratefully acknowledged.

References

[1] M. I. Dyakonov and V. I. Perel' in *Optical orientation*, ed. F. Meier and B. Zakharchenya, North-Holland 1984.
[2] C. Grimaldi, *Phys. Rev. B* **72**, 75307 (2005).
[3] N. S. Averkiev, L. E. Golub, S. A. Tarasenko, and M. Willander, *J. Phys.: Condens. Matter* **13**, 2517 (2001).
[4] N. S. Averkiev, M. M. Glazov, *Semiconductors* (2008).
[5] V. N. Gridnev, *JETP Letters* **74**, 380 (2001). M. M. Glazov, *Solid State Commun.* **142**, 531 (2007).

16th Int. Symp. "Nanostructures: Physics and Technology"
Vladivostok, Russia, July 14–18, 2008

Robust strongly-modulated transmission of a *T*-shaped structure with local Rashba interaction

K. Shen[1] and M. W. Wu[1,2]

[1] Hefei National Laboratory for Physical Sciences at Microscale, University of Science and Technology of China, Hefei, Anhui, 230026, China
[2] Department of Physics, University of Science and Technology of China, Hefei, Anhui, 230026, China

Abstract. A *T*-shaped structure with local Rashba interaction has been studied. The interplay of the Fano–Rashba interference and structure interference makes the transmission strongly-modulated in such structure. A wide energy gap occurs when the structure-induced anti-resonance is tuned close to the Fano–Rashba anti-resonance. A large leakage current from the gap can also be obtained by changing the Rashba strength and the length of the sidearm. The robustness of such gap against strong disorder is demonstrated. The result shows the advantage of our structure as a spin transistor.

Introduction

Utilizing the transport property in mesoscopic system to realize spintronic devices has been paid much attention lately due to the possible application [1]. One of such devices, the Datta–Das spin field effect transistor [2], was proposed depending on the spin precession in Rashba [3] effective magnetic field through the waveguide. After that, the role of Rashba spin orbit coupling in ballistic systems was extensively studied [4,5]. Very recently, the effect of local Rashba spin-orbit coupling in quasi-one dimensional quantum wires was investigated [6]. As reported, there exists at least one bound state localized in the vicinity of the Rashba region due to the equivalent attractive potential from local Rashba interaction. Such bound state can interfere with direct propagating channels leading to Fano asymmetric lineshapes [6,7,8,9]. Therefore, this effect was called Fano–Rashba effect. Similar Fano-type inference effect in the quantum wire with an applied magnetic field was also reported, which was based on the interplay of the transmission channel with certain spin and the evanescent mode with opposite spin [10]. The transmission zero dip at Fano antiresonance was proposed to be helpful to realize spin transistor by Sanchez *et al* [10]. However, the robustness against the disorder, which is essential for real application, remains questionable. In this work, we numerically demonstrate that the occurrence of such dip is rather limited by disorder strength and propose a better scheme of a spin current modulator device using *T*-shaped structure [11,12] with local Rashba interaction.

The waveguide in our study is shown in Fig. 1, where a semiconductor waveguide (the length of the wire is denoted by L) with a sidearm protruding from the center, is connected to the half-metallic leads through perfect ideal ohmic contact. We assume the electron states at the Fermi level are all spin-down ones in the leads, so that only spin-down electrons can propagate into/out of the *T*-shaped structure. The effective length of the sidearm L_s can be adjusted electronically via a gate voltage V_g [12]. The finite width of the waveguide L_w gives the propagation threshold as the first quantized subband along the transversal direction. An entire-spatial perpendicular magnetic field is applied to shift the energy band by Zeeman splitting $V_\sigma = \sigma V_0$. The interference of the different Feynman paths makes it possible to realize spin transistor using *T*-shaped structure [11]. We introduce the local Rashba interaction as

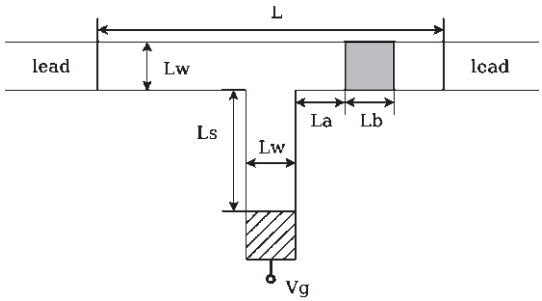

Fig. 1. Schematic of *T*-shaped structure with local Rashba interaction. The Rashba area is shown as the gray square.

the gray square shown in Fig. 1. From Fano-type interference effect due to local Rashba interaction, the transmission of the propagating channel can also be strongly modulated, especially at the Fano antiresonance case [6,10]. We will show such a structure can work as a spin transistor with strong robustness.

1. Method

We describe the *T*-shaped structure by the tight-banding Hamiltonian with the nearest-neighbor approximation

$$H = \sum_{l,m,\sigma} \epsilon_{l,m,\sigma} c^+_{l,m,\sigma} c_{l,m,\sigma} - t \sum_{l,m,\sigma} \left(c^+_{l+1,m,\sigma} c_{l,m,\sigma} + c^+_{l,m+1,\sigma} c_{l,m,\sigma} + \mathrm{H.C.} \right) + H_\mathrm{R} \,, \quad (1)$$

in which two indices l and m denote the site coordinates along the x- and y-direction, respectively. $\epsilon_{l,m,\sigma} = 4t + \sigma V_0$, with the hopping energy $t = \hbar^2/(2m^*a^2)$ and the Zeeman splitting V_0. m^* and a stand for the effective mass and lattice constant. The last term describes the Rashba spin-orbit coupling [3,13]

$$H_\mathrm{R} = \lambda \sum_{l,m,\sigma,\sigma'} \left[c^+_{l+1,m,\sigma} c_{l,m,\sigma'} \left(i\sigma_y^{\sigma\sigma'} \right) - c^+_{l,m,\sigma} c_{l,m+1,\sigma'} \left(i\sigma_x^{\sigma\sigma'} \right) + \mathrm{H.C.} \right], \quad (2)$$

in which $\lambda = \alpha/2a$ with α representing the Rashba coefficient. The sites (l, m) in H_R should lie in the gray area in Fig. 1.

The conductance is obtained from the Landauer–Büttiker

formula [14]

$$G^{\sigma\sigma'}(E) = \left(e^2/h\right) \mathrm{Tr}\left[\Gamma_1^{\sigma} G_{1N}^{\sigma\sigma'+}(E) \Gamma_N^{\sigma'} G_{N1}^{\sigma'\sigma-}(E)\right], \quad (3)$$

where $\Gamma_{1(N)}$ denotes the self-energy of isolated ideal leads and $G_{1N}^{\sigma\sigma'}$ ($G_{N1}^{\sigma'\sigma}$) is the retarded (advanced) of the semiconductor calculated by the Green's function method [15].

2. Results

We calculate the conductance of the only propagating spinor $G^{\downarrow\downarrow}$, and find a zero transmission point, i.e., the structure antiresonance point [12,16], without the Rashba interaction. The presence of the Rashba interaction also strongly influences the conductance and provides another zero transmission point, i.e., the Fano antiresonance due to the Fano–Rashba effect.The former can be moved by tuning the length of sidearm and the later can be moved by tuning the spin-orbit coupling coefficient [10]. A wide energy gap is obtained when the Fano–Rashba antiresonance is close to the structure one. Moreover, one can also tune the gap off via changing the spin-orbit coupling coefficient/the length of the sidearm, and obtain a large leakage current. Therefore, our model can work as a spin transistor with the on- and off-feasibility by tuning Rashba strength as well as remotely controlling of the sidearm length L_s [12] by V_g.

We analyze the robustness of the double-antiresonance gap against the Anderson disorder by averaging over sufficient disorder configurations. We find that the wide gap is much more robust than the single structure or Fano–Rashba antiresonance. This shows the great advantage of our proposed device.

Acknowledgements

This work was supported by the Natural Science Foundation of China under Grant Nos. 10574120 and 10725417, the National Basic Research Program of China under Grant 2006CB922005 and the Knowledge Innovation Project of Chinese Academy of Sciences.

References

[1] *Semiconductor Spintronics and Quantum Computation*, edited by D. D. Awschalom, D. Loss and N. Samarth, (Springer-Verlag, Berlin, 2002); I. Žutić, J. Fabian, and S. Das Sarma, *Rev. Mod. Phys.* **76**, 323 (2004), and references therein.
[2] S. Datta and B. Das, *Appl. Phys. Lett.* **56**, 665 (1990).
[3] E. I. Rashba, *Fiz. Tverd. Tela* (Leningrad) **2**, 1224 (1960).
[4] Y. Sato, S. Gozu, T. Kikutani, and S. Yamada, *Physica B* **272**, 114 (1999).
[5] A. V. Moroz and C. H. W. Barnes, *Phys. Rev. B* **60**, 14272 (1999).
[6] D. Sánchez and Ll. Serra, *Phys. Rev. B* **74**, 153313 (2006).
[7] C. S. Chu and R. S. Sorbello, *Phys. Rev. B* **40**, 5941 (1989).
[8] J. U. Nöckel and A. D. Stone, *Phys. Rev. B* **50**, 17415 (1994).
[9] U. Fano, *Phys. Rev.* **124**, 1866 (1961).
[10] D. Sánchez, Ll. Serra, and M. Choi, *Phys. Rev. B* **77**, 035315 (2008).
[11] F. Sols, M. Macucci, U. Ravaioli, and K. Hess, *J. Appl. Phys.* **66**, 3892 (1989).
[12] X. F. Feng, J. H. Jiang, and M. Q. Weng, *Appl. Phys. Lett.* **90**, 142503 (2007).
[13] F. Mireles and G. Kirczenow, *Phys. Rev. B* **64**, 024426 (2001).
[14] M. Büttiker, *Phys. Rev. Lett.* **57**, 1761 (1986).
[15] S. Datta, *Electronic Transport is Mesoscopic Systems* (Cambridge University Press, New York, 1995).
[16] Q. W. Shi, J. Zhou, and M. W. Wu, *Appl. Phys. Lett.* **85**, 2547 (2004).

16th Int. Symp. "Nanostructures: Physics and Technology"
Vladivostok, Russia, July 14–18, 2008

Simple model of spin polarized state in quantum point contacts

V. A. Sablikov and B. S. Shchamkhalova
Kotel'nikov Institute of Radio Engineering and Electronics, RAS, 141190 Fryazino, Moscow District, Russia

Abstract. We propose a model explaining the formation of spontaneously spin-polarized state in a quantum point contact (QPC) as result of the exchange interaction of one-dimensional electrons passing through the QPC with spin-polarized electron clouds in the near-contact regions of the electron reservoirs. These Kondo-like clouds are formed by electrons which do not pass through the QPC. The model gives a conductance feature close to the 0.7 anomaly.

Introduction

Recent experiments strongly enhanced interest to the nature of the correlated electron state in quantum point contacts (QPC) and quasi-one-dimensional (1D) quantum structures. They have explicitly shown the presence of quasi-bound states in these structures and revealed an important role they play in the electron transport in the regime of opening the QPC before the first quantization plateau. The analysis shows that none of the presently existing theories explain the facts observed. Two main hypothesis are dominating.

The first relates the observed features of the conductance to the Kondo-like effect caused by a quasibound state, while the second appeals to spontaneous spin polarization and splitting the subbands by spin. Recent studies of the temperature dependence of the conductance have shown that "0.7 anomaly" is not a Kondo-like effect [1]. This conclusion is confirmed also by the form of conductance dependence on the gate voltage. The significant argument against the Kondo-like hypothesis was provided by the experiment revealing the spin polarization of the current through the QPC [2].

The idea of spin-splitted subbands also meets difficulties. The spin splitting is supposed to be caused by the exchange interaction of electrons in the quantum wire. However, the existence of this spin polarized state contradicts to the general theorem of Lieb and Mattis according to which the ground state of a 1D system is unpolarized. Even the models constructed with the violation of this theorem do not describe correctly the temperature dependence of the conductance [3].

Meanwhile, the experiments revealed new properties of the electron state in QPCs evidencing that far enough regions of the reservoirs are involved in the formation of the 0.7 anomaly. An unexpectedly strong effect of a spin localed at a considerable distance (>0.5 μm) from the QPC on its conductance was observed [4]. It was also found that the 0.7 anomaly is significantly affected by electron interference caused by nearby side gates [5].

Here we present a new model of spin-polarized state in a QPC which takes into account the above experiments.

1. The model

The model is based on our recent studies [6] showing that clouds of spatially oscillating electron density exists near the QPC in the 2D electron gas reservoirs. They are formed by electrons which do not pass through the QPC. The 1D electrons passing through the QPC interact effectively with these clouds in transition regions between 1D and 2D parts of the structure. The key point of the model we are proposing is the suggestion that the spin polarization arises in the QPC owing to the exchange interaction of 1D electrons with the clouds, which become also spin polarized.

We develop the model in the case of weak interaction when the one-particle energy of spin-up and spin-down electrons is presented in the form

$$\varepsilon_{\uparrow,\downarrow}(k) = \frac{\hbar^2 k^2}{2m} + \varepsilon_{\rm xc} + V_{\rm H}(n_\uparrow + n_\downarrow - n_0) \mp J(n_\uparrow - n_\downarrow) + \varepsilon_1,$$

where k is the wave vector, $\varepsilon_{\rm xc}(n_\uparrow, n_\downarrow)$ exchange-correlation energy in 1D part of the structure; $V_{\rm H}$ describes the Hartree energy, J is the constant of exchange interaction of 1D electrons with the electron clouds in the reservoirs; ε_1 is the quantization energy in the transverse direction; $n_\uparrow$ and $n_\downarrow$ are electron densities with spin up and down; n_0 is the background positive charge density.

The electron densities $n_{\uparrow,\downarrow}$ are expressed in terms of the energy $\varepsilon_{\uparrow,\downarrow}$ via the Fermi distribution function. Using these expressions we obtain a nonlinear equation system describing self-consistently the total electron density $n = n_\uparrow + n_\downarrow$ and the polarization $\zeta = (n_\uparrow - n_\downarrow)/n$ in the QPC. The conductance is calculated in the standard way with using the Landauer formula.

Main advantages of our approach are as follows:

(i) the model explains the existence of quasibound states which are formed due to the electron backscattering from the clouds [7];

(ii) the interaction constant J, which governs the spin polarization, is determined by overlapping the wave functions of 1D

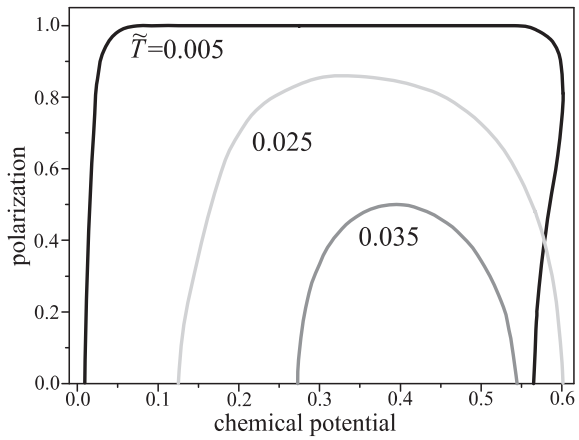

Fig. 1. Spin polarization ζ in the QPC versus the normalized chemical potential for temperatures $\tilde{T} = 0.005, 0.025, 0.035$.

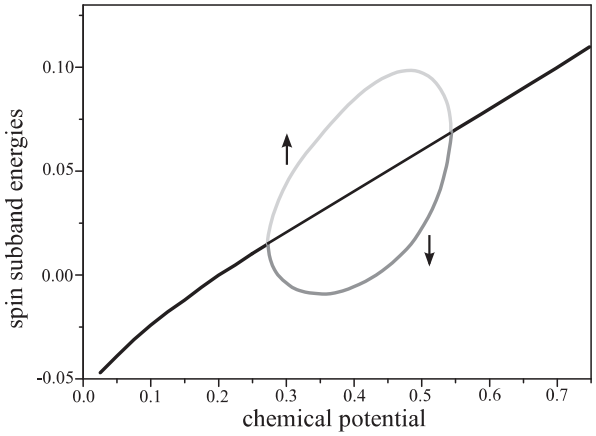

Fig. 2. Spin subband splitting, $\varepsilon_{c;\uparrow\downarrow}/\varepsilon_{\rm N}$, in the QPC.

electrons and the clouds, and therefore depends on interference processes and neighboring spins and gates.

In the next section we show that this model gives the spin polarized state and reasonable dependencies of the conductance on the gate voltage and the temperature even in the simplest case where the electron-electron interaction in the short 1D part of the structure is ignored.

2. The results

The spin polarization ζ, the spin-subband bottom energies $\varepsilon_{c;\uparrow\downarrow}$ and the conductance were calculated as a function of the chemical potential μ in the system for different temperatures. The energies and the temperature are normalized to $\varepsilon_{\rm N} = (\pi\hbar n_0)^2/2m$.

The spin polarization arises if the interaction parameter J exceeds some critical value, and exists in a finite range of μ, as Fig. 1 shows. Here $\tilde{T}$ is the normalized temperature, the normalized chemical potential is $(\mu - \varepsilon_1 + V_{\rm H}n_0)/\varepsilon_{\rm N}$. In these calculations the Hartree interaction parameter $V_{\rm H}n_0/\varepsilon_{\rm N}$ was taken equal 2.

It is seen that the polarization decreases with the temperature and finally disappears at some critical temperature. An interesting feature is the bistability and hysteresis-like behavior of the polarization at low temperatures and high exchange interaction parameter J.

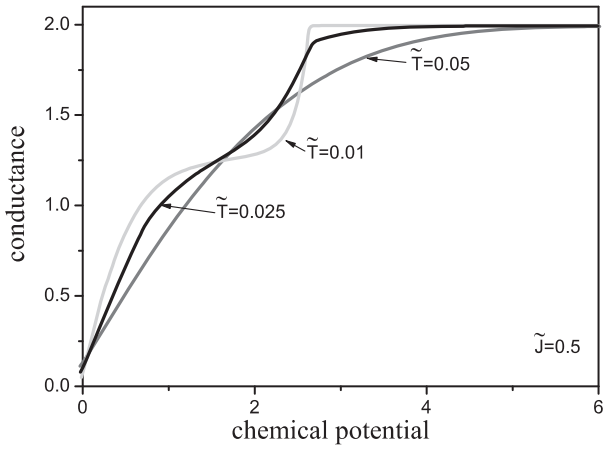

Fig. 3. Conductance (normalized to e^2/h) as a function of the normalized chemical potential for different temperatures.

The splitting of the spin subbands is illustrated in Fig. 2 for $Jn_0/\varepsilon_{\rm N} = 0.5$, $V_{\rm H}n_0/\varepsilon_{\rm N}$=2 and $\tilde{T} = 0.035$.

The conductance dependence on the chemical potential displays features similar to the 0.7 anomaly in the μ range where the spin subbands are splitted. Under such condition, the electron current is spin polarized. While calculating the conductance we take into account that at nonzero temperature both polarized and unpolarized states can be realized with different probabilities. These probabbilities are defined by the free energies of corresponding states.

Acknowledgements

This work was supported by the Russian Foundation for Basic Research, Russian Academy of Sciences (programs "Quantum nanostructures", "Strongly correlated electrons in semiconductors, metals, superconductors, and magnetic materials").

References

[1] F. Sfigakis, C. J. B. Ford *et al*, *Phys. Rev. Lett.* **100**, 026807 (2008).
[2] L. P. Rokhinson, L. N. Pfeiffer, and K. W. West, *Phys. Rev. Lett.* **96**, 156602 (2006).
[3] A. Lassl, P. Schlagheck, and K. Richter, *Phys. Rev. B* **75**, 045346 (2007).
[4] Y. Yoon, L. Mourokh *et al*, *Phys. Rev. Lett.* **99**, 136805 (2007).
[5] Y. Chung, S. Jo *et al*, *Phys. Rev. B* **76**, 035316 (2007).
[6] V. A. Sablikov, *JETP Letters* **84**, 404 (2006).
[7] B. S. Shchamkhalova and V. A. Sablikov, *J. Phys.: Condens. Matter* **19**, 156221 (2007).

16th Int. Symp. "Nanostructures: Physics and Technology"
Vladivostok, Russia, July 14–18, 2008

Generalization of box-model for the description of nuclear spin polarization in quantum dots

M. Yu. Petrov, G. G. Kozlov, R. V. Cherbunin and I. V. Ignatiev
St Petersburg State University, Faculty of Physics, Ulyanovskaya 1, Petrodvorets, 198504 St Petersburg, Russia

Abstract. Two directions of generalization of the box-model for the electron-nuclear spin system in a quantum dot are considered. The first one takes into account the non-uniformity of the electron density over the quantum dot. The second one considers arbitrary values of elementary nuclear spins. The obtained results are discussed.

Introduction

Hyperfine interaction with randomly oriented nuclear spins, which is the most effective mechanism of electron spin relaxation in quantum dots (QDs) [1,2,3], can be suppressed by polarizing the nuclear spins. Due to very large number of nuclei in a QD interacting with the electron spin, $N \simeq 10^4 - 10^5$, the exact solution of the quantum mechanical problem of electron-nuclear spin dynamics is impossible nether analytically nor numerically. This is why the exactly solvable models are of particular interest even when the exact solution is obtained at the expense of assumptions whose plausibility cannot be reliably evaluated.

The simplest model allowing an exact solution of the problem of nuclear spin dynamics in QDs is the box-model which implies that the electron spin is coupled in the same way with all the nuclear spins of the QD [4,5,6]. The main drawback of the box-model is that the model cannot explain a high nuclear polarization for the constant-sign orientation of the electron spin observed experimentally. For quantum dots with 10^4 nuclei, the limiting polarization calculated in framework of the box-model lies in the range of 1% [6], whereas there have been reported experimental observations of the nuclear polarization of several tens of percents in the InAs/GaAs QDs [1,7,8].

In this paper, we report on a generalization of the box-model developed in Ref. [6] in two directions: (i) different elementary nuclear spin momenta $J = 1/2$, 3/2, 9/2 [9], and (ii) inhomogeneous distribution of the electron density over the QD. Such generalization gives rise to more realistic feature of nuclear spin polarization in the QDs.

1. Model

We consider a system comprising the electron spin $S = 1/2$ coupled to even number $2N$ of nuclei with the same elementary spins J. The electron-nuclear interaction strength is proportional to the electron density, $|\psi|^2$, which is considered to be different at different nuclei, on the contrary to what is assumed in the box-model [6]. Let us consider the groups of equivalent nuclei in which all the nuclei interact with the electron equally. In fact, we approximate the smooth space distribution of the electron density by a step-like function. In what follows, we consider n groups with the same number of nuclei in each group.

The hyperfine interaction of the electron with nuclei in this case can be described by the Hamiltonian:

$$\hat{\mathcal{H}}_{hf} = \sum_{i=1}^{n} \hat{H}_i, \tag{1}$$

where each operator, $\hat{H}_i$, describes the hyperfine interaction of the electron with ith group of nuclei:

$$\hat{H}_i = A_i \hat{S}_z \hat{I}_{iz} + \frac{A_i}{2}\left(\hat{I}_i^+ \hat{S}^- + \hat{I}_i^- \hat{S}^+\right). \tag{2}$$

Here $\hat{S}_z$, and $\hat{I}_i$ are the z-projections of the electron spin and total angular momentum of ith group of nuclei, $\hat{S}^{\pm}(\hat{I}_i^{\pm}) = \hat{S}_x(\hat{I}_{ix}) \pm i\hat{S}_y(\hat{I}_{iy})$ are the standard lowering and raising operators for the z-projection of the electron spin (total ith group nuclear spin), and A_i (which is proportional to $|\psi|^2$) is the hyperfine coupling constant for ith group of nuclei.

2. Upper limit of nuclear polarization

We calculate the nuclear polarization achievable in framework of the above model. First, we consider a system with one nuclear group which is correspond to the box-model. As it is shown in Ref. [6], matrix of Hamiltonian (1) has a block-diagonal form in the representation of the functions $|S_z, I_1, L_1, \alpha\rangle$. Here $S_z = \pm 1/2$ is the electron spin z-projection, I_1 and L_1 are the quantum numbers of the total angular momentum of the nuclear system and its z-projection, respectively, α is the set of all other quantum numbers needed for the state to be uniquely specified. Each block in the Hamiltonian is characterized by the angular momentum I_1. The number of blocks with given I_1, $\Gamma_N(I_1)$, equals to the number of ways that yields the state with the total angular momentum I_1. Quantity $\Gamma_N(I_1)$ can be calculated numerically as well as analytically for any elementary nuclear spin J by the method described in Ref. [6]. The density matrix of the nuclear spin system also consist of the blocks corresponding to states with given I_1. These blocks are mutually independent, i.e., the hyperfine interaction may transfer the nuclear spin system from one state to another one within the same block only. So, the nuclear spin polarization of total system corresponds to the polarization of each block. In this case, the average value of the total nuclear spin z-projection is given by:

$$\langle I_z \rangle_1 = \sum_{I=0}^{2NJ} \rho_N(I) I, \tag{3}$$

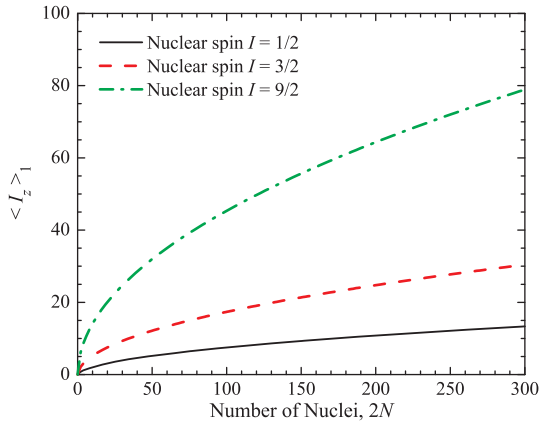

Fig. 1. Average z-projection of the total nuclear spin for the polarized nuclei with different angular momenta as functions of total number of nuclei in the system (box-model).

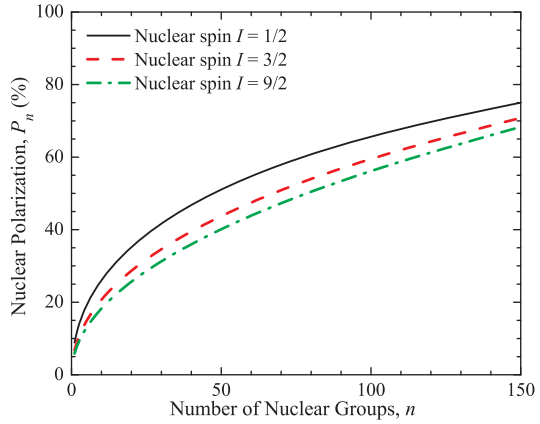

Fig. 2. Dependencies of nuclear polarizations on the number of groups of nuclei for $2N = 300$ nuclei.

where $\rho_N(I) = \Gamma_N(I)(2I+1)/(2J+1)^{2N}$ determines the probability that the nuclear system is in a state with angular momentum z-projection $L_1 = I$ (full polarization of each block). Results of calculations of $\langle I_z\rangle_1$ are shown in Fig. 1. As seen, nuclear momentum $\langle I_z\rangle_1$ as function of number of nuclei increases sub-linearly. The dependence can be approximated by $\langle I_z\rangle_1 \approx C\sqrt{NJ(J+1)}$ with $C \approx 1.3$ for $2N > 50$. Correspondingly, degree of nuclear polarization, $P_1(N) = \langle I_z\rangle_1/(2NJ)$, decreases with the N increase. At large $N \sim 10^4$ the polarization is of about 1%. This is the upper limit of the polarization in the box-model.

At second step of the generalization of box-model, let us consider n groups of equivalent nuclei. We can introduce the representation of functions $|S_z, I_1, L_1, I_2, L_2, \ldots, I_n, L_n, \alpha\rangle$. Here I_i and L_i are the quantum numbers of total angular momentum and its z-projection for ith group, and other quantum numbers S_z and α are chosen as above. In this representation, Hamiltonian (1) and density matrix can be represented also as block-diagonal matrices where each block is characterized by the quantum number set $(I_1, I_2, \ldots, I_n)$. Due to mutual independence of the blocks, the maximum polarization of nuclear system is achievable at full polarization of each block. In this case, average value of angular momentum z-projection of nuclear system can be described as a sum of the respective average values for each group [10]:

$$\langle I_z\rangle_n = \sum_{i=1}^{n}\sum_{I=0}^{2N_i J} \rho_{N_i}(I) I. \qquad (4)$$

The degree of nuclear polarization can be also represented as sum of the weighted polarizations of each block:

$$P_n = \frac{\langle I_z\rangle_n}{2N} = \sum_{i=1}^{n} \frac{N_i}{N} P_1(N_i). \qquad (5)$$

We can easily calculate $\langle I_z\rangle_n$ as a function of number of nuclear group n at fixed number of nuclei in the system and estimate achievable values for nuclear polarization P_n. Results of such calculation for 300 nuclei (for different nuclear spins J) are shown in Fig. 2. Here we used the number of nuclei in each group to be equal to each other so that $N_i = N/n$. As seen from the figure, polarizations P_n increase with increasing number n. So, the experimentally observed degree of nuclear polarization ~40% is achievable at ~50 nuclear groups (i.e. 6 nuclei in each group).

3. Discussion

To describe the nuclear spin polarization in real QDs, both the generalizations of the box-model should be exploited. Important open problem is number of group of equivalent nuclei n and number of nuclei in each group $2N_i$. This problem should be considered for each particular QD because it strongly depends on space distribution of the electron density in QD. Discussion of this problem in detail is out of scope of the present work.

In conclusion, we presented the model of equivalent nuclear groups which generalizes the box-model for both different nuclear spins and non-uniformity of the electron wave-function over the QD. The model gives qualitatively similar results for different elementary nuclear spins. Using the model, the largest achievable values of nuclear polarization can be calculated. This extended model describes real QDs more accurately.

Acknowledgements

This work has been supported in part by Russian Foundation for Basic Research.

References

[1] D. Gammon, Al. L. Efros, T. A. Kennedy *et al*, *Phys. Rev. Lett.* **86**, 5176 (2001).
[2] A. V. Khaetskii, D. Loss, and L. Glazmann, *Phys. Rev. Lett.* **88**, 186802 (2002).
[3] I. A. Merkulov, Al. L. Efros, and M. Rosen, *Phys. Rev. B* **65**, 205309 (2002).
[4] Y. G. Semenov, and K. W. Kim, *Phys. Rev. B* **67**, 073301 (2003).
[5] W. Zhang, V. V. Dobrovitski, K. A. Al-Hassanieh, *et al*, *Phys. Rev. B* **74**, 205313 (2006).
[6] G. G. Kozlov, *JETP* **105**, 803 (2007) [*Zh. Eksp. Teor. Fiz.* **132**, 918 (2007)].
[7] P.-F. Braun, B. Urbaszeck, T. Amand, and X. Marie, *Phys. Rev. B* **74**, 245306 (2006).
[8] B. Urbaszek, P.-F. Braun, T. Amand, *et al*, *Phys. Rev. B* **76**, 201301(R) (2007).
[9] Angular momentum $J = 3/2$ is the momentum of Ga and As nuclei, and $J = 9/2$ is the same of In. We should note, that nuclear spin polarization of InAs/GaAs QDs are widely studied now.
[10] G. G. Kozlov, *Unpublished*; arXiv:0801.1391.

16th Int. Symp. "Nanostructures: Physics and Technology"
Vladivostok, Russia, July 14–18, 2008

Non-radiative recombination of e-h complexes in semimagnetic quantum dot structures

A. V. Chernenko[1], A. S. Brichkin[1], N. A. Sobolev[2] and V. D. Kulakovskii[1]

[1] Institute of Solid State Physics,RAS, 142432,Chernogolovka,Russia
[2] Departamento de Fi'sica, Universidade de Aveiro,3810-193 Aveiro, Portugal

Abstract. It is well known that incorporation of Mn into II–VI semiconductor structures strongly suppresses or even quenches photoluminescence of photoexcited e-h pairs if the energy of the optical transition exceedes the energy gap between the ground and first excited state of Mn ion. This condition is usually satisfied in Cd(Mn)Se/Zn(Mn)Se quantum dots. The quenching of photoluminescence is related with the energy transfer from e-h pairs into the system of Mn ions. However, the detailed mechanism of this process has never been considered carefully. We suggest a model of non-radiative energy transfer, which shows that such type of non-radiative recombination is characteristic one for II–VI semimagnetic semiconductor structures. This model explains variety of experimental results obtained earlier.

Introduction

The great attention to the quantum dot (QD) semimagnetic (diluted magnetic semiconductors (DMS)) structures is attracted due to possibility of their use in various fields of spintronics [1]. The DMS quantum dots are very promising objects because of opportunity to obtain high degree of carriers' polarization in relatively weak magnetic fields. Incorporation of Mn ions into CdSe/ZnSe QDs substantially reduces the quantum yield of radiation if the optical transition energy exceeds the energy of internal Mn transition ∼2.15 eV. Incorporation of Mn ions into CdSe QDs or ZnSe barriers with Mn content x higher than a few percents causes almost complete quenching of PL.

The strong reduction of PL quantum efficiency in semiconductor structures due to presence of deep impurity levels is well known effect. Usually it is related with non-radiative recombination followed by capture of e-h pairs (excitons) by charged impurities. The non-radiative recombination of such complexes is accompanies by excitation of the impurity ion or escape of one electron from the ion's external shell caused by the Coulomb interaction (Auger-like recombination). However, Mn ions incorporated into II–VI matrix are isoelectronic impurities and do not form exciton-impurity complexes of this type. The alternative mechanism of exciton capture by deep isoelectronic impurities was suggested by Hopfield *et al* [2]. According to it one of the carriers (electron or hole) is captured by ion core whereas the other is localized on a hydrogen-like orbital of the formed ion. There are no clear experimental evidences of existence of such complexes in ZnMnSe and CdMnSe, though.

Nevertheless it is widely accepted that the main mechanism of the energy transfer from a photoexcited e-h pair to an Mn ion is Auger-like recombination caused by Coulomb interaction between the crystal electron system and Mn $3d^5$ shell. Such an approach leads to spin-dependent selection rules and allows one to explain the strong increase of the DMS QDs PL intensity in the magnetic field directed perpendicular to the sample plain $B \parallel Oz$ [3].

It was shown in Ref. [3] that matrix elements of the non-radiative recombination vanish due to symmetry if not to take into account the admixture of odd states to 3d-shell even states. It was suggested that these odd-parity states are from the 4p-shell of the same Mn ion. However, there is an additional "source" of p-like states: the p-d mixing of delocalized valence band states with 3d-shell ones. We propose a model of non-radiative recombination which accounts for this mixing.

1. Selection rules of non-radiative recombination

The consideration of the effect of p-d mixing on valence electrons is based on Anderson-like model [4]. It was that model which was used to explain the negative sign of the p-d exchange constant. Being extended by adding the Coulomb interaction of Mn ion core and d-shell with conduction and valence bands it allows one to obtain matrix elements of the Auger recombination.

According to the Anderson model the 3d-electron wave-function of t_2 symmetry in cubic crystal mixes with p-states of the same symmetry:

$$\psi_{\gamma s}(r) = A\left(\phi_{st_2\gamma}(r) - \sum_k g_\gamma(k)\phi_{vs}(k)\right), \qquad (1)$$

where the coefficient

$$g_\gamma(k) = \frac{\langle\phi_{st_2\gamma}(r)|U_{\rm cr}|\phi_{vs}(k)\rangle}{\epsilon_k - \epsilon_{t_2}}. \qquad (2)$$

$\gamma = \eta, \xi, \zeta$ are basis function of t_2 representation, $U_{\rm cr}$ is the crystal field potential, ϵ_k is the energy of zone electron with quasi-moment k, ϵ_{t_2} is the energy level of t_2 d-electron, A is the normalization constant, $\phi_{st_2\gamma}(r)$ and $\phi_{vs}(k)$-wave-functions of t_2 and valence electrons, respectively.

The many-electron 3d-shell wave-function is constructed from the one-electron wave-functions modified by p-d mixing within the intermediate crystal field scheme. The wave-function of the ground and excited states are expressed via modified functions of t_2 and e representation of T_d group [4].

The p-d mixing also modifies wave-function of valence electrons:

$$\psi_{vs}(k) = \phi_{vs}(k) - \sum_\gamma B_\gamma \frac{g_\gamma(k)}{\epsilon_k - \epsilon_\gamma}\left(C_\gamma \frac{g_\gamma(k)}{\epsilon_k - \epsilon_\gamma}\phi_{vs}(k) + \phi_{t_2\gamma s}\right), \quad (3)$$

where coefficients B_γ and C_γ are functions of $\sum_k |g_k|^2/(\epsilon_\gamma(k) - \epsilon_\gamma)^2$.

Cd(Mn)Se /Zn(Mn)Se QDs are characterized by strong splitting of hh $|\pm 3/2\rangle$ and lh $|\pm 1/2\rangle$ hole states. The strong e-h exchange interaction splits exciton $J_z = \pm 1$, $J_z = \pm 2$ states. The PL studies on these QDs revealed, that the valence band states in our QDs are strongly splitted due to the strain and dimensional quantization [5]. Since QDs have very anisotropic lens-like form, where the diameter is few times larger than the hight we apply the model of a QW to find out wave-functions of the carriers. The electron wave-functions in both zones $\phi_c(s_z)$, $\phi_v(j_z)$ are solutions of the effective mass equation for QW at $k = 0$. Such an approximation is valid since $\Delta k < 1/d \simeq 10^6$ cm^{-1}, where d is characteristic lateral QD diameter.

The probability of the resonant energy transfer is given by Fermi's Golden rule:

$$w_{i\to f} = \frac{2\pi}{\hbar} \left|M_{i\to f}\right|^2 \delta(E_i - E_f),$$

where the matrix element $M_{i\to f} = \langle f|\tilde{V}_{\rm in}|i\rangle$. The initial state $|i\rangle$ of the matrix element is the sum of products of antisymmetrized exciton and 3d-shell $^6A_1$ wave-functions. Matrix elements are of the form $M_{i\to f} = \sum_j \sum_\gamma g_\gamma f(r_{\rm e}, r_{\rm e}) U_{\rm Coul\ j\gamma}/(\epsilon_v - \epsilon_{t_2\gamma})$, where $j = x, y, z$ enumerates final states $^4T_{1j}$. The integral $U_{\rm Coul} = \langle\varphi_{t_2}\phi_c\,|V_{\rm in}|\varphi_e\phi_v\rangle = \int \varphi^*_\mu(r_1)\phi^*_c(r_2) V_{\rm in}(\mathbf{r}_1 - \mathbf{r}_2)\ \varphi_v(r_1)\phi_v(r_2)d\mathbf{r}_1 d\mathbf{r}_2$, where $V_{\rm in}(\mathbf{r}_1 - \mathbf{r}_2)$ is the screened Coulomb interaction, $f(r_{\rm e}, r_{\rm e})$ is the envelope function; $\varphi_\mu(r)$ and $\phi_l(r)$ are d- and zone- electrons wave-functions, respectively. The estimation of the matrix elements shows that the contribution of the p-d mixing into Auger recombination matrix elements is compatible with that one due to the upper laying 4p-level.

In the magnetic field $B \parallel Oz$ the e-hh exciton states are characterized not only by the total moment projection $J_z = \pm 3/2$ but also by the spin projection $s_z = 0$. The Coulomb interaction does not change the total spin projection of the system Mn+QD $\Delta S_z = \Delta S_{{\rm Mn},z} + \Delta s_z = 0$. This is valid for any terms of the perturbation series. The conservation of the S_z leads to different selection rules for "bright" $S_z = 0$ ($J_z = 1$) $\Delta S_{{\rm Mn},z} = 0$, $\Delta s_z = 0$ and "dark" $S_z = \pm 1$ ($J_z = \pm 2$) $)\Delta S_{{\rm Mn},z} = \pm 1$, $\Delta s_z = \mp 1$ excitons, respectively.

The considered model supposes resonant energy transfer from e-h pairs to Mn ions. However, experimental results indicate that the non-radiative recombination remains efficient even when the exciton transition energy substantially exceeds the energy of the intra-ionic transition ~2.15 eV. The non-resonant energy transfer is allowed since exited states ($^4T_2$, $^4A_1$, ^4E) are located 0.2–0.7 meV above the lowest $^4T_1$ one. The interaction between isolated Mn ions as well as inhomogeneous strain distribution and spin-lattice interaction broaden the Mn ion levels which leads to the quasi-continuous density of states. The non-radiative recombination is allowed into higher laying excited states with following relaxation onto the $^4T_1$ state by means of interaction with vibration modes of Mn ions. An alternative mechanism of the phonon assisted non-radiative recombination was proposed in the paper of Yassievich *et al* [6] where the problem of the phonon-assisted energy transfer from semiconductors to rear-earth impurities was considered. According to this mechanism, the energy transfer is accompanied by the excitation of vibration modes of the impurity ion. The excited vibration state of the ion slowly relaxes via multiple phonon emission. Both of these paths lead to the dissipation of excess energy which is necessary for the non-resonant recombination.

Abramishvili *et al*proposed that the non-radiative recombination takes place via creation of so called "donor" and "acceptor" excitons [7]. The "acceptor" exciton is formed by capture of the excitonic electron on the 3d-shell and the hole on external hydrogen-like orbital of the created d^6 ion, whereas the "donor exciton" is formed by the capture of the hole on the 3d-shell (escape of one d-electron into the valence band) and localization of the electron on the external orbital of d^4 ion. An estimation gives one the binding energy of the "donor" exciton $\epsilon_{{\rm d},n} \simeq 10$ meV, $a_{\rm D} \simeq 60$ nm. Similarly, for the "acceptor" exciton $\epsilon_{{\rm a},n} \simeq 50$ meV, one obtains $a_{\rm A} \simeq 15$ nm i.e. dimensions of these complexes exceed QDs ones. The presence of these complexes could accelerate the non-radiative recombination in CdSe/ZnMnSe QDs structures indeed. However, the only experimental observation of such excitons in ZnSe or CdSe matrixes was reported in [4].

To conclude we developed the model of non-radiative recombination of e-h complexes located within II–VI DMS quantum dots. This model can be extended to any II–VI semiconductor structures doped by 3d-metals. It clarifies the mechanism of non-radiative recombination and allows one to estimate the effect of the p-d mixing. This model explains variety of experimental results; for example it explains why the the magnetic field perpendicular to the sample growth plane in DMS quantum wells and quantum dot structures strongly increases their PL intensity, whereas the effect of magnetic field on the excitonic PL in bulk materials is not so pronounced. It also explains the strong anisotropy of this effect. The obtained selection rules of the non-radiative recombination allows us to explain peculiarities in PL spectra of individual DMS quantum dots [5].

Acknowledgements

This work has been supported by RFBR grants.

References

[1] D. D. Awschalom, D. Loss, N. Samarth *Semiconductor Spintronics and Quantum Computations*, Springer-Verlag, Berlin (2002).
[2] J. J. Hopfield, D. G. Thomas and R. T. Lynch, *PRL* **17**, 312 (1966).
[3] A. V. Chernenko *et al*, *Phys. Rev. B* **72**, 045302 (2005).
[4] K. A. Kikoin and V. N. Fleurov, *Transition Metal Impurities in Semiconductors. Electronic Structure and Physical Properties*, World Scientific Publishers, Singapore, London, New York, 360 pp (1994).
[5] A. S. Brichkin, A. V. Chernenko, A. S. Chekhovish *et alJETP* **132**, 426 (2007).
[6] I. N. Yassievich and L. C. Kimerling, *Semicond Sci.Technol* **8**, 718 (1993).
[7] V. G. Abramishvili, A. M. Komarov, S. M. Ryabchenko, and Yu. G. Semenov, *Solid State Commun.* **78**, 1069 (1991).

16th Int. Symp. "Nanostructures: Physics and Technology"
Vladivostok, Russia, July 14–18, 2008

Variable threshold for giant magnetoresistance in Ni-polymer-Cu system

N. V. Vorob'eva[1], A. N. Lachinov[1], Jan Genoe[2] and A. A. Lachinov[1,2]

[1] Institute of Physics of Molecules and Crystals UNC RAS, Ufa, Russia
[2] IMEC Leuven, Belgium

Abstract. While applying external magnetic field on some threshold value the conductivity of the Ni-polymer-Cu system was switching "on" or "off". Giant magnetoresistance threshold could be shifted with bias voltage value or by annealing of ferromagnet in external magnetic field. Giant magnetoresistance was also destroyed by thin copper film inserted between ferromagnet and polymer. Copper layer depolarized partially spin-polarized electrons that had been injected in polymer from nickel.

Introduction

It is known that the magnetic state of the ferromagnetic electrode can essentially change the characteristics of the contact and transport properties of multi-layers structure. Probably, one of the first examples of this interaction applicability appears in [1]. This patent suggested to detect bubble domains using Fermi level shifting in ferromagnet. The Fermi level shifting appears as a result of influence of domains' magnetic field on tunnel barrier parameters and consequently flowing current changes. Later the analogous ideas were developed in papers [2,3], where also the chemical potential change in magnetic field had been used for magnetic state indication. In [4] magnetic phase transition in ferromagnet-polymer-nonmagnetic metal system was described as sharp change of current proceeding via structure at Curie temperature. Here Cr was used as magnetic field sensitive layer.

In 2002 in [5] there was at first shown that spin- oriented electrons injected in organic semiconductor sexithienyl, can keep orientation up to 200 nm thickness of barrier layer between ferromagnet electrodes. This is much more than 1–2 nm — thickness for tunnel electron percolation. Such enlarging of spin penetration length in organic materials is connected, in particular, with the suppression of the superfine interaction by delocalized sexithienyl π-orbitals. So, using of organic transport layer instead of the usual dielectric has serious prospects. Polymers deserve special attention. The presence of traps in polymer layer was suggested in [6] to use for current amplification and also for memory cells [7].

In 2004 in experimental research of Xiong Z. H. *et al* [8], the investigation of the ferromagnet-π-conjugated polymer-ferromagnet had been described. The authors discovered the difference between working cell resistance with parallel and antiparallel orientations of magnetizations of ferromagnetic electrodes. They built classical spin valve. But polymer barrier layer thickness in this valve exceeds for 2 orders the thickness of really putted into practice dielectric layers that are transparent for the electron tunnel junction. Measurements were done at 11 K, and relative change of resistance was up to 40 percents. At room temperature the effect vanished. Recently the sufficiency of only one interface with ferromagnetic metal was shown for the observation of giant magnetoresistance (GMR) effect in metal-transport layer-metal structure [9]. It was determined, that this effect could be realized at room temperature and could have GMR coefficient almost at 100 percents with relative resistance change for 6 orders [10].The peculiarity of the phenomenon is that we can choose the sign of the effect by making up initial state of systems' conductivity. But if the phenomenon has been demonstrated enough convincingly, than its explanation and description demand some additional experiments. Particularly, for spin-polarized charge carriers. So in the present work we explore the possibility of shifting of the field threshold or vanishing of GMR in Ni-polymer-Cu system with the aid of spin polarization and any other external factors.

1. Experiment for destroying GMR

The idea of the experiment is presented in Fig. 1. If we propose spin polarization factor to be important for GMR, than while diminishing the polarization we delete the effect. At first we checked the structure Ni-polymer-Cu, there was no GMR. For spin-polarization disordering in ferromagnet-polymer-copper structure we inserted thin copper layer between ferromagnet and polymer. As ferromagnet we used nickel polycrystalline plate.

Polydiphenylenphtalide was used as polymer material. Polymer film was formed by centrifugation on nickel. Polymer film thickness was $\sim$0.8 μm and was estimated with microinterfer-

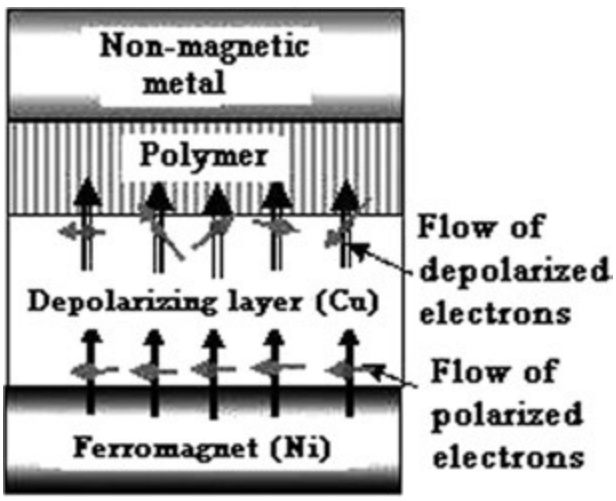

Fig. 1. The scheme of the experiment for destroying of spin polarization of current by thin copper layer.

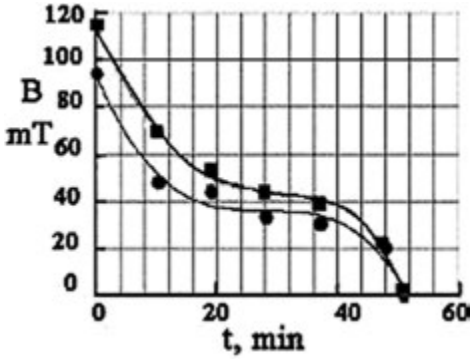

Fig. 2. Switching "on" and "off" dependencies of the system from total time in external magnetic field normal to ferromagnetic electrode plane. Circles — switching "on" field, squares — switching "off" field.

ometer MII-4. The initial conductance of polymer film was made up by external pressure with method described in [11]. Maximal pressure on the film did not exceed 0.15 MPa.

Copper electrode was made by thermal vacuum evaporation on polymer film surface. The copper layer between the ferromagnet and polymer film was obtained also by vacuum evaporation under pressure of $\sim 10^{-5}$ mm Hg. Copper layer thickness was controlled with field-emission microscope. Magnetic field was normal to the film surface and did not exceed 0.35 T. All measurements were done at room temperature. The microscopic measurements showed that copper film had been continuous down to ∼8 nm thickness.

Copper layer existence leads to the significant decrease of GMR coefficient, and when copper layer thickness over 12 nm giant magnetoresistance vanishes. At 8–10 nm we see magnetic field influence and relative magnetoresistance change is not over 5 percents. Further decrease of depolarizing copper layer thickness gives GMR coefficient increase. If copper layer absences, than GMR is maximal.

The experiments show that GMR in ferromagnet-copper-polymer-copper system takes place only if copper layer between ferromagnet and polymer does not exceed some value. For the conditions of the present work this thickness is 10 ± 2 nm.

In [11] it was proposed that Fermi level position of ferromagnet in the magnetic field affects on injective properties of ferromagnet-polymer interface and, consequently, on GMR in the structure. But from the experiments with internal copper layer we can conclude that partial spin-polarization ordering of electrons in ferromagnet is also important for GMR.

2. GMR threshold shifting

The dependence of the threshold field from time of system standing in external magnetic field is shown in Fig. 2. Apparently, the obtained values of threshold field diminish after preliminary staying in external magnetic field. For each subsequent point in Fig. 2 total time of standing in external magnetic field increases on 10 minutes. Switching "off" field always exceeds switching "on" field.

The time of preliminary standing of the system in external magnetic field leads to ferromagnet domain structure changing. The value of saturation field for thin ferromagnetic plate

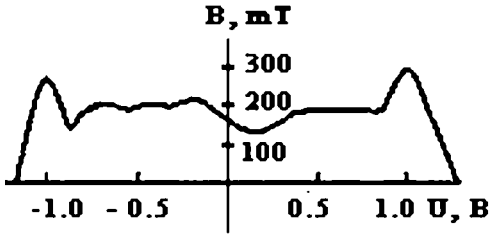

Fig. 3. The dependence of value of threshold switching off magnetic field B vs. bias voltage value U.

is too great when external field is oriented normally to the plate surface. Standing in such field gives thermomagnetic annealing even at room temperature. Initial domain structure (without external magnetic field) become oriented nearer to external magnetic field direction. So small changes of magnetic anisotropy lead to great changes of switching "on" and "off" fields.

The dependence of switching off magnetic field value from bias voltage is presented in Fig. 3. Threshold field value change is not significant with voltage less than 0.7 V. Near 1 V we have threshold increase from ∼200 mT up to almost 300 mT. Then there is sharp decreasing of threshold and near 1.5 V we have no switching off at all.

Such behavior of the dependence in Fig. 3 is the evidence of injection of carriers. The applied electric field lowers the potential barrier, so threshold field value diminishes. And when potential barrier is deformed enough the external magnetic field have no influence on the current, so as we have high conductivity state caused by electric field. Besides, the result presented in Fig. 3 is the evidence of possibility to affect on switching conductivity magnetic field in Ni-polymer-Ñu system by changing voltage on sandwich-structure.

Acknowledgements

This work has been supported by Federal Agency on Science and Innovations of Federal special program Researches and elaborations on primary directions of the development of the science and technology complex in Russia for 2007–2012 years on lot No. 1 (2007-7-5.2-00-01) of arrangement 5.2 "The development of the network of collective scientific equipment using", and also partially by grants of fundamental research program OFN-5, project 1.15. and program of presidium RAS P-8.

References

[1] F. Holtzberg *et al*, *US Patent* **3972035**, (1976).
[2] S. A. Ignatenko *et al*, *Tech. Phys.* **50**, 680 (2005).
[3] S. A. Ignatenko *et al*, *Semiconductors* **39**, 1048 (2005).
[4] A. N. Lachinov *et al*, *Phys. Usp.* **49/12**, 1 (2006).
[5] V. Dediu *et al*, *Solid State Comm.* **22**, 181 (2002).
[6] Yu. A. Berashevich *et al*, *Semiconductors* **35/1**, 112 (2001).
[7] A. S. Borukhovich, *Phys. Usp.* **42**, 653 (1990).
[8] Z. H. Xiong *et al*, *Nature* **427**, 821 (2004).
[9] A. N. Lachinov *et al*, *JETP Lett.* **84**, 604 (2006).
[10] N. V. Vorob'eva *et al*, *Poverhnost* **5**, 22 (2006).
[11] A. N. Lachinov *et al*, *Mol. Cryst. Liq. Cryst.* **467**, 135 (2007).

16th Int. Symp. "Nanostructures: Physics and Technology"
Vladivostok, Russia, July 14–18, 2008

Observation of 2DEG transport in helical geometry at low filling factors

Yu. S. Yukecheva[1], A. B. Vorob'ev[1], V. Ya. Prinz[1], A. I. Toropov[1] and D. K. Maude[2]

[1] Institute of Semiconductor Physics, Russian Academy of Science, Acad. Lavrent'ev Ave. 13, 630090 Novosibirsk, Russia

[2] Grenoble High Magnetic Field Laboratory, Centre National de la Recherche Scientifique, B.P. 166, F-38042 Grenoble Cedex 9, France

Abstract. Helical shaped Hall bar was fabricated from the heterostructure containing high-mobility two-dimensional electron gas. Longitudinal and Hall resistances of such structure were investigated at high magnetic fields for different sample positions with respect to the magnetic field vector. A strong asymmetry of the longitudinal magnetoresistance was observed; the ratio $R_{xx}(B)/R_{xx}(-B)$ was shown to be higher than 10^4. Longitudinal magnetoresistance peak positions at low filling factors are discussed.

Introduction

Curved two-dimensional electron gases (2DEGs) hold much promise for investigation of new physical effects that appear both due to curvature itself [1] and due to modification of the external magnetic-field influence. The influence of uniform magnetic field on electrons in such gases is spatially non-uniform because only the normal-to-surface component of the magnetic field governs the electron transport in 2DEG samples. In quantizing magnetic fields this non-uniformity results in spatial curving of Landau levels and manifests itself in magnetotransport characteristics which depend on the relative directions of magnetic field and current, and locations of current and voltage probes. In this work helices containing two-dimensional electron gas with electrical contacts were fabricated by method [2]. Here we present and discuss experimental results of magnetotransport in such structures at high magnetic fields for different rotation angles.

1. Experimental

A high-mobility 2DEG in a free-standing thin film was realized using GaAs quantum wells with spacers consisting of short-period AlAs/GaAs superlattices. In these superlattices heavy X electrons smooth fluctuations of the scattering potential induced by ionized impurities [3] and surface states on both surfaces of free-standing layers. The multi-layered heterostructures were grown on a GaAs (100) substrate by molecular beam epitaxy (MBE). These structures comprised a 50-nm thick AlAs sacrificial layer and a strained multi-layered film with thickness of 192 nm to be detached from the substrate. The multi-layered film contains a 20-nm thick $In_{0.15}Ga_{0.85}As$ stressor and the stack of hereterostructure, including a central 13-nm-thick GaAs QW clad with δ-doped AlAs/GaAs SPSL-spacers. The rolled-up Hall bars used in the present study were prepared by directional rolling of two-level-lithography defined mesastructures [4]. As far as mobility in heterostructures was anisotropic the Hall bar was oriented along $[1\bar{1}0]$ that corresponds to maximal mobility. The rolling is directed along [100], that leads to formation of Hall bar shaped as a coil of helix. Magnetotransport measurements were made using a.c techniques and 28T superconducting magnet with a dilution refrigerator. Measurements were made at 40 mK for both magnetic field directions.

2. Results and discussion

Fig. 1 shows longitudinal and Hall resistances of the flat sample measured at magnetic fields from -28 T to 28 T. The measured electron mobility and electron sheet density are 41 $m^2/(V\,s)$ and 5.9×10^{15} m^{-2}, respectively.) Under the highest magnetic field, the filling factor of $\nu = 1$ is reached. Between $\nu = 1$ and $\nu = 2$ there are also distinguishable R_{xx} minima corresponding to filling factors of $\nu = 4/3$, 5/3 and 7/5. Longitudinal resistance of the rolled sample at different rotation angle is shown on Fig. 2. Rotation occurred around the cylinder axis. It is surprising that with tube rotation peaks and minima of R_{xx} corresponding to integer and fractional quantum Hall effects, smooth out but do not appreciably shift in external magnetic field with respect to their position in flat samples. This behavior was observed both for integer quantum Hall effect (IQHE) and fractional quantum Hall effect (FQHE) minima. In addition, longitudinal magnetoresistance revealed strong asymmetry with respect to external magnetic field direction. With the angle increasing, magnetic field maximum shifts towards the current probes, and the asymmetry of R_{xx} versus B increases and exceeds 10^4. To explain the dependence of the longitudinal magnetoresistanse on rotation angle, Landauer–Büttiker formalism adapted for the systems with selectively populated

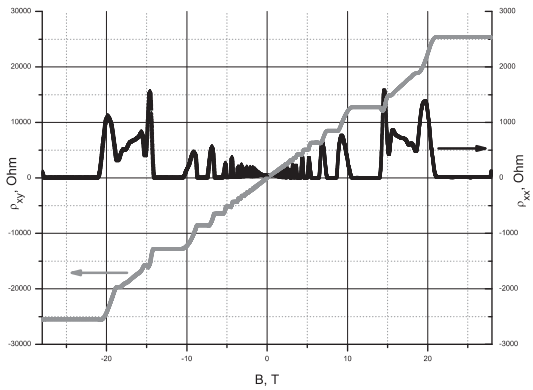

Fig. 1. Hall (left axis) and longitudinal (right axis) resistances of the flat sample with 2DEG.

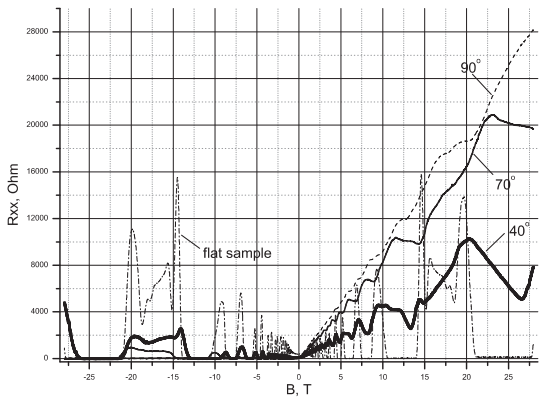

Fig. 2. Longitudinal resistances of the helix with 2DEG at different rotation angles with respect to magnetic field maximum. For comparison, R_{xx} of flat sample with values multiplied by 10 is drawn by dash-dot line.

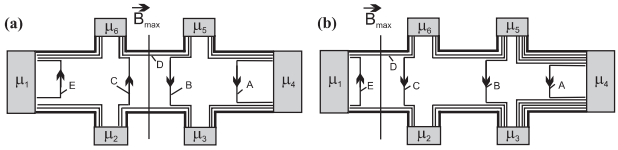

Fig. 3. Edge state distribution in the helix in external magnetic field. Letters A, B, C, D, E mean numbers of corresponding channels. Only D channels travel through the whole sample, all the rest are reflected.

edge states [5] was used. Taking into account relative positions of Fermi level intersections with curved Landau levels and voltage probes, one obtains spatial distribution of the edge states shown in Fig. 3. Letters A, B, C, D, E mean numbers of corresponding channels. Here, two cases are distinguishable: magnetic field maximum lies inside the region between voltage probes (Fig. 3a), and outside of it (Fig. 3b). The latter case was analyzed in details earlier [6], so we concentrated on the first case.

$$I_i = (e/h) T_{ij} \mu_j,$$

where I is the current, T_{ij} — components of the transmission matrix, μ_j — electrochemical potential in the contact j. In case of the absense of interchannel scattering the transmission matrix for the situation shown in Fig. 3a can be written as

$$\hat{T} = \begin{pmatrix} -c-d & 0 & 0 & 0 & 0 & c+d \\ c+d & -c-d & 0 & 0 & 0 & 0 \\ 0 & d & -b-d & 0 & b & 0 \\ 0 & 0 & b+d & -b-d & 0 & 0 \\ 0 & 0 & 0 & b+d & -b-d & 0 \\ 0 & c & 0 & 0 & d & -c-d \end{pmatrix}$$

From here, longitudinal resistances are easily obtained:

$$R_{23} = \frac{\mu_3 - \mu_2}{eI} = \frac{h}{e^2} \frac{b}{(b+d)\,d},$$

$$R_{56} = \frac{\mu_6 - \mu_5}{eI} = \frac{h}{e^2} \frac{c}{(c+d)\,d}.$$

This simple model shows (Fig. 4) that :

(1) sample rotation around cylinder axis results in peak broadening, however, in contrary to the flat 2DEGs its front is not shifted to the higher fields with rotation. This conclusion is in agreement with the described experiment.

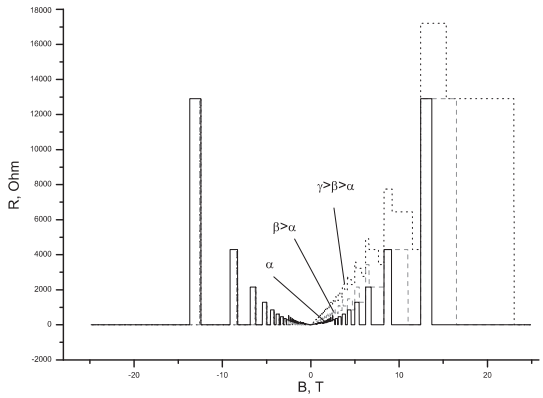

Fig. 4. Longitudinal resistances of the helix with 2DEG at different rotation angles with respect to magnetic field maximum, obtained by Landauer–Büttiker formalism.

(2) magnetoresistance grows at the starting region of the quantizing positive external magnetic field. At qualitative level, this is in agreement with the experiment. Quantitative analysis of the magnetoresistance value and explanation of longitudinal resistance behavior in the FQHE region requires more complicated models.

To summarize, 2DEG of helical shape with contacts was fabricated for the first time. Magnetotransport measurements of such structure at high magnetic fields revealed IQHE and FQHE minima in longitudinal magnetoresistance and its strong asymmetry with respect to external magnetic field direction. It was observed that with sample rotation in external magnetic field peaks of longitudinal magnetoresistance stay near the same places as in the flat sample. The peak positions and longitudinal magnetoresistance asymmetry were qualitatively explained with Landauer–Büttiker formalism.

Acknowledgements

This work has been supported by Russian Foundation for Basic Research (Grants 07-02-01472-a and 06-02-16005-a).

References

[1] R. C. T. da Costa, *Phys. Rev. A* **23**, 1982 (1981).
[2] V. Ya. Prinz, V. A. Seleznev, A. K. Gutakovsky, A. V. Chehovskiy, V. V. Preobrazhenskii, M. A. Putyato, and T. A. Gavrilova, *Physica E* **6**, 828 (2000).
[3] K.-J. Friedland, R. Hey, H. Kostial, R. Klann, and K. Ploog, *Phys. Rev. Lett.* **77**, 4616 (1996).
[4] A. B. Vorob'ev and V. Ya. Prinz, *Semicond. Sci. Technol.* **17**, 614 (2002).
[5] D. K. Ferry, S. M. Goodnick, *Transport in nanostructures*, Cambridge University Press (1997).
[6] A. B. Vorob'ev, K.-J. Friedland, H. Kostial, R. Hey, U. Jahn, E. Wiebicke, Ju. S. Yukecheva, and V. Ya. Prinz, *Phys. Rev. B.* **75**, 205309 (2007).

16th Int. Symp. "Nanostructures: Physics and Technology"
Vladivostok, Russia, July 14–18, 2008

Weak localization in patterned 2D structures with a single quantum well

A. V. Germanenko[1], G. M. Minkov[1,2], O. E. Rut[1], A. A. Sherstobitov[1,2] and A. K. Bakarov[3]

[1] Institute of Physics and Applied Mathematics, Ural State University, 620083 Ekaterinburg, Russia
[2] Institute of Metal Physics, 620041 Ekaterinburg, Russia
[3] Institute of Semiconductor Physics, 630090 Novosibirsk, Russia

Abstract. The results of experimental study of the weak localization phenomenon in 2D system with artificial inhomogeneity of potential relief are presented. It is shown that the shape of the magnetoconductivity curve is determined by the statistics of closed paths. The area distribution function of closed paths has been obtained using the Fourier transformation of the magnetoconductivity curves taken at different temperatures. The experimental results are found in a good agreement with the results of computer simulation.

We present the results of experimental studies of the weak localization phenomenon in the structures with a single quantum well with an artificial potential relief. The heterostructure represents the AlGaAs/GaAs/AlGaAs quantum well heterostructure grown by molecular beam epitaxy. It consists of a 250 nm-thick undoped GaAs buffer layer grown on semi-insulator GaAs, a 50 nm $Al_{0.3}Ga_{0.7}As$ barrier, Si δ layer, a 6 nm spacer of undoped $Al_{0.3}Ga_{0.7}As$, a 8 nm GaAs well, a 6 nm spacer of undoped $Al_{0.3}Ga_{0.7}As$, a Si δ layer, a 50 nm $Al_{0.3}Ga_{0.7}As$ barrier, and 200 nm cap layer of undoped GaAs. Artificial relief was fabricated using the electron lithography. As a result the lattice of pits was formed on the surface (Fig. 1). The typical distance between centers of neighbor pits is about 1 μm, the depth is 0.6–0.7 μm. An Al gate electrode was deposited on so patterned cap layer. This allows us to control electron density and conductivity of 2D gas and to change the potential relief of the conducting area. Analysis of the results of transport measurements shows that the depletion of 2D gas in quantum well under piths takes place at $V_g < -1.8$ V, where V_g is the gate voltage. In this case the electric current flows through 2D networks (bright areas in Fig. 1) which parameters depend on V_g value. So varying the gate voltage within the interval from -1.8 V to -2.95 V we are able to change the mean width of channels from 0.3 μm to 0.06 μm. The electron density and local conductivity are changed within the range $(9 - 5.5) \times 10^{11}$ cm^{-2} and $(120 - 30)\, G_0$, respectively, where $G_0 = e^2/(2\pi^2\hbar)$.

The measurements of transport properties at low temperatures ($T = 1.5 - 20$ K) show that the formation of the electric

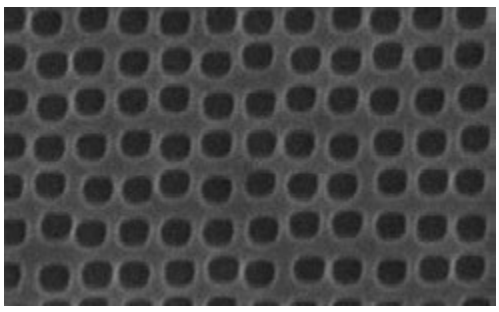

Fig. 1. 7×12 μm^2 electron microscopy image of the surface before the gate electrode deposition.

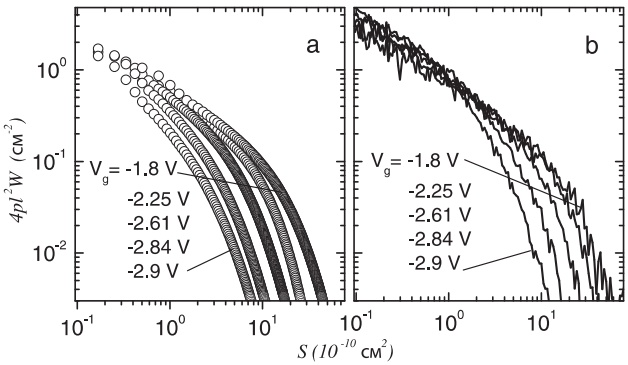

Fig. 2. Area distribution function of closed paths recovered from the experimental magnetoconductivity curves (a) and obtained from the simulation (b).

potential relief results in strong modification of the magnetoconductivity at low magnetic field corresponding to suppression of the weak localization. Although the negative magnetoresistivity due to suppression of quantum interference correction is observed, the shape of the magnetoconductivity curve differs drastically from that for unpatterned sample. It cannot be already described by the well-known formula obtained for the homogeneous 2D gas in Ref. [1]. This fact makes it impossible the use of the standard procedure of the determination of inelastic phase relaxation time, τ_ϕ.

Therefore, the analysis of the experimental results has been performed using the method described in Refs. [2] and [3]. It is shown in these papers that a new kind of information can be extracted from the Fourier transform of negative magnetoresistance in two-dimensional structures. In particular, this procedure provides the information on the area distribution function of closed paths. Based on this line of attack the method of analysis of the negative magnetoresistance is suggested. The method is used to process the experimental data on negative magnetoresistance in homogeneous 2D structures. The results of such a data treatment applied to our samples for different gate voltages are shown in Fig. 2(a). As seen the area distribution function shifts with the lowering gate voltage towards the lower areas.

The results presented are interpreted with the use of the computer simulation of the motion of classical particle over 2D plane. It is represented as a lattice with scatterers of two types

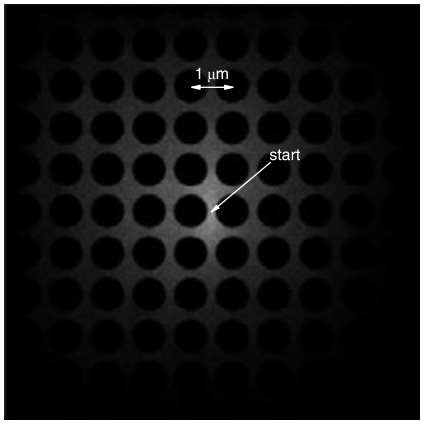

Fig. 3. Closed paths in the model 2D system.

placed in a part of lattice site. The scatterers of the first type with isotropic differential cross-section correspond to ionized impurity. The scatterers of the second type are hard discs with specular reflection from the boundaries. Particle motion is forbidden within disks. They correspond to the areas of 2D gas under the holes. A particle is launched from some random point, then it moves with a constant velocity along straight lines, which happen to be terminated by collisions with the scatterers. After collision it changes the motion direction. If the particle passes near the starting point at the distance less than some prescribed value, which is small enough, the path is perceived as being closed. Its length and enclosed algebraic area are calculated and kept in memory. The particle walks over the plane until it escapes the lattice. As this happens one believes that the particle has left to infinity and will not return. A new start point is chosen and all is repeated. In more details the simulation procedure is described in Ref. [2]. As an example the trajectories of the particle with several tens of thousand collisions launched from the center of 2D model system with the parameters corresponding to $V_g = -2.25$ V are shown in Fig. 3.

The area distribution functions obtained from the simulation for several gate voltages are shown in Fig. 2(b). When statics of closed paths is collected, only the relatively short paths (shorter than $2v_F\tau_\phi$, where v_F is the Fermi velocity) are taken into account. Namely statistics of such closed paths can be reliably obtained from the weak localization experiments from our point of view. It is clearly seen that the results of computer simulation are in qualitative agreement with those of real experiment. Quantitative difference can be explained by some roughness of our model. So, we supposed the areas forbidden for classical particles had the form of hard disks. As seen from Fig. 1 it is not exactly. Moreover, it was suggested that the mean free path and Fermi velocity are constant over all the sample that should not fulfilled in the real structure with inhomogeneity of classical scale.

Acknowledgements

This work has been supported in part by the RFBR (Grant Nos. 07-02-00528 and 06-02-16292) and by CRDF (Grant Y1-P-05-11).

References

[1] S. Hikami *et al*, *Prog. Theor. Phys.* **63**, 707 (1980).
[2] G. M. Minkov *et al*, *Phys. Rev. B* **61**, 13164 (2000).
[3] G. M. Minkov *et al*, *Phys. Rev. B* **61**, 13172 (2000).

16th Int. Symp. "Nanostructures: Physics and Technology"
Vladivostok, Russia, July 14–18, 2008

Current oscillations in a correlated quantum wire with an impurity

S. N. Artemenko and D. S. Shapiro
Institute for Radioengineering and Electronics of Russian Academy of Sciences, Moscow, Russia

Abstract. We study theoretically electronic transport through a single impurity in 1D conductors in the Luttinger liquid (LL) state, and find that above a threshold voltage related to a strength of the impurity potential the DC current $\bar{I}$ is accompanied by coherent oscillations with frequency $f = \bar{I}/e$. Frequency range of the oscillations is determined by the strength of the impurity potential and by the inter-electronic interaction. There is an analogy with the Josephson effect.

Basic electronic properties of 3D solids are usually well described within Landau's Fermi-liquid picture where low-energy excitations are quasiparticles that in many respects behave like non-interacting electrons. This is not the case in 1D systems where the usual Fermi liquid picture breaks down. In one dimension single-electron quasiparticles do not exist, the only low energy excitations are charge and spin collective modes. Such a state which is an alternative to Fermi liquid in one dimension is called the Luttinger liquid (LL) (for a review see Ref. [1]). There are different realizations of the 1D electronic systems, the examples are semiconductor-based quantum wires [2], metallic linear chains on Si surfaces [3], carbon nanotubes [4], conducting polymers [5], quantum Hall effect edge states [6]. There are evidences that the LL state can be stabilized in strongly anisotropic quasi-1D conductors by defects [7] or by formation of the CDW gap induced by electron-phonon coupling [8]. The transport properties of the LL are also very different from those of the Fermi liquid. In particular, impurities in 1D systems with repulsive inter-electronic interaction strongly suppress the current which leads to a power-law dependence of conductivity [9]. This effect can be described in terms of tunnelling between different minima of a periodic potential describing interaction of the electronic system with the impurity, the periodic potential is associated with Friedel oscillations induced by impurity. In the LL Hamiltonian describing interaction with the impurity reads [1]

$$H_{\rm imp} = -\frac{e}{\pi}\int dx\, V_i \cos 2\hat{\Phi}(t,x)\delta(x), \qquad (1)$$

where $\hat{\Phi}$ is the bosonic (plasmon) displacement field, and V_i is related to $2k_{\rm F}$-component of the impurity potential. The particle density operator is expressed as $\hat{\rho} = -\frac{1}{\pi}\frac{\partial\hat{\Phi}}{\partial x} + \frac{k_{\rm F}}{\pi}\cos(2k_{\rm F}x - 2\hat{\Phi})$, where the first term describes smooth variations of the particle density and the second is rapidly oscillating. Fluctuations of $\hat{\Phi}$ make the expectation value of the second term in a free LL equal to zero. However, near the impurity the second term survives resulting in Friedel oscillations, i.e., in $2k_{\rm F}$ modulation of charge density. As long as the current operator in the LL is given by relation $\hat{I} = (e/\pi)\partial_t\hat{\Phi}$ the current flow through the impurity means an increase of $\hat{\Phi}$ with time, which corresponds to a shift of the Friedel oscillations. So the Friedel oscillations is an obstacle for the current through the impurity. The power-law I–V curves [9] are induced by tunneling between minima of slightly inclined by external voltage washboard potential (1) [1]. This resembles Josephson junctions where fluctuations result in a finite voltage drop at currents below the Josephson critical current, $\bar{I} < I_{\rm c}$ (for a review see Ref. [10]). However, in superconducting junctions at $\bar{I} > I_{\rm c}$ the Josephson oscillations start, and this corresponds to an increase of the superconducting phase difference with time in the washboard potential inclined to an amount exceeding the critical value. Below we show that a similar regime must occur in the LL with an impurity when the applied voltage exceeds a threshold slope of the washboard potential at which the system can roll out from the minimum. Above the threshold the current is larger than the tunneling current in the sub-threshold regime corresponding to power-law I–V curves and is accompanied by oscillations with the washboard frequency $f = \bar{I}/e$.

For brevity we consider first the response of the spinless repulsive LL to DC voltage using Tomonaga–Luttinger (TL) model with short range interaction between electrons. Such interaction describes gated quantum wires where the long-range part of the interaction is screened by 3D gate electrodes. At the end we will discuss essential modifications induced by the long-range Coulomb interaction and spin.

We start with the Hamiltonian that includes the impurity term (1), the standard TL Hamiltonian, and the term with an external electric field E

$$H_{\rm TL} = \int dx\Big\{\frac{\hbar\pi v_{\rm F}}{2}\Big[\hat{\Pi}^2 + \frac{1}{\pi^2 K_\rho^2}\big(\partial_x\hat{\Phi}\big)^2\Big] - \frac{e}{\pi}E\hat{\Phi}\Big\}, \qquad (2)$$

where K_ρ is the LL parameter measuring the strength of the interaction: $K_\rho < 1$ for repulsive and $K_\rho > 1$ for attractive interaction. Commuting field operators with the Hamiltonian we derive equation of motion for the Heisenberg operator $\hat{\Phi}$

$$\Big(v^2\partial_x^2 - \partial_t^2 - \gamma\partial_t\Big)\hat{\Phi}(t,x) = \frac{ev_{\rm F}}{\hbar}\Big[2V_i\sin 2\hat{\Phi}_0(t)\delta(x) - E\Big], \qquad (3)$$

where $\hat{\Phi}_0(t) \equiv \hat{\Phi}(t, x=0)$, $v = v_{\rm F}/K\rho$ is the plasmon velocity, and γ describes small damping induced by coupling of electrons to a dissipative bosonic bath (to phonons or to density fluctuations in a metallic gate [11]). Using Eq. (3) with boundary conditions at the contacts one can express $\hat{\Phi}(t,x)$ in terms of its value at the impurity site. We apply boundary conditions [12] derived for a wire adiabatically connected to ideal Fermi-liquid reservoirs at $x = \pm L/2$ with voltage difference U. We consider a long wire, $L \gg v_{\rm F}/\gamma$, and neglect reflection of current pulses generated by the impurity from the contacts. Then we obtain equation of motion for $\hat{\Phi}_0(t)$ at the

impurity position supplemented by relation between time averaged values

$$\partial_t \hat{\Phi}_0(t) + \int_0^\infty dt_1 e Z(t-t_1) \sin 2\hat{\Phi}_0(t_1) = \frac{\pi}{e}\bar{I},$$
$$\bar{I} = G_0(U-U_i),\ Z(t) = V_i K_\rho \int \frac{d\omega}{2\pi} e^{-i\omega t} \sqrt{\frac{\omega}{\omega + i\gamma}}, \quad (4)$$

where $\bar{I} = e^2 E v_F/\pi\hbar\gamma$ is the DC current, $G_0 = e^2/h$ is the conductance quantum per spin orientation, and $U_i = 2V_i \langle \sin 2\hat{\Phi}_0(t)\rangle_t$ is the DC voltage drop at the impurity.

As $\hat{\Phi}_0(t)$ is an operator, it is not easy to solve Eq. (4). However, in the limit of strong inter-electron interaction ($K_\rho \to 0$) when fluctuations of $\hat{\Phi}_0(t)$ at the impurity are small, $\hat{\Phi}_0(t)$ can be treated as the ordinary function. So we consider first the simple case $K_\rho \to 0$ when fluctuations can be neglected and Eq. (4) can be easily solved analytically. When $U \le U_T = 2V_i$ the solution is stationary, $2\Phi_0 = \arcsin(U/U_T)$, with zero current $I = 0$. At $U > U_T$ the solution is oscillatory with fundamental frequency $f = \bar{I}/e$

$$\partial_t \Phi_0(t) = \frac{\pi \bar{I}^2/e}{\sqrt{\bar{I}^2 + (G_0 U_T K_\rho)^2} + G_0 U_T K_\rho \sin(2\pi \bar{I}/e)t}. \quad (5)$$

Eq. (5) determines the current at the impurity site, $I(t, x = 0) = e\dot{\Phi}_0(t)/\pi$. Current at the clean part of the channel is equal to $I(t,x) = e\partial_t \Phi_0(t - |x|/v)$ at $|x| \ll v_F/\gamma$, and $I(t,x) = \bar{I}$ at large distances from the impurity.

For the DC voltage drop at the impurity we obtain

$$U_i = \left[\sqrt{\bar{I}^2 + (G_0 U_T K_\rho)^2} - \bar{I}\right]/(G_0 K_\rho). \quad (6)$$

Thus the oscillatory regime starts at $U > U_T$ and the amplitude of the oscillations decreases as voltage increases decaying at large voltages $U \gg U_T$.

At finite values of K_ρ fluctuations cannot be neglected. In this case we extract the expectation value $\Phi_0(t) = \langle\hat{\Phi}_0\rangle$, and obtain an equation for $\Phi_0(t)$. We ignore the soliton-like fluctuations that are responsible for sub-threshold tunneling, but take into account Gaussian fluctuations, that strongly reduce the threshold voltage. These fluctuations can be treated with the self-consistent harmonic approximation. Acting in this way we find the threshold voltage renormalized by fluctuations

$$U_T = 2V_i \left(\frac{2K_\rho^{3/2}\, eV_i}{\Lambda}\right)^{\frac{K_\rho}{1-K_\rho}} \sqrt{1-K_\rho}. \quad (7)$$

where $\Lambda \sim p_F v_F$ is a large cut-off energy.

It is not simple to take into acount fluctuations analytically in a general time-dependent case, but this can be done easily near the threshold value when the DC current is small, $\bar{I} \ll G_0 U_T K_\rho$. Then we again find (5) and (6) with different value of the threshold voltage U_T given by (7).

So far we considered the spinless LL. In the spinful LL the spin-charge separation is violated at the impurity. This leads to modification of the results, in particular, of the threshold voltage. For a spin-independent electronic repulsion Eq. (7) is substituted by

$$U_T = \sqrt{2}V_i \left(\frac{2eV}{\Lambda}\right)^{\frac{1+K_\rho}{1-K_\rho}} K_\rho^{\frac{1+K_\rho}{3K_\rho}} \sqrt{2(1-K_\rho)}. \quad (8)$$

We considered also the case of the long-range Coulomb repulsion, and find that it does not result in important qualitative difference. One of the distinctions is the smaller role of fluctuations. An estimate for the threshold field in this case with the logarithmic accuracy gives

$$U_T = 2V_i \exp\left(-\frac{2}{a}\sqrt{\ln\frac{e}{\epsilon d V_i}}\right),$$

where d is the wire diameter, and $a^2 = \frac{4e^2}{\pi\hbar v_F \epsilon}$ is the dimesionless parameter measuring the strength of the Coulomb interaction, and ϵ is a background dielectric constant.

In conclusion, we found that above the threshold voltage U_T the current through an impurity generates coherent oscillations with the fundamental frequency $f = \bar{I}/e$. If in addition there is also an AC applied voltage with frequency f_0 then an analog of the resonanse Shapiro steps observed in Josephson junctions will appear on the I–V curves. In our problem these are the steps of a constant voltage, the fundamental step being located at the current value $\bar{I} = ef_0$. Characteristic frequencies of the oscillations are determined by the strength of the impurity potential. In semiconducting quantum wires typical values of the impurity potential can be of the order of several meV, so depending on the strength of the electronic repulsion the frequency may fall into gigahertz or terahertz frequency region. Direct application of our results to real systems are limited by voltages smaller than distances to other electronic subbands. The results can be modified also due to different coupling of the 1D system to 3D environment.

Acknowledgements

We thank K. E. Nagaev and V. A. Sablikov for useful discussions. The work was supported by Russian Foundation for Basic Research, and a part of it was performed in the frame of the CNRS-RAS-RFBR Associated European Laboratory "Physical properties of coherent electronic states in condensed matter" between Institut Néel and IRE RAS.

References

[1] T. Giamarchi, *Quantum Physics in One Dimension*, Clarendon Press, Oxford (2003).
[2] O. M. Auslaender *et al*, *Science* **308**, 88 (2005).
[3] H. W. Yeom *et al*, *Phys. Rev. Lett.* **95**, 205504 (2005).
[4] H. Ishii *et al*, *Nature* **426**, 540 (2003).
[5] A. N. Aleshin *et al*, *Phys. Rev. Lett.* **93**, 196601 (2004).
[6] X. G. Wen, *Phys. Rev. Lett.* **64**, 2206 (1990).
[7] S. N. Artemenko, *JETP Lett.* **79**, 335 (2004); S. N. Artemenko and S. V. Remizov, *Phys. Rev. B*, **72**, 125118 (2005).
[8] S. N. Artemenko, T. Nattermann, *Phys. Rev. Lett.* **99**, 256401 (2007).
[9] C. L. Kane and M. P. A. Fisher, *Phys. Rev. Lett.* **68**, 1220 (1992); K. A. Matveev and L. I. Glazman, *Phys. Rev. Lett.* **70**, 990 (1993); A. Furusaki and N. Nagaosa, *Phys. Rev. B* **47**, 4631 (1993).
[10] J. Clarke *et al*, *Science* **29**, 992 (1988).
[11] M. A. Cazalilla, F. Sols, and F. Guinea, *Phys. Rev. Lett.* **97**, 076401 (2006).
[12] R. Egger, H. Grabert, *Phys. Rev. B* **58**, 10761 (1998).

16th Int. Symp. "Nanostructures: Physics and Technology"
Vladivostok, Russia, July 14–18, 2008

The effect of long-range Coulomb interaction on slow relaxation of excess conductance in two-dimensional array of tunnel-coupled Ge/Si quantum dots

N. P. Stepina, E. C. Koptev, A. V. Nenashev, A. V. Dvurechenskii and A. I. Nikiforov
Institute of Semiconductor Physics, Lavrenteva 13, 630090 Novosibirsk, Russia

Abstract. The effect of e-e interaction on the relaxation phenomena in two-dimensional array of tunnel-coupled Ge/Si QDs was studied using the method of screening the long-range Coulomb interaction between carriers located in different dots. It was shown that the screening of the electron-electron interaction suppresses the dependence of the relaxation behavior on the bias voltage and accelerates the relaxation process. Analysis of distribution of the transition rates indicates that the long-range Coulomb interaction excludes some of the transition rates from the hopping transport rather than changes the correlations between them.

Introduction

The atomic-like density of electronic states (DOS) in ensembles of QDs is the crucial issue when QDs are considered for both device applications and fundamental physical studies. In practice, the DOS is determined by (i) spatial confinement of charge carriers in three dimensions, (ii) intradot Coulomb interaction, (iii) interdot tunneling influenced by Coulomb correlations, and (iv) spatial disorder originated from the statistical distribution of dot sizes as well as from fluctuating Coulomb potentials created by charged QDs and background impurity centers. As it has been established earlier [1,2], the electronic states of high density array of weakly coupled and randomly distributed Ge/Si QDs with quite inhomogeneous dot sizes are strongly localized in space, and the electrical charge transfer is due to the hole hopping between dots. Moreover, this structure shows the slow non-exponential relaxation of excess conductivity [3] after the light excitation.

If the formation of the Coulomb gap in the density of state and crossover from Mott to Efros–Shklovskii (ES) variable range hopping (VRH) is obviously associated with the electron-electron (e-e) interaction, the question how is the interaction affects the relaxation process, remains open up to now. At the first glance, slow relaxation of the excess conductivity may be obtained even in non-interacting systems due to the exponential dependence of the transition rates on the hopping length. However, a lot of experimental data in strongly localized systems is difficult to explain without the assumption of interaction being involved [4]. It is proposed [5] that the interaction should further enhance the glassiness of the system, with the relaxation behavior being dependent on the type and strength of the interaction. However, to our best knowledge, no direct experimental proof for such influence has been provided so far.

In this work the contribution of the electron-electron interaction to the relaxation of excess conductivity was studied in two-dimensional array of tunnel-coupled Ge/Si QDs. The excitation from the equilibrium was carried out biasing the samples with pulse of high electric field. To reveal the influence of the long-range Coulomb interaction on the conductivity behavior, we applied the method of interaction screening using the metal plane placed on the top of the sample parallel to the dot layer. Relaxation behavior was compared in the samples with and without screening.

1. Experimental

The samples were grown on a (001) p-Si substrate with a resistivity of 20 cm by molecular-beam epitaxy of Ge in the Stranskii–Krastanov growth mode. The growth temperature for Ge layer was 300 °C and the growth rate was 0.2 monolayer per second, which allows to reach areal density of the dots $\sim 3 \times 10^{11}$ cm^{-2}. 2 holes per dot were supplied from a boron δ-doped Si layer inserted 5 nm below the Ge QDs layer. Details of sample preparation and structure characterization of QDs array have been described elsewhere [3]. The silicon cap layer has a thickness of 40 nm. Al source and drain electrodes were deposited on top of the structure and heated at 450 °C to form reproducible Ohmic contacts. Al screening electrode was deposited over Si cap layer without intermediate isolator parallel to the dot layer. Relaxation measurements were carried out at 4.2 K with the samples immersed in liquid 4He inside a storage dewar. The conductivity of the structures was measured using two-terminal configuration by Keithley electrometer. We made sure that up to 4 K the resistance between the screening plane and the source or drain is much larger (by ≈100 times) than the channel resistance.

2. Results and discussion

The temperature dependence of conductance G(T) for screened and unscreened samples is shown in the Fig. 1(a) as Arrhenius plots. To determine the behavior of $G(T)$, we analyze the temperature dependence of the reduced activation energy $w(T)$ using the method proposed in [6]. As a results, we found (Fig. 1(b)) that in unscreened samples the slopes x of w plots yields $x \approx 0.56$, close to ES VRH, over the whole investigated temperature range. Screened sample exhibits a crossover to the Mott VRH with $x \approx 1/3$ at a temperature ≈13 K. Thus, we showed that the metal plane put as the Shottky barrier at a distance of 40 nm from the quantum dot layer leads to the screening of long-range interactions forming the Coulomb gap in density of state.

The typical curves obtained for the series of relaxation experiments are shown in Fig. 2 for screened and unscreened samples. The conductance G was monitored continuously versus

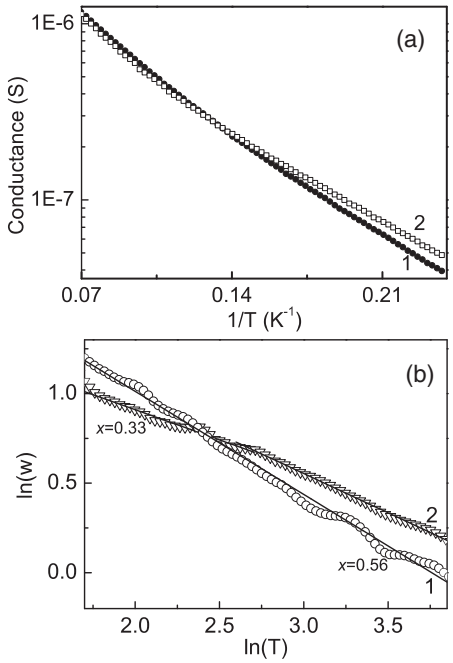

Fig. 1. Temperature dependence of conductance (a) and the logarithmic derivative of the activation energy w (b) for unscreened (1) and screened (2) samples.

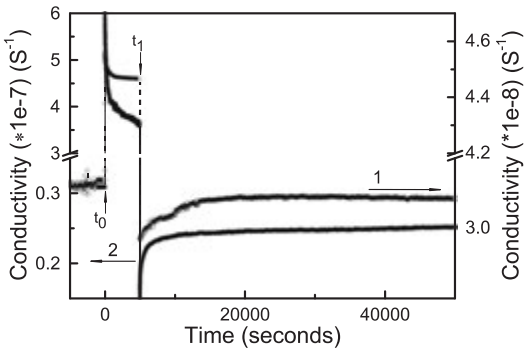

Fig. 2. Conductivity versus time traces for a typical excitation experiment for unscreened (1) and screened (2) samples ($F_1 = 20$ V). The break in the ordinate is to accommodate the large dynamic range.

time. Initially, $G(t)$ is recorded while keeping bias field F=F_0 chosen to be in the Ohmic regime. At the time t_1 (5000 seconds for this experiment), the electrical field was switched back to its original value. Conductivity relaxation curves were analyzed in an attempt to obtain a law describing the relaxation behavior. It was shown, that the $G(t)$ dependence in screened sample may be described by the Kohlrausch law: $F(t) = A\exp[(-t/\tau)^{\beta}]$ with $\beta \approx 0.17$ and being scarcely affected by the bias voltage. In unscreened sample relaxation is also described by the stretched exponential law with $\beta \approx 0.66$ and τ linearly depending on the bias voltage.

The simplest way to obtain a Kohlrausch law is to postulate a statistical distribution $N(w)$ of relaxation rates w. Then, assuming an additive contribution to the relaxing quantity $Q(t)$, it is natural to write $Q(t) = \int N(w)e^{-wt}dw$. Palmer *et al* [7] also found the stretched exponential behaviour describing glassy relaxation when proposed the model of hierarchically constrained relaxation dynamics. It was suggested that a series interpretation is more appropriate than parallel one, with

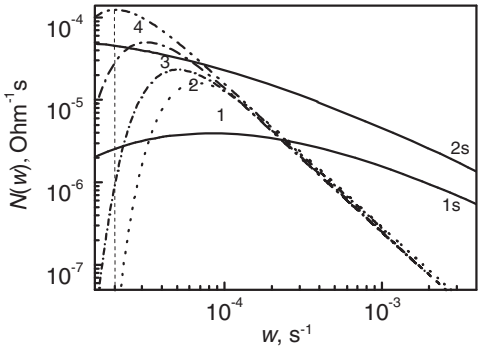

Fig. 3. Distribution function $N(w)$ for the relaxation of screened (1s — for 15 V excitation, 2s — 25 V) and unscreened samples (curves 1 — 4 correspond to 10 — 20 V).

the path to equilibrium involving many sequential correlated activation steps. In this model the same equation may be used, but the $N(w)$ distribution must have a microscopic source in correlations — or constrains — between different degrees of freedom. To restore the distribution function of the relaxation rates, $N(w)$, we carried out the inverse Laplace transformation of the relaxation laws, describing our experimental data. Fig. 3 shows the $N(w)$ derived from such a transformation for both kind of samples and different excitation voltage. One can see that the screening of Coulomb interaction introduces the additional transition rates over almost all experimental time range. Hierarchically constrained relaxation model suggests that interaction will change the correlation between different transition events, keeping the fastest degrees of freedom practically invariable. In this case the distribution functions for interacting and non-interacting systems, should converge at the limit of $t \to 0$. One can see the strong divergence of these functions at the smallest times. Thus, a simple model with parallel channels of relaxation seems to be more convenient than Palmer's one [7]. In the frame of the uncorrelated model, the interaction simply removes some of the transition events, delaying the relaxation process.

References

[1] A. I. Yakimov *et al*, *Phys. Rev.* **B 61**, 10868 (2000).
[2] A. I. Yakimov *et al*, *Phys. Rev.* **B 68**, 205310 (2003).
[3] N. P. Stepina *et al*, *Journal of Exp. and Theor. Phys.* **103**, 269 (2006).
[4] Z. Ovadyahu, *Phil. Magazine B* **81**, 1225 (2001).
[5] M. Pollak *et al*, *Phys. Rev.* **B 59**, 5328 (1999).
[6] A. G. Zabrodskii *et al*, *Zh. Eksp. Theor. Fiz.* **86**, 727 (1984).
[7] R. G . Palmer *et al*, *Phys. Rev. Lett.* **53**, 958 (1984).

16th Int. Symp. "Nanostructures: Physics and Technology"
Vladivostok, Russia, July 14–18, 2008

Electrical conductance of Cu nanowires on Si(111)'5×5'-Cu surface

D. A. Tsukanov[1,2], M. V. Ryzhkova[1], D. G. Larkovich[2], D. V. Gruznev[1], O. A. Utas[1], V. G. Kotlyar[1], A. V. Zotov[1,2,3] and A. A. Saranin[1,2]

[1] Institute of Automation and Control Processes FEB RAS, 690041 Vladivostok, Russia
[2] Far Eastern State University, 690000 Vladivostok, Russia
[3] Department of Electronics, Vladivostok State University of Economics and Service, 690600 Vladivostok, Russia

Abstract. In present paper the electric conductivity of the Cu nanowires on Si(111)'5 × 5'-Cu surface has been studied using LEED and four-point probe conductivity measurement techniques in ultrahigh vacuum. Upon room-temperature deposition onto Si(111)'5 × 5'-Cu surface, Cu atoms migrate over extended distances to become trapped at the step edges, where they form Cu nanowires (NWs). The NWs are 20–60 nm wide, 1–3 nm high and characterized by the resistivity of $\simeq 8\ \mu\Omega$ cm.

Introduction

Metal nanowires (NWs) are important building blocks for the nanoscale devices. Hence, design of the effective and reliable procedures for fabricating NW arrays is considered currently as a challenging task for the researchers. Methods based on the self-assembled NW growth have received especial attention. Self-assembly of the epitaxial silicide NWs on Si surface furnishes an example [1–5]. The silicide NWs have a simple preparation process, which is to deposit metal film onto Si surface in ultrahigh vacuum and then anneal at high temperatures to induce epitaxial regrowth or to deposit metal onto the heated Si substrate to achieve silicide formation already at the deposition stage. Usually atomic mechanism for generating NWs is related to the anisotropic lattice mismatch: the NW is long in the direction of small mismatch and short in large one. Electrical characterization of the silicide NWs have revealed that in the best cases they demonstrate the resistivity, close to that for the high-quality epitaxial films [6–7]. However, in many instances the resistivity of NWs is much greater [8,9].

To fabricate atomic-size NWs, deposition of Au films onto the high-index stepped Si surface, like Si(335), Si(557), Si(553), etc., have been employed [10–13]. In this case, regular arrays of gold atom chains, which spacings depend on the surface are formed. Electrical characterization of the Si(557)-Au surface have shown [11] that the surface exhibits the anisotropy of the surface conductivity: conductivity parallel to the Au chains ($\sigma_{\parallel} = 9.3\ \mu$S/□) is greater than in the perpendicular direction ($\sigma_{\perp} = 2.7\ \mu$S/□).

The goal of the present work was to fabricate arrays of NWs made of copper, the metal with one of the highest conductivities, and to characterize their conductance properties. The basic idea for the Cu-NW self-assembly is to employ the preferential nucleation of Cu islands along the atomic step edges. The Si(111)'5 × 5'-Cu reconstruction appears to be most suitable surface, as Cu atoms adsorbed on it at room temperature (RT) can freely migrate over terraces for long distances to become trapped at the step edges to form there NWs. Growth of the NWs was monitored by scanning tunneling microscopy (STM), conductance properties of the fabricated NW arrays were measured by square four-point probe (4PP) method. Electrical characterization revealed conductance anisotropy of the Cu-NW array and showed that NWs have a resistivity of $\simeq 8\ \mu\Omega$ cm, which is among the lowest values ever reported for the metal NWs.

1. Experimental

The experiments were carried out in two separate UHV chambers with a base pressure in both being in the $\simeq 10^{-10}$ Torr range. The first chamber was the Omicron scanning tunneling microscope, where the NW growth was investigated and regimes for fabricating the NW arrays were established. In the second home-made chamber, the NW arrays were fabricated according established regimes and their electrical properties were measured using 4PP method with tungsten probes making a square of $\simeq 0.6 \times 0.6$ mm^2. Substrates were cut from a standard n-type Si(111) wafers (10–25 Ω cm). The sample size was $12 \times 2 \times 0.45$ mm^3 for STM observations and $15 \times 5 \times 0.45$ mm^3 for electrical characterization. Copper was deposited by resistive heating a tungsten filament wrapped with a Cu wire. A typical deposition rate was about 0.5 monolayer (ML)/min. 1 ML $= 7.8 \times 10^{14}$ cm^{-2}, the density of the top Si atoms on the Si(111) plane. In particular, 1 ML of Cu is equivalent to the 0.93 Å thick Cu film on Si(111), assuming that the film has the same atom density as the bulk Cu.

2. Results and discussions

Fig. 1a shows a typical STM image (800×500 nm^2) of the Si(111) surface prepared *in situ* by flashing to 1250 °C after the sample were first outgases at 600 °C for several hours. The surface comprises a system of terraces separated by atomic steps. An average terrace width was about 150 nm, hence average step density was $\simeq 7 \times 10^4$ cm^{-1}. However, along the sample these parameters vary in wide range (from 50 to 500 nm and from 2×10^5 to 2×10^4 cm^{-1}, respectively), due to local variations in the tilt angle from (111) plane. In atomic scale the surface displats a 7×7 reconstruction, a signature of the atomically-clean Si(111) surface. 4PP method demonstrates that the samples prepared in such a way display a surface conductivity of $\simeq 12\ \mu$S/□.

Deposition of ≃2–3 ML of Cu onto Si(111)7×7 surface at 550 °C results in developing Cu/Si(111)'5×5' reconstruction (Fig. 1b), which is essentially a Cu_2Si-silicide monolayer [14].

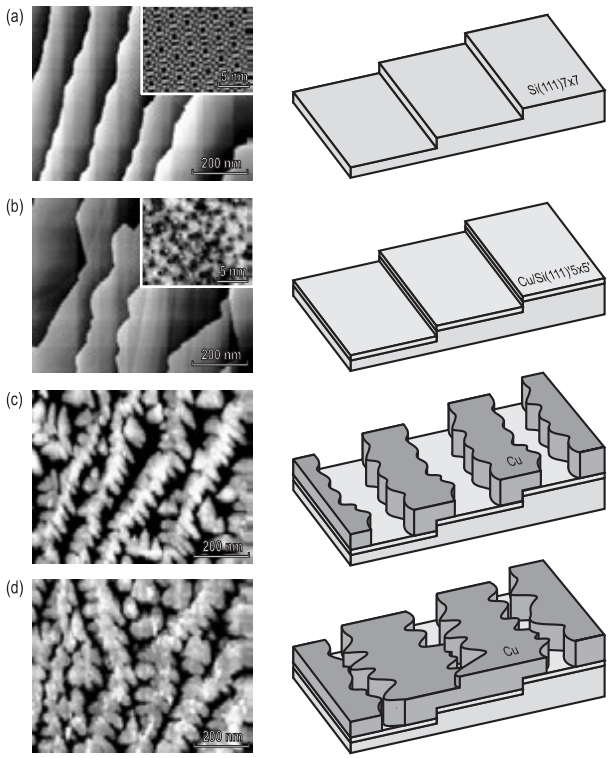

Fig. 1. STM images and schematic diagram illustrating the consequent stages of fabrication NW array. (a) Atomically clean Si(111)7 × 7 surface. (b) Cu/Si(111)'5 × 5' reconstructed surface. (c) NW array prepared by RT deposition of 15 ML of Cu onto the Cu/Si(111)'5 × 5'reconstructed surface. (d) Sample surface after RT deposition of 25 ML of Cu, when interconnected NWs form a percolated Cu film.

After Cu/Si(111)'5 × 5' layer formation, 4PP method reflects a twofold isotropic increase in the surface conductivity, which becomes ≃24 μS/□.

Being deposited onto Cu/Si(111)'5 × 5' surface at RT, Cu adatoms easily migrate over terraces, but are trapped at the step edges where they agglomerate into islands having triangular shape (Fig. 1c). With increasing Cu coverage, islands grow in size and contact with each other to form NWs along the step edges. Typical width of these NWs ranges from 20 to 80 nm and their height from 1 to 3 nm. To characterize conductance properties of NW arrays, a "rotational square 4PP method" was employed, in which the sample resistance $R = \Delta V/I$ (where ΔV is voltage drop measured by a pair of adjacent probes and I is measuring current through another pair of probed) was measured as a function of the rotational angle θ. The rotational angle θ is defined between the line linking the current source probes and the long side of the sample. It has been found that sample conductivity grows by about three orders of magnitude with Cu deposition onto Cu/Si(111)'5 × 5' surface and when Cu-NWs become continuous over sufficient length (at ≃10–20 ML of Cu) the conductance anisotropy is apparent (maximal $R_\perp/R_\parallel \simeq 5.0$).

From the data plotted in Fig. 2, taking into account that

$$R = \frac{1}{2\pi\sqrt{\sigma_x\sigma_y}} \ln\left(1 + \frac{\sigma_x}{\sigma_y}\right),$$

where σ_x and σ_y are surface conductivities along x and y directions [15], one obtains that the surface conductivity along the

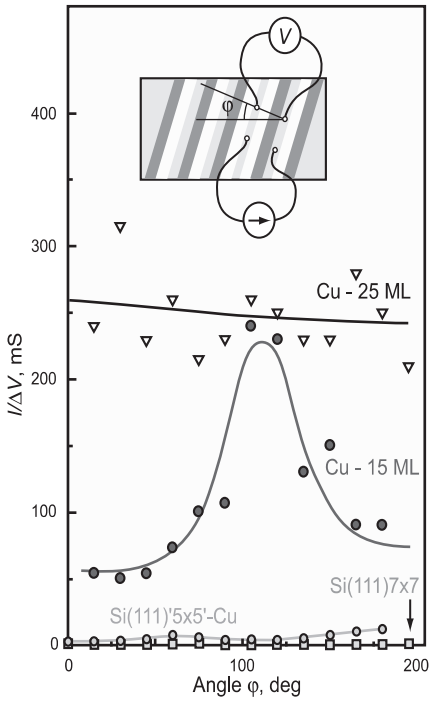

Fig. 2. Conductivity anisotropy of the sample measured using "rotational square 4PP method" (illustrated in the upper panel) at the stages shown in Fig. 1.

NWs $\sigma_\parallel = 19.2$ μS/□ and that in the perpendicular direction $\sigma_\perp = 6.3$ μS/□. Consequently, the resistivity of the NWs can be estimated as $\rho = d/\sigma_\parallel \simeq 8\,\mu\Omega$ cm, where $d \simeq 1.5$ nm is the nominal thickness of the deposited Cu layer, constituting Cu-NWs. As one can see, the resistivity of the Cu-NWs is about 5 times higher than that for bulk copper (1.7 $\mu\Omega$ cm). Enhanced resistivity of the Cu-NWs might be due to surface scattering of the electrons within the NWs or to possible presence of the less-conductive Cu-silicide inclusions in the Cu-NWs. In any case, this value is about twice lower than 17 $\mu\Omega$ cm reported for the Cu-NWs (with a diameter of 60 nm and a lenght of 2.4 μm) electrochemically grown in etched ion-track membranes [16].

Acknowledgements

This work has been supported in part by Russian Foundation for Basic Research (Grant 07-02-00650).

References

[1] C. Preinesberger *et al*, *J. Phys. D* **31**, L43 (1998).
[2] J. Nogami *et al*, *Phys. Rev. B* **63** 233305 (2001).
[3] Y. Chen *et al*, *J. Appl. Phys.* **91**, 3213 (2002).
[4] B. Z. Liu *et al*, *Nanotechnology* **14**, 873 (2003).
[5] W. Zhou *et al*, *Nanotechnology* **17**, 852 (2006).
[6] J. Okino *et al*, *Appl. Phys. Lett.* **86**, 233108 (2005).
[7] J. Kim *et al*, *Nano Lett.* **6**, 1356 (2006).
[8] J. F. Lin *et al*, *Appl. Phys. Lett.* **85**, 281 (2004).
[9] Z. Li *et al*, *J. Phys. D: Appl. Phys.* **39**, 2839 (2006).
[10] P. Starowics *et al*, *Phys. Rev. Lett.* **89**, 256402 (2002).
[11] H. Okino *et al*, *Phys. Rev. B* **70**, 113404 (2004).
[12] J. N. Crain *et al*, *Phys. Rev. B* **69**, 125401 (2004).
[13] H. Okino *et al*, *Phys. Rev. B* **76**, 035424 (2004).
[14] J. Zegenhagen *et al*, *Phys. Rev. B* **46**, 1860 (1992).
[15] T. Kanagawa *et al*, *Phys. Rev. Lett.* **91**, 036805 (2003).
[16] M. E. T. Morales *et al*, *Appl. Phys. Lett.* **82**, 2139 (2003).

16th Int. Symp. "Nanostructures: Physics and Technology"
Vladivostok, Russia, July 14–18, 2008

High frequency blockade and local states in a periodic lattice of quantum dots

M. V. Entin[1] and *M. M. Mahmoodian*[1,2]

[1] Institute of Semiconductor Physics, Siberian Division of Russian Academy of Sciences, Novosibirsk, 630090, Russia
[2] Novosibirsk State University, Novosibirsk, 630090, Russia

Abstract. We study 1D tight-binding lattice of quantum dots, one of which has harmonically vibrating level. The states of non-interacting electrons incident with fixed energy from infinity are considered. It is shown that at definite conditions the site reflects electrons *absolutely and elastically* (high-frequency blockade). The problem is studied numerically and analytically. Together with the blockade states the local states are examined. Possible realizations of the system are discussed.

The system with vibrating local potential attracted attention as possible quantum pumps [1–7]. The study of their regimes tended to the conclusion that at some condition [6–9] such systems with limited potential can ideally reflect electrons. This phenomenon, called "high-frequency blockade" [6, 7], is very interesting, because it permits produce very narrow resonances (quasilocal states in continuum) in transmission, conductance.

Here we concentrate on the study of states of tight-binding 1D lattice expressed by the system of equations

$$i\dot{a}_m - \delta_{m,0}(u + v\cos(\omega t))a_0 + \frac{\Delta}{2}(a_{m+1} + a_{m-1}) = 0. \quad (1)$$

The Eq. (1) corresponds to a periodic chain (for example, planar) of equivalent single-level quantum dots, one of levels vibrates. The energy levels of equivalent dots are chosen as reference point, $\Delta/2$ denotes the overlapping amplitudes.

In the absence of vibrating site the eigenstates of the system with quasimomentum p are running waves $a_m = e^{ipm - iE(p)t}$. The energy of propagating electron $E(p) = -\Delta\cos p$ lies within the permitted band $-\Delta < E < \Delta$. The presence of single site with different level leads to scattering of electrons. Due to vibrations the energy of scattered electrons changes by some quanta ω. We use the quantities u, v, Δ, E measured in units of ω, $\hbar = 1$. The solution of the scattering problem reads

$$\begin{aligned} a_{m\le 0} &= \sum_n \left(\delta_{n,0}e^{ip_n m} + r_n e^{-ip_n m}\right) e^{-i(E+n)t}, \\ a_{m\ge 0} &= \sum_n t_n e^{ip_n m} e^{-i(E+n)t}. \end{aligned} \quad (2)$$

Here p_n is the solution of the equation $E + n = -\Delta\cos p_n$, in accordance with causality corresponding to positive value of velocity for the states inside the permitted band. Some of states occur in the forbidden band; for them positive imaginary value of p_n should be chosen that guarantee the decaying of states apart from the zero site.

The transition amplitudes t_n yield

$$t_n(\Lambda(E+n) - u) - \frac{v}{2}(t_{n+1} + t_{n-1}) = \Lambda(E)\delta_{n,0}. \quad (3)$$

Here

$$\Lambda(E) = i\sqrt{\Delta^2 - (E + i\,0)^2}\,. \quad (4)$$

Physically, the solutions can be tested by measurement of conductance of the system. The presence of mentioned blockade states reflects in the vanishing of conductance at definite conditions.

1. Numerical results

The calculated conductance is depicted in the Figs. 1–3 for different values of Δ. The Fermi energy runs from the bottom $-\Delta$ to the top Δ of the permitted band. The picture for large $\Delta > 1$ exhibits the singularities connected with the thresholds $\pm\Delta$, namely $\pm(\Delta - n)$. They arise as photon repetitions of the threshold singularities. The singularities ease with n. The conductance oscillates with v, that reflects interference nature of the process. At $u = 0$ the figure is symmetric with respect to the band center in accordance with Eq. (3).

There are two other important features of the conductance dependence. One is the vanishing of the conductance at specific energies $E(u, v)$ (blockade states). This means that at corresponding energy all channels of transmission become closed,

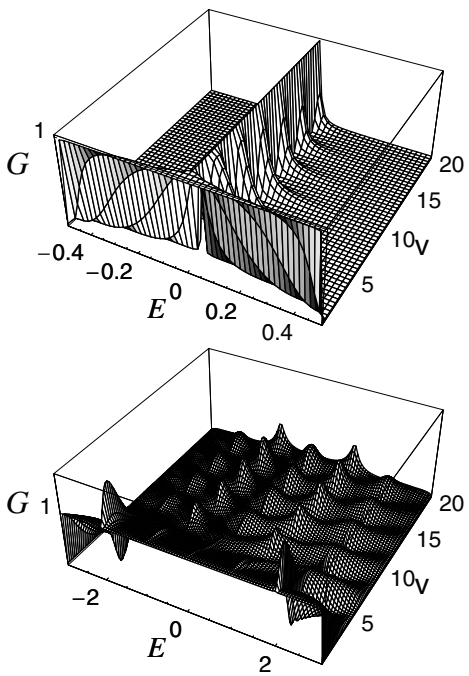

Fig. 1. Conductance versus the Fermi energy and parameter v at $u = 0$, $\Delta = 0.5$ (top) and $\Delta = 2.5$ (bottom).

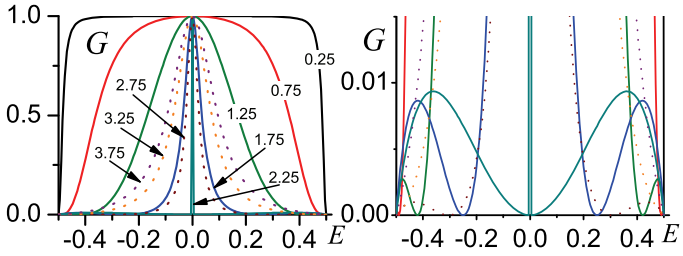

Fig. 2. Dependence of conductance on the Fermi energy E for $\Delta = 0.5$, $u = 0$ and different v (marked on the curves). The right plot is magnified to resolve blockade states (zeros of conductance). Zero-width transmission resonance occur at $v \approx 2.25$, $E = 0$ when blockade states intersect.

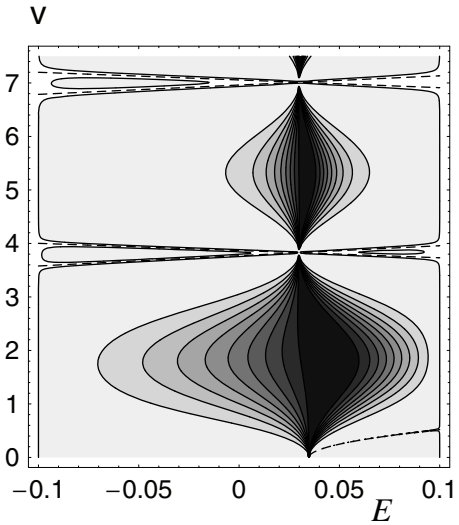

Fig. 3. Map of conductance levels (in relative units) in the tight-binding model as a function of the Fermi energy and the parameter v at $u = 0.13$, $\Delta = 0.1$. The levels run equidistantly from <0.1 (white) to ≥1 (black). The blockade states are depicted by dashed curves.

$t_n = 0$ for $|E + n| < \Delta$. Another feature is the existence of a state with absolute transmission. For $u = 0$ this state corresponds to $E = 0$. It exists if $\Delta < 1$.

2. Analytical results

Let us consider the limit $\Delta \ll 1$. The solution of the system (3) in this limit can be expressed in the form

$$t_n = \frac{\Lambda(E)\sum\limits_k \frac{J_{n-k}(v)J_{-k}(v)}{k-\lambda}}{1 + [\Lambda(E) - E]\sum\limits_k \frac{J_k^2(v)}{k-\lambda}}. \qquad (5)$$

Here $J_n(v)$ are the integer Bessel functions, $\lambda = u - E$. In the considered case only channel $n = 0$ belongs to the propagating states. Hence zeros of t_0 determine the blockade states, while the poles do the localized states.

Blockade states. If the fractional part of u, $\{u\} \equiv \tilde{u} \ll 1$ and $v \ll 1$ the blockade state reads

$$E_0 = \tilde{u} + \frac{N}{(N!)^2}\left(\frac{v}{2}\right)^{2N}, \qquad (6)$$

where $N = [u]$ is integer part of u. The blockade states exist also near points $v = v_{N,m}$, where $v_{n,m}$ are zeros of the Bessel functions $J_n(v)$. For small $v - v_{N,m}$,

$$E_m = \tilde{u} \pm \frac{J_{N+1}(v_{N,m})(v - v_{N,m})}{\left[\sum\limits_{k\neq N} J_k^2(v_{N,m})/k^2\right]^{\frac{1}{2}}}. \qquad (7)$$

Local states satisfy to an equation

$$u = N + E\left[1 - \left(1 - \sqrt{1 - \Delta^2/E^2}\right) J_N^2(v)\right]. \qquad (8)$$

If $N = 0$ and $v = 0$, the local states convert to static impurity states $E = u\sqrt{1 + \Delta^2/u^2}$. For weak, but finite v the level move to the boundaries of the permitted band:

$$E = u\left[\sqrt{1 + \Delta^2/u^2} - \frac{v^2}{2}\left(1 + \frac{1}{\sqrt{1 + \Delta^2/u^2}}\right)\right]. \qquad (9)$$

The obtained analytical results are in accord with numerical results.

One of intriguing features of the systems under examination is possibility to construct local states on the background of free motion band using potential of finite strength. This states appear in the crossing points of blockade states (see Figs. 2 and 3). The similar but almost local states appear in systems with double vibrating sites.

How to realize local high-frequency perturbation? The most interesting domain of parameters is the domain where blockade states exist. In this region the Fermi energy should be less than the frequency. The application of so high frequency is difficult by using of ordinary electrodes. More natural way is utilization of a freely propagating electromagnetic wave. (Neglecting the corrections caused by low-dimensional system itself). The wavelength of electromagnetic wave for typical frequency $\omega \gtrsim E$ exceeds the electron wavelength, that mean non-locality of electromagnetic wave action. Nevertheless, the ways for locality exist. We shall discuss two variants, namely curved quantum wire and utilization of local plasmon resonances.

In conclusion, we have demonstrated that the local vibrating potential in 1D system can act as an ideal mirror, despite the openness of the system. These blockade states co-exist with the states of ideal transparency and local states. We have also found, that such system with double wells can near-ideally confine electrons with energies lying in the continuum. The conditions for these interesting phenomena are reasonable to realize them experimentally.

Acknowledgements

The work was supported by grant of RFBR No. 08-02-00506, the grant of the President of the Russian Federation No. MK-271.2008.2 and the grant of the Russian Science Support Foundation.

References

[1] M. Moskalets and M. Büttiker, *Phys. Rev. B* **66**, 205320 (2002).
[2] S. W. Kim, *Int. J. Mod. Phys. B* **18**, 3071 (2004).
[3] L. S. Braginsky, M. M. Mahmoodian, M. V. Entin, *JETP* **100**, 920 (2005).

[4] M. M. Mahmoodian, L. S. Braginsky, M. V. Entin, *Phys. Rev. B* **74**, 125317 (2006).
[5] M. M. Mahmoodian, M. V. Entin, *Europhys. Lett.* **77**, 67002 (2007); cond-mat/0610832.
[6] M. M. Makhmudian, M. V. Entin, and L. S. Braginskii, *JETP* **105**, 495 (2007).
[7] M. M. Mahmoodian, M. V. Entin and L. S. Braginsky, *Physica E* **40**, 1205 (2008).
[8] O. A. Tkachenko, V. A. Tkachenko, and D. G. Baksheev, *Phys. Rev. B* **54**, 13 452 (1996).
[9] D. F. Martinez and L. E. Reichl, *Phys. Rev. B* **64**, 245315 (2001).

16th Int. Symp. "Nanostructures: Physics and Technology"
Vladivostok, Russia, July 14–18, 2008

Carrier localization in silicon nanocrystals embedded in SiO_x films and exchanging of charge

S. A. Arzannikova, M. D. Efremov, G. N. Kamaev, G. A. Kachurin, D. V. Marin and V. A. Volodin
Institute of Semiconductor Physics of SB RAS, pr. ak. Lavrentjeva 13, Novosibirsk 630090, Russia

Abstract. The presented work is devoted to investigation of electrical properties of MOS-structures containing nanocrystals in silicon dioxide. SiO_x film deposition was elaborated using silicon-organic materials as precursors. Also treatment in plasma of pure O_2 gas was approved to achieve very thin SiO_2 films in a range of thickness 3–20 nm owing to oxidation of silicon surface. Three layer SiO_x dielectric films with large amount of excess silicon in the middle layer were made and correspondent MOS-structures were prepared for electrical measurement. Excimer laser treatments were applied for phase transformation of Si nanoclusters to nanocrystals. Electrical characteristics were measured using CV, GV, IV methods in a range of frequencies from static up to 2 MHz. Exchange of carriers between substrate and nanoclusters and nanocrystals leaded to increasing of MOS capacity at enrichment biases, meanwile this effect dissapear with frequency increase. Correlation of differential capacitance and conductivity versus voltage was observed. Calculation and estimation of possibility of carrier transfer to nanocrystals in the middle layer were provided including comparison with the case of thermal oxide doped with Si nanocrystals.

Introduction

Earlier we have published the work been demonstrated step-like static IV characteristic for MOS-structure with Si nanocrystals ad the middle of thermal oxide, introduces by means of ion implantation. The temperature of the NC formation was about 1100 °C. Plasma-chemical technology offers some advantages at significantly low temperatures of the substrate heating. One of them is possibility to form more abrupt transitions between layers of SiO_x with different contents of silicon. Other one, in spite of common opinion, it is conductivity through the oxide layer. It means, that direct tunnelling through best quality oxide is impossible taking into account reasonable technology possibilities. Transport due to multiple jumps of carriers could provide efficient probability to reach the middle layer, where majority of nanocrystals could be formed. Adding of silicon atoms inside of SiO_x layers provides both decreasing of bandgap and appearance of electronic states, which could be responsible for electron transport between nanocrystals even in the case of quite thick SiO_x layers. For crystallisation of nanoclusters formed just at deposition excimer laser annealing was applied to prevent overheating of substrate due to short pulses of irradiation (20ns). So, main topic of the papers is to realise low-temperature method to form thin dielectric with nanocrystals inside.

Experimental

Induction type reactor was used for deposition. Layers of $SiO_2/SiO_x/SiO_2$ were subsequently grown. Regimes of deposition were chosen such a way to obtain good quality SiO_2 layers using approved method of deposition marked in preface. In the middle layer SiO composition was intentionally created for sample N 7, and with some amount of Si (SiO_x, $x < 1$) for sample N 5. Correspondent thickness of layers was 20 nm/2 nm/6 nm starting from substrate of p-type conductivity (KDB-12). Spectral ellipsometry was applied to examine composition of the dielectric film. Capacity-voltage (CV), conductivity voltage (GV) characteristics were measured at various frequencies from 20 Hz up to 2 MHz at room temperature, as well as static current-voltage (IV) curves. Raman spectra were measured for detection of phase composition, and photoluminescence spectra were recorded at room temperature. Raman polarisation geometry was chosen to suppress signal from substrate.

1. Plasma-chemical SiO_2:NC

As evident from Raman spectra for as deposited films silicon clusters give signal around 480 cm^{-1}, meanwhile peak at 520 cm^{-1} corresponds to substrate (Fig. 1). Contents of silicon in the film of sample N 5 much larger, than for N 7 as was intentionally grown. Meanwhile in the sample N 7 some excess of silicon atoms is displayed due to small feature at 480 cm^{-1}. Peak at 480 cm^{-1} corresponds to amorphous phase of silicon, or Si-Si bonds vibrations within some surrounding of Si atoms, what requires interpretation as clusters inclusions. Results of laser impact are reflected in Fig. 2. It is interesting that after one short of laser irradiation broad peak in 440–500 cm^{-1} region was appeared. Pulse energy was chosen correspondently to usual for transforming amorphous silicon into crystalline phase in liquid phase crystallization regime, in other words with melting of the a-Si film. Similar behavior was observed for transformation of amorphous structure without crystallization, but with increasing of Raman intensity or for so-called amorphization of the silicon liquid due to rapid cooling. Ex-

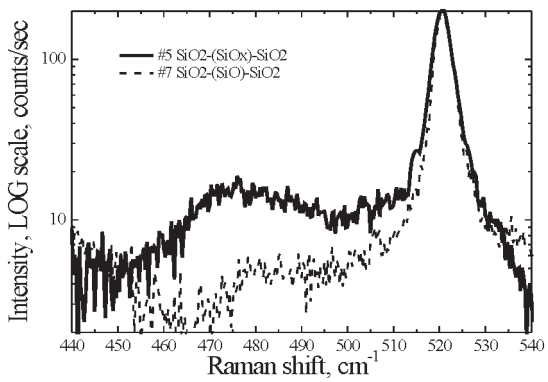

Fig. 1. Raman spectra for as deposited samples N 5, N 7.

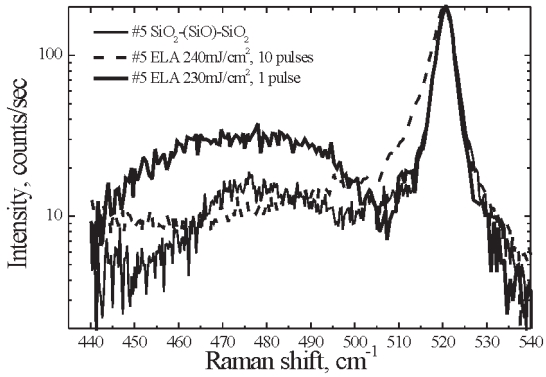

Fig. 2. For sample N 7 depending on laser treatment regime.

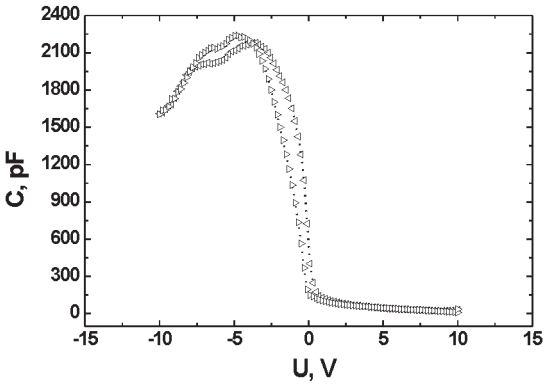

Fig. 3. CV characteristics for ELA treated sample N 5 (10 pulses) at room temperature and frequency 3 kHz.

act answer requires additional study of rapid phase transition for nanoparticles. Ten pulses leaded to crystallization of nanoclusters, peak at 480 cm^{-1} disappears and crystalline phase add Raman signal at left wing of the peak at 520 cm^{-1} (Fig. 2). So, nanocrystals were successfully formed in dielectric film.

CV, GV, IV characteristics were examined for fabricated samples for different frequencies. Both as grown oxides and laser treated were used in experiments with MOS-structures. Some effects were detected for both type of structures and interpreted accordingly. Differential capacities were detected at enrichment biases with much large values than estimated capacity of dielectric layer (Cd). It should be noted, that for non conducting dielectric the theory of MOS structures require up limit of MOS capacitance equal to Cd. With increasing of testing frequency maximal capacitance became significantly less. The effect is illustrated in Fig. 3, Fig. 4 for correspondent frequencies of 3,1000 kHz and interpreted as exchange of carriers with substrate within period of oscillations. When carriers are not in time to transfer inside to dielectric film and to return back, maximal capacitance became comparable with Cd. Significant deviation of capacitance from classical values is following with features for differential conductivity versus voltage. That fact support proposed interpretation, that namely alternative current through dielectric is responsible for the effect. Features in conductivity were observed as in the form of plateau, as sharp peaks at the voltage where capacitance changes. Sharp peaks could correspond to either mono-energetic states in SiO_2 or in the middle layer SiO_x corresponding to silicon clusters. For as grown SiO_2 electronic state distributions were calculated to be smooth, so possibly transfer of cluster onto Si nanoclusters

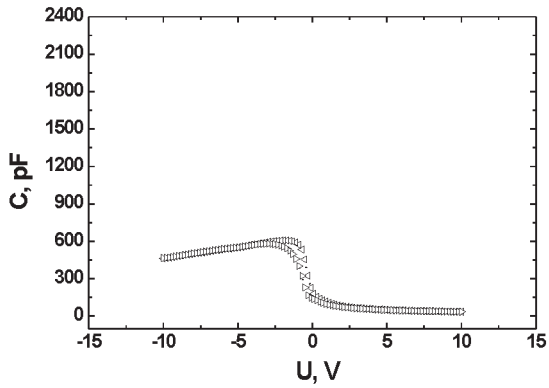

Fig. 4. CV characteristics for ELA treated sample N 5 (10 pulses) at room temperature and frequency 1000 kHz.

(nanocrystals) were discovered.

As shown, some hysteresis is detected for direct and reverse scanning of voltage. Flat band voltage is close to zero. At inversion bias decreasing of characteristic high frequency "inversion capacitance" (Ci) was detected, may be due to the same reason. It should be noted, that as for nanocrystals, as for nanoclusters similar quantum electronic spectrum may be expected, but less finest in the second case. So, both cases could be compared with round nanocrystals in thermal oxide films.

2. Thermal SiO_2:NC

Earlier results for Si nanocrystals inside of thermal oxide films demonstrated step-like IV characteristics [1]. It is interesting that capacitance behavior was detected to look similar to observed for plasma-chemical films. So, one could expect to observe single electron phenomena in the PCVD films. In order to take account possibly large values of parallel conductivity calculation were provided. Besides of parallel conductivity nonlinear character of equivalent scheme was adopted, taking into account diode characteristic for substrate. Calculation of electron energies was made taking into account different effective mass of electrons in silicon nanocrystals and in surrounding SiO_2. Steps due to Coulomb blockade effect on spin degenerated levels in nanocrystals are resolved in calculations, but steps was evaluated could be with slope on voltage due to parallel conductivity through the film. Influence of illumination on CV characteristics and processes of recharging of electronic states were detected in experiment.

3. Conclusion

Preliminary experiments demonstrated perspectives of plasmochemical multi-layer structures for further study of single-electrons effects.

References

[1] M. D. Efremov *et al*, *Semiconductors* **39**, 910–916 (2005).

16th Int. Symp. "Nanostructures: Physics and Technology"
Vladivostok, Russia, July 14–18, 2008

The dc voltage proportional to the persistent current observed on system of asymmetric mesoscopic loops

V. L. Gurtovoi, A. I. Il'in, *A. V. Nikulov* and V. A. Tulin

Institute of Microelectronics Technology, Russian Academy of Sciences, 142432 Chernogolovka, Moscow region, Russia

Abstract. The observations of the dc voltage proportional to the persistent current on system of asymmetric superconductor loops at a non-zero resistance raise a question on a nature of this quantum phenomenon and its possibility in semiconductor and normal metal mesoscopic loops.

Introduction

It is well known that a potential difference $V = (R_{ls} - R_l l_s/l)I = R_{\rm an} I$ is observed on a segment l_s (with a resistance R_{ls}) of an asymmetric conventional metal loop l (with a resistance R_l) when a circular current $I = \oint_l dl\, E/R_l$ is induced by the Faraday's voltage $\oint_l dl\, E = -d\Phi/dt$ in this loop. On the other hand the magnetization measurements give evidence a circular direct current observed in semiconductor [1] normal metal [2] and normal state of superconductor [3] nano-structures in a constant magnetic field, i.e. without the Faraday's voltage $d\Phi/dt = 0$. The observed periodical change of the magnetization with magnetic field at the period corresponding to the flux quantum for single electron $\Phi_0 = 2\pi\hbar/e$ or pair $\Phi_0 = \pi\hbar/e$ gives unambiguous evidence that this equilibrium quantum phenomenon, as well as flux quantization in superconductor [4], is a consequence of the persistent current $I_{\rm p}(\Phi/\Phi_0)$ existing because of the quantization of the velocity circulation

$$\oint_l dl\, v = \frac{2\pi\hbar}{m}(n + \frac{\Phi}{\Phi_0})$$

But in contrast to the flux quantization observed as far back as 1961 [5] the experimental results [1–3] give evidence of the persistent current along the loop with non-zero resistance $R_l > 0$.

The persistent current at $R_l > 0$ was predicted as far bag as 1970 both in normal state $T > T_{\rm c}$ of superconductor [6] and in non-superconductor mesoscopic structures [7]. It was written in [7] and the later theoretical works [8,9] have corroborated that the persistent current can be observed at electron scattering (at a finite mean free path $L_{\rm f.p.}$), i.e. at non-zero dissipation. Thus, the persistent current can be observed at non-zero dissipation like conventional circular current. Nevertheless most experts are fully confident that a potential difference $V_{\rm p}(\Phi/\Phi_0) = R_{\rm an} I_{\rm p}(\Phi/\Phi_0)$ can not be observed on a segment l_s when the persistent current $I_{\rm p}(\Phi/\Phi_0)$ is observed along the asymmetric mesoscopic loop with non-homogeneous dissipation $R_{\rm an} = R_{ls} - R_l l_s/l \neq 0$ along its circumference l. The observation [10] of the quantum oscillation of the dc voltage $V_{\rm p}(\Phi/\Phi_0)$ on a system of aluminum loops in the temperature region corresponding to the superconducting resistive transition, i.e. at $R_l > 0$, call this confidence in question.

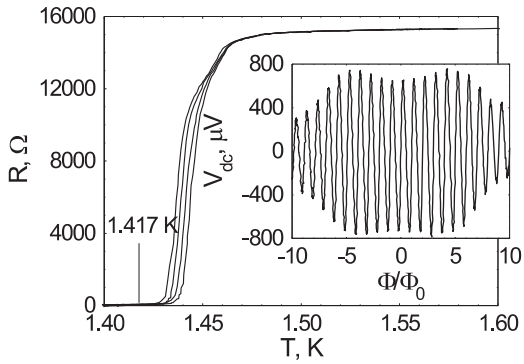

Fig. 1. The superconducting resistive transition of the nano-structure containing 1050 asymmetric aluminum loops with diameter $2r = 4$ μm written at the measuring current with different values $I_{\rm ext} =$ 100 nA, 200 nA, 300 nA, 400 nA. The inset shows the quantum oscillation of the dc voltage $V_{\rm dc}(\Phi/\Phi_0)$ induced by the external as current with the frequency $f = 1$ kHz and the amplitude $I_0 = 2$ μA at the temperature $T = 1.417$ K corresponding to superconducting state of this nano-structure.

1. The persistent current in superconductor and in non-superconductor loops

The persistent current observed in normal state of superconductor and non-superconductor (semiconductor and normal metal) has seminar nature and the theorists demonstrate this likeness. I. O. Kulik made the theory of the persistent current in non-superconductor nano-structure [7] just after the work [6] on this phenomenon in normal state of superconductor and in twenty years F. von Oppen and E. K. Riedel have calculated the flux-periodic persistent current in mesoscopic superconducting rings close to $T_{\rm c}$ [11] after the calculation of the disorder-averaged persistent current for a non-superconductor mesoscopic ring [9]. The persistent current can be observed in a loop when the wave function of electron or superconducting condensate is closed now and again in this loop. Therefore the persistent current can have an appreciable value only if the mean free path $L_{\rm f.p.}$ is not smaller than the loop length l [8,9].

In the superconducting state the mean free path of pairs is infinite $L_{\rm f.p.} = \infty$ and the persistent current has a value $I_{\rm p} = 2eN_s v_s/l$ much large then in a non-superconductor loop $|I_{\rm p}| < ev_{\rm F}/l$ [8,9]. Although the Fermi velocity exceeds the pair velocity $max|v_s| = \pi\hbar/ml$ determined by the relation (1) the pair number N_s in any real loop is so great at $T < T_{\rm c}$

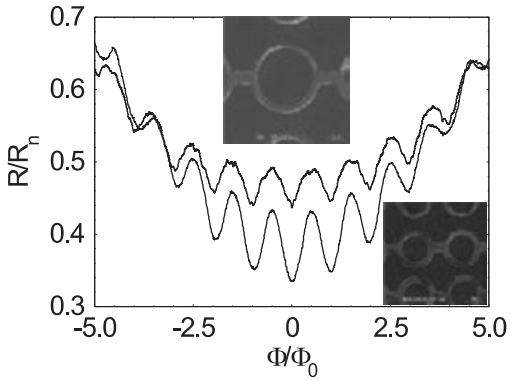

Fig. 2. The Little–Parks oscillations of the resistance R reduced to the one in the normal state R_n measured on two nano-structures containing aluminum loops with diameter $2r = 4\ \mu$m (the upper curve) and $2r = 2\ \mu$m (the lower curve) demonstrate the increase of the amplitude of the superconducting transition shift $\Delta T_c(\Phi/\Phi_0)$ in magnetic field with the loop decrease.

that $2eN_s\pi\hbar/ml^2 \gg ev_F/l$. Because of the large I_p value the quantum oscillation of the dc voltage $V_{dc}(\Phi/\Phi_0)$ with high amplitude can be observed at $T < T_c$, Fig. 1. But because of zero resistance $R_{an} = 0$ an external ac current with the amplitude I_0 exceeding the superconducting critical current $I_c = I_c(0)(1 - T/T_c)^{3/2}$ should be applied at $T < T_c$ [12].

The $I_p(\Phi/\Phi_0)$ and $V_{dc}(\Phi/\Phi_0)$ decrease with the temperature increase together with the I_c value [13]. But because of the thermal fluctuation there is a critical region near T_c where $I_c = 0$ and $R_l > 0$ (at $I_{ext} = 0$) but $I_p \neq 0$ [3,6,11]. The fluctuations switching [14] loop segments in the normal state destroy the phase coherence along the superconductor loop just as scattering of electron destroys its phase coherence along the non-superconductor loop.

2. Shift because of the persistent current and width of superconducting resistive transition

Such switching between quantum states with different connectivity of the wave function can induce a potential difference $V_p(\Phi/\Phi_0) \propto I_p(\Phi/\Phi_0)$ on segment of an asymmetric loop [14,15]. It is expected that its value in the normal state $T > T_c$ may be larger than in non-superconductor loop since the I_p value in the first case [3] is larger than in the second one [1,2]. The persistent current $I_p \propto v_s \propto 1/l$ increases with the loop length $l = 2\pi r$ decrease. But at a too small loop $r < \xi(0)(\delta T_c/\Delta T_{c,sh})^{1/2}$ the switching between states with different connectivity of the wave function becomes impossible [14] because of the critical temperature shift $\Delta T_c = \Delta T_{c,sh}(n - \Phi/\Phi_0)^2 = -(\xi(0)/r)^2(n - \Phi/\Phi_0)^2$ [16]. Here $\xi(0)$ is the superconductor coherence length at $T = 0$ and δT_c is the width of the superconducting transition. Our measurements have corroborated the $\Delta T_c(\Phi/\Phi_0) \propto \Delta R(\Phi/\Phi_0)/R_n$ amplitude increase with the $2r$ loop decrease, Fig. 2. We have found that $\Delta T_{c,sh} = \delta T_c$ at the diameter of our aluminum loop $2r = 2\ \mu$m. We intend to present results of the $V_p(\Phi/\Phi_0)$ measurements on nano-structures with great number of such loops, Fig. 3. It may be these results will answer on the question on a possibility to observe the like phenomenon in semiconductor and normal metal loops.

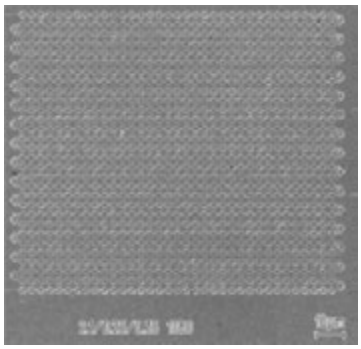

Fig. 3. An electron micrograph of the nano-structure containing 1080 asymmetric aluminum loops with diameter $2r = 2\ \mu$m.

Acknowledgements

This work has been supported by grant of the Program "Quantum Nanostructures" of the Presidium of RAS, grant 08-02-99042-r-ofi of the Russian Foundation of Basic Research and grant "Quantum bit on base of micro- and nano-structures with metal conductivity" of the Program "Technology Basis of New Computing Methods" of ITCS department of RAS.

References

[1] D. Mailly, C. Chapelier, and A. Benoit, *Phys. Rev. Lett.* **70**, 2020 (1993); B. Reulet *et al*, *Phys. Rev. Lett.* **75**, 124 (1995); W. Rabaud *et al*, *Phys. Rev. Lett.* **86**, 3124 (2001); R. Deblock *et al*, *Phys. Rev. Lett.* **89**, 206803 (2002); R. Deblock *et al*, *Phys. Rev. B* **65**, 075301 (2002); N. A. J. M. Kleemans *et al*, *Phys. Rev. Lett.* **99**, 146808 (2007).

[2] L. P. Levy *et al*. *Phys. Rev. Lett.* **64**, 2074 (1990); V. Chandrasekhar *et al*, *Phys. Rev. Lett.* **67**, 3578 (1991); E. M. Q. Jariwala *et al*, *Phys. Rev. Lett.* **86**, 1594 (2001).

[3] X. Zhang and J. C. Price, *Phys. Rev. B* **55**, 3128 (1997).

[4] T. I. Smith and H. E. Rorschach, *Rev. Mod. Phys*. **36**, 277 (1964).

[5] B. S. Deaver, Jr. and W. M. Fairbank, *Phys. Rev. Lett.* **7**, 43 (1961); R. Doll and M. Nabauer, *idid.* **7**, 51 (1961).

[6] I. O. Kulik, *Zh. Eksp. Teor. Fiz.* **58**, 2171 (1970).

[7] I. O. Kulik, *Pisma Zh. Eksp. Teor. Fiz.* **11**, 407 (1970) (*JETP Lett.* **11**, 275 (1970)).

[8] Ho-Fai Cheung, E. K. Riedel, and Y. Gefen *Phys. Rev. Lett.* **62**, 587 (1989); V. Ambegaokar and U. Eckern *idid.* **65**, 381 (1990); Ho-Fai Cheung, Y. Gefen, E. K. Riedel, and Wei-Heng Shih, *Phys. Rev. B* **37**, 6050 (1988).

[9] F. von Oppen and E. K. Riedel, *Phys. Rev. Lett.* **66**, 587 (1991).

[10] A. A. Burlakov *et al*, *Pisma Zh. Eksp. Teor. Fiz.* **86**, 589 (2007) (*JETP Lett.* **86**, 517 (2007)).

[11] F. von Oppen and E. K. Riedel, *Phys. Rev. B* **46**, 3203 (1992).

[12] S. V. Dubonos *et al*, *Pisma Zh. Eksp. Teor. Fiz.* **77**, 439 (2003) (*JETP Lett.* **77**, 371 (2003)).

[13] V. L. Gurtovoi *et al*, *Zh. Eksp. Teor. Fiz.* **132**, 1320 (2007) (*JETP* **105**, 1157 (2007)).

[14] A. V. Nikulov and I. N. Zhilyaev, *J. Low Temp.Phys*. **112**, 227 (1998).

[15] A. V. Nikulov, *Phys. Rev. B* **64**, 012505, (2001).

[16] M. Tinkham, *Introduction to Superconductivity.* McGraw-Hill Book Company (1975).

16th Int. Symp. "Nanostructures: Physics and Technology"
Vladivostok, Russia, July 14–18, 2008

Emitting a-SiO$_x$(Er) films and a-SiO$_x$(Er)/a-Si:H microcavities with a controlled erbium doping profile

A. V. Medvedev, A. B. Pevtsov, S. A. Grudinkin, N. A. Feoktistov, V. A. Sakharov, I. T. Serenkov and V. G. Golubev

Ioffe Physico-Technical Institute, St Petersburg, Russia

Abstract. We have developed the technique of growing a-SiO$_x$(Er) films and a-SiO$_x$(Er)/a-Si:H multilayer structures based on spatial separating the processes of the decomposition of an oxygen-silane gas mixture in a RF glow discharge plasma and remote magnetron sputtering of an Er-target. This approach allows us to control independently the film deposition rate, the Er-ion concentration and its depth-distribution in the film. The method we suggest is a way to produce effectively emitting microcavity structures, in which the distribution profile of emission centers coincides with that of the electromagnetic field in individual layers of the structure.

Introduction

Interest in Er-doped materials is due to their application in optoelectronic devices, in particular, in amplification media for optical fiber communication systems, primarily because Er^{3+} ions have their major emitting transition $^4I_{13/2} \rightarrow {}^4I_{15/2}$ at a wavelength of ∼1540 nm coinciding with the minimum loss region in optical fibers [1].

The emission lifetime of the first excited state of an Er^{3+} ion (the $^4I_{13/2} \rightarrow {}^4I_{15/2}$ transition) usually lies in the millisecond range; the absorption and emission cross sections are small, $10^{-21}-10^{-20}$ cm^2. Therefore, a high ion concentration of 0.1–1% is necessary to achieve a large gain in device structures. It is known that for increasing the operation efficiency of emitting structures the depth concentration profile of doping ions must optimally coincide with the profile of the fundamental optical mode in the structure [2].

The commonly used Er-ion implantation technique [3] can only provide a Gaussian distribution of emitting centers. The peak position and the doping profile dispersion are defined by the energy of implanted ions, so they cannot be controlled independently. As a result, ion implantation is unable to match adequately the doping and microcavity eigenmode profiles, leading to ineffective excitation of emitters when the eigenmodes have a complex profile. Another method of Er introduction in, for instance, a-Si:H films is magnetron-assisted silane decomposition [4]. Here the ion concentration closely depends on the area ratio of silicon and erbium in the target and cannot be varied during the growth.

In this work, we have developed a technological approach which allows varying the concentration and depth distribution of Er ions introduced in a-SiO$_x$ and a-Si:H films directly during the growth. This method can produce multilayered structures with a well-defined doping profile in any layer. We synthesized both a-SiO$_x$(Er) films and periodic a-SiO$_x$/a-Si:H structures and studied the erbium distribution profile over the film thickness, steady-state photoluminescence and its kinetics. It is shown that the developed technique can provide fabricating of the structures emitting at 1540 nm with a 75% internal quantum yield.

1. Experimental

Our technological approach is based on the spatial separation of two processes: the decomposition of an oxygen-silane gas mixture in a RF glow discharge plasma and remote magnetron sputtering of an Er target. The magnetron unit is located outside the main RF discharge region, in which a-SiO$_x$ and a-Si:H films are grown. This allows an independent control of the growth rate (by varying the discharge power) and the ion concentration in the film (from the dependence of the Er sputtering rate on the magnetron current). The advantages of this technological approach are especially evident when Er is introduced in *multilayered* structures made up of periodic a-SiO$_x$ and a-Si:H layers: distributed Bragg reflectors (DBR) and microcavities [5,6]. In this case, one can obtain a desired doping profile and a controlled ion concentration in both a-SiO$_x$ and a-Si:H layers during the structure growth. The Er ion concentration and depth distribution were found from the middle energy ion scattering (MEIS) data [7]. Photoluminescence (PL) was excited by a semiconductor laser operating in a continuous mode at 980 nm (in the vicinity of the intra-4f $^4I_{15/2} \rightarrow {}^4I_{11/2}$ transition of the Er^{3+} ion).

2. Results and Discussion

Figure 1 demonstrates the depth distribution of Er^{3+} ions, obtained from the analysis of the MEIS spectra for two films grown in different doping modes. Curve 1 is for the depth distribution profile of an a-SiO$_x$ film Er-doped during the whole growth time. Curve 2 is for the profile when the Er ion source was turned on for a short time at the moment of half a-SiO$_x$ layer thickness. The arrows indicate the layer boundaries (the position of the a-SiO$_x$(Er)/Si interface) for both profiles. Zero on the depth scale denotes the outer film surface. The simulation yielded the doped layer thickness of 6.8 nm with the ion concentration in this layer 2.72×10^{19} atoms/cm^3. The thicknesses of the depth distribution fronts were found to be 0.9 nm each. The actual front of the impurity distribution is likely to be sharper, since the experimental data used in the simulation were limited by the resolution of the MEIS detector.These results show a conceptual possibility to create a well-defined distribution profile of emission centers, adjusting it exactly to the electromagnetic field profile determined by the mode structure of,

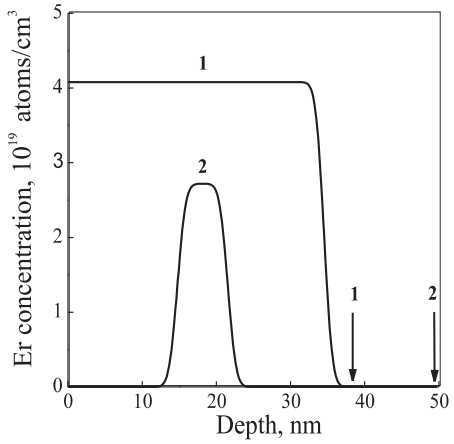

Fig. 1. The depth distribution profiles of Er ions in two a-SiO_x(Er) films. Zero on the depth scale is the film surface: 1 — the distribution profile for the a-SiO_x film which was doped with Er during the whole growth time, 2 — the distribution profile for the a-SiO_x film which was doped for a short time at the a-SiO_x half layer. Arrows indicate the a-SiO_x layer boundaries, i.e., the position of the a-SiO_x(Er)/Si interface for both distribution profiles.

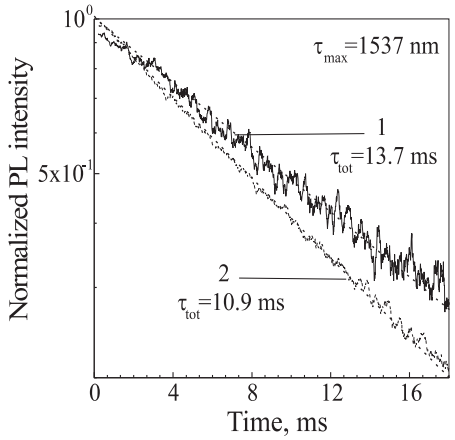

Fig. 2. The time dependence of the PL decay at the wavelength $\lambda_{max} = 1537$ nm (semi-logarithmic scale): 1 — a-SiO_x (Er) film, 2 — a-SiO_x/a-Si:H microcavity with a-SiO_x active layer doped with Er. Both plots are normalized to the maximum PL intensity at $t = 0$. Straight lines — single exponential fits with the decay parameters τ_{tot} of 13.7 ms (curve 1) and 10.9 ms (curve 2), respectively.

for instance, a DBR or a microcavity. The emission efficiency of a-SiO_x(Er) films can be evaluated from the internal quantum yield of PL: $\eta = \tau_{tot}/\tau_r$, where $\tau_{tot} = \tau_r \times \tau_{nr}/(\tau_r + \tau_{nr})$ is the total lifetime of an emission center, τ_r is the radiative lifetime, and τ_{nr} is the nonradiative lifetime. The τ_{tot} value can be derived by processing the experimental data on the PL time decay. Figure 2 shows the time dependence of the PL signal for an a-SiO_x(Er) film (curve 1) measured at the wavelength $\lambda_{max} = 1537$ nm corresponding to the maximum intensity in the emission spectrum. The PL decay trace is well described by means of an exponential curve (the dashed line in Figure 2) with the parameter $\tau = \tau_{tot} = 13.7$ ms. For a quantitative evaluation of η, we used the radiative lifetime of Er ions in the silicon oxide $\tau_r \approx 18$ ms [8]. It was found that the internal quantum yield from a-SiO_x(Er) films was as high as 75%, which is an evidence for a good effectiveness of our approach to producing Er^{3+} emission centers in a-SiO_x films during their growth. To test the potentialities of this technological approach for creating effective emitters at 1.5 μm, we produced a microcavity structure made up of two DBRs and an a-SiO_x(Er) half-wave active layer sandwiched between them. The cavity eigenmode wavelengths were tuned to the 1537 nm emission line of Er^{3+} ions.

Figure 2 (curve 2) shows the time dependence of the PL signal for the microcavity structure. It is seen that the experimental data are well approximated by an exponential fit with the parameter $\tau_{tot} = 10.9$ ms. The total ion lifetime is shorter than their lifetime in a single a-SiO_x(Er) film, which is due to the change in the spontaneous emission rate in the microcavity structure (the Purcell effect). Thus, this result demonstrates that the technological approach we have suggested provides an effective ion introduction in any spatial region of a multilayered structure.

3. Conclusion

We have developed a method of growing a-SiO_x(Er) films and a-SiO_x/a-Si:H multilayer structures doped with Er, in which the process of decomposition of an oxygen-silane gas mixture by a RF glow discharge plasma is spatially separated from magnetron sputtering of an Er target. This technique provides an independent control of the a-SiO_x film deposition rate, the concentration of Er ions and their depth distribution in the film. We have grown films and microcavities with the internal quantum yield of Er^{3+} ions emission ~75%. A precise introduction of emission centers in any given region in the sample directly during its growth is a further step in enhancing microcavity emission owing to a good adjustment of the spatial distribution profile of emission centers to that of the electromagnetic field in the microcavity layers.

Acknowledgements

We acknowledge A. A. Dukin for fruitful discussions. This work was financially supported in part by the EC-funded project PHOREMOST (FP6/2003/IST-2-511616), and by the Alexander von Humboldt-Foundation.

References

[1] A. J. Kenyon, *Progress in Quantum Electronics* **26**, 225 (2002).
[2] J. Kalkman, A. Polman, T. J. Kippenberg, K. J. Vahala and M. L. Brongersma, *Nuclear Instruments and Methods in Physics Research B* **242**, 182 (2006).
[3] A. Polman, D. C. Jacobson, D. J. Eaglesham, R. C. Kistler and J. M. Poate, *J. Appl. Phys.* **70**, 3778 (1991).
[4] M. S. Bresler, O. V. Gusev, V. Kh. Kudoyarova, A. N. Kuznetsov, P. E. Pak, E. I. Terukov, I. N. Yassievich, B. P. Zakharchenya, W. Fuhs and A. Sturm, *Appl. Phys. Lett.* **67**, 3599 (1995).
[5] A. A. Dukin, N. A. Feoktistov, V. G. Golubev, A. V. Medvedev, A. B. Pevtsov, and A. V. Sel'kin, 2000 *Appl. Phys. Lett.* **77**, 3009 (2000).
[6] A. V. Medvedev, A. A. Dukin, A. B. Pevtsov, C. Sibilia, N. A. Feoktistov and V. G. Golubev, *Tech. Phys. Lett.* **33**, 976 (2007).
[7] V. V. Afrosimov, R. N. Il'in, V. I. Sakharov and I. T. Serenkov, *Semiconductors* **41**, 487 (2007).
[8] de M. J. Dood, L. H. Sloof, A. Polman, A. Moroz, and van A. Blaaderen, *Phys. Rev. A* **64**, 033807 (2001).

16th Int. Symp. "Nanostructures: Physics and Technology"
Vladivostok, Russia, July 14–18, 2008

Synthesis of thin-film opal-iron oxide photonic crystals

D. A. Kurdyukov, S. A. Grudinkin, S. F. Kaplan, N. F. Kartenko and V. G. Golubev
Ioffe Physico-Technical Institute, St Petersburg, Russia

Abstract. The developed method of lateral infiltration (LI) under capillary forces allows introduction of iron oxides into opal film pores from a liquid precursor without depositing a bulk layer on the outer film surface. The method provides a uniform filler distribution in pores and controllable photonic band gap properties of the nanocomposite obtained. The combination of LI and thermodynamically driven synthesis is an effective and inexpensive way of producing 3D photonic crystals based on opal films filled with dielectrics and metals.

1. Introduction

Three-dimensional (3D) thin-film photonic crystals (PCs) are needed to develop all-optical planar microdevices (integrated circuits, waveguides, superprisms, etc.). Synthetic opal films are regarded as promising and cheap templates for 3D PCs based on direct and inverted opal-filler composites [1]. At present, the most common filling techniques for opal films are thermal chemical vapour deposition, atomic layer deposition and electrodeposition [1]. Some of these methods require the use of costly equipment and reagents, and all of them are special-purpose techniques. In contrast, a fairly inexpensive and versatile technology of pore filling in various templates is the infiltration from aqueous solutions.

Solution techniques, however, have not found a wide application for opal films, because they involve several immersion runs which produce a bulk layer on the sample surface preventing further penetration of the precursor into the pores [2]. Here we describe a method of opal film infiltration with aqueous solutions of salts under capillary forces in a lateral direction. This practically excludes the presence of the solution on the outer film surface, thus preventing the formation of a bulk layer on it.

We have used this method to fill opal films with the iron oxides α-Fe_2O_3 (hematite) and Fe_3O_4 (magnetite). Recent interest in iron oxides has been due to their unique physical properties and wide potential applications. Its magnetic properties find application in optical media such as magnetophotonic crystals [3] which can control light beams when an external magnetic field is applied.

2. Infiltration of α-Fe_2O_3 and synthesis of Fe_3O_4

The experimental opal films were grown from a-SiO_2 spheres on glass substrate by using the vertical deposition method [4]. Spheres of 545 nm in diameter were fabricated by Stöber technique [5]. The typical dimensions of a sample were: the substrate $15\times8\times1.5$ mm^3, the film thickness 10 μm. The film surface was parallel to the (111) planes. The precursor we used in this study for filling opal films by lateral infiltration (LI) under capillary forces was an aqueous solution of $Fe(NO_3)_3{\cdot}9H_2O$ (Aldrich). An opal film was immersed into the solution to 1 mm depth (Fig. 1a). The sample was fixed vertically so that gravity prevented spreading of the solution on the film surface. The processes occurring in the pores and on the film surface are the following : (1) LI due to the capillary force; (2) hydraulic resistance; (3) the solvent evaporation and capillary condensation, whose rates depend on the setup humidity; (4) the liquid surface bending at the contact with the film (meniscus).

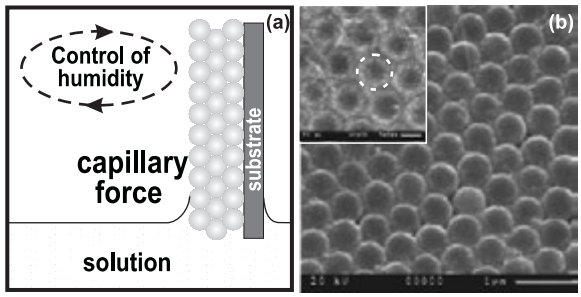

Fig. 1. (a) Scheme of the LI technique, (b) SEM image of the opal-Fe_2O_3 (24 LI runs). The inset shows the enlarged top-down view. The white dash circle marks a silica sphere.

The meniscus height at the contact with a vertical plane in a fully wetting liquid is equal to the capillary length ($\sim$2 mm for water). Therefore, the lower film portion in contact with the salt solution was about 3 mm long (including the immersed 1 mm length). The capillary water pressure in the pores of the opal sample was found from Laplace's equation to be 14 bars (293 K). The calculation from Poiseuille's equation of hydraulic resistance in the pores of this size, showed that the pressure drop of 14 bars would be reached at the sample length of $\sim$1 m at the filling rate of 10^{-5} m/s (the rate value was found experimentally). For the liquid to remain inside the opal pores, the condensation and evaporation rates must be the same. If the evaporation rate is higher, there will be an uncontrollable drying of the upper film portion. If the condensation rate becomes greater because the ambient vapour pressure is higher than the saturated vapour pressure in the pores, liquid droplets will appear on the film due to the condensation in the intersphere spaces. Using Kelvin's formula, we calculated the saturated vapor pressure at the narrowest sites of contact between the tetrahedral and octahedral pores with the minimum diameter of $\sim$70 nm and found it to be 3% lower than that over the plane surface. For this reason, the relative humidity in the setup was maintained at a value of $97 \pm 1\%$.

We carried out 24 LI runs, each followed by thermal decomposition of iron nitrate, which completely transforms to hematite. There was no salt solution on the film; therefore, the solid decomposition products were contained only in the template pores. The scanning electron microscopy (SEM) measurements of opal$-\alpha$-Fe_2O_3 composite proved that the pores are filled uniformly (Fig. 1b). Some bulk material was found only on the film portion of $\sim$3 mm long, which had been in contact with the solution. The rest of the film ($\sim$12 mm length) did not contain bulk α-Fe_2O_3, as evidenced by the SEM data.

The composite X-ray diffraction (XRD) pattern was typical for those of α-Fe_2O_3.

Magnetite was synthesized in opal pores by hematite reduction with hydrogen under thermodynamic equilibrium conditions, using argon as a carrier gas. To find equilibrium composition as a function of the temperature and the hydrogen partial pressure, we use the VCS (Villars–Cruise–Smith) algorithm [6]. The calculations show that α-Fe_2O_3 completely transforms to Fe_3O_4 at the hydrogen partial pressure of 0.2 bar, the partial pressure of water vapour of 10^{-4} bar and the total pressure of 1 bar at temperatures below 650 K; the amount of impurities was below 0.01 %mol. These calculations were supported by experimental data. The sample reduced at 630 K (15 h) was found by X-ray analysis to contain only one crystalline substance — magnetite, whose lattice parameter was 0.839(1) nm, in agreement with the reported value of 0.8396 nm (JCPDS 19-629). These findings indicate that it was thermodynamically driven synthesis of Fe_3O_4 that occurred in the opal template pores.

3. Photonic band gap properties

An essential feature of opal-iron oxide composites is the manifestation of properties typical of PCs [1]. We could control and estimate the hematite filling degree from the dip position in the transmission spectra and the corresponding maximum in the reflection spectra caused by Bragg diffraction from the (111) planes of the f.c.c. lattice of the composite (Fig. 2). The reflection and transmission spectra were measured at near normal incidence from the sample area of 3 mm^2 by a Bruker IFS 113v spectrometer.

The position of the extremum in the diffraction line λ_{111} can be described by Bragg's formula $\lambda_{111} = 2d_{(111)}\sqrt{0.74\varepsilon_s + 0.26\varepsilon_p}$, where $d_{(111)}$ — the interplane distance, x — the filling degree of pores, $\varepsilon_p = (x\,\varepsilon_f + 1 - x)$, ε_s, ε_f — the dielectric permittivity of pores, spheres and the filling material, correspondingly. As the number of LI runs increased, the amount of filling material in the pores became larger, making the Bragg line shift to the long wavelength region (Fig. 2). Simultaneously, we observed a reduction in the dielectric contrast of the opal-hematite composite, which was assumed to be $q = |1 - \varepsilon_s/\varepsilon_p|$. The fact that the dielectric contrast tends to be zero is the reason for the Bragg line to become narrower and for the transmittance to be larger at the Bragg wavelength. After 7–10 LI runs, there were no Bragg lines in the spectra (Fig. 2). However, further increase in the filling degree gave rise to a Bragg line again. The dielectric permittivity of pores became greater than that of SiO_2 spheres. Each subsequent LI run increased the dip depth and the Bragg line width because of the enhanced dielectric contrast of the composite (Fig. 2, curves 4 and 5). The observable poorer transparency of the opal-hematite composite as compared with the bare opal film out of the Bragg line associated with Rayleigh light scattering.

The photonic band gap properties of the opal-magnetite composite were determined from the reflection spectra because of a magnetite absorption in this spectral region [7] (Fig. 2, inset). The filling degrees of opal-hematite after 24 LI runs and of opal-magnetite, calculated from the reflection spectra using the Bragg formula, appeared to be similar and equal to ~52% of the pore volume.

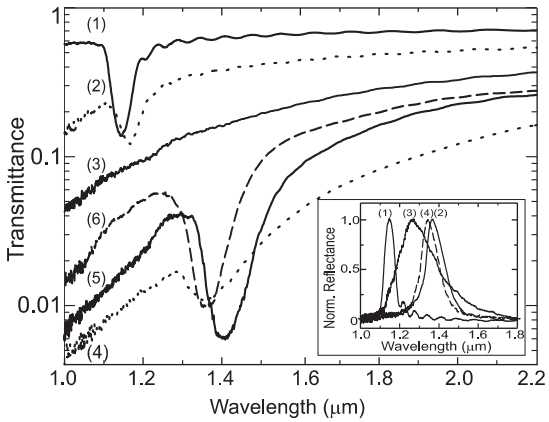

Fig. 2. Transmission spectra. (1–5) opal−α-Fe_2O_3 at selected LI runs: (1) 0, (2) 4, (3) 7, (4) 18, (5) 24. (6) opal−α-Fe_2O_3 after oxidation of Fe_3O_4. Inset: reflection spectra: (1) bare opal, (2) opal−α-Fe_2O_3 (24 LI runs), (3) opal-Fe_3O_4, (4) opal−α-Fe_2O_3 after oxidation of Fe_3O_4.

After an opal-magnetite sample was annealed in oxygen flow at 1 bar, we again detected α-Fe_2O_3 (hematite) in the opal pores by XRD analysis. The Bragg lines in both the transmission and reflection spectra measured following the oxidation are seen to be shifted toward shorter wavelengths as compared with those for the opal−α-Fe_2O_3 composite after 24 LI runs. It is quite likely that the long-term annealing in oxygen (750 K, 20 h) somewhat decreased the interplane distance $d_{(111)}$ due to the sintering of silica spheres. The widths of the Bragg lines in the opal-hematite spectra measured after the annealing in oxygen and of the opal-hematite composite after 24 LI runs are practically the same (Fig. 2, curves 5 and 6). Evidently, the thermodynamically driven processes of oxidation and reduction of iron oxides do not produce structural defects in the composite, which might be responsible for the Bragg line broadening. The reflection line broadening for opal-magnetite by over a factor of 2, as compared with the diffraction line for opal-hematite, is likely to be due to a large value of the imaginary part of dielectric permittivity of Fe_3O_4 [7].

It should be emphasized that we have first performed a reversible chemical transformation of fillers in opal pores: α-$Fe_2O_3 \rightarrow Fe_3O_4 \rightarrow \alpha$-$Fe_2O_3$. A combination of lateral infiltration and thermodynamically driven synthesis could allow to fabricate 3D PCs based on opal films filled with A^3B^5, A^2B^6, and A^4B^6 semiconductors, oxides, and metals.

Acknowledgements

This work has been supported in part by Russian Academy of Sciences, the EC-funded project PHOREMOST (FP6/2003/IST/2-511616), the RFBR project (08-02-00450), and the NWO-RFBR Cooperation project (047.011.2005.026)

References

[1] C. López, *Adv. Mater.* **15**, 1679 (2003).
[2] T. Kodama *et al*, *Phys. Stat. Sol. (b)* **241**, 1597 (2004).
[3] M. Inoue *et al*, *J. Mater. Chem.* **16**, 678 (2006).
[4] P. Jiang *et al*, *Chem. Mater.* **11**, 2132 (1999).
[5] W. Stöber *et al*, *J. Colloid Interface Sci.* **26**, 62 (1968).
[6] Smith W. R. *et al*, *Chemical Reaction Equilibrium Analisys: Theory and Algorithm*, Weinheim:Willey-VCH, 1982.
[7] B. Karlsson *et al*, *Physica Scripta* **25**, 826 (1982).

16th Int. Symp. "Nanostructures: Physics and Technology"
Vladivostok, Russia, July 14–18, 2008

Laser action and spectral and spatial characteristics of radiation of 1D and 2D photonic crystal structure with active layers

O. N. Kozina[1] and L. A. Melnikov[1,2]

[1] Institute of Radio Engineering and Electronics (Saratov Branch), Russian Academy of Sciences, 410019 Saratov, Russia
[2] Saratov State University, 410026 Saratov, Russia

Abstract. We present the result of theoretical investigations of gain and attenuation properties, spectral and spatial characteristics of radiation and laser action in 1D and 2D PC with air-glass-doped layers. The model of active medium corresponds to Nd^{3+} doped glass. For these calculations we used the transfer matrix formalism. The laser power and laser frequency are presented on the dependence from gain, angle of propagation , gain bandwidth, refraction index and others parameters for the both case: axial and off-axial propagation of radiation. The lazing optimum condition is determined. The spatial distributing of electromagnetic field, the angular spectrum of radiation in such structures will present too.

As well known, a photonic crystal (PC) is the dielectric material with a periodic modulation of the dielectric constant that strongly perturbs optical modes and causing photonic band gaps (PBG) to occur [1–2]. The presence of gain or loss in PC dielectrics can change its characteristic [2–6]. Namly, leads to the amplification or losses depending on the sign of the imaginary part of the refraction index [5,6]. It was shown numerically for nonlinear 1D PBG structure that more than five times increase of transmission in one direction relatively to the opposite direction should be possible using realistic materials and intensities [7]. The enhanced gain in a photonic band edge medium has potential application in vertical-cavity surface-emitting lasers (VCSEL's), for example [4]. Exploration of nonlinear properties of photonic band-gap (PBG) materials may open new applications of PC for all-optical signal processing and switching [9]. In our investigation the model of active medium corresponds to Nd^{3+} doped glass. Early we presented the results of calculations of the transmission/reflection characteristics of the finite length 1D PC with air-glass-doped layers [8]. For these calculations we used the transfer matrix formalism [5,6,8]. We have shown the noticeable enhancement of the transmission at wavelength near 1.06 μ occurs, when unsaturated gain is about 10 cm^{-1}. The results of calculation accounting nonlinear deformation of the field distribution

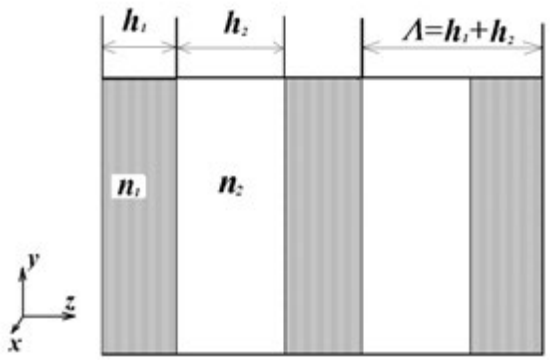

Fig. 1. The schematic view of 1D air-dielectric PC. The first and ending layers are dielectric.

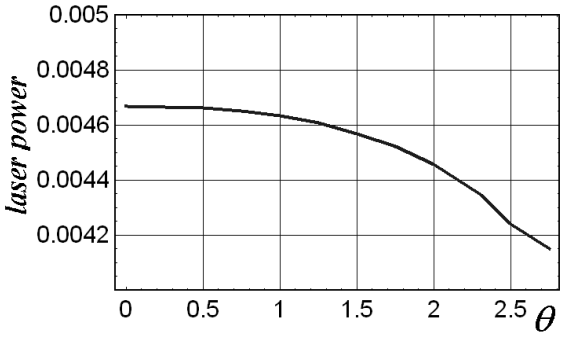

Fig. 2. The dependence of the laser power from angle of propagation. The angle of propagation varies from $\theta = 0$ to $\theta = 3$.

along the structure due to gain and refraction index saturation were presented too. We have shown, by iteration method, that at real gain parameters the field deformation is negligible. Using this approximation the results of calculations of laser power and laser frequency were presented on the dependence from gain, angle of propagation, gain bandwidth, refraction index and others parameters for the both case axial and off-axial propagation of radiation. The lazing optimum condition is determined. The spatial distributing of electromagnetic field, the angular spectrum of radiation in such structures will present too. The results for 2D PC will be present. Firstly, we considered 1D PC, shown in Fig. 1, which consists of two layers (air and dielectric), repeated periodically along the z-axes. The model of active medium corresponds to Nd^{3+} doped glass [8] (refractive index n_1 on Fig. 1). The refractive index for an active medium is complex. We use relation for refractive index corresponded to high-index layers as follows:

$$n = n' - i\kappa = n_0 + \frac{iG\Delta(1 - i\Delta)}{1 + \Delta^2 + \|E \times E\|^2}.$$

Here n_0 is linear refractive index and second term described its nonlinear property. $G = \sigma N$ is value of gain, is the stimulated transition cross-section, N is active atoms density, $\Delta = (\omega - \nu)/\Gamma$ is detuning, is the linewidth, last term in denominator describe the saturation. For these calculations we used the transfer matrix formalism [5,7]. The transformation of

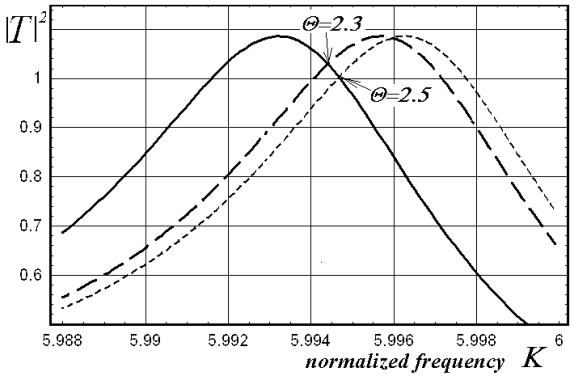

Fig. 3. The transmission spectrum for $\theta = 0$ (the solid line) and the transmission spectrums for $\theta = 2.3$ (the heavy dashed line) and for $\theta = 2.5$ (the thin dashed line) vs wave vector.

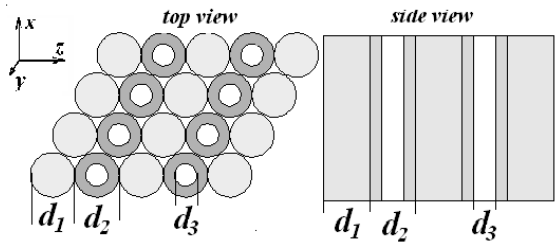

Fig. 4. The schematic view of 2D air-dielectric PC. The first and ending layers are dielectric (Nd^{3+} doped glass).

electric and magnetic field vectors per period describes by the transfer matrix M. The matrix M is a product of partial transfer matrices for each layers M_j, contain the direction and polarization dependence and parameters of the structure, see [8]: $\hat{M} = \Pi M_j$. The transmission (and reflection, see [8,10]) coefficients are defined by elements of transfer matrix M and as follows:

$$t = M_{11} + M_{12}\cos\theta + \frac{M_{11}+M_{12}\cos\theta - M_{21}/\cos\theta - M_{22}}{M_{12}\cos\theta - M_{11} + M_{21}/\cos\theta - M_{22}}(M_{11} - M_{12}\cos\theta),$$

We have shown [6] that the reflection and transmission coefficients on the band edges oscillate. Maximum peak is observed near the band gap edge. The noticeable enhancement of the transmission at wavelength near 1.06 μ occurs, when unsaturated gain is about 10^4 cm^{-1} [6,8]. The parameters for the case considered are as follows: $G = 0.0001$, $\Delta\nu = 200$ GHz, $\lambda = 1.06$ μ, $\Delta = 0.001$, $\Gamma = 2\pi 200$ GHz, ω_0 is the frequency of transition, in our case corresponds main peak frequency $K_{\max} = 5.993$, $K = 2\pi\lambda^{-1}$ is the wave vector [8]. The oscillation condition is satisfied when the denominator (Z in the figure) of expression for reflection (or transmission) coefficient tends to zero [6]. This requirement is satisfied if the real and imaginary parts of Z simultaneously vanish. In previous paper [6,8], we have shown the $\mathrm{Re}(Z)$ and $\mathrm{Im}(Z)$ simultaneously vanish at the frequencies at which we observe when the frequency corresponds to the maximum transmission peak. Therefore, at these frequencies, the gain can reach the level corresponding to the oscillation threshold [6]. Using this method we calculated the dependence of the laser power from angle of propagation (from $\theta = 0$ to $\theta = 3$) (Fig. 3). It is

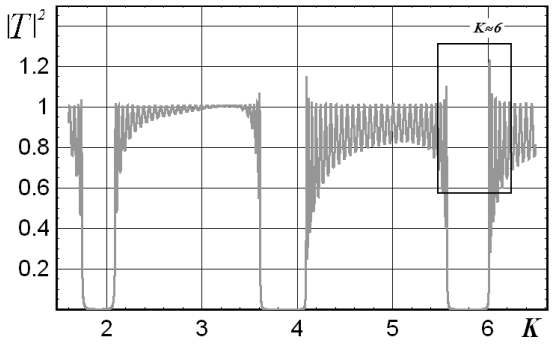

Fig. 5. The transmission spectrums of the 2D air-Nd3+ doped glass PC.

easy to see, that the lazing has reached its maximum for $\theta = 0$. Then laser power decreases when the angle of propagation is increasing. This happened because the main peak shift from the frequency of transition (corresponds $K = 5.993$) to higher frequencies, Fig. 4. So obviously, for angles more than $\theta = 2.3$ the main peak of transmission coefficient goes off the line of amplification. This means that we can consider this structure like restrict in $x - y$ plane, as the amplification will observed only within the small range, namely in limits of the little spatial angle from $\theta = 0$ to $\theta = 2.3$. Now let us present the investigation of 2D PC structures, shown on Fig. 5. The dark areas correspond for Nd^{3+} doped glass roads with refraction index $n_1 = 1.58 - i\,0.0001$, more light areas correspond glass, refraction index $n_2 = 1.5$ with air holes (white areas), $n_3 = 1$. If we assumed that this 2D PC structures is close-packed roads, we can observe it like 1D band structure (side view). Then we can use the same theoretical method for calculation of transmission coefficient for 2D PC structures.

In this approximation we can investigate transmission vs normalized frequency for such PC. We observed the 2D PC with parameters as follow: $d_1 = 0.6$ μ, $d_2 = 0.6$ μ, $d_3 = 0.3$ μ. The transmission coefficients for 2D PC have shown on Fig. 6. The maximum peak of the transmission coefficient is observed for $K \approx 6$. This fact, as before, means amplification. This method allows for analysis of the possible amplification of the 2D PC at various values of its parameters and makes it possible to estimate the threshold oscillation condition. We should note that the making of described 2D PC is possible. So the generation conditions for the laser with 1D and 2D PC structures are determinate. The parameters of this lasers can choose by aforementioned method.

References

[1] P. S. Russel, T. A. Birks, F. D. Lloud-Lukasü, *IPlenum Press, New York,*, 250 (1995).
[2] E. Yablonovitch, *J. Mod. Opt.* **41**, 173 (1994).
[3] K. Sakoda *et al*, *Opt. Express* **4**, 167 (1999).
[4] K. P. Dowling, M. Skarola, M. J. Bloemer, *J. Appl. Phys.* **75**, 1896 (1994).
[5] L. A. Mel'nikov, O. N. Kozina, *Opt. Spectrosc.* **94**, 411 (2003).
[6] L. A. Mel'nikov, O. N. Kozina,, *Laser Physics* **14**, 1 (2004).
[7] J. Fogel *et al*, *Pure Appl. Opt* **7**, 393 (1998).
[8] O. Kozina, L. Melnikov. *Journal of Non-Crystalline Solids* **353**, 968 (2007).
[9] V. Sukhorukov, Y. Kivshar. *Phys. Rev. Let* **87**, 083901 (2001).

16th Int. Symp. "Nanostructures: Physics and Technology"
Vladivostok, Russia, July 14–18, 2008

Evanescent waves contribution into efficiency of light-emitting diodes with grating patterned top surface

M. Barabanenkov[1], I. Schelokov[1], Yu. Kholopova[1], A. Kovalchuk[1], N. Antonova[2], E. Polushkin[1] and S. Shapoval[1]

[1] Institute of Microelectronics Technology RAS, 142432 Chernogolovka, Moscow region, Russia
[2] R&D Corporation "Istok", Fryazino, Moscow region, Russia

Abstract. In this report we apply a consequence of the recently derived optical theorem for near field electromagnetic wave scattering by, in particular, one dimensional diffraction grating to the problem of external efficiency of light-emitting diodes.

Introduction

An importance of light-emitting diodes (LEDs) as an instrumental ingredient in solid-state lighting is of common knowledge. The development of high efficiency and brightness LEDs is limited mainly due to the difficulty for light to escape from high refractive index semiconductors. The escape cone θ_c for internal light, for example, in GaN film of refractive index $n_{GaN} = 2.5$ is only $\theta_c = \sin^{-1}(n_{air}/n_{GaN}) = 23°$, as imposed by Snell's law. Among a number of schemes considered for increasing the external quantum efficiency (based on the old idea [1] of coupling the light out of the semiconductor by means of a high refractive index hemispherical lens), surface roughening [2] or surface texturing with a rear reflector [3] are considered as one of the simpler methods. For example, Windisch *et al* [3] achieved an external quantum efficiency of 40% from unencapsulated top-emitting oxide-confined GaAs/AlGaAs nonresonant cavity LED. The LED structure surface was textured using a nanolayer of randomly positioned polystyrene spheres as a mask for dry etching. In this method there are at least three parameters which have to be optimized: spheres size and distribution on the surface, etching depth). The roughened surface morphology can be irregular and uncontrolled [4] along with a significant problem to eliminate the strong parasitic absorption at the electrodes [2]. Aiming to overcome the latter problem it was suggested [5] formation of active emitters in a two dimensional (2D) inverse photonic crystal (PC). Besides, 2D PCs enhance the light output from LEDs by extracting lateral guided modes of light in the vertical direction due to the so called photonic band gap phenomenon. From the other hand, getting LED's p-contact into shape of laminar diffraction grating promises additional light output. Stripe-like grooves of grating can spatially homogeneous spread of applied current driving across the whole structure being the grating covered structure surface totally. The grating itself can be resonantly transparent for the generated light [6]. In Ref. [6] the optics of LED with metal grating patterned p-contact has been considered in the approximation that a radiance of electroluminescent area of the structure consists only of propagating (homogeneous) electromagnetic (EM) waves. In this report we present more rigorous study of the coupling efficiency of LED radiance to the air via laminar diffraction grating taking into consideration exponentially decaying (evanescent) emitted EM waves.

1. p-contact pad shaped as grating

We start with our previous grating-LED calculations of the current density in the p-n junction area as a function of the voltage across the LED. We demonstrated [6] that the higher is the voltage the closer is the potential distribution to the linelike light sources, i.e. to the top contact grating shape. Therefore, we currently suppose the planelike source $j(x)$ (see the inset in Fig. 1) has the form of a periodical array of linelike sources of EM waves of pure evanescent nature (we omit a homogeneous part of EM waves).

Let this evanescent wave be scattered by a laminar diffraction grating, whose rulings are parallel to the y axis and placed periodically along the x axis with a period Λ. The grating occupies a region $0 < z < h < L$ (see Fig. 1). The wave, with electric field being parallel to the rulings (TE-polarization), is incident upon a plane $z = L$ and has the form of series in the grating spectral orders $\nu = 0, \pm1, \pm2, \ldots$ (the phases of the spectral orders are evaluated from the reference plane $z = L$)

$$\tilde{E}^0_y(x, z) = \sum_\nu \exp\left[i\frac{2\pi\nu}{\Lambda}x - i\gamma(\nu)(z - L)\right]\tilde{E}^0_y(\nu). \quad (1)$$

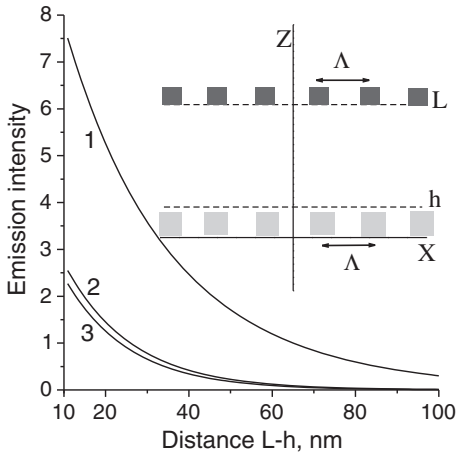

Fig. 1. Solid curves are the results of numerical calculations of the dimensionless emission intensity Ik^2/j_0^2 [Eq. (9)] versus distance L–h between grating rulings (gray filled boxes in the inset) and linelike sources (black filled boxes). The values of the parameters are taken from our previous work [6]: $\lambda_0 = 0.45\ \mu$m (in the air), $\lambda = \lambda_0/n_{GaN} = 0.18\ \mu$m, $\Lambda = 0.4\ \mu$m (curve 1), $0.65\ \mu$m (curve 2), and $0.8\ \mu$m (curve 3).

Here

$$\gamma_\nu = \sqrt{1 - \left(\frac{2\pi\nu}{k\Lambda}\right)^2}, \tag{2}$$

k is the wave number of EM wave in a semiconductor with refractive index n_{GaN}. Denote the minimum (lowest) evanescent wave spectral order ν, where $2\pi \mid \nu \mid /\Lambda > k$, by n_1, and $n_2 = n_1 + 1, n_3 = n_1 + 2, \ldots$, all other higher spectral orders of evanescent waves. Take further $E_k = \tilde{E}_y^0(n_k) + \tilde{E}_y^0(-n_k)$, where $k = 1, 2, 3, \ldots$, to be an amplitude of a symmetrical function with respect to the variable x of an evanescent wave of the spectral order n_k and $\gamma_k = \mid \gamma(n_k) \mid$. Using these denotations we reduce natural expression for energy emission from an evanescent wave $I(L) = \mid \tilde{E}_y^0(x = 0, z = 0) \mid^2$ to the form [7]

$$\begin{aligned} I(L) &= \sum_k \exp(-2\gamma_k L) \mid E_k \mid^2 \\ &+ \sum_{k'>k} \exp\left[-(\gamma_{k'} + \gamma_k) L\right] \Gamma(k', k) \\ &= \exp(-2\gamma_1 L) \mid E_1 \mid^2 + \exp\left[-(\gamma_2 + \gamma_1) L\right] \Gamma(2, 1) \\ &+ \exp(-2\gamma_2 L) \mid E_2 \mid^2 + \ldots \end{aligned} \tag{3}$$

Here a coefficient of interference $\Gamma(k', k)$ between evanescent spectral orders $n_{k'}$ and n_k is defined by $\Gamma(k', k) = E_{k'} E_k^* + E_{k'}^* E_k = 2 \mid E_{k'} \mid\mid E_k \mid \cos(\varphi_{k'} - \varphi_k)$, with $\varphi_{k'}$ and φ_k being phases of $E_{k'}$ and E_k, respectively. The second Eq. (3) is written in approximation of two evanescent spectral orders n_1 and n_2 in the series Eq. (1).

2. Linelike periodical source and energy emission

Incident electric field represented by Eq. (1) may be created by the linelike sources $j(x)$ periodically varying along the x axis

$$j(x) = \sum_\nu \exp\left(i\frac{2\pi\nu}{\Lambda}x\right) j_\nu. \tag{4}$$

Bearing in mind that the incident electric field $\tilde{E}_y^0(x, z)$ in Eq. (1) is expressed through the current density $j_y(x, z)$ with the aid of the scalar Green function in the background, we can obtain the following relation

$$\tilde{E}_y^0(\nu) = \frac{1}{2i\gamma(\nu)} j_\nu. \tag{5}$$

Let periodic linelike source has the form $j(x) = j_0\Lambda \sum_\nu \delta(x - x_\nu)$ where $x_\nu = \nu\Lambda - (\varphi_0/2\pi)\Lambda$ are the points of the x axis intersection by linelike sources and j_0 is an electric current density. The quantity φ_0 in the expression for x_ν defines possible detuning between the positions of line-like sources in the plane $z = L$ and positions of the line-like grating rulings. This planelike electric current distribution is situated at a distance L–h below the LED outer surface and functions as a source of exponentially decaying in the z direction EM waves. Evanescent waves scattering by a grating results in appearing of an EM energy flux in the direction of incident evanescent waves decay. This energy flux is the crux of the energy emission effect theoretically predicted in [7].

Substituting expression for $j(x)$ into Eq. (4) gives j_ν, which after the insertion into Eq. (5) leads to

$$\tilde{E}_y^0(\nu) = \frac{1}{2i\gamma(\nu)} j_0 \exp(i\nu\varphi_0). \tag{6}$$

The evaluation of the quantities $\mid E_{1,2} \mid^2$ and $\Gamma(2, 1)$ enables us to specify the second Eq. (3).

Finally, the energy emission from an evanescent wave becomes periodically varying with a detuning parameter φ_0 according to expression [7]

$$I = j_0^2 \left[d_1 \cos n_1\varphi_0 + d_2 \cos n_2\varphi_0\right]^2 + \ldots \tag{7}$$

where

$$d_\nu = \gamma_\nu^{-1} \exp(-kL\gamma_\nu). \tag{8}$$

It is seen that at an exact tuning, $\varphi_0 = 0$, when the line-like sources are positioned exactly under the line-like rulings of the grating, the emission intensity has a maximum. This maximum intensity I of the energy emission from near field of the luminescent layer depends upon the distance L–h between the layer and grating position according to expression

$$\frac{Ik^2}{j_0^2} = (d_1 + d_2)^2. \tag{9}$$

Note, we take into account only two lowest evanescent wave spectral orders.

Fig. 1 demonstrates that the emission intensity does not practically depends upon the distance between currents in the electroluminescent area of the LED and grating shaped LED top electrode provided that the grating period becomes grater than the emitted wavelength in air.

3. Conclusion

We have considered theoretically a contribution of evanescent electromagnetic waves in external efficiency of LED with upper p-contact as a laminar diffraction grating. In the report some experimental results will be presented. We would like to note here that Eq. (8) predicts also a zero emission intensity at some special detuning between the linelike sources and rulings of the grating. A situation of zero emission intensity may be useful for optical coupling of generated photons and strip like waveguide at the top of LED structure.

Acknowledgements

This work has been supported in part by two projects of the Russian Academy of Sciences (RAS) and by the project of the fundamental investigation program of Presidium of RAS.

References

[1] W. N. Carr, G. E.Pittmann, *Appl. Phys. Lett.* **3**, 173 (1963).
[2] I. Schnitzer, E. Yablonovitch, *Appl. Phys. Lett.* **63**, 2174 (1993).
[3] R. Windisch *et al*, *IEEE Trans. Electron Devices* **47**, 1492 (2000).
[4] C. Huh *et al*, *J. Appl. Phys.* **93**, 9383 (2003).
[5] J. Shakya *et al*, *Appl. Phys. Lett.* **85**, 142 (2004).
[6] S. Shapoval *et al*, *Proc. WOCSDICE*, Padova, Italy 2007, p. 29.
[7] Yu. Gulyaev *et al*, *Phys. Rev. E* **72**, 026602 (2005).

16th Int. Symp. "Nanostructures: Physics and Technology"
Vladivostok, Russia, July 14–18, 2008

Slow light in GaN

T. V. Shubina[1], M. M. Glazov[1], A. A. Toropov[1], N. A. Gippius[2,5], J. P. Bergman[3], B. Monemar[3], A. Usui[4], A. Vasson[5], J. Leymarie[5], S. V. Ivanov[1] and P. S. Kop'ev[1]

[1] Ioffe Physico-Technical Institute, St Petersburg, Russia
[2] General Physics Institute RAS, Moscow 119991, Russia
[3] Department of Physics, Chemistry and Biology, Linköping University, Sweden
[4] Furukawa Co., Ltd. Tsukuba, Ibaraki 305-0856, Japan
[5] LASMEA-UMR 6602 CNRS-UBP, 63177 Cedex, France

Abstract. Slow light is a subject of extensive studies nowadays due to its potential application in all-optical systems of quantum communication and information processing. We report the first observation of the slow light in GaN by time-of-flight spectroscopy and demonstrate a resonant nature of this phenomenon. It has been shown that both light diffusion and ballistic propagation can contribute to the light retardation. The observed light delay amounts 470 ps for 1-mm propagation length, corresponding to a velocity of light as slow as 2100 km/s.

The realization of all-optical schemes of quantum communication and information processing implies frequently a deterministic retardation of photon pulses [1]. It includes quantum logics and non-linear devices, exploiting the effect of electromagnetically induced transparency [2], random-access memory, data synchronization, pattern correlation, and network buffering. For all these purposes, it is necessary to have the delay of the light (T) by several times exceeding the pulse duration T_0. However the delayed output pulses suffer from substantial distortion (broadening) or have short delay times [3]. The maximal value T/T_0 of $\approx$4 has been reported by Kasari *et al* for an atomic medium [4]. Thus a search of new systems with the efficient light retardation is in progress.

The phenomenon of the light delay can also be very important for a set of optoelectronic devices, including vertical cavity surface emitting lasers, polariton lasers with a semiconductor microcavity, solar cells, etc., whose total thicknesses can be a few tens of micrometers. Moreover, it may by significant for laser heterostructures, where the light traveling through a planar waveguide passes a distance of 1–2 mm. Threshold and frequency characteristics in these devices depend on the mechanism of the light transfer (Fig. 1).

Generally, the propagation of an electromagnetic wave may be either ballistic, with the conservation of wave vector, or diffusive, when the vector can change during multiple scattering processes in a medium [5]. The energy transport with ballistic light propagation through a dispersive medium with a resonant absorption line is retarded in the vicinity of the resonance [6]. It has been noted that the light velocity can be zero and even negative here [7]. This consideration is closely related to the exciton-polariton concept [8]. Reasonable agreement between the pulse propagation time and the time calculated from the group velocity of polaritons has been obtained in GaP:N around an isolated bound exciton (BX) line [9], in CuCl near a free exciton resonance [10], and in ZnO in the vicinity of a BX [11]. These experiments seem to demonstrate the dominance of the ballistic light propagation in the semiconductors.

The light diffusion can also provide a strong slow-down of the light transfer time [12–17]. The discussion of the fundamental issue of the light transport velocity in the strongly scattering media has revealed that it can be significantly smaller than the phase velocity [12]. The multiple scattering process is associated with intriguing fundamental phenomena, such as weak localization and coherent backscattering of light [13]. Experimentally, photon diffusion has been studied in various disordered media, including dielectric [14] and polymer [15] micro-spheres, liquid crystals [16] and ZnS nanocrystals [17]. It is somewhat surprising that practically no experiments of this kind have been done in conventional bulk semiconductors, where the light scattering by imperfections also might take place.

In this work, we demonstrate that these two mechanisms of the light delay — ballistic and diffusive, can coexist in bulk GaN crystals in the vicinity of excitonic resonances [18,19]. The delay of 470 ps for the 1-mm path results in a velocity of light as slow as 2100 km/s. This delay value markedly exceeds the pulse duration, making the observed effect interesting for device applications. Besides, the combined consideration of the light delay spectra together with reflection and transmission ones permits us to refine some GaN excitonic parameters.

The studies have been performed by time-of-flight spectroscopy using high-quality free-standing GaN layers grown by HVPE with the width of neutral donor bound exciton (BX) lines $\sim$0.5 meV, pronounced A and B exciton lines, and the carrier concentration as low as 8×10^{15} cm^{-3}. The sample thickness L varies from 0.3 to 2 mm. A Hamamatsu streak camera with a $\sim$20 ps temporal resolution was exploited to

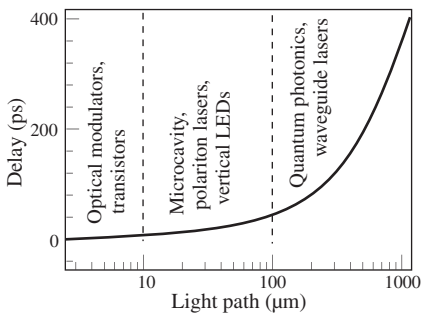

Fig. 1. An illustrative dependence of delay time on a length of the path which light propagates in a semiconductor in the vicinity of strong exciton resonances, calculated as described below using GaN parameters. Dashed lines indicate roughly the length limits in various devices.

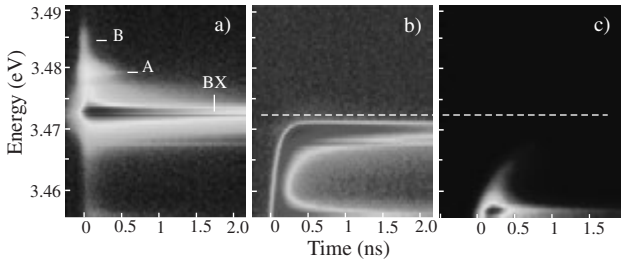

Fig. 2. (a) Backward and (b,c) forward TR PL images recorded in (a,b) 1-mm and (c) 2-mm-long samples with excitation by a 4.66 eV laser line at 2 K (logarithm scale). A, B and BX denote respective excitons; a dashed line marks the light transfer cut-off.

record the time-resolved (TR) images. A tunable Ti:sapphire femtosecond pulsed laser was used as a light source. Two geometries of measurement have been exploited: i) the conventional backward one; ii) forward transmission spectroscopy, when the light was detected from the opposite side of a sample with respect to excitation.

In the latter geometry with the 4.66 eV laser line excitation, the transmitted photoluminescence (PL) quenches completely above a certain boundary, which is in close vicinity of the BX doublet. The sharp cut-off is at 3.470 eV in the 1-mm sample, being smoother and red-shifted in the 2-mm sample. Below the cut-off energy the transmitted PL resembles that registered in the conventional geometry with one remarkable exception. It appears with a delay in time, which increases gradually towards the cut-off, attaining 470 ps in the 1-mm sample (Fig. 2).

To study the propagation of the laser pulse solely, without excited PL, the excitation pulse energy was tuned to 3.464 eV. The similar bending of the pulse towards BX is observed. Besides, an additional curved streak ("reflex") was recorded, which appears at times corresponding to the triple coherent passage of a wave packet with reflection at the sample boundaries (Fig. 3a). The appearance of the reflex indicates that the pulse propagation in our samples is predominantly ballistic, because a photon should lose the direction memory after a few acts of scattering. However the far-field angular dependence, measured using a Xe lamp, revealed a superposition of two components in the transmitted signal — relatively narrow and broad ones (Fig. 3b). The intensity ratio between these two components depends on the photon energy. The ballistic part dominates in the region of relative transparency, while the diffusive one prevails in the vicinity of the BX resonances.

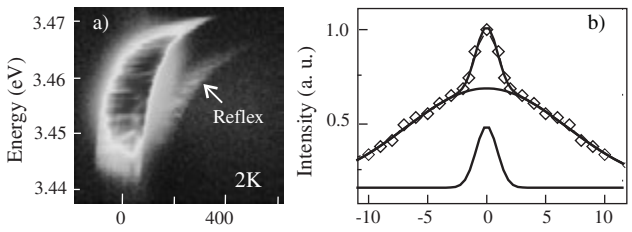

Fig. 3. (a) The TR image of the 3.486 eV laser pulse recorded after passing through the 1-mm sample. The interference reflex is marked by an arrow. (b) Normalized angular diagrams of the transmitted light intensity measured in the sample at 3.4671 eV shown together with its deconvolution into ballistic (narrow) and diffusive (broad) components.

The coexistence of two regimes of light propagation without significant broadening of the pulse implies that their delay times do not differ strongly. However, it is known that the ballistic propagation time $T_B(\omega)$ depends linearly on the sample thickness $T_B(\omega) = L/v_g(\omega)$, where $v_g(\omega)$ is the ballistic group velocity, while the conventional diffusion delay time would increase quadratically with the sample thickness. To clarify this contradiction we model both processes separately. The group velocity $v_g(\omega) = d\omega/dk$, where the wave vector $k(\omega) = (\omega/c)\sqrt{\varepsilon(\omega)}$. The dielectric constant in the vicinity of exciton resonances neglecting spatial dispersion can be written as

$$\varepsilon(\omega) = \varepsilon_b + \sum_j \int \frac{f_j \omega_{0,j}}{\omega_{0,j} + \xi - i\Gamma_j - \omega} \frac{1}{\sqrt{\pi}\Delta_j} \exp\left(\frac{-\xi^2}{{\Delta_j}^2}\right) d\xi. \quad (1)$$

Here, ε_b is the background dielectric constant, $j = A, B, C$, and BX denotes an exciton resonance. Each resonance is described by a frequency $\omega_{0,j}$, an oscillator strength f_j, and a damping term Γ_j. The inhomogeneous broadening of the exciton line is taken into account by means of convolution with the Gaussian having a width Δ_j.

The modeling has been done assuming $\varepsilon_b = 9.5$ and $\hbar\omega_{0,j}$ equal to 3.4720, 3.4785, 3.4837, and 3.5016 eV for BX, A, B, and C excitons, respectively. (The energies are obtained from the fitting of reflection spectra.) For each of the resonances, $\hbar\Gamma_j$ is taken as 0.012 meV, which is comparable with the homogeneous line width of an exciton-polariton in other semiconductors [20]. The inhomogeneous width $\hbar\Delta_j$ is taken as 0.75 meV, close to the average PL linewidth in our spectra. The oscillator strength for the bound exciton has been estimated in accord with [5], as depending on the donor concentration [18]. With this estimation, the exciton localization radius is assumed to be approximately equal to the Bohr radius [21]. The oscillator strength for the A, B and C excitons is taken as 0.0026, 0.0017, and 0.00037, respectively. These values, differing from the previously reported parameters for GaN [22], are obtained as a result of simultaneous fitting of the reflection, transmission and delay time spectra (Fig. 4). We emphasize that only the developed approach allows such a simultaneous fitting. The conventional method (see, e.g. [22]) neglecting the inhomogeneous broadening gives a reasonable fitting of reflection spectra but strongly overestimates absorption near the exciton resonances (Fig. 4a, dashed line). Similarly, excluding from consideration the BX resonance markedly underestimate the delay in the BX vicinity (Fig. 4c, dashed line).

For the diffusive propagation, we assume that elastic neutral donor scattering dominates the delay [23]. All the photons with the concentration $n(\omega, x, t)$ at frequency ω, coordinate x, and time t are assumed to be initially created in a thin layer near the sample surface: $n(\omega, x, 0) = n(\omega, 0)\delta(x)$. The light reflection at the boundaries is neglected. The respective diffusion equation is

$$\frac{\partial n(\omega, x, t)}{\partial t} = D(\omega)\frac{\partial^2 n(\omega, x, t)}{\partial x^2} - \frac{n(\omega, x, t)}{\tau(\omega)}. \quad (2)$$

Here $D(\omega)$ and $\tau(\omega)$ are a diffusion coefficient and photon lifetime, respectively. The latter is $\tau(\omega) = \tau_0(l_A(\omega)/l_0)$, where l_0 and τ_0 are a photon mean free path and time between two

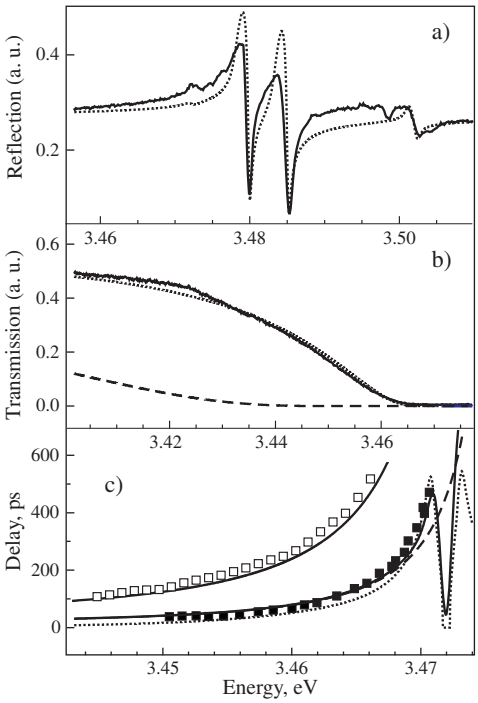

Fig. 4. Reflection (a), transmission (b), and delay (c) spectra measured in the 1-mm sample shown together with their simulations. (a,b) Fittings taking into account the inhomogeneous exciton line broadening are shown by dotted lines, neglecting that — by a dashed line. (c) Delay times corresponding to the main signal and reflex are marked by solid and open squares, respectively. The fitting curves are presented for diffusive (dotted line) and ballistic propagations, taking into account the BX resonance (solid lines) and neglecting that (dashed line).

acts of scattering in the region of relative transparency; $l_A(\omega)$ is the absorption length. The delay time due to diffusive photon motion, $T_D(\omega)$, is found from the condition $\partial n(\omega, L, t)/\partial t = 0$ which corresponds to the intensity maximum. In the general case it is written as

$$T_D(\omega) = \sqrt{\frac{\tau(\omega)^2}{16} + \frac{L^2\tau(\omega)}{4D(\omega)}} - \frac{\tau(\omega)}{4}. \qquad (3)$$

Two limiting cases are important: i) small absorption, $\tau(\omega) \gg L^2/D(\omega)$, where the delay scales as a second power of the sample thickness, $T_D(\omega) = L^2/[2D(\omega)]$; ii) strong absorption, $\tau(\omega) \ll L^2/D(\omega)$, where the delay is proportional to the sample thickness as with the ballistic propagation, $T_D(\omega) = (L/2)\sqrt{\tau(\omega)/D(\omega)}$. The latter result describes the light scattering in the vicinity of strongly absorbing exciton lines.

The diffusion constant $D(\omega) = v_g(\omega)l_{tr}(\omega)/3$, where the photon mean free path $l_{tr}(\omega) = (N\sigma(\omega))^{-1}$ is determined by the light scattering cross-section $\sigma(\omega)$ and the concentration of scattering centers N. For the scattering caused by the individual BX resonances, $\sigma(\omega)$ can be written as [24].

$$\sigma(\omega) = \frac{f^2}{4\pi N^2 c^4} \frac{\omega_{0,BX}^6}{(\omega_{0,BX} - \omega)^2 + \gamma^2}. \qquad (4)$$

Here, γ is an effective broadening parameter. In real samples, the inhomogeneous spatial distribution of the donors provides virtual scattering centers with an effective concentration and localization radius. Figure 4c demonstrates a reasonable fit using Eq. (4) with $N = 8 \times 10^{15}$ cm^{-3}, $\gamma = 0.75$ meV, $\tau_0/l_0 = 2 \times 10^{-9}$ s/cm, and f estimated in similar way as for the ballistic propagation. It clarifies the origin of the sharp cut-off. The calculated dependencies have a strong dip near the BX resonance. It appears because the phase and group velocity of light strongly decrease here, while the absorption is enhanced [7]. That influences both diffusive and ballistic propagation.

In conclusion, we report a strong light transfer retardation in high-quality bulk GaN samples and present a quantitative description of this phenomenon in the frameworks of optical dispersion and resonant elastic scattering models. The registered delay value of 470 ps for the 1-mm-long path exceeds significantly the pulse duration of (∼50) ps, that makes the discovered effect useful for photonics. We believe that the proposed application of three independent measurements — time-resolved transmission, reflection and absorption, gives most reliable data on exciton oscillator strength and line broadening, both homogeneous and inhomogeneous, in GaN. Our findings can be important for a set of smart optoelectronic devices, which rely on a controlled delay of light propagation.

Acknowledgements

We thank Profs. E. L. Ivchenko and M. I. Dyakonov for fruitful discussions. This work is supported in part by the RFBR and ANR grants. A. A. T. and M. M. G. acknowledge Wenner–Gren Foundation and Dynasty Foundation — ICFPM, respectively.

References

[1] M. Bigelow *et al*, *Science* **301**, 200 (2003); Q. Yang *et al*, *Phys. Rev. Lett.* 95, 063902 (2005).
[2] H. Schmidt and A. Imamoğlu, *Opt. Lett.* **21**, 1936 (1996).
[3] R. W. Boyd *et al*, *Phys. Rev. A* **71**, 023801 (2005).
[4] A. Kasapi *et al*, *Phys. Rev. Lett.* **74**, 2447 (1995).
[5] E. L. Ivchenko, *Optical spectroscopy of semiconductor nanostructures* (Alpha Science, Harrow UK) (2005).
[6] R. Loudon, *J. Phys. A* **3**, 233 (1970).
[7] C. G. B. Garrett and D. E. McCumber, **1**, 305 (1970). *Phys. Rev. A* **1**, 305 (1970).
[8] S. I. Pekar, *Zh. Eksp. Teor. Fiz.* **33**, 1022 (1957) [*Sov. Phys. JETP* **6**, 785 (1958)].
[9] S. Chu and S. Wong, *Phys. Rev. Lett.* **48**, 738 (1982).
[10] M. Kuwata *et al*, *Phys. Rev. Lett.* **61**, 1226 (1988).
[11] G. Xiong *et al*, *J. Phys.: Condens. Matter* **17**, 7287 (2005).
[12] Yu. N. Barabanenkov and V. D. Ozrin, *Phys. Rev. Lett.* **69**, 1364 (1992); B. A. Van Tiggelen *et al*, *ibid* **71**, 1284 (1993).
[13] M. P. van Albada and A. Lagendijk, *Phys. Rev. Lett.* **55**, 2692 (1985).
[14] M. P. van Albada *et al*, *Phys. Rev. Lett.* **66**, 3132 (1991).
[15] N. Garcia *et al*, *Phys. Rev. B* **46**, 14475 (1992).
[16] B. A. van Tiggelen *et al*, *Phys. Rev. Lett.* **77**, 639 (1996).
[17] A. Kurita *et al*, *Phys. Rev. Lett.* **83**, 1582 (1999).
[18] T. V. Shubina *et al*, *Phys. Rev. Lett.* **100**, 087402 (2008).
[19] T. V. Shubina *et al*, *PLMCN7 Havana, Cuba*, 18 (2007).
[20] Y. Masumoto*et al*, *Phys. Rev. Lett.* **51**, 923 (1983).
[21] M. Suffczynski and L. Wolniewicz, *Phys. Rev. B* **40**, 6250 (1989).
[22] K. Torii *et al*, *Phys. Rev. B* **60**, 4723 (1999).
[23] T. Steiner *et al*, *Phys. Rev. B* **34**, 1006 (1986).
[24] V. B. Berestetskii, E. M. Lifshitz, and L. P. Pitaevskii, *Relativistic Quantum Theory* (Pergamon Press, Oxford) (1971).

16th Int. Symp. "Nanostructures: Physics and Technology"
Vladivostok, Russia, July 14–18, 2008

Fabrication and characterization of one monolayer InN-based novel nanostructures embedded in GaN matrix

A. Yoshikawa, S. B. Che, Y. Ishitani, X. Q. Wang, H. Saito, T. Fujimoto, N. Hashimoto, A. Hikida, K. Matsui, A. Yuki, M. Otsuki, K. Soudalin and E. S. Hwang

Graduate School of Electrical and Electronics Engineering, InN-Project as a CREST-program of JST, and VBL, Chiba University, Chiba 263-8522, Japan

Abstract. Novel structure InN/GaN MQWs are proposed and demonstrated. The MQWs consists of very fine and narrow 1 monolayer (ML)-thick InN wells embedded in GaN matrix. The thickness of InN wells can be fractional ML and/or two MLs depending on the growth conditions, resulting in different wavelength light emissions from deep violet to blue. Unique epitaxy processes for the MQWs fabrication are discussed on the basis of self-ordering and coherent growth mode for atomically flat ∼1 ML InN well deposition on GaN template. Further the epitaxy temperature for 1 ML InN wells can be much higher than the highest epitaxy temperature of thick InN layer due to the effects of GaN matrix, resulting in higher quality MQWs.

Introduction

AlN/GaN/InN III-nitrides (III-N) are promising materials system in the application for new functionality photonic devices, where their possible covering wavelengths have extended nowadays to much wider wavelength range. In the longer side it is from green to near IR corresponding to the InN bandgap of about 0.63 eV [1–4]. There are two important problems which seriously affect the device performance in LEDs: one is the defects arising from large lattice mismatch between barriers and wells, and the other is the quantum confined Stark effect (QCSE) in the wells arising from extremely large piezoelectric field caused by large strains in the MQW structure. Further, in particular for extending the working wavelength of the LDs to the longer side, spatial compositional inhomogeneity in the InGaN ternary-alloy wells arising from serious immiscible nature between GaN and InN is also another problem resulting in wider lasing gain spectrum. As one of the ideas to solve these problems stated above, we propose here a novel structure InN/GaN MQWs whose basic structure is consisting of coherently grown one monolayer-thick binary InN wells embedded in GaN matrix [5]. The working wavelengths confirmed by photoluminescence properties are ranging from 390 to 450 nm at room temperature, and the wavelengths are expected to extend in longer side to achieve pure blue and green laser diodes.

In this paper, we describe the features of proposed novel structure InN/GaN MQW structures grown by rf-MBE. We first investigate unique epitaxy behavior inherent to this heterostructure system and also characterize their structural properties. A series of MQW samples were grown at different growth temperatures under +c polarity growth regime by rf-MBE, and they showed marked improvements in both crystalline quality and achieving precise control of 1 ML InN well thickness due to the self-organized epitaxy processes at intentionally highered growth temperatures above 600 °C.

1. Experimental

InN/GaN MQW structures were grown by rf-MBE under +c polarity growth regime. Ga-polarity GaN (∼2 μm-thick) grown by MOVPE was used as a template. In and Ga fluxes were supplied from standard Knudsen effusion cells, and an rf plasma cell was used to obtain excited-nitrogen flux. Prior to the MQWs growth, the GaN template was thermally cleaned at 860 °C for 15 min and re-growth of 100 nm-thick GaN was carried out at 845 °C. One basic period of the MQW studied here consisted of ∼1-ML InN well and ∼15 nm GaN barrier. In order to reduce the effect of accumulated strain in the MQW structure, we inserted a ∼150 nm-thick GaN spacer after depositing 5 ∼ 6 periods of this basic structure. Then this process was repeated 8 times, resulting in 40 ∼ 48 InN well insertions in GaN matrix. Finally the top surface was caped by a 100 nm GaN layer.

We first fabricated a series of samples with this structure for different growth temperatures from 500 to 650 °C with 50 °C step. We also fabricated the 1-ML InN/GaN MQW structure without inserting the spacer layer. Typical deposition rate of InN well layers examined first was 0.5 Å/sec but it was later increased to 1.5 Å/sec to assure the InN deposition at higher growth temperatures above 600 °C. Total supply of InN for two different deposition rates was 1-ML and 3-MLs, respectively. Growth processes such as surface stoichiometry and in-plane lattice parameters were in-situ monitored and real-time controlled by using spectroscopic ellipsometry together with RHEED measurements. Structural properties of MQWs were characterized by high resolution XRD and XTEM.

2. Fabrication and characterization of InN/GaN MQWs

Figure 1 shows XRD $\theta - \omega$ diffraction patterns around GaN (0002) planes and [1–100] RHEED diffraction patterns for samples grown at temperatures of (a) 500 °C, (b) 550 °C, (c) 600 °C, and (d) 650 °C under conditions of with GaN spacer layer and 1-ML InN supply with deposition rate of 0.5 Å/sec.

It was found that the InN QW structures could be fabricated at up to 600 °C and also found from the number and sharpness of those satellite peaks that the structural properties of these MQWs were remarkably improved with increasing growth temperature. In particular, the sample grown at 600 °C indicated sharp satellite peaks up to 5th order. Improvement in the surface/interface flatness with increasing growth temperature was also confirmed by in-situ observation of RHEED patterns changing from spotty to streaky with temperature. These results indicate that very thin InN well layers with flat/abrupt interface quality can be fabricated at much high temperature of

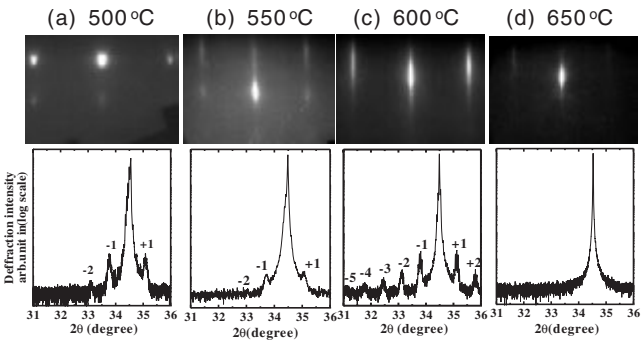

Fig. 1. XRD $2\theta - \omega$ scans and [1–100] RHEED patterns of InN/GaN MQW samples grown at different temperatures of (a) 500 °C, (b) 550 °C, (c) 600 °C, and (d) 650 °C, respectively.

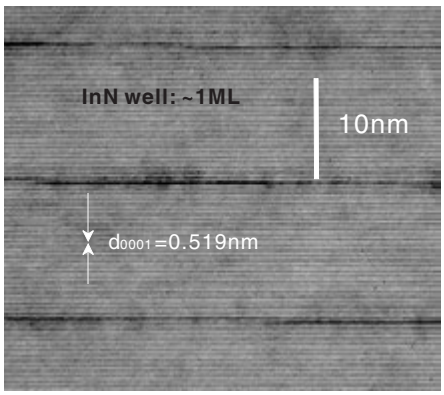

Fig. 2. XTEM dark field image ($g = 0002$) for the sample grown at 600 °C.

600 °C and the increase in growth temperature plays an important role in improvement of the qualities of interface and GaN barrier. When the temperature was raised to 650 °C, however, no such satellite peak was observed, indicating that InN well layers did not stick during source supply and/or decomposed/ re-evaporated during growth. This means that nominal thickness of InN well layers decreases due to the increase in decomposition and re-evaporation rates at the high growth temperature, and no InN well layer can be formed at 650 °C under the deposition rate of 0.5 Å/sec.

To investigate the structural quality of the MQW samples in detail and also to precisely determine the inserted InN well layer thickness, high resolution XTEM characterization was carried out. Figure 2 shows the XTEM dark field image for the sample grown at 600 °C, where the image was taken for the condition under $g = 0002$.

It is obvious that interface quality of the MQWs is remarkably high, and surprisingly sharp and atomically flat InN well layer insertion in GaN matrix is achieved. The thickness of InN well layer was estimated to be about 1°2 ML (0.3°0.6 nm) and GaN layer was about 14 nm. Another important point is that we do not observe any serious generation of misfit dislocations at the hetero-interfaces at least in the TEM image.

Then in order to achieve InN layer deposition at higher temperatures than 600 °C, we examined the fabrication of MQW structure at 650 °C under conditions without GaN spacer and 3-MLs InN supply with higher InN deposition rate of 1.5 Å/sec. Figures 3(a) and (b) show the XRD pattern and a dark field

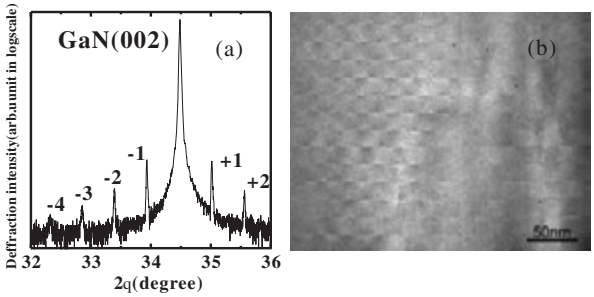

Fig. 3. (a) XRD $2\theta - \omega$ scan and (b) XTEM dark field image for the sample grown at 650 °C.

XTEM image of this sample. Very clear and sharp satellite peaks up to 4th order are observed in Fig. 6(a).

It was confirmed here that the deposition of InN was possible at as high temperatures as 650 °C and the structural quality of obtained MQW was significantly improved with increasing growth temperature as expected. In fact, the XTEM image indicates that very clear and sharp MQW structure is fabricated in this sample, but InN is not a continuous layer any more because of lowered sticking coefficient for In and N species at such high temperature as 650 °C and/or enhanced dissociation and re-evaporation of InN at this high temperature. As clearly shown in this figure, this resulted in fabrication of a fractional ML InN insertion in GaN matrix. As explained already, although 3-MLs of InN was supplied under 3 times increased deposition rate at the 650 °C growth, very thin 1-ML thick InN well layers with high degree of structural perfection were formed. This suggests that at such high temperature, the 1 ML or FML InN wells are formed by self-ordering growth mode. Therefore, fabrications of 1 ML or FML InN/GaN QWs by rf-MBE can be achieved with good reproducibility by self-ordering growth mode, which is very important to realize InN-based fine nano-device structures. Finally we explain PL properties of these MQWs. It should be noted that stronger PL was observed in higher growth temperature samples. Figure 4 shows room-temperature PL spectra of samples grown at 650 °C for three different InN deposition rates of (a) 0.5, (b) 1.5, and (c) 2.5 Å/s, corresponding total InN supply of 1, 3, and 5 ML, respectively. The sample for (a) is the same one of which the XRD pattern is shown in Fig. 1(d) and no InN layer is inserted in this sample. The sample for (b) is the same one indicating FML InN insertion in GaN matrix of which the XRD pattern and its XTEM image are indicated in Figs. 3(a) and (b), respectively. The sample for (c) was newly grown to confirm thicker InN insertion in GaN matrix and it was found from the XRD pattern analysis that the InN layers were more than 1 ML and resulted in poorer structural quality than that of the sample for (b). The PL emission peak for (a) is located at 363 nm and originated from GaN. The peaks for (b) and (c) are located at 398 and 437 nm, respectively, and these correspond to 1 ML and 2 MLs-thick InN wells. We consider that skillful design of the MQW structures and properties, such as the in-plane coverage of FML InN, the size of each fractional InN well, the distance between neighboring fractional InN wells, the thickness of InN well, the composition of well and matrix, etc., will give us a development of exciton-based functionality photonic devices, which are working in much longer wavelengths

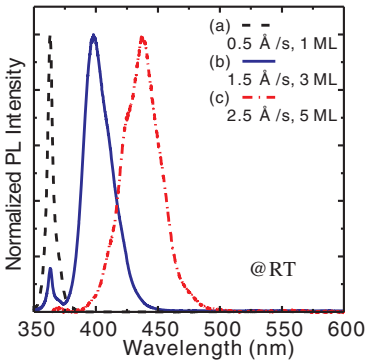

Fig. 4. Room temperature PL spectra of InN/GaN MQWs grown at 650 °C under InN deposition rates of (a) 0.5, (b) 1.5, and (c) 2.5 Å/sec.

than those available at present, i.e., green for LDs/LEDs. In fact, LED structures consisting of the proposed novel structure InN/GaN MQWs were successfully fabricated and very bright EL emission was observed at 418 nm. Moreover, the small blue-shift in EL emission spectra under the different current injection was confirmed indicating QCSE was remarkably reduced in the QW structure.

3. Summary

We have proposed and demonstrated the first achievement of a novel structure InN/GaN MQW consisting of 1-ML and FML InN well insertion in GaN matrix under In-polarity growth regime. It was found that 1-ML InN insertion can be done at remarkably higher temperatures than that of conventional thicker In-polarity InN epilayer due to the effect of GaN matrix. The MQW indicated surprisingly high quality structure probably due to the self-ordering effect between InN and GaN. The proposed structure has physically and practically significant meaning because the excitons in GaN can be effectively localized at InN well even at room temperature, leading to the development nitride-based visible light emitters probably approaching up to green in LDs.

Acknowledgements

This work was partly supported by the Grant-in-Aid for Science Research on Priority Areas (18069002, 2007).

References

[1] J. Wu, W. Walukiewicz, K. M. Yu, J. W. Ager III, E. E. Haller, H. Lu, W. J. Schaff, Y. Saito and Y.Nanishi, *Appl. Phys. Lett.* **80**, 3967 (2002).

[2] V. Yu. Davydov, A. A. Klochikhin, R. P. Seisyan, V. V. Emtsev, S. V. Ivanov, F. Bechstedt, J. Furthmuller, H. Harima, A. V. Mudryi, J. Aderhold, O. Semchinova and J. Graul, *Phys. Status Solidi B* **229**, r1 (2002).

[3] K. Xu, W. Terashima, T. Hata, N. Hashimoto, M. Yoshitani, B. Cao, Y. Ishitani and A. Yoshikawa, *Phys. Status Solidi C* **0**, 2814 (2003).

[4] K. Xu and A.Yoshikawa, *Appl. Phys. Lett.* **83**, 251 (2003).

[5] A. Yoshikawa, S. B. Che, W. Yamaguchi, H. Saito, X. Q. Wang, Y. Ishitani and E. S. Hwang, *Appl.Phys.Lett.* **90**, 073101 (2007).

16th Int. Symp. "Nanostructures: Physics and Technology"
Vladivostok, Russia, July 14–18, 2008

Theoretical and experimental investigations on Boron-incorporated III–V materials for relevant heterostructures

Xiaomin Ren, Qi Wang, Hui Huang, Yongqing Huang, Aiguang Ren, Deping Xiong, Shiwei Cai, Xia Zhang and Peida Ye

Key Laboratory of Optical Communication and Lightwave Technologies (Beijing University of Posts and Telecommunications), Ministry of Education
P.O. Box 66, Beijing, 100876, P.R.China

Abstract. The possibilities for obtaining new quaternary III–V compounds with properly engineered band-gaps and lattice-constants have been investigated to meet the requirements of future heterostructure optoelectronic devices for optical fiber communications and the relevant PIC/OEICs. The properties of a series of boron incorporated materials such as BGaInAs/GaAs, BAlInAs/GaAs, BGaAsSb/GaAs, BInAsP/GaAs, BInAsP/Si and BGaPSb/Si are theoretically analyzed. The LP-MOCVD growths of BGaAs/GaAs, BAlAs/GaAs, BGaInAs/GaAs and relevant MQW structures have be experimentally investigated. The boron composition of 5.8% in BGaAs and the PL peak wavelength of 1.24 μm for BGaInAs at 11 K have been achieved.

Introduction

New material systems should be always interesting for most scientists in the field of semiconductor heterostructure optoelectronics. Both GaAlAs/GaAs and InGaAsP/InP systems proposed in the early years are typical examples and they have made great impact on the optoelectronic devices used in optical fiber communications and other information technologies. In recent years, GaInNAs/GaAs system has attracted increasing interest and attention of scientists. Boron-incorporated III–V materials related to GaAs or Si substrate described in this paper as a whole is another kind of new material systems (it should be noted that the boron-incorporated nitrides on GaN/sapphire substrate are not included here). We began to work on this kind of systems in 2003 and our purpose is mainly to find a system or some systems with suitable application-oriented energy-gap (say, covering the long wavelength region for optical fiber communications) and lattice-matched to GaAs and even to Si (equivalently to GaP or AlP) [1–2]. We believe that this work, if we could do it successfully, would make a significant impact on the monolithic photonic integrated circuits (PIC) and optoelectronic integrated circuits (OEIC). At the same time, a new variety of optoelectronic devices, featuring much lowered cost, based on GaAs substrate and even Si substrate would appear.

To our best knowledge, only a few other groups from France, USA, Germany, Russia and few other countries have devoted to this quite new subject [3–7]. H. Dumont' group from France have pursued the similar goal with ours and other groups have their own various purposes such as the application for solar cells, nano- or micro-tube fabrications and strain compensation in multilayer heterostructures.

The relevant theoretical and experimental research works in our laboratory are described as follows.

1. Theoretical predictions

We surveyed all the III–V binary and ternary alloys and analyzed various possibilities for obtaining new quaternary compounds with the properly engineered band-gaps and lattice-constants to meet the requirements mentioned in the introduction. Finally, our interest has been focused on the most promising new material systems, namely, BGaInAs/GaAs, BAlInAs/GaAs, BGaAsSb/GaAs, BInAsP/GaAs, BInAsP/Si and BGaPSb/Si (by the way, TlGaPN/Si, TlAlPN/Si may also be promising. However, they will not be discussed in this paper because no boron is incorporated in them).

Firstly, the fulfillment of Vegard's law allows us to get the lattice matching conditions of these materials.

The expression form for each of these materials can be generally written either as $A_x^{III}B_y^{III}C_{1-x-y}^{III}D^V$ or as $A_x^{III}B_{1-x}^{III}C_y^VD_{1-y}^V$ (Note: here the letter B is just a general symbol for a specified element, not surely the element boron). The corresponding bandgap $E_g(x, y)$ can be expressed respectively as

$$\begin{aligned} &E_g^{ABCD}(x, y) = xE_g^{AD} + yE_g^{BD} + (1-x-y)E_g^{CD} \\ &-b_{ABD}xy - b_{ACD}x(1-x-y) \\ &-b_{BCD}y(1-x-y) - b_{ABCD}xy(1-x-y) \end{aligned} \quad (1)$$

and

$$\begin{aligned} &E_g^{ABCD}(x, y) = xyE_g^{AC} + x(1-y)E_g^{AD} \\ &+(1-x)yE_g^{BC} + (1-x)(1-y)E_g^{BD} - b_{ABC}x(1-x)y \\ &-b_{ABD}x(1-x)(1-y) - b_{ACD}xy(1-y) \\ &-b_{BCD}(1-x)y(1-y) - b_{ABCD}x(1-x)y(1-y), \end{aligned} \quad (2)$$

where b_{ABCD} is the quaternary bowing parameter and b_{XXX} (i.e. b_{ABC}, b_{ABD}, b_{ACD}, b_{BCD}) the ternary bowing parameter. The latter can be determined from the equations below when the energy gaps $E_g^{XXX}(x)$ of all related boron incorporated ternary alloys have been known. Actually, $E_g^{XXX}(x)$ can be calculated by the first-principles technique based on density-functional theory (DFT).

For

$$\begin{aligned} &A^{III}B_x^VC_{1-x}^V : E_g^{ABC}(x) = xE_g^{AB} \\ &+(1-x)E_g^{AC} - b_{ABC}x(1-x) \end{aligned} \quad (3)$$

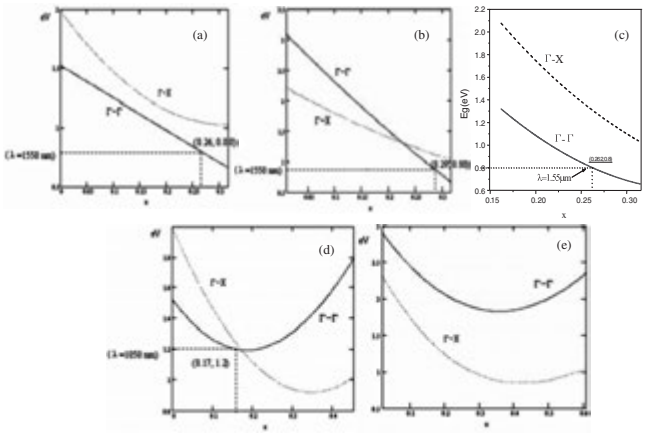

Fig. 1. Energy gap vs boron composition for (a) BGaInAs/GaAs, (b) BAlInAs/GaAs, (c) BInAsP/GaAs, (d) BGaAsSb/GaAs, (e) BGaPSb/Si.

and for

$$A_x^{\mathrm{III}} B_{1-x}^{\mathrm{III}} C^{\mathrm{V}} : E_{\mathrm{g}}^{\mathrm{ABC}}(x) = x E_{\mathrm{g}}^{\mathrm{AC}} + (1-x) E_{\mathrm{g}}^{\mathrm{BC}} - b_{\mathrm{ABC}} x(1-x). \quad (4)$$

Assuming the bandgap bowing parameters of quaternary alloy were zero and the energy gaps for all binary alloys appearing in the above equations were specified as their Γ-Γ energy gaps (E_{g}^{Γ}), the dependences of the emission wavelength on boron composition x for some of the above-mentioned quaternary materials lattice-matched to GaAs or Si have been theoretically investigated.

It has been shown that the emission wavelength of BGaInAs/GaAs, BAlInAs/GaAs, BInAsP/GaAs can reach 1.55 μm with the boron composition (x) of 26%, 29.7%, and 26.2% respectively while all their bandgaps are direct. It is also reasonably believed that BInAsP/Si could be as good as BInAsP/GaAs for its emission wavelength and bandgap type. However, the simulations show that the bandgap of BGaAsSb/GaAs would be indirect when their emission wavelength reaches 1.55 μm and the bandgap of BGaPSb/Si seems to be indirect over a wide range of the boron composition (see Fig. 1).

Some of the calculated results in one of our earlier papers [2] are different from that of this paper and we believe that the results provided here should be more accurate due to some improvements of the theoretical model. Further modification of the model based on comparison with the experimental results is just on the way.

2. Material growths and characterizations

We have grown $B_xGa_{1-x}As$, $B_xAl_{1-x}As$ and $B_xGa_{1-x-y}In_yAs$ alloys on exactly-oriented (001) GaAs by low pressure metalorganic chemical vapor deposition (LP-MOCVD) with a $3 \times 2''$ vertical reactor. The sources of triethylboron (TEB), trimethylgallium (TMGa), trimethylaluminium (TMAl), trimethylindium (TMIn), pure arsine (AsH_3) and the carrier gas of Pd-cell purified hydrogen (H_2) have been used in the growth with a total flowrate of 12 slpm (standard litre per minute). The wafer-susceptor rotation speed was 100 rpm. The growth temperature (T_g) was 550–650 °C and the pressure was kept as 100 Torr.

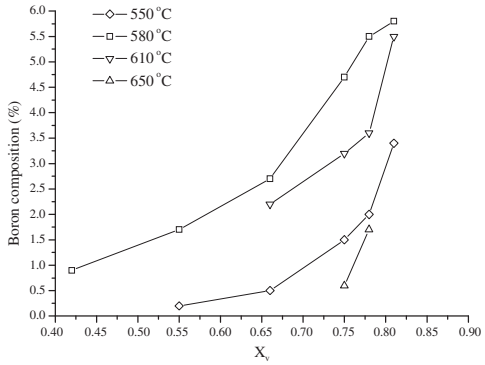

Fig. 2. Boron composition of $B_xGa_{1-x}As$ epilayers measured by DCXRD as a function of Xv at (a) $T_g = 550$ °C, (b) $T_g = 580$ °C, (c) $T_g = 610$ °C, (d) $T_g = 650$ °C.

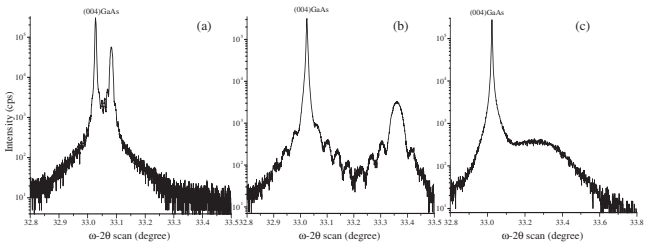

Fig. 3. DCXRD $\omega - 2\theta$ scan pattern of $B_xGa_{1-x}As$ epilayers grown at 580 °C with (a) Xv=0.42; (b) Xv=0.81; (c) Xv=0.85.

The respective epilayer thickness of bulk BGaAs, BAlAs and BGaInAs was nearly 100 nm.

The Input gas phase TEB mole fraction Xv is defined as [TEB]/([TEB]+[TMGa]), [TEB]/([TEB]+[TMAl]) and [TEB]/([TEB]+[TMGa]+[TMIn]) for the growths of $B_xGa_{1-x}As$, $B_xAl_{1-x}As$, and $B_xGa_{1-x-y}In_yAs$, respectively. While, [TEB], [TMGa], [TMAl] and [TMIn] represent the input mole flowrates of TEB, TMGa, TMAl and TMIn, respectively.

2.1. $B_xGa_{1-x}As$ and $B_xAl_{1-x}As$

For the growth of $B_xGa_{1-x}As$, the dependences of boron composition x on the TEB mole fraction Xv at different temperatures such as 550, 580, 610, 650 °C are shown in Fig. 2. The growth temperature was optimized as 580 °C and the highest incorporation of boron was 5.8%. There were critical values of Xv at which the crystalline growth turned to polycrystalline growth for different given growth temperatures. It was observed in our experiments that this critical value of Xv was approximately in a range of 0.8 to 0.85. In comparison, the highest boron compositions (x) in $B_xGa_{1-x}As$ realized by other groups is 7% [7].

DCXRD $\omega - 2\theta$ scan patterns of the $B_xGa_{1-x}As$ samples grown at 580 °C are shown in Fig. 3. When Xv increased, the diffraction peak of $B_xGa_{1-x}As$ moved apart from the GaAs peak gradually to the right side and the width of the peak was broaden. The peak disappeared when the value of Xv reached 0.85 and a polycrystalline growth began.

The depth profiles of elements in $B_{0.058}Ga_{0.942}As$ samples were measured by SIMS. The measurement result has been an evidence of a remarkable incorporation of boron in such an alloy.

It was shown that as long as Xv was less than its critical value, the RMS roughness of $B_xGa_{1-x}As$ samples kept very

low (less than 0.2 nm). In fact, it increased with increasing Xv and the surface became gradually covered with some randomly-distributed conical shape islands. However, the increment of roughness was very small and the surface looked still specular. At the critical value of Xv, the roughness increased dramatically. A roughness as high as 38.6 nm was measured when Xv reached 0.85.

For the growth of $B_xAl_{1-x}As$, the boron incorporation behaviors were also investigated. The optimized growth temperature T_g was also 580 °C. It was observed in the DCXRD patterns that the diffraction peak of $B_xAl_{1-x}As$ moved gradually from one side to another side of the GaAs peak when x increased first from 0.4% (550 °C) to 1.0% (610 °C), and then to 1.3% (580 °C).

2.2. $B_xGa_{1-x-y}In_yAs$

For the growth of $B_xGa_{1-x-y}In_yAs$, the growth temperature was also set as 580 °C and the flowrates of TEB, TMGa and AsH_3 kept the same as in the growth of $B_xGa_{1-x}As$ mentioned above while TMIn was introduced. As the flow-rate of TMIn was increased, the value of the TEB mole fraction Xv naturally decreased and the diffraction peak of $B_xGa_{1-x-y}In_yAs$ in the DCXRD pattern moved gradually along the direction at which the Bragg angle decreased. The diffraction peak of $B_xGa_{1-x-y}In_yAs$ coincided with GaAs peak when Xv=0.714, which indicated that in this case the $B_xGa_{1-x-y}In_yAs$ epilayer had been lattice matched to GaAs. With the approximate assumption of $x = 0.04$, the compositions of the material could be determined and written as $B_{0.04}Ga_{0.87}In_{0.09}As$ according to the lattice-matching condition, $y = 2.16x$, derived from Vegard's law. The PL spectrum at 11 K excited by a 514.5 nm argon-ion laser is shown in Fig. 4. The peak of the spectrum appeared at the wavelength of 1.24 μm (the corresponding energy gap was 1 eV) and the full width at half maximum of the peak was about 210 meV. The peak wavelength at room temperature is reasonably expected to be longer. In comparison, the longest PL peak wavelength at room temperature of $B_xGa_{1-x-y}In_yAs$ realized by other groups is 1.07 μm [3].

It can be found that the boron composition x in $B_xGa_{1-x-y}In_yAs$ corresponding to the emission wavelength about 1.24 μm ($x \approx 4\%$) in our experiment is much smaller than $x \approx 19\%$ predicted theoretically. This fact means that our theoretical model have to be modified.

2.3. MQWs of BGaAs/GaAs and BGaInAs/GaAs

On the basis of above mentioned works, both structures of $B_{0.027}Ga_{0.973}As$/GaAs MQW and $B_{0.027}Ga_{0.913}In_{0.060}As$/GaAs MQW had been grown in our laboratory (the element compositions here were evaluated approximately). These structures featured 10 periods in which the thickness of each GaAs layer was 50 nm and of each $B_{0.027}Ga_{0.973}As$ or $B_{0.027}Ga_{0.913}In_{0.060}As$ layer 10 nm. The DCXRD patterns are shown in Fig. 5 and it is clear that the quality of each interface between different layers was quite good.

3. Conclusions

This work is just at its very beginning. It seems possible to extend the luminescence wavelength of BGaInAs to the long-wavelength (1.3–1.55 μm) region of optical fiber communi-

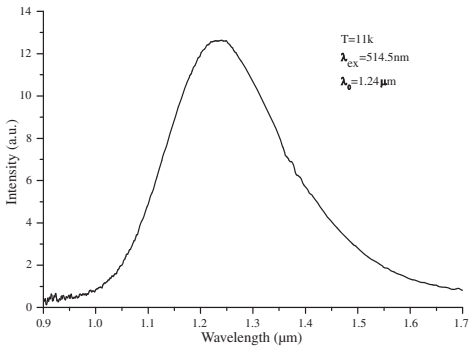

Fig. 4. 11 K PL pectrum of the $B_xGa_{1-x-y}In_yAs$/GaAs sample.

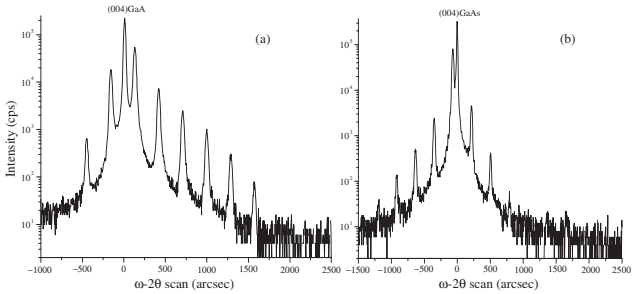

Fig. 5. DCXRD $\omega-2\theta$ scan pattern of MQW samples with 10-periods of (a) $B_{0.027}Ga_{0.973}As$/GaAs, (b) $B_{0.027}Ga_{0.913}In_{0.060}As$/GaAs grown at 580 °C.

cations at a reasonable boron incorporation ratio. Most theoretical predictions for a series of boron incorporated materials are encouraging although a modification of the relevant theoretical model would be necessary. More intensive study on BGaInAs/GaAs system should be done and more quaternary III–V compounds with boron incorporated would be grown and investigated. Particularly, the Si based band-gap engineering with some of these compounds would attract stronger interest. We believe that greater efforts will be paid on this subject due to various promising applications of this kind of materials.

Acknowledgements

This work was supported by the National Basic Research Program of China (also called 973 Program, No. 2003 CB314901), the 111 Program of China (No. B07005), Program of Key International Science and Technology Cooperation Projects, MOST (No. 2006DFB11110) and Program for Changjiang Scholars and Innovative Research Team in University, MOE (No. IRT0609). The authors would like to thank senior engineer Nongnong Ma and Dr. Wenjuan Wang for their helps in SIMS and PL spectrum (low temperature) measurements.

References

[1] Xiaomin Ren *et al*, *Optics Valley of China International Symposium on Optoelectronics*, Wuhan, China, Nov. 2005, pp. 22–23.
[2] Xiaomin Ren *et al*, *Fourth Joint Symposium on Opto- and Microelectronic Devices and Circuits (SODC)*, Duisburg, Germany, 2006, pp. 69–73.
[3] Philippe Rodriguez *et al*, *J. Cryst. Growth.* **298**, 81–84 (2007).
[4] J. F. Geisz *et al*, *Appl. Phys. Lett.* **76**, 1443–1445 (2000).
[5] H. Paetzelt *et al*, *J. Cryst. Growth.* **298**, 648–651 (2007).
[6] D. A. Pryakhin *et al*, *Semiconductors* **39**, 11–13 (2005).
[7] F. Saidi *et al*, *Mater. Sci. Eng. C* **26**, 236–239 (2006).

16th Int. Symp. "Nanostructures: Physics and Technology"
Vladivostok, Russia, July 14–18, 2008

Spin dynamics in semiconductor nanostructures

M. W. Wu

Hefei National Laboratory for Physical Sciences at Microscale and Department of Physics,
University of Science and Technology of China, Hefei, Anhui, 230026, China

In this talk we are going to present our theoretical investigations on spin dynamics of semiconductor nanostructures under various conditions. It is shown from a fully microscopic kinetic-spin-Bloch-equation (KSBE) approach that the single-particle approach is inadequate in accounting for the spin relaxation/dephasing (R/D) both in the time domain and the spacial domain. The momentum dependence of the effective magnetic field (the Dresselhaus and the Rashba terms) and the momentum dependence of the spin diffusion rate along the spacial gradient all serve as inhomogeneous broadenings. It is pointed out that in the presence of inhomogeneous broadening, any scattering, including the carrier-carrier Coulomb scattering, can cause irreversible spin R/D. Moreover, besides the spin R/D channel the scattering provides, it also gives rise to the counter effect to the inhomogeneous broadening. The scattering tends to drive carriers to a more homogeneous states and therefore suppresses the inhomogeneous broadening. Finally, this approach is valid in both strong and weak scattering regime and can be used to study systems far away from the equilibrium such as electrons of high spin polarization and/or electrons with strong electric field (hot electrons).

Many novel effects are predicted from our theory and some have been realized experimentally very recently.

Author Index